

nature



STEM CELL ADVANCES

- Affairs of the heart
- Yamanaka on iPS cells
- Anemia cells reprogrammed

NATURE

Journal of Science

Volume 458 | May 7, 2009

Abstractions



FIRST AUTHOR

Have you ever noticed that when you buy, say, a red convertible, every other car on the road suddenly seems to be a red convertible? According to findings by Marius

Peelen and his colleagues in the psychology department of Princeton University in New Jersey, neural mechanisms in the visual cortex are responsible for the phenomenon. When the researchers tested neural responses in the visual cortices of volunteers who had been instructed to look for certain objects in photographs that flashed up on a screen, they discovered that people are extremely adept at spotting objects of interest, even in situations in which the items are difficult to find (see page 94). He tells *Nature* why.

How did you conduct your experiment?

We tested neural activity in volunteers' visual cortices during two tasks using functional magnetic resonance imaging. In the first task, the volunteers were shown isolated images of cars and people; in the second, they were asked to try to spot a car or person during brief viewings of complex real-life photos. Their visual-system responses were very similar in both situations. This tells us that the visual cortex can filter out, or ignore, irrelevant visual information.

What was the most striking result?

We flashed four photos up on the screen simultaneously and told volunteers to look for cars or people in two of the photos, and to ignore the other two. But the volunteers' cortical activity was high regardless of whether the specified objects were in the photos that they were supposed to be watching or in those they had been told to ignore. Thus, they visually registered the cars or people in photos they were trying to ignore, even though they didn't consciously realize it.

What does this mean for real-life situations?

That you can quickly detect things you are looking for by biasing the processing of a scene in favour of those objects. For example, after buying a red convertible, you may select items in a scene that are similar to your new interest, red convertibles. Looking for someone in a crowd may follow the same basic mechanism. Knowing what you are looking for primes the visual system in favour of objects similar to your 'search template'.

Is there a downside to this phenomenon?

It might result in your missing useful things that you are not actively searching for. For example, you might walk up and down supermarket aisles looking for sugar until you find it. Then, if you also want coffee, you might have to check all the aisles again, even though you may have passed the coffee minutes earlier. ■

MAKING THE PAPER

Juan Carlos Izpisua Belmonte

Healthy cells derived from diseased ones offer treatment hope.

In 2006, scientists in Japan rocked the biomedical world when their manipulations prompted mouse skin cells to revert to an embryonic-like state, from which they could potentially be turned into any type of body cell. The cells were dubbed induced pluripotent stem (iPS) cells, and the following year two groups successfully generated human iPS cells. These could obviate the need to destroy human embryos to generate stem cells, and may offer a new way to treat human diseases using a patient's own cells.

A group of scientists led by Juan Carlos Izpisua Belmonte, a developmental biologist at the Salk Institute for Biological Studies in La Jolla, California, wasted no time in testing whether iPS cells could one day replace diseased cells in patients with Fanconi anaemia. This inherited blood disorder results from mutations in any of 13 known genes, the products of which maintain genetic stability. It can lead to bone-marrow failure, cancer and other problems. As a first step, the team has demonstrated that a patient's skin cells can be turned into disease-free blood-cell progenitors that could potentially be transplanted into humans.

Izpisua Belmonte's previous research, which focused on understanding how some animals — such as frogs and salamanders — are able to regenerate limbs, fuelled his foray into human stem-cell research. To negotiate this new territory, he partnered with basic scientists and clinicians in Spain, Italy and California. "For someone with my background to help to produce this type of focused regenerative-medicine study speaks to the importance of collaboration in science," he says.

The team's first task was to turn skin cells from a patient with Fanconi anaemia into iPS cells. The researchers used viruses to introduce four 'reprogramming' genes into the cells, but



repeated efforts with the Fanconi anaemia cells didn't work. One team member pointed out that the cells might have too many abnormalities to be successfully reprogrammed. "We realized that we had to correct the genetic defects first," says Izpisua Belmonte. To do so, they used viral vectors to introduce corrected versions of two of the Fanconi anaemia genes into cells.

Once the genetic defects had been corrected, the group was able to generate iPS cells. Turning these cells into progenitors of healthy blood cells was relatively straightforward. However, it did take several attempts to work out the experimental details, because there was no well-established protocol. Eventually, though, the group succeeded — creating the first patient-specific, disease-corrected cells (see page 53).

"We cured a cell, but we haven't cured a patient," says Izpisua Belmonte, calling this work a "proof of principle". One crucial hurdle remains. Introducing foreign genes — such as those used to reprogram skin cells — can cause tumours to form, a particularly troublesome side effect for the already tumour-prone individuals with Fanconi anaemia. "Before this technology can be brought into the clinic, we will have to be able to generate cells that do not produce tumours," says Izpisua Belmonte, "or find a way to readily kill any potentially tumorigenic cell before transplanting them into patients."

But he remains cautiously optimistic that it can be done. "Just a few years ago, the ability to reprogram mature cells caused the entire community to change its perspective, so you never know where the science will lead," he says. ■

FROM THE BLOGOSPHERE

Throw away those chemistry lab-course 'cookbooks', says Aaron Finke, guest blogger at The Sceptical Chymist (<http://tinyurl.com/lvjw5q>).

A graduate student in organic chemistry at the University of Illinois in Urbana-Champaign, Finke recently oversaw an organic chemistry lab course attended primarily by students aiming to study medical or veterinary science. The

absurdity of having students perform basic extractions, chromatography and syntheses was not lost on Finke: "It is highly unlikely they will actually use the specific skills implemented in the course, unless they plan on distilling their own whiskey!" Furthermore, the course failed to deliver what students should be learning — the process of scientific inquiry, how scientific knowledge is validated and

exposure to modern chemistry instrumentation such as nuclear magnetic resonance (NMR) and mass spectroscopy.

One commenter on the the post reported learning how to gather NMR and mass-spectroscopy data on an organic chemistry course, so the tide may be turning. In his next post, Finke will explore how some educators are looking to make such courses more relevant. ■

Visit *Nautilus* for regular news relevant to *Nature* authors ▶ <http://blogs.nature.com/nautilus> and see Peer-to-Peer for news for peer reviewers and about peer review ▶ <http://blogs.nature.com/peer-to-peer>.

We are all Iranians

Iran's endogenous civil-rights movement needs international solidarity, not political meddling. Academics, universities and non-governmental organizations can help.

"Bomb, bomb, bomb, bomb-bomb, Iran," sang John McCain to the tune of The Beach Boys' *Barbara Ann* at a US presidential campaign event in 2007. McCain, a Republican senator for Arizona, later insisted he was joking. Yet the spur-of-the-moment instinct behind the 'joke' sums up aptly the tendency of some politicians both in the West and in Iran to demonize each other's peoples as a faceless enemy.

But that kind of demonization has become passé over the past few weeks, as images of mass protests against Iran's allegedly fraudulent presidential election on 12 June have allowed many in the West to see faces of ordinary Iranians who are far from the crude stereotype. And many Iranians, although suspicious of the reactions of foreign governments, have been struck by the worldwide outpouring of empathy for their quest for fundamental civil liberties and self-determination.

In the past, unfortunately, Western governments and research organizations have bought into former US president George W. Bush's 'axis of evil' rhetoric by discriminating against Iranian researchers, denying or delaying visa applications, subjecting them to disproportionate vetting and showing lacklustre interest in collaborating. Moreover, the international scientific community has been laggard and passive in responding to the current situation. But Iranian scientists say that the solidarity of the international academic and scientific community is needed now more than ever.

They are quick to caution that the last thing the civil-rights movement needs is overt or covert support from Western governments. That would simply play into the Iranian regime's portrayal of the home-grown uprising as a foreign-inspired velvet revolution. The consensus among Iranian researchers is that the only steps that foreign governments should take are to refuse to recognize Mahmoud Ahmadinejad as president, and to condemn human-rights violations such as denying Iranians their constitutional right to freedom of peaceful assembly. Much more useful, they say, is broader pressure from Western academics, their institutions and other non-governmental organizations, which can impartially yet forcefully endorse Iranians' human rights, and condemn attacks on Iran's universities and the detention of Iranian academics (see *Nature* doi:10.1038/news.2009.597; 2009).

Non-governmental assistance

Research bodies and universities — and perhaps a few Nobel laureates — need to speak out louder. They should encourage, rather than discourage, collaboration, and replace past discrimination by welcoming Iranian researchers and students.

With the continuing Iranian crackdown on academics, for example, an exodus of young researchers can be expected. They will need the kind of assistance being provided by organizations such as the Scholars at Risk Network based in New York, an international network of universities and colleges that helps to find work for researchers seeking political asylum anywhere in the world. The international research

community should find ways to support and expand such efforts. Likewise, with Iran's decision on Monday to confirm the re-election — albeit under a cloud of illegitimacy — of Ahmadinejad, who is backed by the Supreme Leader Ayatollah Ali Khamenei, who controls nuclear policy, hopes for intergovernmental progress on curbing Iran's nuclear ambitions have been dealt a severe setback. The research community should thus do everything possible to promote continued contacts with colleagues in Iran, if only to promote détente between Iran and the West when relations are bellicose.

Meanwhile, the diaspora of Iranian academics is playing a key part in helping to get across the complexity of the situation in Iran. In informal public meetings, newspaper opinion pieces and discussions with governments and reporters, they say that, in contrast to what is often reported by Western media, the uprising has little to do with any desire to topple the regime. It is above all a broad civil-rights movement that extends far beyond the 'Twittering' classes. It is led by young people — 70% of Iranians are under 30 — who are not ideologically motivated, but instead are hungry for the greater freedoms that were one of the main, but unrealized, goals of the 1979 Iranian revolution. The majority of Iranian scientists are behind the movement.

"The research community should do everything possible to promote continued contacts with colleagues in Iran."

The green wave

Iranian émigré scientists also point out that Mir-Hossein Mousavi — who ran against Ahmadinejad in this year's elections — is an unlikely leader of the protest movement. As prime minister of Iran from 1981 to 1989 he presided over a cultural revolution in which Iranian universities were violently purged of influences other than Islam, and many scientists fled the country to avoid death or imprisonment. But Mousavi, although a conservative, is now part of a broad coalition of political and ethnic forces — ethnic Iranians make up just half of the population of Iran — who want greater democracy and openness to the world. The protests surpass the issues of the contested election, and the green colour of Mousavi's presidential campaign has now become the symbol of this broader civil-rights movement.

Ahmadinejad is another matter entirely. Iranian expatriate academics explain that, after stalling immediately after the 1979 revolution, science gained momentum under reformist governments starting in the late 1990s. Ahmadinejad has maintained government support for science since his election as president in 2005. However, his regime has systematically savaged academic freedom in general, by purging universities of reformists and social scientists, and appointing government stooges to many senior university positions. His term in office has also been marked by the arrests of Iranian and foreign academics on trumped up charges of fomenting a revolution — having a damaging

effect on international collaboration (see *Nature* **457**, 511; 2009, and **447**, 890–891; 2007). In the short term, academic freedom and the isolation of Iran's scientists are likely to worsen under a regime desperate to cling onto power by crushing reformist elements, and targeting thousands of students, academics and other intellectuals for arrest. Seventy academics were arrested on 24 June after meeting Mousavi to give their analysis of current Iranian society, and other academics are reported to have been detained since, although reliable information is scarce. Academics are now in the front line, says one Iranian researcher who returned from Iran just days ago.

In the face of this bleak news, however, Iranian academics are surprisingly optimistic. They tend to buy into the argument that,

despite the current crackdown, greater democracy is inevitable in Iran, which will provide an open society that is more conducive to science and critical thinking. They point out that Iran and Turkey are the two Muslim countries with the strongest democratic and secular traditions — and that academics have played a major part in helping the society resist religious obscurantism. Iran is not the only country in the region where human rights and democracy are violated; and the West has hypocritically been relatively silent on similar abuses by several of its allies in the Middle East. But in Iran at least, the country's long traditions of democracy, education and free thinking — suppressed for decades by the regime, and in particular the current hard-line leadership — are now out in the open. ■

Time for early action

Carbon dioxide is not the only warming agent worth tackling now in the bid to cool the planet.

The US House of Representatives must be commended for passing a comprehensive climate bill last week that would finally set the United States on a path to lower its greenhouse-gas emissions. The pending legislation is far from perfect and will face a tough test in the Senate. But it is a necessary first step for the country that has so far added the most carbon dioxide to the atmosphere.

However, it will take several decades, if not longer, for the United States and other nations to significantly reduce carbon dioxide emissions. This fact has spurred many scientists to intensify research into techniques that might provide a more immediate way to turn down the planetary thermostat. Some solutions seek to fine-tune Earth's climate through large-scale geoengineering projects, such as pumping sulphates into the atmosphere to reflect more sunlight back into space. But another approach — an 'early action' climate agenda increasingly being pushed by environmentalists and some scientists — might prove safer and much easier to sell to governments and populations around the world.

A good place to start is with black carbon, the sooty, dark component of smoke that emanates from diesel engines, inefficient cooking stoves, forest fires and the like. Black carbon is a danger to human health, having been implicated in a variety of cardiovascular and respiratory diseases, and may also be a major player when it comes to global warming, particularly in regions that spend at least part of the year covered with ice and snow (see page 29). But unlike carbon dioxide, which stays in the atmosphere for centuries, black-carbon particles remain in the air for just a matter of weeks. So, in principle, efforts to eliminate emissions could quickly reduce the warming power of this pollutant.

Unfortunately, it is not that simple. First, not all black carbon is anthropogenic in origin. Second, black carbon is accompanied to varying degrees by its lighter-coloured cousin, organic carbon, which cools the planet along with most other reflective aerosols. Third, despite more than a decade of research, the chain of reactions by which black carbon warms the atmosphere and melts snow remains surprisingly hazy. All of these factors make black carbon's effect on climate difficult to quantify.

However, none of the caveats is a reason for nations not to try their utmost to control it. Even if the climate benefits turn out to be less than hoped, cleaner air would save hundreds of thousands of lives a year. Governments should already be working to clean up diesel emissions and to improve cooking stoves in southeast Asia, where the health problems are most acute. But it may be that the threat of global warming is more effective than health advocacy.

Accompanying black carbon on the early-action agenda are methane and hydrofluorocarbons (HFCs). The latter are used predominantly as refrigerants, and can be more than a thousand times more powerful than CO₂ as greenhouse gases (see *Nature* **459**, 1040–1041; 2009).

The international 'Methane to Markets' programme provides money and expertise to help countries to capture methane from sources such as landfills, farms and coal mines. Once up and running, these projects produce energy at a profit by making use of a clean-burning compound that would otherwise have wreaked havoc in the atmosphere for years. The programme has been a resounding success, and other nations should find the money and will to replicate it.

The case for HFCs is a bit more complicated, but no less strong. HFCs were developed to replace ozone-depleting chlorofluorocarbons that were phased out in response to the 1989 Montreal Protocol. Because they don't affect atmospheric ozone levels, they were pulled under the United Nations' Kyoto climate treaty. But there are now calls to take the chemicals out of the climate treaty and put them into the Montreal Protocol. This is the right thing to do. Montreal regulators have already proved their ability to implement worldwide curbs on emissions, and there is little doubt that they could handle this problem faster and more cost-effectively than could a cumbersome treaty aimed at targeting CO₂.

Notably, each of these solutions could be pursued immediately, precisely because they make sense on multiple levels; global warming might be a driving factor, but it is not the only one. There is no need to wait for international negotiators to strike a deal on a climate treaty that would lay the groundwork for a global carbon market. And they do not pose the ethical or legal challenges that geoengineering schemes so often face.

Some fear that even talking about such subjects could distract from the main problem, which is CO₂. The opposite is true. Providing workable solutions in other areas will build momentum and simultaneously ease the burden that remains. What is there to lose? ■

RESEARCH HIGHLIGHTS

Losing Louisiana

Nature Geosci. 2, 488–491 (2009)

The Mississippi Delta is sinking, and to rebuild it some have proposed diverting the Mississippi River to carry sediment to coastal areas. But a new study shows that the delta's rivers don't have enough sediment to counter predicted sea-level rise.

Mike Blum and Harry Roberts, both then working at Louisiana State University in Baton Rouge, found that the rivers currently transport less sediment than the amount that was needed for delta formation. Sinking land and accelerating sea-level rise will submerge 10,500–13,500 square kilometres by 2100, they predict.

Even if sediment trapped in dams was freed, the duo found, the rivers still couldn't supply the 18–24 billion tonnes needed to keep the delta above water until the end of the century.



M. BLUM/NASA

CANCER BIOLOGY

Double agent

Science 324, 1713–1716 (2009)

A protein associated with some cancers acts in the energy-producing organelles of the cell called mitochondria.

The protein, STAT3, regulates gene expression. It is activated by the addition of a phosphate group, which sends the protein into the nucleus. Transformation of healthy cells into cancerous ones by the small protein Ras is inhibited by an absence of normal STAT3. But David Levy of New York University School of Medicine and his colleagues found that STAT3 mutants that cannot accept the phosphate or cannot bind to DNA still allow Ras to transform cells.

Surprisingly, the researchers found that STAT3 is active in mitochondrial metabolism, and during transformation mediates metabolic changes necessary for cancers to grow.

NEUROSCIENCE

Early bird learns the tune

PLoS ONE doi:10.1371/journal.pone.0005929 (2009)

Scientists have assumed that vocal learning in songbirds starts with subsongs — the bird equivalent of infant babbling. But Wan-chun Liu from the Rockefeller University, New York, and his colleagues, have determined that vocal learning begins much earlier — when juveniles first beg for food.

When begging, juvenile male chipping sparrows (*Spizella passerina*) exhibit neural activity in part of the forebrain associated with learned song, the team found. And begging patterns appear in the sparrows' first subsongs.

Auditory feedback is crucial to vocal learning, and distinguishes it from innate

calls. Deafening affected the structures of males' begging calls, but had no such effect on females; female chipping sparrows do not sing and their begging calls are innate.

PHYSIOLOGY

Ground control

Biol. Lett. doi:10.1098/rsbl.2009.0360 (2009)

The limits on acceleration are commonly described in terms of horsepower, be it from internal combustion or accompanied by real hoofbeats.

But motorbike and drag-racing aficionados know that too much acceleration can lift front wheels off the ground, sacrificing control. Sarah Williams and her colleagues from the Royal Veterinary College in Hatfield, UK, have found that quadrupeds face the same problem.

Data from racing greyhounds (pictured, below) and polo ponies showed that acceleration limits at high speeds are predicted by models of muscle power. At

lower speeds, however, animals do not reach the acceleration theoretically possible from muscle power. Instead they seem to be limited by the rate that would cause the quadruped equivalent of a 'wheelie'.

ECOLOGY

Putting height on the map

J. Ecol. doi:10.1111/j.1365-2745.2009.01526.x (2009)

Average plant height peaks in the tropics and declines towards the poles, says an international team after analysing a data set of almost 6,000 species. Plants living near to the equator are 29 times taller on average than those found between 60–75 °N (in Iceland, say) and 31 times taller than those at 45–60 °S (such as on the South American archipelago of Tierra del Fuego).

Plant height drops 2.4-fold at the edge of the tropics, suggesting that temperate and tropical species pursue different ecological strategies, according to Angela Moles of the University of New South Wales in Sydney, Australia, and her colleagues. Cold or dry places support plants with a range of heights, but there are few short species in warm, wet environments. Rainfall in the wettest month of the year is the best predictor of plant height, the researchers say.

EVOLUTIONARY DEVELOPMENT

The birth of a thymus

Cell doi:10.1016/j.cell.2009.04.017 (2009)

In a broad-ranging study, Thomas Boehm of the Max Planck Institute of Immunobiology in Freiburg, Germany, and his colleagues attempt to reconstruct the evolutionary history of the thymus, the immune-system organ where T cells accumulate and mature.

The authors looked at the expansion and diversification of genes implicated in T-cell



R. PIERSE/GETTY

and thymus development in 13 species spanning the chordate phylogenetic tree. They paid special attention to the jawed vertebrates, which have a thymus, and jawless fishes such as lampreys, which do not. The authors conclude that the latter have many but not all of the genes required to develop a thymus. The study begins to show how the duplication and cooption of genetic pathways leads to the development of a complex organ.

BIOLOGY

Shell shocker

J. Zool. doi:10.1111/j.1469-7998.2009.00596.x (2009) Big eggs risk being crushed by the big birds that sit on them. Eggshells must be sturdy, but not so sturdy that they entomb chicks. These conflicting demands placed on eggshells set the upper size limit for birds, according to Geoffrey Birchard of George Mason University in Fairfax, Virginia, and Charles Deeming of the University of Lincoln, UK. They are also, the authors suggest, the reason that females outweigh males in the largest of species.

The researchers analysed shell thickness, body mass and incubation behaviour for 968 species of bird. Having relatively small males do the incubating allows eggs to be bigger yet thinner-shelled. The largest specimens of extinct giants such as the 400-kilogram elephant bird might all be female, they speculate.

CHEMISTRY

Fire boxed

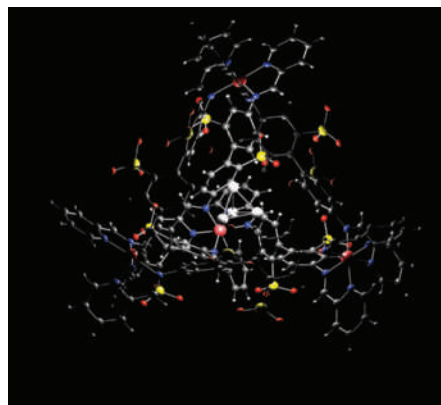
Science 324, 1697–1699 (2009)

White phosphorus combusts violently in air, making it a dangerous agent, and one that has become controversial for its military uses.

Now Jonathan Nitschke at the University of Cambridge, UK, and his co-workers have constructed a molecular cage to defuse this version of phosphorus. The cage self-assembles in water from organic groups and iron ions. A solution of the cage can suck up solid white phosphorus, trapping its small, tetrahedral molecules within the cages' larger ones (pictured, below).

The cage doesn't prevent oxygen reaching the white phosphorus, but does stop it reacting because there isn't enough room within the cage for the normal products of the reaction to form.

Benzene can displace the incendiary molecule, releasing it from its confinement.



ASTRONOMY

Little neighbours

Astrophys. J. 699, 649–666 (2009)

How does one find dwarves in a crowd of giants? Evgenya Shkolnik at the Carnegie Institution of Washington in Washington DC and her colleagues searched X-ray data gathered by the now-defunct German satellite ROSAT for nearby M-class dwarf

stars less than 300 million years old.

Previous surveys placed greater emphasis on higher mass, higher luminosity Sun-like stars. The team identified 185 likely candidates before ruling out older interlopers by spectroscopy. The 144 remaining, some as small as 10% of the mass of the Sun, have a better chance than easier-to-spot, higher-mass stars of revealing the early formation of rocky Earth-like planets.

If any of the dwarves do host planets, their proximity to Earth (most are within 25 parsecs) will make them relatively easy to study in detail.

GENOMICS

Murky associations

Am. J. Hum. Genet. doi:10.1016/j.ajhg.2009.05.011 (2009)

Genome-wide association studies have been hailed for their ability to find genetic variations that may contribute to disease risk. But assigning meaning to these variations is more difficult. Peter Holmans of the MRC Centre for Neuropsychiatric Genetics and Genomics in Cardiff, UK, and his colleagues have developed an approach that they call ALIGATOR.

They look for gene ontology categories — agreed-upon terms used to define the function and activity of gene products — that regularly pop up in the candidates exposed by genome-wide association, reasoning that many associations in the same category signal functional relevance. For Crohn's disease, which is immunological in origin, overrepresented ontological categories included immune functions, as expected. For bipolar disorder, they included hormone activity and RNA splicing, processes with as yet unknown roles in the condition.

JOURNAL CLUB

Subhajyoti De
Medical Research Council,
Cambridge, UK

A biologist looks at the effect of a dynamic nuclear environment on gene expression.

In many organisms, including animals, genes are arranged linearly on chromosomes. But this linear order is largely meaningless during transcription, when RNA is made from DNA. Instead, a very different three-dimensional arrangement of genomic regions emerges in which structural flexibility and ability to

reorganize become crucial to gene expression. Some regions loop out dynamically, moving far from their neighbours. Genes can participate in 'transcription hotspots' in close association with genes from other chromosomes. But the question remains as to what leads this dance. Is the chromosomal reorganization a cause or a consequence of transcription?

Using *Hox* clusters — groups of genes important in development — Wendy Bickmore of the Medical Research Council in Cambridge and her colleagues start to answer this question. *Hoxb* and *Hoxd* have very different environments

in terms of their location on the chromosome and expression of their neighboring genes. The authors found that during tissue differentiation, *Hox* genes loop out and undergo active transcription. This reorganization then spreads from the *Hox* locus into adjacent genomic regions, but does not necessarily affect transcription of neighbouring genes (C. Morey *Genome Res.* doi:10.1101/gr.089045.108; 2009).

The authors propose that on activation, structural changes alter the constraints on genes' expression, allowing them to loop out and explore a much larger

transcriptional environment within the nucleus. The team concludes that positioning outside of a chromosomal region is important for, but not a driver of, transcriptional activation.

These findings have broad implications: first, dynamic reorganization of chromosome territories is necessary but not sufficient for activation. Second, this reorganization is associated with modification to DNA's structural packaging, which can permanently alter a cell's nature.

Discuss this paper at <http://blogs.nature.com/nature/journalclub>

NEWS

African science drops down G8 agenda

Researchers lament poor progress on commitments to developing nations.

In the run-up to the G8 summit meeting in Italy from 8–10 July, African science leaders are counting the cost of unfulfilled commitments to their continent made at previous G8 meetings.

At the 2005 Gleneagles Summit in the United Kingdom, the rich G8 nations endorsed many of the proposals put forward by the Commission for Africa, launched by former British prime minister Tony Blair in 2004. These included creating centres of excellence in science and technology across the continent, and setting up African institutes of technology.

“To my knowledge, no new centres of excellence have been set up,” says Mohamed Hassan, executive director of the Academy of Sciences for the Developing World (TWAS) in Trieste, Italy, and president of the African Academy of Sciences. “It’s very disappointing.”

The agenda of this year’s G8 summit, which is being held in the earthquake-ravaged town of L’Aquila, renews the focus on Africa, with goals such as tackling the effects of climate change and safeguarding biodiversity on the continent. Yet support for African science is unlikely to be a priority for discussion, says Hassan.

At a G8 satellite meeting on science and international development, organized by TWAS and the Italian foreign ministry and held on 26 June in Trieste, the focus was firmly on Afghanistan. The delegates agreed that international science academies should work with Afghanistan’s science ministry to establish a development plan for the coming decade. But African science was not discussed, says Hassan: “I don’t think it will be on the G8 agenda.”

Myles Wickstead, head of the Commission for Africa secretariat until late 2005, also has low expectations for the forthcoming G8 meeting, not least because the Italian government cancelled a meeting of the G8 science and technology ministers that was due to take place on 25 June (see *Nature* 459, 1041; 2009). “There is very little we can expect for science and technology at the Italian summit,” Wickstead says.

The United Kingdom’s former chief science adviser, David King, who was involved in drawing up the Commission for Africa proposals and is now director of the Smith School of Enterprise and the Environment in Oxford, UK, says that continued pressure needs to be placed on the G8 nations to deliver on their promises. “Questions need to be asked about the priorities set out in Gleneagles,” he told *Nature*. “What has



The G8 summit will boost the fortunes of L’Aquila — but the news might not be so good for African science.

happened to the concept of African institutes of science and technology?”

A key stumbling block has been the G8’s failure to commit to donating US\$3 billion over 10 years to set up the centres and \$500 million a year over 10 years to strengthen universities, as recommended by the Commission for Africa in 2005. But Hassan says that some of the blame must rest with the African nations. With the exception of South Africa and possibly Rwanda, African nations will not reach the target agreed

in 2003 by the African Union, a confederation of 53 African states, of investing 1% of their gross domestic product in science by 2010, he says. “African governments have

to put their house in order first. If they show progress in investing in science and technology, this will encourage donors.”

Red tape

Tensions over who should be responsible for African science-and-technology aid have certainly hampered progress, says Wickstead. Despite high-level discussions in December last year between the two key players — the African Union and its implementing partner, the New Partnership for Africa’s Development (NEPAD) — a single fund for African science still does not exist, he says (see *Nature* 457, 14; 2009). “Africa has not yet developed a comprehensive plan for science that the donor community can get behind and support,” he says.

Despite this, bioscientists in Africa have benefited from four networks set up by the NEPAD and the African Union since 2003, aided by a Can\$30-million (US\$26-million) grant from the Canadian government. Diran Makinde, director of the West African Biosciences Network, says that Spain has contributed €3 million (US\$4.2 million) and Finland €400,000 to bioscience initiatives in Africa. But he adds that the contribution from G8 nations has been small in comparison to what was promised, and that the networks could face tough times if they are not able to secure longer-term funding.

Calestous Juma, a Kenyan professor of international development at the John F. Kennedy School of Government in Cambridge, Massachusetts, says that a better forum is now needed for discussions about harnessing science for African development. If the momentum generated by Tony Blair before Gleneagles bore little fruit, he says, it is unlikely that a less-engaged Italian leadership will be able to achieve much.

Although progress on the G8 commitments to science has been slow, other forums are moving forwards. The European Union, for example, launched a science partnership with the African Union in October 2008. Several initiatives are being funded through the partnership, including grants for Africa researchers that total €36 million over 3 years — with the first call for proposals to be launched at the end of 2009. ■

Natasha Gilbert

See ‘African institutions gain support networks’, page 23.

PERI-PERCOSSI/EPA/CORBIS



IRANIAN SCIENTISTS SPEAK OUT

Universities targeted in government crackdown.

www.nature.com/news

M. TREZZINI/AP PHOTO

Chief scientist quits California stem-cell agency

The California Institute for Regenerative Medicine (CIRM) in San Francisco is again under the microscope, following the resignation of its chief scientific officer and a call for its restructuring.

Marie Csete, a doctor and stem-cell biologist, has resigned from CIRM's top science job, effective from 1 August. The move leaves CIRM without medical leadership as it prepares to issue US\$210 million in grants for stem-cell research that aim towards clinical trials. "When it became clear to me that my considered clinical advice was not respected, I concluded that it made no sense for me to stay at CIRM," she says.

When Csete left Emory University in Atlanta, Georgia, to join CIRM in March 2008, she gave up her lab and divorced her husband John Doyle. He is a professor at the California Institute of Technology in Pasadena, an institution she would be inviting to apply for research funding and so needed to avoid contravening state conflict-of-interest laws. "We were willing to sacrifice a lot for me to be in a position to make a positive impact at CIRM," she says. "I wanted to see it to the end."

Her accomplishments at the agency include restructuring CIRM's grant programmes, cultivating relationships with grantees and laying the groundwork for international collaborations. "Her medical and scientific experience made her a superb proponent of CIRM's main mission, which is to make stem cells medically useful," says Jeanne Loring, a stem-cell researcher at the Burnham Institute in La Jolla, California. "It won't be easy to replace her."

In a message to staff, CIRM president Alan Trounson praised Csete's "highly valuable contributions to our science operations".

Csete says she hopes her leaving will mark "a new start" for the agency. "I had tried everything I could to change what I think needed to change from the inside, and that was not going to happen," she says. "I felt I would have more impact by stepping away and advising the leadership of the board on my way out about ways to revise the structure and management of the agency to make it more optimal."

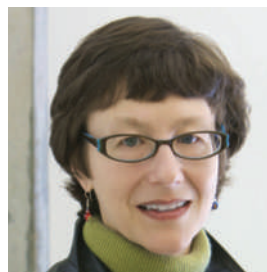
Csete would not provide details on what changes she feels are needed. But her frustration echoes previous tensions over leadership structure that led in part to the early departure of CIRM's first president,

Zach Hall, in 2007. The agency's structure is spearheaded by Robert Klein, CIRM's architect, and includes Trounson and a 29-member governing board.

Last year, two state senators asked California's bipartisan, independent oversight agency, the Little Hoover Commission, to study CIRM's governance.

"I felt I would have more impact by advising the leadership of the board on my way out."

— Marie Csete



On 25 June, the commission reported that CIRM's governance structure "locks in inefficiencies" and "inhibits CIRM's ability to adjust to changing scientific and political landscapes". The commission recommended that CIRM downsize its board to 15 members, add members without ties to CIRM grantees, boost the efficiency and transparency of grant reviews, clarify

the overlapping roles of chair and president, and "create succession plans for board leadership", a reference to Klein's statement that he will leave the agency next year.

Hall says the recommendations are "useful, thoughtful and should be seriously considered", but says "the leadership of the agency has taken a position that any change at all threatens the entirety of stem-cell research, and that's unfortunate".

Indeed, CIRM said in a statement that it was disappointed with the Little Hoover Commission's recommendations, which would "slow the agency's progress toward cures". But CIRM board member Jeff Sheehy wrote on a blog that CIRM's "knee jerk" reaction, delivered in a statement dated 24 June — before the Hoover group released its final report — "suggests a renegade agency outside the control of its board or the state of California".

The report is unlikely to spur immediate change, as the state legislature, which would need to enact many of the recommendations, is preoccupied with California's budget crisis.

Erika Check Hayden

N. PRIESTLEY

SNAPSHOT Vanishing meadows

Seagrass meadows around the world are in dire shape, according to the first comprehensive global assessment of these economically and biologically essential areas.

More than a quarter of all seagrass meadows have disappeared in the past 130 years, says a new synthesis of quantitative data from 215 sites (M. Waycott et al. *Proc. Natl Acad. Sci. USA* doi:10.1073/pnas.0905620106; 2009). The rate of decline has grown from less than 1% per year before 1940, to 7% per year since 1990.

As well as supporting wildlife such as dugong (*Dugong dugon*, right) and green turtles (*Chelonia mydas*), seagrass meadows also serve as a vital nursery for fish, supporting populations for coral reefs and commercial fisheries.

Daniel Cressey

For a longer version of this story, see <http://tiny.cc/u4qzg>



J. FREUND

How to fix a broken heart?

Clues about how human hearts form hint at routes to cell-based therapies.

Heart disease kills more people than any other condition, yet cell therapies for it remain frustratingly elusive. On page 113 of this issue, Kenneth Chien of the Massachusetts General Hospital, in Boston, and his colleagues report a finding that could move this treatment closer to reality: human 'progenitor' cells that generate various types of heart tissue as they develop.

Chien's work remains a long way from the clinic, however, and clinical trials of other cell types for heart ailments have yielded mixed results. "Even the most ardent advocates are calling the long-term benefit modest," says Christine Mummery, a stem-cell researcher at Leiden University in the Netherlands. That leaves open the question of what cell types, if any, could turn stem-cell research into reality for patients with heart disease.

Chien's team had previously identified, in mice, heart progenitor cells that expressed a transcription factor called Isl1 (A. Moretti *et al.* *Cell* 127, 1151–1165; 2006). Their latest paper finds that these cells also exist in humans. After identifying cell populations in human fetal tissue, the researchers produced them from human embryonic stem cells. They also showed that the cells were multipotent — they could generate more progenitors as well as the major heart cell types of heart-muscle, smooth-muscle and blood-vessel cells.

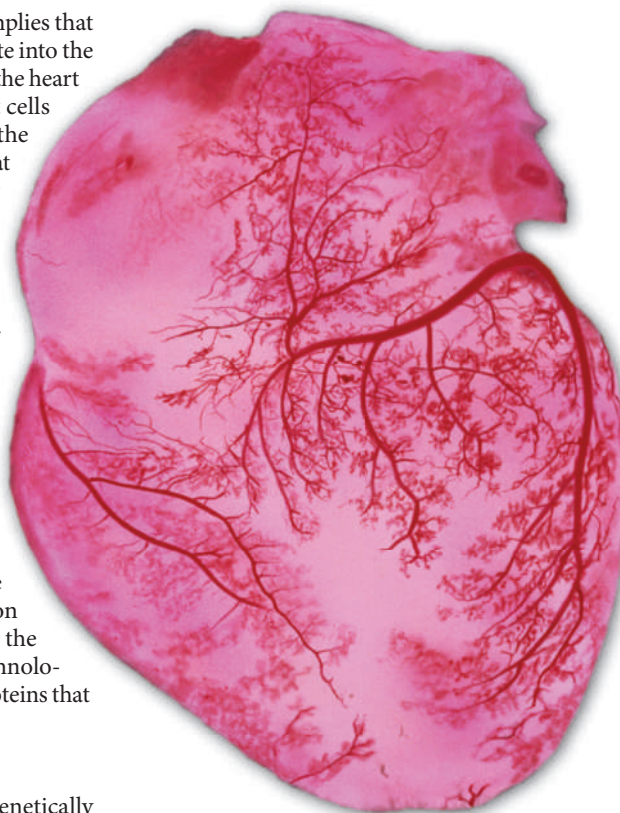
The work provides an explanation for how heart cells differentiate. Although the cells exist for just a couple of days in mice, they persist

for weeks in human fetuses. This implies that cells do not immediately differentiate into the major types of heart tissue, but that the heart is built from a pool of multipotent cells that persists and differentiates as the heart grows. The findings suggest that an effective approach to cell therapy might be "to put heart progenitors in, because that's the way the heart is built in the first place", says Chien.

Philippe Menasche, a cardiac surgeon at the Georges Pompidou European Hospital in Paris, has some doubts. He calls the work "a very interesting basic research paper", but says that "when you are identifying progenitors like this, the first question is, 'is it possible to isolate these cells selectively and use them [to treat patients]?'". And that isn't possible, he says, because the telltale Isl1 is a protein that turns genes on and off and so must lie deep within the nucleus of the cell. Most robust technologies to purify cells do so through proteins that are found on the cell surface.

Early stages

At the moment, Chien has to use genetically engineered fluorescent tags to identify cells that produce Isl1. Wariness over using genetically engineered cells, plus the fact that his cells are not genetically matched to patients', make



Stem cells have a way to go to treat failing hearts.

them less suitable for clinical trials. But for now, he says, they could be used to help screen potential heart drugs, and to help model childhood congenital diseases in which the heart is malformed. Chien hopes that researchers will eventually identify a set of surface markers that can isolate his cells reliably without genetic engineering.

Raj Makkar, a cardiologist at Cedars-Sinai Medical Center in Los Angeles, California, adds that researchers should look at the effects of Isl1 on other cells, including damaged heart tissue *in situ*. Adding or activating Isl1 could make some of the cells being tested in clinical trials more effective, he suggests.

Current trials for heart-disease therapies use cells collected from bone-marrow, heart and skeletal-muscle biopsies (see 'Selected heart cell-therapy trials'). Much of the focus has been on cells that are easy to collect — mainly bone-marrow cells taken from the patients who will ultimately receive them. These cells do not seem to be able to generate heart-muscle cells, called

SELECTED HEART CELL-THERAPY TRIALS

Trials of bone-marrow cells dominate the field of heart stem-cell therapy. All except the Osiris trial use patients' own cells.

Sponsor	Cell type	Phase	Expected enrolment
Bioheart, Munich, Germany	Skeletal myoblasts	II/III	390
Osiris Therapeutics, Columbia, Maryland	Mesenchymal stem cells	II	220
Cedars-Sinai Medical Center, Los Angeles, California	Cells from heart biopsies	I	30
Ministry of Health, Brazil	Bone-marrow cells	III	300
Johann Wolfgang Goethe University Hospitals, Frankfurt, Germany	Bone-marrow cells	III	200
Barts and The London NHS Trust, UK	Bone-marrow cells	II/III	165
Seoul National University Hospital, Korea	Circulating blood cells	II/III	116

Source: clinicaltrials.gov



**SPOOKY COMPUTERS
CLOSER TO REALITY**
Solid-state quantum
processing demonstrated.
www.nature.com/news

MM_PHOTO/ALAMY

cardiomyocytes, but that doesn't mean they aren't helpful, argues Menasche. "It doesn't imply they don't have any effect," he says.

Several large-scale trials are under way to determine whether bone-marrow cells might instead benefit patients through the 'paracrine' effect: secreting growth factors that encourage hearts to grow new blood vessels and thereby preserve existing heart tissue. So far, says Mummery, the results have been ambiguous: the cells seem to be safe, but are not particularly effective.

But others think that the efficacy of the cells has not yet been tested properly. Cells delivered too soon after a heart attack are unlikely to survive, for example, and their effects in very sick patients might be masked if healthier patients are also included in a trial, says Makkar.

Approaches using skeletal-muscle cells have also been mixed. In 2002, Menasche led a large clinical trial studying whether injecting skeletal muscle into the heart could restore heart function. In 2006 that trial was stopped early because of a lack of efficacy, and Menasche has since decided to work on cells derived from embryonic stem cells. These readily generate beating cardiomyocytes in laboratory dishes, but are difficult to integrate productively into damaged heart tissues. Problems include purifying cells, getting enough of them, making sure they are not attacked by the immune system and controlling for the possibility of unwanted growth — to say nothing of making sure that the introduced cells beat in time with the motion of the failing heart.

Most bone-marrow trials focus on blood-forming stem cells, but another cell type found in bone marrow, called mesenchymal stem cells, is also being studied. Joshua Hare, of the University of Miami in Florida, says his team will soon report results from a phase II trial of mesenchymal stem cells, run by Osiris Therapeutics of Columbia, Maryland, showing that the cells both engraft as new cardiomyocytes and help through the paracrine effect.

Indeed, Hare believes that doctors might eventually use a variety of cell therapies to treat heart disease. Mesenchymal stem cells could be used as a first-generation therapy, followed perhaps by cells derived from cardiac biopsies, followed by other cell types that have not yet entered clinical trials. He predicts that cardiac cell therapy will follow the same path as antibiotics. "Just because we have third-generation cephalosporins now," he says, "doesn't mean that penicillin didn't work."

Monya Baker

Italians sue over stem cells

Three scientists are appealing against the Italian government's decision to exclude human embryonic stem cells from a recent call for proposals to fund stem-cell biology.

The scientists' lawyer, Vittorio Angiolini, who specializes in bioethics and human rights, filed the appeal with Rome's administrative court on 24 June. He argues that excluding human embryonic stem cells infringes on the constitutional freedom of scientific research. The use of established lines of human embryonic stem cells in research is legal in Italy.

The original draft of the funding call did not exclude any type of stem cell. "We don't know where the sentence that was added came from," says Elisabetta Cerbai, a pharmacologist at the University of Florence who is one of the appellants. "But we suspect that a compromise deal may have been made at high political levels."

The stem-cell research fund, run by the ministry responsible for health, has a turbulent history. In 2007, the then health minister, Livia Turco, cancelled a €3-million (US\$4.2-million) fund after some scientists complained that monies were being distributed without a public call for proposals and without appropriate peer review. At the time, Turco referred to the people complaining as "gangsters", but agreed to start again, with an €8-million pot and transparent reviewing procedures.

The centre-left government to which Turco belonged fell in spring last year. The following June, Turco's successor, Ferruccio Fazio, established a committee of experts to draft a call that he promised would be administered in a transparent way.

Giulio Cossu, a developmental biologist at the San Raffaele scientific institute in Milan and one of the five members of that committee, says that the group formulated a carefully worded text that would neither exclude any type of stem-cell proposal, nor incite controversy.

But when that text became public, a sentence had been added that explicitly excluded projects with human embryonic stem cells. It appeared online after a 26 February meeting of the State-Regions Conference, the body comprising representatives of the 20 Italian regions



Stem-cell proponent Elisabetta Cerbai.

that decides how national health funds are distributed. "I was obviously disappointed," says Cossu, who notes that he joined the committee on the condition that there would be no exclusions based on ideology.

In media interviews at the time, Fazio dismissed rumours that the sentence had been added by someone within his ministry. He declined to comment to *Nature*, but in media reports has said that the sentence was added by the regions. However, the representative for Tuscany, Enrico Rossi,

said publicly that no changes were made or requested when it was discussed by the conference.

Angiolini argues that "the ministry can change the text of the call only with the regions' consent".

"Our appeal is a matter of principle," says Cerbai. "Politicians should decide strategic research objectives and leave scientists to choose how best to achieve those objectives."

The other two appellants are Elena Cattaneo, a neuroscientist at the University of Milan, and Silvia Garagna, a developmental biologist at the University of Pavia. The three are financing the action with their own money.

The case is likely to be heard by the court in the first half of July, before the funding call's closing date of 20 July.

"We expect to win," says Cerbai. But if that does not happen, they hope to take their appeal to a higher court.

Alison Abbott

UNIV. FLORENCE CENTER OF MOLECULAR MEDICINE

Budget request tackles habitat changes

US wildlife agency bids to revitalize research with focus on effects of global warming.

The US Fish and Wildlife Service (FWS) is looking to get back on its research feet, in the wake of revelations in recent years that a top official manipulated scientific results involving endangered species. A budget request now wending its way through Congress could provide an 11–14% budget increase, including beefed-up funding to investigate how species will be affected by climate change.

There's "no question" that the agency needs more resources, says John Eadie, a wildlife biologist at the University of California, Davis. "Particularly with climate change, there's so much uncertainty," he says. "It's a huge science undertaking."

The agency has requested \$10 million to establish eight new 'landscape conservation cooperatives' across the country that would identify key locations for species protection and develop management strategies. Another \$10 million would fund research, both at the FWS and other agencies and universities, to assess the effects of climate change on wildlife populations and habitats.

Strong science support will be necessary to defend management decisions that could be taken to court, says Dan Ashe, science adviser to the agency's director. For instance, the FWS must issue a critical-habitat decision by 30 June 2010 for the polar bear, listed last year as threatened, and create a recovery plan for it. "Those are going to be very controversial documents," says Ashe. The state of Alaska sued the agency in an attempt to overturn the decision, three months after the polar bear was listed.

The agency maintains recovery plans for more than 1,000 species listed under the Endangered Species Act, and many of those will need to be updated to address the issue of climate change, says Nancy Green in Arlington, Virginia, a scientist with the FWS's endangered-species programme. The agency is prioritizing which plans to update first, says Ashe.

The 2010 budget request for the Department of the Interior, which includes the \$1.6-billion FWS, passed the Senate appropriations committee on 25 June and a House of Representatives vote on 26 June. The requested Interior increase of \$4.7 billion over 2009 levels is an attempt to reverse underfunding and emphasizes climate change as a priority, said Norman Dicks (Democrat, Washington), chair of the



S. KAZLOWSKI/NATUREPL.COM

A recovery plan must be drawn up for the polar bear, which was last year listed as 'threatened'.

House Subcommittee on Interior, Environment, and Related Agencies, in a statement.

The FWS has faced a "chronic" lack of science resources ever since its biology research programme was moved to a separate Interior agency — the National Biological Survey — in 1993, says Ashe. That became part of the US Geological Survey (USGS) in 1996. Today, the FWS usually has to pay part of the project costs to acquire biological, geographical and water research from the USGS, he says.

Sue Haseltine, associate director for biology at the USGS in Reston, Virginia, agrees that the USGS — considered to be the main research arm for the Interior — doesn't have enough resources to satisfy all of the federal and state agencies it serves. The problem has worsened

recently because challenges such as climate change are creating higher-priority research needs, she says: "The urgency has increased."

The USGS has requested its own funding boost in the 2010 budget to help it investigate the effects of climate change on wildlife. \$15 million of the \$1.1-billion budget it has requested would go towards the new National Climate Change and Wildlife Science Center, a network of research hubs meant to translate global climate data to regional scales and

predict effects on habitats and populations.

The agency is also seeking \$5 million to lend ecological- and population-modelling support to the FWS's proposed landscape conservation cooperatives, and \$4.2 million to expand its forecasting of changes in Arctic ecosystems.

Ashe says that the FWS is trying to restore some of the scientific credibility that it lost during the last administration. Interior official Julie MacDonald, who oversaw the FWS, resigned in 2007 after an investigation found that she had manipulated scientific conclusions in endangered-species reports and shared internal information outside the agency. The FWS has since decided to revise seven of MacDonald's Endangered Species Act decisions.

Jeff Ruch, executive director of Public Employees for Environmental Responsibility in Washington DC, says that the critical question is whether the agency will pay attention to its scientific findings. "There's no absence of science it could use now," he says. But if it's not funnelled into management decisions, he says, "it's \$20 million window dressing".

The FWS may soon get new leadership from a 30-year veteran: Sam Hamilton, who currently oversees its southeast region, has been nominated to head the agency. His nomination must be confirmed by the Senate.

Roberta Kwok

"Strong science support will be necessary to defend management decisions that could be taken to court."



FLEEING CLIMATE CHANGE

Mass migration fears questioned.

www.nature.com/news

P. RAHMAN/AP

Lawsuit puts flu-vaccine contract in doubt

A US office tasked with readying the country for influenza pandemics received an unpleasant surprise last week, when creditors filed a lawsuit intended to force one of its new grantees into bankruptcy.

The lawsuit was filed the day before the Biomedical Advanced Research and Development Authority (BARDA) in Washington DC announced it had awarded a US\$35-million contract to Protein Sciences, a biotechnology company in Meriden, Connecticut. The contract is to support the development of vaccines against pandemic flu viruses, such as the H1N1 strain circling the globe. The award could be extended to \$147 million over five years, and require 50 million doses of vaccine to be produced.

But the company's success or failure may depend on the outcome of a lawsuit filed on 22 June by vaccine maker Emergent BioSolutions of Rockville, Maryland, and two other creditors that say Protein Sciences has failed to pay back more than \$11 million in loans.

Protein Sciences has developed a way to produce flu vaccines in insect cells — a method that some hope will break the industry's reliance on the tried-and-

tested but slow process of making them in chicken eggs. Its seasonal-flu vaccine is being considered by the Food and Drug Administration; a decision about its approval could come this year, says chief operating officer Manon Cox.

In March 2008, the company received word that it would probably win a contract from BARDA; but then Emergent offered to buy it,

Pandemic update

ARGENTINA: Reports an infection in a pig farm in Buenos Aires province, the first known infection in pigs outside Canada.

See also www.nature.com/swineflu

and the two firms entered into negotiations. Concerned that the merger might threaten the company's ability to produce an influenza vaccine, BARDA held back its final decision. "Emergent BioSolutions at that time did not have the necessary know-how, resources and people to use the technology that Protein Sciences had developed," says BARDA director Robin Robinson.

Negotiations between the two companies

collapsed when Protein Sciences' shareholders voted against the agreement, but by then the company had already accepted a \$10-million loan from Emergent. BARDA conducted two financial audits of Protein Sciences last year, Robinson says, and assured itself that the company would be able to pay back its creditors. But Cox says that the financial climate, and lawsuits filed by Emergent after negotiations broke down, made it difficult to raise funds.

Although the loan was due to be repaid at the end of May, Robinson says he had not expected a lawsuit, and he declined to speculate about the fate of BARDA's contract until the case is heard in court later this month. "Basically, we just see this as feuding between two companies," he says.

BARDA, meanwhile, will receive an influx of funds from the \$7.7-billion spending on pandemic flu that was signed into law last week. Spending on vaccines is not specified, but the money will be used mainly for the public-health programmes and supplies needed to cope with the H1N1 pandemic, says Robinson, without sacrificing its investments in vaccine technology.

Heidi Ledford

CDC

UK Met Office hit by cuts to climate project

The UK government has slashed its financial support for the Met Office's climate programme. The move came in the same week that prime minister Gordon Brown laid out ambitious talk of a US\$100-billion fund to help developing countries to cope with climate change (see <http://tinyurl.com/m22pq9>).

The Ministry of Defence (MOD) has withdrawn its £4.3 million (US\$7 million) in funding for climate research — roughly a quarter of the Met Office's total funding in this area. The change will affect the Hadley Centre for Climate Change in Exeter, the world-class climate-modelling institute whose researchers made key contributions to the most recent assessment report of the Intergovernmental Panel on Climate Change in 2007.

"This news comes as a shock," says climate scientist Martin Parry, formerly of the Met Office and now at the Grantham Institute for Climate Change at Imperial College London. "The UK's core modelling work on climate change has been funded from this source, up to now," he says.

The change does, however, bring the centre more in line with other national climate research centres, very few of which have links to defence funding.

In a statement, an MOD spokesperson said that the cuts, which are effective immediately, were made with a view to "prioritizing success in current operations, such as Afghanistan".

This will be the first time that Met Office climate research has gone without MOD cash.

One-sixth of the agency's total budget of £176.5 million comes from commercial services, but the government, and the MOD in particular, remains its main customer and funder.

In 2007, the MOD signed a three-year deal worth £12 million with the Met Office to part-fund its Integrated Climate Programme, which makes up the bulk of its climate research. Although the MOD has withdrawn its remaining funding, a Met Office spokesman insisted that the programme is not threatened.

The Department of the Environment, Food and Rural Affairs is committed to providing £4 million per year until 2011 to the climate programme, and the Department

of Energy and Climate Change will provide about £10 million in annual funding over the same period.

The Met Office is now in negotiations with these departments, and with the Department for International

Development, in an effort to recoup some of the lost funding.

"If they don't recoup it, they are going to

be in serious trouble," said Gavin Schmidt, a climate modeller at NASA's Goddard Institute of Space Studies in New York. "Losing 25% of your funding is a huge deal. Five per cent is generally containable, but 25% is not an amount you can hope to absorb easily."

Olive Heffernan

For a longer version of this story, see <http://tinyurl.com/mlcn7y>

"Losing 25% of your funding is a huge deal."

Indian university system overhauled

Indian universities are likely to find themselves under a new oversight body, human resource development minister Kapil Sibal announced last week.

Physicist Yash Pal led the committee that recommended setting up a six-member National Commission for Higher Education and Research (NCHER) to reform higher education. The commission would replace nearly a dozen regulatory bodies and bring all streams of higher education, including engineering, medicine, agriculture and law, under its purview.

Many Indian scientists welcomed the move, although some are sceptical. Chemist C. N. R. Rao, former science adviser to Prime Minister Manmohan Singh, says that the current infrastructure has led to graduates without the quality to compete on the world stage. India ranks behind such smaller powerhouses as Taiwan, Singapore and South Korea in the number of high-impact scientific papers published.

Adding another regulatory body is unlikely to address such problems, Rao says. "It is fine if it remains just an advisory body," he says. "But if it starts controlling the entire educational sectors from medicine to law, it will be simply weighed down by bureaucracy."

According to the committee's report, the NCHER will create new norms for accrediting universities. Approvals for "deemed" universities, which are aspiring independent institutions wanting university status, will be stopped, and the existing ones must be re-accredited. India's deemed universities have mushroomed in recent years, to 123 in total. The report also proposes bolstering funding of state universities and encourages recruitment of foreign faculty.

Pushpa Bhargava, a biologist and founder of the Centre for Cellular and Molecular Biology in Hyderabad, says the recommendations "should be implemented seriously". As an

example of shoddy accreditation, he says he has been approached by a private college that asked to borrow academic staff on a short-term basis so that it could have professors on hand for a three-day visit from regulatory body the All India Council for Technical Education. That council, along with others, would be subsumed under the new commission.

Sibal said the recommendations would be implemented within 100 days. The NCHER's chairman will be appointed by President Pratibha Patil, and its members selected by a search committee that will include the prime minister and the leader of the opposition.

"It is a very good thing that has happened for educational reform," Mamannamana Vijayan, president of the Indian National Science Academy, told *Nature*. "We now need to turn to the question of how to reform the structure of Indian science." ■

K. S. Jayaraman

Impasse at talks leaves whales high and dry

The 2009 meeting of the International Whaling Commission (IWC) in Madeira, Portugal, has ended in deadlock.

No consensus could be reached on Japan's proposal that it be allowed to resume commercial whaling in its own coastal waters — banned since 1986 — in exchange for reducing its quota of whales killed for 'scientific research' in Antarctic waters.

Scott Baker, a researcher at Oregon State University's Marine Mammal Institute in Newport, told the meeting that the number of coastal whales killed as 'by-catch' in fishing nets, and sold on Japanese markets, is under-reported. His team found that by-catch numbers approach 150 minke whales a year, roughly equivalent to those killed in Japan's North Pacific offshore whaling programme. A 2007 study (C. S. Baker *et al. Mol. Ecol.* 16, 2617–2626; 2007) found similar coastal by-catch depletion in South Korea.

The IWC also postponed a decision on Denmark's request for Greenland's indigenous Inuits to hunt 10 humpback whales a year.

Key polar research centres sign up to cooperative deal

European polar researchers could enjoy easier access to funding thanks to a cooperative deal between key institutes.

Twenty-six institutions associated with polar research signed up to the European Polar Framework on 24 June, including the British Antarctic Survey, Germany's Alfred-Wegener Institute and the Norwegian Polar Institute. Paul Egerton, executive director of the polar board for the European Science Foundation, which is behind the framework, told *Nature* he

F. FUNDEL/ALFRED-WEGENER-INSTITUT



Polar scientists can expect easier access to funds.

Heritage alert for Central American reef

Belize's barrier-reef system (pictured) — the largest of its kind in the Northern Hemisphere — has been put on a danger list by the World Heritage Committee to encourage international support for its preservation.

The committee, part of the United Nations Educational, Scientific and Cultural Organization (UNESCO), included the reef because it is threatened by development and the cutting back of mangroves. It has been on the World Heritage List of naturally important sites since 1996.

Also placed on the danger list is the Los Katios National Park in Colombia, which is at risk from logging. UNESCO added a further two natural sites to its World Heritage List: the Wadden Sea wetlands belonging to Germany and the Netherlands, and the Dolomites mountain range in Italy.



N. WU/SCIENCEFACTORY/CORBIS

hoped Russia would soon sign up too.

Funding rounds from separate national research programmes may be combined, and it should also be easier for researchers to secure places at other countries' research stations, says Egerton. The new framework, he adds, continues the spirit of International Polar Year, which ended in March 2009 (see *Nature* 457, 1074; 2009).

Recession deals a glancing blow to nanomaterials

Markets for carbon nanotubes, ceramic nanoparticles, nanocomposites and coatings have been dented following the downturn in the construction, electronics and automotive industries. But according to a report released last week, they should recover swiftly.

The report, by Lux Research, a market-analysis company in New York, projects that the revenue from products incorporating nanotechnology will reach US\$2.5 trillion worldwide in 2015 — a cut of 21% from the company's July 2008 projection.

But in a few years, revenue from affected nanomaterials and intermediates will bounce back to approach the previous estimates, the report says. And it notes that expected growth for nano-related products in the health-care and life-sciences sectors has hardly been affected by the recession.

African institutions gain support networks

African research, by many measures the least competitive in the world, got a financial pick-me-up this week.

On 2 July, the UK Wellcome Trust launched a £30-million (US\$50-million) plan to support more than 50 institutions

across the continent, organized in themed networks that will study water and sanitation, infectious diseases and population health.

"There are other collaborations and networks but the lack of research capacity in Africa is a huge problem and it's going to take more than one initiative to achieve this," says Jimmy Whitworth, the Wellcome Trust's head of international activities.

The funding will be used to revamp laboratories, to train laboratory personnel and to support competitive grants aimed at encouraging African scientists to remain working in their home countries.

For a longer version of this story, see <http://tinyurl.com/africafund>

SOUNDBITES: TALKING CLIMATE TARGETS

"The most ambitious and comprehensive piece of climate change legislation anywhere in the world."

Scotland's climate-change minister, Stewart Stevenson, as his country passed legislation on 24 June to reduce greenhouse-gas emissions by 42% by 2020, and by 80% by 2050.

"A bold and necessary step."

US President Barack Obama hails the passage of the Waxman-Markey energy and climate-change bill through the House of Representatives on 26 June — by the narrow margin of 219 to 212 votes (see *Nature* 459, 493; 2009).

"We must move the debate from a stand-off over hypothetical figures to active negotiation on real mitigation actions and real contributions."

UK prime minister Gordon Brown suggests on 26 June that an international fund of US\$100 billion a year will be needed by 2020 to help developing countries to mitigate and adapt to climate change (see <http://tinyurl.com/m22pq9>).

Don't cry politicization

To call biomedical research proposals political distorts the issue, says **David Goldston**.

Last month, three of the leading proponents of biomedical research in the US Congress levelled an unlikely charge at President Barack Obama's proposal to focus health research on cancer and autism: they said the plan amounted to the 'politicization' of science.

The first response to such a claim might be to marvel that any member of Congress could even pretend to take umbrage that a politician was involved in allocating money to the National Institutes of Health (NIH). It's even more surprising that the critique should come from three leaders on congressional spending committees: Representative David Obey of Wisconsin and Senators Tom Harkin of Iowa and Arlen Specter of Pennsylvania, all Democrats although Specter was, until recently, a Republican. After all, every year, in the documents that accompany spending legislation, Congress directs the NIH to focus on specific diseases and even specific populations. If targeting spending on cancer is illegitimate politicization, then what would one call urging the NIH to "increase research that is focused on understanding heart disease and cerebrovascular disease among Native Hawaiians", as the Senate did, not atypically, in 2007?

But the fundamental problem with the politicization charge is not its disingenuousness or its lack of perspective. Rather the almost reflexive resort to that word is a sign that it has been drained of all genuine meaning, and that, in turn, reflects fundamental misunderstandings about how decisions concerning science have to be made.

Decisions about how to allocate taxpayer funds among scientific fields or diseases cannot be politicized because they are inherently political. Apportioning public monies is a matter of making policy choices, of applying values and setting priorities; it is not some cold, mathematical exercise to be solved for the 'right' answer. (There can turn out to be wrong answers, but only measured against whatever politically selected criteria were used to make the original allocation.)

Congress could decide to delegate the NIH budget decisions to NIH officials, or to a group of scientists or selected lay people, all of whom would certainly have their own politics. But the delegation itself would be a political choice about whose priorities and what



PARTY OF ONE

kinds of politics should determine funding.

Alternatively, Congress could devise some methodology for choosing priorities, based on, say, the number of citizens suffering from a disease, its seriousness, the likelihood of finding a cure, the cost of treatment and even the fear the disease engendered. But just beginning to list such factors underscores the political nature of the decision. What factors should be included and how should they be weighed? Would diseases of the young or the old get higher priority? Research on men or women? What about illnesses that primarily affect just one ethnic group? Evaluating each factor would require judgment calls, and Congress would have to decide who would make those calls.

This is more than an academic point, and tossing around the word politicization is more than harmless sloganeering. The term is often used, consciously or not, as a way to obscure or shut down debate on issues that ought to engage the public and their representatives. Indeed, it's hard to know exactly why Obey, Harkin or Specter (who has very publicly battled his own cancer in recent years) object to the Obama plan because of the way they've framed the issue.

One possibility is that they're concerned that dollars that go to cancer and autism research will be unavailable to be spent on diseases that they see as equal or higher priorities. Or they may be worried that Obama will use his initiatives to parry their efforts to increase total NIH spending. Or they may fear that the proposal will unravel the unwritten pact that increases the budget of every NIH institute by about the same percentage, uniting NIH constituencies to fight for the agency's bottom line.

Those concerns are all worth discussing. The president's proposed budget for the fiscal year that begins on 1 October includes a 5% increase for cancer research and a 16% rise for autism, while proposing that overall NIH spending grow by only 1.4%, to about \$31 billion.

But if congressional appropriators think the president has picked the wrong priorities or is stinting on overall research funding, then there ought to be a full debate about the proposals, their rationale and any alternatives. Crying "politicization" is a strategy for circumventing all that by making the proposals seem illegitimate and unworthy of discussion. That can distract attention long enough to smuggle one's own favoured approaches into legislation.

That is bad enough, but the profligate use of the word politicization has other detrimental consequences. There are times when the charge is warranted — when, for example, politicians try to manipulate a scientific conclusion — and the term will gradually lose its bite if it comes to mean nothing more than "you made a choice I don't like". Crying politicization should not become a case of crying wolf.

Perhaps worse still, constant talk of politicization can erode public faith in the political system and deepen the misconception that there is something automatically suspect about political decision-making, when it is ultimately the only tool a democracy has. One might think that politicians would be more worried than anybody about demonizing the process that is the very reason their jobs exist, but instead they try to gain favour by posing as being 'above' politics. This is an old strategy — politician has long been synonymous with rascal and worse in the American lexicon — but it can gradually delegitimize the entire system.

It's rare to have a direct debate on the role of politics in making decisions about science. Scientists and their patrons have long tried to perpetuate the myth that the allocation of science funds is somehow more pure (not just better done) than the mad scramble for funding in every other policy area. Perhaps the last time the issue was fully argued was when President Harry Truman vetoed an early version of the National Science Foundation in the late 1940s because a panel of scientists, rather than the president, was to select the agency's director. But the myth becomes pernicious when it enables politicians to try to shut down debate by playing on the sense that science spending decisions can or should be apolitical.

Obama's cancer and autism proposals may or may not be a good idea. But that's for politicians to decide; there is no higher authority. ■

David Goldston (partyofonecolumn@gmail.com) is a visiting lecturer at Harvard University's Center for the Environment.

The hybrid returns

Slotting a fusion reactor into the heart of a nuclear fission plant could accelerate the development of waste-free nuclear energy. So why are all the designs still on paper, asks **Ed Gerstner**.

It seems like such a natural fit. Nuclear fission has proved that it can produce greenhouse-gas-free energy: the roughly 440 nuclear plants operating in 31 countries around the world collectively have the capacity to generate some 370 gigawatts of electrical power, or about 15% of the global total. But fission power also produces a stream of radioactive nuclear waste, laced with potentially bomb-grade plutonium — some 12,000 tonnes of waste per year, worldwide. That's quite a disposal problem.

Thermonuclear fusion, meanwhile, promises to generate an even greater supply of clean energy. But so far no human-induced fusion reaction has produced more energy than was used to fire it up.

What fusion does generate, however, is neutrons. And therein lies the fit: fusion's neutrons could burn up fission's waste almost completely, leaving a residue greatly reduced

in both volume and radioactivity. So why not combine the two into a fusion-fission hybrid reactor, and let each technology solve the problems of the other?

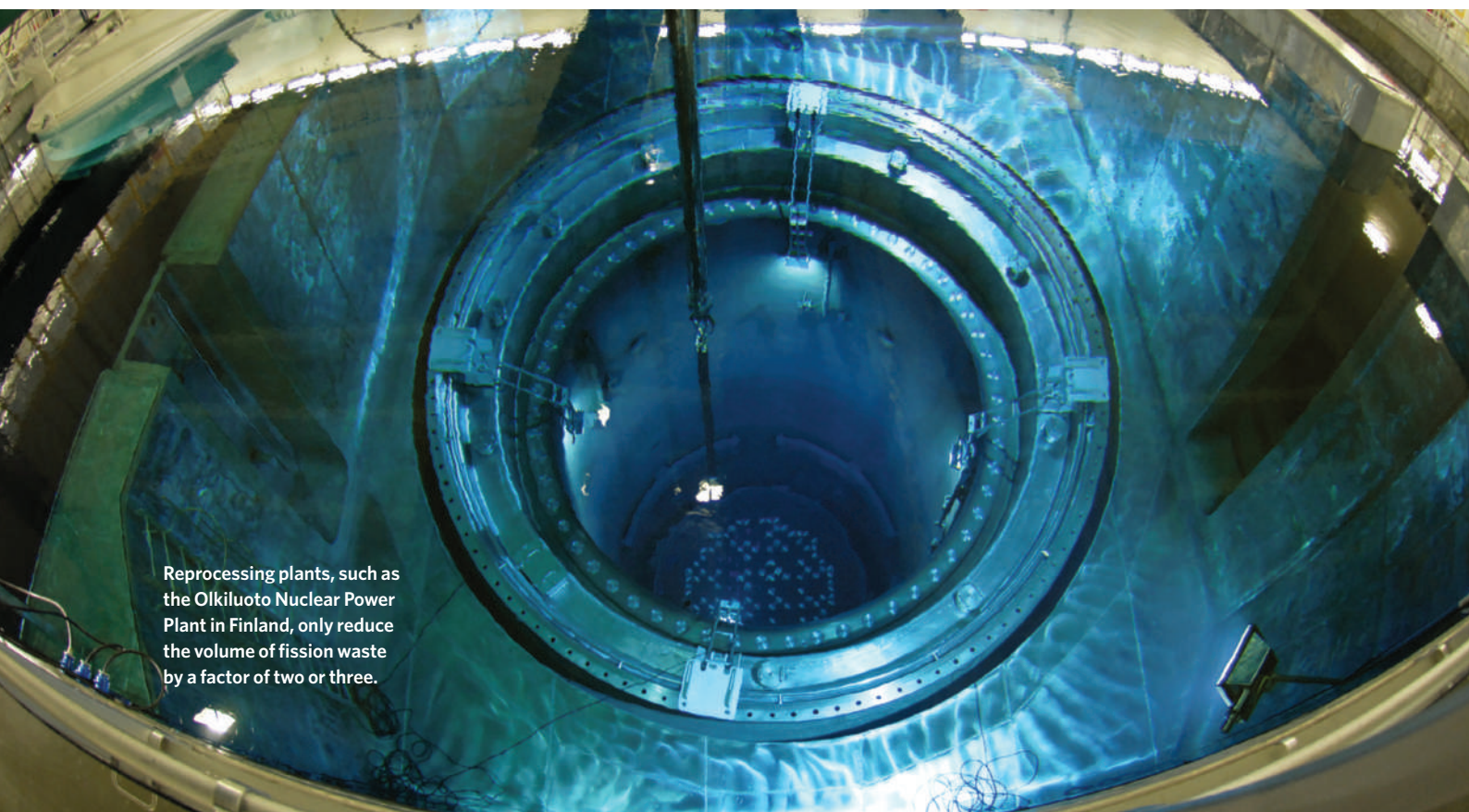
There are several reasons why not. One is that nobody knows how. Building a fusion reactor is complicated enough without trying to build one inside a nuclear fission reactor — which is why hybrids currently exist only as designs on paper. Another is the unquantified risk factor: a hybrid reactor would almost inevitably put a potentially unstable thermonuclear plasma next to radioactive fission products.

Still, a growing number of researchers around the world are convinced that it is worth tackling those challenges — because pure fusion power isn't getting much closer, and the piles of fission wastes are mounting ever faster. After decades of stagnation because of concerns about safety and waste,

the fission-power industry seems on the verge of a renaissance. The need to cut greenhouse-gas emissions and to reduce the reliance on fossil fuels has prompted staunch opponents of nuclear power, such as Italy and Sweden, to reverse long-standing embargoes against the construction of new nuclear plants. Finland, France and the United Kingdom are preparing for new reactor building programmes. China is planning to build 40–50 fission plants within the next two decades. The US Nuclear Regulatory Commission has received applications for licenses to construct another 26 reactors in the United States, which has 104 already. And almost 45 fission plants are under construction around the globe.

Clearly, a plan is needed for dealing with the resulting increase in nuclear waste. Such plans generally centre on burying it deep underground. The question, is where?

H. HUOVILA/TVO



Reprocessing plants, such as the Olkiluoto Nuclear Power Plant in Finland, only reduce the volume of fission waste by a factor of two or three.

Disposal can be a very politically sensitive issue. For example, a site at Yucca Mountain in Nevada was considered for more than two decades for use as a US national repository for spent nuclear fuel. But the plan sparked so much resistance from local residents and politicians that the US energy secretary, Steven Chu, announced in March that the underground facility was no longer an option. For the foreseeable future, the spent fuel from each US nuclear plant will continue to be stored on site.

Many countries reduce the volume of waste by a factor of two or three by reprocessing the spent fuel — extracting the still-fissionable isotopes of uranium and plutonium, and fashioning them into new fuel elements. But reprocessing is expensive, inefficient and poses a nuclear proliferation risk: the extracted plutonium is usable in nuclear weapons. And it still leaves tonnes of highly radioactive residue to be disposed of.

All of which is why hybrid reactors are suddenly starting to look good again.

Nuclear roots

The hybrid idea dates back to the 1950s, when nuclear engineers were first struggling to harness nuclear reactions for generating electrical power.

They were already aware of the waste problem that arises from the nature of the fission reaction itself. The reaction starts when a neutron strikes the nucleus of a fissile

isotope such as uranium-235 or plutonium-239, causing it to split apart. The result is a pair of lighter nuclei, a burst of energy and a number of new neutrons. The energy can be extracted as heat and used to drive an electricity turbine. But to keep the fission reaction going, some of the newly created neutrons must collide with other fissile nuclei, causing them to split and to release still more neutrons in a chain reaction. This happens easily as long as the fuel is fresh and there is nothing else for the neutrons to hit. As the reactions continue, however, the fuel accumulates more fission-product nuclei, most of which absorb the neutrons without doing anything else. Eventually, so many neutrons are absorbed that the chain reaction can no longer sustain itself, at which point the fuel becomes waste — even though most of the original fissile material is still there.

Engineers realized that they could get around this problem by supplementing the chain reaction with an independent source of neutrons. If there were enough neutrons, they would use up much more of the uranium and plutonium in the fuel, and would also burn

through most of the long-lived radioactive fission products, greatly reducing waste.

And so the idea of the fusion–fission hybrid was born, because fusion reactions — in which various isotopes of hydrogen fuse to become helium nuclei — produce a torrent of neutrons (one per fusion event). In principle, building a hybrid was simply a matter of wrapping a blanket of fissile material around a fusion reactor, and letting the energy flow (see graphic, below).

In practice, though, the technology of the day was not up to the task. Harnessing fusion, whether for neutrons or energy, amounts to recreating the conditions that drive

the reaction in the Sun. Somehow, a gas of hydrogen isotopes — usually deuterium and tritium — has to be compressed and heated until it becomes plasma at more than 150 million °C. And somehow, that plasma has to be confined in its dense, superheated state for long enough for the reactions to proceed.

Faced with what seemed like insurmountable difficulties, the hybrid idea was shelved and physicists focused their efforts on the separate development of pure-fission and pure-fusion reactors. And except for a brief flurry of interest following the energy crisis of the late 1970s, when the Nobel laureate physicist Hans Bethe tried to drum up support for hybrids¹, the idea has stayed on the shelf — until now.

The advance of fusion

One reason for the renewed optimism about hybrids is half a century of progress in plasma containment. The most common approach today is to trap the plasma inside a doughnut-shaped device known as a tokamak, which holds it in place with an intense magnetic field. It is a measure of the difficulty of the task that the longest-lived fusion reaction demonstrated so far, achieved in 1997 in the Joint European Torus at the UK Atomic Energy Authority's (UKAEA) Culham Science Centre near Oxford, lasted no more than a few seconds. It generated fusion energy equivalent to 70% of the energy that was used to produce it. But many scientists in the tokamak-fusion community think that the next big machine — the International Thermonuclear Experimental Reactor (ITER), being built at Cadarache in the south of France — will have an energy output up to ten times its input.

At about 19 metres wide and 11 metres tall, ITER's toroidal containment vessel will be twice



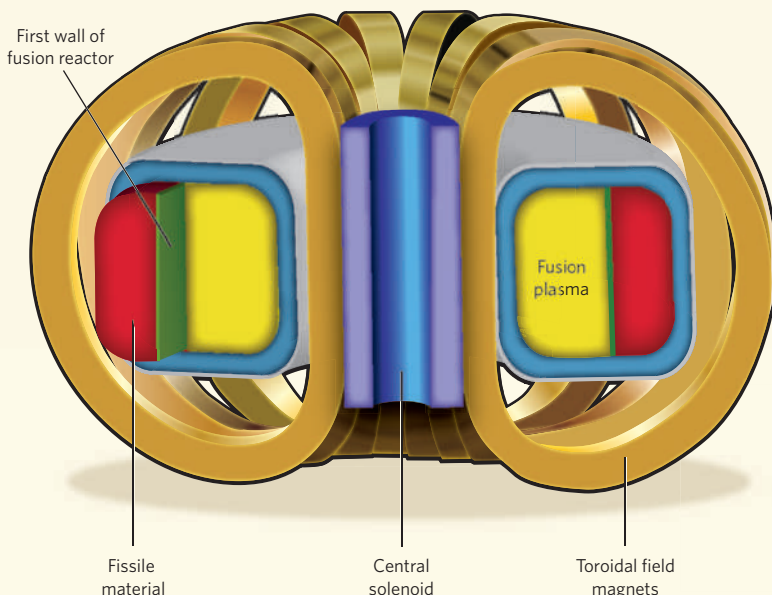
"I'm not saying a hybrid can't be done, but we should focus on getting all the way to pure fusion first."

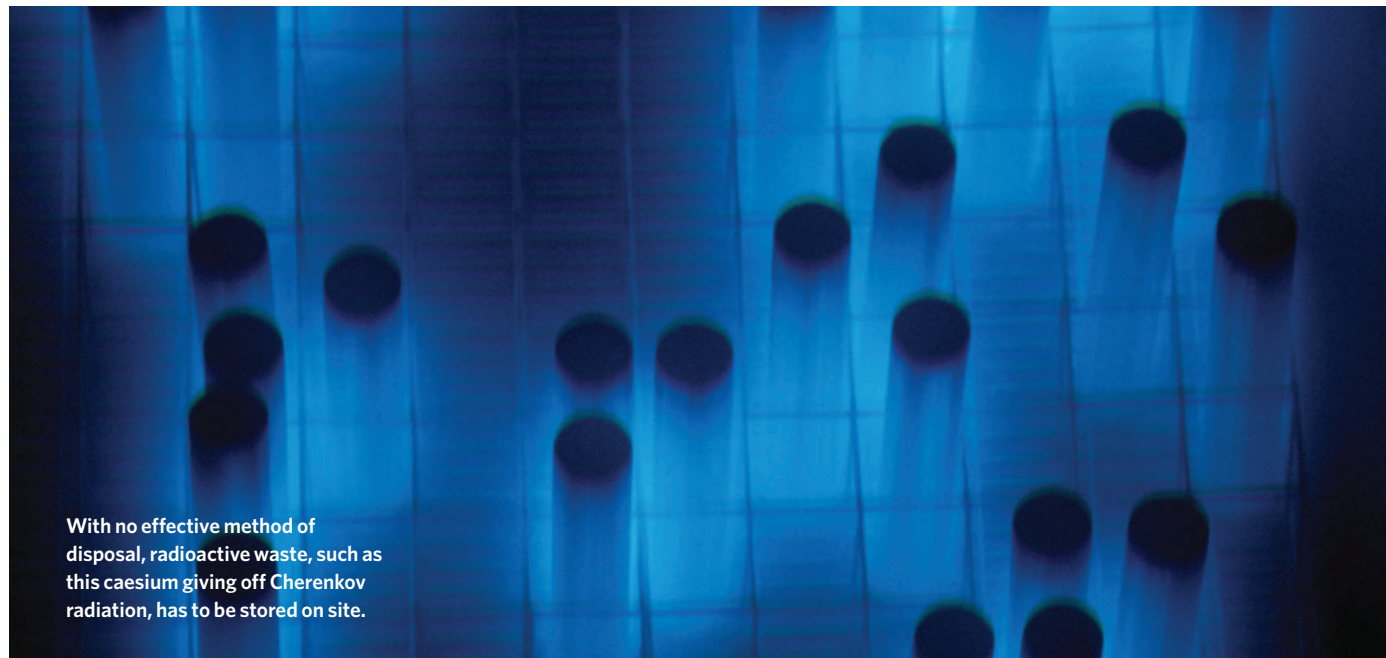
— Steve Cowley

UKAEA CULHAM

ANATOMY OF A FUSION-FISSILE HYBRID

A fusion reactor, based on a doughnut-shaped tokamak, generates high-energy neutrons that drive fission in the surrounding blanket of fissile material. Putting nuclear waste in this blanket should in principle burn up all the long-lived radioactive by-products produced by the fission process.





With no effective method of disposal, radioactive waste, such as this caesium giving off Cherenkov radiation, has to be stored on site.

P. ESSICK/AURORA/GETTY IMAGES

the size of that of the Joint European Torus and, at an estimated construction cost of some €10 billion (US\$14 billion), it will be one of the most expensive experiments ever undertaken². However, the project has come under criticism for its cost overruns and delays and it will not start operation until 2018. Experiments on whether fusion would be viable for power aren't planned to begin until the end of 2026.

Nonetheless, says Weston Stacey, a professor of nuclear engineering at the Georgia Institute of Technology in Atlanta, "the physics and technology that are being developed at ITER are more than enough to build a good neutron source for a hybrid".

That's why Stacey, a leading proponent of the hybrid idea, has used the ITER design as the basis for the concept of a subcritical advance burner reactor³, a fusion-fission hybrid design that he and his team at Georgia Tech have been working on for more than 10 years.

Once we have a fusion reactor, says Stacey, "the problem will be to fit all this together". He laughs at himself for implying that putting a fusion reactor the size of ITER into the core of a fission reactor will merely be 'an engineering challenge'. But it is his engineering approach to design that has prompted people to take notice.

"One of the problems with designs in the past was that nobody who was interested in the hybrid had done very much serious engineering," says Jeff Freidberg, a nuclear scientist and engineer at the Massachusetts Institute of Technology in Cambridge. "But the one that has perhaps done the best job so far is Stacey, because he's spent a lot of

time to put some real engineering in there."

China is also pursuing the hybrid idea: it is one of the goals of the country's High-Tech Research and Development Programme. "At the moment it's mainly calculations to assess the various conceptual designs for a hybrid," says Jiangang Li, director of the Chinese Academy of Sciences' Institute of Plasma Physics in Hefei. But the country's big push into nuclear fission power gives the effort urgency, he says: "China will be faced by both a need to be able to reprocess a lot of radioactive waste and a shortage of nuclear fuel because the country has relatively limited fission fuel resources."

Freidberg is cautious about how realistic many of the ideas that are emerging in the field

are in the short term, but is optimistic about their contribution in the longer term. In particular, he sees the hybrid as potentially easing some of the technical challenges posed by a pure fusion reactor.

Because the fusion core of a hybrid would only have to generate neutrons, for example, it could be operated well below the power levels that a pure fusion reactor would need to work at to produce electricity. As a result, the plasma in a hybrid device would probably be less susceptible to instabilities and other disruptions.

A real beast

Lower power levels should also ease the 'first wall' problem — the difficulty of finding materials for a fusion reactor's inside wall, which will be exposed to such an intense flux of high-energy neutrons that it will probably need to be replaced after just a year or two of operation. "The problem of that first wall is a real beast," says Freidberg.

That will still leave Stacey's engineering challenge to solve: building a fusion reactor inside an equally complex fission device. But Freidberg remains optimistic. "None of these problems are insurmountable, but you can't solve them with paper studies, you ultimately need to build some devices. And maybe you can start to build things sooner than you could do for pure fusion electricity, because the end goal is a little bit nearer."

Not everyone is convinced, however. Steven Cowley, director of the Culham Science Centre, speaks for many in the fusion community who are sceptical of the need to revisit the hybrid



Nuclear fission plants generate about 12,000 tonnes of waste annually.

F. MORI/AP

concept, and who are concerned that it is a distraction from the goal of sustainable, clean, pure fusion power. "I'm not saying a hybrid can't be done," says Cowley. "But if what you need is post-ITER in its abilities, then you should focus your attention at getting all the way to pure fusion. Because even though in principle it looks easier, you have to solve all these other problems as well."

Beyond ITER

Hybrid designs don't have to be based on ITER. For example, a group of researchers at the Institute for Fusion Studies at the University of Texas in Austin argues that a practical hybrid will require a fusion core that is far smaller than that of ITER.

"A typical light-water fission reactor runs at about a gigawatt of electric power," explains Swadesh Mahajan, a senior research scientist with the institute. That gigawatt is generated within a certain volume, which means that the reactor has a power density of so many gigawatts per unit volume. And as it turns out, says Mahajan, that number is about five times higher than the power density of ITER. This creates a problem for the design of a hybrid. For the fission blanket to capture the fusion-generated neutrons efficiently, the fusion core and the blanket have to have roughly the same power density. So the fusion system has to have a power density about five times that of ITER, says Mahajan. Or to put it another way, the fusion core has to put out the same amount of energy (and neutrons) in a volume five times as small.

The problem is that ITER's planned power density is already at the limits of current technology. These limits are set by the materials used to construct the exhaust of the reactor — the divertor. The materials have to withstand the high volume of superheated gas that must be continually vented from its plasma.

To overcome this problem, Mahajan's group has come up with the Super-X Divertor⁴. The concept involves engineering the magnetic fields around the exhaust of a tokamak to increase the distance hot gases have to travel, giving them a chance to cool down before they come into contact with the solid walls of the exhaust. This enables the divertor to handle the exhaust from much higher power-density tokamaks.

"I think the Super-X Divertor is a big step forwards. A huge step forwards," says Cowley.

He is excited about the prospect of a compact neutron source based on Mahajan's ideas, but nevertheless says that the UKAEA's fusion efforts are focused on ITER, and that it has no interests in developing a hybrid. "The Super-X Divertor could certainly enable the high-power devices that the Texas group want for their hybrid. But I think it'll do more than that. It will be the model of the kind of divertor that we will have on any demo reactor." As well as testing the Super-X concept itself, a compact neutron source built with its help could be used to develop and test the materials needed for a commercial fusion reactor. However, adding the untested divertor to ITER would be too risky.

Mahajan, for his part, is hoping that Cowley's work will further another of his group ideas, that of a disposable fusion 'battery'⁴⁻⁵ — a much smaller fusion device than ITER that can be replaced in its entirety at the end of its operational life.

"The biggest engineering nightmare if you ask any fusion engineer is the problem of the first wall," says Mahajan. "So we decided that if we had a fusion neutron source that was sufficiently small, not in the sense that you could put it in your handbag, but small enough that a crane could easily lift it, we could design a neutron source that is replaceable."

With a reactor that can be lifted in an out of the middle of a hybrid's fission blanket, Mahajan argues, you no longer have to worry as much about the stability of the materials you use to make it. He envisages that the fusion part of such a device could be removed and replaced at the same time as the fission blanket's waste-fuel rods, about every 2 years. What's more, he says, in the test phase of such a device, this 2-year lifespan should enable the technology in the battery to be developed at a much faster pace than a conventional reactor. "If we needed five iterations to improve the stability of our device, with a turn-around time of just 2 years, that would take us only 10 years. For other designs the same process would take 50 years."

And it's not just the materials problems that the Texas approach would address, but the plasma physics as well. For ITER to produce ten times more energy from a fusion plasma than is put in, it will require the generation

of unprecedented plasma temperatures, densities and confinement times. But because the fusion component of a hybrid need not produce energy, merely neutrons, the plasma conditions needed will be more modest.

"Because the Super-X Divertor takes care of the heat-flux issue, we can operate our device in the sorts of conventional plasma modes that every Tom, Dick and Harry in the plasma community are already producing in their laboratories," says Mahajan.

And it could even deal with potential concerns about generating a hot thermonuclear plasma in the middle of a blanket of concentrated,

highly radioactive, nuclear waste. "Even if something did go wrong with the fusion module of our hybrid, the toroidal field coils of the module, which are made of strong metal, will shield the fission blanket from any stupid thing that the plasma is capable of doing," says Mahajan. This would not be the case in a conventional hybrid design, in which the components are more intimately connected.

The Texas group is in talks with groups at Princeton University in New Jersey and Oak Ridge National Laboratory in Tennessee to investigate these ideas.

Mahajan says he sees their work as essential to rebuilding the world's nuclear power capacity: "One of the things I've been arguing for — because in 20 years we will be ready to destroy the waste — is to start building nuclear reactors now. Don't wait. The rate at which nuclear capacity has been destroyed is an act of monumental stupidity." If scientist don't start aggressively pursuing this form of clean energy, he says, "We can forget about solving global warming. We will have screwed the planet royally if we don't take action fast."

Ed Gerstner is a senior editor of *Nature Physics*.



"Our device operates in the plasma modes that every Tom, Dick and Harry in the plasma community can produce in their lab."
— Swadesh Mahajan



"Once we have a fusion reactor, the problem will be to fit all this together."
— Weston Stacey

1. Bethe, H. *Phys. Today* **32**, 44–51 (1979).
2. Brumfiel, G. *Nature* **459**, 488–489 (2009).
3. Stacey, W. M. et al. *Nucl. Technol.* **162**, 53–79 (2008).
4. Valanju, P. M., Kotschenreuther, M., Mahajan, S. M. & Canik, J. *Phys. Plasmas* **16**, 056110 (2009).
5. Kotschenreuther, M., Valanju, P. M., Mahajan, S. M. & Schneider, E. A. *Fusion Eng. Design* **84**, 83–88 (2009).



CLIMATE'S SMOKY SPECTRE

With their focus on greenhouse gases, atmospheric scientists have largely overlooked lowly soot particles. But black carbon is now a hot topic among researchers and politicians. **Jeff Tollefson** investigates.

Steve Warren spent his spring break island-hopping with a couple of friends, but they didn't go to bask in the sun. Instead, his team from the University of Washington in Seattle toured the Canadian Arctic, digging pits in the snow and collecting hundreds of samples to take back to the lab. The targets of their expedition, hidden in all the whiteness, were specks of something called black carbon.

These dark particles, the major constituents of soot, are the legacy of incomplete combustion in diesel engines, coal power plants, agricultural burning and wildfires far to the south. Prevailing winds sweep black carbon and other pollutants into the Arctic, where they circulate in a dirty yellow haze (pictured above) until storms wash them out of the air. Warren's team was collecting those that fell among the snow flakes.

The aerosol haze has long plagued the Arctic, but scientists are only now taking stock of a different and potentially uglier dimension of soot. As its name would suggest, black carbon absorbs sunlight. These particles heat the atmosphere while aloft; when they settle on the snow, they hasten its melting. This exposes the dark land and water, which absorb more of the sun's energy and thereby drive up the region's

temperature. Recent research¹ suggests that black carbon could be responsible for a large fraction of the Arctic warming. Soot also takes a toll elsewhere. In southeast Asia, studies suggest² that it is choking the moisture supply for the Indian monsoons and contributing to the retreat of mountain glaciers that provide fresh water for more than a billion people.

At this point, scientists lack enough data to definitively conclude how strongly black carbon is affecting the climate. But some studies suggest that it could be second behind carbon dioxide in terms of its contribution to global warming. There is a crucial difference between the two pollutants, however: soot particles hang in the atmosphere for just a few weeks, whereas CO₂ molecules can remain in the air for centuries. This means that efforts to curb soot emissions could reap immediate climatic benefits. That possibility has recently pulled soot, which has conventionally been seen as a public-health issue, into the climate-policy arena.

"There's an urgency about this: we still don't have a viable way of cutting down CO₂," says Veerabhadran Ramanathan, an atmospheric scientist at Scripps Institution of Oceanography in La Jolla, California. By comparison, reducing soot emissions seems remarkably

simple and cheap. "It's not going to take 30 or 100 years to do it. If you halt the black carbon now, it will be gone in two weeks."

A. CLARKE

Hazy data

Long before the current interest in black carbon, an accidental observation by Warren led him to do some pioneering work on the pollutant. In 1980, he and Warren Wiscombe of the National Center for Atmospheric Research in Boulder, Colorado, were having trouble developing a mathematical model of snow reflectance, or albedo. The two couldn't make their calculations align with the latest albedo measurements in the Arctic because the snow in their study was reflecting less light than expected. "It turned out the snow was being collected downwind from a diesel generator," Warren says.

Warren went on to collaborate with Antony Clarke at the University of Washington, who organized the first survey of black-carbon deposition in the Arctic, largely using samples collected by researchers who were going there for other reasons. On the basis of those data, Clarke concluded in 1985 that soot could have a measurable effect on the Arctic climate³. But his paper had little influence until Jim Hansen, the man known for alerting the world to the threat of CO₂ pollution, pressed the issue years later.

In 2000, Hansen, director of New York's Goddard Institute for Space Studies, proposed⁴

"Sea ice may be melting anyway, but black carbon can cause more melting and earlier melting."
— Andreas Stohl

Stephen Warren uses snow from Canada's Ellesmere Island to look at effects of soot on the climate.



that the quickest way to combat global warming was to reduce black carbon, methane and other powerful warming pollutants that could be controlled more easily, and to greater effect, than CO₂. Other studies soon followed. Building on earlier research on Californian smog, Mark Jacobson of Stanford University, California, reached a similar conclusion the following year⁵. He has since become a leading advocate for curbing black-carbon emissions and was invited to make his case before a congressional committee chaired by California Democrat Henry Waxman in 2007. Waxman, who is now chairman of the House energy and commerce committee, took the message on board. In a comprehensive climate bill that was passed by the House of Representatives last week, he calls on the US Environmental Protection Agency to analyse potential black-carbon strategies.

Jacobson calculates that humans have pumped enough pollutants into the air to warm the planet by about 2 °C. More than half that effect, however, is masked by other aerosol pollutants — including sulphates and light-coloured soot particles — which cool the planet by reflecting sunlight and seeding clouds. Jacobson estimates that altogether, the climate has warmed 0.75–0.85 °C and black carbon is responsible for 0.25 °C of that.

“In other words, you could control up to 30% of global warming if you could control soot,” he says. Given that black carbon has its strongest effect in the Arctic, he suggests that such a

strategy could slow sea-ice retreat until international controls on greenhouse gases kick in. “It’s the only mechanism that you have,” he says, “in the absence of putting in a bunch of refrigerators” (see ‘Stopping the soot’).

A recent study of the Arctic supports Jacobson’s assessment. Drew Shindell, a modeller at the Goddard Institute, recently used a coupled ocean–atmosphere climate model to reconstruct twentieth-century influences on climate, or forcings, with and without black carbon. His results suggest that increases in black carbon from Asia and reductions in sulphate pollution have caused about 45% of the observed warming in the Arctic¹. In Ramanathan’s global assessment², the forcing from black carbon equals 0.9 watts per square metre, which is more than the forcing from methane and 55% of that from CO₂.

These numbers are much higher than the estimates produced by the Intergovernmental Panel on Climate Change (IPCC) in its 2007 report. The IPCC pegged the direct influence of black carbon — not including its ability to speed the melting of ice — at 0.05 to 0.35 watts per square metre (ref. 6). Overall, the effect of all aerosols — both the heat-absorbing black carbon and the reflective light-coloured ones — produces a net cooling of 0.5 watts per square metre, according to the panel. That’s enough to offset roughly one-third of the warming driven by CO₂, but the estimate comes with a huge uncertainty range of 0.1–0.9 watts per square metre. It also does not include the indirect

effect that aerosols have on cloud particles.

Last month, Gunnar Myhre, a climate modeller at the Center for International Climate and Environmental Research in Oslo, attempted to lessen the uncertainty. He compared global aerosol models with observations derived from NASA’s ground-based AERONET system, a network of passive aerosol sensors, as well as those from the MODIS (Moderate Resolution Imaging Spectroradiometer) instruments on NASA satellites. After accounting for historical emissions and tweaking the way his model handled clouds, Myhre produced a new estimate⁷ of 0.3 watts per square metre of cooling and halved the IPCC’s uncertainty range. In explaining his lower estimate for net cooling, Myhre notes that black-carbon emissions have increased roughly sixfold in the industrial era, whereas reflective aerosols have only increased three- or fourfold.

Questions in the clouds

Although few doubt that black carbon has a warming effect, particularly in icy regions, some scientists are concerned that the policy debate is getting in front of the science. Uncertainties abound about everything from current and historical emissions to the actual chemical and physical processes that are driving black carbon’s influence on snow and in the atmosphere.

For his part, Hansen says that there have been some “excessive claims” about black carbon. He calls greenhouse gases “the predominant

R. BRANDT

cause” of global and Arctic warming and believes methane remains the number two forcing agent. At the same time, he says soot’s effect is amplified over snow, which means the numbers put forth by Shindell cannot be ruled out. “Assuming greenhouse gases are reined in,” he says, “other things that we can do such as reducing black-carbon emissions will be useful.”

All this uncertainty has put a premium on solid information, which is why Warren and his colleagues set out in 2006 to conduct the first survey of black-carbon deposition in the Arctic. Since then, they have collected samples in Siberia, Greenland and Alaska, as well as at the North Pole. In their most recent trip in April, they hired a ski plane in Inuvik in Canada’s Northwest Territories and flew east, setting down on lakes, tundra and sea ice as well as on fields of permanent ice.

Each of the team’s sample pits captures an entire season of snow, providing clues about when different kinds of black-carbon pollution were deposited. They plan to feed this vast new resource to climate modellers, who are still trying to sort out ways that black carbon could affect temperatures.

The samples that Warren’s team have collected tell only part of the story. Researchers have also used instruments on the ground, on planes and on satellites to measure soot in the air. But the task is particularly difficult because soot’s darkness makes it hard to detect.

NASA hopes to get a better fix on black carbon around the globe when it launches the Glory satellite next year. A passive aerosol sensor will scan the atmosphere using seven wavelengths from visible light to short-wave-length infrared. It won’t be able to pinpoint the amount of black carbon at specific altitudes, but it should be able to measure the total concentration from the ground up with an accuracy of 3%, says the Goddard Institute’s Brian Cairns, who designed the instrument.

Other clues to black carbon’s influence are coming from deep below the surface of Greenland, where ice layers record how much soot wafted around the Arctic each year since before the industrial revolution. In 2007, Joe McConnell, a hydrologist at the Desert Research Institute in Reno, Nevada, measured black-carbon concentrations within an ice core from central Greenland dating back to 1788. He found a sevenfold increase between 1850 and about 1910, particularly in winter. Soot levels fell after that until about 1950 and then largely remained close to pre-industrial levels⁸. These data, and findings from a second Greenland core, seem to align fairly well with estimates of historical emissions in North America, a likely source of the soot.

Stopping the soot



Some Indian cooking methods are contributing to atmospheric soot levels.

Last month the eight-nation Arctic Council appointed a task force to look at ways to reduce black carbon and other key pollutants responsible for rapid Arctic warming. It was a sign that the scientists pushing the link between black carbon and climate (see main article) are getting their message through to governments. The question faced by the council, and by policy-makers across the world, is what to do.

Black carbon, a primary component of soot, is a ubiquitous product of incomplete combustion, formed by natural forest fires, motor vehicles, coal plants and myriad other sources. Soot contains both black carbon and light-coloured particles that cool the planet; smoke produced by sources such as cooking stoves and diesel engines tends to be rich in darker particles. Reducing black-carbon emissions isn’t a technical problem — modern stoves and filters can do most of the work — so much as an issue of governance and resources.

“Black carbon is perhaps the biggest, fastest bite we can take out of the climate problem,” says Durwood Zaelke, who heads the Institute for Governance and Sustainable Development in Washington DC and has helped spearhead the movement internationally. “It needs, however, to be followed with aggressive regulatory action.”

Global soot emissions have been rising steadily since the mid-1800s, although in recent decades the source of emissions has shifted from industrialized to developing nations. Pinning down actual emissions is difficult, but Tami Bond, a researcher at the University of Illinois, Urbana-Champaign, estimates that diesel combustion and residential fuel use (from coal, wood and agricultural debris) each produce roughly one-quarter of the total; another 40% comes from wildfires and controlled agricultural burning; various industrial sources make up the remainder.

Industrialized nations could clean up fossil fuels further

and reduce agricultural emissions at home. But much of the focus will be on developing countries. The hope there is that current concerns over climate change will energize existing efforts to clean up diesel emissions and replace inefficient cooking stoves.

The precedent is there. China delivered roughly 150 million stoves to rural areas in the 1980s and early 1990s in an effort to reduce fuel use, says Kirk Smith, a rural energy expert at the University of California, Berkeley. Smith is working with local communities to encourage the use of locally produced, clean-burning biomass stoves, which reduce emissions of carbon dioxide, methane and other dangerous compounds. The impetus for the work has been to improve public health and reduce greenhouse-gas emissions, but the new attention on black carbon doesn’t hurt, says Smith. “It’s sort of the pollutant of the month and you need to take advantage of what’s on people’s minds.”

J.T.

G. JECAN/CORBIS

Taken at face value, it is difficult to match up the Greenland records with the contention that black carbon is now a major player in the Arctic. Arctic temperatures have surged in recent decades, when black-carbon levels have all but returned to historic levels.

McConnell cautions against reaching too strong a conclusion about black carbon on the basis of his two published cores. And he has already started analysing another pair of ice cores from Alaska. The amount of soot in snow depends both on how much is emitted and on how it gets transported. There is no way to differentiate changes in one from the other on the basis of just a few sites.

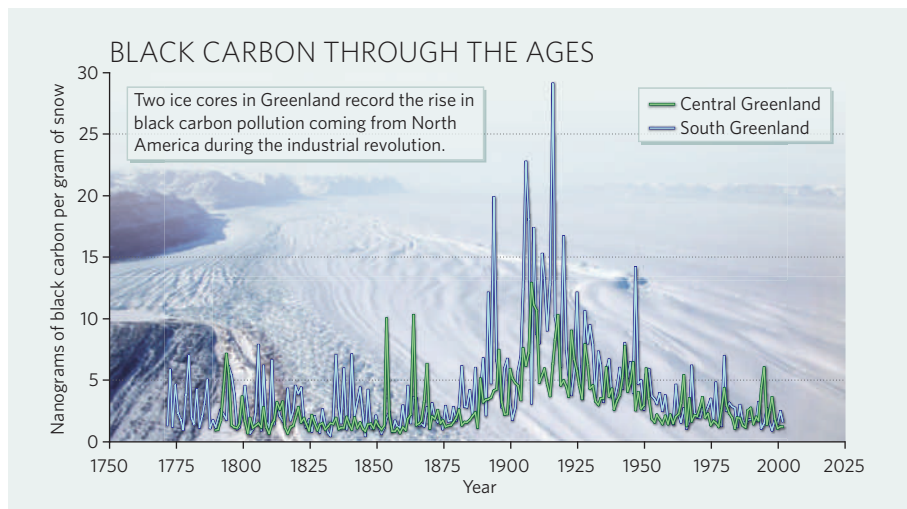
Primed to melt

Arctic circulations might have shifted at some point, or Greenland may simply not be representative of the entire Arctic. Variations on both arguments have been used to explain the apparent discrepancy. Another possibility is that the Arctic is more sensitive today than it used to be: decades of warming may have primed the climate system for early spring thaws.

"If you melt the snow just a few days earlier, that's quite a dramatic effect already," says Andreas Stohl, a researcher at the Norwegian Institute for Air Research in Kjeller who has been studying how black carbon gets into the Arctic. "The same is true for sea ice. It may be melting anyway, but black carbon can cause more melting and earlier melting. That has quite a big effect."

Last year Stohl led a project called POLARCAT, which involved using aircraft and satellites as part of an intensive mission that sampled Arctic aerosols. The project documented a number of smoke plumes from agricultural activities and open burning in Siberia. Such findings support data collected by Warren and his colleagues, suggesting that black carbon from fires — rather than industrial sources — has a dominant role during the melting season in the Arctic⁹.

Those results, which surprised some researchers, could help explain how reduced levels of black carbon today could nevertheless have a strong influence on temperatures. Agricultural fires rarely happen during the dark Arctic winter, when black carbon has little effect; they tend to occur during the spring and summer, when the dark soot particles are particularly effective at melting snow.



The story is different in southeast Asia, where China and India are in the midst of rapid development that combines industrial-scale fossil-fuel burning with extensive use of coal, wood and crop residues for home heating and cooking. The lowly cooking stove may contribute about 40% of the black-carbon pollution in China and about two-thirds of the total in places such as India, Pakistan and Bangladesh, says Ramanathan.

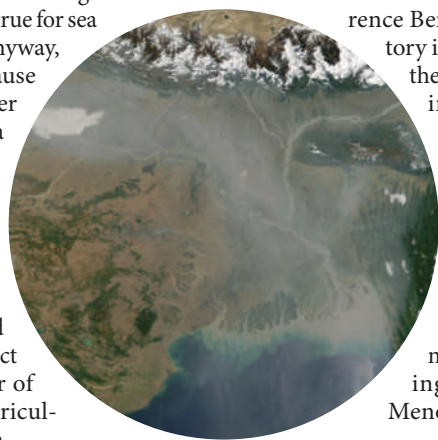
Surabi Menon, a researcher at Lawrence Berkeley National Laboratory in California, was among the first, with Hansen, to dig into the effects of black carbon in southeast Asia. Using general circulation climate models to test the effects of aerosols in 2002, they found that black carbon and other particles could help explain droughts in northern China and flooding in southern China¹⁰. Menon has recently finished some modelling indicating that black carbon could be responsible for

and cuts down on evaporation. At the same time, it cools the continent enough to weaken the monsoonal winds from the Indian Ocean. Overall, those changes contribute to glacial retreat by denying precipitation that would otherwise replenish the snowpack each year.

Ramanathan now heads a consortium involving scientists from countries such as India, China, Japan and South Korea that is trying to document effects in the Himalayas, the source of the region's fresh water. The team is even detecting strong signs of soot around Mount Everest.

"We're finding as much black carbon at altitudes of 3–6 kilometres as you are finding in downtown Los Angeles," he says, suggesting that the problem seems to grow the more he looks at it. Ramanathan is already convinced of the need to act on black carbon, although he realizes that effecting change in villages and cities across southeast Asia won't be easy. "Politically, of course, it's a tough issue," he says. "Thank goodness I'm not a politician."

Jeff Tollefson covers climate from Nature's office in Washington DC.



A thick haze lingers over the Ganges delta.

roughly one-third of the glacial retreat in the past two decades.

Ramanathan took things a step further in March 2006, leading a team that sent a trio of unmanned aerial vehicles to sample black-carbon levels above the Indian Ocean¹¹. Building on these results, he suggests that the Himalayas are hit twice: in addition to the direct effect on glaciers, black carbon and other aerosols also reduce snowfall by inhibiting the Indian monsoon². One effect is that black carbon absorbs sunlight high in the atmosphere over the Indian Ocean, which shades the ocean surface

1. Shindell, D. & Faluvegi, G. *Nature Geosci.* **2**, 294–300 (2009).
2. Ramanathan, V. & Carmichael, G. *Nature Geosci.* **1**, 221–227 (2008).
3. Clarke, A. D. & Noone, K. J. *Atmos. Environ.* **19**, 2045–2053 (1985).
4. Hansen, J., Sato, M., Ruedy, R., Lacis, A. & Oinas, V. *Proc. Natl Acad. Sci. USA* **97**, 9875–9880 (2000).
5. Jacobson, M. Z. *Nature* **409**, 695–697 (2001).
6. Forster, P. et al. *Climate Change 2007: The Physical Science Basis* (eds. Solomon, S. et al.) Ch. 2, 165 (Cambridge Univ. Press, 2007).
7. Myhre, G. *Science* doi:10.1126/science.1174461 (2009).
8. McConnell, J. R. et al. *Science* **317**, 1381–1384 (2007).
9. Hegg, D. A. et al. *Environ. Sci. Tech.* **43**, 4016–4021 (2009).
10. Menon, S., Hansen, J., Nazarenko, L. & Luo, Y. *Science* **297**, 2250–2253 (2002).
11. Ramanathan, V. et al. *Nature* **448**, 575–578 (2007).

See Editorial, page 12.

CORRESPONDENCE

Invitation to help compile an index of biodiversity in cities

SIR — In 2002 the World Summit on Sustainable Development assigned to the Convention on Biological Diversity (CBD) a target for 2010 of significantly reducing the rate of biodiversity loss. If we hope to chart positive trends in biodiversity conservation, then cities must now make a pivotal contribution.

For the first time in history, there are now more people living in cities than in rural areas; cities are likely to become larger, and the number of cities will increase. However, their contribution to the achievement of the CBD's objectives is difficult to measure today. There are tested environmental sustainability and performance indices for countries, but none is applicable to cities. There is therefore an urgent need to compute an aggregate of several indicators of biodiversity conservation for cities.

To enable cities to evaluate their biodiversity conservation efforts better, Singapore proposed that a self-assessment evaluation tool be developed (<http://tinyurl.com/q9aj75>). This will take the form of an index, devised by the secretariat of the CBD and the Global Partnership on Cities and Biodiversity, and will allow city officials to evaluate their efforts and help them to improve their management of biodiversity.

The index is being designed to be simple, scientifically credible, fair and objective. It focuses on three key components in cities: their indigenous biodiversity; the ecosystem services this provides; and the governance and management of this biodiversity. Balancing a robust number of indicators with manageability led to 26 indicators. Our task-force manual on the computation of the Singapore Index on Cities' Biodiversity will be posted on the CBD website (<http://tinyurl.com/lpmwtb>).

Most universities are based in

cities, so we invite scientists to contribute to this global effort by helping to collect relevant data for the computation of this index. The partnership then aims to table the index for adoption at the 10th meeting of the Conference of the Parties to the CBD in Nagoya, Japan, in October 2010. Data can be e-mailed to L. C.

Lena Chan National Parks Board, Singapore Botanic Gardens, 1 Cluny Road, Singapore 259569
e-mail: lena_chan@nparks.gov.sg
Ahmed Djoghlaif Convention on Biological Diversity, 413 R. St Jacques, Suite 800, Montreal H2Y 1N9, Canada

We must reverse the Bush legacy of stem-cell problems

SIR — Your Editorial 'Stem-cell clarity' (*Nature* **459**, 615–616; 2009) calls for reason in deliberations by the US National Institutes of Health (NIH) on public comments about proposed NIH guidelines for stem-cell research. We agree that rules barring the use of the 21 previously approved human embryonic stem-cell lines at the US National Stem Cell Bank (NSCB) are bad policy, and stand in the way of scientific progress. We trust that the NIH will permit use of approved and other lines derived by the US National Academies' standards.

The draft guidelines reignited a contentious issue that dominated the Bush years — the need for a diversity of lines for research and therapeutic use. In 2001, the NIH announced 78 registered lines. In the end, only 21 were available. Our research using data on cell-line shipments indicates that fewer federally approved lines are available than is generally believed, and only a handful of those are commonly used (J. McC., J. O.-S. and C.T. S. *Cell Stem Cell* **4**, 107–110; 2009).

No more than 18 cell lines have ever been available from NSCB. The 1,217 unique requests for materials between 1998 and 2008 are quite clustered.

Only three lines — H1, H7 and H9 — routinely made it to the bench. These three have quickly become experimental standards. Preliminary results from a systematic search of 534 peer-reviewed publications using human embryonic stem-cell lines during the same period show that H9 was used in 83.3% of these, H1 in 60.9% and H7 in 24.2%, and that 68.2% used one or more in combination with other NSCB lines. Also, derivatives of H9 will be transplanted in the world's first clinical trial for spinal injury.

Over time, researchers routinely discard ill-behaved or less useful lines. But our data raise serious questions about how best to calibrate the number and variety of a controversial research tool that is in short supply. Now that the NIH has made a tentative step towards a coherent national policy, the agency should take a pragmatic approach to the dual problems of diversity and fragmented ethical oversight that are the Bush administration's legacy. The field needs a repository containing an adequate number of high-quality, ethically derived, diverse lines. We must work to ensure availability and widespread use of diverse materials.

Every effort should be made to investigate the provenance of existing lines carefully and expeditiously. Local oversight committees must individually grapple with this time-consuming and exacting task; currently, they often repeat each other's efforts. To avoid redundancy and to speed the accession of new lines, we suggest the creation of a national clearing house specifically charged with certifying provenance. If there are indeed 700 lines worldwide (as the NIH hopes), then this is a necessary step to build a rich and diverse resource that can be used widely and efficiently.

Christopher Thomas Scott Program on Stem Cells in Society, Center for Biomedical Ethics, Stanford University, Stanford, California 94304, USA
e-mail: cscott@stanford.edu
Jason Owen-Smith Department of

Sociology and Organizational Studies Program, University of Michigan, Ann Arbor, Michigan 48109, USA
Jennifer McCormick Departments of Medicine and Health Sciences Research, Bioethics Research Program, Mayo Clinic, and College of Medicine, Rochester, Minnesota 55905, USA

The pleasure and importance of printed journals

SIR — I am shocked to read in *Nature News* online that the American Chemical Society intends to stop all personal subscriptions to its printed journals by 2010, and to start introducing major changes this year ('Chemistry publisher moving towards online-only journals' <http://tinyurl.com/llae53>).

The attractive printed versions of *Journal of the American Chemical Society*, *Journal of Organic Chemistry*, *Accounts of Chemical Research* and *Organic Letters* provide distinct advantages in letting me browse their content (during breakfast at home, for example) and readily take in information, without the lengthy opening of individual web pages, article by article.

But I also find this decision to stop the print journals disturbing in my capacity as a board member of the German chemical society, the GDCh, and as head of the editorial board of the journal *Angewandte Chemie*. I believe that high-quality journals such as *Nature* and *Science* and, in chemistry, *Angewandte Chemie* and *Journal of the American Chemical Society* should continue to appear in all their published formats, including print. Otherwise, there is a risk that the quality of these prestigious journals could gradually decline to the standard of many of today's web-only journals.

François Diederich Laboratorium fuer Organische Chemie, Department of Chemistry and Applied Biosciences, ETH-Zürich, Hönggerberg HCI G313, 8093 Zürich, Switzerland
email: diederich@org.chem.ethz.ch

BOOKS & ARTS

When DNA goes on trial

The science of DNA profiling is firm, but the way that the adversarial justice system interprets probability can cause controversy, argues **Peter Gill**.

At the heart of *Truth Machine* lies the fundamental debate about the evaluation of probabilistic risk. The book examines the use of DNA tests in legal proceedings and the development of DNA-profiling methods in the United Kingdom and the United States. Used in British courts for more than 20 years, DNA profiling has spread worldwide. Large national databases of DNA samples are held by many countries; Britain's database alone hosts more than 4 million samples.

Inevitably, questions arise about the robustness of DNA-profiling systems and how frequently errors will occur. However, this draws us into the long-running scientific debate between Bayesian and frequentist camps over how probability should be reasoned. Bayesians include prior knowledge in evaluating probabilities, which they see as quantifying degrees of belief in a proposition. Frequentists derive probabilities from statistical distributions, and complain that the Bayesian prior probabilities are *ad hoc*.

Science relies on peer review to decide whether theories should be accepted. However, this process does not fit well with an adversarial system of justice. In what is ultimately a competition between lawyers representing the defence and the prosecution, each side in an adversarial court case relies on opinion-based evidence given by a handful of expert witnesses.

The authors bring a breadth of experience: Michael Lynch and Simon Cole in science and technology studies, Ruth McNally in economic and social aspects of genomics, and Kathleen Jordan in sociology. To demonstrate the controversies surrounding DNA profiling, they focus on landmark appeal-court decisions.

Two cases from the UK courts of appeal are analysed in detail. In the first, *The Queen v. Deen* in 1994, a jury was found to have been misled by incorrect wording of probability in the original trial. Where a DNA random-match probability of 1 in 3 million had been



Many countries hold large databases of DNA profiles.

reported, the counsel for the prosecution remarked, "So the likelihood of this being any other man but Andrew Deen is 1 in 3 million?" The expert agreed — but this statement was incorrect. The reasoning contained a logical flaw that confused the rarity of the DNA profile with the probability of innocence. This error

— that of the 'transposed conditional' — is well recognized by statisticians.

In the second appeal-court ruling, *The Queen v. Adams* in 1996, the defence

used Bayes's theorem to convert the prosecution's statistic of a 1-in-200-million chance of random DNA match into a lower probability of guilt. The calculation involved setting and combining odds for the probability of a DNA match with subjective prior 'facts' — such as that a local man would have committed the

offence and that the victim would not have identified the defendant. The resulting estimate was given as 1 chance in 55 that Denis Adams was innocent.

Both defence and prosecution scientists in this case agreed on the use of Bayes's theorem. If the prosecution scientist had been a frequentist and had avoided the use of prior probabilities, then a different debate could have ensued. Thus, court presentations based on the opinions of experts do not necessarily reflect scientific consensus. The problem is exacerbated because some lawyers, motivated to win the case, may deliberately pick scientists who support particular views.

Paradoxically, in the *Adams* appeal, the court ruled the use of Bayes's theorem to be inadmissible because the mathematical reasoning was too difficult for a jury to follow. The scientific approach of combining probabilities was thus rejected in favour of an intuitive approach. Controversy can therefore arise even when there is agreement on the science.

Experts sometimes make mistakes in court. For example, in a recent miscarriage of justice, a mother was falsely accused of murder as a result of a misdiagnosis of a natural cot death, based on faulty statistics. A scientist acting for the prosecution wrongly assumed that the chance of two deaths in the same family was remote, under the assumption that they were independent events. Ideally, a scientist for the defence would have challenged this statistic at the trial. That this failed to happen implies a failure of the adversarial system. The authors put it thus: "Junk science is a legal problem, not a scientific one. It is cultivated by the adversarial nature of legal proceedings and it depends on the difficulty many laypeople have in evaluating technical arguments."

The dangers for scientist experts in court are implicit in the adversarial system. Evaluative thinking is not encouraged in the binary courtroom, which seeks yes or no answers. Scientists cannot indulge in open debate, but can only respond to the questions put to them by the lawyers. If the wrong questions are asked, the situation is difficult to rectify. If one team lacks the necessary experience, justice may suffer as

Truth Machine: The Contentious History of DNA Fingerprinting

by Michael Lynch, Simon A. Cole, Ruth McNally and Kathleen Jordan
University of Chicago Press: 2009.
416 pp. \$37.50

a result, and its slow-turning wheels mean that errors can take years to correct. The human cost can be great.

Even so, there has never been a miscarriage of justice in the United Kingdom that was attributed to evidence from DNA profiling. By contrast, miscarriages of justice have been uncovered by the later application of DNA technology. In the two appeals described, it is important to note that both Deen and Adams were sent for retrial and were eventually convicted of the crimes of which they had been charged. Only the appeals were controversial; the initial guilty verdicts were upheld.

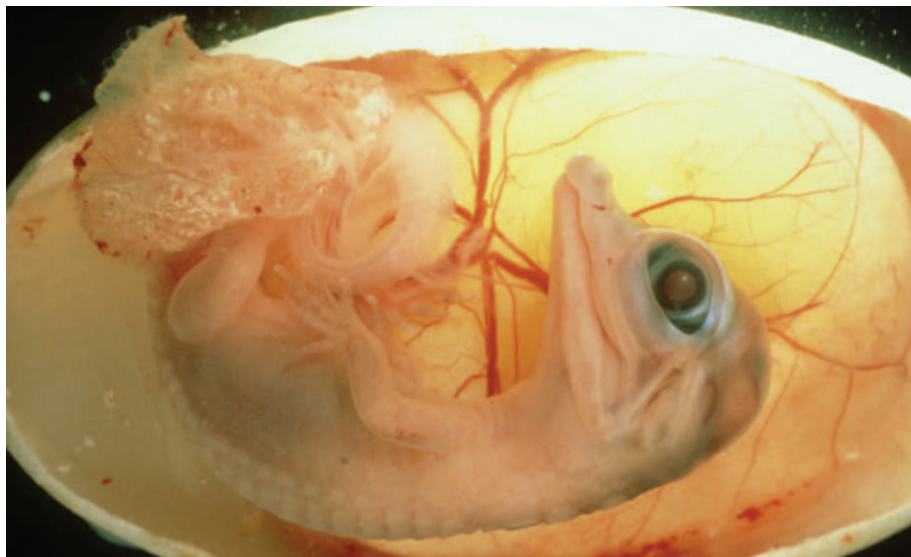
Truth Machine concludes with a section on fingerprinting — of the dermal kind. Fingerprint examiners identify ‘friction ridge details’, or marks, at particular positions within the image. If the relative positions of sufficient marks are consistent with the reference sample from a known person, then the fingerprint is deemed to match. Statistics are not used because fingerprints are considered to be unique: geneticist Francis Galton estimated the chance of a random match to be 1 in 64 billion.

However, there is no reason to preclude probabilistic estimation, for example in assessing partial fingerprints. Models exist for doing so, but they require knowledge of the rarity of various marks. Surprisingly, as Lynch and his co-authors point out, such population studies have not yet been done. The challenges are different from those of DNA profiles because a set of dermal fingerprint marks may not be definitive: prints from the same finger may differ simply because of distortion or substrate variations.

Fingerprinting has entered the public psyche as being synonymous with unique identification, and such ideas are difficult to shift once lodged. Applying the same ‘fingerprint’ phrase to DNA profiles, as in this book’s title, implies that they too are unique — but they are not. The term ‘DNA fingerprint’ should be avoided.

Truth Machine is an interesting read — it illustrates that the controversy of DNA profiling is rooted not in the science, but mainly in the restrictions of the adversarial system. A discussion of how science is applied in jurisdictions that use the inquisitorial system, in countries other than the United States and the United Kingdom, would also be welcome. ■

Peter Gill is a senior lecturer in chemistry at the University of Strathclyde, Glasgow, UK, and professor of legal medicine at the University of Oslo, Norway. He was principal scientist for the UK Forensic Science Service from 1982 until 2008. e-mail: peter.gill@strath.ac.uk



N. BROMHALL/PHOTOLIBRARY.COM

Evolutionary embryos

The Origin of Individuals

by Jean-Jacques Kupiec

World Scientific Publishing: 2009. 276 pp.

\$72, £54

A central question in biology is how multicellular organisms develop from a single cell and how development is controlled. The standard view is that the process is deterministic, following directives governed by information located in the genome. Molecular biologist Jean-Jacques Kupiec contradicts this picture. In the fascinating *The Origin of Individuals* he argues that there is no plan, pre-pattern or program encoded in the genome. Instead, cell differentiation and development include a random element.

In the standard view, development is controlled by the binding of protein transcription factors to promoters that activate genes in the DNA. These genes in turn generate proteins, including other transcription factors and signalling molecules that activate yet more genes. A cascade of gene activation results, leading to the proliferation and differentiation of cells that ultimately generates the organism. Assuming that molecular interactions and gene activation are predictable, the development process should be deterministic.

Kupiec argues that this picture is wrong. Gene activation is inherently stochastic, he says, and, therefore, cell differentiation must also be stochastic. Transcription factors attach with certain probabilities to many binding sites in gene promoters, implying that chance plays a dominant role in gene activation and expression. Similarly, cell signalling pathways,

and thereby cell interactions, are stochastic, as proteins may bind promiscuously to many partners with various odds. Many interactions and pathways are possible.

As a result of this underlying unpredictability, Kupiec claims, stochastic cellular actions such as cell growth, cell differentiation and cell death must be constrained somehow to ensure that the correct sequence of development occurs. Otherwise, a fertilized egg could grow into any organism.

The problem that ordered biological structures are rarer than the many possible random states led the physicist Erwin Schrödinger in his 1944 book *What is Life?* to contrast the science of life with physics: in statistical thermodynamics, macroscopic order is generated from disorder, whereas for life to develop, order must be generated from order. Schrödinger introduced the notion of a code script — analogous to a program — contained in the chromosomes, which acts as both plan and operative factor to prevent disorder by guiding the development process.

Kupiec disagrees with the idea of programs. Because of the stochastic nature of protein interaction and gene expression, he says, there can be no Aristotelian form or program to give order to life and ward off entropic chaos and death.

But without a code to follow, how can a particular organism develop from a single cell? Kupiec’s radical solution is to apply Darwin’s theory of evolution. Put simply, evolution requires two processes — variation and selection. An organism’s offspring each varies slightly; natural selection picks out those that

survive to generate more such organisms, again with their own subtle variations. In the development of an organism the stochastic nature of gene activation and protein interactions permits a vast array of possible developmental outcomes. Darwinian selection, Kupiec argues, constrains development so as to consistently form a particular organism. The local environment of the cell is the selecting agent, choosing which cells survive, differentiate, divide or die. He demonstrates his concept through computer simulations that generate simple patterns of two cell types. Each cell reacts with some probability to its local conditions to determine its next state.

In setting up local environment and metabolic interactions, cells must, however, use signalling protocols or programs that specify how the cells react — even if they involve probabilities. Yet Kupiec claims that because of stochastic protein interactions such programs cannot exist. But even if we allow simple reactive protocols to control any cell's reaction to its local environment, such strategies can produce only simple patterns. They cannot achieve the complex structures and functions generated in many multicellular organisms. Such reactive strategies can, at best, pass on information to determine the cell's next state.

Thus, in Kupiec's proposal, the local environment must host the constraining information necessary to form an organism. But it is not clear how this information could be stored and conveyed. In his view, the environment

functions like a complex, external 'homunculus', magically controlling embryonic development at every step. Kupiec also fails to explain why differentiated cells remain stable if gene activation is stochastic, or why cellular control strategies and protocols exist at all.

Kupiec's version of a Darwinian-like cell-selection process needs to be robust and invariant. It must be more restrictive than typical Darwinian selection, which permits the formation of a diverse array of organisms and species to form. It must explain why a particular embryo forms, not just any embryo. It must account for the similarity of identical twins; the precision with which the left side mirrors the right in bilaterally symmetrical organisms; and why a mouse differs from a horse or a potato. A further issue is that even if there is local molecular randomness, it need not be passed on to the cell or to the developmental control architecture of the organism. Organisms consistently pass through the same stages during development, irrespective of minor variations in their local and maternal environments.

By treating the genome only as a generator of proteins, Kupiec adopts an implicitly reductionist view of development. But organisms of many species have virtually identical protein structures, yet their control architecture is vastly different, just as a house and a skyscraper can be made of the same parts. Every complex structure needs specific control information to develop, and the only reasonable source of that information is the genome, not some blind local

evolutionary selection process. The genome and cell cooperate by means of an epigenetic interpretation system by which control information in the genome is interpreted and executed by the cell. Thus the genome encodes more than protein building-blocks — it contains a hidden control code. Such a feature could explain the vast non-coding regions in the genome; Kupiec prefers to think of these regions as mere space fillers determining gene-activation probabilities.

Kupiec's model also fails to account for global and temporal relationships. Local information is not powerful enough to generate global relationships in an organism — all the more so if it is probabilistic. Because the growth process of an embryo is ordered in time, directives from the genome must be linked to form control networks. The architecture of an organism is complex both spatially and temporally.

Kupiec is a very successful writer, deservedly so. I enthusiastically recommend this courageous book with its iconoclastic viewpoint. *The Origin of Individuals* is a pleasure to read, presenting complex ideas clearly and effectively. Whether one agrees with him or not, Kupiec's is an inspiring work, a thought-provoking rollercoaster ride through the history of ideas about the origins of ontogeny.

Eric Werner is in the Department of Physiology, Anatomy and Genetics, and the Computing Laboratory, University of Oxford, South Parks Road, Oxford OX1 3QX, UK.
e-mail: eric.werner@dpag.ox.ac.uk

Stuffed spectacular

Extreme Mammals: The Biggest, Smallest, and Most Amazing Mammals of All Time

American Museum of Natural History, New York City

Until 3 January 2010

Roll up, roll up! See the giant *Indricotherium*, a plant-eating mammal from Mongolia that weighed as much as four adult African elephants! Gaze at the tiny bumblebee bat, which can hover in place like a hummingbird! Marvel at the wide-eyed sugar gliders, sailing nimbly through the branches! All can be seen in *Extreme Mammals*, the latest exhibition at the American Museum of Natural History that showcases the largest, smallest, toothiest, brainiest, prickliest, slowest, fastest and lustiest mammals on the planet.

Although its title suggests a circus, the show lacks the pizzazz of a real one. Except for the

sugar gliders and the human visitors, none of the mammals in the exhibition is moving or breathing: all are models, skeletons or stuffed.

The museum has more than a million stuffed animals in its collection, and never misses an opportunity to haul them out for display, preferably in one of its beloved dioramas.

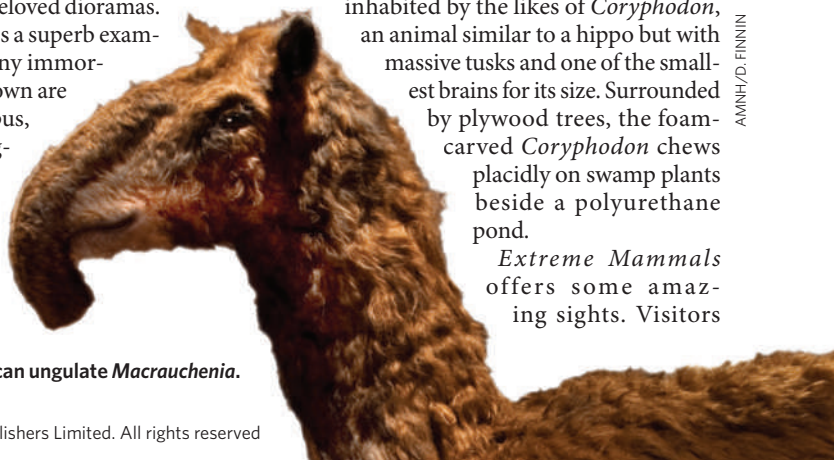
Extreme Mammals is a superb example. Among the many immortalized creatures shown are a duck-billed platypus, a fluffy koala, a long-tailed howler monkey, a spectacled bear and a striped Tasmanian wolf or thylacine, which went extinct in

1936 when the last of its kind died in an Australian zoo.

One diorama depicts Ellesmere Island — now an expanse of frozen tundra some 1,000 kilometres from the North Pole — when it was a warm paradise 50 million years ago, inhabited by the likes of *Coryphodon*, an animal similar to a hippo but with massive tusks and one of the smallest brains for its size. Surrounded by plywood trees, the foam-carved *Coryphodon* chews placidly on swamp plants beside a polyurethane pond.

Extreme Mammals offers some amazing sights. Visitors

Extinct: South American ungulate *Macrauchenia*.



AMNH/D. FINNIN



Extant: the duck-billed platypus.

enter the exhibition by walking under the belly of a model of a 34-million-year-old adult *Indriacotherium* — at 18 tonnes, it is the largest land mammal ever found. They are then treated to

a stupendous array of mammalian headgear, such as a cast of a 2.5-metre-long, bendable tusk of the narwhal; some 2-metre-wide moose antlers; the giant fossil jaw of the 14-million-year-old extinct *Platybelodon grangeri* — an elephant relative that may have used its platter-like teeth to scoop up swamp grasses; and the curved upper canines of the Indonesian male babirusa pig that stick upwards through its skull.

The exhibition includes plenty of basic biology: all mammals have three bones in the middle ear, some sort of hair, large brains for their body size and females that produce milk for their young. The show also offers a plethora of weird facts: the Shaw's jird, a small African desert rodent, can mate 224 times in 2 hours; the aardvark, or 'earth pig', can dig for and eat

40,000 termites in a night; the bony, armoured shell of a glyptodont — an extinct South American armadillo relative that grew up to 3 metres long — could weigh more than 500 kilograms. A model easily fits three children inside.

A quarter of all living mammal species are now threatened with extinction. Among those that are endangered are some species that have only recently been found, such as the shy saola, *Pseudoryx nghetinhensis*, a beautiful horned ox discovered in 1992 in the wet evergreen forests of Vietnam's Annamite Mountains that is now threatened by road construction and hunting.

And the striped rabbit, *Nesolagus timminsi*, was discovered in 1999 on sale at a food market near the border of Laos and Vietnam. A taxidermized specimen sits at the end of the exhibition and seems a fitting symbol of the fate of so many of its threatened mammal brethren. Unless we protect them, the only place we might be able to see these fascinating animals in future is in a museum, stuffed. ■

Josie Glausiusz is a writer based in New York. e-mail: jg@planetjosie.net

Evolution's influence on art nouveau

Emile Gallé, *Nature and Symbolism: Influences from Japan*

Georges de La Tour Departmental Museum, Vic-sur-Seille, Moselle, France
Until 30 August 2009

Characterized by sinuous shapes and subtle colours, the glass vases, bowls and other objects made by the nineteenth-century French artist-designer Emile Gallé and his factory are still highly regarded. But his interest in botany and evolution is less well known. An exhibition this summer in Moselle, northeastern France, explores how Gallé's work was influenced by nature and by Japanese art and design. The show is co-curated by scientist François Le Tacon of the French National Institute for Agronomic Research in Nancy, France.

Gallé was one of the founders of art nouveau, an influential art and design movement. He learnt glass-making skills as an apprentice, but after taking over his father's factory in Nancy in 1875, he created designs that were made by its artisan employees. He exploited the sensual properties of glass, using acid etching to form opaque vessels with layered colours and shaped surfaces. His organic designs did not simply borrow from nature — they expressed contemporary thought and politics. Gallé was aware of Dar-

win's work by 1877 and owned a copy of Ernst Haeckel's *Art Forms in Nature* (1899–1904).

Plant, insect and animal motifs were derived from his careful observations, but also held deeper meanings. "Beetles symbolized industriousness; the thistle symbolized Nancy, Lorraine and separation from Germany; the rose symbolized France and the lover," note Jennifer Hawkins Opie in *Art Nouveau 1890–1914* (V&A Publications, 2000). Gallé was also inspired by aquatic flora and fauna, as

shown in nine works incorporating themes such as undulating strands of seaweed and deep sea colours.

Japanese artwork displayed in Europe at the end of the nineteenth century captivated many western artists and designers. Gallé himself owned woodblock prints by Hokusai and others, and he befriended the Japanese botanist Hokkai Takashina after meeting him at a horticultural exhibition in Nancy in 1886. They were both interested in chrysanthemums, a potent symbol in Japan, which Gallé used as a decorative motif. The internally cracked and coloured glass used by Gallé and his artisans, although made in France, was inspired by Japanese watercolours and lacquerware, as well as carved rock crystal and jade from China.

From 1886 until his death in 1904, Gallé investigated evolutionary mechanisms in botany, an interest covered in the exhibition. Displayed, for example, are plates illustrating the orchid *Aceras hircina*, from a paper on polymorphisms in orchids local to Lorraine that Gallé presented at an international botanical congress in Paris in 1900. They underscore how Gallé's biological exactitude and interest in symbolism generated his incomparable designs. ■

Colin Martin is a writer based in London.



Emile Gallé vase with etched dragonfly.

DEVELOPMENTAL BIOLOGY

A cellular view of regeneration

Alejandro Sánchez Alvarado

How the salamander regrows an entire limb after injury has flummoxed the wisest of scientists. A closer look at the cells involved in limb regeneration shows that remembering past origins may be crucial for this feat.

When a salamander loses an appendage, such as a limb, a remarkable series of events unfolds: a clump of cells forms at the site of the injury, and this deceptively simple structure, known as a blastema, regenerates the missing body parts. Skin, muscle, bone, blood vessels and neurons all arise from this collection of nondescript cells through patterning and self-assembly. So complete is the repair that it is difficult — if not impossible — to tell that the animal has been injured. It has long been believed that the cells responsible for this repair process are pluripotent, capable of giving rise to all tissue types. On page 60 of this issue, Kragl *et al.*¹ describe a novel cell-tracking technique that reveals some surprising findings about the origins and fates of cells involved in salamander limb regeneration.

Far from being a mere curiosity confined to a few species, regeneration is a phenomenon that is broadly but unevenly distributed among the animal and plant kingdoms. Body-part regeneration is found in most animal phyla thus far examined, indicating that this biological attribute may actually be an ancient evolutionary invention². Yet how new body parts arise from old ones has been a riddle within a mystery dating back to antiquity. Regeneration in animals and plants has astounded successive generations of great thinkers, including Aristotle, Lazzaro Spallanzani, Voltaire, Charles Darwin and the biologist Thomas Hunt Morgan.

Persistent efforts by current researchers in the field^{3–7} have begun to reveal crucial insights into this biological phenomenon. Nevertheless, much remains to be understood. Key to elucidating the mechanism of regeneration is defining the origins, lineages and fates of the cells that mount a regenerative response after injury. Because the cells that collect in the blastema look identical, it has long been thought that they have dedifferentiated from tissues near to the plane of amputation into a single population of pluripotent cells⁵. However, it is quite possible that blastema cells involved in regeneration have instead entered a migratory or proliferative state without changing their tissue identity or their lineage potential. Without robust methods to track the fate of cells from

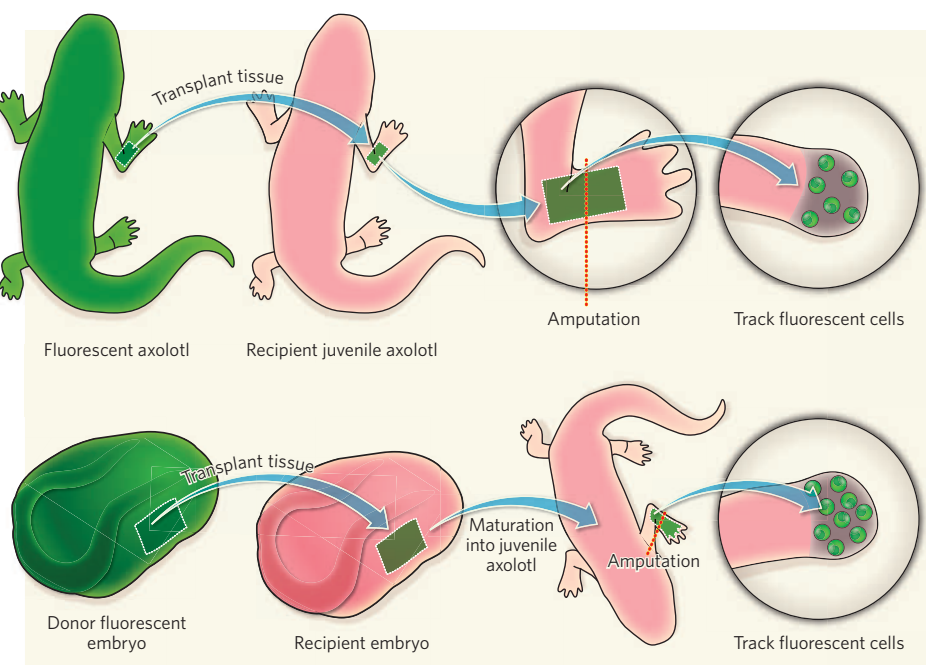


Figure 1 | Cell-tracking techniques used by Kragl and colleagues¹. Tissue from axolotls expressing a transgene encoding the green fluorescent protein (GFP) molecule is transplanted into juvenile non-transgenic axolotls (upper panel). The transplanted tissue is included in the amputation site, and the fluorescently labelled cells are followed during limb regeneration. Alternatively, specific embryonic tissue is transplanted from GFP-labelled axolotl embryos into non-transgenic embryos (lower panel), which mature into juvenile axolotls with a tissue-specific fluorescent marker. These glowing cells can also be tracked after amputation.

the time of amputation to their differentiation during regeneration, definitive conclusions about the nature of the regenerative cells are difficult to reach.

Kragl *et al.*¹ investigate limb regeneration in the axolotl (*Ambystoma mexicanum*), a salamander endemic to Mexico and a favourite model system for studying vertebrate development. The authors use transgenic technology to introduce DNA coding for a green fluorescent protein molecule into the genome of axolotl cells. Once marked out by its permanent, glowing, green fluorescent 'tattoo', a specific tissue type (for instance, muscle or skin) can be transplanted into a host animal and followed in time and space after the host tissues have been amputated (Fig. 1).

Kragl *et al.* find that the cells that regenerate the amputated body parts in the axolotl

are not pluripotent. Instead, they respect their developmental origins and restrict their differentiation potential accordingly (Fig. 2, overleaf). For instance, labelled muscle cells at the site of amputation differentiate only into muscle and do not differentiate into other tissue types in the regenerating limb. The authors observed similar lineage restriction for epidermal cells, cartilage cells and Schwann cells (a type of cell that ensheathes nerve axons). Dermal cells are the sole exception — they contribute cells to both the dermis and the skeleton of the regenerating limb. These data strongly suggest that cells tasked with regeneration retain a memory of their previous identity and, in some cases, of their position in the limb.

The use of transgenic methodologies to map cell behaviour and population dynamics during vertebrate regeneration¹ is without

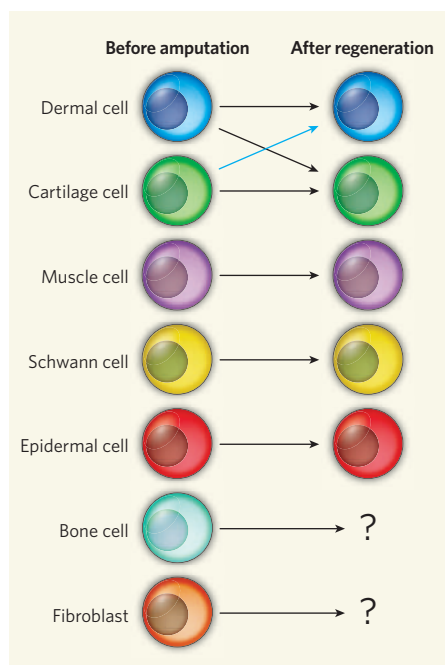


Figure 2 | Lineages are respected during axolotl limb regeneration. Kragl *et al.*¹ find that, with the exception of cells in the dermis, the dedifferentiated cells contributing to limb regeneration largely remain lineage restricted. Because the experiments were carried out in juveniles, in which the bones have not fully ossified, the fate of bone cells after amputation is unknown. Similarly, owing to the paucity of markers, the fate of connective-tissue fibroblasts contributing to limb regeneration remains undefined. The blue arrow indicates that cartilage cells can sometimes contribute to the dermis.

doubt a significant technical accomplishment that adds a new dimension to our understanding of regeneration. Like all important work, it also leaves us with questions that will probably occupy researchers for the next few years. One question concerns the

contribution of connective-tissue fibroblast cells to the regenerating limb. Fibroblasts are relatively abundant in the limb and are known to contribute significantly to regenerative activities in salamanders⁸. Are these cells lineage restricted, or can they give rise to other types of tissue? Because there are no reliable markers for identifying connective-tissue fibroblasts yet, Kragl and colleagues could not definitively answer this particularly interesting question.

Is lineage restriction in regenerating cells unique to the axolotl, or can these principles be applied to other commonly studied species of salamander? The animals used for these studies were juveniles, with a skeletal system made up of cartilage rather than bone. Most other studies in salamanders have been done in adult newts, which have ossified skeletons. Also, there are well-documented differences between the regenerative properties of newts and axolotls. For instance, whereas newts can regenerate the lens of the eye after its removal, the axolotl cannot⁹. These and other issues will have to be resolved before the biological significance of Kragl and colleagues' findings¹ can be fully appreciated.

Alejandro Sánchez Alvarado is in the Department of Neurobiology and Anatomy, Howard Hughes Medical Institute, University of Utah School of Medicine, Salt Lake City, Utah 84132, USA. e-mail: sanchez@neuro.utah.edu

1. Kragl, M. *et al.* *Nature* **460**, 60–65 (2009).
2. Birnbaum, K. D. & Sánchez Alvarado, A. *Cell* **132**, 697–710 (2008).
3. Grogg, M. W. *et al.* *Nature* **438**, 858–862 (2005).
4. Gurley, K. A., Rink, J. C. & Sánchez Alvarado, A. *Science* **319**, 323–327 (2008).
5. Kumar, A., Godwin, J. W., Gates, P. B., Garza-Garcia, A. A. & Brockes, J. P. *Science* **318**, 772–777 (2007).
6. Morrison, J. I., Löff, S., He, P. & Simon, A. *J. Cell Biol.* **172**, 433–440 (2006).
7. Reddien, P. W. *et al.* *Dev. Cell* **8**, 635–649 (2005).
8. Bryant, S. V., Endo, T. & Gardiner, D. M. *Int. J. Dev. Biol.* **46**, 887–896 (2002).
9. Tsonis, P. A., Madhavan, M., Tancous, E. E. & Del Rio-Tsonis, K. *Int. J. Dev. Biol.* **48**, 975–980 (2004).

Over the same interval, levels of atmospheric CO₂ have fallen from around 1,400 p.p.m. at the end of the Eocene to possibly as low as 200 p.p.m. during the Miocene³ — the geological period between around 24 million and 5 million years ago.

This long-term history of atmospheric CO₂ is the result of the interplay between several processes. The degassing of the Earth through magmatic activity (for instance volcanic eruptions) is the main source of CO₂, and the dissolution of continental rocks captures atmospheric CO₂, which is eventually stored as marine carbonate sediments⁴. The efficiency of the dissolution process — chemical weathering — is heavily dependent on climate, but also depends on vegetation and physical erosion. The last two parameters boost CO₂ uptake by rock weathering. In particular, land plants promote rock dissolution through the mechanical action of roots, and by acidifying the water in contact with rocks⁵. Acidification occurs through the release of organic acids and the large-scale accumulation of CO₂ in soil through root respiration. Removing plants, particularly trees, may strongly decrease the dissolution rate of rocks and the ability of this process to consume atmospheric CO₂.

In their paper, Pagani and colleagues¹ consider the potential role of the rise of many mountainous regions (orogens) over the past 40 million years, especially in the warm and humid low-latitude areas. In these mountain ranges, physical erosion would break down rocks and expose them to intense chemical weathering. The uptake of atmospheric CO₂ would consequently increase, as indicated by the levels of CO₂ measured, which could have declined to the lowest levels since multicellular life evolved on Earth some 500 million years ago.

But what could stop this CO₂ uptake pump? Degassing through magmatic activity was probably declining at the same time (at best it remained constant), and tectonic activity accelerated mountain uplift over the past 24 million years. According to this line of evidence, CO₂ levels should have plunged to below 200 p.p.m., with ice ultimately covering large surfaces of the Earth as a consequence. But that was not the case. Earth even experienced a warm spell between 18 million and 14 million years ago².

Pagani *et al.*¹ propose an exciting hypothesis to explain why, 24 million years ago, CO₂ might have levelled off at about 200 p.p.m., and then stuck there. They suggest that, when CO₂ levels became too low, forests became starved and were progressively replaced by grasslands, particularly in the low-latitude orogens. Grasslands exert a much less vigorous effect on rocks than do trees. In consequence, runs the thinking, CO₂ consumption due to weathering declined because of changing terrestrial ecosystems, which in turn stabilized atmospheric CO₂ at around 200 p.p.m.

Overall, the authors' model provides an elegant twist on several ideas about the Earth system that emphasize the role of vegetation

BIOGEOCHEMISTRY

Climatic plant power

Yves Goddérès and Yannick Donnadieu

Levels of atmospheric carbon dioxide constrain vegetation types and thus also non-biological uptake during rock weathering. That's the reasoning used to explain why CO₂ levels did not fall below a certain point in the Miocene.

The world is currently at risk of overheating in response to all the carbon dioxide being pumped into the atmosphere from the use of fossil fuels: the current atmospheric concentration of CO₂ is about 385 parts per million (p.p.m.), compared with a 'pre-industrial' level of around 280 p.p.m. But overheating is an atypical menace in the recent history of the Earth. Over most of the past 24 million years, it was the possibility of cooling that posed the

main threat to life. Cooling, however, did not reach the levels of severity that might have been expected, and on page 85 of this issue Pagani *et al.*¹ put forward a thought-provoking case as to why that was so.

Since the end of the Eocene, around 40 million years ago, Earth's climate has been naturally getting colder. In temporal terms, the cooling has sometimes occurred in discrete steps, sometimes as a long-term trend².

in dynamically regulating and fixing the lower limit of atmospheric CO₂. But it also raises contentious issues.

First, in the model¹, forest starvation is triggered by the low level of atmospheric CO₂, and by elevated temperature. But do proxy estimates of conditions at that time confirm this paradoxical combination? Proxy measurements of CO₂ levels include marine carbonate boron isotopes⁶, carbon-isotope values of alkenones produced by oceanic algae³ and the density of stomata — a measure of gas exchange — in fossil leaves⁷. Unlike the geochemical proxy records^{3,6}, the more recent estimates based on the stomatal index⁷ depict a highly variable CO₂ trend over the Miocene (in good agreement with climatic fluctuations), rather than a CO₂ level stuck at 200 p.p.m. Furthermore, the estimates show that CO₂ concentrations are above the forest-starvation level most of the time, oscillating between 300 and 500 p.p.m.

Second, in their model Pagani *et al.* assume that rock weathering generated by mountain uplift would have continuously consumed atmospheric CO₂ until it reached the forest-starvation level. But there is evidence that the extra consumption of CO₂ due to the Himalayan uplift, the most important orogeny of the recent past, occurred mainly through the burial of organic matter in the Bengal fan, and not through rock weathering^{8,9}. In addition, the tectonic history of the past 24 million years is still subject to debate, and the timing of the uplift of the main mountain ranges, such as the Himalaya and Andes, is far from fully constrained¹⁰.

Finally, the link between weathering and continental vegetation is well recognized. But it is complex. Apart from acidifying water and mechanical effects, land plants also control the hydrology of soils. In humid tropical environments, about 70% of the rainfall is absorbed by land plants and then evaporates through their leaves. This effect should inhibit weathering reactions by limiting the amount of water available for rock dissolution. Also, in equatorial uplifted areas, intense erosion occurs through landslides triggered by heavy rainfall¹¹. These landslides bring fresh rock material in contact with water by removing the soil mantle, promoting weathering and CO₂ consumption. The role of vegetation cover in these systems might not be as significant as Pagani *et al.* suggest.

The authors themselves acknowledge some of these limitations, and all in all have put forward a bold and provocative hypothesis. But accounting for all of the processes and constraints involved is probably beyond the capabilities of the first-order global models that Pagani *et al.* used, and more-complex and process-based modelling^{12,13} will be required to test their conclusions. Whatever the outcome, that should prove to be a fruitful exercise for carbon-cycle modellers intent on understanding the processes that drove climate and CO₂ oscillations during the Miocene. ■

Yves Godd  ris is at the LMTG-Observatoire Midi-Pyr  n  es, CNRS, Universit   de Toulouse III, Toulouse F-31400, France. Yannick Donnadi  u is at LSCE, CNRS-CEA, Gif-sur-Yvette F-91191, France.
e-mails: godderis@lmtg.obs-mip.fr;
yannick.donnadi  u@lsce.ipsl.fr

1. Pagani, M., Caldeira, K., Berner, R. & Beerling, D. J. *Nature* **460**, 85–88 (2009).
2. Zachos, J. C., Dickens, G. R. & Zeebe, R. E. *Nature* **451**, 279–283 (2008).
3. Pagani, M. *et al.* *Science* **309**, 600–603 (2005).
4. Walker, J. C. G., Hays, P. B. & Kasting, J. F.

5. Berner, R. A. *The Phanerozoic Carbon Cycle* (Oxford Univ. Press, 2004).
6. Pearson, P. N. & Palmer, M. R. *Nature* **406**, 695–699 (2000).
7. K  rschner, W. M., Kva  ek, Z. & Dilcher, D. L. *Proc. Natl Acad. Sci. USA* **105**, 449–453 (2008).
8. Galy, V. *et al.* *Nature* **450**, 407–410 (2007).
9. France-Lanord, C. & Derry, L. A. *Nature* **390**, 65–67 (1997).
10. Sempere, T., Hartley, A. & Roperch, P. *Science* **314**, 760 (2006).
11. Bhatt, M. P. & McDowell, W. H. *Water Resour. Res.* **43**, doi:10.1029/2007WR005915 (2007).
12. Donnadi  u, Y. *et al.* *Geochem. Geophys. Geosyst.* **7**, doi:10.1029/2006GC001278 (2006).
13. Donnadi  u, Y., Godd  ris, Y. & Bouttes, N. *Climate Past* **5**, 85–96 (2009).

IMMUNOLOGY

A metabolic switch to memory

Martin Prlic and Michael J. Bevan

Two therapeutic drugs have been found to enhance memory in immune cells called T cells, apparently by altering cellular metabolism. Are changes in T-cell metabolism the key to generating long-lived immune memory?

T lymphocytes respond to an acute infection with a massive burst of proliferation, generating effector T cells that counteract the pathogen. When the infection is cleared, most of these effector T cells die (the contraction phase of the immune response), but a minority lives on and changes into resting memory T cells that rapidly respond to future encounters with the same pathogen¹. In this issue, Pearce *et al.*² (page 103) and Araki *et al.*³ (page 108) report that two drugs, one used to control diabetes and the other to prevent organ-transplant rejection, markedly enhance memory T-cell development. Through their actions on major metabolic pathways in the cell, these drugs seem to promote the switch from growth to quiescent survival.

While investigating the role of a protein called TRAF6, which is a negative regulator of T-cell signalling, Pearce *et al.*² noted that, although T cells in which TRAF6 was knocked out mounted a normal effector response to a pathogen, they left behind few if any memory cells. The authors performed a microarray analysis comparing the genes expressed by normal and TRAF6-deficient T cells at the time they change from effector to memory cells. In a eureka moment, they realized that TRAF6-knockout T cells display defects in the expression of genes involved in several metabolic pathways, including the fatty-acid oxidation pathway, implying that a metabolic switch in T cells might be affecting memory-cell generation.

Pearce *et al.* followed up on this clue, and showed that the inability of TRAF6-deficient T cells to spawn long-lived memory T cells could be reversed by treatment with either the antidiabetes drug metformin or the immunosuppressant rapamycin. Both drugs are known

to affect cellular metabolism, and treatment with either drug not only restored the memory T-cell response in TRAF6-deficient cells, but also greatly enhanced memory T-cell formation in normal cells, resulting in a superior recall response to a second infection.

In an independent study, Araki *et al.*³ examined the effect of treating mice with rapamycin during the various phases of a T-cell response to viral infection. Giving rapamycin during the first 8 days after infection (the proliferative phase) markedly increased the number of memory T cells 5 weeks later. This was due to an enhanced commitment of effector T cells to become memory precursor cells. When the authors administered rapamycin during the contraction phase of the T-cell response (days 8–35 after infection), the number of memory T cells did not increase, but there was a speeding up of the conversion of effector T cells to long-lived memory T cells with superior recall ability.

Rapamycin inhibits mTOR ('mammalian target of rapamycin'), a protein-kinase enzyme found in at least two multiprotein complexes — mTORC1, which is rapamycin sensitive, and mTORC2, which is largely resistant to inhibition by rapamycin⁴. To pinpoint the cellular target of rapamycin in their studies, Araki *et al.*³ used RNA-interference knock-down techniques to demonstrate that the mTORC1 complex, acting intrinsically in T cells, regulates memory-cell differentiation.

So both rapamycin and metformin seem to enhance T-cell memory formation. But do both drugs affect the same pathway(s), are the pathways interconnected, or do two different mechanisms lead to a similar outcome? Metformin activates AMPK, an enzyme that can inhibit mTOR activity in several ways,

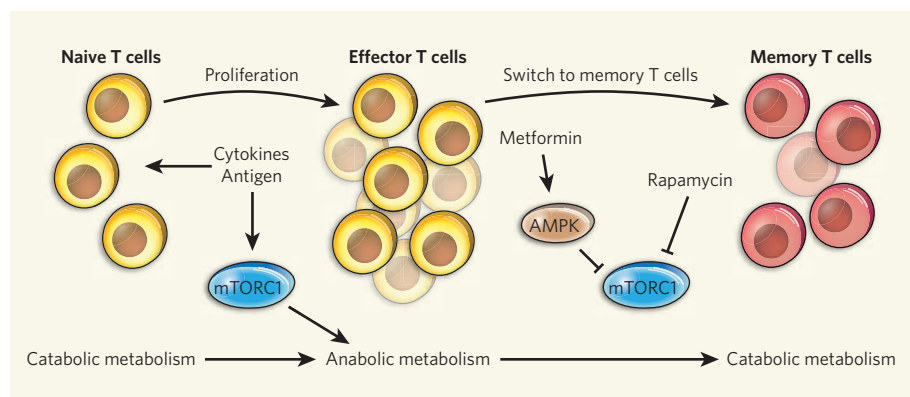


Figure 1 | The metabolic state of T-cell memory. Naive T cells that have not been exposed to antigen are quiescent, but undergo metabolic conversion (catabolic metabolism to anabolic metabolism) on stimulation with an antigen such as a pathogen. This switch allows effector T cells to use mTORC1-dependent glycolytic energy production (anabolic metabolism) to sustain rapid proliferation and biosynthetic needs. At the end of the effector stage, T cells either die by programmed cell death or enter the quiescent memory stage and switch back to catabolic metabolism. Pearce *et al.*² and Araki *et al.*³ show that rapamycin and metformin can enhance memory T-cell formation by inhibiting the protein complex mTORC1, thus leading to changes in cell metabolism.

including directly targeting raptor, a component of rapamycin-sensitive mTORC1 (ref. 5). Both AMPK and mTOR sense and control the energy status of a cell (ATP:AMP ratio) and regulate key aspects of cell growth and, as part of this, glucose metabolism.

In a quiescent cell, most energy (in the form of ATP) is generated in the mitochondria through oxidative phosphorylation, including the oxidation of fatty acids and amino acids — catabolic metabolism. On activation, T cells massively increase their glucose uptake and shift to producing ATP by glycolysis (anabolic metabolism) instead of catabolically (Fig. 1). mTOR is activated by signalling molecules, growth factors and antigen-induced T-cell-receptor signalling, and its activity enables a cell to increase glycolysis and ATP accumulation, which opposes AMPK activation⁶. Although some of the processes involved in the switch from catabolic to anabolic metabolism are fairly well understood, the reversal from an anabolic to a catabolic state is not as well characterized. One could speculate that rapamycin and metformin facilitate the switch from a glucose-dependent anabolic state (effector T cell) to a catabolic state of metabolism (memory T cell) by blocking mTORC1 activity (Fig. 1). But how a change in the metabolic signature of a T cell could enhance memory T-cell numbers and function is unknown.

How can rapamycin, a drug known for its immunosuppressive effects, enhance the function and formation of T-cell memory? The answer may lie in dosage and, more importantly, timing. Whereas treatment with a low dose of rapamycin during the first 8 days after T-cell activation enhanced the numbers and function of memory T cells, a higher dose, closer to therapeutic levels, hampered the T-cell response, as would be expected of an immunosuppressant³. Interestingly, both papers^{2,3} clearly show that the higher dose of rapamycin enhanced memory T-cell function and recall ability if

administered after day 8. At this point, the vigorous cell proliferation that is characteristic of the effector stage has ceased and cells begin to enter the more quiescent memory state. Recent data⁴ suggest that mTOR can form different complexes (aside from mTORC1 and mTORC2) depending on the phase of the cell cycle, and little is known about their interaction with rapamycin. In addition, as the metabolic signature of a cell changes along with its activation state, rapamycin might differentially affect a cell depending on its cell cycle and metabolic state.

A long-standing paradigm in immunology proposes that, after the peak of the proliferative response, the programmed cell death of effector T cells is caused by a lack of growth

and survival factors — conditions that could also affect cell metabolism. However, recent experiments⁷ indicate that, in a physiological setting, effector T-cell viability and conversion to memory T cells are not regulated by competition for growth and survival factors. Thus, it is more likely that the metabolic switch is either programmed early after T-cell activation or occurs as a secondary effect after a quiescent stage has been entered.

Both Pearce *et al.*² and Araki *et al.*³ establish a crucial role for mTOR-mediated metabolic changes in enhancing T-cell memory. Does changing the metabolism of T cells through manipulation of mTOR hold promise for improving future vaccination strategies? mTOR is involved in regulating a plethora of functions in many cell types, and rapamycin administration is associated with many side effects. Thus, a more targeted approach will be required to harness their memory-enhancing ability. Identifying the downstream signalling pathways that lead to enhanced T-cell memory on inhibition of mTOR complexes will be a first step in that direction.

Martin Prlc and Michael J. Bevan are in the Department of Immunology, University of Washington, Seattle, Washington 98195-7370, USA.

e-mails: mprlc@u.washington.edu; mbevan@u.washington.edu

1. Williams, M. A. & Bevan, M. J. *Annu. Rev. Immunol.* **25**, 171–192 (2007).
2. Pearce, E. L. *et al.* *Nature* **460**, 103–107 (2009).
3. Araki, K. *et al.* *Nature* **460**, 108–112 (2009).
4. Thomson, A. W., Turnquist, H. R. & Raimondi, G. *Nature Rev. Immunol.* **9**, 324–337 (2009).
5. Gwinn, D. M. *et al.* *Mol. Cell* **30**, 214–226 (2008).
6. Jones, R. G. & Thompson, C. B. *Immunity* **27**, 173–178 (2007).
7. Prlc, M. & Bevan, M. J. *Proc. Natl Acad. Sci. USA* **105**, 16689–16694 (2008).

NANOOPTICS

Photons pushed together

Michel Orrit

Photons don't interact well with each other, which is a real headache for researchers developing all-optical transistors for computing applications. But a single molecule can mediate photon-photon affairs.

Transistors in computers generally modify electrical signals (source currents) using other electrical signals (gate voltages). The nonlinear interactions in and between networks of transistors thus underpin all electronic computing. Similar nonlinear networks can be found in the brain¹, where neuron firing is triggered by the outputs of other neurons, or in microfluidic chips², in which fluid pressures govern fluid flow. But on page 76 of this issue, Hwang *et al.*³ describe how the transmission of a light beam can be modulated by another light beam: the basic process of an all-optical transistor.

Optical transistors are a long-sought goal because they could form the basis of optical computers that use photons instead of electrons as signal carriers. Not only are photonic signals faster than their electronic counterparts, but they are also easier to transmit directly over large distances. And because photons carry no electrical charge, photonic signals do not perturb each other (unlike electronic signals). Furthermore, photons offer advantages for future quantum-computing applications, because the coherence of their quantum states can be maintained at practically useful temperatures;

the same feat in electrons is possible only at temperatures below 1 kelvin (ref. 4).

Previous attempts at all-optical data processing have been thwarted by the weakness of photon–photon interactions. Such interactions depend on the strengths of the electric fields of the photons, but these fields are far weaker than those of the atoms and molecules of the medium through which they travel. The interactions between photons, which have to be mediated by atoms (or molecules), are therefore usually negligible. Hwang *et al.*³ have overcome this problem by using a single absorber — an atom, a quantum dot or a molecule — to mediate photon–photon interactions.

The basic principle is as follows. A light beam (the gate beam) is aimed at a suitable dye molecule, so that the molecule absorbs every photon and enters an excited state. The excited molecule can then alter the propagation of photons from another incident beam (the source beam). In effect, the molecule ‘slows down’ gate photons so that they can interact with source photons in a nonlinear way. The single molecule is analogous to a crossing between a railway line (the gate beam) and a road (the source beam). For short, fast trains, the road traffic is hardly perturbed. However, if trains are long and slow, every train blocks a large number of cars, heavily perturbing road traffic.

Unfortunately, the probability of photon absorption by a single molecule is usually tiny, so that merely detecting the nonlinear interaction of optical waves at a molecule is difficult. But theoretical studies show that, for tightly focused light beams that cause ‘lifetime-limited’ molecular transitions (which create excited states that relax to the ground state only by emitting photons, rather than by other mechanisms), the probability grows and can even reach 100% (ref. 5). So, for example, a molecule that reflects source photons in its ground state might absorb gate photons and enter an excited state that is transparent to source photons. It has therefore been proposed⁶ that a single gate photon could switch a whole beam of source photons from being reflected to being transmitted (Fig. 1). Hwang *et al.*³ provide the first experimental proof of this concept.

In their experiment, Hwang and colleagues excited a dye molecule to a vibrational sublevel of its electronic excited state using a continuous laser beam (the gate beam). The authors needed to be able to distinguish between the gate and source beams, and the easiest way to do this is to use different frequencies for each beam. But different frequencies wouldn’t ordinarily be able to excite the absorber molecule to the same electronic state. The authors therefore chose a system in which both the gate and source beams can access the same electronic state, albeit at different vibrational sublevels. This is rather inefficient for practical applications, because the probability of photon absorption generating vibrational excited states

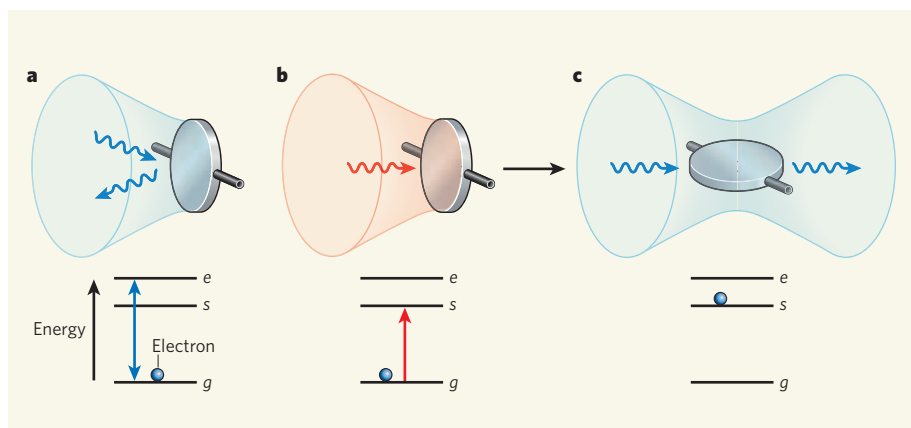


Figure 1 | Design for an all-optical transistor. A single molecule, represented here as a rotating mirror, can in principle behave as an all-optical transistor — it can modulate the transmission of a beam of light (the source beam, blue) in response to another beam of light (the gate beam, red). The waist-shaped surface represents a beam of light, focused on the molecule. The diagrams under each of the transistors represent the electronic energy levels of the molecule. **a**, If the molecule is in its ground state (*g*) and the source photons are equivalent in energy to the electronic energy transition from *g* to an excited state (*e*), then the source photons are resonantly scattered (totally reflected) as electrons oscillate between the *e* and *g* states. **b**, A gate photon of appropriate energy (different from that of the source photons) excites the molecule to a long-lived excited state (*s*). **c**, The excited molecule no longer absorbs source photons, which are instead perfectly transmitted. Hwang *et al.*³ report the first all-optical transistor that works on similar principles.

is small (about 1 in 1,000), but for the purposes of Hwang and colleagues’ experiment it was a convenient ploy.

The authors probed photon absorption of the molecule’s main electronic state using a laser source beam that produced light at the same narrow range of frequencies as those absorbed by the molecule. They found that the molecule allowed more source photons to pass through after it had been irradiated by the gate beam. Again, the design of the experiment is not perfect, because the desired effect is reduced by relaxation of the excited state to vibrational sublevels of the ground state. Nonetheless, the authors observed that the absorption of just one gate photon led to an approximately 10% modulation of the source beam. Because the source beam is faint, this corresponds to each gate photon interacting with one source photon.

This demonstration³ of photon–photon interactions in an all-optical transistor is a milestone in the field, but real applications are still far away. Too many gate photons are required to create an effect, and the modulation of the source beam is too weak to act as a signal for another transistor in a network. Furthermore, because both source and gate beams excite the absorber molecule to the same electronic state, one gate photon cannot efficiently influence the behaviour of more than one source photon. This is a problem, because in real-world applications, the source beam will be much stronger (consisting of more photons) than the gate beam, and so the proportion of source photons perturbed by gate photons will be smaller than in Hwang and colleagues’ experiment (which uses a weak source beam).

So how could this device be developed into a practical all-optical transistor? First, it would

be better to use a metastable state rather than an excited state⁶, because a single gate photon would then enable the molecule to transmit many source photons for a long time. For example, the lifetime of a ‘triplet’ metastable state is a thousand to a million times longer than that of the excited state used in Hwang and colleagues’ experiment. Second, the ideal absorber for all-optical transistors would involve transitions to just two excited levels, whereas the light absorption of all molecules in condensed matter corresponds to many transitions, each associated with different vibrational sublevels of electronic states. An atom would be much closer to the ideal three-level system, but atoms cannot easily be immobilized in optical circuits. A possible alternative would be to enhance the coupling of light to two molecular transitions only — one for the source and one for the gate — by concentrating the optical field so that the frequency matches only one vibrational sublevel. This can be done using devices known as optical cavities⁷, or by using a ‘lightning-rod effect’ close to a metallic nanoantenna⁸.

Hwang and colleagues’ work³ is not only an experimental tour de force, but it also provides a clear road map towards practical, single-molecule switching systems, and identifies the major obstacles to be overcome. The authors use an organic molecule at low temperatures as the absorber for their study, because this offers practical advantages for demonstration purposes. But the underlying principle of their transistor applies to many other materials⁹, ranging from cold atoms and trapped ions to quantum dots. So the future is certainly bright for photon manipulations at molecular scales.

Michel Orrit is in the Huygens Laboratory, Leiden

Institute of Physics, Leiden University, 2300 RA Leiden, the Netherlands.
e-mail: orrit@molphys.leidenuniv.nl

1. Livet, J. *et al. Nature* **450**, 56–62 (2007).
2. Psaltis, D., Quake, S. R. & Yang, C. *Nature* **442**, 381–386 (2006).
3. Hwang, J. *et al. Nature* **460**, 76–80 (2009).

4. Koppens, F. H. L. *et al. Nature* **442**, 766–771 (2006).
5. Zumofen, G., Mojarad, N. M., Sandoghdar, V. & Agio, M. *Phys. Rev. Lett.* **101**, 180404 (2008).
6. Chang, D. E., Sørensen, A. S., Demler, E. A. & Lukin, M. D. *Nature Phys.* **3**, 807–812 (2007).
7. Duan, L.-M. & Kimble, H. J. *Phys. Rev. Lett.* **92**, 127902 (2004).
8. Merlein, J. *et al. Nature Photon.* **2**, 230–233 (2008).
9. Lounis, B. & Orrit, M. *Rep. Prog. Phys.* **68**, 1129–1179 (2005).

CELL BIOLOGY

The not-so-odd couple

Sarah E. Millar

Actively dividing cells do so at a risk — with each division, chromosome ends tend to shorten. Pairing proteins that promote cell division with a chromosome-end repair factor is a smart way to solve this problem.

Embryonic development and homeostasis of adult tissues are regulated by a relatively small number of signalling pathways with astoundingly diverse functions. These include controlling the rate of cell division, regulating the differentiation of cells into organs with complex structures, and activating adult stem cells. The functional complexity of signalling pathways is achieved in part by the interaction of proteins in specific cell types with core components of signalling pathways, which modulates pathway activity and confers cell-type-specific functions. A study by Park *et al.*¹ on page 66 of this issue identifies one such protein that functions in tissue-progenitor cells to increase the transcription of genes activated by the Wnt- β -catenin signalling pathway. Unexpectedly, this protein turns out to be an essential component of telomerase, a protein–RNA complex that has an apparently unrelated role in protecting the ends of chromosomes (telomeres) from shortening during DNA replication². Park *et al.* propose an intriguing functional connection.

The Wnt- β -catenin signalling pathway stimulates proliferation of embryonic progenitor cells and adult stem cells in self-renewing tissues such as the intestine, the haematopoietic system and hair follicles³. Wnt proteins bind to membrane-bound Frizzled receptors and LRP co-receptors, and this binding prevents degradation of cytoplasmic β -catenin. β -catenin translocates to the nucleus, where it activates target genes by binding to LEF/TCF transcription factors³.

The first inklings of a link between β -catenin and telomerase came from studies of adult stem cells in the hair follicle. Throughout adult life, hair follicles undergo cycles of growth and regression that are dependent on stem cells located in a region of the follicle

known as the bulge. Expression of stable, active β -catenin protein in skin epithelial cells causes proliferation of bulge stem cells and initiation of a new phase of hair growth⁴. Previous work⁵ had created mice in which extra copies of the gene encoding TERT, the protein component of telomerase, can be switched on in adult life in skin epithelial cells. Surprisingly, this study⁵ revealed that extra TERT mimics the proliferative and hair-growth-promoting effects of β -catenin. Another group⁶, working independently, found that continuous expression of TERT in skin epithelial cells enhances stem-cell proliferation in response to hair plucking or topical treatment with a tumour-promoting chemical. Subsequent experiments in hair

follicles showed that extra TERT enhances the expression of genes targeted by β -catenin⁷. However, exactly how TERT affects gene activity was unclear. TERT provides the reverse transcriptase enzyme activity of telomerase — it synthesizes DNA at the ends of chromosomes, transcribing from an RNA template provided by the telomerase RNA component, TERC. Interestingly, the effects of TERT on hair-follicle growth are independent of its reverse transcriptase activity and of TERC, suggesting that, in this context, TERT has an atypical function^{5,7}.

Park *et al.*¹ provide a molecular basis for these unexpected observations. They purified TERT protein complexes from mammalian cells to identify any novel components, and were surprised to discover that these complexes contained BRG1. BRG1 is a subunit of a complex of proteins that alters the conformation of chromatin to facilitate transcription. β -catenin is known to bind directly to BRG1, resulting in enhanced expression of β -catenin target genes⁸. Thus, the existence of TERT–BRG1 complexes provided a possible molecular link between TERT and β -catenin. Subsequent experiments showed that TERT interacts directly with BRG1, and that complexes of TERT, β -catenin and a TCF protein bind to β -catenin target genes in cells from mouse small intestine.

The authors¹ found that, in several cell types, TERT is required for expression of Wnt-regulated genes. In mouse embryonic stem (ES) cells, deletion of TERT reduces expression of Wnt target genes. This inhibition is overcome by the addition of enzymatically inactive TERT, indicating that, similarly to its effects on hair growth, the effect of TERT on Wnt target genes in ES cells is independent of telomerase's reverse transcriptase activity. Strikingly, depletion of TERT in embryos of the frog *Xenopus laevis* produces developmental defects similar to those seen in mouse embryos that lack β -catenin⁹. Excess Wnt signalling in *X. laevis* embryos causes duplication of the embryo's anterior–posterior axis, resulting in the development of two-headed tadpoles¹⁰. Park and colleagues¹ discovered that TERT overexpression in *X. laevis* embryos synergizes with β -catenin to promote expression of Wnt reporter genes and axis duplication. Taken together, these findings provide convincing evidence for TERT as a key component of β -catenin transcriptional complexes in various contexts.

Telomerase activity is particularly important in stem cells and other progenitor cells to maintain their extensive proliferative capacity and to prevent cellular senescence — a form of cell-cycle arrest that can be triggered by shortened telomeres^{11,12}.

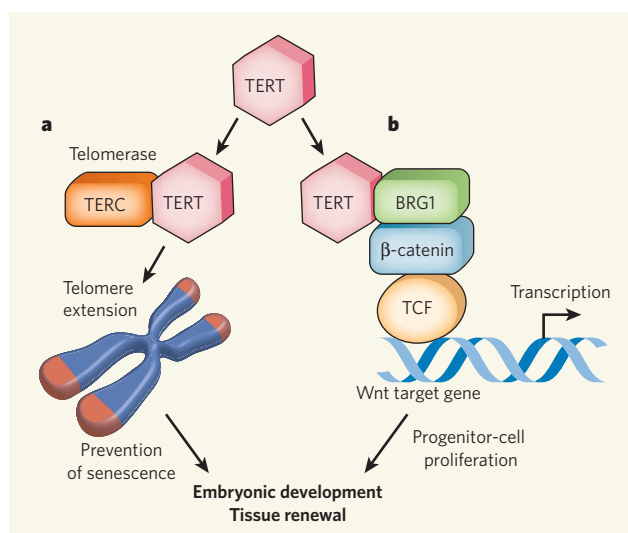


Figure 1 | The TERT- β -catenin connection. **a**, The telomerase complex functions in progenitor cells to repair chromosome ends, known as telomeres, during cell division. TERT provides reverse transcriptase activity to the complex, and uses TERC, the RNA component of telomerase, as a template. **b**, Park *et al.*¹ find that TERT also increases the transcriptional activity of β -catenin/TCF complexes through interaction with BRG1, a factor that binds the Wnt signalling molecule β -catenin and alters the conformation of chromatin. These two separate functions of TERT may simultaneously prevent cellular senescence and increase proliferation of progenitor cells, permitting embryonic development and renewal of adult tissues.

Thus the link between β -catenin and TERT may not be so surprising after all. Park *et al.*¹ argue that the functional interaction between β -catenin and TERT may have evolved to coordinate mechanisms regulating progenitor-cell proliferation and chromosome integrity (Fig. 1), permitting embryonic development and renewal of adult tissues.

Given the identification of this exciting new partnership, and the significant effects of TERT deletion on Wnt-target-gene expression in mouse ES cells, it is perhaps surprising that first-generation knockout mice lacking TERT look normal¹². In these mice, and in mice lacking TERC, obvious defects in self-renewing tissues become apparent only after continued breeding, and are associated with progressive telomere shortening, reflecting the absence of a mechanism to protect chromosome ends^{11,12}.

Park and colleagues wondered whether subtle developmental defects resulting from decreased Wnt signalling in TERT-knockout mice might have been overlooked in previous studies. As *X. laevis* embryos that were depleted of TERT showed abnormal development of embryonic structures that give rise to vertebrae, a process known to require the Wnt

protein Wnt3a¹³, the authors examined vertebral development in TERT-deficient mice. A significant proportion of these mice showed abnormalities of the vertebrae similar to those seen in mice with reduced Wnt3a expression. Thus mammals also seem to require TERT for normal Wnt signalling during embryonic development. Notwithstanding these findings, the limited developmental defects found in TERT-deficient mice remain puzzling.

It is possible that the modulating effects of TERT on activity of the Wnt pathway are relatively small in mice *in vivo*, and only become significant during cellular stress (for instance, when ES cells are removed from their embryonic environment and grown on a plastic dish). Alternatively, TERT may function semi-redundantly with factors that are yet to be discovered, or TERT-deleted embryos may compensate for lack of TERT by activating other pathways. The latter hypothesis could be tested by generating embryos that have a mix of labelled TERT-deficient cells and normal cells. If true, TERT-deficient cells should be out-competed by the normal cells during development. Similarly, the extent to which the Wnt-promoting functions of

TERT are required in adult stem cells *in vivo* remains unclear. This central issue could be addressed by deleting TERT in specific adult tissues. The molecular tools for such an experiment are readily available for tissues such as the hair follicle, which can be counted on once again to release more of its treasure trove of secrets¹⁴.

Sarah E. Millar is in the Departments of Dermatology, and of Cell and Developmental Biology, University of Pennsylvania, M8D Stellar-Chance Laboratories, 422 Curie Boulevard, Philadelphia 19104, USA. e-mail: millars@mail.med.upenn.edu

1. Park, J.-I. *et al.* *Nature* **460**, 66–72 (2009).
2. Blackburn, E. H. *FEBS Lett.* **579**, 859–862 (2005).
3. Reya, T. & Clevers, H. *Nature* **434**, 843–850 (2005).
4. Fuchs, E. *J. Cell Biol.* **180**, 273–284 (2008).
5. Sarin, K. Y. *et al.* *Nature* **436**, 1048–1052 (2005).
6. Flores, I., Cayuela, M. L. & Blasco, M. A. *Science* **309**, 1253–1256 (2005).
7. Choi, J. *et al.* *PLoS Genet.* **4**, e10 (2008).
8. Barker, N. *et al.* *EMBO J.* **20**, 4935–4943 (2001).
9. Huelsken, J. *et al.* *J. Cell Biol.* **148**, 567–578 (2000).
10. McMahon, A. P. & Moon, R. T. *Cell* **58**, 1075–1084 (1989).
11. Rudolph, K. L. *et al.* *Cell* **96**, 701–712 (1999).
12. Rajaraman, S. *et al.* *Proc. Natl Acad. Sci. USA* **104**, 17747–17752 (2007).
13. Ikeda, M. & Takada, S. *Mech. Dev.* **103**, 27–33 (2001).
14. Hardy, M. H. *Trends Genet.* **8**, 55–61 (1992).

APPLIED PHYSICS

A leak of information

Pavlo Zubko and Jean-Marc Triscone

As capacitors, the ubiquitous components of electronic circuitry, get smaller, keeping them insulating is a challenge. But that's not necessarily bad news — some conductivity might be just the thing for data storage.

A general problem in the electronics industry is that the insulating materials used in the continually shrinking capacitors and transistors start to leak charge when they become too thin. This leads to large power consumption and, in the case of memory, to difficulties in storing and retrieving information. But on page 81 of this issue, Garcia *et al.*¹ show that this generally undesirable leakage current can in fact be very useful. They find that the leakage current flowing through ultrathin (1–3 nanometres) ferroelectric films of barium titanate (BaTiO₃) is strongly dependent on their electric polarization states — that is, on whether the net electric dipole of the material is in one or the other of the two possible orientations. The authors' result, which allows direct reading of the polarization state through a simple measurement of the material's electrical resistance, may be just what is needed to put ferroelectric random access memories (FeRAMs) — those based on storing information in the polarization states of ferroelectric materials — back on track in the race for faster and better memory.

The ability of ferroelectrics to retain a

permanent dipole in the absence of an electric field, and the possibility of reversing its direction with a modest voltage, has been a driving force behind decades of intense research in ferroelectric memory, where the 'up' and 'down' polarization states are used to code the 'ones' and 'zeros' of binary information². Offering the non-volatility — the ability to retain information even when power is switched off — of hard disks, combined with speeds at which data are read and written comparable to those of 'dynamic random access memories' (DRAMs), FeRAMs were touted as the potential replacement for the flash memories found in today's mobile phones and digital cameras.

But despite huge technological advances and the successful commercialization of FeRAMs by several leading electronics manufacturers, the dream of the ultimate memory is at present still beyond reach, and FeRAMs remain competitive only in a number of niche applications. Industrial forecasts for the role of FeRAMs in the memory market have become more mixed. Whereas Samsung has recently presented its new vision of a FeRAM as part of a fusion memory³, rather than as a stand-alone solution, and

subsequently shelved its FeRAM programme altogether, other manufacturers remain optimistic. For example, Toshiba has just announced a new 128-megabit prototype with writing speeds of 1.6 gigabytes per second (ref. 4).

The obstacles encountered by FeRAMs in the memory race are as much financial as technical. One of the main disadvantages of current FeRAMs is that they are charge-sensing devices. The information is stored in the dipole orientation of the ferroelectric, the insulating layer that is sandwiched between two metallic electrodes to make a tiny capacitor. To determine this orientation, a voltage is applied that, depending on the dipole's original direction, either reverses it or leaves it unchanged. A reversal of the polarization is accompanied by a current pulse that can be detected and so allows the dipole's orientation to be determined. The magnitude of this current pulse depends on the charge stored on the capacitor plates, and therefore on the area of the capacitor. With lateral dimensions approaching 100 nm, the charge available for sensing during the read operation is reduced. A concomitant increase in parasitic conduction (leakage) currents associated with downscaling of the capacitors further complicates the memory readout. What's more, the read process is destructive, in that each bit must be rewritten after being read. Achieving non-destructive readout is a major quest, and NASA's Jet Propulsion Laboratory in the 1990s⁵, and more recently Tonouchi's group⁶, have investigated various optical routes.

In their experiment, Garcia *et al.*¹ explore another promising non-destructive readout technique. They use the conducting tip of

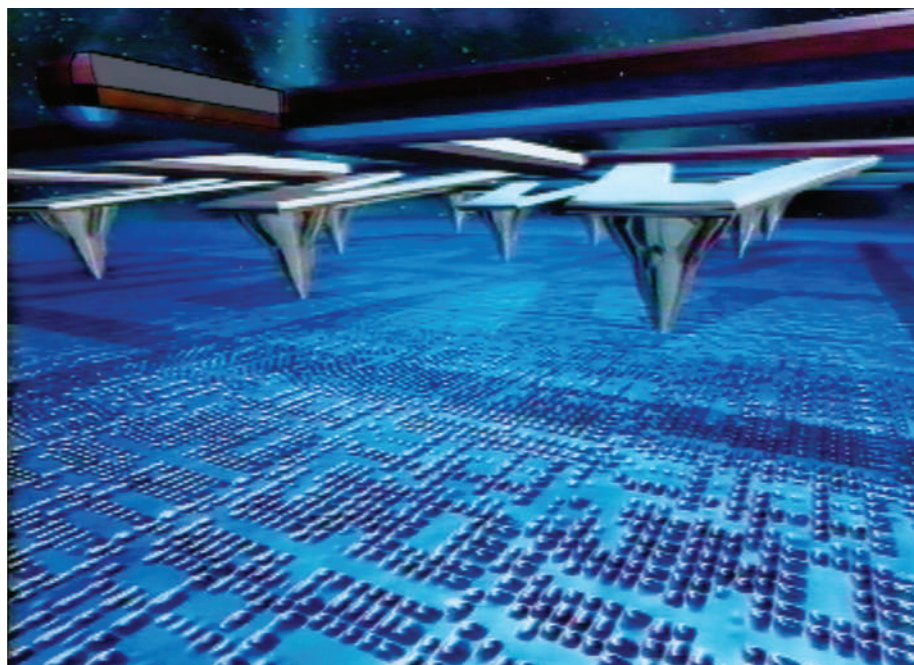


Figure 1 | An approach to data storage. IBM's Millipede project involves a technique, depicted here in an artist's impression, for reading and writing data that consists of operating, in parallel, an array of atomic-force-microscopy cantilevers with sharp tips. Just as punch cards were used in the first computers, the tips are used to punch nanometre-scale indentations, representing the 'ones' and 'zeros' of binary information, into a silicon chip coated with a thin plastic film. Garcia and colleagues' demonstration¹ of the operation of a single tip to read and write ferroelectric domains could be generalized to use a similar array of cantilevers.

an atomic force microscope (AFM) to create and then image ferroelectric domains (tiny ferroelectric regions with polarization 'up' or 'down' that can constitute the memory bits) on ultrathin ferroelectric films of BaTiO_3 , a well-known ferroelectric from the perovskite family of compounds. They show that films as thin as 1 nm are still ferroelectric at room temperature. With ferroelectricity expected to disappear below a certain film thickness, the value of which is still a matter of debate among both theoreticians and experimentalists⁷, this by itself is a major result, setting a new lower-size limit for ferroelectricity in BaTiO_3 .

Next, the conducting AFM tip was used to apply a small voltage and measure the leakage current through the film while scanning the tip across the sample surface, thus mapping the resistance of the ferroelectric domains. The resistance map showed remarkable homogeneity within each domain, and most importantly, a dramatic change (up to a factor of 750) between oppositely polarized domains. Hence, by measuring this resistance (or the leakage current for a given voltage), the direction of the polarization could be easily determined without altering it, allowing the highly desirable non-destructive readout of the ferroelectric memory to be obtained by exploiting the leakage currents.

So what is the source of leakage currents? Various imperfections in the material's crystal structure, and even the boundaries between the different ferroelectric domains, may lead to localized conducting channels through an

insulator, sometimes with rather interesting properties^{8,9}. Alternatively, electrons can surmount the insulating barrier by jumping over it, if given enough thermal energy, or passing through it via the quantum-mechanical process of tunnelling. The key to understanding the results of Garcia *et al.* is to note that the height and shape of the barrier that the insulator presents to the flow of electrons might be modified by changing its polarization state¹⁰, hence altering the probabilities of electrons being thermally excited over the barrier or tunnelling through it.

Both thermally activated and tunnelling conduction can lead to the desired giant changes in resistance^{11,12}, which allow the two polarization states to be distinguished with ease. But discriminating between the different conduction mechanisms is not trivial. Measurements of resistance as a function of temperature may be crucial, as tunnelling conduction generally has a weaker dependence on temperature, making it the preferred mechanism from the point of view of applications where temperature stability of the devices is essential. More detailed studies of the (nonlinear) dependence of leakage currents on applied voltage would be worthwhile to clarify the complexities at the interface with the AFM tip and the physical mechanism that underlies the resistance changes reported by Garcia and colleagues.

Although highly motivating for the FeRAM community, within the broader field of resistive memory, the discovery of Garcia *et al.* will encounter some serious rivalry with the

various contenders in the non-volatile-memory category¹³. The most mature technology is phase-change memory, which exploits switching upon heating between conducting crystalline and highly resistive amorphous phases. In 2006, Samsung announced a prototype 512-Mbit phase-change memory featuring a cell size of 46.7 nm. Whether devices based on Garcia and colleagues' development can, with the help of current FeRAM or DRAM processing techniques, be made more compact and make their way into the memory market, is an open question. Although a multi-AFM-tip approach, such as that developed at IBM for the Millipede project (Fig. 1), is a possible path to a ferroelectric memory device and bears the closest resemblance to the current work, conventional capacitor arrays with standard row-and-column memory addressing may be the preferred choice.

The work of Garcia *et al.*¹ may profit from recent advances in oxide deposition methods, which allow the growth of 'perfectly' ordered (epitaxial) strontium titanate (SrTiO_3) films on silicon wafers¹⁴. These SrTiO_3 layers can be used as templates for further growth of perovskite oxides that include not only BaTiO_3 and other technologically important ferroelectrics, but a whole spectrum of materials displaying a huge diversity of functional properties — from superconductivity and colossal magnetoresistance (the material's ability to change its electrical resistance when placed in a magnetic field) to multiferroicity (the coexistence in a material of both electric and magnetic ordering, which offers innovative means for memory storage¹⁵). The quality of many perovskite thin films is now comparable to that of group III–V semiconductors, and thus the successful integration of epitaxial oxide films onto silicon opens the door to a new era in oxide electronics and possibly to the next generation of non-volatile memory devices. ■

Pavlo Zubko and Jean-Marc Triscone are in the Department of Condensed Matter Physics, University of Geneva, 24 Quai Ernest-Ansermet, CH-1211 Geneva 4, Switzerland.
e-mails: pavlo.zubko@unige.ch;
jean-marc.triscone@unige.ch

- Garcia, V. *et al.* *Nature* **460**, 81–84 (2009).
- Scott, J. F. & Araujo, C. A. *Science* **246**, 1400–1405 (1989).
- Kim, K. & Jung, D. J. *Integr. Ferroelectrics* **96**, 100–111 (2008).
- www.toshiba.com/taec/news/press_releases/2009/mem_09_554.jsp
- Thakoor, S. *Appl. Phys. Lett.* **60**, 3319–3321 (1992).
- Takahashi, K., Kida, N. & Tonouchi, M. *Phys. Rev. Lett.* **96**, 117402 (2006).
- Rabe, K. M., Ahn, C. H. & Triscone, J.-M. (eds) *Physics of Ferroelectrics* (Springer, 2007).
- Szot, K., Speier, W., Bihlmayer, G. & Waser, R. *Nature Mater.* **5**, 312–320 (2006).
- Seidel, J. *et al.* *Nature Mater.* **8**, 229–234 (2009).
- Tsymbal, E. Y. & Kohlstedt, H. *Science* **313**, 181–183 (2006).
- Blom, P. V. M., Wolf, R. M., Cillesen, J. F. M. & Krijn, M. P. C. M. *Phys. Rev. Lett.* **73**, 2107–2110 (1994).
- Maksymovych, P. *et al.* *Science* **324**, 1421–1425 (2009).
- Meijer, G. I. *Science* **319**, 1625–1626 (2008).
- McKee, R. A., Walker, F. J. & Chisholm, M. F. *Phys. Rev. Lett.* **81**, 3014–3017 (1998).
- Gajek, M. *et al.* *Nature Mater.* **6**, 296–302 (2007).

OBITUARY

Robert Furchgott (1916–2009)

Nobel laureate who pioneered research into nitric oxide.

In 1992, *Science* heralded nitric oxide (NO) as 'molecule of the year', less than six years after it had been identified as a physiological dilator of blood vessels, accounting for the activity of a molecule known as endothelium-derived relaxing factor (EDRF). On 19 May 2009, Robert Furchgott, whose research was most influential in leading to the discovery that NO is EDRF, died peacefully in Seattle, Washington, aged 92.

Bob, as he was known to friends (Robert to family), was born in Charleston, South Carolina, in 1916, and spent his high-school years in the small town of Orangeburg. He began college at the University of South Carolina, then transferred to the University of North Carolina in Chapel Hill a year later, when his father became a North Carolina resident. Furchgott worked his way through college as a technician in a laboratory studying the physical chemistry of cellulose.

His fascination with physical chemistry led to a graduate-school placement at Northwestern University Medical School in Chicago, Illinois, in a laboratory addressing the physical properties of red blood cells, the subject of his PhD thesis. In 1940, he joined Ephraim Shorr's group at Cornell University Medical School in New York City, where he spent nine years focusing on cardiovascular research. With the onset of the Second World War, the laboratory turned its attention to wartime issues, especially the physiology of irreversible haemorrhagic shock. Furchgott found evidence for a natural substance that contributes to irreversible vasodilation, and attempted to isolate it using strategies that presaged his approach to studying EDRF some 40 years later.

Furchgott's first faculty position, in 1949, was in the pharmacology department at Washington University in St Louis, Missouri, where he began examining the effects of drugs on blood vessels. His first publication there, in 1953, includes a description of the effects of acetylcholine and sodium nitrite on the contraction of strips of rabbit aorta. In this work he made an observation that could have predicted the source of EDRF — acetylcholine, well known as a vasodilator in the intact organism, produced contractions only in blood vessels that he had prepared with consummate care, presumably inadvertently removing the EDRF-producing endothelial layer.

In St Louis, Furchgott also discovered photorelaxation when one of his preparations, which sat beneath a sunlit window, dilated much more than preparations in a darker section of the



laboratory — in retrospect, it seems likely that photorelaxation reflects the release of NO by blood vessels in response to light.

After seven years in St Louis, Furchgott moved to what is now called the State University of New York (SUNY) Downstate Medical Center in Brooklyn as chair of pharmacology, where he continued his research on blood-vessel pharmacology as well as developing theories of blood-vessel-receptor activity. Experiments leading to the EDRF concept began about 22 years later, in 1978, when his technician failed to follow the standard protocol for preparing the rabbit aorta strips and, instead of contraction in response to acetylcholine, Furchgott saw relaxation. He was eager to troubleshoot this 'accident', and after several weeks realized that gentle rubbing of the endothelial layer of blood vessels transformed relaxation into contraction. One explanation was that acetylcholine acts on receptors on endothelial cells (removed by the rubbing) to trigger the release of a substance with relaxing activity — EDRF. He obtained direct evidence for this by making a 'sandwich' of a strip of aorta freed of endothelial cells to which he applied the endothelium of another aortic strip; this procedure transformed contraction into relaxation.

Over the next few years, various clues emerged that ultimately led to the identification of NO as EDRF. Calcium ionophores were effective in eliciting EDRF activity, which we now know reflects the requirement of NO synthase

for calcium/calmodulin. Ferid Murad had shown that NO is the active metabolite of nitroglycerine, a drug that mediates its vasorelaxant effects by stimulating guanylyl cyclase, converting GTP to cyclic GMP. EDRF was also shown to stimulate cyclic GMP formation. Haemoglobin, known to interfere with the effects of NO on cyclic GMP, inhibited EDRF. And methylene blue, which inhibits stimulation of guanylyl cyclase by nitroglycerine-like drugs, also blocked EDRF activity. Billy Martin, working in the Furchgott lab, had noted that acidification of a tissue extract enhanced its vasorelaxant activity, and acidification is known to convert nitrite to NO. At about this time, Salvador Moncada and Paul Vanhoutte reported that superoxide rapidly inactivates EDRF and that superoxide dismutase prevents this.

On the basis of these clues, Furchgott carried out definitive experiments testing whether NO might be EDRF. Relaxation by both NO and EDRF was inhibited by haemoglobin, methylene blue and superoxide generators, and was potentiated by superoxide dismutase. Moreover, both NO and EDRF augmented levels of cyclic GMP. At a July 1986 symposium, Furchgott proposed that NO is EDRF. At the same meeting, Louis Ignarro presented findings using similar experimental approaches and with the same conclusion.

The identification of NO as EDRF was made when Furchgott was 70 years old, a feat of late-life productivity reminiscent of Hans Kosterlitz, who published his identification of the enkephalin pentapeptides as 'the brain's own morphine' in December 1975, when he was 72.

In 1996, Furchgott shared the Albert Lasker Basic Medical Research Award with Ferid Murad. In 1998, Murad, Ignarro and Furchgott shared the Nobel Prize in Physiology or Medicine "for their discoveries concerning nitric oxide as a signalling molecule in the cardiovascular system".

In contrast to many self-promoting, hyper-ambitious scientists, Furchgott was ever mild mannered, self-effacing and generous to a fault. With his first wife Lenore Mandelbaum, he had three daughters, Terry, Jane and Sue, who survive him along with four grandchildren and a great-grandchild. Lenore died in 1983, after which he married Maggie Roth, who died several years ago.

In 2008 he moved to a retirement community in Seattle. His voracious curiosity never flagged. According to Sue, "he visited every single museum, even obscure ones at least once, many more than once". She summarized her father's principal attributes: "He was a real southern gentleman." I concur.

Solomon H. Snyder

Solomon H. Snyder is in the Department of Neuroscience, Johns Hopkins Medical School, Baltimore, Maryland 21205, USA.
e-mail: ssnyder@jhmi.edu

PROGRESS

Elite and stochastic models for induced pluripotent stem cell generation

Shinya Yamanaka^{1,2}

Induced pluripotent stem cells offer unprecedented potential for disease research, drug screening, toxicology and regenerative medicine. However, the process of reprogramming is inefficient and often incomplete. Here I consider reasons for bottlenecks in induced pluripotent stem cell generation, and propose a model in which most or all cells have the potential to become pluripotent.

In 2000, my laboratory began testing the idea that factors that maintain pluripotency in embryonic stem (ES) cells might induce pluripotency in somatic cells. Twenty-four factors were selected as initial candidates, on the basis of their important roles or specific expression in mouse ES cells.

To evaluate these factors, we introduced combinations of the genes into mouse embryonic fibroblasts (MEFs) using a retroviral vector. The cells were engineered to carry an antibiotic-resistance gene that would only be expressed when *Fbxo15*, one of the mouse ES cell pluripotency genes, was turned on. We predicted that this gene could also be turned on if pluripotency was induced by a combination of the 24 genes¹.

When each candidate gene was individually introduced into the fibroblasts, no colonies grew. However, when we mixed retroviruses expressing all 24 of the candidate genes, several colonies emerged. Much to our surprise, we found that only four of these factors were needed to generate a small number of stem-cell-like colonies. All of the four genes were transcription factors: namely Oct3/4 (also known as Pou5f1), Sox2, Klf4 and c-Myc, and we found they could reprogram fibroblasts from both embryonic and adult mice².

The reprogrammed cells, which we termed 'induced pluripotent stem (iPS) cells', were similar to ES cells in their morphology, expression of important ES cell marker genes, and their ability to form teratomas (tumours comprised of diverse tissue types) when injected into mouse testes. However, the initial iPS cells possessed different global gene expression patterns, and when injected into early mouse embryos, they failed to populate the embryo and form adult chimaeric mice. These characteristics indicated that the iPS cells were not fully reprogrammed. However, eventually, by modification of the induction protocols, our group and others generated mouse iPS cells competent for adult chimaeric mice and germline transmission^{3–5}. In 2007, human fibroblasts were reprogrammed using the same or slightly modified combination of genes introduced by retroviruses or lentiviruses^{6–9}.

Although it is possible to reproducibly generate iPS cells by viral transduction of these defined factors, only a small portion of the transduced cells become pluripotent. In the original report of germline-competent iPS cells, the efficiency was only ~0.05%—that is, on average only one out of 2,000 plated fibroblasts formed pluripotent cells⁴. Furthermore, several groups reported that the cells that seemed to be pluripotent were in fact often only partially reprogrammed, being dependent on continuous transgene expression of the reprogramming factors for their self-renewal^{2,10,11}.

Low efficiency and partial reprogramming are barriers for applying human iPS cells to basic research, drug screening, toxicology and

regenerative medicine. In this Progress article, I will consider two models, the elite and stochastic models, to explain the low efficiency and partial nature of iPS cell generation (Fig. 1). The elite model predicts that direct reprogramming only take place in a subset of

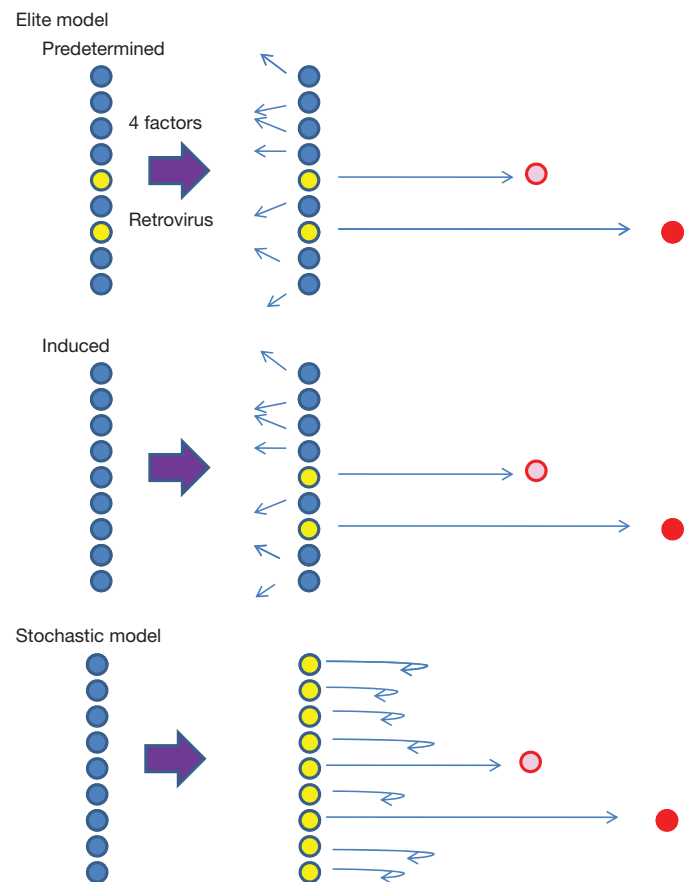


Figure 1 | Two models explaining the low efficiency of iPS cell generation. In the elite model, only a small number of cells, determined either before or after retroviral transduction, can be reprogrammed either partially or completely. In the stochastic model, most cells initiate the reprogramming process, but only a few can achieve complete reprogramming. Yellow, cell competent for reprogramming; pink, partially reprogrammed cells; red, iPS cells.

¹Center for iPS Cell Research and Application (CiRA), Kyoto University, Kyoto 606-8507, Japan. ²Gladstone Institute of Cardiovascular Disease, San Francisco, California 94158, USA.

transduced cells, whereas the stochastic model predicts that most or all cells are competent for reprogramming. My review of the current literature supports the stochastic model.

Elite model

This model presupposes that only a few cells are competent for reprogramming. This model can be further divided into two models: a 'predetermined elite' and an 'induced elite' model (Fig. 1).

Predetermined elite model. In the predetermined model, small numbers of cells are competent for reprogramming even before retroviral transduction of the four factors. Tissue stem cells and other undifferentiated cells existing in regenerative tissues are good candidates for 'elite' cells, predisposed to reprogramming. In reprogramming by nuclear transfer (somatic cell nuclear transfer, or SCNT), higher efficiencies were achieved using nuclei from less-differentiated, progenitor-like neural stem cells, as well as from ES cells, than with nuclei from terminally differentiated neuronal donor cells such as lymphocytes¹². Similarly, in inducing pluripotency using defined factors, more primitive stem cells may be preferentially reprogrammed. Multipotent stem cells are known to exist in adult organs and tissues such as the skin. In skin, stem cells comprise ~0.067% of the population¹³, a number markedly similar to the efficiency of iPS cell generation in our initial report.

However, four lines of evidence contradict the predetermined elite model. First, the efficiency of iPS cell generation is now much higher than originally reported. By simply delaying the timing of drug selection for Nanog expression, we increased the efficiency 10-fold, showing that ~0.5% of MEFs can become iPS cells¹⁴. Furthermore, retroviral infection of MEFs routinely results in ~2% reprogramming efficiency in my laboratory. This can be further increased by the use of specific chemicals. It has been reported that up to 10% of MEFs are reprogrammed by the four factors when treated with a small molecule, valproic acid¹⁵. It is unlikely that tissue stem cells or otherwise undifferentiated cells comprise 2–10% of primary fibroblast cultures. Although reprogramming factors or chemical treatments might preferentially enhance the proliferation of tissue stem or progenitor cells, it is more likely that a wider spectrum of somatic cells is reprogrammed in the formation of iPS cells.

A separate line of evidence for the stochastic model arose from genetic lineage tracing analyses. In addition to fibroblasts, iPS cells have been generated from various tissues, including the liver¹⁶ and pancreas¹⁷. Genetic lineage tracing analyses, using the *Cre-loxP* system, showed that most iPS cells obtained from liver originate from cells that have expressed albumin. Similarly, many iPS cells from pancreas originate from cells that have expressed insulin. These data do not prove that terminally differentiated cells can become iPS cells, because albumin and insulin are expressed in precursor cells as well as mature hepatocytes and pancreatic beta-cells. Nevertheless, these findings clearly demonstrate that the four factors can reprogram lineage-committed cells that had at least differentiated into stages in which the expression of either albumin or insulin is turned on.

More directly, Hanna *et al.* generated iPS cells from B lymphocytes¹⁸. They confirmed the origin to be terminally differentiated B cells by showing genetic recombination of the globulin locus. Although the ectopic expression of the myeloid transcription factor CCAAT/enhancer binding protein alpha (CEBP α) or specific knock-down of the B cell transcription factor Pax5 was required, as well as the introduction of the four reprogramming factors, their data nevertheless demonstrated that lineage-committed cells can be reprogrammed by these defined factors.

The lines of evidence described earlier suggest that many, if not all, lineage-committed somatic cells can become iPS cells. However, some cell types might be more easily reprogrammed by defined factors than others. Indeed, mouse neural stem cells can be directly reprogrammed by only one factor, Oct3/4 (ref. 19).

Induced elite model. In the induced model, genes of factor(s) other than the four factors must be activated or inactivated by viral integration

into the host genome (Fig. 1). Therefore, only cells with specific viral integration sites are competent for reprogramming. Many lines of evidence, however, do not support this model.

iPS cells derived from epithelial cells and tissues, such as the liver, gastric mucosa and skin²⁰, have less retroviral integration than iPS cells derived from fibroblasts. Taking advantage of this phenomenon, we performed inverse PCR to determine the retroviral integration sites in two iPS cell clones from hepatocytes and two from the stomach¹⁶. No common integration sites were identified. More recently, it was reported that six iPS cell clones derived from mouse fibroblasts showed no common retroviral vector insertions²¹. These data suggest that retroviral integration into specific sites is not required for iPS cell generation.

Further direct evidence came from several groups who generated iPS cells without retroviruses. iPS cells were generated from mouse adult hepatocytes by introducing the four reprogramming factors with adenoviruses²². Another group generated iPS cells from MEFs with two plasmids—one with Oct3/4, Sox2 and Klf4 complementary DNAs connected by the 2A self-cleavage peptides, and the other with *c-Myc* (also known as *Myc*) cDNA²³. Both groups showed that these iPS cells did not contain the integration of adenoviruses or plasmids into the genomes of the established iPS cells. More recently, mouse iPS cells were generated by protein transduction of the four factors²⁴. Furthermore, human iPS cells have been generated with episomal expression vectors²⁵. In some of their iPS cell clones, the episomal DNA spontaneously disappeared during the course of culture.

However, iPS cell generation without retroviruses is far less efficient. For the episomal induction, seven factors, including the potent oncogene SV40, were required. This may suggest that insertional mutagenesis is not required for iPS cell generation but does promote the process. In this case, integration sites do not have to be common among different clones. The generation of iPS cells could be promoted by activating or inactivating endogenous genes by retroviruses or lentiviruses, so as to enhance proliferation, decrease apoptosis, or enhance reprogramming. Furthermore, the amount, balance, continuity and silencing of transgene expression can be greatly influenced

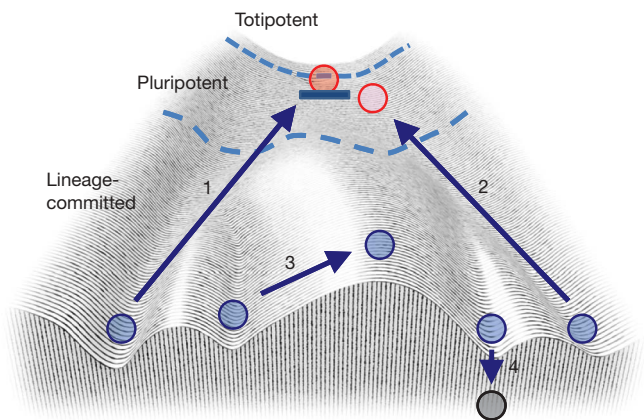


Figure 2 | Stochastic model. Totipotent fertilized eggs differentiate into various lineages through the pluripotent status. Here I depict this process in the context of the epigenetic landscape proposed by Conrad Waddington²⁶. The iPS cell is like a ball rolling down the slope of a valley. The reprogramming factors cooperatively push cells up the slope to the pluripotent zone. Some cells are blocked by an epigenetic bump (closed rectangle) on the slope and thus become able to self-renew (1). Other cells are only partially reprogrammed and are not blocked by the bump; therefore, without the exogenous reprogramming factors, they would roll down again (2). When the expression of the reprogramming factors is not appropriate, cells may transform to other types of cell (3), or even undergo apoptosis or senescence (4). For cells that are located on the middle of the valley (that is, somatic stem cells) it might be easier to go back to the pluripotent state. Figure modified from Waddington, 1957 (ref. 26).

by the positions of retroviral integrations. This may explain why only a small portion of transduced cells complete the reprogramming process, as discussed later.

Stochastic model

In the stochastic model, most, if not all, differentiated cells have the potential to become iPS cells after the introduction of the four factors. Cell differentiation is often described as a ball rolling down an epigenetic landscape, first depicted by Conrad Waddington in 1957, starting from the totipotent state, going through the pluripotent state, and rolling down to a lineage-committed state²⁶ (Fig. 2). In normal development, pluripotent cells appear transiently. They cannot stop on the slope and are pulled by gravity to rapidly differentiate into various lineages. In contrast, ES cells can self-renew and maintain pluripotency for a long time. Thus, it is as if ES cells are blocked by a bump or a roadblock formed by their particular epigenetic status. In this metaphor, the four reprogramming factors cooperatively push the cells up into the pluripotent state.

There are at least two requirements for complete reprogramming. First, the four factors must be expressed in a pattern that provides a sufficient push in the right direction. Because available technologies cannot precisely control the expression levels of the four transgenes, this first requirement can only be achieved stochastically. Second, cells must be blocked by the epigenetic bump so that they can remain in the pluripotent zone even when the transgene expression disappears. Because the four reprogramming factors alone cannot constitute such an epigenetic roadblock, stochastic events again are required during iPS cell generation. As has been demonstrated in reprogramming by nuclear transfer, DNA methylation and histone modifications probably have important roles in iPS cell generation.

Expression patterns of reprogramming factor. Direct reprogramming probably depends on the amount, balance, continuity and silencing of the transgene expression of the four factors. The high copy numbers of proviruses in each iPS cell clone suggest that strong transgene expression is initially required. *Klf4* is expressed in fibroblasts, but its endogenous expression is not sufficient for iPS cell generation. The endogenous *c-Myc* gene is also expressed in fibroblasts, but its ectopic expression significantly enhances the efficiency of iPS cell generation in both mice and humans^{14,27}.

iPS cell induction may also depend on the specific stoichiometric balance of the four factors. For example, excess Oct-3/4 (ref. 28) and Sox2 (ref. 29) are detrimental to the maintenance of pluripotency. In fact, in neural stem cells that express the endogenous Sox2 gene, the efficiency of iPS cell generation is higher with ectopic expression of three factors devoid of Sox2 than with the combination of all four factors³⁰. The balance between *c-Myc* and *Klf4* may also be crucial for preventing apoptosis and senescence caused by the overexpression of these tumour-related genes³¹. An inappropriate balance of the four factors would result in improper reprogramming, senescence or apoptosis.

The continuity and silencing of the transgene expression are also important. Transgene expression must be maintained during the first 10 to 14 days^{32,33}. In this respect, retroviral vectors clearly have an advantage over plasmids and adenoviruses. However, to achieve complete reprogramming, transgene expression should be silenced and then taken over by the endogenous genes after this initial stage. The failure to achieve such transgene silencing could result in so-called partially reprogrammed cells, which possess ES cell morphology and express some ES cell marker genes, but have a limited ability to differentiate^{2,10,11}.

The amount, balance, continuity and silencing of the transgene expression can be greatly influenced by gene-delivery methods. With retroviruses and lentiviruses, positions of proviral integrations should have strong effects. This may explain why only a small portion of transduced cells complete the reprogramming process, because each transduced cell has a unique integration pattern. If this is the case, then one would expect a marked increase in efficiency when iPS

cells are generated from fibroblasts containing the reprogramming-competent integration of transgenes.

This experiment was first performed by Wernig *et al.*, who isolated MEFs from chimaeric embryos after the injection of doxycycline-induced iPS cells into blastocysts, and then generated 'secondary' iPS cells by treating these MEFs with doxycycline³⁴. A similar approach was also used in human cells³⁵. Primary human iPS cells were generated with doxycycline-regulated lentiviruses, which induced differentiation into fibroblasts, and then secondary iPS cells were generated with doxycycline. In these experiments, up to 4% of fibroblasts became iPS cells. More recently, a comparable method using the *piggyBac* transposon system demonstrated ~20% reprogramming efficiency³⁶. These findings indicate that cells containing the proper patterns of transgene integration could efficiently become iPS cells.

Epigenetic requirements for reprogramming. Even when the four factors are suitably expressed and able to move cells up the valleys, cells would roll down again without the transgene expression. Cells have to be blocked by a bump formed by a specific epigenetic status (Fig. 2). The endogenous loci of the four factors should be fully activated. An important requirement is proper DNA methylation. The promoter regions of many pluripotency associated genes are heavily methylated in fibroblasts and somatic cells, but are hypomethylated in ES cells and iPS cells³⁷. Therefore, during direct reprogramming, DNA demethylation of these regions should be accomplished. Because the four factors do not have intrinsic DNA demethylation activity, the process is probably a secondary effect, requiring several cell divisions. This may be one reason why iPS cell generation is so slow and inefficient. The fact that demethylation-promoting agents, such as 5-azacytidine, promote iPS cell generation supports this model¹⁰.

Generation of iPS cells should also require the proper reprogramming of histone modifications. In both ES cells and iPS cells, histone H3 and H4 are hyperacetylated in the promoter regions of pluripotency associated genes. In contrast, differentiated cells have hypoacetylated H4. Therefore, H4 of these regions should be acetylated during iPS cell generation. Because the three transcription factors themselves do not have histone modification activities, other factors are required. One function of *c-Myc* may be to recruit histone acetyltransferase to the target genes³⁸. The fact that a histone deacetylase inhibitor, such as valproic acid, enhances the efficiency of iPS cell generation supports the notion that histone acetylation is important in direct reprogramming^{15,39}.

Histone methylation also is likely to be important in suppressing iPS cell generation. In both ES cells and iPS cells, H3 is methylated at lysine 4 and demethylated at lysine 9 in the promoter regions of pluripotency associated genes. Fibroblasts have the opposite patterns of histone modifications. Furthermore, both ES cells and iPS cells have a so-called bivalent chromatin structure of developmental genes, consisting of methylation of both of H3 lysines 27 and 4 (ref. 40). These histone methylation states have to be established for iPS cell generation.

The iPS technology is still at its infancy. Nevertheless, its potential is enormous. Patient- or disease-specific iPS cells should provide unprecedented cell sources for better understanding the pathogenesis of diseases and for developing safer and more effective drugs. Furthermore, iPS cell technology should some day make it possible to perform cell transplantation therapies for a wide variety of diseases and injuries, while circumventing ethical issues and immune rejection. To realize the clinical applications, we have to achieve complete and uniform reprogramming in iPS cells. Failure to do this would result in resistance to differentiation and increase the risk of teratoma formation. The stochastic model predicts that iPS cells can be generated from a variety of somatic cells with a variety of methods. We have to evaluate different original cells and induction methods to determine the best combination to allow us to generate the safest iPS cells for clinical application.

Received 20 February; accepted 29 May 2009.

1. Tokuzawa, Y. *et al.* Fbx15 is a novel target of Oct3/4 but is dispensable for embryonic stem cell self-renewal and mouse development. *Mol. Cell. Biol.* **23**, 2699–2708 (2003).
2. Takahashi, K. & Yamanaka, S. Induction of pluripotent stem cells from mouse embryonic and adult fibroblast cultures by defined factors. *Cell* **126**, 663–676 (2006).
- This paper is the first demonstration of direct reprogramming by defined factors.**
3. Wernig, M. *et al.* In vitro reprogramming of fibroblasts into a pluripotent ES cell-like state. *Nature* **448**, 318–324 (2007).
4. Okita, K., Ichisaka, T. & Yamanaka, S. Generation of germ-line competent induced pluripotent stem cells. *Nature* **448**, 313–317 (2007).
5. Maherali, N. *et al.* Directly reprogrammed fibroblasts show global epigenetic remodelling and widespread tissue contribution. *Cell Stem Cell* **1**, 55–70 (2007).
6. Takahashi, K. *et al.* Induction of pluripotent stem cells from adult human fibroblasts by defined factors. *Cell* **131**, 861–872 (2007).
7. Yu, J. *et al.* Induced pluripotent stem cell lines derived from human somatic cells. *Science* **318**, 1917–1920 (2007).
8. Lowry, W. E. *et al.* Generation of human induced pluripotent stem cells from dermal fibroblasts. *Proc. Natl Acad. Sci. USA* **105**, 2883–2888 (2008).
9. Park, I. H. *et al.* Reprogramming of human somatic cells to pluripotency with defined factors. *Nature* **451**, 141–146 (2008).
10. Mikkelsen, T. S. *et al.* Dissecting direct reprogramming through integrative genomic analysis. *Nature* **454**, 49–55 (2008).
11. Silva, J. *et al.* Promotion of reprogramming to ground state pluripotency by signal inhibition. *PLoS Biol.* **6**, e253 (2008).
12. Blelloch, R. *et al.* Reprogramming efficiency following somatic cell nuclear transfer is influenced by the differentiation and methylation state of the donor nucleus. *Stem Cells* **24**, 2007–2013 (2006).
13. Toma, J. G. *et al.* Isolation of multipotent adult stem cells from the dermis of mammalian skin. *Nature Cell Biol.* **3**, 778–784 (2001).
14. Nakagawa, M. *et al.* Generation of induced pluripotent stem cells without Myc from mouse and human fibroblasts. *Nature Biotechnol.* **26**, 101–106 (2008).
15. Huangfu, D. *et al.* Induction of pluripotent stem cells from primary human fibroblasts with only Oct4 and Sox2. *Nature Biotechnol.* **26**, 1269–1275 (2008).
16. Aoi, T. *et al.* Generation of pluripotent stem cells from adult mouse liver and stomach cells. *Science* **321**, 699–702 (2008).
17. Stadtfeld, M., Brennand, K. & Hochedlinger, K. Reprogramming of pancreatic Beta cells into induced pluripotent stem cells. *Curr. Biol.* **18**, 890–894 (2008).
18. Hanna, J. *et al.* Direct reprogramming of terminally differentiated mature B lymphocytes to pluripotency. *Cell* **133**, 250–264 (2008).
19. Kim, J. B. *et al.* Oct4-induced pluripotency in adult neural stem cells. *Cell* **136**, 411–419 (2009).
20. Aasen, T. *et al.* Efficient and rapid generation of induced pluripotent stem cells from human keratinocytes. *Nature Biotechnol.* **26**, 1276–1284 (2008).
21. Varas, F. *et al.* Fibroblast-derived induced pluripotent stem cells show no common retroviral vector insertions. *Stem Cells* **27**, 300–306 (2008).
22. Stadtfeld, M., Nagaya, M., Utikal, J., Weir, G. & Hochedlinger, K. Induced pluripotent stem cells generated without viral integration. *Science* **322**, 945–949 (2008).

This paper is the first demonstration of integration-free iPS cell generation.

23. Okita, K., Nakagawa, M., Hyenjong, H., Ichisaka, T. & Yamanaka, S. Generation of mouse induced pluripotent stem cells without viral vectors. *Science* **322**, 949–953 (2008).
24. Zhou, H. *et al.* Generation of induced pluripotent stem cells using recombinant proteins. *Cell Stem Cell* **4**, 381–384 (2009).
- This paper is the first demonstration of iPS cell generation by protein transduction.**
25. Yu, J. *et al.* Human induced pluripotent stem cells free of vector and transgene sequences. *Science* **324**, 797–801 (2009).
26. Waddington, C. H. *The Strategy of the Genes. A Discussion of Some Aspects of Theoretical Biology* (Allen & Unwin, 1957).
27. Wernig, M., Meissner, A., Cassady, J. P. & Jaenisch, R. c-Myc is dispensable for direct reprogramming of mouse fibroblasts. *Cell Stem Cell* **2**, 10–12 (2008).
28. Niwa, H., Miyazaki, J. & Smith, A. G. Quantitative expression of Oct-3/4 defines differentiation, dedifferentiation or self-renewal of ES cells. *Nature Genet.* **24**, 372–376 (2000).
29. Kopp, J. L., Ormsbee, B. D., Desler, M. & Rizzino, A. Small increases in the level of Sox2 trigger the differentiation of mouse embryonic stem cells. *Stem Cells* **26**, 903–911 (2008).
30. Eminli, S., Utikal, J. S., Arnold, K., Jaenisch, R. & Hochedlinger, K. Reprogramming of neural progenitor cells into induced pluripotent stem cells in the absence of exogenous Sox2 expression. *Stem Cells* **26**, 2467–2474 (2008).
31. Rowland, B. D. & Peeper, D. S. KLF4, p21 and context-dependent opposing forces in cancer. *Nature Rev. Cancer* **6**, 11–23 (2006).
32. Brambrink, T. *et al.* Sequential expression of pluripotency markers during direct reprogramming of mouse somatic cells. *Cell Stem Cell* **2**, 151–159 (2008).
33. Stadtfeld, M., Maherali, N., Breault, D. T. & Hochedlinger, K. Defining molecular cornerstones during fibroblast to iPS cell reprogramming in mouse. *Cell Stem Cell* **2**, 230–240 (2008).
34. Wernig, M. *et al.* A drug-inducible transgenic system for direct reprogramming of multiple somatic cell types. *Nature Biotechnol.* **26**, 916–924 (2008).
35. Maherali, N. *et al.* A high-efficiency system for the generation and study of human induced pluripotent stem cells. *Cell Stem Cell* **3**, 340–345 (2008).
36. Woltjen, K. *et al.* piggyBac transposition reprograms fibroblasts to induced pluripotent stem cells. *Nature* **458**, 766–770 (2009).
37. Imamura, M. *et al.* Transcriptional repression and DNA hypermethylation of a small set of ES cell marker genes in male germline stem cells. *BMC Dev. Biol.* **6**, 34 (2006).
38. Knoepfler, P. S. *et al.* Myc influences global chromatin structure. *EMBO J.* **25**, 2723–2734 (2006).
39. Huangfu, D. *et al.* Induction of pluripotent stem cells by defined factors is greatly improved by small-molecule compounds. *Nature Biotechnol.* **26**, 795–797 (2008).
- This paper presents considerable improvement of iPS cell generation by a defined chemical.**
40. Bernstein, B. E. *et al.* A bivalent chromatin structure marks key developmental genes in embryonic stem cells. *Cell* **125**, 315–326 (2006).

Acknowledgements I thank B. Conklin and G. Howard for critical reading of the manuscript, and members of my laboratory for scientific and administrative support. I apologize to researchers whose work could not be cited owing to space constraints.

Author Information Reprints and permissions information is available at www.nature.com/reprints. Correspondence should be addressed to S.Y. (yamanaka@cira.kyoto-u.ac.jp).

Disease-corrected haematopoietic progenitors from Fanconi anaemia induced pluripotent stem cells

Ángel Raya^{1,2,3}, Ignasi Rodríguez-Pizà¹, Guillermo Guenechea^{4,5}, Rita Vassena¹, Susana Navarro^{4,5}, María José Barrero¹, Antonella Consiglio^{1,6}, Maria Castellà^{5,7}, Paula Río^{4,5}, Eduard Sleep^{1,3}, Federico González¹, Gustavo Tiscornia¹, Elena Garreta^{1,3}, Trond Aasen^{1,3}, Anna Veiga¹, Inder M. Verma⁸, Jordi Surrallés^{5,7}, Juan Bueren^{4,5} & Juan Carlos Izpisua Belmonte^{1,9}

The generation of induced pluripotent stem (iPS) cells has enabled the derivation of patient-specific pluripotent cells and provided valuable experimental platforms to model human disease. Patient-specific iPS cells are also thought to hold great therapeutic potential, although direct evidence for this is still lacking. Here we show that, on correction of the genetic defect, somatic cells from Fanconi anaemia patients can be reprogrammed to pluripotency to generate patient-specific iPS cells. These cell lines appear indistinguishable from human embryonic stem cells and iPS cells from healthy individuals. Most importantly, we show that corrected Fanconi-anaemia-specific iPS cells can give rise to haematopoietic progenitors of the myeloid and erythroid lineages that are phenotypically normal, that is, disease-free. These data offer proof-of-concept that iPS cell technology can be used for the generation of disease-corrected, patient-specific cells with potential value for cell therapy applications.

The possibility of reprogramming mature somatic cells to generate iPS cells^{1–5} has enabled the derivation of disease-specific pluripotent cells, thus providing unprecedented experimental platforms to model human disease^{6–9}. In addition, the generation of patient-specific iPS cells may have a wide range of applications in cell and gene therapy, and could be particularly relevant for the treatment of inherited bone marrow failure (BMF) syndromes, where the progressive decline in haematopoietic stem cell (HSC) numbers limits the production of peripheral blood cells.

Among the different inherited BMF syndromes, Fanconi anaemia (FA) is the most common¹⁰. FA is a rare recessive, autosomal or X-linked, chromosomal instability disorder caused by mutations in any of the 13 genes so far identified in the FA pathway¹¹. Cells from these patients display typical chromosomal instability and hypersensitivity to DNA crosslinking agents, characteristics that are used to make the diagnosis of FA¹². Most FA patients develop BMF, which typically appears during the first decade of life, and some patients show increased predisposition to develop malignancies (cumulative incidence of ~30% by 40 years of age)¹³. Currently, the therapy of choice for BMF in FA patients is the transplantation of haematopoietic grafts from HLA-identical siblings, whereas the output of transplants from non-related donors is more limited^{14,15}. Somatic mosaicism, acting as a natural gene therapy in FA patients, showed that genetic correction confers a selective growth advantage to HSCs from FA patients, a process that can ultimately restore the haematopoietic system of the patient with phenotypically normal cells^{16–18}. A selective proliferation advantage has also been observed in FA mouse models after *ex vivo* genetic correction of their HSCs with lentiviral vectors¹⁹. In spite of

these observations, gene therapy trials conducted so far in FA patients have not been clinically successful^{20,21}, owing to the paucity and poor quality of HSCs in the bone marrow of FA patients^{20–23}.

As a consequence of the genetic instability of FA cells, genetic defects eventually produced before gene therapy correction would not be repaired. Nevertheless, the generation of genetically corrected FA-specific iPS cells by the reprogramming of non-haematopoietic somatic cells would result in the production of large numbers of autologous, genetically stable HSCs that may be used to treat BMF in FA patients.

Generation of patient-specific iPS cells

We obtained samples from six FA patients, four from the FA-A complementation group (patients FA5, FA90, FA153 and FA404) and two from the FA-D2 complementation group (FA430 and FA431). Samples from patients FA5, FA90, FA153, FA430 and FA431 were cryopreserved primary dermal fibroblasts that had undergone an undetermined number of passages. From patient FA404 we obtained a skin biopsy, from which we established primary cultures of dermal fibroblasts and epidermal keratinocytes. We first attempted to optimize the reprogramming protocol using primary dermal fibroblasts from a foreskin biopsy of a healthy donor (see Supplementary Information and Supplementary Fig. 1). Our improved reprogramming protocol consisted of two rounds of infection with mouse-stem-cell-virus-based retroviruses encoding amino-terminal Flag-tagged versions of OCT4 (also known as POU5F1), SOX2, KLF4 and c-MYC (also known as MYC), performed 6 days apart. Transduced fibroblasts were passaged after 5 days onto a feeder layer

¹Center for Regenerative Medicine in Barcelona, Dr. Aiguader 88, 08003 Barcelona, Spain. ²Institució Catalana de Recerca i Estudis Avançats (ICREA). ³Networking Center of Biomedical Research in Bioengineering, Biomaterials and Nanomedicine (CIBER-BBN). ⁴Hematopoiesis and Gene Therapy Division, Centro de Investigaciones Energéticas, Medioambientales y Tecnológicas (CIEMAT), Av. Complutense 22, 28040 Madrid, Spain. ⁵Networking Center of Biomedical Research in Rare Diseases (CIBERER). ⁶Department of Biomedical Science and Biotechnology, University of Brescia, Viale Europa 11, 25123 Brescia, Italy. ⁷Department of Genetics and Microbiology, Universitat Autònoma de Barcelona, 08193 Bellaterra, Spain. ⁸Laboratory of Genetics, ⁹Gene Expression Laboratory, Salk Institute for Biological Studies, 10010 North Torrey Pines Road, La Jolla, California 92037, USA.

of primary human fibroblasts and switched to human embryonic stem (ES) cell medium the next day. We also included a selection step based on the combined inhibition of MAP2K1 and GSK3B with inhibitors PD0325901 and CT99021 (a combination termed 2i that enhances derivation and growth of mouse ES cells²⁴) for 1 week, starting 1 week after plating onto feeders.

Because of the genetic instability and apoptotic predisposition of FA cells²⁵, somatic cells were reprogrammed either directly or after genetic correction with lentiviral vectors encoding FANCA or FANCD2, respectively. We have previously shown that genetic complementation of human and mouse FA cells with these vectors efficiently corrects the FA phenotype^{19,23,26}. We were not successful at obtaining iPS-like colonies from fibroblasts of patients FA5, FA153 or FA430, either unmodified or corrected, after at least five reprogramming attempts, probably owing to the cells having accumulated too many passages and/or karyotypic abnormalities (Supplementary Table 1). However, from patient FA90 we readily obtained iPS-like colonies when using genetically corrected fibroblasts (Fig. 1a). Overall, we obtained 10–15 iPS-like colonies in each of 3 independent experiments. Of these, we randomly picked ten colonies, all of which could successfully be expanded and grew as colonies morphologically indistinguishable from human ES cells (Fig. 1b) that stained strongly positive for alkaline phosphatase activity (Fig. 1c). Five of these lines (cFA90-44-1, -11, -14, -20 and -21) were selected for further characterization. All of them displayed a normal karyotype (46 XX) at passages 12–16 and could be maintained in culture for, at least, 20 passages. At the time of the writing, cFA90-44-14 had undergone 43 passages without signs of replicative crisis, while maintaining a normal karyotype (Supplementary Fig. 2). Immunofluorescence analyses of the five lines revealed expression of transcription factors (OCT4, SOX2, NANOG) and surface markers (SSEA3, SSEA4, TRA1-60, TRA1-81) characteristic of pluripotent cells (Fig. 1d–f and Supplementary Fig. 3).

With somatic cells from another FA-A patient, patient FA404, we obtained similar results. Fibroblasts that had been transduced with lentiviruses encoding FANCA (Fig. 1g) were readily reprogrammed to generate iPS-like cells (Fig. 1h). We established two cell lines

(cFA404-FiPS4F1 and cFA404-FiPS4F2), which displayed typical human ES-like morphology and growth characteristics, stained positive for alkaline phosphatase activity and expressed all the pluripotency-associated markers tested (Fig. 1i–l and Supplementary Fig. 4). From patient FA404 we also derived primary epidermal keratinocytes, which we reprogrammed using a protocol recently set up in our laboratory²⁷. We generated three iPS cell lines (cFA404-KiPS4F1, -KiPS4F3 and -KiPS4F6) from genetically corrected keratinocytes, which displayed all the main characteristics of bona fide iPS cells and human ES cells (Supplementary Fig. 4) and a normal 46 XY karyotype (Supplementary Fig. 2).

We were also successful at reprogramming fibroblasts from patient FA431 (Supplementary Fig. 5a), a FA-D2 patient. In this case, iPS-like colonies appeared in roughly equal numbers from either unmodified or genetically corrected fibroblasts (Supplementary Table 1). We picked two iPS-like colonies from either condition, which grew after passaging and stained positive for alkaline phosphatase activity (Supplementary Fig. 5c, g). However, whereas those derived from corrected fibroblasts (cFA431-44-1 and cFA431-44-2) could be maintained in culture for extended periods of time (18 passages at the time of writing) and showed expression of pluripotency-associated transcription factors and surface markers (Supplementary Fig. 5d–f and data not shown), those derived from unmodified fibroblasts experienced a progressive growth delay and could not be maintained over the third passage (Supplementary Fig. 5g). The observation that uncorrected FA-D2 fibroblasts from patient FA431 could be reprogrammed, while we only obtained iPS cells from FANCA-complemented fibroblasts from patients FA90 or FA404, could be explained by the fact that FA-D2 patients, in particular FA431, carry hypomorphic mutations compatible with the expression of residual FANCD2 protein²⁸. Therefore, it appears that restoration of the FA pathway is a pre-requisite for iPS cell generation from somatic cells of FA patients (in total, 12 out of 28 independent reprogramming attempts were successful when using genetically corrected cells—also including the patients for which reprogramming was never successful—versus 0 out of 28 successful attempts when uncorrected cells were used; $\chi^2 [1] = 15.27$, $P = 9.3 \times 10^{-5}$).

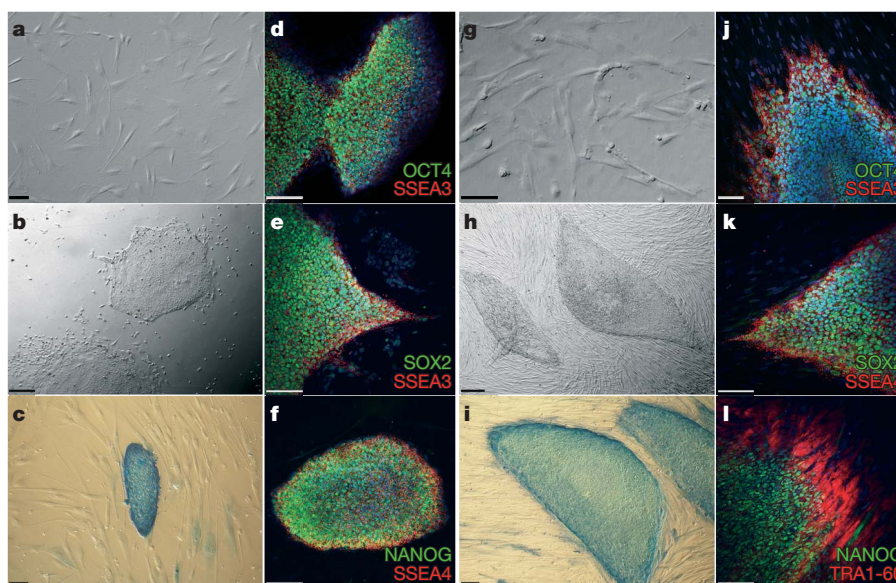


Figure 1 | Derivation of patient-specific induced pluripotent stem cells from Fanconi anaemia patients. **a–f**, Successful reprogramming of genetically corrected primary dermal fibroblasts (**a**) derived from patient FA90. **b**, Colony of iPS cells from the cFA90-44-14 line grown on Matrigel-coated plates showing human-ES-cell-like morphology. **c–f**, The same iPS cell line shows strong alkaline phosphatase staining (**c**) and expression of the transcription factors OCT4 (**d**), SOX2 (**e**) and NANOG (**f**) and the surface markers SSEA3 (**d**, **e**) and SSEA4 (**f**). **g**, Genetically corrected fibroblasts

from patient FA404. **h**, Colony of iPS cells from the cFA404-FiPS4F1 line grown on feeder cells displaying typical human ES cell morphology. **i–l**, The same iPS cell line shows strong alkaline phosphatase staining (**i**) and expression of the pluripotency-associated transcription factors OCT4 (**j**), SOX2 (**k**) and NANOG (**l**) and surface markers SSEA3 (**j**), SSEA4 (**k**) and TRA1-80 (**l**). Cell nuclei were counterstained with 4,6-diamidino-2-phenylindole (DAPI) in **d–f** and **j–l**. Scale bars, 100 μ m (**a**, **c–g**, **i–l**) and 250 μ m (**b**, **h**).

Characterization of iPS cells

Out of the 19 FA-iPS cell lines generated in these studies, we selected 10 for more thorough characterization (Supplementary Table 1). We confirmed the presence of the reprogramming transgenes integrated in their genome by polymerase chain reaction (PCR) of genomic DNA (Fig. 2a and Supplementary Fig. 6), as well as the origin of the iPS cell lines by comparing their HLA type and DNA fingerprint with those of patients' somatic cells (Supplementary Table 2). In all lines tested, transgenic expression of the four reprogramming factors was reduced to low or undetectable levels, compared to an iPS cell line (KiPS4F3) previously shown not to have silenced the retroviral expression of *OCT4* and *c-MYC*²⁷ (Fig. 2b). Furthermore, all the FA-iPS cell lines tested showed re-activation of endogenous *OCT4* and *SOX2* expression, as well as of other pluripotency-associated transcription factors such as *NANOG*, *REX-1* (also known as *ZFP42*) and *CRIP1* (also known as *TDGF1*; Fig. 2c). Taking advantage of the fact that our retroviral transgenes were Flag-tagged, we confirmed by immunofluorescence that iPS cells displayed negligible anti-Flag immunoreactivity (Fig. 2d–g). Finally, the promoters of the pluripotency-associated transcription factors *OCT4* and *NANOG*, heavily methylated in patients' fibroblasts, were demethylated in FA-iPS cells (Fig. 2h), indicating epigenetic reprogramming to pluripotency.

We next analysed the differentiation ability of FA-iPS cells. *In vitro*, iPS-derived embryoid bodies readily differentiated into endoderm, ectoderm and mesoderm derivatives as judged by cell morphology and specific immunostaining with antibodies against α -fetoprotein/FOXA2, TuJ1/GFAP and α -actinin, respectively (Fig. 3a–c, and Supplementary Fig. 7). Following specific *in vitro* differentiation protocols, iPS cells gave rise to specialized mesoderm-derived cell types such as rhythmically beating cardiomyocytes (Supplementary Movie

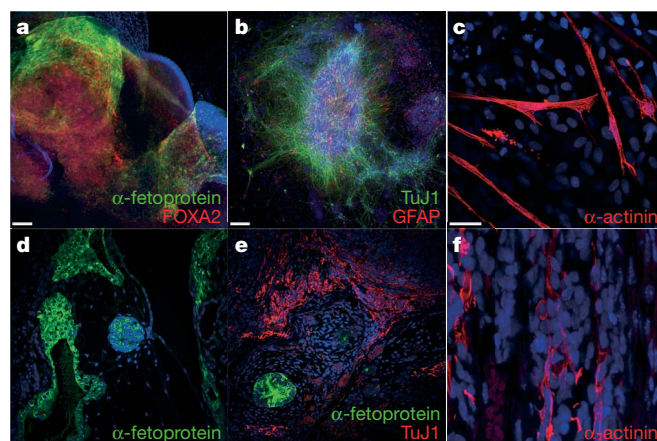


Figure 3 | Pluripotency of FA-iPS cells. a–c, *In vitro* differentiation experiments of cFA404-FiPS4F2 iPS cells reveal their potential to generate cell derivatives of all three primary germ cell layers. Immunofluorescence analyses show expression of markers of a, endoderm (α -fetoprotein, green; FOXA2, red), b, neuroectoderm (TuJ1, green; GFAP, red), and, c, mesoderm (α -actinin, red). d–f, Injection of cFA90-44-14 iPS cells into the testes of immunocompromised mice results in the formation of teratomas containing structures that represent the three main embryonic germ layers. Endoderm derivatives (d, e) include glandular structures that stain positive for endoderm markers (α -fetoprotein, green); ectoderm derivatives (e) include structures that stain positive for neuroectoderm markers (TuJ1, red); mesoderm derivatives (f) include structures that stain positive for muscle markers (α -actinin, red). All images are from the same tumour. Scale bars, 100 μ m (a, b, d, e) and 25 μ m (c, f).

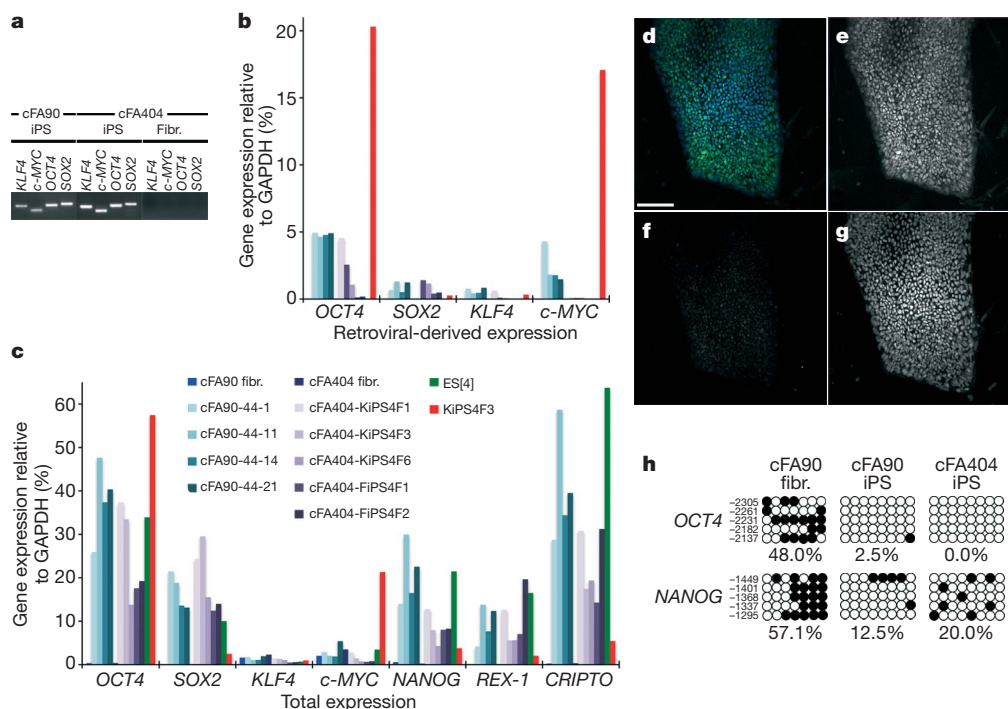


Figure 2 | Molecular characterization of FA-iPS cell lines. a, PCR of genomic DNA to detect integration of the indicated retroviral transgenes in FA-iPS cell lines cFA90-44-14 (cFA90) and cFA404-FiPS4F1 (cFA404). Genetically corrected fibroblasts (Fibr.) from patient FA404 before reprogramming were used as negative control. b, c, Quantitative PCR with reverse transcription (RT-PCR) analyses of the expression levels of retroviral-derived reprogramming factors (b) and of total expression levels of reprogramming factors and pluripotency-associated transcription factors (c) in the indicated patients' fibroblasts (fibr.) and FA-iPS cell lines. Human ES cells (ES[4]) and partially silenced iPS cells (KiPS4F3) are included as

controls. Transcript expression levels are plotted relative to GAPDH expression. d–g, Colony of cFA90-44-14 iPS cells showing high levels of endogenous *NANOG* expression (e, green channel in d) and absence of Flag immunoreactivity (f, red channel in d). Cell nuclei were counterstained with DAPI (g, blue channel in d). h, Bisulphite genomic sequencing of the *OCT4* and *NANOG* promoters showing demethylation in FA-iPS cell lines cFA90-44-14 and cFA404-KiPS4F3, compared to patient's fibroblasts. Open and closed circles represent unmethylated and methylated CpGs, respectively, at the indicated promoter positions. Scale bar, 100 μ m.

1) and haematopoietic progenitor cells (see below). We also subjected our FA-iPS cells to the most stringent test available to assess pluripotency of human cells, the formation of bona fide teratomas²⁹. For this purpose, we injected cells from eight different lines into the testes of immunocompromised mice. In all cases, teratomas could be recovered after 8–10 weeks that were composed of complex structures representing the three main embryonic germ layers, including glandular formations that stained positive for definitive endoderm markers, neural structures that expressed neuroectodermal markers, and mesoderm derivatives such as muscle and cartilage (Fig. 3d–f, Supplementary Fig. 8 and data not shown). Using comparable assays, we have recently characterized the *in vitro* differentiation and teratoma induction abilities of a variety of normal human pluripotent stem cell lines, including human ES cells³⁰ and iPS cells generated from healthy donors²⁷. Overall, we did not detect conspicuous differences in the differentiation ability of FA-iPS cell lines compared to that of either human ES cells or normal iPS cells.

FA-specific iPS cells are disease-free

Consistent with the previous genetic correction of somatic cells used for reprogramming, we could detect the presence of integrated copies of the gene therapy vectors by quantitative PCR of genomic DNA in all FA-iPS cell lines tested (Supplementary Fig. 9a). A concern with gene therapy strategies is the silencing of the correcting transgene. For this reason, we chose lentiviruses as gene therapy vectors, because lentiviral transgenes are particularly resistant to silencing in human ES cells³¹. However, this resistance appears to be promoter-dependent³² and nearly complete silencing of lentiviral transgenes has been recently

observed in the context of induced reprogramming^{3,8}. In our experiments, the *FANCA* lentivirus was partially silenced in FA-iPS cells, as evidenced by the loss of *IRES*-GFP (internal ribosome entry site-green fluorescent protein) fluorescence (data not shown), which was detectable in transduced fibroblasts (Supplementary Fig. 9b). However, transgene silencing was not complete, as we could detect *FANCA* expression in all the FA-iPS cell lines analysed, but not in the patients' fibroblasts (Fig. 4a). To test the functionality of the FA pathway in FA-iPS cells, we induced subnuclear accumulation of stalled replication forks by high-energy local ultraviolet irradiation across a filter with 5 μ m pores and checked whether FANCD2 relocated to the locally damaged subnuclear areas³³. In those experiments, fibroblast-like cells derived from FA-iPS cells showed normal relocation of FANCD2 (Fig. 4b). In addition, we induced replication fork collapse by treating FA-iPS-derived cells with the DNA replication inhibitor hydroxyurea. Also, in this case, FA-iPS-derived cells displayed normal relocation of FANCD2 (Supplementary Fig. 10). These results, together with the persistent *FANCA* expression in FA-iPS cells, clearly show that iPS cells generated from genetically corrected FA somatic cells maintain a fully functional FA pathway and are, thus, phenotypically disease free.

Our findings that successful reprogramming of FA cells only occurred in those that had been transduced with *FANCA*-expressing lentiviruses (in spite of only 35–50% of cells being actually transduced with the correcting lentiviruses; see Supplementary Fig. 9b), and that lentiviral transgenes were not completely silenced in FA-iPS cells, indicate that a functional FA pathway confers a strong selection advantage for iPS cell generation and/or maintenance. To address

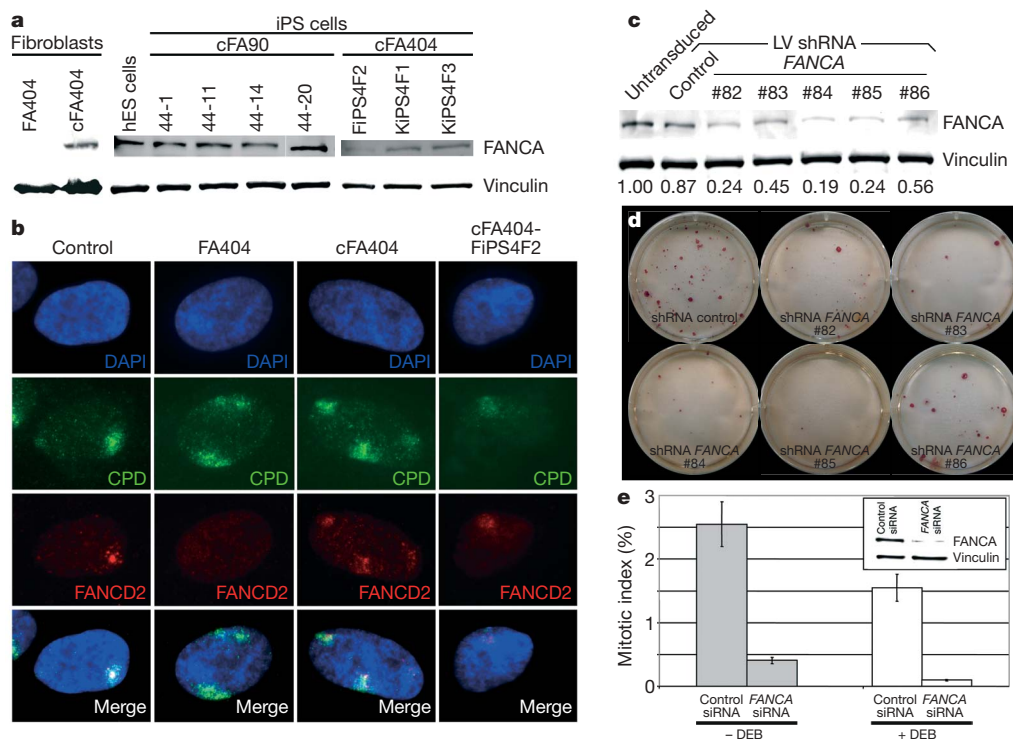


Figure 4 | Functional FA pathway in FA-iPS cells. **a**, Western blot analysis of FANCA in protein extracts from the indicated cell lines, showing expression of FANCA in FA-iPS cells. The expression of vinculin was used as a loading control. hES, human ES. **b**, FANCD2 (red channel) fails to relocate to UVC-radiation-induced stalled replication forks, visualized by immunofluorescence with antibodies against cyclobutane pyrimidine dimers (CPD, green channel), in fibroblasts from patient FA404, whereas it shows normal accumulation to damaged sites in wild-type fibroblasts (control), corrected fibroblasts (cFA404) or FA-iPS-derived cells (cFA404-FIPS4F2). **c**, Western blot analysis of FANCA in protein extracts from untransduced cFA404-KIPS4F3 cells or 6 days after transduction with lentiviruses expressing scramble shRNA (control) or the indicated *FANCA*

shRNAs. The expression of vinculin was used as a loading control. Values at the bottom represent FANCA expression levels measured by densitometry quantification normalized by vinculin expression and referred to untransduced cFA404-KIPS4F3 cells. **d**, Alkaline phosphatase staining of cFA404-KIPS4F3 cells one passage after being transduced with lentiviruses expressing scramble shRNA (control) or the indicated *FANCA* shRNAs, one week after seeding. **e**, Mitotic index values in cFA404-FIPS4F2-derived cells transfected with scramble (control) or *FANCA* siRNAs and incubated in the absence or in the presence of diepoxybutane (DEB). The inset shows FANCA depletion induced by *FANCA* siRNAs in these experiments, as visualized by western blot using vinculin as a loading control. Data are presented as mean \pm s.d.

this possibility directly, we knocked down the transgenic expression of *FANCA* in FA-iPS cells by lentiviral delivery of *FANCA* short hairpin RNAs (shRNAs). Of the five different shRNAs tested, three achieved greater than 70% downregulation of *FANCA* expression in cFA404-KiPS4F3 cells (Fig. 4c). Notably, iPS cells with the lowest *FANCA* levels failed to proliferate after one passage (Fig. 4d). Similar results were obtained with cFA90-44-14 cells (data not shown). In a complementary approach, transient downregulation of *FANCA* expression in FA-iPS-derived cells by small interfering RNA (siRNA) transfection led to a marked decrease in cell proliferation (~ 7 -fold) compared to scramble-siRNA-transfected cells (Fig. 4e), which was even more pronounced (~ 15 -fold) in response to diepoxybutane-induced DNA damage (Fig. 4e). These results provide further evidence for the FA disease-free status of our FA-iPS cells and, importantly, unveil a previously unsuspected role of the FA pathway as a critical player in the maintenance of pluripotent stem cell self-renewal.

Disease-free haematopoietic progenitors

To test the haematopoietic differentiation ability of FA-iPS cells, embryoid bodies from six different lines (cFA90-44-11 and -44-14,

cFA404-FiPS4F2, -KiPS4F1, -KiPS4F3 and -KiPS4F6) were co-cultured with OP9 stromal cells³⁴ in the presence of haematopoietic cytokines. In all cases, we could detect CD34⁺ cells by flow cytometry starting at day 5 and peaking at day 12 ($7.23 \pm 2.57\%$, $n = 7$). We could also detect CD45⁺ cells in those cultures from day 10, which reached $0.95 \pm 0.38\%$ ($n = 6$) by day 12 (Fig. 5a). The timing of appearance and frequency of haematopoietic progenitors obtained from FA-iPS cells were similar to those obtained using iPS cells from healthy individuals ($7.24 \pm 3.43\%$ of CD34⁺ cells at day 12, $n = 5$ from 2 independent iPS cell lines) and human ES cells ($6.62 \pm 1.03\%$ of CD34⁺ cells at day 12, $n = 5$ from 2 independent human ES cell lines; see also ref. 35).

We purified FA-iPS-derived CD34⁺ cells at day 12 of the differentiation protocol by two rounds of magnetic-activated cell sorting (MACS) to test their haematopoietic differentiation ability in clonogenic progenitor assays. FA-iPS-derived CD34⁺ cells generated large erythroid (burst-forming unit-erythroid (BFU-E)) and myeloid (colony-forming unit-granulocytic, monocytic (CFU-GM)) colonies (Fig. 5b, c). The myeloid nature of CFU-GM colonies was confirmed by the expression of the CD33 and CD45 markers in these colonies (Fig. 5d). The haematopoietic potential of FA-iPS-derived CD34⁺

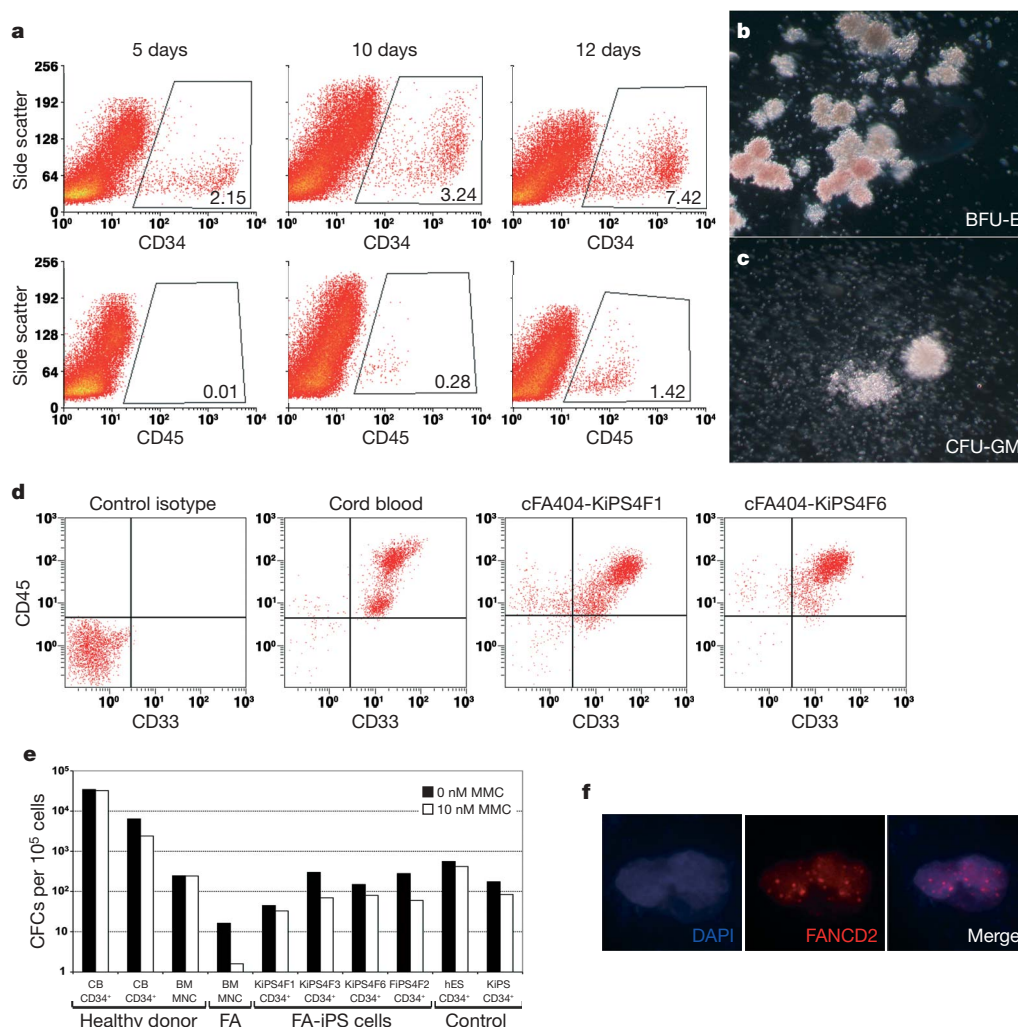


Figure 5 | Generation of disease-free haematopoietic progenitors from FA-iPS cell lines. **a**, Expression of CD34 and CD45 markers in FA-iPS cells subjected to haematopoietic differentiation. **b**, **c**, Representative erythroid (BFU-E) and myeloid (CFU-GM) colonies generated 14 days after the incubation of iPS-derived CD34⁺ cells in semisolid cultures. **d**, The myeloid nature of CFU-GM colonies was confirmed by the co-expression of the CD33 and CD45 markers in CFU-GM colonies. **e**, Total number of CFCs generated in the absence and the presence of 10 nM mitomycin C (MMC) from CD34⁺

cells derived from the indicated FA-iPS cell lines. For comparison, clonogenic assays were also performed using haematopoietic progenitors from healthy donors (purified CD34⁺ cord blood cells from two independent donors, CB CD34⁺; and mononuclear bone marrow cells, BM MNC), from a FA patient and from CD34⁺ cells derived from control human pluripotent stem cells, including ES[2] cells (hES) and KiPS4F1 (KiPS) cells. **f**, Immunofluorescence analysis showing FANCD2 foci in mitomycin-C-treated CD34⁺ cells derived from FA-iPS cells (line cFA90-44-14).

cells was robust and the numbers of colony-forming cells (CFCs) obtained in clonogenic assays were comparable to those obtained from CD34⁺ cells derived from human ES cells or control iPS cells (Fig. 5e, solid bars). These results indicate that FA-iPS cells successfully differentiated into haematopoietic progenitors of the erythroid and myeloid lineages. We also attempted to generate blood cells in nonobese diabetic/severe combined immunodeficient mice transplanted with FA-iPS-derived CD34⁺ cells, but no engraftment was observed, in agreement with the reported technical limitation for repopulating immunodeficient mice with *in-vitro*-differentiated human ES cells³⁶.

To test whether FA-iPS-derived haematopoietic progenitors maintained the disease-free phenotype of FA-iPS cells, haematopoietic colonies were also cultured in the presence of mitomycin C, because hypersensitivity to DNA crosslinking agents is a hallmark of FA cells¹². The proportion of mitomycin-C-resistant colonies obtained from FA-iPS-derived CD34⁺ cells was similar to that obtained from mononuclear bone marrow cells from healthy donors, or from human ES- or control iPS-derived CD34⁺ cells, and contrasted sharply with the hypersensitivity to mitomycin C shown by FA mononuclear bone marrow cells (Fig. 5e, white bars). Moreover, FA-iPS-derived CD34⁺ cells were able to form nuclear foci after exposure to mitomycin C (Fig. 5f), demonstrating a functional FA pathway.

Discussion

Before the clinical application of iPS-based strategies is realized, a number of caveats must be resolved. Retroviral transduction of adult somatic cells with OCT4, SOX2, KLF4 and c-MYC, although currently the most efficient method for generating human iPS cells, results in permanent undesirable transgene integrations. Although the retroviral transgenes become silenced during reprogramming, their re-activation during cell differentiation (particularly that of the proto-oncogene c-MYC) has been associated with tumour formation³⁷. Human iPS cells can be generated without c-MYC, but reprogramming efficiency in this case is markedly reduced^{27,38}. To ascertain whether FA-iPS cells could be generated without c-MYC, we used primary keratinocytes from patient FA404. After three reprogramming attempts, we generated one iPS cell line (cFA404-KiPS3F1), which expanded robustly and showed all the characteristics and differentiation ability of iPS cells generated with four factors, and gave rise to haematopoietic progenitors *in vitro* (Supplementary Fig. 11). As expected, the genome of cFA404-KiPS3F1 cells did not contain integrations of the c-MYC retrovirus, as revealed by Southern hybridization with probes specific for the reprogramming factors (Supplementary Fig. 12) and PCR of genomic DNA (data not shown). These results demonstrate that 'safer' patient-specific iPS cells can be generated with just three factors, although at efficiencies that may not be compatible with practical application. Moreover and ideally, permanent modification of the genome of iPS cells should be avoided, and integrating retroviruses omitted altogether. The recent implementation of reprogramming protocols that do not rely on viral integration^{39–42}, if their applicability to human cells was confirmed, would bring the realization of this possibility closer.

The use of patient-specific iPS cells to generate disease-corrected cells could potentially overcome the risks of insertional oncogenesis⁴³ that currently limit gene therapy strategies, because genetically corrected iPS cells lend themselves to the screening of safe integration sites of the therapeutic transgenes. In addition, homologous recombination⁴⁴ could be used to correct genetic defects of patient-specific iPS cells. Our studies also unveil a critical role of the FA pathway in the self-renewal of pluripotent stem cells, which we postulate provided strong selection advantage to iPS cells that had not completely silenced the therapeutic transgene. The ability of human pluripotent stem cells to silence viral transgenes should be carefully taken into account when devising future iPS-cell-based gene therapy strategies

for conditions in which genetic correction does not confer selection advantage.

METHODS SUMMARY

Somatic cells of FA patients were obtained after approval by the competent authorities. Patients FA5, FA90 and FA153 have been previously described⁴⁵; patients FA430 and FA431 correspond to patients 2 and 10, respectively, in ref. 28. Patient FA404 was newly recruited for the study and typed by standard methods⁴⁵. Somatic cells were reprogrammed with retroviruses encoding Flag-tagged OCT4, SOX2 and KLF4, with or without c-MYC(T58A). The gene therapy lentiviral vectors used to correct FA somatic cells have been previously described²⁶ and were prepared essentially as reported⁴⁶. Characterization of iPS cells was performed essentially as described^{27,30}. The functionality of the FA pathway was assessed by subnuclear accumulation of stalled replication forks induced by local ultraviolet-C (UVC) irradiation essentially as described³³. Haematopoietic differentiation of iPS cells was done by co-culturing embryoid bodies with OP9 stromal cells³⁴ in the presence of BMP4, VEGF, Kit ligand, FGF2, TPO and Flt ligand. For knocking down *FANCA* expression, we used transient transfection of *FANCA* siRNA (ref. 47) as reported⁴⁸, with luciferase siRNA as a control, or lentiviral delivery of five different *FANCA* shRNAs (Sigma, MISSION shRNA NM_000135), with scramble shRNA as a control.

Full Methods and any associated references are available in the online version of the paper at www.nature.com/nature.

Received 20 January; accepted 14 May 2009.

Published online 31 May 2009.

1. Takahashi, K. & Yamanaka, S. Induction of pluripotent stem cells from mouse embryonic and adult fibroblast cultures by defined factors. *Cell* **126**, 663–676 (2006).
2. Takahashi, K. *et al.* Induction of pluripotent stem cells from adult human fibroblasts by defined factors. *Cell* **131**, 861–872 (2007).
3. Yu, J. *et al.* Induced pluripotent stem cell lines derived from human somatic cells. *Science* **318**, 1917–1920 (2007).
4. Park, I. H. *et al.* Reprogramming of human somatic cells to pluripotency with defined factors. *Nature* **451**, 141–146 (2008).
5. Lowry, W. E. *et al.* Generation of human induced pluripotent stem cells from dermal fibroblasts. *Proc. Natl Acad. Sci. USA* **105**, 2883–2888 (2008).
6. Park, I. H. *et al.* Disease-specific induced pluripotent stem cells. *Cell* **134**, 877–886 (2008).
7. Dimos, J. T. *et al.* Induced pluripotent stem cells generated from patients with ALS can be differentiated into motor neurons. *Science* **321**, 1218–1221 (2008).
8. Ebert, A. D. *et al.* Induced pluripotent stem cells from a spinal muscular atrophy patient. *Nature* **457**, 277–280 (2009).
9. Soldner, F. *et al.* Parkinson's disease patient-derived induced pluripotent stem cells free of viral reprogramming factors. *Cell* **136**, 964–977 (2009).
10. Tischkowitz, M. D. & Hodgson, S. V. Fanconi anaemia. *J. Med. Genet.* **40**, 1–10 (2003).
11. Wang, W. Emergence of a DNA-damage response network consisting of Fanconi anaemia and BRCA proteins. *Nature Rev. Genet.* **8**, 735–748 (2007).
12. Auerbach, A. D. & Wolman, S. R. Susceptibility of Fanconi's anaemia fibroblasts to chromosome damage by carcinogens. *Nature* **261**, 494–496 (1976).
13. Kutler, D. I. *et al.* A 20-year perspective on the International Fanconi Anemia Registry (IFAR). *Blood* **101**, 1249–1256 (2003).
14. Guardiola, P. *et al.* Outcome of 69 allogeneic stem cell transplantations for Fanconi anemia using HLA-matched unrelated donors: a study on behalf of the European Group for Blood and Marrow Transplantation. *Blood* **95**, 422–429 (2000).
15. Wagner, J. E. *et al.* Unrelated donor bone marrow transplantation for the treatment of Fanconi anemia. *Blood* **109**, 2256–2262 (2007).
16. Waisfisz, Q. *et al.* Spontaneous functional correction of homozygous fanconi anaemia alleles reveals novel mechanistic basis for reverse mosaicism. *Nature Genet.* **22**, 379–383 (1999).
17. Gregory, J. J. Jr *et al.* Somatic mosaicism in Fanconi anemia: evidence of genotypic reversion in lymphohematopoietic stem cells. *Proc. Natl Acad. Sci. USA* **98**, 2532–2537 (2001).
18. Gross, M. *et al.* Reverse mosaicism in Fanconi anemia: natural gene therapy via molecular self-correction. *Cytogenet. Genome Res.* **98**, 126–135 (2002).
19. Rio, P. *et al.* *In vivo* proliferation advantage of genetically corrected hematopoietic stem cells in a mouse model of Fanconi anemia FA-D1. *Blood* **112**, 4853–4861 (2008).
20. Liu, J. M. *et al.* Engraftment of hematopoietic progenitor cells transduced with the Fanconi anemia group C gene (FANCC). *Hum. Gene Ther.* **10**, 2337–2346 (1999).
21. Kelly, P. F. *et al.* Stem cell collection and gene transfer in Fanconi anemia. *Mol. Ther.* **15**, 211–219 (2007).
22. Larghero, J. *et al.* Hematopoietic progenitor cell harvest and functionality in Fanconi anemia patients. *Blood* **100**, 3051 (2002).

23. Jacome, A. *et al.* Lentiviral-mediated genetic correction of hematopoietic and mesenchymal progenitor cells from Fanconi anemia patients. *Mol. Ther.* (in the press).
24. Ying, Q. L. *et al.* The ground state of embryonic stem cell self-renewal. *Nature* **453**, 519–523 (2008).
25. Taniguchi, T. & D'Andrea, A. D. Molecular pathogenesis of Fanconi anemia: recent progress. *Blood* **107**, 4223–4233 (2006).
26. Almaraz, E. *et al.* Characteristics of lentiviral vectors harboring the proximal promoter of the *vav* proto-oncogene: a weak and efficient promoter for gene therapy. *Mol. Ther.* **15**, 1487–1494 (2007).
27. Aasen, T. *et al.* Efficient and rapid generation of induced pluripotent stem cells from human keratinocytes. *Nature Biotechnol.* **26**, 1276–1284 (2008).
28. Kalb, R. *et al.* Hypomorphic mutations in the gene encoding a key Fanconi anemia protein, FANCD2, sustain a significant group of FA-D2 patients with severe phenotype. *Am. J. Hum. Genet.* **80**, 895–910 (2007).
29. Brivanlou, A. H. *et al.* Stem cells. Setting standards for human embryonic stem cells. *Science* **300**, 913–916 (2003).
30. Raya, A. *et al.* Generation of cardiomyocytes from new human embryonic stem cell lines derived from poor-quality blastocysts. *Cold Spring Harb. Symp. Quant. Biol.* (in the press).
31. Pfeifer, A., Ikawa, M., Dayn, Y. & Verma, I. M. Transgenesis by lentiviral vectors: lack of gene silencing in mammalian embryonic stem cells and preimplantation embryos. *Proc. Natl Acad. Sci. USA* **99**, 2140–2145 (2002).
32. Xia, X., Zhang, Y., Zieth, C. R. & Zhang, S. C. Transgenes delivered by lentiviral vector are suppressed in human embryonic stem cells in a promoter-dependent manner. *Stem Cells Dev.* **16**, 167–176 (2007).
33. Bogliolo, M. *et al.* Histone H2AX and Fanconi anemia FANCD2 function in the same pathway to maintain chromosome stability. *EMBO J.* **26**, 1340–1351 (2007).
34. Nakano, T., Kodama, H. & Honjo, T. Generation of lymphohematopoietic cells from embryonic stem cells in culture. *Science* **265**, 1098–1101 (1994).
35. Vodyanik, M. A., Bork, J. A., Thomson, J. A. & Slukvin, I. I. Human embryonic stem cell-derived CD34⁺ cells: efficient production in the coculture with OP9 stromal cells and analysis of lymphohematopoietic potential. *Blood* **105**, 617–626 (2005).
36. Ji, J., Vijayaragavan, K., Bosse, M., Weisel, K. & Bhatia, M. OP9 stroma augments survival of hematopoietic precursors and progenitors during hematopoietic differentiation from human embryonic stem cells. *Stem Cells* **26**, 2485–2495 (2008).
37. Okita, K., Ichisaka, T. & Yamanaka, S. Generation of germline-competent induced pluripotent stem cells. *Nature* **448**, 313–317 (2007).
38. Nakagawa, M. *et al.* Generation of induced pluripotent stem cells without *Myc* from mouse and human fibroblasts. *Nature Biotechnol.* **26**, 101–106 (2008).
39. Okita, K., Nakagawa, M., Hyenjong, H., Ichisaka, T. & Yamanaka, S. Generation of mouse induced pluripotent stem cells without viral vectors. *Science* **322**, 949–953 (2008).
40. Stadtfeld, M., Nagaya, M., Utikal, J., Weir, G. & Hochedlinger, K. Induced pluripotent stem cells generated without viral integration. *Science* **322**, 945–949 (2008).
41. Zhou, H. *et al.* Generation of induced pluripotent stem cells using recombinant proteins. *Cell Stem Cell* **4**, 381–384 (2009).
42. Gonzalez, F. *et al.* Generation of mouse-induced pluripotent stem cells by transient expression of a single nonviral polycistronic vector. *Proc. Natl Acad. Sci. USA* doi:10.1073/pnas.0901471106 (2009).
43. Hacein-Bey-Abina, S. *et al.* Insertional oncogenesis in 4 patients after retrovirus-mediated gene therapy of SCID-X1. *J. Clin. Invest.* **118**, 3132–3142 (2008).
44. Zwaka, T. P. & Thomson, J. A. Homologous recombination in human embryonic stem cells. *Nature Biotechnol.* **21**, 319–321 (2003).
45. Casado, J. A. *et al.* A comprehensive strategy for the subtyping of patients with Fanconi anaemia: conclusions from the Spanish Fanconi Anemia Research Network. *J. Med. Genet.* **44**, 241–249 (2007).
46. Gonzalez-Murillo, A., Lozano, M. L., Montini, E., Bueren, J. A. & Guenechea, G. Unaltered repopulation properties of mouse hematopoietic stem cells transduced with lentiviral vectors. *Blood* **112**, 3138–3147 (2008).
47. Bruun, D. *et al.* siRNA depletion of BRCA1, but not BRCA2, causes increased genome instability in Fanconi anemia cells. *DNA Repair (Amst.)* **2**, 1007–1013 (2003).
48. Nijman, S. M. *et al.* The deubiquitinating enzyme USP1 regulates the Fanconi anemia pathway. *Mol. Cell* **17**, 331–339 (2005).

Supplementary Information is linked to the online version of the paper at www.nature.com/nature.

Acknowledgements The authors are indebted to FA patients and their families for their cooperation. We are grateful to I. Badell, J. Couselo, A. Almeida and D. Schindler for collaboration in providing samples from FA patients, J.A. Casado for subtyping studies, M. Edel, J. Bilic, V. Pekarik and members of the laboratory for comments on the manuscript, J. M. Andrés-Vaquero for assistance with flow cytometry, R. Pujol for assistance with cytogenetics, M. J. Ramirez for immunofluorescence studies, B. Arán, M. Carrió and Y. Muñoz for assistance with cell culture techniques, E. Melo, L. Mulero and M. Martí for bioimaging assistance, and Y. Richaud, T. Lopez Rovira and M. L. Lozano for technical assistance. I.R.-P. and E.S. were recipients of pre-doctoral fellowships from MEC and DIUE, respectively. M.J.B. and G.T. were partially supported by the Ramón y Cajal program, and J.S. by the ICREA-Academia program. This work was partially supported by the Ministerio de Educación y Ciencia grants BFU2006-12251, SAF2005-00058, SAF2006-3440, and Genoma España (FANCOGENE), European Commission 'Marie-Curie Reintegration Grant' MIRG-CT-2007-046523 and European Program CONSERT LSHB-CT-2004-5242, the Fondo de Investigaciones Sanitarias (RETIC-RD06/0010/0016, PI061897, PI061099), Marató de TV3 (063430), the G. Harold and Leila Y. Mathers Charitable Foundation, Fundación Marcelino Botín, and Fundación Cellex.

Author Information Reprints and permissions information is available at www.nature.com/reprints. Correspondence and requests for materials should be addressed to J.C.I.B. (belmonte@salk.edu or izpisua@cmbr.eu).

METHODS

Patients. Studies were approved by the authors' Institutional Review Board and conducted under the Declaration of Helsinki. Patients were encoded to protect their confidentiality, and written informed consent obtained. The generation of human iPS cells was done following a protocol approved by the Spanish competent authorities (Commission on Guarantees concerning the Donation and Use of Human Tissues and Cells of the Carlos III Health Institute). FA patients were diagnosed on the basis of clinical symptoms and chromosome breakage tests of peripheral blood cells using a DNA crosslinker drug. Patients FA5, FA90 and FA153 have been previously described⁴⁴; patients FA430 and FA431 correspond to patients 2 and 10, respectively, in ref. 28. Patient FA404 was subtyped by analysing the G2-phase arrest of dermal fibroblasts transduced with enhanced GFP (EGFP) and FANCA retroviral vectors and then exposed to mitomycin C, as previously described⁴⁴.

Cell lines. 293T and HT1080 cells (ATCC CRL-12103) were used for the production and titration of lentiviruses, respectively. These cell lines were grown in Dulbecco's modified medium (DMEM, Invitrogen) supplemented with 10% fetal bovine serum (FBS; Biowhitaker). The ES[2] and ES[4] lines of human ES cells were maintained as originally described³⁰. The control iPS cell lines KiPS4F1 and KiPS3F1 and the partially silenced KiPS4F3 cell line were cultured as reported²⁷.

Generation of iPS cells. Fibroblasts were cultured in DMEM supplemented with 10% FBS (all from Invitrogen) at 37 °C, 5% CO₂, 5% O₂ and used between 2 and 6 passages. For reprogramming experiments, about 50,000 fibroblasts were seeded per well of a 6-well plate and infected with a 1:1:1:1 mix of retroviral supernatants of Flag-tagged OCT4, SOX2, KLF4 and c-MYC (T58A) (ref. 27) in the presence of 1 µg ml⁻¹ polybrene. Infection consisted of a 45-min spinfection at 750g after which supernatants were left in contact with the cells for 24 h at 37 °C, 5% CO₂. One or two rounds of three infections on consecutive days were performed at the times indicated in Supplementary Information. Five days after beginning the last round of infection, fibroblasts were trypsinized and seeded onto feeder layers of irradiated human foreskin fibroblasts in the same culture medium. After 24 h, the medium was changed to human ES cell medium, consisting of KO-DMEM (Invitrogen) supplemented with 10% KO-Serum Replacement (Invitrogen), 0.5% human albumin (Grifols), 2 mM Glutamax (Invitrogen), 50 µM 2-mercaptoethanol (Invitrogen), non-essential aminoacids (Cambrex) and 10 ng ml⁻¹ bFGF (PeproTech). Cultures were maintained at 37 °C, 5% CO₂, with media changes every other day. Starting 1 week after plating onto feeders, medium was supplemented with 1 µM PD0325901 and 1 µM CT99021 (both from Stem Cell Sciences) for 1 week. Colonies were picked based on morphology 45–60 days after the initial infection and plated onto fresh feeders. Lines of patient-specific iPS cells were maintained by mechanical dissociation of colonies and splitting 1:3 onto feeder cells in human ES cell medium or by limited trypsin digestion and passaging onto Matrigel-coated plates with human ES cell medium pre-conditioned by mouse embryonic fibroblasts. Other inhibitors were used as indicated in Supplementary Information at the following concentrations: 10 µM U0126 (Calbiochem), 25 µM PD098059 (Calbiochem), 5 µM BIO (Sigma), 10 µM Y27632 (Calbiochem). Generation of patient-specific KiPS cells was essentially as previously reported²⁷, except that primary epidermal keratinocytes were derived from small biopsy explants in the presence of irradiated fibroblasts in DMEM/Hams-F12 (3:1) supplemented with 10% FBS, 1 µg ml⁻¹ EGF (BioNova), 0.4 µg ml⁻¹ hydrocortisone, 5 µg ml⁻¹ transferrin, 5 µg ml⁻¹ insulin, 2 × 10⁻¹¹ M liothyronine (all from Sigma) and 10⁻¹⁰ M cholera toxin (Quimigen).

Quantitative RT-PCR, transgene integration and promoter methylation analyses. Expression of retroviral transgenes and endogenous pluripotency-associated transcription factors, integration of retroviral transgenes by genomic PCR or Southern blot, and methylation status of OCT4 and NANOG promoters were assessed as previously reported²⁷.

HLA typing and DNA fingerprinting. Molecular typing of cell lines was performed by Banc de Sang i Teixits (Barcelona, Spain). HLA typing human ES cell lines used sequence-based typification with the AlleleSEQR HLA Sequencing Kit (Atria Genetics). Microsatellite DNA fingerprinting was performed using multiplex polymerase chain reaction of nine microsatellites and short tandem repeats plus amelogenin gene using AmpliFISTR Profiler Plus Kit (Applied Biosystems).

Analysis of proviral copy number and transgene expression. Quantification of proviral copy number per cell was analysed by qPCR in a Rotor Gene RG-3000 (Corbett Research Products) using primers against FANCA transgene: FANCA-F, 5'-GCTCAAGGGTCAGGGCAAC-3', and FANCA-R, 5'-TGTGAGAA GCTCTTTTCGGG-3', and detected with the Taqman probe FANCA-P, 5'-FAM-CGTCTTTTCTGCTGCAGTTAATACCTCGGT-BHQ1-3'. To quantify the number of cells, β-actin primers were used: DNA-RNA-β-actin-F,

5'-ATTGGCAATGAGCGGTTCC-3', and DNA-β-actin-R, 5'-ACAGTCTCCAC TCACCCAGGA-3', and detected with the probe DNA-RNA-β-actin-P, 5'-Texas Red-CCCTGAGGCACTCTTCCAGCCTTCC-BHQ1-3'. To measure the average proviral DNA per transduced cell a standard curve of lentiviral vector (FANCA-IRES-EGFP) and β-actin DNA amplification was made. Next, the average proviral number per cell was estimated by interpolation of the FANCA-to-β-actin ratio from each DNA sample in the standard curve. The expression of the FANCA transgene was analysed by real-time quantitative RT-PCR on complementary DNA obtained from total RNA. Samples from a healthy donor and a FA patient were used as controls. To distinguish between endogenous expression of FANCA and the expression due to the transgene, total FANCA expression was analysed using FANCA primers and probe and the endogenous expression was analysed using 3'FANCA-F, 5'-TCTTCTGACGGGACCTGCC-3', and 3'FANCA-R, 5'-AAGAGCTCCATGTTATGCTTGTAATAAAT-3', and detected with the Taqman probe, 3'FANCA-P, 5'-FAM-CACACCAGCCAGCTCCCGTGTA-BHQ1-3'. For housekeeping control expression β-actin was analysed using DNA-RNA-β-actin-F primer, RNA-β-actin-R primer, 5'-CACAGGACTCCA TGCCCA-3', and Taqman probe DNA-RNA-β-actin-P. Differences between the expression obtained with the FANCA and that obtained using the 3'FANCA indicate the expression of the integrated provirus.

Western blot. Cell extracts were prepared using standard RIPA buffer. The total protein concentration in the supernatant was then measured using the Bio-Rad protein assay (Biorad) according to the manufacturer's instructions. Forty micrograms of total proteins were then loaded on a 6% SDS-PAGE and subjected to standard western blot procedure followed by immunodetection with an anti-human FANCA antibody provided by the Fanconi Anemia Research Fund, Eugene, Portland, USA. Vinculin (Abcam, catalogue number ab18058; 1:5,000) was used as an internal loading control.

Functional studies of the FA pathway in iPS-derived cells. Subnuclear accumulation of stalled replication forks was induced by local UVC irradiation of cells growing on 22 × 22 mm coverslips through polycarbonate filters with pores of 5 µm diameter, essentially as described³³, and processed for immunofluorescence 6 h later. In parallel experiments, primary fibroblast and iPS-derived cells were exposed to hydroxyurea (2 mM) for 24 h and then fixed and processed for immunofluorescence as previously described³³.

For FANCD2 detection at UV-induced stalled replication forks, a primary rabbit antibody against FANCD2 (Abcam; 1:1,000) mixed with an anti-CPD antibody (Kamiya Biomed, MC-062; 1:500) were used. Cells were then incubated with the secondary antibodies anti-mouse Alexa Fluor 488 (Molecular Probes) and anti-rabbit Alexa Fluor 555 (Molecular Probes), and finally mounted in anti-fading medium containing DAPI (Sigma). In the hydroxyurea experiments, immunodetection was identical with the exception that the HCl washing step and a primary mouse antibody against anti-γH2AX (Upstate; 1:3,000) was used instead of an anti-CPD to visualize nuclei foci representing stalled and broken replication forks. Microscopic analysis and image capturing were performed in identical optical and exposure conditions for all cell types using a Zeiss Axio Observer A1 epifluorescence microscope equipped with a AxioCam MRc 5 camera and the AxioVision Rel. 4.6 software.

Immunofluorescence and alkaline phosphatase analyses. Patient-specific iPS cells were grown on plastic coverslide chambers and fixed with 4% paraformaldehyde (PFA). The following antibodies were used: TRA1-60 (MAB4360, 1:100), TRA1-81 (MAB4381, 1:100) and SOX2 (AB5603, 1:500) from Chemicon, SSEA4 (MC-813-70, 1:2) and SSEA3 (MC-631, 1:2) from the Developmental Studies Hybridoma Bank at the University of Iowa, Tuj1 (1:500; Covance), TH (1:1,000; Sigma), α-fetoprotein (1:400; Dako), α-actinin (1:100; Sigma), CT4 (C-10, SantaCruz, 1:100), NANOG (Everest Biotech; 1:100), GFAP (1:1,000; Dako), vimentin (1:500, Chemicon) and FOXA2 (1:100; R&D Biosystems). Secondary antibodies used were all the Alexa Fluor Series from Invitrogen (all 1:500). Images were taken using Leica SP5 confocal microscope. Direct alkaline phosphatase activity was analysed using an alkaline phosphatase blue/red membrane substrate solution kit (Sigma) according to the manufacturer's guidelines. For FANCD2 immunofluorescence assays, cells were grown in plastic coverslide chambers and treated with 30 nM mitomycin C. After 16 h, cells were fixed with 3.7% PFA in PBS for 15 min followed by permeabilization with 0.5% Triton X-100 in PBS for 5 min. After blocking for 30 min in blocking buffer (10% FBS, 0.1% NP-40 in PBS), cells were incubated with polyclonal rabbit anti-FANCD2 antibody (Novus Biologicals, NB 100-182, 1/250). Anti-rabbit Texas red-conjugated antibody (Jackson ImmunoResearch Laboratories) was used as secondary antibody (1:500). Slides were analysed with a fluorescence microscope Axioplan2 (Carl Zeiss) using a ×100/1.45 oil working distance 0.17 mm objective.

In vitro differentiation. Differentiation towards endoderm, cardiogenic mesoderm and neuroectoderm was carried out essentially as described³⁰. Differentiation towards fibroblast-like cells was accomplished by plating embryoid bodies onto

gelatin-coated plates in 90% DMEM, 10% FBS and repeated passaging of differentiated cells with fibroblast-like morphology. For haematopoietic differentiation, embryoid bodies were produced by scraping of confluent iPS wells and cultured in suspension in embryoid body medium (90% DMEM, 10% FBS) for 24–48 h. Embryoid bodies were then placed over a feeder layer of confluent OP9 stromal cells and allowed to attach. The medium used for the first 48 h of differentiation was 50% embryoid body medium and 50% haematopoietic differentiation medium. The haematopoietic differentiation medium was StemSpan serum-free medium (StemCell Technologies) supplemented with cytokines BMP4 (10 ng ml⁻¹), VEGF (10 ng ml⁻¹), SCF (25 ng ml⁻¹), FGF (10 ng ml⁻¹), TPO (20 ng ml⁻¹) and Flt ligand (10 ng ml⁻¹). After 48 h, cells were cultured with haematopoietic differentiation medium, with medium changes every 48 h until the end of the differentiation protocol, day 13 after embryoid body plating. At day 13, OP9 and embryoid bodies were collected by trypsinization (0.25% trypsin), washed and labelled with anti-CD34 bead-conjugated antibody (Miltenyi Biotec) according to manufacturer's specification. The CD34⁺ fraction was purified by MACS, and fraction purity was increased by a second round of MACS. Final purity of the collected cells for CD34 was checked on a fraction of the MACS eluate by flow cytometry. The remaining CD34⁺ cells were frozen in medium IMDM containing 10% DMSO and 20% FBS and stored in liquid nitrogen until further use. For the assessment of CFCs, samples were cultured in triplicates, in Methocult H4434 (Stem Cell Technologies) at 37 °C, in 5% CO₂, 5% O₂ and 95% humidified air. Colonies were scored after two weeks in culture. To analyse the mitomycin C resistance of the haematopoietic progenitors, CFC cultures were treated with 10 nM mitomycin C. In some experiments, iPS-derived CD34⁺ cells were cultured for 7 days in StemSpan serum-free medium (Stem Cell Technologies) supplemented with haematopoietic growth factors SCF (Amgen, 300 ng ml⁻¹), TPO (R&D Systems, 100 ng ml⁻¹) and Flt ligand (BioSource, 100 ng ml⁻¹).

Flow cytometry analyses. For surface phenotyping the following fluorochrome (phycoerythrin (PE) or allophycocyanin (APC))-labelled monoclonal antibodies were used (both from Becton Dickinson Biosciences): anti-CD34 PE (581/CD34) and anti-CD45 APC (HI30). Gating was done with matched isotype control monoclonal antibodies. Hoechst 33258 (H258) was included at 4 µg ml⁻¹ in the final wash to exclude dead cells. All analyses were performed on a MoFlo cell sorter (DakoCytomation) running Summit software. To analyse the phenotype of haematopoietic progenitors, CFU-GM colonies were picked and washed with PBS. Cells were stained with antihuman CD45-PECy5 monoclonal antibody (Clone J33, Immunotech) in combination with anti-human CD33-PE monoclonal antibody (D3HL60.251, Immunotech). Cells were then washed in PBA (phosphate-buffered salt solution with 0.1% BSA and 0.01% sodium azide), resuspended in PBA plus 2 µg ml⁻¹ propidium iodide, and analysed using an

EPICS ELITE-ESP cytometer (Coulter). Off-line analysis was done with CXP Analysis 2.1 flow-cytometry software (Beckman Coulter Inc.).

Teratoma formation. Severe combined immunodeficient beige mice (Charles River Laboratories) were used to test the teratoma induction capacity of patient-specific iPS cells essentially as described²⁷. All animal experiments were conducted following experimental protocols previously approved by the Institutional Ethics Committee on Experimental Animals, in full compliance with Spanish and European laws and regulations.

Genetic correction of FA cells with lentiviral vectors. Lentiviral (LV) vectors carrying the human *FANCA*-IRES-EGFP cassette under the control of the internal spleen-focus-forming virus (*SFFV*) U3 promoter (*FANCA*-LV; ref. 26) were used to transduce fibroblasts and keratinocytes from FA-A patients. Fibroblasts from FA-D2 patients were transduced with a lentiviruses carrying the *FANCD2* cDNA under the control of the *vas* promoter (*FANCD2*-LV, ref. 26). Lentiviral vectors carrying either of these promoters were equally efficient to correct the phenotype of human FA cells²⁶. Vector stocks of VSV-G pseudotyped lentiviruses were prepared by four-plasmid calcium-phosphate-mediated transfection in 293T cells, essentially as described⁴⁵. Supernatants were recovered 24 h and 48 h after transfection and filtered through 0.45 µm. Functional titres of infective lentiviruses were determined in HT1080 cells, plated at 3.5 × 10⁴ cells per well in 24-well plates and infected overnight with different dilutions of either lentivirus-supernatant. Cells were washed and incubated with fresh medium, and the proportion of EGFP-positive cells was determined 5 days later by flow cytometry, or after 8 days by qPCR.

Knockdown of *FANCA*. Lentiviral vectors expressing scramble shRNA and five different *FANCA* shRNAs (Sigma, MISSION shRNA NM_000135) were used to generate viral particles according to the manufacturer's instructions. For infection, FA-patient-specific iPS cells were incubated with viral supernatants in 6-well plates for 24 h. Puromycin selection (2 µg ml⁻¹) was applied for 24 h 3 days after lentiviral infection and cells were allowed to recover for 3 days before splitting. Transient RNA interference experiments with siRNA were performed as previously described⁴⁷. In brief, cells were grown in OPTI-MEM medium (Gibco, catalogue number 31985) with 10% FCS without antibiotics and transfected with 10 nM *FANCA* siRNA (ref. 46) or luciferase siRNA as a control (5'-CGUACGCGGAUACUUCGA[dT][dT]-3'), with Lipofectamin RNAiMAX transfection reagent (Invitrogen, catalogue number 13778-075) twice over a period of 24 h. Twenty-four hours after the second transfection, cells were left untreated or were treated with DEB at 0.02 µg ml⁻¹ for 3 days and subsequently harvested for protein lysates or processed following standard cytogenetic methods. Mitotic indexes were calculated by counting the number of mitotic cells in 500–6,000 cells per point in duplicate.

ARTICLES

Cells keep a memory of their tissue origin during axolotl limb regeneration

Martin Kragl^{1,3,*†}, Dunja Knapp^{1,3,*}, Eugen Nacu^{1,3}, Shahryar Khattak^{1,3}, Malcolm Maden⁴, Hans Henning Epperlein² & Elly M. Tanaka^{1,3}

During limb regeneration adult tissue is converted into a zone of undifferentiated progenitors called the blastema that reforms the diverse tissues of the limb. Previous experiments have led to wide acceptance that limb tissues dedifferentiate to form pluripotent cells. Here we have reexamined this question using an integrated GFP transgene to track the major limb tissues during limb regeneration in the salamander *Ambystoma mexicanum* (the axolotl). Surprisingly, we find that each tissue produces progenitor cells with restricted potential. Therefore, the blastema is a heterogeneous collection of restricted progenitor cells. On the basis of these findings, we further demonstrate that positional identity is a cell-type-specific property of blastema cells, in which cartilage-derived blastema cells harbour positional identity but Schwann-derived cells do not. Our results show that the complex phenomenon of limb regeneration can be achieved without complete dedifferentiation to a pluripotent state, a conclusion with important implications for regenerative medicine.

The salamander is a powerful regeneration model because it can reconstitute a fully functional limb after injury. Amputation anywhere between the shoulder and the hand triggers the formation of a progenitor cell zone called the blastema that regenerates the missing portion. The mature limb consists of multiple tissues, including the epidermis, dermis, muscle, nerve, blood vessels and skeletal elements that potentially contribute to the blastema, and these tissues must regenerate coordinately to restore functionality. In addition, the limb is structured into three major segments—upper arm, lower arm and hand, generically termed the proximo-distal axis—that must be properly patterned. Remarkably, the fundamental questions of which tissues contribute to the blastema, and whether blastema cells are a multipotent or pluripotent cell type have remained largely unanswered, owing to the complexity of the adult limb as an experimental starting point and the lack of tools with which to follow different cell types precisely over the course of regeneration.

Histologically, the blastema appears to be a homogeneous group of cells and has been commonly viewed as a single cell type. Considering that multiple tissue types in the limb are regenerated, this would imply that blastema cells are pluripotent. Indeed, many studies have suggested that cells become multipotent or pluripotent in the limb blastema¹. When the bones were removed from salamander limbs before amputation, the resulting regenerates contained all limb tissues including the bone, implying that non-skeletal cells converted to bone during regeneration, and skin was identified as one potential source of skeleton^{2–6}.

Muscle and Schwann cells have also been proposed to achieve a multipotent or pluripotent state during limb regeneration. Wallace and Wallace observed full limb regeneration after implanting nerve pieces into irradiated hosts and hypothesized that Schwann cells become pluripotent⁷. Muscle was also thought to acquire broad plasticity (for review see ref. 8). Experiments tracking dextran-injected newt myotubes implanted into the limb blastema found the label in cartilage, implying dedifferentiation of muscle into a multipotent

progenitor⁹. Complementarily, BrdU was used to track cultured newt muscle satellite cells *in vivo*, where labelled cells populated cartilage, muscle and even epidermis¹⁰. Such apparent plasticity could, however, have been acquired during culturing, through BrdU incorporation into DNA or through label transfer to the host¹¹. These experiments pointed out the need to mark the different limb cell types indelibly with high resolution, specificity and minimal perturbation.

Here, by comprehensively tracking limb tissues marked by an integrated green fluorescent protein (GFP)–transgene in the salamander *Ambystoma mexicanum* (the axolotl), we show that cells do not become pluripotent during limb regeneration and retain a strong memory of their tissue or embryonic origin. This leads to the important conclusion that the blastema is a heterogeneous pool of restricted progenitor cells from its outset. Using this information, we further show that proximo-distal positional identity is a tissue-specific property of blastema cells: blastema cells deriving from cartilage harbour positional identity but Schwann cells do not. This means that tissue-specific origin must be considered when studying any aspect of the limb blastema.

Dermis makes cartilage but not muscle or Schwann cells

We achieved specific labelling of each major limb tissue either by grafting the embryonic region that produces that limb tissue from GFP⁺ transgenic donors¹² into GFP[−] host embryos¹³ or by direct grafting of a given GFP⁺ limb tissue to an unlabelled host (see Figs 1, 2, 3, 4, Supplementary Fig. 3 and the online-only Methods). To draw our conclusions we examined thousands of cells in multiple individuals (quantification in Supplementary Tables). An important requirement of the donors is stable GFP–transgene expression. No chimaeric expression in the regenerate to indicate silencing was observed (Supplementary Fig. 2 and Supplementary Table 1).

Immediately after amputation, a layer of epidermal cells migrates over the stump and has long been considered to remain separate from the internal blastema^{4,14}. Grafting of embryonic GFP⁺ epidermis to label limb epidermis confirmed these results (Supplementary Fig. 3).

¹Max Planck Institute of Molecular Cell Biology and Genetics, Pfotenhauerstrasse 108, ²Institute of Anatomy, Medical Faculty, University of Technology Dresden, Fetscherstrasse 74, ³Center for Regenerative Therapies, University of Technology Dresden, Tatzberg 47/49, 01307 Dresden, Germany. ⁴The Regeneration Project, McKnight Brain Institute, University of Florida, Rm 326 Bartram Hall, Gainesville, Florida 32611, USA. [†]Present address: Institute of Metabolic Physiology, Heinrich-Heine-Universität Düsseldorf, Universitätsstrasse 1, 40225 Düsseldorf, Germany.

*These authors contributed equally to this work.

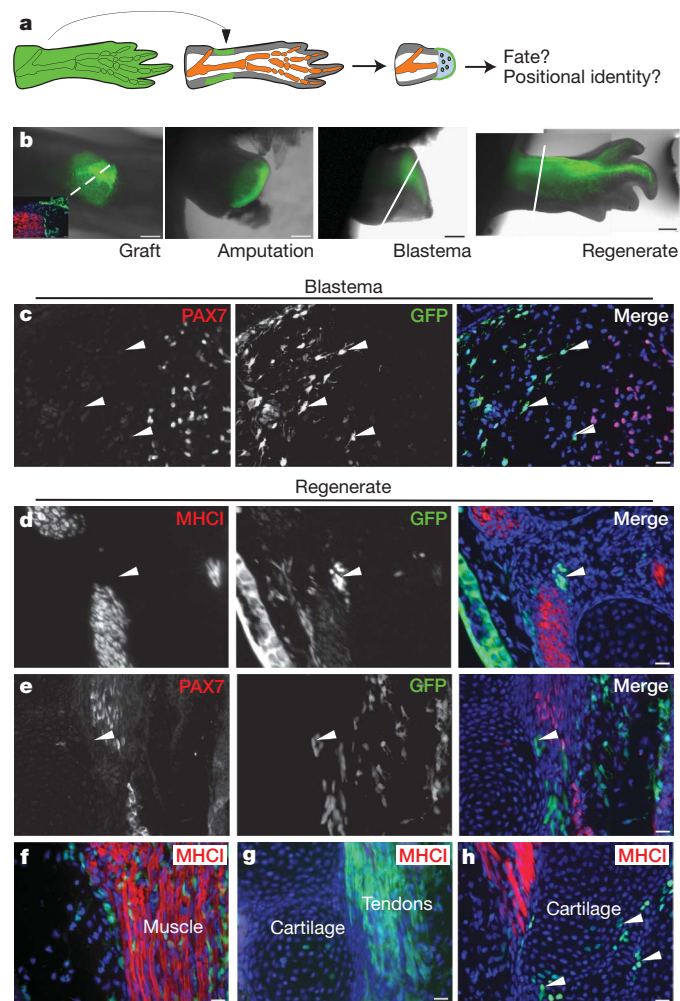


Figure 1 | Dermis does not make muscle but makes cartilage and tendons. **a**, Schematic of experiment. **b**, Representative time course. Inset shows cross-section at dashed line immunostained for MHCI (see Supplementary Fig. 4a, b). **c**, Longitudinal section of 12-day blastema. GFP⁺ (arrowhead) and PAX7⁺ signals did not overlap. **d**, **e**, Cross-sections through regenerated limbs. GFP⁺ cells (arrowheads) were negative for the indicated muscle markers (red). **f**–**h**, Longitudinal sections immunostained for anti-MHCI. Fluorescent cells contributed to connective tissue (**f**), tendons (**g**) and cartilage (**h**, arrowheads). Blue shows DAPI in merge panels (**d**–**h**). Scale bars: **b**, 0.5 mm; **c**–**h**, 50 µm.

In contrast, the dermal layer of skin is a major contributor to the blastema, and has been proposed to have potent patterning effects on regeneration^{15–19}. To determine whether dermis produces a pluripotent cell, we grafted full-thickness skin from GFP⁺ transgenic 8-cm-long donors onto GFP[−] hosts (Fig. 1a). Although this type of transplant also labelled epidermis, Schwann cells and blood vessels, it cleanly excluded muscle (Supplementary Fig. 4a, b). As shown in Fig. 1b, the skin grafts generated a large swath of GFP⁺ cells in the regenerated limb.

To analyse whether GFP⁺ skin transplants produced skeletal muscle during regeneration, PAX7 immunofluorescence was used to identify muscle progenitors. Mid-bud-stage blastemas harbouring dermis-derived GFP⁺ cells showed no overlap between GFP⁺ and PAX7⁺ cells, indicating that dermal cells did not enter the myogenic lineage (Fig. 1c, Supplementary Fig. 5 and Supplementary Table 2a). In addition, single-cell polymerase chain reaction (Supplementary Fig. 9a) of GFP⁺ blastema cells showed that no dermis-derived blastema cells scored positive for *Myf5* expression, whereas 31% of control skeletal muscle-derived blastema cells expressed detectable *Myf5* (Fig. 3d).

We confirmed these results by examining fully regenerated limbs using muscle-specific-myosin heavy chain (MHCI) and PAX7 as molecular muscle markers. Although abundant GFP⁺ cells intermingled

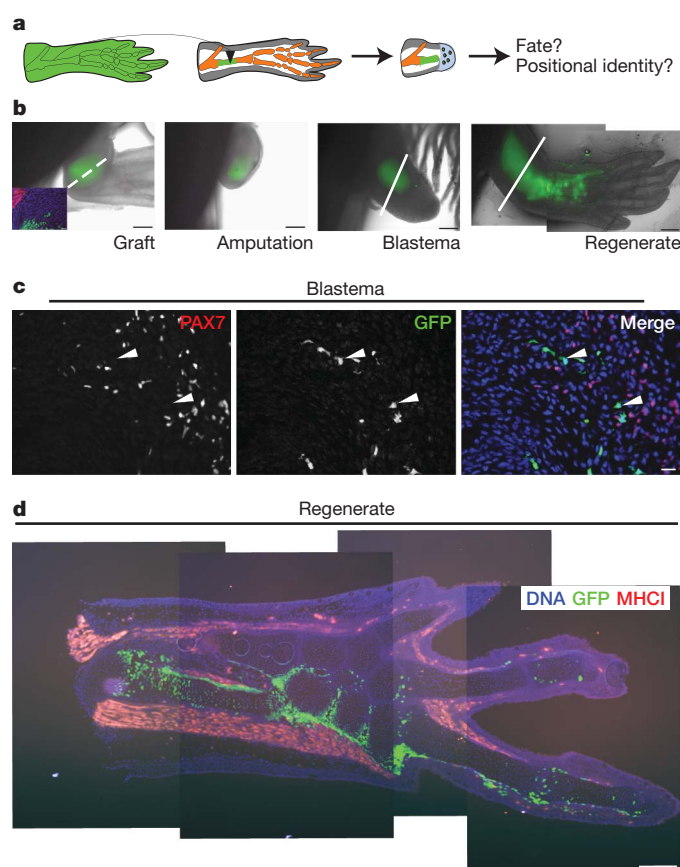


Figure 2 | Cartilage cells do not make muscle. **a**, Schematic of experiment. **b**, Time course through regeneration. Inset shows cross-section at dashed line immunostained for MHCI (see Supplementary Fig. 4c, d). **c**, Longitudinal section of a 12-day blastema. GFP⁺ cells (arrowheads) were negative for PAX7⁺ signals. **d**, Longitudinal section of a regenerated limb 30 days post-amputation immunostained for MHCI (red). The majority of fluorescent cells were found located in the regenerated skeleton; no signal was found in muscle. Blue shows DAPI in merge panels (**b**–**d**). Scale bars: **b**, 0.5 mm; **c**, 50 µm; **d**, 100 µm.

with muscle tissue, no GFP⁺, MHCI⁺ muscle fibres or GFP⁺, PAX7⁺ cells were found, indicating that dermal cells do not make muscle (Fig. 1d–f, Supplementary Table 2b). We did, however, observe significant numbers of GFP⁺ cells in cartilage and tendons (Fig. 1g, h and Supplementary Table 2b). Furthermore, the cells intermingling with muscle presumably represent connective-tissue fibroblasts for which there is currently no reliable marker.

The full-thickness skin transplants contained several cell types, so limited conclusions could be drawn from the above experiments. To determine whether cartilage cells truly derived from the dermis and second, if dermal cells can transdifferentiate into Schwann cells, we cleanly labelled the dermis by transplanting GFP⁺ embryonic lateral plate mesoderm (which forms limb dermis, connective fibroblasts and cartilage) (see Supplementary Materials and Methods). After growing the animals to 8 cm length, limb skin (unlabelled epidermis and labelled dermis) was transplanted from the labelled animals onto GFP[−] hosts and then amputated. Cartilage cells formed from these clean dermis-labelled limbs. Second, GFP⁺ Schwann cells were not found in the regenerate (Supplementary Table 2c). Taken together, our dermis tracking indicates that dermis cells do not enter the myogenic or the Schwann cell lineage but do form cartilage, connective tissue and tendons.

Cartilage does not produce muscle

We also tracked the descendants of the limb skeleton. At the juvenile stages used in our experiments, the skeleton consists of cartilage. To follow limb cartilage, pieces of GFP⁺ upper-arm cartilage were used

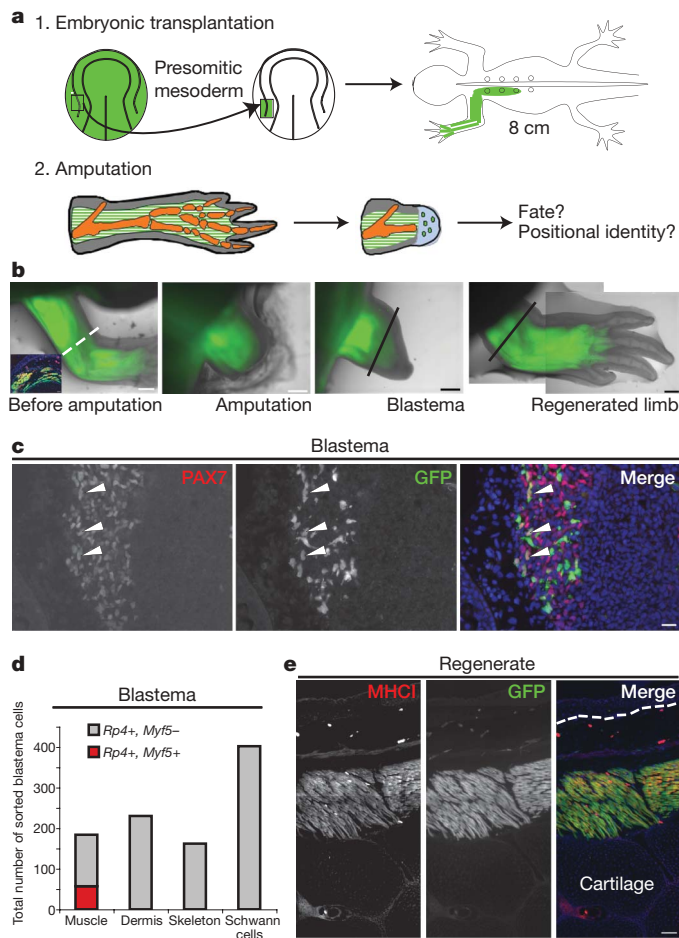


Figure 3 | Muscle does not make cartilage or epidermis. **a**, Schematic of labelling. **b**, Time course. Inset shows cross-section at dashed line (see Supplementary Fig. 4e). **c**, Section of 12-day blastema. GFP⁺ cells (arrowheads) were positive for PAX7. **d**, Single-cell PCR showed that GFP⁺ muscle-derived blastema cells expressed *Myf5* (see also Supplementary Fig. 9a) but GFP⁺ cells from other tissues did not. RP4 acted as quality control. Numbers of cells/blastemas/animals/experiments analysed were as follows for each tissue. Skeleton: 152/8/8/4, Schwann cells: 402/6/6/6, dermis: 230/12/12/6, muscle: 184/6/6/3. **e**, Longitudinal section through regenerated limb. No GFP⁺ cells were found in cartilage or epidermis (above dotted line). Scale bars: **b**, 0.5 mm; **c**, 50 μ m; **e**, 100 μ m.

to replace a section of cartilage in GFP⁻ hosts before amputation (Fig. 2a, Supplementary Fig. 4c, d). GFP⁺ cells contributed significantly to the blastema and then to the regenerated cartilage (Fig. 2b).

Analogously to the dermis analysis, we looked for muscle formation. No GFP⁺, PAX7⁺ or GFP⁺, *Myf5*⁺ cells were found in the blastema (Fig. 2c, 3d, Supplementary Table 3a), nor any GFP⁺, MHCII⁺ muscle fibres or GFP⁺, PAX7⁺ satellite cells in the regenerated limbs (Fig. 2d, Supplementary Table 3b). GFP⁺ cells were observed in tendons, perichondrium and perhaps dermis (Fig. 2d). This indicates that the cells in the cartilaginous skeleton do not form myogenic cells and the vast majority contribute back to cartilage.

Muscle does not make cartilage or epidermis

Muscle was of particular interest because previous experiments indicated that muscle may produce a generalized stem cell^{9,10,20,21}. We therefore transplanted GFP⁺ embryonic presomitic mesoderm (Fig. 3a) to label limb muscle fibres and satellite cells (Supplementary Figs 4e and 6, Supplementary Table 4a). This method also labelled some blood vessels, as shown by autofluorescent blood cells circulating within GFP⁺ vessel segments (Supplementary Fig. 6d). Amputation of the labelled limbs resulted in abundant GFP⁺ cells in

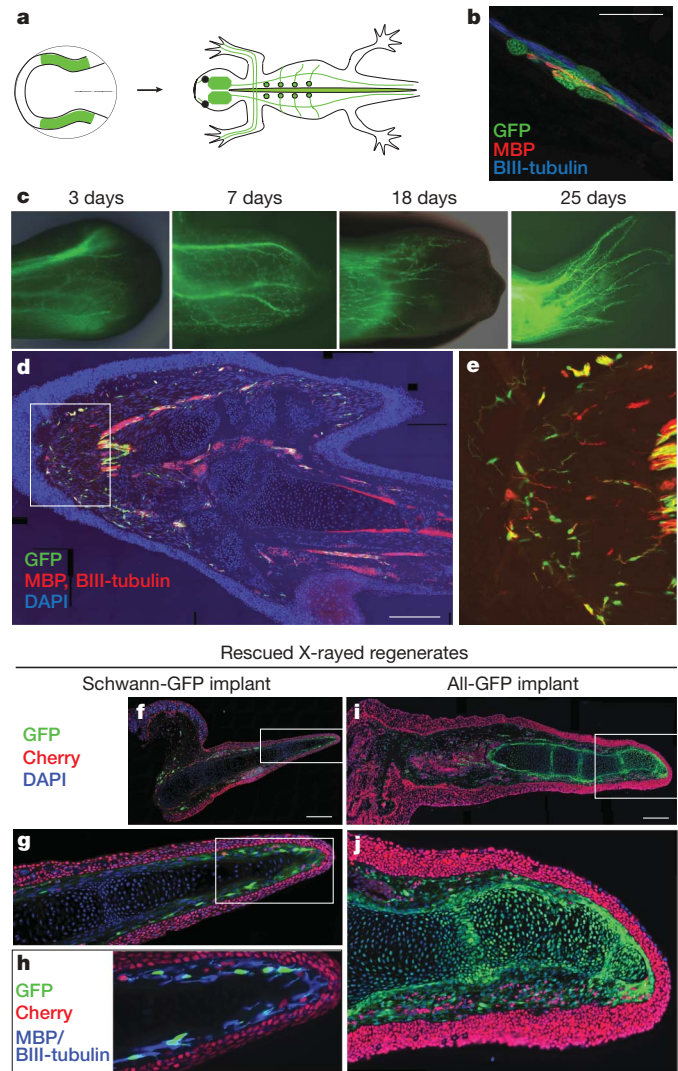


Figure 4 | Schwann cells give rise to Schwann cells and do not form cartilage even during nerve-rescue of irradiated limbs. **a**, Schematic of labelling. **b**, Confocal fluorescence image of GFP⁺ Schwann cells in the hand. **c**, Time course of regeneration. Note that Schwann cells did not enter the distal tip until 25 days post amputation. **d**, Longitudinal section through a regenerated hand. GFP⁺ Schwann cells were closely associated to MBP and BIII-tubulin staining. **e**, Enlarged part of **d** shown without DAPI. **f–j**, Sections of regenerating limbs that had been X-rayed and rescued by a non-irradiated nerve implant. **f–h**, A regenerate rescued by nerve with GFP-labelled Schwann cells. Cartilage was negative for both GFP and nuclear Cherry. **i, j**, A regenerate rescued by nerve tissue in which all cells expressed GFP. Cartilage cells were GFP⁺, indicating that they derived from non-Schwann cells in the nerve. **g, j**, Higher magnification of the regions framed in **f** and **i** respectively. **h**, Higher magnification of the frame in **g** showing MBP and BIII-tubulin staining. Scale bars: **b**, 50 μ m; **d, f, i**, 0.5 mm.

the regenerate (Fig. 3b–e, Supplementary Table 4b, c). Longitudinal sections representing labelling of over 25,000 nuclei in GFP⁺ muscle fibres revealed no GFP⁺ cells in the cartilage or epidermis (Fig. 3e, Supplementary Table 4c), indicating that muscle remains restricted primarily or exclusively to the muscle lineage.

Irradiation rescue does not increase potency

Schwann cells have also been proposed to dedifferentiate into diverse cell types during limb regeneration and such plasticity seemed plausible considering their neural crest origin^{7,22,23}. To label Schwann cells we grafted GFP⁺ neural fold using *white* mutant embryos as hosts and donors²⁴ (Fig. 4a, see Supplementary Information and the online-only Methods). The specificity of cell labelling was confirmed by the close association of the GFP signal with neuronal-specific

BIII-tubulin and glia-specific myelin basic protein (MBP) (Fig. 4b). Upon limb amputation and regeneration, surprisingly, GFP expression was clearly restricted to nerve tracts and we observed no label in cartilage or muscle (Fig. 4d, e, Supplementary Table 5a).

Our results so far found restricted cell potential during normal regeneration. To test whether cells display increased potency when forced to reconstitute other limb tissues, we examined the ability of implanted nerves to rescue irradiated limbs. To track Schwann cells versus host cells we irradiated host forelimbs transgenic for the nuclear Cherry gene. After limb amputation, we implanted nerves from the animals described above in which the Schwann cells were specifically GFP⁺ (termed 'Schwann-GFP'). Longitudinal sections of the nerve-rescued samples revealed the formation of cartilage but little if any muscle. Surprisingly, the vast majority of GFP label was limited to BIII-tubulin/MBP-positive nerve tracts and the cartilage was completely negative for both transgenes (Fig. 4f–h, Supplementary Table 5b).

These results raised two alternatives; either Schwann cells were transdetermining to cartilage and the GFP transgene became silenced or the regenerated cartilage derived from an unlabelled, non-Schwann cell in the nerve. To address these possibilities we rescued nuclear Cherry-irradiated limbs with nerves from fully transgenic GFP animals ('all-GFP'). Representative sections from two of the rescued limbs revealed that all cartilage cells were GFP⁺ and that no observable muscle had formed (Fig. 4i, j, Supplementary Table 5b). These results demonstrate that cartilage does not derive from Schwann cells when nerve implants rescue irradiated limbs but rather come from another cell population, presumably connective-tissue fibroblasts. Consistent with our tracking of cell potential during normal regeneration, we also saw no evidence of muscle being formed from the implanted or host tissue.

Positional identity is tissue specific

These tracking experiments have established that the blastema is a heterogeneous pool of progenitor cells from the outset of regeneration. This result has important implications for another central problem in limb regeneration—the control of positional identity along the proximal/distal limb axis. So far, experiments addressing this issue have treated the blastema as a homogeneous pool of cells^{25–28}. Considering the results above, we examined whether blastema cells deriving from different tissues all harbour similar molecular and cellular features of positional identity.

We first compared cartilage and Schwann-derived blastema cells for their expression of molecular markers associated with proximo-distal identity, namely nuclear MEIS 1+2 protein and *HoxA13* messenger RNA. During limb regeneration, nuclear-localized MEIS is found in the proximal half of the upper-arm blastema (Supplementary Fig. 7a) and functions to specify upper-arm cell identity during both limb development and regeneration^{29,30}. We examined whether blastema cells derived from upper-arm GFP cartilage or upper-arm GFP Schwann-cell transplants expressed nuclear-localized MEIS, and found contrasting results for the two cell types. While 95% of upper-arm-cartilage-derived blastema cells at the base of the blastema displayed nuclear-localized MEIS, no Schwann-cell-derived blastema cells displayed nuclear MEIS (Supplementary Fig. 8a–d). A portion of dermis and muscle-derived blastema cells displayed nuclear MEIS. All blastemas eventually produced a hand, so we also examined the distal-identity-associated marker *HoxA13* by single-cell PCR. *HoxA13* plays an important role in hand formation and is re-expressed in the blastema^{31,32} (Supplementary Fig. 7b). 15% of upper-arm-cartilage-derived cells were positive for *HoxA13*, while so far no Schwann cells have scored positive for *HoxA13* (Supplementary Fig. 9b). This molecular data predicts that cartilage cells possess proximo-distal positional identity while Schwann cells do not.

To test the molecular prediction, we asked whether cartilage and Schwann cells behave differently in a functional assay of proximo-distal positional identity. Previous studies showed that a wrist-level

blastema grafted onto an upper-arm blastema homes to the hand region during regeneration, indicating that the transplanted cells stably retain their distal identity^{25,28}. To examine tissue-specific behaviours in this assay, we grafted GFP⁺ fingertip cartilage into the upper arm and allowed healing before amputation. In a parallel set of limbs, we grafted upper-arm cartilage into the upper arm (Fig. 5a–c). Upon limb amputation the finger-cartilage-derived blastema cells homed to the regenerated hand (Fig. 5c, d and Supplementary Table 6), whereas control upper-arm-cartilage transplants were found all along the limb (Fig. 5b, d and Supplementary Table 6). In contrast, when we transplanted hand-derived Schwann cells into the upper arm they spread all along the proximo-distal limb axis, behaving indistinguishably from upper-arm Schwann cells (Fig. 5e, Supplementary Table 6).

The functional assays combined with the molecular results strongly indicate that cartilage cells have proximo-distal positional identity while Schwann cells are neutral and probably spread along the limb promiscuously. In general, these results indicate that the tissue origin of the blastema cell must be considered when studying positional identity.

Discussion

This work resolves many ambiguities surrounding cell plasticity during limb regeneration and points out the importance of high-resolution, genetic methods to map cell fate accurately in complex tissues *in vivo*. Our results show that limb blastema cells do not switch between embryonic germ layers and most cell types are largely restricted to their own tissue identity during limb regeneration (Supplementary Fig. 1a). Dermis was the most flexible tissue,

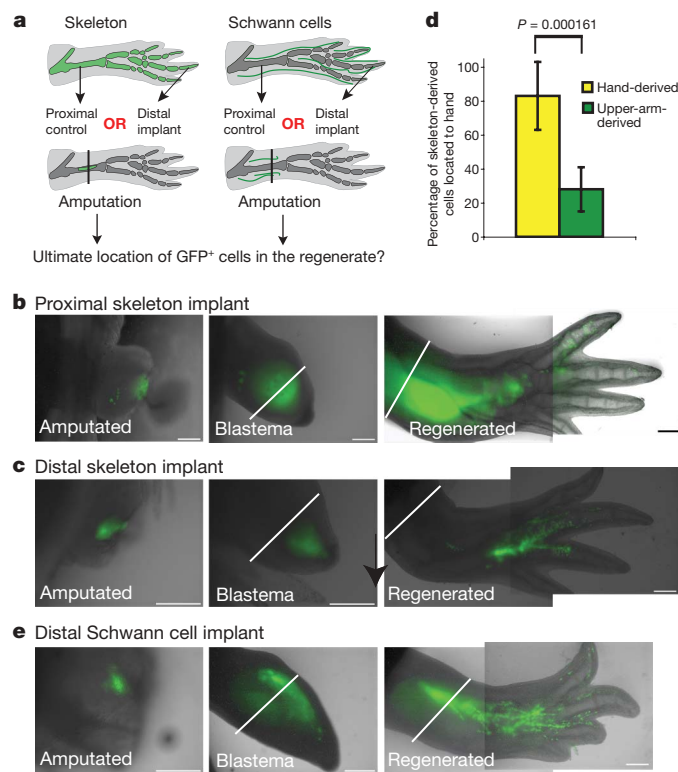


Figure 5 | Schwann cell-derived blastema cells do not possess proximo-distal positional identity but cartilage-derived cells do. **a**, Schematic to show the experimental design. **b**, **c**, **e**, Time course through regeneration of the indicated graft type. Progeny of distal skeletal cells localize distally while Schwann-cell-derived cells show no positional preference. $n = 14$ (**b**), 20 (**c**) and 15 (**e**) limbs. Scale bars: 0.5 mm. **d**, Percentage of cartilage-derived progeny originating from upper arm (six limbs) or hand transplants (seven limbs) that contribute to hand skeleton after regeneration. Error bars are standard deviations; P value is from Student's t -test (Welch; unpaired).

forming cartilage and tendons but not muscle. This attribute probably reflects the common origin of limb dermis and cartilage in the lateral plate mesoderm and suggests that dermal tissue contributes a lateral plate-like restricted progenitor in the blastema, either via a resident stem cell or reversion of a fibroblast phenotype.

Muscle and Schwann cell dedifferentiation to a multi- or pluripotent state has been an important theme in limb regeneration studies^{8–10,22,33–36}. We posit that the discrepancy between our results and previous ones derives either from previous contamination of implanted cells, plasticity induced by culturing and/or labelling with invasive or leaky methods. Although we clearly demonstrate that muscle makes muscle but not cartilage or epidermis, we did not resolve here whether the regenerated muscle derives from satellite cells, dedifferentiation of muscle or both, because our current experiments labelled both muscle satellite cells and differentiated fibres. It will clearly be important to apply genetic labelling methods to resolve whether muscle dedifferentiation does indeed occur during limb regeneration.

Cell plasticity of neural cells has also been reported during tail regeneration, in which cell tracking by transient electroporation of expression plasmids led to the conclusion that spinal cord radial glia can cross lineage boundaries to form muscle and cartilage³⁷. We are currently re-exploring this issue using transgenesis methods (V. Mazurov, L. Mchedlishvili and E.M.T., unpublished work)³⁸.

Limb regeneration studies have historically been performed on various species at different life stages, so whether the cell behaviours observed here are somehow specific for the species or the developmental stage of the animals that were used in this study is still unclear. We recapitulated a number of these experiments on sexually mature animals, so the results are unlikely to be a stage-dependent trait (data not shown). It will clearly be important to perform analogous experiments in *Notophthalmus viridescens*, in which much of the work examining muscle cell plasticity has been performed. Muscle dedifferentiation to a mononucleate state has been described in both *Notophthalmus viridescens* and *Ambystoma mexicanum*, but results showing contributions to other tissues such as cartilage has been described only in the former^{9,34,35}.

Importantly, this knowledge changes our common conception of the blastema from a homogeneous pool of progenitors to a group of cells that are heterogeneous from the outset. In fact, our tracking data indicate that blastema cells from the different tissues occupy distinct subregions, as summarized in Supplementary Fig. 1b. Interestingly, the dermis occupies the distal tip of the blastema and has potential to form cartilage, so a significant part of the regenerated hand skeleton derives from the dermis (Supplementary Fig. 10).

These results strikingly point to salamander blastema cells behaving, in terms of tissue-specific restrictions, like their counterparts in the mammal or like progenitors observed in the limb bud. Nonetheless, the adult salamander tissue uniquely generates these blastema cells to reconstitute an entire limb after amputation, a property that other systems do not have. It is likely that cells at the amputation plane are indeed undergoing reprogramming events that allow them to re-enter embryonic programs of tissue formation, even if they do not revert back to the earliest pluripotent state. How this is achieved in the salamander and why it does not occur in mammals remains an important question.

METHODS SUMMARY

To obtain tissue-specific GFP labelling, transgenic embryos ubiquitously expressing GFP or nuclear Cherry were used as donors for transplanting various embryonic anlagen (lateral ectoderm, neural fold, presomitic mesoderm, lateral plate mesoderm) to normal host embryos of the same stage that were then allowed to grow to a size of 8 cm. In a separate set of experiments, 8-cm-long juveniles were used as donors for transplanting full-thickness skin or cartilage to normal hosts of the same age. Limbs were amputated and descendants of fluorescently labelled tissues were followed over time and imaged using a fluorescence stereomicroscope coupled to a digital imaging system (Olympus). At different time points, limbs were processed for cryosectioning and immunofluorescence

using antibodies to different cell populations (see full list of antibodies in Supplementary Information and the online-only Methods). Alternatively, blastema cell samples were dissociated by digestion with liberase (Roche), and then sorted by fluorescence-activated cell sorting (FACS) based on GFP fluorescence and DRAQ5 staining, followed by single-cell PCR (see Supplementary Information and the online-only Methods for additional information).

Full Methods and any associated references are available in the online version of the paper at www.nature.com/nature.

Received 26 February; accepted 22 May 2009.

1. Umanski, E. E. The regeneration potencies of axolotl skin studied by means of exclusion of the regeneration capacity of tissues through exposure to x-rays. *Bull. Biol. Med. Exp. USSR* **6**, 141–145 (1938).
2. Weiss, P. Unabhängigkeit der Extremitätenregeneration vom Skelett (bei *Triton cristatus*) 'Wilhelm Roux'. *Arch. Entwicklungsmech. Organ.* **104**, 359–394 (1925).
3. Thornton, C. S. The histogenesis of the regenerating fore limb of larval *Amblystoma* after exarticulation of the humerus. *J. Morphol.* **62**, 219–235 (1938).
4. Namenwirth, M. The inheritance of cell differentiation during limb regeneration in the axolotl. *Dev. Biol.* **41**, 42–56 (1974).
5. Dunis, D. A. & Namenwirth, M. The role of grafted skin in the regeneration of x-irradiated axolotl limbs. *Dev. Biol.* **56**, 97–109 (1977).
6. Lheureux, E. The origin of tissues in the X-irradiated regenerating limb of the newt *Pleurodeles waltlii*. *Prog. Clin. Biol. Res.* **110**, 455–465 (1983).
7. Wallace, B. M. & Wallace, H. Participation of grafted nerves in amphibian limb regeneration. *J. Embryol. Exp. Morphol.* **29**, 559–570 (1973).
8. Echeverri, K. & Tanaka, E. M. Mechanisms of muscle dedifferentiation during regeneration. *Semin. Cell Dev. Biol.* **13**, 353–360 (2002).
9. Lo, D. C., Allen, F. & Brookes, J. P. Reversal of muscle differentiation during urodele limb regeneration. *Proc. Natl Acad. Sci. USA* **90**, 7230–7234 (1993).
10. Morrison, J. I., Loof, S., He, P. & Simon, A. Salamander limb regeneration involves the activation of a multipotent skeletal muscle satellite cell population. *J. Cell Biol.* **172**, 433–440 (2006).
11. Burns, T. C. *et al.* Thymidine analogs are transferred from prelabeled donor to host cells in the central nervous system after transplantation: a word of caution. *Stem Cells* **24**, 1121–1127 (2006).
12. Sobkow, L., Epperlein, H. H., Herklotz, S., Straube, W. L. & Tanaka, E. M. A germline GFP transgenic axolotl and its use to track cell fate: dual origin of the fin mesenchyme during development and the fate of blood cells during regeneration. *Dev. Biol.* **290**, 386–397 (2006).
13. Gargioli, C. & Slack, J. M. Cell lineage tracing during *Xenopus* tail regeneration. *Development* **131**, 2669–2679 (2004).
14. Hay, E. D. & Fischman, D. A. Origin of the blastema in regenerating limbs of the newt *Triturus viridescens*. An autoradiographic study using tritiated thymidine to follow cell proliferation and migration. *Dev. Biol.* **3**, 26–59 (1961).
15. Carlson, B. M. Morphogenetic interactions between rotated skin cuffs and underlying stump tissues in regenerating axolotl forelimbs. *Dev. Biol.* **39**, 263–285 (1974).
16. Maden, M. & Mustafa, K. The structure of 180 degrees supernumerary limbs and a hypothesis of their formation. *Dev. Biol.* **93**, 257–265 (1982).
17. Slack, M. J. Morphogenetic properties of the skin in axolotl limb regeneration. *J. Embryol. Exp. Morphol.* **58**, 265–288 (1980).
18. Muneoka, K., Fox, W. F. & Bryant, S. V. Cellular contribution from dermis and cartilage to the regenerating limb blastema in axolotls. *Dev. Biol.* **116**, 256–260 (1986).
19. Rollman-Dinsmore, C. & Bryant, S. V. The distribution of marked dermal cells from small localized implants in limb regenerates. *Dev. Biol.* **106**, 275–281 (1984).
20. Asakura, A., Komaki, M. & Rudnicki, M. Muscle satellite cells are multipotential stem cells that exhibit myogenic, osteogenic, and adipogenic differentiation. *Differentiation* **68**, 245–253 (2001).
21. Wada, M. R., Inagawa-Ogashiwa, M., Shimizu, S., Yasumoto, S. & Hashimoto, N. Generation of different fates from multipotent muscle stem cells. *Development* **129**, 2987–2995 (2002).
22. Wallace, H. The components of regrowing nerves which support the regeneration of irradiated salamander limbs. *J. Embryol. Exp. Morphol.* **28**, 419–435 (1972).
23. Horstadius, S. & Sellmann, S. Experimentelle Untersuchungen über die Determination des knorpeligen Kopfskelettes bei Urodelen. *Nova Acta Regiae Soc. Sci. Ups. Ser. 13*, 1–170 (1946).
24. Epperlein, H., Meulemans, D., Bronner-Fraser, M., Steinbeisser, H. & Selleck, M. A. Analysis of cranial neural crest migratory pathways in axolotl using cell markers and transplantation. *Development* **127**, 2751–2761 (2000).
25. Crawford, K. & Stocum, D. L. Retinoic acid coordinately proximalizes regenerate pattern and blastema differential affinity in axolotl limbs. *Development* **102**, 687–698 (1988).
26. Iten, L. E. & Bryant, S. V. The interaction between the blastema and stump in the establishment of the anterior–posterior and proximal–distal organization of the limb regenerate. *Dev. Biol.* **44**, 119–147 (1975).
27. Nardi, J. B. & Stocum, D. L. Surface properties of regenerating limb cells: evidence for gradation along the proximodistal axis. *Differentiation* **25**, 27–31 (1983).
28. Echeverri, K. & Tanaka, E. M. Proximodistal patterning during limb regeneration. *Dev. Biol.* **279**, 391–401 (2005).
29. Mercader, N. *et al.* Conserved regulation of proximodistal limb axis development by Meis1/Hth. *Nature* **402**, 425–429 (1999).

30. Mercader, N., Tanaka, E. M. & Torres, M. Proximodistal identity during vertebrate limb regeneration is regulated by Meis homeodomain proteins. *Development* **132**, 4131–4142 (2005).
31. Gardiner, D. M., Blumberg, B., Komine, Y. & Bryant, S. V. Regulation of HoxA expression in developing and regenerating axolotl limbs. *Development* **121**, 1731–1741 (1995).
32. Fromental-Ramain, C. *et al.* Hoxa-13 and Hoxd-13 play a crucial role in the patterning of the limb autopod. *Development* **122**, 2997–3011 (1996).
33. Kumar, A., Velloso, C. P., Imokawa, Y. & Brockes, J. P. Plasticity of retrovirus-labelled myotubes in the newt limb regeneration blastema. *Dev. Biol.* **218**, 125–136 (2000).
34. Kumar, A., Velloso, C. P., Imokawa, Y. & Brockes, J. P. The regenerative plasticity of isolated urodele myofibers and its dependence on MSX1. *PLoS Biol.* **2**, E218 (2004).
35. Echeverri, K., Clarke, J. D. & Tanaka, E. M. *In vivo* imaging indicates muscle fiber dedifferentiation is a major contributor to the regenerating tail blastema. *Dev. Biol.* **236**, 151–164 (2001).
36. Tanaka, E. M. Regeneration: if they can do it, why can't we? *Cell* **113**, 559–562 (2003).
37. Echeverri, K. & Tanaka, E. M. Ectoderm to mesoderm lineage switching during axolotl tail regeneration. *Science* **298**, 1993–1996 (2002).
38. Mchedlishvili, L., Epperlein, H. H., Telzerow, A. & Tanaka, E. M. A clonal analysis of neural progenitors during axolotl spinal cord regeneration reveals evidence for both spatially restricted and multipotent progenitors. *Development* **134**, 2083–2093 (2007).

Supplementary Information is linked to the online version of the paper at www.nature.com/nature.

Acknowledgements This work was supported by grants from the Volkswagen Foundation I/78 766; DFG SFB655, SPP1109, SPP 1356, the BMBF Biofutures program, funds from the Max Planck Institute, and the Center of Regenerative Therapies, Dresden. D.K. was a fellow of the Alexander von Humboldt Foundation. We are grateful to K. Agata, H. Tarui, T. Hayashi and M. Saitou for advice on the single-cell PCR technique. We thank I. Nüsslein for assistance on FACS analysis and A. Merseburg for assistance on the nerve rescue experiments. We thank H. Andreas, T. Richter and M. Schuez for technical assistance. We are grateful to L. Rohde, C. Antos, G. Weidinger and A. Tóth for comments on the manuscript.

Author Contributions M.K., D.K. and E.M.T. designed the experiments. M.K., D.K., E.N. and H.H.E. performed embryonic grafting and specificity assessment. M.K. imaged and performed the histological analysis of regenerating limbs, cell counting and single-cell PCR on all experiments. D.K. performed all work related to Schwann cells, with M.M.'s advice. S.K. generated the nucCherry transgenic animals. E.M.T. advised on experiments, examined samples and evaluated data. M.K., D.K. and E.M.T. wrote the manuscript.

Author Information Reprints and permissions information is available at www.nature.com/reprints. Correspondence and requests for materials should be addressed to E.M.T. (elly.tanaka@crt-dresden.de).

METHODS

Axolotl care. *Ambystoma mexicanum* individuals (axolotls) were bred in our facility, where they were kept at 18 °C in Dresden tap water and fed daily with artemia or fish pellets. For all surgery, animals were anaesthetized in 0.01% ethyl-*p*-aminobenzoate (Sigma). The experiments described here were performed on 8-cm-long juvenile axolotls.

Transgenesis. The generation of transgenic animals ubiquitously expressing GFP under the control of the CAGGS promoter has been described before³⁹. Following the same protocol, transgenic animals expressing nuclear Cherry under the control of the CAGGS promoter were generated.

Fluorescent cells were imaged live using a 25× or 40× plan-neofluar objective on a Zeiss Axiovert 200 system with a Spot digital camera, controlled by MetaMorph image acquisition software.

Embryonic transplantation. We labelled the respective tissues by transplantation of GFP⁺ embryonic or mature tissue to normal hosts. After the embryos had developed into juveniles (~8 cm snout to tail), limbs were amputated through regions containing fluorescent cells. Such grafts ultimately labelled a significant portion of a given limb tissue so that when we observed no contribution of labelled cells to another tissue layer after regeneration, the result securely reflected a tissue-specific restriction. This level of numerical significance would not have been achievable by tracing techniques, in which one cell is labelled per animal to determine cell lineage. A similar approach has been used successfully to analyse *Xenopus* tail regeneration⁴⁰.

An important requirement of the donors is the stability of transgene expression. We used the ubiquitous CAGGS promoter to drive GFP, resulting in stable expression except in some blood cells^{39,41}. No evidence of chimaeric expression in regenerating limbs to indicate silencing was observed (Supplementary Fig. 2 and Supplementary Table 1).

To specifically label epidermis, Schwann cells or muscle tissue in the axolotl limb, we performed transplantation of the respective embryonic anlage to host embryos. Briefly, normal and transgenic embryos were allowed to reach late gastrulae (stage 13) before being dejected. For the surgical procedure, stage 14–18 embryos were transferred to agar dishes containing 1× Steinberg's saline with antibiotics. Prior to operations, they were kept for 1 h at 4 °C. Then the vitelline membrane was removed.

Epidermis: an epidermal sheet of about 1 mm² was excised from the limb fields of stage 18 embryos (ventro-lateral region at somite level 3–4). At this stage, the epidermal layer can be removed without contaminating underlying mesodermal tissue. From GFP⁺ transgenic animals, an epidermal piece of the same size was removed and transplanted onto the operated site of the host embryo. Embryos that received a fluorescent epidermal graft were grown to the size of 2 cm larvae before experimental analyses were performed (Supplementary Fig. 3a). The transplanted cells were restricted to the epidermal layer as assessed by Fibronectin localization, which demarcates the epidermal basement membrane (Supplementary Fig. 3b). In the regenerated limb, GFP⁺ cells were still restricted to the epidermal layer, confirming the previous findings that epidermis does not contribute to other limb tissues (Supplementary Fig. 3c).

Dermis: in stage 17–20 embryos the epidermal layer was lifted up and the underlying lateral plate mesoderm was removed from the host. Equivalent pieces of lateral plate mesoderm were taken from the GFP⁺ donors and placed into the hosts, after which the epidermal flap was closed over the transplanted cells.

Muscle: at stage 14–15 the neural fold of host embryos at somite level 3–5 was detached using tungsten needles and pieces of the underlying presomitic mesoderm were removed from the region where progenitors of the limb muscle tissue normally reside. Transgenic embryos were opened in the same way, and fluorescent grafts of the respective tissue layer were transferred to the host. After the surgery, the epidermis was folded back. We observed labelling of muscle fibres and satellite cells after the embryos had developed into juveniles (Supplementary Figs 4e and 6a). We also observed labelling in some blood vessels, presumably owing to endothelial precursors contaminating the original graft.

Schwann cells: neural folds of stage 14–16 *white* mutant host embryos were removed all along the antero-posterior axis and replaced by GFP⁺ fluorescent neural folds derived from transgenic, *white* mutant stage 14–16 donor embryos. Several neural-crest-derived cell types were fluorescently labelled in adults that received fluorescent neural fold transplants during their embryogenesis. However, melanophores and Schwann cells are the only neural-crest-derived cell types present in the limb. This operation produced specific labelling of Schwann cells in the limb because in *white* embryos melanophores do not migrate away from the neural tube region, leaving the limb free of melanophores. Axolotls whose limbs harboured fluorescent Schwann cells were either directly used for experiments, or pieces of tissue containing GFP⁺ Schwann cells were transplanted and analysed in normal hosts.

Axolotl surgery. Surgeries to specifically label animals for skin or skeleton were performed on 8-cm-long (snout to tail) juveniles. As donors, we used GFP-transgenic animals.

Full-thickness skin: squares of ~1 mm × 1 mm were excised from the dorsal upper arm skin of GFP⁺ transgenic donors. After removal of contaminating pieces of muscle and large nerves, they were grafted to the dorsal site of a normal host where a large piece of skin had been removed before surgery. After an integration period of 2 weeks, limbs were amputated through the grafts.

Skeleton: upper arm and hand skeletal elements were removed from GFP⁺ transgenic donors and incubated for 30–60 min in 80% PBS containing 30 U ml⁻¹ papain (Sigma) and 10 U ml⁻¹ DNase IV (Roche) to clear them of contaminating tissues such as muscle and nerves. Fluorescent tissues were then implanted into the upper arms of normal hosts from which a large piece of skeletal tissue had been removed before surgery. After a healing period of 2 weeks, limbs were amputated through the grafts.

X-ray irradiation and nerve implantation. Experiments were performed on 6–8-cm-long animals. The limbs of narcotized animals were irradiated in an X-ray machine (YXLON International, Maxishot, 1000426 B) at 200 kV and 20 mA for 3.3 min, which at a 16 cm distance from the source gave a dose of 20 Gy. The other body parts were shielded by 3-mm-thick lead plates, which transmitted less than 5% of the incident dose.

Nerves from non-irradiated donors containing either GFP-labelled Schwann cells or all cells GFP⁺ were explanted in 80% PBS, cleaned of contaminating sticking cells, implanted into the irradiated lower arms through a small incision in the skin, and two days later the limbs were amputated through the implant. Within 22–40 weeks (a period much longer than is sufficient to allow the regeneration of unirradiated control limbs) a significant number of the X-rayed limbs that received a nerve implant produced limbs that were not completely patterned. Five of 17 irradiated limbs were rescued by Schwann-GFP nerve, and five of 16 irradiated limbs were rescued by the 'all-GFP' nerve implants. The unrescued controls continuously lost tissue up to the shoulder.

Antibody staining on axolotl limb cryosections. Axolotl limbs were fixed in fresh 4% paraformaldehyde overnight at 4 °C, washed in PBS, incubated in 30% sucrose overnight and frozen in Tissue-Tek (O.C.T. compound, Sakura) or in 7.5% gelatin (Merck). Cross- and longitudinal-limb sections (14–20-μm-thick) were washed in TBS/0.3% Tween and blocked for one hour in 20% goat serum, followed by an overnight incubation with anti-Pax7 mAb (Developmental Studies Hybridoma Bank), anti-MEIS pAb (Upstate Cell Signalling solution), anti-MBP pAb (Gene Tex Industries) and anti-BIII-tubulin mAb (R&D Systems). After several washes in TBS/Tween, a Cy5-labelled anti-mouse secondary antibody (Dianova) was used at 1:200 dilution in combination with anti-PAX7, anti-MEIS and anti-BIII-tubulin primary antibodies, while a Cy3- or Cy5-labelled anti-rat secondary antibody was used at a 1:100 dilution in combination with the anti-MBP primary antibody. To visualize MHCI⁺ muscle fibres, we used the monoclonal antibody 4A1025 (the kind gift of S. Hughes), which was directly coupled to rhodamine-NHS (Molecular Probes). Nuclear stainings were performed using DAPI or 1 μg ml⁻¹ of Hoechst in TBS/Tween20.

Images were taken on an Olympus BX61 microscope using a digital camera (Diagnostic Instruments Inc.) under the control of the Spot Advanced program. Mosaic images in Supplementary Figs 5 and 7 were stitched using the Adobe Photoshop CS3 program. Mosaic images in Supplementary Fig 4d–j were taken on a Zeiss Observer Z1 and stitched using the AxioVision program. Confocal images were acquired on a Zeiss LSM 510 microscope.

Cell dissociation and FACS. In each experiment, two limb blastemas were manually dissected in 2 ml liberase based dissociation solution (100 U ml⁻¹ DNase IV, 0.35 mg ml⁻¹ liberase blendzyme both Roche, in 80% PBS), until a single-cell suspension was visible (depending on the tissue, 10–60 min). The cell suspension was transferred into a new tube incubated with 5 μM DRAQ5 (Axxora). Cells were then passed through a 22-μm filter and analysed by FACS. Single events of maximum GFP intensity, which were verified to be GFP⁺ transgenic cells, were gated and sorted into reverse transcription buffer.

Single-cell PCR. Single-cell PCR was performed as described⁴² with the following modifications.

Reverse transcription: cells were sorted into a 96-well plate in which each well contained 5 μl reverse transcription buffer. The plate was centrifuged and incubated for 1 min at 65 °C and 3 min at 22 °C. 2.6 μl RNase-free water and 0.4 μl SSII reverse transcriptase (Invitrogen) were then added to each well so that the reverse transcription buffer reached a final volume of 8 μl containing 50 mM Tris-Cl pH 8.3, 75 mM KCl, 0.1 ng μl⁻¹ reverse transcription primer (sequence: TGG ACT AAC TAT GAA TTC TTT TTT TTT TTT TTT TTT TTT V), 2 μM dNTPs, 0.5% NP40 (Sigma), 0.08 μl RNAGuard (GE Healthcare) and 0.27 μl Prime RNase inhibitor (VWR). For reverse transcription, the plate was incubated at 42 °C for 15 min and 70 °C for 10 min.

Poly A tailing: to each reaction well, 8 μ l polyadenylation solution was added to reach a final concentration of 100 mM of potassium cacodylate (Roche), 2 mM of CoCl_2 (Roche), 0.2 mM of DTT, 100 μ M of dATP and 0.2 μ l terminal transferase (Roche) were added to reach a final volume of 16 μ l. The plate was incubated at 37 °C for 15 min and at 65 °C for 10 min.

PCR: the reaction volume was increased to 50 μ l for PCR amplification to reach a final concentration of 1 \times reaction buffer, 1 mM dNTPs, 0.07 μ g μ l⁻¹ PCR primer (sequence: CAT GTC GTC CAG GCC GCT CTG GGA CAA AAT ATG AAT TC TTT TTT TTT TTT TTT TTT TTT) and 0.1 U μ l⁻¹ TAQ polymerase (MPI-CBG protein expression facility). After one complete run (1 cycle of 37 °C for 5 min and 72 °C for 20 min; 25 cycles of 94 °C for 1 min, 42 °C for 2 min and 72 °C for 6 min plus 10 s extension/cycle), fresh TAQ polymerase was supplied along with buffer, dNTPs and PCR primer to a final volume of 60 μ l and maintaining the final concentrations of each component. After the addition of the fresh components, the amplification reaction was repeated. After the completion of the second run, we normally generated a total amount of 8–10 mg complementary DNA, which was analysed subsequently in a quantitative PCR using gene-specific primers.

Real time PCR on cDNA generated by single-cell PCR. The cDNAs were diluted 1:300 and used as a template to perform quantitative PCR. Reactions were performed in a total volume of 10 μ l using the SYBR Green kit (Stratagene) following the instructions given by the manufacturer. We used the recommended

final primer concentration of 300 nM. Sequences of gene-specific primers were designed based on the published sequences obtained from our cDNA library⁴³.

The primer sequences were TGA AGA ACT TGA GGG TCA TGG forward and CTT GGC GTC TGC AGA TTT TTT reverse (*Rp4*), GGG CAC ACT AAA AAG GTT AAA forward and GCA GGG TTT ACG ACA ATG TAC reverse (*HoxA13*), and AGC AGA TTC CTG CGA TGT TT forward and GCA CCA CAT GAC AAA ACA CA reverse (*Myf5*).

Statistical analyses. Localization of cells to lower arm versus hand skeleton were analysed using the Student's *t*-test for unpaired samples (Welch modification). *P* values were determined using the Matlab software.

39. Sobkow, L., Epperlein, H. H., Herklotz, S., Straube, W. L. & Tanaka, E. M. A germline GFP transgenic axolotl and its use to track cell fate: dual origin of the fin mesenchyme during development and the fate of blood cells during regeneration. *Dev. Biol.* **290**, 386–397 (2006).
40. Gargioli, C. & Slack, J. M. Cell lineage tracing during *Xenopus* tail regeneration. *Development* **131**, 2669–2679 (2004).
41. Okabe, M., Ikawa, M., Kominami, K., Nakanishi, T. & Nishimune, Y. 'Green mice' as a source of ubiquitous green cells. *FEBS Lett.* **407**, 313–319 (1997).
42. Brady, G. & Iscove, N. N. Construction of cDNA libraries from single cells. *Methods Enzymol.* **225**, 611–623 (1993).
43. Habermann, B. et al. An *Ambystoma mexicanum* EST sequencing project: analysis of 17,352 expressed sequence tags from embryonic and regenerating blastema cDNA libraries. *Genome Biol.* **5**, R67, 1–19 (2004).

ARTICLES

Telomerase modulates Wnt signalling by association with target gene chromatin

Jae-Il Park¹, Andrew S. Venteicher^{1,2*}, Ji Yeon Hong^{4*}, Jinkuk Choi^{1,3}, Sohee Jun¹, Marina Shkreli¹, Woody Chang¹, Zhaojing Meng⁵, Peggie Cheung¹, Hong Ji⁴, Margaret McLaughlin⁶, Timothy D. Veenstra⁵, Roel Nusse⁷, Pierre D. McCrea⁴ & Steven E. Artandi^{1,2,3}

Stem cells are controlled, in part, by genetic pathways frequently dysregulated during human tumorigenesis. Either stimulation of Wnt/ β -catenin signalling or overexpression of telomerase is sufficient to activate quiescent epidermal stem cells *in vivo*, although the mechanisms by which telomerase exerts these effects are not understood. Here we show that telomerase directly modulates Wnt/ β -catenin signalling by serving as a cofactor in a β -catenin transcriptional complex. The telomerase protein component TERT (telomerase reverse transcriptase) interacts with BRG1 (also called SMARCA4), a SWI/SNF-related chromatin remodelling protein, and activates Wnt-dependent reporters in cultured cells and *in vivo*. TERT serves an essential role in formation of the anterior–posterior axis in *Xenopus laevis* embryos, and this defect in Wnt signalling manifests as homeotic transformations in the vertebrae of *Tert*^{−/−} mice. Chromatin immunoprecipitation of the endogenous TERT protein from mouse gastrointestinal tract shows that TERT physically occupies gene promoters of Wnt-dependent genes. These data reveal an unanticipated role for telomerase as a transcriptional modulator of the Wnt/ β -catenin signalling pathway.

Mammalian tissues require strict regulation of progenitor cell proliferation and differentiation to facilitate both tissue maintenance with normal homeostasis and efficient repair in settings of organ damage. This exquisite control of tissue progenitor cells is executed by both secreted and cell-intrinsic factors. Dysregulation of pathways controlling normal progenitor cell function is a common event in human cancer, suggesting that altered progenitor cell regulation is an important step in carcinogenesis. One such pathway is controlled by Wnt proteins, secreted glycoproteins crucial for development, stem-cell maintenance and stem-cell activation¹. Overexpression of β -catenin, a critical mediator of Wnt signalling, causes activation of epidermal stem cells and induces anagen in mouse skin^{2–4}. A similar phenotype is elicited by overexpression of telomerase, the enzyme that adds DNA repeats to chromosome ends, although the mechanisms by which telomerase activates tissue progenitor cells remain poorly understood^{5,6}. The central role of Wnt/ β -catenin signalling in stem-cell biology and in differentiation explains how alterations in this pathway are frequently initiating lesions in human tumorigenesis⁷.

Another pathway essential for maintaining stem cells involves telomere repeat addition by telomerase. In settings of insufficient telomerase, telomeres shorten with each cell division, eventually compromising end protection at a subset of chromosome ends, which results in a local DNA-damage response that impairs stem-cell self renewal and progenitor cell survival^{8,9}. In addition to this role for telomerase in supporting tissue progenitor cells by maintaining telomeres, gain-of-function experiments revealed that telomerase serves a more direct function in tissue progenitor cells. Conditional overexpression of TERT in mouse skin activated quiescent bulge stem cells and caused a rapid developmental transition in the hair

follicle from telogen, the resting phase of the hair follicle cycle, to anagen, the active phase⁵, which strikingly phenocopies the effects of β -catenin overexpression in mouse skin^{2–4}. The ability of TERT to activate tissue stem cells required neither the telomerase RNA TERC nor the reverse transcriptase activity of TERT and is therefore independent of its catalytic role in adding telomere repeats^{5,10}. Gene expression studies on inducible TERT mouse skin together with pattern-matching algorithms suggested that the TERT-controlled gene expression pattern significantly resembled the transcriptional programs regulated by Wnt and Myc¹⁰.

Other experiments have suggested the existence of telomere length-independent activities for telomerase in cellular transformation^{11–13}, proliferation¹⁴, stem-cell biology^{15–17}, cell survival¹⁸ and chromatin regulation¹⁹. However, the mechanisms by which TERT exerts these effects in progenitor cells and cancers remain unknown. Here we report the unexpected finding that telomerase is a direct modulator of the Wnt/ β -catenin pathway. TERT interacts with BRG1, occupies specific chromatin sites of Wnt/ β -catenin target genes, activates Wnt reporters in culture and *in vivo*, and is important for the Wnt program in mouse embryonic stem (ES) cells and in *Xenopus* embryos. These data reveal a significant level of integration between two pathways required for stem-cell proliferation and self-renewal with profound implications for understanding stem-cell regulation, development and carcinogenesis.

TERT interacts with BRG1 and activates Wnt reporters

To understand telomerase-mediated signalling, we purified TERT protein complexes from HeLa cells using tandem affinity chromatography coupled with nano liquid chromatography tandem mass

¹Department of Medicine, ²Biophysics program, ³Cancer Biology Program, Stanford University School of Medicine, Stanford, California 94305, USA. ⁴Department of Biochemistry and Molecular Biology, University of Texas M.D. Anderson Cancer Center, Houston, Texas 77030, USA. ⁵Laboratory of Proteomics and Analytical Technologies, Advanced Technology Program, SAIC-Frederick Inc., NCI-Frederick, Frederick, Maryland 21702, USA. ⁶Koch Institute for Integrative Cancer Biology and Department of Biology, Massachusetts Institute of Technology, Cambridge, Massachusetts 02139, USA. ⁷Department of Developmental Biology, Howard Hughes Medical Institute, Stanford University School of Medicine, Stanford, California 94305, USA.

*These authors contributed equally to this work.

spectrometry²⁰. In replicate purifications, we identified numerous peptides derived from BRG1, a SWI/SNF-related ATP-dependent chromatin-remodelling factor that acts to modulate chromatin conformation²¹ (Supplementary Fig. 1). To circumvent significant challenges in studying endogenous TERT protein²², we introduced epitope tags into the *Tert* locus in knock-in mouse ES cells (Fig. 1a and Supplementary Fig. 2) and in knock-in mice (see below). Endogenous TERT was readily detected by immunoprecipitation and western blot analysis from ES cells in which a haemagglutinin (HA) epitope tag was inserted at the start codon of the *Tert* gene through homologous recombination (Fig. 1a, b). Immunoprecipitation of endogenous TERT revealed the presence of BRG1 in TERT complexes (Fig. 1b and Supplementary Figs 3–5). Domain mapping experiments showed that TERT interacts with the bromodomain of BRG1 in glutathione S-transferase pull-down experiments (Supplementary Fig. 6).

Because BRG1 had been implicated as a β -catenin-interacting protein in the Wnt pathway^{23,24}, we tested whether BRG1 was required for transactivation of Wnt reporter plasmids. Stabilization of β -catenin caused by LiCl-mediated inhibition of GSK3- β led to strong upregulation of luciferase from a transfected reporter plasmid driven by multimerized TCF-binding sites (TOP-FLASH). Depletion of BRG1 with retroviral-encoded short hairpin RNAs (shRNAs) reduced luciferase expression by more than 50%, consistent with a role for BRG1 in controlling β -catenin-mediated transcription at TCF-dependent promoters (Fig. 1c, d). These data showing that TERT interacts with BRG1, and that BRG1 is involved in the Wnt pathway, together with the similarities between the effects of Wnt proteins and those of TERT in hair follicle stem-cell activation prompted us to investigate a role for TERT in the Wnt/ β -catenin signalling pathway.

We asked whether TERT could activate the Wnt pathway by co-transfecting a TERT expression plasmid together with TOP-FLASH.

Remarkably, overexpression of TERT was sufficient to hyperactivate the TOP-FLASH reporter in cells treated with LiCl (Fig. 1e) without altering β -catenin protein level or subcellular localization (Supplementary Fig. 7). Similarly, reporter plasmids driven by promoters of other β -catenin target genes, including cyclin D1, *c-myc* (hereafter referred to as *Myc*) and *siamois*²⁵, were also hyperactivated by TERT upon LiCl treatment (Fig. 1f). Overexpression of TERT in SW-13 cells, which do not express BRG1, failed to enhance β -catenin reporter activity upon lithium treatment, and this defect in TERT signalling was restored through BRG1 overexpression (Fig. 1g). Furthermore, BRG1 depletion using RNA interference abrogated the ability of TERT to hyperactivate TOP-FLASH reporter plasmids in HeLa cells (Fig. 1h). TERT stimulated TOP-FLASH plasmids in *Terc*^{-/-} mouse embryonic fibroblasts (MEFs) and a catalytically inactive TERT mutant (TERT^{ci}) stimulated Wnt reporters, indicating that the catalytic function of telomerase is not required for transcriptional co-activation (Supplementary Fig. 8). These results suggest that TERT protein interacts with BRG1 to regulate Wnt-dependent promoters.

TERT activates the Wnt axis *in vivo* and in ES cells

To determine if the ability of TERT to activate the Wnt pathway extends to an *in vivo* context, we investigated the stem-cell niche of the gastrointestinal tract, where Wnt signalling through β -catenin and TCF proteins is required for maintenance of stem cells and progenitor cells²⁶. Wnt signalling in the gastrointestinal tract was monitored using *Axin2*^{lacZ/+} reporter mice, a knock-in strain in which β -galactosidase is expressed from the *Axin2* promoter²⁷. *Axin2*^{lacZ/+} mice were intercrossed with inducible TERT (*i-TERT*^{ci}) mice, which allow tetracycline-regulated expression of catalytically inactive TERT^{5,10}. β -galactosidase activity in crypts in the small intestine and colon was significantly enhanced by induction of TERT^{ci} in *i-Tert*^{ci}

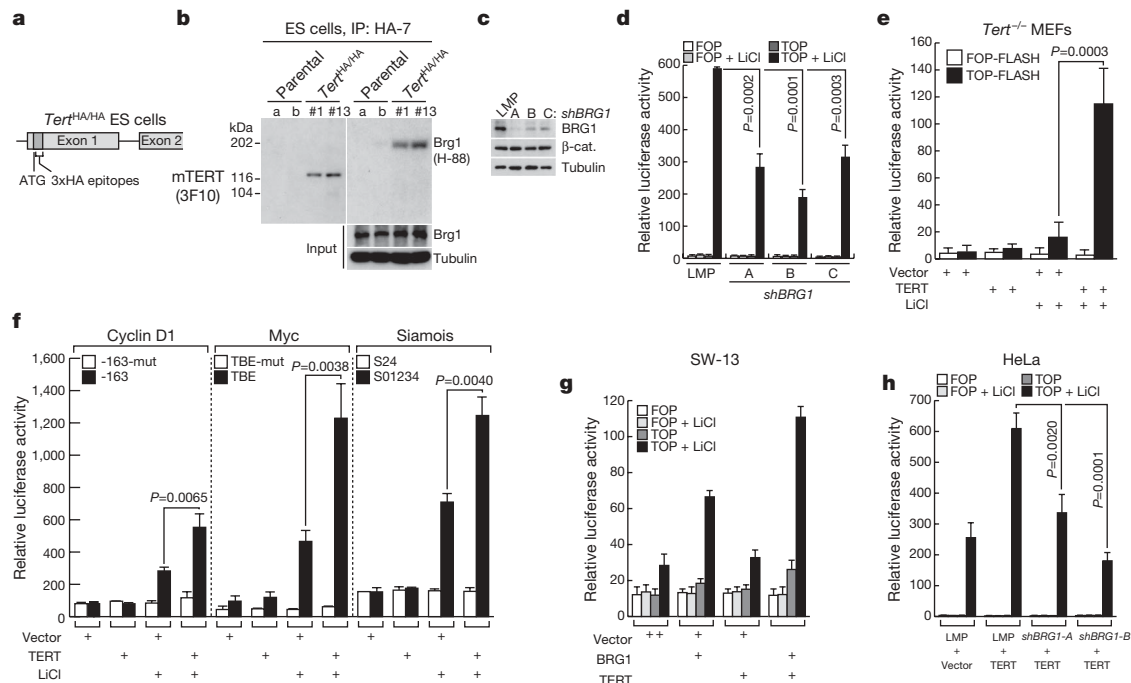


Figure 1 | TERT activates Wnt reporter plasmids in a BRG1-dependent manner. **a**, Diagram of HA-TERT knock-in ES cells. **b**, Interaction of endogenous TERT with BRG1 in *Tert*^{HA/HA} ES cells by immunoprecipitation (IP) and immunoblot (IB). HA-7 and 3F10, anti-HA antibodies. **c**, Depletion of BRG1 protein by shRNAs in HeLa cells by immunoblot. **d**, TOP-FLASH reporter activity in HeLa cells transduced with empty vector (LMP) or shRNA *BRG1* retroviruses, then transfected with TOP-FLASH plasmid (wild-type TCF sites) and treated with LiCl ($n = 3$) (FOP-FLASH, mutant TCF sites). **e**, TOP-FLASH activity in *Tert*^{-/-} MEFs co-transfected with empty vector or mouse TERT expression plasmid and treated with or

without LiCl ($n = 4$). **f**, Luciferase activity after transient co-transfection of reporter plasmids comprising cyclin D1, *Myc*, or *siamois* promoters driving luciferase with TERT plasmid or empty vector in HeLa cells, followed by LiCl treatment ($n = 3$). Filled bar, wild-type TCF binding elements (TBE); open bar, mutant TBEs. **g**, Effect on TOP-FLASH activity of transient co-transfection of BRG1, TERT or BRG1 combined with TERT in SW-13 cells lacking BRG1 ($n = 2$). **h**, Effect of *BRG1* depletion with shRNA on TERT-mediated activation of TOP-FLASH activity in HeLa cells ($n = 3$). Error bars indicate standard deviation; *P* values produced by Student's *t*-test.

Axin2^{lacZ/+} mice by both whole mount and histology (Fig. 2a, b). In addition, CD44, a transcriptional target of β -catenin in crypts, was upregulated by TERT^{ci} overexpression (Fig. 2c). These data show that TERT overexpression is sufficient to enhance significantly the transcriptional output of the Wnt/ β -catenin pathway in progenitor cells of the small intestine.

To understand if TERT is required for Wnt signalling, we generated TERT conditional knockout mouse ES cells, incorporating a ROSA26-CreER allele, which enabled efficient deletion of TERT with tamoxifen treatment (Fig. 2d, e and Supplementary Fig. 9)²⁸. WNT3A ligand efficiently induced *Axin2* messenger RNA in TERT conditional knockout ES cells that retained TERT sequences. However, deletion of TERT in TERT conditional knockout ES cells with tamoxifen significantly diminished induction of *Axin2* by WNT3A treatment (Fig. 2f). Furthermore, deletion of TERT reduced basal expression of *Axin2*, which was rescued by overexpression of mouse TERT^{ci} (Fig. 2g, h). Thus, TERT is required for efficient induction of Wnt target genes in mouse ES cells treated with WNT3A ligand.

TERT is required for *Xenopus* anterior–posterior axis formation

Activation of Wnt/ β -catenin signalling in the ventral vegetal region of *Xenopus* embryos causes duplication of the anterior–posterior axis²⁹. Injecting increasing amounts of *Xenopus Tert* mRNA together with a low amount of *Xenopus* β -catenin mRNA promoted formation of a

duplicate anterior–posterior axis in a dose-dependent manner (Fig. 3a, b). Similarly, injection of *Xenopus* (x)TERT^{ci} (D770A) mRNA in conjunction with *Xenopus* β -catenin mRNA also promoted secondary axis formation, indicating that this activity does not require reverse transcriptase catalytic function (Fig. 3c).

Endogenous Wnt/ β -catenin signalling has an important role in axial development and patterning of the ventrolateral mesoderm^{30,31}. We therefore asked if inhibiting TERT through injection of specific morpholinos altered *Xenopus* embryo development (Fig. 3d). Remarkably, xTERT depletion by TERT morpholinos (TMO) caused a pronounced defect in anterior–posterior axis formation³² (Fig. 3e and Supplementary Table 1; dorso–anterior index score: TMO1, 3.7; TMO2, 3.2; StdMO control, 5.0). TERT inhibition led to ectopic neural tube formation and loss of the notochord, phenotypes also seen in knockout mouse embryos defective in components of the Wnt pathway (Fig. 3f)³³. These TERT phenotypes were efficiently rescued by co-injection with *xTert*, *xTert*^{ci} or human TERT^{ci} mRNAs resistant to TMO1, ruling out off-target effects of the TMOs and revealing that the developmental defects in TMO-treated embryos are due to impaired TERT-mediated signalling rather than a defect in catalytic function (Fig. 3g and Supplementary Fig. 10). Overexpression of *xTert* mRNA strongly activated co-injected TOP-FLASH reporter plasmids and xTERT depletion significantly reduced TOP-FLASH expression (Fig. 3h). These results show that

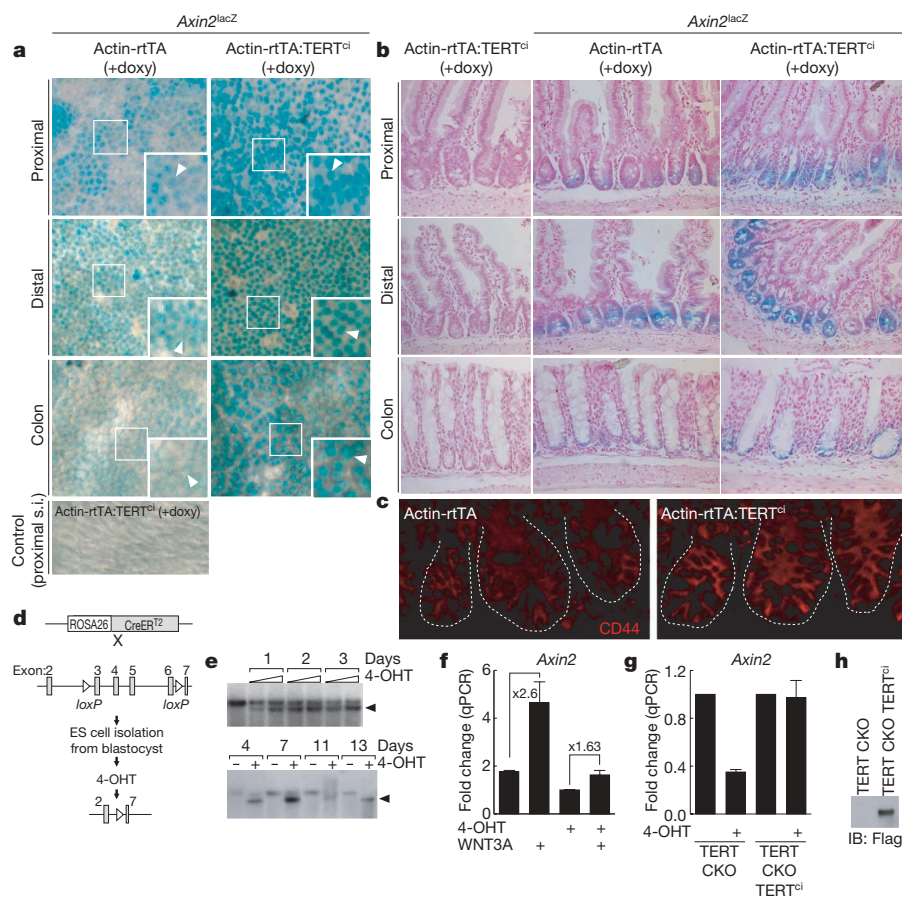


Figure 2 | TERT activates the Wnt pathway *in vivo* and is required for efficient target gene activation by WNT3A ligand in mouse ES cells.

a, b, X-Gal staining for β -galactosidase activity in small intestine and colon of *Axin2*^{lacZ/+} reporter mice, *i-Tert*^{ci} *Axin2*^{lacZ/+} mice or controls. Whole mounts seen from abluminal side (**a**); histology, nuclear fast red (**b**). Arrowheads indicate crypts. Doxy, doxycycline; s.i., small intestine. **c**, CD44 protein in small intestine crypts by immunofluorescence. **d**, Schematic for deletion of TERT by 4-OHT treatment of conditional TERT knockout (CKO) ES cells. **e**, Cre-mediated recombination in ES cells by

Southern blot. Arrowhead, recombined *Tert* allele. **f**, Induction of *Axin2* by WNT3A ligand in TERT conditional knockout (CKO) mouse ES cells treated with vehicle or with 250 nM 4-OHT for 3 days, exposed to WNT3A (100 ng ml⁻¹) for 24 h and analysed by qPCR (*n* = 3). **g**, **h**, Basal expression of *Axin2* mRNA by qPCR in TERT conditional knockout mouse ES cells treated with vehicle or 4-OHT, and *Axin2* mRNA levels in TERT conditional knockout cells with stable overexpression of mouse TERT^{ci} (*n* = 3), shown in **h** by immunoprecipitation and western blot analysis. Error bars indicate s.d. Original magnification: **a**, $\times 4$ (insets $\times 8$); **b**, $\times 20$; **c**, $\times 40$.

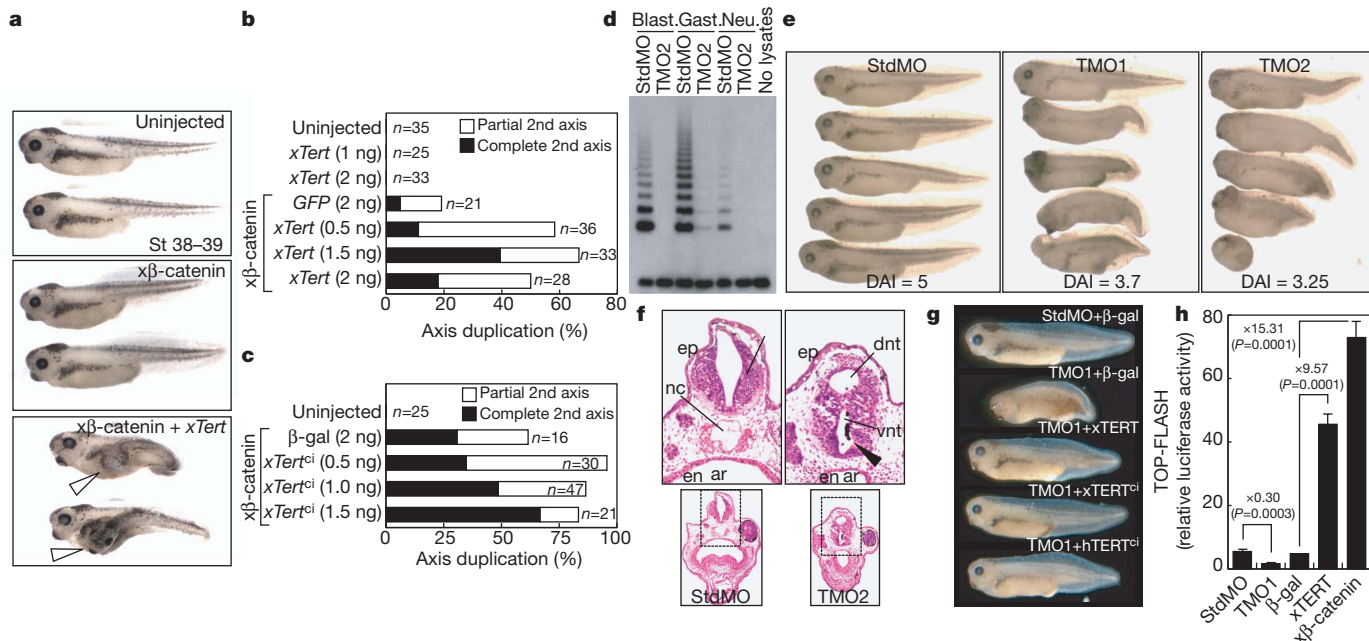


Figure 3 | TERT promotes anterior–posterior axis duplication and is required for efficient anterior–posterior axis in *Xenopus*. **a, b**, Duplicate anterior–posterior axis formation in *Xenopus* embryos co-injected with *Xenopus* (x)β-catenin mRNA (0.2 ng) and increasing amounts of xTert mRNA. Open arrowheads, extra axes. **c**, Duplicate axis with co-injection of xTert^{ci} and xβ-catenin mRNA (0.4 ng). **d**, TRAP activity at blastula, gastrula and neurula stages in embryos injected with TERT morpholino (TMO2) or control (StdMO). **e**, Defects in anterior–posterior axis development in embryos injected with TERT morpholinos (TMO1 or TMO2), but not

StdMO, scored using dorso-anterior index (DAI). **f**, Ectopic neural tube formation (arrowhead) in TMO2-injected embryos. ar, archenteron; dnt, dorsal neural tube; en, endoderm; ep, epidermis; nc, notochord; vnt, ventral neural tube. Transverse sections; haematoxylin and eosin staining. **g**, Rescue of developmental phenotypes with xTERT, xTERT^{ci} and human (h)TERT^{ci}, stages 37–38. **h**, TOP-FLASH analysis by co-injecting reporter plasmid at the 2-cell stage with either StdMO or TMO1, or co-injecting reporter plasmid with β-gal, xTERT or β-catenin ($n = 3$, P values produced by Student's t -test, error bars indicate s.d.).

TERT is required for proper Wnt signalling and for formation of the anterior–posterior axis during frog development.

Homeotic transformations in *Tert*^{−/−} mice

In addition to its critical role in formation of the anterior–posterior axis, Wnt signalling is also required for formation of the paraxial mesoderm³³ and subsequent generation of the somites from presomitic mesoderm³⁴. We speculated that impaired Wnt signalling caused by TERT inhibition might therefore result in defects in somitogenesis. Somite-specific staining of *Xenopus* embryos revealed that TERT depletion disrupted somitogenesis, resulting in abnormal somite shape and impaired segment polarity (Fig. 4a). Notably, the effect of TERT morpholinos on caudal development was particularly pronounced, consistent with the established role of WNT3A in posterior development in vertebrates³⁵. WNT3A regulates posterior development in part through transcriptional regulation of *Cdx1*, a homeobox gene that directly regulates posterior Hox gene expression³⁶. WNT3A ligand induced expression of *Cdx1* in mouse ES cells by 12 fold, whereas conditional deletion of TERT in TERT conditional knockout ES cells strongly suppressed induction of *Cdx1* by WNT3A (Fig. 4b). Moreover, depletion of xTERT reduced levels of x*Cdx1*, x*Cdx2* and x*Cdx3*, as well as the Wnt target gene siamois, in TMO-treated *Xenopus* embryos at the late gastrulation stage (Fig. 4c). *Cdx* genes are also regulated by FGF, retinoic acid and BMP signalling, in addition to Wnts^{36–38}; however, we detected no change in these pathways with TERT depletion, indicating that TERT contributes to *Cdx* gene regulation through its specific role in the Wnt/β-catenin pathway (Supplementary Fig. 11). These data show that the endogenous TERT protein is required for appropriate regulation of *Cdx* genes by the Wnt/β-catenin pathway in mouse ES cells and in *Xenopus* embryos.

Analysis of telomerase knockout mice, including germline deletion of either *Terc* or *Tert*, led to the paradigm that first generation (G1)

telomerase knockout mice are normal, but that continued breeding of telomerase-deficient strains leads to defects in renewing tissues caused by progressive telomere shortening and eventual loss of telomere protection^{39,40}. On the basis of our data showing clear involvement of TERT in Wnt/β-catenin signalling in diverse contexts, we analysed *Tert*^{−/−} mice, focusing on the vertebrae of the spinal column, which derives from somites and depends on proper expression of *Cdx* and Hox genes⁴¹. G1 *Tert*^{−/−} mice lacked telomerase activity but retained functional telomeres and showed none of the apoptotic defects seen in late generation (G5–G6) *Tert*^{−/−} mice (Supplementary Fig. 12)^{42,43}. Detailed analyses using skeletal preparations and high-resolution CT scanning revealed that G1 *Tert*^{−/−} mice have homeotic transformations of the vertebrae (T13 to L1), characterized by loss of the thirteenth rib on one or both sides (6 out of 13 G1 *Tert*^{−/−} mice with T13 to L1 transformation versus 0 out of 15 *Tert*^{+/+} controls, $P = 0.0046$; Fig. 4d–f and Supplementary Table 2). In addition, some G1 *Tert*^{−/−} mice showed an L6 to S1 transformation (Supplementary Fig. 13). These homeotic defects in G1 *Tert*^{−/−} mice strikingly resemble those in vestigial tail mice, which harbour a hypomorphic mutation in WNT3A and have homeotic transformations with similar penetrance (Supplementary Fig. 14)³⁶.

TERT occupies Wnt target gene promoters

To address the mechanism by which TERT regulates transcription of Wnt/β-catenin target genes, we investigated occupancy of β-catenin-dependent gene promoters by chromatin immunoprecipitation (ChIP). Upon lithium treatment of HeLa cells, β-catenin and BRG1 became associated with promoter fragments containing known TCF binding elements (TBEs), including those within cyclin D1 and *Myc*, two genes directly regulated by β-catenin. ChIP revealed that stably expressed Flag–TERT was also associated with the TBE-containing promoter fragments of the cyclin D1 and *Myc* promoters in a lithium-dependent manner (Fig. 5a, b). Furthermore, sequential

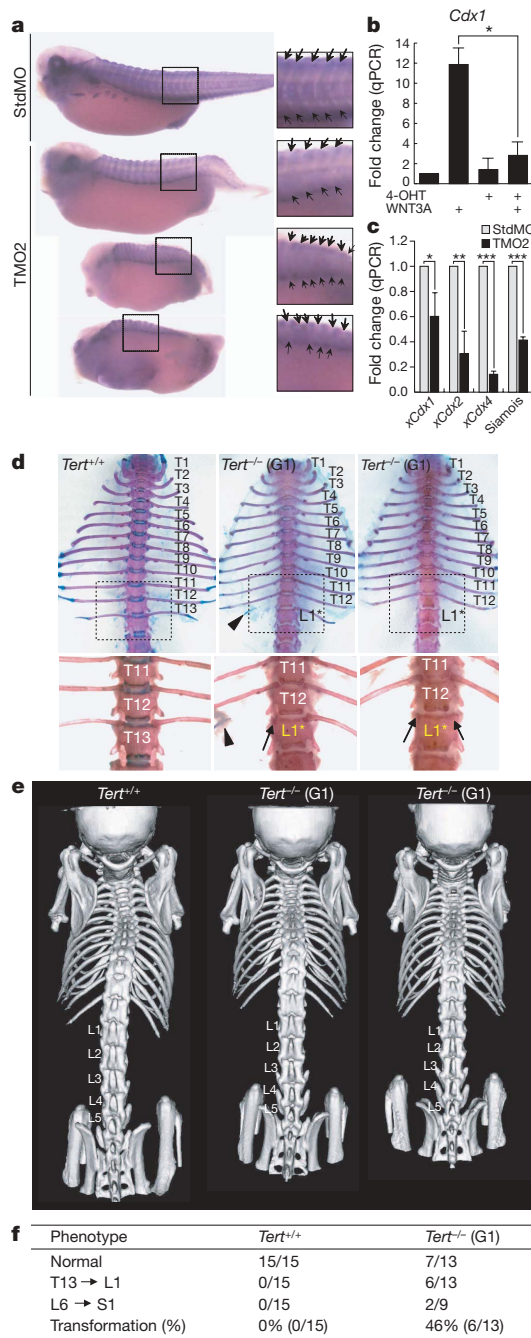


Figure 4 | Somite defects in *Xenopus* embryos treated with TERT morpholino and homeotic transformations in *Tert*^{-/-} mice. **a**, Somite staining using 12/101 antibody of *Xenopus* embryos injected with either StdMO or TMO2. Arrows show somite boundaries. **b**, WNT3A-mediated induction of *Cdx1* in TERT conditional knockout ES cells treated with vehicle or 4-OHT for 3 days, followed by WNT3A for 24 h. **P* = 0.002 by Student's *t*-test (*n* = 3). **c**, Levels of *xCdx1*, *xCdx2* and *xCdx4* measured by qPCR in *Xenopus* embryos injected with StdMO or TMO2 and collected at the late gastrulation stage. **P* = 0.0066, ***P* = 0.0003, ****P* < 0.0001 by Student's *t*-test (*n* = 4). **d**, **e**, T13 to L1 vertebral homeotic transformations in G1 *Tert*^{-/-} mice. Unilateral loss of 13th rib (middle) or bilateral loss of 13th ribs (right). Arrowhead, 13th rib remnant; arrows, missing 13th ribs. Adult skeletons were stained with alcian blue and alizarin red (ventral; **d**). Three-dimensional reconstruction of microCT scan images of independent mice (dorsal; **e**). **f**, Summary of axial skeletal defects in G1 *Tert*^{-/-} mice. *P* = 0.0046 by Fisher's exact test.

ChIP revealed that Flag-TERT was bound to the same promoter elements as BRG1 and β-catenin (Supplementary Fig. 15). TERT binding to TCF elements was analysed further through quantitative ChIP experiments using primer pairs spanning 20 kb upstream of

the *Axin2* and *Myc* genes at average intervals of 1 kb. The profile of Flag-TERT binding closely resembled that of TCF3 at both the *Axin2* and *Myc* genes in HeLa cells stimulated with lithium (Fig. 5c). Notably, the Flag antibody ChIP performed on parental HeLa cells lacking expression of Flag-TERT did not detect these promoter fragments, indicating that the Flag-TERT ChIP signals depended on the presence of stably overexpressed TERT protein. These data reveal that Flag-TERT physically associates with TBE-containing promoter fragments, along with BRG1 and β-catenin.

To understand if endogenous TERT protein participates in regulatory complexes at β-catenin-dependent genes, we engineered knock-in mice in which a multiple epitope tag was inserted in frame at the beginning of the *Tert* gene (AFH-TERT) (Fig. 5d and Supplementary Fig. 16). *Tert*^{AFH/AFH} mice were viable and telomerase activity from small intestine extracts measured by the telomere repeat amplification protocol (TRAP assay) was equivalent in *Tert*^{AFH/AFH} mice and in wild-type littermate controls (Fig. 5e). Immunoprecipitation and western blot analysis from protein extracts of the small intestine using anti-HA antibodies revealed an AFH-TERT band of the expected size specifically in *Tert*^{AFH/AFH} mice (Fig. 5f). Chromatin association of endogenous TERT with TCF sites was assessed by performing *in vivo* ChIP on small intestine using anti-HA antibodies and TCF3 antibodies. Primer pairs spanning 20 kb of the mouse *Myc* promoter at an average of 1-kb intervals were used in quantitative PCR to detect chromatin fragments associated with AFH-TERT and TCF3. AFH-TERT and TCF3 were bound to several chromatin regions spanning the *Myc* genomic sequences in a remarkably similar pattern (Fig. 5g). Importantly, ChIP experiments performed in parallel using anti-HA antibodies and wild-type small intestine samples did not pull down *Myc* promoter chromatin, indicating that the chromatin fragments in the AFH-TERT samples were dependent on the presence of AFH-TERT protein. Consistent with these findings, HA-TERT was associated with chromatin from the *Axin2* promoter in a pattern that overlapped with β-catenin in *Tert*^{HA/+} mouse ES cells (Supplementary Fig. 17). Furthermore, β-catenin was detected in AFH-TERT complexes purified from small intestine extracts of *Tert*^{AFH/AFH} mice, but not in *Tert*^{+/+} controls, indicating that endogenous TERT and β-catenin exist in a common complex (Fig. 5f and Supplementary Fig. 18). These data show that endogenous TERT and TCF3 occupy similar chromatin sites in the *Myc* gene in small intestine, consistent with a role for TERT in β-catenin-mediated transcriptional responses *in vivo*.

Conclusions

Wnt signalling serves a critical role in development, in proliferating tissue progenitor cells and in human cancers¹. In the absence of a Wnt signal, TCF/LEF transcription factors occupy their cognate sites in Wnt responsive gene promoters, where they recruit repressor proteins such as CtBP and Groucho/TLE⁴⁴. In the setting of Wnt ligand, β-catenin displaces these repressors and recruits proteins that help to confer transcriptional activation at TCF/LEF binding sites, although the mechanisms governing this activation are not fully understood⁴⁵. Proteins recruited by β-catenin to promoters include several complexes that modify or remodel histones, such as BRG1, CBP/p300, TRAAP, Mll1/Mll2 and SWR1, as well as proteins coupled to initiation and elongation by RNA polymerase II, such as MED12, hyrax, pygopus and CDK8 (refs 44, 46–48). Thus, many modulators may be required for efficient tuning of the Wnt response and it is likely that some cofactors may be context-specific to explain how Wnt signalling leads to alternative cell fates, such as proliferation or differentiation. Our data indicate that telomerase represents one such cofactor that probably acts in a progenitor cell context to facilitate a Wnt-regulated program of self-renewal, proliferation or survival.

This unexpected role for TERT as a regulatory molecule modulating transcription complements the more widely appreciated function of telomerase in maintaining telomere repeats at chromosome ends. Dysfunctional telomeres that arise in settings of insufficient telomerase

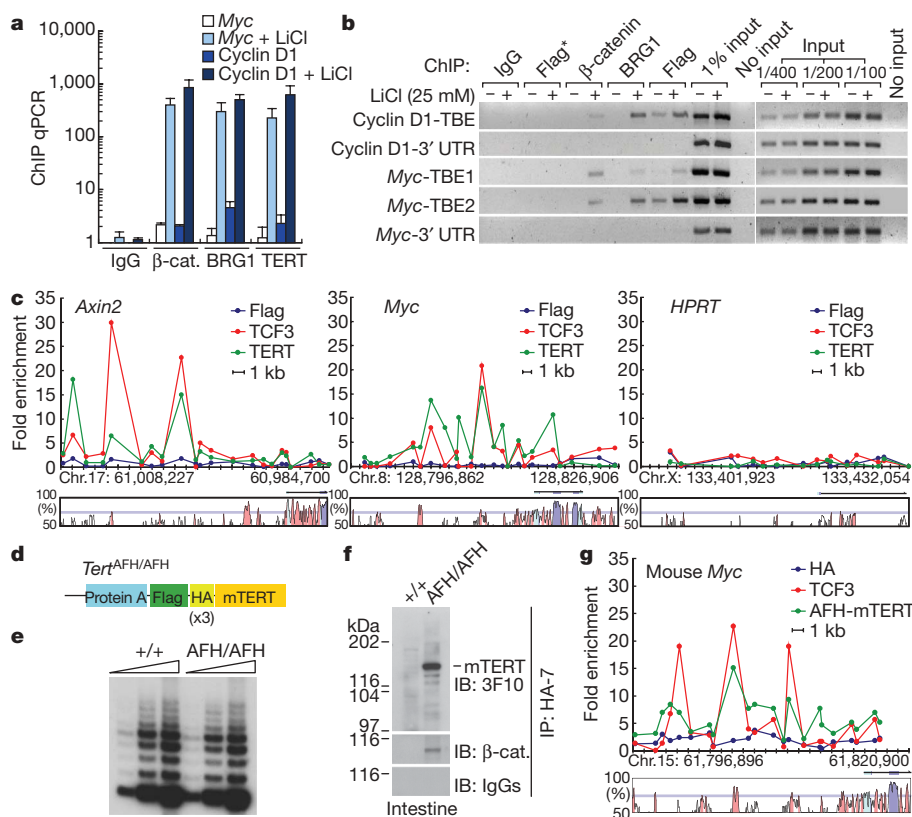


Figure 5 | TERT occupies Wnt target gene promoters in HeLa cells and in mouse small intestine. **a, b**, Association of Flag–TERT, BRG1 or β -catenin with TBE-containing fragments of the cyclin D1 and Myc promoters in Flag–TERT HeLa cells with or without LiCl treatment by ChIP qPCR (**a**) and semi-qPCR (**b**). Error bars indicate s.d. 3' UTR sequences lacking TBEs, negative controls. Flag*, Flag ChIP from HeLa parental cells. **c**, Scanning ChIP across 20 kb of *Axin2*, *Myc* and *HPRT* promoters in lithium-treated HeLa parental and Flag–TERT HeLa cells by qPCR. Non-coding sequences conserved between human and mouse genomes are shown (VISTA graphs: exon, purple; 5' UTR, blue; conserved non-coding sequence, pink). **d**, AFH–

TERT knock-in mouse allele. **e**, Telomerase activity in small intestine from wild-type and *Tert*^{AFH/AFH} mice (TRAP). **f**, Association of AFH–TERT and β -catenin at the endogenous level in extracts from small intestine of *Tert*^{AFH/AFH} mice. Anti-HA antibody immunoprecipitation, followed by immunoblot with anti-HA antibody or anti- β -catenin antibody. IgGs, negative control for immunoblot. **g**, *In vivo* ChIP from *Tert*^{+/+} and *Tert*^{AFH/AFH} mouse small intestine shows co-occupancy across 20 kb of the Myc promoter for TCF3 (red) and AFH–TERT (green). ChIP from *Tert*^{+/+} mouse with anti-HA-7 antibody, negative control (blue).

strongly inhibit stem-cell self-renewal and impair survival of tissue progenitor cells, resulting in defects in telomerase knockout mouse tissues with high renewal requirements, including blood, gastrointestinal tract and testis^{39,49}. Similarly, mutations in telomerase components underlie the human stem-cell disorder dyskeratosis congenita, which is characterized by defects in blood, lung epithelium and epidermal structures⁵⁰. Thus, it is likely that activation of the Wnt pathway to support progenitor cell proliferation also requires coordinated regulation of telomerase at telomeres to ensure that telomere dysfunction does not undermine the effects of Wnt proteins. This need for coordinated regulation of telomere maintenance and Wnt signalling in progenitor cells may have led to the direct incorporation of telomerase into the Wnt signalling pathway as a cofactor for β -catenin.

The contrast between the modest effects on Wnt signalling seen with germline deletion of *Tert* in mouse and the more severe consequences of inhibiting TERT in ES cells or in *Xenopus* embryos suggests the possibility that TERT function in the Wnt pathway is partially compensated in germline knockout mice. Such developmental compensation may occur through adaptation of the Wnt network and explain the mild phenotypes in mouse knockouts of other Wnt regulators, such as *Axin2*, *Nkd1*, *Nkd2*, *Pygo1* and *Pygo2*. Our findings provide a mechanism to understand previous observations showing that TERT overexpression activates epidermal stem cells, as well as previous findings linking TERT to proliferation, survival and stem-cell biology in diverse contexts. Our data reveal an

unanticipated level of convergence between the telomerase and Wnt/ β -catenin signalling pathways with important implications for understanding development, stem-cell regulation and cancer.

METHODS SUMMARY

ES cell targeting strategy and generation of knock-in mice. In-frame epitope tags at the initiating methionine were introduced in the *Tert* gene by homologous recombination in ES cells. For *Tert*^{HA/+} ES cells, a triple HA epitope tag was cloned into a TERT genomic plasmid isolated from a BAC, and the plasmid was transfected into ES cells expressing CreER from the endogenous ROSA26 promoter. The positive selection cassette was flanked by *loxP* sites and deleted by treatment with 4-OHT in culture. *Tert*^{AFH/+} ES cells were generated similarly to introduce a compound epitope tag comprising a Staph protein A sequence, a Flag epitope and a triple HA epitope in-frame with the initiating methionine. Correctly targeted ES cells were identified by Southern blot using both 5' and 3' probes. *Tert*^{AFH/+} germline mice were generated by blastocyst injection. All mice were treated in accordance with AAALAC approved guidelines at Stanford University.

Wnt/ β -catenin reporter assays. pMegaTOP-FLASH (14 wild-type TCF binding elements: CTTTGAT) or pMegaFOP-FLASH (8 mutant TCF binding elements: CAAAGGG) reporter plasmids were co-transfected with pRL-SV40 plasmid (an internal control) into HeLa S3 cells and luciferase activities were measured.

Detection of endogenous TERT protein. Mouse ES cells (*Tert*^{HA/HA}) or homozygous small intestine (*Tert*^{AFH/AFH}) were lysed with NP-40 lysis buffer (0.5% NP-40, 1.5 mM MgCl₂, 25 mM HEPES, 150 mM KCl, 10% glycerol) for 15 min followed by centrifugation (13,200 r.p.m., 10 min). Whole-cell lysates were immunoprecipitated with anti-HA (HA-7, Sigma) antibody and immunoblotted with anti-HA (3F10, Roche) antibody.

Full Methods and any associated references are available in the online version of the paper at www.nature.com/nature.

Received 28 January; accepted 13 May 2009.

- Reya, T. & Clevers, H. Wnt signalling in stem cells and cancer. *Nature* **434**, 843–850 (2005).
- Gat, U., DasGupta, R., Degenstein, L. & Fuchs, E. De Novo hair follicle morphogenesis and hair tumors in mice expressing a truncated β -catenin in skin. *Cell* **95**, 605–614 (1998).
- Van Mater, D., Kolligs, F. T., Dlugosz, A. A. & Fearon, E. R. Transient activation of β -catenin signaling in cutaneous keratinocytes is sufficient to trigger the active growth phase of the hair cycle in mice. *Genes Dev.* **17**, 1219–1224 (2003).
- Lo Celso, C., Prowse, D. M. & Watt, F. M. Transient activation of β -catenin signalling in adult mouse epidermis is sufficient to induce new hair follicles but continuous activation is required to maintain hair follicle tumours. *Development* **131**, 1787–1799 (2004).
- Sarin, K. Y. et al. Conditional telomerase induction causes proliferation of hair follicle stem cells. *Nature* **436**, 1048–1052 (2005).
- Flores, I., Cayuela, M. L. & Blasco, M. A. Effects of telomerase and telomere length on epidermal stem cell behavior. *Science* **309**, 1253–1256 (2005).
- Polakis, P. The many ways of Wnt in cancer. *Curr. Opin. Genet. Dev.* **17**, 45–51 (2007).
- Maser, R. S. & DePinho, R. A. Connecting chromosomes, crisis, and cancer. *Science* **297**, 565–569 (2002).
- Smogorzewska, A. & de Lange, T. Regulation of telomerase by telomeric proteins. *Annu. Rev. Biochem.* **73**, 177–208 (2004).
- Choi, J. et al. TERT promotes epithelial proliferation through transcriptional control of a Myc- and Wnt-related developmental program. *PLoS Genet.* **4**, e10 (2008).
- Artandi, S. E. et al. Constitutive telomerase expression promotes mammary carcinomas in aging mice. *Proc. Natl Acad. Sci. USA* **99**, 8191–8196 (2002).
- Gonzalez-Suarez, E. et al. Increased epidermal tumors and increased skin wound healing in transgenic mice overexpressing the catalytic subunit of telomerase, mTERT, in basal keratinocytes. *EMBO J.* **20**, 2619–2630 (2001).
- Stewart, S. A. et al. Telomerase contributes to tumorigenesis by a telomere length-independent mechanism. *Proc. Natl Acad. Sci. USA* **99**, 12606–12611 (2002).
- Smith, L. L., Collier, H. A. & Roberts, J. M. Telomerase modulates expression of growth-controlling genes and enhances cell proliferation. *Nature Cell Biol.* **5**, 474–479 (2003).
- Armstrong, L. et al. Overexpression of telomerase confers growth advantage, stress resistance, and enhanced differentiation of ESCs toward the hematopoietic lineage. *Stem Cells* **23**, 516–529 (2005).
- Imamura, S. et al. A non-canonical function of zebrafish telomerase reverse transcriptase is required for developmental hematopoiesis. *PLoS ONE* **3**, e3364 (2008).
- Yang, C. et al. A key role for telomerase reverse transcriptase unit in modulating human embryonic stem cell proliferation, cell cycle dynamics, and *in vitro* differentiation. *Stem Cells* **26**, 850–863 (2008).
- Lee, J. et al. TERT promotes cellular and organismal survival independently of telomerase activity. *Oncogene* **27**, 3754–3760 (2008).
- Masutomi, K. et al. The telomerase reverse transcriptase regulates chromatin state and DNA damage responses. *Proc. Natl Acad. Sci. USA* **102**, 8222–8227 (2005).
- Venteicher, A. S., Meng, Z., Mason, P. J., Veenstra, T. D. & Artandi, S. E. Identification of ATPases pontin and reptin as telomerase components essential for holoenzyme assembly. *Cell* **132**, 945–957 (2008).
- Wu, J. I., Lessard, J. & Crabtree, G. R. Understanding the words of chromatin regulation. *Cell* **136**, 200–206 (2009).
- Wu, Y. L. et al. Immunodetection of human telomerase reverse-transcriptase (hTERT) re-appraised: nucleolin and telomerase cross paths. *J. Cell Sci.* **119**, 2797–2806 (2006).
- Barker, N. et al. The chromatin remodelling factor Brg-1 interacts with β -catenin to promote target gene activation. *EMBO J.* **20**, 4935–4943 (2001).
- Major, M. B. et al. New regulators of Wnt/ β -catenin signaling revealed by integrative molecular screening. *Sci Signal* **1**, ra12 (2008).
- Henriksson, M. & Luscher, B. Proteins of the Myc network: essential regulators of cell growth and differentiation. *Adv. Cancer Res.* **68**, 109–182 (1996).
- Korinek, V. et al. Depletion of epithelial stem-cell compartments in the small intestine of mice lacking Tcf-4. *Nature Genet.* **19**, 379–383 (1998).
- Lustig, B. et al. Negative feedback loop of Wnt signaling through upregulation of conductin/axin2 in colorectal and liver tumors. *Mol. Cell Biol.* **22**, 1184–1193 (2002).
- Ventura, A. et al. Restoration of p53 function leads to tumour regression *in vivo*. *Nature* **445**, 661–665 (2007).
- McMahon, A. P. & Moon, R. T. Ectopic expression of the proto-oncogene int-1 in *Xenopus* embryos leads to duplication of the embryonic axis. *Cell* **58**, 1075–1084 (1989).
- Huelsken, J. et al. Requirement for β -catenin in anterior-posterior axis formation in mice. *J. Cell Biol.* **148**, 567–578 (2000).
- Heasman, J. et al. Overexpression of cadherins and underexpression of β -catenin inhibit dorsal mesoderm induction in early *Xenopus* embryos. *Cell* **79**, 791–803 (1994).
- Kao, K. R. & Elinson, R. P. The entire mesodermal mantle behaves as Spemann's organizer in dorsoanterior enhanced *Xenopus laevis* embryos. *Dev. Biol.* **127**, 64–77 (1988).
- Yoshikawa, Y., Fujimori, T., McMahon, A. P. & Takada, S. Evidence that absence of Wnt-3a signaling promotes neuralization instead of paraxial mesoderm development in the mouse. *Dev. Biol.* **183**, 234–242 (1997).
- Dubrulle, J. & Pourquie, O. Coupling segmentation to axis formation. *Development* **131**, 5783–5793 (2004).
- Greco, T. L. et al. Analysis of the vestigial tail mutation demonstrates that Wnt-3a gene dosage regulates mouse axial development. *Genes Dev.* **10**, 313–324 (1996).
- Ikeya, M. & Takada, S. Wnt-3a is required for somite specification along the anteroposterior axis of the mouse embryo and for regulation of cdx-1 expression. *Mech. Dev.* **103**, 27–33 (2001).
- Pownall, M. E., Tucker, A. S., Slack, J. M. & Isaacs, H. V. eGFP, Xcad3 and Hox genes form a molecular pathway that establishes the anteroposterior axis in *Xenopus*. *Development* **122**, 3881–3892 (1996).
- Houle, M., Prinos, P., Iulianella, A., Bouchard, N. & Lohnes, D. Retinoic acid regulation of Cdx1: an indirect mechanism for retinoids and vertebral specification. *Mol. Cell Biol.* **20**, 6579–6586 (2000).
- Lee, H.-W. et al. Essential role of mouse telomerase in highly proliferative organs. *Nature* **392**, 569–574 (1998).
- Erdmann, N., Liu, Y. & Harrington, L. Distinct dosage requirements for the maintenance of long and short telomeres in mTert heterozygous mice. *Proc. Natl Acad. Sci. USA* **101**, 6080–6085 (2004).
- Lohnes, D. The Cdx1 homeodomain protein: an integrator of posterior signaling in the mouse. *Bioessays* **25**, 971–980 (2003).
- Farazi, P. A., Glickman, J., Horner, J. & Depinho, R. A. Cooperative interactions of p53 mutation, telomere dysfunction, and chronic liver damage in hepatocellular carcinoma progression. *Cancer Res.* **66**, 4766–4773 (2006).
- Rajaraman, S. et al. Telomere uncapping in progenitor cells with critical telomere shortening is coupled to S-phase progression *in vivo*. *Proc. Natl Acad. Sci. USA* **104**, 17747–17752 (2007).
- Willert, K. & Jones, K. A. Wnt signaling: is the party in the nucleus? *Genes Dev.* **20**, 1394–1404 (2006).
- Daniels, D. L. & Weis, W. I. β -catenin directly displaces Groucho/TLE repressors from Tcf/Lef in Wnt-mediated transcription activation. *Nature Struct. Mol. Biol.* **12**, 364–371 (2005).
- Firestein, R. et al. CDK8 is a colorectal cancer oncogene that regulates β -catenin activity. *Nature* **455**, 547–551 (2008).
- Carrera, I., Janody, F., Leeds, N., Duvieu, F. & Treisman, J. E. Pygopus activates Wingless target gene transcription through the mediator complex subunits Med12 and Med13. *Proc. Natl Acad. Sci. USA* **105**, 6644–6649 (2008).
- Kim, S., Xu, X., Hecht, A. & Boyer, T. G. Mediator is a transducer of Wnt/ β -catenin signaling. *J. Biol. Chem.* **281**, 14066–14075 (2006).
- Wong, K.-K. et al. Telomere dysfunction impairs DNA repair and enhances sensitivity to ionizing radiation. *Nature Genet.* **26**, 85–88 (2000).
- Armanios, M. Syndromes of telomere shortening. *Annu. Rev. Genomics Hum. Genet.* doi:10.1146/annurev-genom-082908-150046 (2009).

Supplementary Information is linked to the online version of the paper at www.nature.com/nature.

Acknowledgements We thank P. Chu of the Stanford Comparative Medicine Histology Research Core Laboratory for technical assistance. We thank F. Ishikawa for *Xenopus* TERT plasmid, G. Crabtree for antibodies and plasmids, T. Jacks for ROSA^{CreER} mice, and K. Park for constructive comments. J.-I.P. was supported by a Stanford Comprehensive Cancer Center Fellowship. This work was supported by NCI grants CA111691 and CA125453 and by a grant from the California Breast Cancer Research Program to S.E.A.

Author Contributions J.-I.P., A.S.V., J.Y.H., J.C., M.S., T.D.V., R.N., P.D.M. and S.E.A. designed the experiments and analysed data; J.-I.P., A.S.V., J.Y.H., J.C., S.J., M.S., W.C., Z.M., P.C., H.J. and M.M. performed the experiments; and J.-I.P. and S.E.A. wrote the manuscript.

Author Information Reprints and permissions information is available at www.nature.com/reprints. Correspondence and requests for materials should be addressed to S.E.A. (sartandi@stanford.edu).

METHODS

TERT protein complex purification and mass spectrometry. Lysates from HeLa S3 cells expressing AH3-TERT were used for protein purification and mass spectrometry as described previously²⁰. In brief, TERT was fused at its amino terminus to a Staph protein A domain and an HA-epitope tag (AH3), separated by a TEV protease cleavage site. Telomerase complexes from HeLa AH3-TERT extracts were purified on IgG-agarose, released by TEV protease, and captured again on anti-HA antibody resin. After final elution, TERT complexes were fractionated by SDS-PAGE and TERT-associated proteins were excised from the gel and analysed by LC MS/MS.

X-gal staining. *Axin2^{lacZ/+}* reporter mice were intercrossed with actin-rtTA⁺ tetop-TERT^{ci} double transgenic mice (i-TERT^{ci}) and TERT was induced by administration of doxycycline (2 mg ml⁻¹, 5% sucrose) in drinking water beginning at age 21 days. After 14 days of doxycycline treatment, tissues were processed for X-gal staining. Tissues were fixed with 4% paraformaldehyde for 1 h at 4 °C, rinsed in PBS, washed 5 times for 30 min in wash buffer (2 mM MgCl₂, 0.01% deoxycholate, 0.02% NP-40 in PBS), then stained with X-gal solution (4 mM K₃Fe(CN)₆, 4 mM K₄Fe(CN)₆, 20 mM Tris pH 7.4, 1 mg ml⁻¹ X-gal in wash buffer) overnight at room temperature. The stained samples were washed, post-fixed and analysed.

Immunoprecipitation and immunoblot. The following antibodies were used: anti-Flag (M2, Sigma), BRG1 (H-88, SantaCruz and J1 from G. Crabtree), β -catenin (Transduction) and tubulin (Sigma). For immunoblotting, whole-cell lysates were prepared using NP-40 lysis buffer (0.5% NP-40, 1.5 mM MgCl₂, 25 mM HEPES, 150 mM KCl, 10% glycerol, 1 mM PMSF, 1 mM Na₃VO₄, 1 mM NaF and 1 μ g ml⁻¹ each of aprotinin, leupeptin and pepstatin) for 15 min at 4 °C, followed by centrifugation (13,200 r.p.m., 10 min). Supernatant fractions were denatured with 5 \times SDS sample buffer (200 mM Tris-Cl, pH 6.8, 40% glycerol, 8% SDS, 200 mM DTT, 0.08% bromophenol blue) at 95 °C for 5 min, fractionated by SDS-PAGE and transferred onto nitrocellulose membrane. For immunoblot blocking and antibody incubation, 1% non-fat dry milk in TBST (25 mM Tris-HCl, pH 8.0, 125 mM NaCl, 0.5% Tween-20) was used. SuperSignal WestPico (Pierce Biotechnology) reagents were used to detect HRP (horseradish peroxidase)-conjugated secondary antibodies. For immunoprecipitation, the cells on 10-cm plates were lysed with 1 ml NP-40 lysis buffer for 15 min at 4 °C, followed by spinning at 13,200 r.p.m. for 10 min. 100 μ l extract (10% of input) was saved for later immunoblotting. The cell lysates were pre-cleared with either mouse or rabbit IgG (SantaCruz) for 30 min and 30 μ l of protein A/G agarose PLUS (SantaCruz) beads for an additional 30 min. After spinning down (2,000 r.p.m., 2 min), the supernatant was transferred into fresh tubes and incubated with antibodies at 4 °C overnight. Subsequently, 20 μ l of protein A/G agarose PLUS was added and incubated for 1 h. Immunoprecipitates were washed with NP-40 lysis buffer and PBS, then eluted by boiling in loading buffer and analysed by immunoblotting. For quantification of immunoblots, ImageJ (NIH) was used.

Xenopus embryo culture, microinjections and duplicate axis formation assay.

Fertilization, embryo culture and microinjections were performed in accordance with standard methods. Embryos were microinjected with 5'-capped mRNAs synthesized *in vitro* (mMessage mMachine, Ambion), or with morpholinos (Gene Tools, TMO1, 5'-CATAGTGAGCACAATGGCAAAGTCC-3'; TMO2, 5'-TGGCTCCTCCTGTACGCAAAGGCAT-3' and Std-MO). For duplicate axis formation assays, mRNAs were injected into ventral vegetal region of blastomere at the four-cell stage and ectopic axis formation was visually scored at embryonic stages 17 (late neurulation) through to 32 (tadpole). Partial axis duplication was scored based on incomplete formation of a duplicate head structure including eyes and cement gland pigmentation from the additional axis, whereas complete axis duplication required a complete head from the duplicated axis. *Xenopus* β -catenin mRNA was titrated to yield approximately 20% axis duplication and co-injected with increasing amounts of *Xenopus Tert* mRNA. For loss-of-function studies, morpholinos (40 ng) were injected at the one-cell stage. Average DAI (dorso-anterior index) score was calculated from more than 50 embryos of each condition. For rescue experiments, each mRNA (50 pg) was co-injected with TMO1 at the one-cell stage. Somites were analysed by 12/101 antibody staining of embryos fixed in MEMFA (0.1M MOPS (pH 7.4), 2 mM EGTA, 1 mM MgSO₄ and 4% formaldehyde).

MicroCT and skeleton staining. ImTek microCT images (ImTek microCT scanner) were analysed by Microview 2.2 software (GE healthcare). Alcian blue/alizarin red staining was performed as previously described³⁶.

Chromatin immunoprecipitation assays. ChIP assays were performed using Flag (M2, Sigma), β -catenin (Transduction), BRG1 (H-88, SantaCruz), TCF3 (M-20, SantaCruz) and HA (3F10, Roche) antibodies. HeLa cells were treated with 25 mM LiCl for 4 h before ChIP. For *in vivo* ChIP assays, mouse small intestine was dissected, opened longitudinally, washed twice in cold PBS and immediately cross-linked with 1% formaldehyde for 30 min at room temperature. Formaldehyde was quenched by adding glycine (final 0.125 M concentration). Tissues were homogenized (maximum speed, 30 s), and processed in ChIP-RIPA buffer (50 mM Tris pH 8.0, 150 mM NaCl, 0.1% SDS, 0.5% deoxycholate, 1% NP40, 1 mM EDTA) containing proteinase inhibitors and further incubated on ice for 15 min. Tissue lysates were sonicated (70% output, 10 times, 30 s) with glass beads (Sigma) and centrifuged (13,200 r.p.m., 30 min). Supernatants were removed, diluted with ChIP-RIPA lysis buffer and pre-cleared with protein A/G agarose PLUS (SantaCruz) overnight at 4 °C. Supernatant from pre-cleared lysates was immunoprecipitated with antibodies overnight at 4 °C and pulled down using protein A/G agarose PLUS by centrifugation (3,400 r.p.m., 2 min). Immunoprecipitates were further washed serially with ChIP-RIPA, high salt (50 mM Tris pH 8.0, 500 mM NaCl, 0.1% SDS, 0.5% deoxycholate, 1% NP40, 1 mM EDTA), LiCl wash buffer (50 mM Tris pH 8.0, 1 mM EDTA, 250 mM LiCl, 1% NP40, 0.5% deoxycholate) and TE buffer. Finally, immunoprecipitates cross-linked were reversed by incubation at 65 °C overnight and treated with RNaseA and proteinase K to extract DNA. The isolated DNAs were analysed by real-time PCR.

An intermediate-mass black hole of over 500 solar masses in the galaxy ESO 243-49

Sean A. Farrell^{1,2,†}, Natalie A. Webb^{1,2}, Didier Barret^{1,2}, Olivier Godet³ & Joana M. Rodrigues^{1,2}

Ultraluminous X-ray sources are extragalactic objects located outside the nucleus of the host galaxy with bolometric luminosities¹ exceeding $10^{39} \text{ erg s}^{-1}$. These extreme luminosities—if the emission is isotropic and below the theoretical (Eddington) limit, where the radiation pressure is balanced by the gravitational pressure—imply the presence of an accreting black hole with a mass of $\sim 10^2$ – 10^5 solar masses (M_\odot). The existence of such intermediate-mass black holes is in dispute, and though many candidates have been proposed, none are widely accepted as definitive. Here we report the detection of a variable X-ray source with a maximum 0.2–10 keV luminosity of up to $1.1 \times 10^{42} \text{ erg s}^{-1}$ in the edge-on spiral galaxy ESO 243-49, with an implied conservative lower limit for the mass of the black hole of $\sim 500 M_\odot$.

Apart from the super-Eddington luminosities of ultraluminous X-ray sources, other circumstantial evidence exists for intermediate-mass black holes. Low-temperature disk blackbody spectral components and quasi-periodic oscillations believed to originate at the inner regions of the accretion disk are seen in some ultraluminous X-ray sources implying black-hole masses above the stellar range^{2,3}. However, neither can be conclusively linked to the innermost disk radius, precluding a definitive mass estimate. In the globular cluster ω Cen the presence of an intermediate-mass black hole was inferred from the rise in the velocity dispersion profile towards the cluster centre, although a concentration of stellar remnants or a radially biased orbital structure are also valid explanations⁴. Modelling showed that the cluster dynamics and the current mass are consistent with an accreted stripped dwarf galaxy nucleus⁵ with a mass of $\sim 10^7 M_\odot$. The blackbody X-ray spectrum and bolometric luminosity of $\sim 10^{39} \text{ erg s}^{-1}$ of the ultraluminous super-soft X-ray source in M81 may imply the presence of an intermediate-mass black hole⁶, but the source properties are also consistent with a massive white dwarf accreting at a high rate. The luminosity can alternatively be explained through mild super-Eddington accretion and/or beaming⁷. In addition, the black-hole mass was derived by estimating the shape of the X-ray spectrum from widely spaced optical observations. This assumes a smooth continuation between the optical and X-ray spectra, and that the spectra were stable over the approximately six-year time span of the observations. The latter assumption is inconsistent with observational data, because black holes of all sizes demonstrate significant spectral variability over a wide range of timescales⁸.

While investigating the 2XMM Serendipitous Source catalogue⁹, we identified 2XMM J011028.1–460421 (HLX-1 for simplicity) at right ascension 01 h 10 min 28.2 s, declination $-46^\circ 04' 22.2''$ (J2000) with a 3σ positional uncertainty of $0.83''$, observed on 23 November 2004 as part of Obs-Id 0204540201. The position of HLX-1 is coincident with the absorption-line galaxy ESO 243-49, at a redshift¹⁰ of $z = 0.0224 \pm 0.0001$, $8''$ from the nucleus, yet within the confines of the galaxy (Fig. 1). The position and error in each observation were

derived in accordance with the methods used for the creation of the 2XMM catalogue⁹, with the final position and error determined by taking the weighted mean of the two positions. No indication for disruption of the galactic disk, as would be expected following a galaxy merger, is visible. Unlike ω Cen, HLX-1 is not likely to represent the stripped nucleus of an accreted dwarf galaxy. The XMM-Newton European Photon Imaging Camera spectra (Fig. 2) of HLX-1 are best-fitted by an absorbed power-law model, with parameters consistent with other ultraluminous X-ray sources¹ (Table 1).

The derived luminosity (assuming the ESO 243-49 distance) is ~ 400 times larger than the Eddington value for a $20 M_\odot$ black hole, and almost an order of magnitude greater than that of the previously reported most-luminous ultraluminous X-ray source¹¹ (0.2–10 keV unabsorbed X-ray luminosity $< 2 \times 10^{41} \text{ erg s}^{-1}$). A deeper follow-up observation performed with XMM-Newton on 28 November 2008 (Obs-Id: 0560180901) showed a change in the luminosity and the spectral shape (Fig. 2). Fourier power spectra were computed using the pn camera light curves for this observation (6 ms resolution) to test for high-frequency quasi-periodic oscillations. No significant modulation was found at frequencies less than 83 Hz. Fitting of the spectrum required the addition of a soft disk blackbody component ($\Delta\chi^2 = 155$ for 2 fewer degrees of freedom, Table 1), consistent with other ultraluminous X-ray sources. Adding this component to the fit of observation 1 did not improve the χ^2 significantly ($\Delta\chi^2 = 2.1$ for 2 fewer degrees of freedom).

Using the posterior predictive p -values method¹², we simulated 5,000 data sets with exposure times, background and energy response

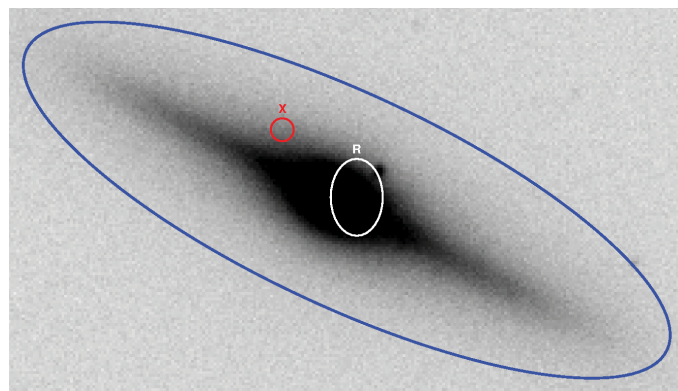


Figure 1 | R-band optical image of ESO 243-49 obtained with the Very Large Telescope. The centre of the red circle (X) indicates the position of HLX-1, with the radius representing a 3σ positional uncertainty of $0.83''$. The centre of the white ellipse (R) indicates the position of the radio detection from the Phoenix Deep Survey¹⁰, with the radii representing the 3σ uncertainty. The blue ellipse indicates the elliptical confines of the galaxy.

¹Université de Toulouse, UPS, CESR, 9 Avenue du Colonel Roche, F-31028 Toulouse Cedex 9, France. ²CNRS, UMR5187, F-31028 Toulouse, France. ³Department of Physics and Astronomy, University of Leicester, University Road, Leicester, LE1 7RH, UK. [†]Present address: Department of Physics and Astronomy, University of Leicester, University Road, Leicester, LE1 7RH, UK.

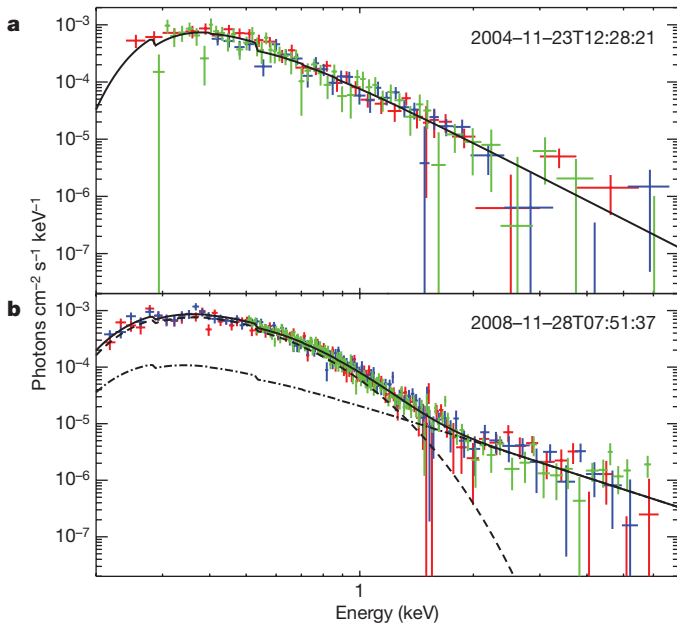


Figure 2 | European Photon Imaging Camera X-ray spectra of HLX-1. **a**, The unfolded pn (green), MOS1 (red) and MOS2 (blue) spectra of the first observation fitted with the best-fit absorbed power-law model (solid black line). **b**, The unfolded spectra of the second observation, fitted with the best-fit absorbed power law (black dot-dashed line) plus disk blackbody (dashed line) model. The error bars indicate the 68% confidence limits.

identical to the first observation using the best-fit spectral parameters of the second observation, and fitted them with an absorbed power law. In less than 1% of the cases the power-law fit is acceptable and the fitted parameters are consistent with the values reported in Table 1 for the first observation (within the 90% confidence errors). Further, using the same method and an additional 5,000 simulations, we evaluated the significance of the disk blackbody component in the first observation to be $\sim 70\%$, which is insufficient to claim it is real. These simulations demonstrate unambiguously that HLX-1 has varied between the two observations.

The case for the hyperluminous nature of HLX-1 depends on its association with ESO 243-49. The probability that any of the real 2XMM sources surrounding ESO 243-49 could be randomly aligned with any of the background galaxies in the field, calculated by 1,000,000 Monte Carlo simulations, is $\sim 9\%$. However, by taking into account the X-ray spectral shape we can confidently rule out a foreground source. The X-ray spectrum allows us to exclude coronal emission from a star, which is typically fitted by multi-temperature thermal models¹³. Non-thermal emission has been detected from supernovae and from shock-boundaries in shell-type supernova remnants¹⁴ with X-ray luminosities of 10^{37} – 10^{41} erg s⁻¹. However, the non-thermal flux decays rapidly after the supernova explosion¹⁴, with thermal emission dominating after ~ 100 days.

A Galactic white dwarf accreting from a low-mass companion could be visible in X-rays but not show up in our optical image.

The spectra of these objects are consistent with emission from a thermal plasma with temperatures of over 2 keV and non-zero elemental abundances^{15,16}. The spectra from both observations are inconsistent with this model. A quiescent neutron star low-mass X-ray binary is also inconsistent with our data, because its spectrum should be thermal (representing emission from the neutron-star atmosphere) possibly with the addition of a flat power-law component¹⁷. The steep power-law spectrum of HLX-1 during observation 1 is not consistent with a neutron star in either the high or low states, and instead indicates the presence of an accreting black hole in the high/soft state¹⁸. The derived luminosity for HLX-1 at 10 kpc is only $\sim 10^{34}$ erg s⁻¹, too low for a Galactic black-hole binary undergoing near-Eddington accretion. Therefore HLX-1 cannot be a foreground Galactic object.

Some blazars (a subclass of radio-loud active galactic nuclei with the jet pointing close to our line of sight) have steep power-law spectra¹⁹. However, even the faintest blazars have flux densities over 2 mJy at 1.4 GHz (ref. 20). Previous radio observations¹⁰ detected a source consistent with the core of ESO 243-49 with a 1.4 GHz flux density of 0.16 ± 0.03 mJy, inconsistent with the position of HLX-1 (Fig. 1). The relatively low intrinsic absorption also rules out the possibility that we are observing a blazar through the disk of ESO 243-49, yet is consistent with a number of other ultraluminous X-ray sources²¹. The association of HLX-1 with ESO 243-49 is thus almost certain, and so our derived luminosity is valid.

The observed variability between observations indicates that HLX-1 cannot be a superposition of multiple lower-luminosity sources. The maximum luminosity derived from the first observation therefore implies a mass lower limit of $\sim 5,400 M_{\odot}$, assuming Eddington accretion and isotropic emission. Relativistic jets have been observed in a number of Galactic black-hole X-ray binaries during the low/hard state⁸, where the accretion rate and luminosity decrease and the spectrum flattens. If the source is viewed at angles close to the jet axis, relativistic boosting could amplify the flux so that the luminosity appears to exceed the Eddington value. Modelling of stellar-mass black-hole binaries has shown that relativistic boosting could produce apparent luminosities of five times the Eddington limit²², implying a black-hole mass exceeding $1,000 M_{\odot}$ for HLX-1. However, relativistic boosting is unlikely because a flat spectrum—as opposed to the steep spectrum we observe in the first observation—is predicted²², and still requires an intermediate-mass black hole for luminosities exceeding 10^{41} erg s⁻¹.

Geometric beaming, whereby a thick accretion disk collimates the X-ray emission, coupled with super-Eddington accretion, can explain apparent luminosities up to $\sim 10^{40}$ erg s⁻¹, with higher luminosities for hydrogen-poor accretion⁷. A $20 M_{\odot}$ black hole with an apparent luminosity of 10^{42} erg s⁻¹ implies a low beaming factor of 0.01, with a mass accretion rate of ~ 2.6 times the Eddington value for hydrogen-poor accretion⁷. However, the derived luminosity is high enough above the Eddington limit that matter would be easily accelerated to Lorentz factors of ~ 5 – 10 , leading to relativistic jets and flat spectra²³. The combination of the derived luminosity and steep spectrum of HLX-1 in the first observation thus rules out relativistic and geometric beaming.

Table 1 | X-ray spectral parameters of HLX-1

Parameter	Observation 1	Observation 2	Unit
Total neutral hydrogen column density	$0.08^{+0.03}_{-0.03}$	$0.04^{+0.01}_{-0.01}$	10^{22} atoms cm ⁻²
Neutral hydrogen column density intrinsic to the source*	$0.06^{+0.03}_{-0.03}$	$0.02^{+0.01}_{-0.01}$	10^{22} atoms cm ⁻²
Temperature at inner disk radius	...	$0.18^{+0.01}_{-0.01}$	keV
Normalization of disk blackbody component	...	29^{+6}_{-5}	
Power-law photon index	$3.4^{+0.3}_{-0.3}$	$2.2^{+0.4}_{-0.3}$	
Normalization of power-law component	9^{+1}_{-1}	$2.2^{+0.8}_{-0.6}$	10^{-5} photons cm ⁻² s ⁻¹ keV ⁻¹
χ^2 statistic (and associated degrees of freedom for the spectral fitting)	113.4 (108)	333.9 (329)	
Unabsorbed X-ray luminosity in the 0.2–10 keV band	$11^{+0.1}_{-4.0}$	$6.4^{+0.6}_{-0.6}$	10^{41} erg s ⁻¹

* After taking into account the Galactic absorption²⁵ of 0.0179×10^{22} atoms cm⁻².

Accreting stellar-mass black holes may exceed the Eddington luminosity by up to a factor of ten²⁴, implying an Eddington luminosity of $\sim 10^{41} \text{ erg s}^{-1}$ (0.2–10 keV), and a lower mass limit of $\sim 500 M_{\odot}$ for HLX-1. This limit is derived assuming a bolometric luminosity, whereas our derived luminosity is in the 0.2–10 keV band. The bolometric luminosity is likely to exceed our value, so our mass lower limit is a conservative estimate. HLX-1 therefore presents the strongest case thus far for the existence of intermediate-mass black holes.

Received 25 August 2008; accepted 20 April 2009.

- Roberts, T. P. X-ray observations of ultraluminous X-ray sources. *Astrophys. Space Sci.* **311**, 203–212 (2007).
- Miller, J. M., Fabbiano, G., Miller, M. C. & Fabian, A. C. X-ray spectroscopic evidence for intermediate-mass black holes: cool accretion disks in two ultraluminous X-ray sources. *Astrophys. J.* **585**, L37–L40 (2003).
- Casella, P. et al. Weighing the black holes in ultraluminous X-ray sources through timing. *Mon. Not. R. Astron. Soc.* **387**, 1707–1711 (2008).
- Noyola, E., Gebhardt, K. & Bergmann, M. Gemini and Hubble space telescope evidence for an intermediate-mass black hole in ω Centauri. *Astrophys. J.* **676**, 1008–1015 (2008).
- Bekki, K. & Freeman, K. C. Formation of ω Centauri from an ancient nucleated dwarf galaxy in the young Galactic disc. *Mon. Not. R. Astron. Soc.* **346**, L11–L15 (2003).
- Liu, J. & Di Stefano, R. An ultraluminous supersoft X-ray source in M81: an intermediate-mass black hole? *Astrophys. J.* **674**, L73–L76 (2008).
- King, A. R. Accretion rates and beaming in ultraluminous X-ray sources. *Mon. Not. R. Astron. Soc.* **385**, L113–L115 (2008).
- Fender, R. in *Compact Stellar X-ray Sources* (eds Lewin, W. & van der Klis, M.) 381–419 (Cambridge University Press, 2006).
- Watson, M. G. et al. The XMM-Newton serendipitous survey. VI. The second XMM-Newton serendipitous source catalogue. *Astron. Astrophys.* **493**, 339–373 (2009).
- Afonso, J. et al. The phoenix deep survey: spectroscopic catalog. *Astrophys. J.* **624**, 135–154 (2005).
- Miniutti, G. et al. Have we detected the most luminous ULX so far? *Mon. Not. R. Astron. Soc.* **373**, L1–L5 (2006).
- Hurkett, C. P. et al. Line searches in Swift X-ray spectra. *Astrophys. J.* **679**, 587–606 (2008).
- Güdel, M. X-ray astronomy of stellar coronae. *Astron. Astrophys. Rev.* **12**, 71–237 (2004).
- Immler, S. & Lewin, W. H. G. in *Supernovae and Gamma-Ray Bursters* (ed. Weiller, K.) 91–111 (Springer, 2003).
- Baskill, D. S., Wheatley, P. J. & Osborne, J. P. The complete set of ASCA X-ray observations of non-magnetic cataclysmic variables. *Mon. Not. R. Astron. Soc.* **357**, 626–644 (2005).
- Hilton, E. J. et al. XMM-Newton observations of the cataclysmic variable GW Librae. *Astron. J.* **134**, 1503–1507 (2007).
- Jonker, P. G. Constraining the neutron star equation of state using quiescent low-mass X-ray binaries. *AIP Conf. Proc.* **983**, 519–526 (2008).
- Done, C., Gierliński, M. & Kubota, A. Modelling the behaviour of accretion flows in X-ray binaries. *Astron. Astrophys. Rev.* **15**, 1–66 (2007).
- Giommi, P. et al. in *Blazar Astrophysics with BeppoSAX and Other Observatories* (eds Giommi, P., Massaro, E. & Palumbo, G.) 63–99 (ESA-ESRIN, 2002).
- Turriziani, S., Cavazzuti, E. & Giommi, P. ROXA: a new multi-frequency large sample of blazars selected with SDSS and 2dF optical spectroscopy. *Astron. Astrophys.* **472**, 669–704 (2007).
- Berghea, C. T., Weaver, K. A., Colbert, E. J. M. & Roberts, T. P. Testing the paradigm that ultra-luminous X-ray sources as a class represent accreting intermediate-mass black holes. *Astrophys. J.* **687**, 471–487 (2008).
- Freeland, M., Kuncic, Z., Soria, R. & Bicknell, G. V. Radio and X-ray properties of relativistic beaming models for ultraluminous X-ray sources. *Mon. Not. R. Astron. Soc.* **372**, 630–638 (2006).
- Abramowicz, M. A., Ellis, G. F. R. & Lanza, A. Relativistic effects in superluminal jets and neutron star winds. *Astrophys. J.* **361**, 470–492 (1990).
- Begelman, M. C. Super-Eddington fluxes from thin accretion disks? *Astrophys. J.* **568**, L97–L100 (2002).
- Kalberla, P. M. W. et al. The Leiden/Argentine/Bonn (LAB) survey of Galactic HI. Final data release of the combined LDS and IAR surveys with improved stray-radiation corrections. *Astron. Astrophys.* **440**, 775–782 (2005).

Supplementary Information is linked to the online version of the paper at www.nature.com/nature.

Acknowledgements We thank N. Scharfel for granting an observation under the XMM-Newton project scientist discretionary time programme. We thank R. Belmont, A. King, J.-P. Lasota, K. Mukai, T. Roberts, S. Rosen, S. Sembay and M. Watson for discussions. S.A.F. acknowledges funding from the CNES. S.A.F. and O.G. acknowledge STFC funding. This work made use of the 2XMM Serendipitous Source Catalogue constructed by the XMM-Newton Survey Science Centre on behalf of ESA. We thank the Swift team for performing a TOO observation that provided justification for an additional observation with XMM-Newton. This work was based on observations obtained with XMM-Newton, an ESA science mission with instruments and contributions directly funded by ESA Member States and NASA.

Author Information Reprints and permissions information is available at www.nature.com/reprints. Correspondence and requests for materials should be addressed to S.A.F. (saf28@star.le.ac.uk) or N.A.W. (natalie.webb@cesr.fr).

LETTERS

A single-molecule optical transistor

J. Hwang¹, M. Pototschnig¹, R. Lettow¹, G. Zumofen¹, A. Renn¹, S. Götzinger¹ & V. Sandoghdar¹

The transistor is one of the most influential inventions of modern times and is ubiquitous in present-day technologies. In the continuing development of increasingly powerful computers as well as alternative technologies based on the prospects of quantum information processing, switching and amplification functionalities are being sought in ultrasmall objects, such as nanotubes, molecules or atoms^{1–9}. Among the possible choices of signal carriers, photons are particularly attractive because of their robustness against decoherence, but their control at the nanometre scale poses a significant challenge as conventional nonlinear materials become ineffective. To remedy this shortcoming, resonances in optical emitters can be exploited, and atomic ensembles have been successfully used to mediate weak light beams⁷. However, single-emitter manipulation of photonic signals has remained elusive and has only been studied in high-finesse microcavities^{10–13} or waveguides^{8,14}. Here we demonstrate that a single dye molecule can operate as an optical transistor and coherently attenuate or amplify a tightly focused laser beam, depending on the power of a second ‘gating’ beam that controls the degree of population inversion. Such a quantum optical transistor has also the potential for manipulating non-classical light fields down to the single-photon level. We discuss some of the hurdles along the road towards practical implementations, and their possible solutions.

The central phenomenon behind the operation of a transistor is nonlinearity. A simple two-level atom is known to undergo nonlinear interaction with light¹⁵, but it is usually not considered as a sufficiently strong medium for manipulating laser beams in free space. In a recent theoretical study, however, we showed that in the weak excitation regime, an atom can block a propagating light beam fully if it is in a directional dipolar mode, and by up to 85% if it is a tightly focused plane wave¹⁶. In these cases, photons are confined to an area comparable with the scattering cross-section of the atom, and their electric fields become large enough to achieve atomic excitation with unity or near unity probability. As we shall see below, this strong coupling between an emitter and light also makes it possible to observe stimulated emission from a single molecule, and paves the way for the realization of various nonlinear phenomena at the single-emitter level.

The emitters of choice in our study are dye molecules embedded in organic crystalline matrices. These are highly suitable for quantum optical investigations because under cryogenic conditions, the zero-phonon lines (ZPLs) connecting the vibronic ground states of their electronic ground ($|1\rangle$) and excited ($|2\rangle$) states become lifetime limited¹⁷ (Fig. 1a). If the doping concentration is low enough, single dye molecules can be selectively addressed spectrally¹⁸. The most common way of achieving this is through fluorescence excitation spectroscopy, where the frequency of a narrow-band laser is scanned across the inhomogeneous distribution of the ZPLs¹⁹, and the Stokes-shifted fluorescence to the vibronic excited states ($|4\rangle$) in Fig. 1a) of the electronic ground state is recorded. In addition, it has been demonstrated that single molecules can be detected resonantly by

the interference of a laser beam with its coherent scattering²⁰. Recently, the latter technique was extended to show that a molecule can attenuate a strongly confined laser beam by about 10%, both in the near and far fields^{21,22}. The degree of this attenuation has been found to be smaller than its theoretical limit for a two-level atom¹⁶, mainly because the Stokes-shifted fluorescence acts as a loss channel and reduces the coherent scattering cross-section of the ZPL^{21,22}. Another

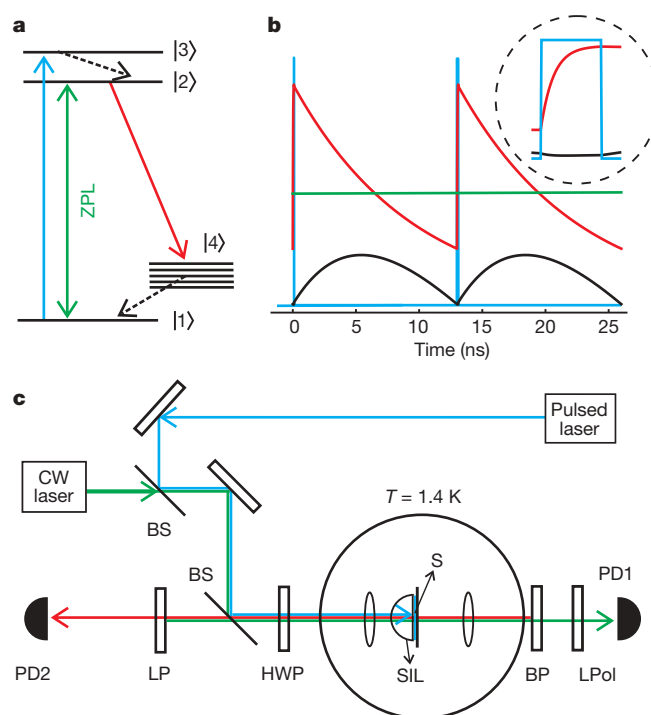


Figure 1 | Diagrams of the experiment. **a**, Energy level scheme of a molecule with ground state ($|1\rangle$), and ground ($|2\rangle$) and first excited ($|3\rangle$) vibrational states of the first electronic excited state. Manifold $|4\rangle$ shows the vibronic levels of the electronic ground state, which decay rapidly to $|1\rangle$. Blue arrow, excitation by the gate beam; green double-headed arrow, coherent interaction of the CW source beam with the zero-phonon line (ZPL); red arrow, Stokes-shifted fluorescence; black dashed arrows, non-radiative internal conversion. **b**, Time-domain description of laser excitations and corresponding response of the molecule simulated by the Bloch equations with periodic boundary conditions. Blue spikes and red curve represent the pump laser pulses and the population of the excited state $|2\rangle$, respectively. Black curve shows the time trajectory of $\text{Im}(\rho_{21})$. Straight green line indicates the constant probe laser intensity that is on at all times. Inset, magnified view of curves during a laser pulse. **c**, Schematic diagram of the optical set-up. BS, beam splitter; LP, long-pass filter; BP, band-pass filter; HWP, half-wave plate; LPol, linear polarizer; S, sample; SIL, solid-immersion lens; PD1, PD2, avalanche photodiodes. Transmission of the probe beam (green) is monitored on PD1, and the Stokes-shifted fluorescence (red) is recorded on PD2.

¹Laboratory of Physical Chemistry and optETH, ETH Zurich, 8093 Zurich, Switzerland.

source of decoherence is the weak coupling of the dye molecule to the host matrix. These two effects can vary in different systems, and amount roughly to a 2–5 times reduction of the scattering cross-section.

The first step in our experiment was to detect single dibenzanthanthrene (DBATT) molecules doped in a *n*-tetradecane matrix. To do this, we used a continuous-wave (CW) ring dye laser (wavelength ~ 590 nm, linewidth ~ 1 MHz) to perform fluorescence excitation and extinction spectroscopy on the $|1\rangle \leftrightarrow |2\rangle$ ZPL transitions. Once a molecule was selected, we used a synchronously pumped pulsed dye laser (wavelength ~ 582 nm, pulse width $t_{\text{pul}} \approx 50$ ps, repetition period $t_{\text{rep}} = 13$ ns) to populate the vibronic excited state of its first electronic excited state ($|3\rangle$ in Fig. 1a). The $|1\rangle \leftrightarrow |3\rangle$ transition has a broad linewidth of about 30 GHz (ref. 23), determined by the fast vibrational relaxation of $|3\rangle$ to $|2\rangle$. State $|2\rangle$, on the other hand, has a relatively long fluorescence lifetime of 9.5 ns (ref. 24) so that population inversion in this state could be achieved right after each pulse. Figure 1b gives a pictorial temporal view of the excitation and emission processes. As we shall see below, the pulsed and the CW laser beams served as the transistor gate and source, respectively. The experimental arrangement of the single-molecule microscope operating at $T = 1.4$ K, as well as the excitation and detection paths, are sketched in Fig. 1c and are described in more detail in ref. 22. Here we emphasize that in order to provide a high coupling efficiency to the molecule, both laser beams were strongly focused to near the diffraction limit.

The data points in Fig. 2a–e display a series of transmission spectra recorded on a weak CW laser beam for various powers of the pulsed laser beam. Figure 2a shows that in the absence of the pump beam, the molecule attenuates the source beam by about 7%. However, as the gate power is raised and the population is transferred from the ground to the excited state, the dip decreases, until the $|1\rangle \rightarrow |2\rangle$ transfer rate equalizes the spontaneous decay rate of $|2\rangle$ and the molecule becomes fully transparent to the probe beam (Fig. 2c). If the pump power is increased even further, population inversion is achieved and we observe amplification of the probe laser beam (Fig. 2d and e). These data demonstrate that a single molecule can indeed act as a transistor, in which the pulsed gate beam regulates the flow of the CW source beam by controlling the populations of the molecular ground and excited states. The data points in Fig. 2f summarize the transistor characteristic curve by plotting the visibility (the ratio of the peak or dip magnitude to the off-resonance signal) for the transmission of the source as a function of the gate power.

The underlying mechanism of light amplification by a population-inverted molecule is analogous to its extinction by a ground-state molecule. The dip in Fig. 2a arises from the destructive interference between the excitation laser beam and the light that is coherently scattered by the molecule^{21,22}, causing the reflection of the incident beam¹⁶. Similarly, amplification by stimulated emission can be understood as a constructive interference of the two fields when the molecule is in the excited state. To elucidate the coherent nature of light amplification experimentally, we allowed a slight polarization ellipticity for the source beam and placed a polarizer to select a projection of the molecular and laser fields with a relative phase of 90° (more details may be found in ref. 22). Figure 3a shows the resulting dispersive transmission spectrum in the absence of pumping. When a strong gate beam was turned on, the spectrum was

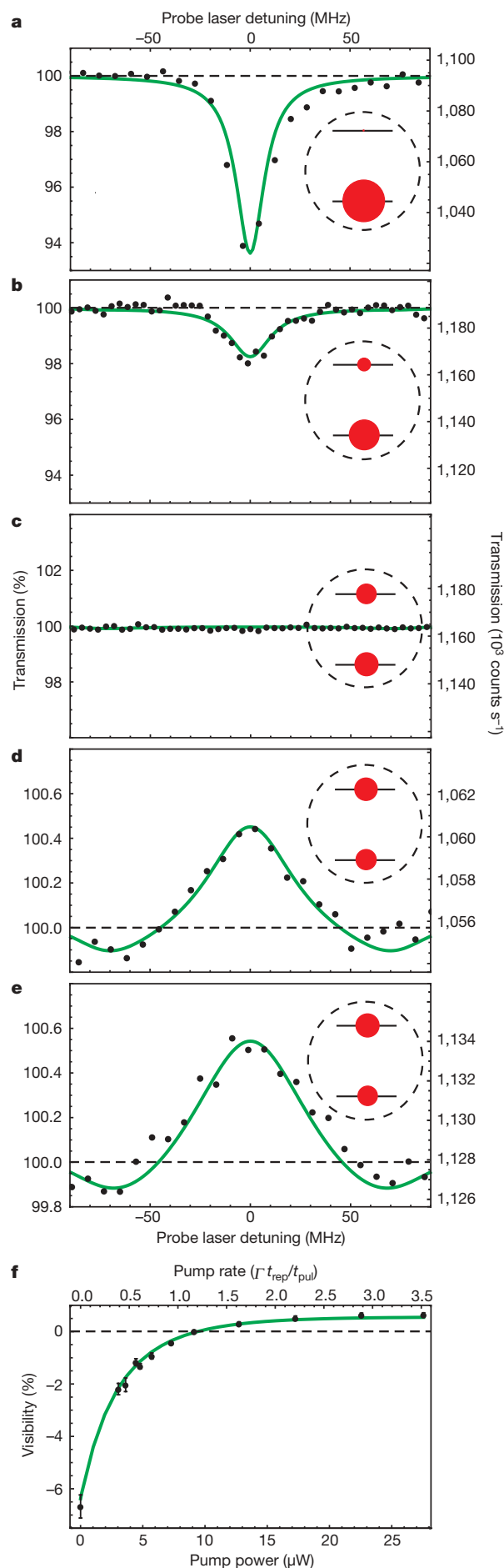


Figure 2 | Attenuation and amplification of a laser beam by a single molecule. **a–e**, Filled circles, transmission of a weak CW laser beam as a function of its frequency detuning with respect to the ZPL of a single dye molecule. Average pump laser powers (μW) were: 0 (**a**), 3.6 (**b**), 9.1 (**c**), 17.3 (**d**) and 27.6 (**e**). Insets indicate the time-averaged populations of states $|1\rangle$ and $|2\rangle$. The radii of the circles are proportional to the populations. **f**, Filled circles, visibility of the transmission spectra with respect to the pump power. Solid curves in all panels are outcomes of calculations (see text for details). Error bars in **f** were determined by propagating errors based on the 95% confidence intervals of the amplitude and background in Lorentzian fits to the experimental spectra.

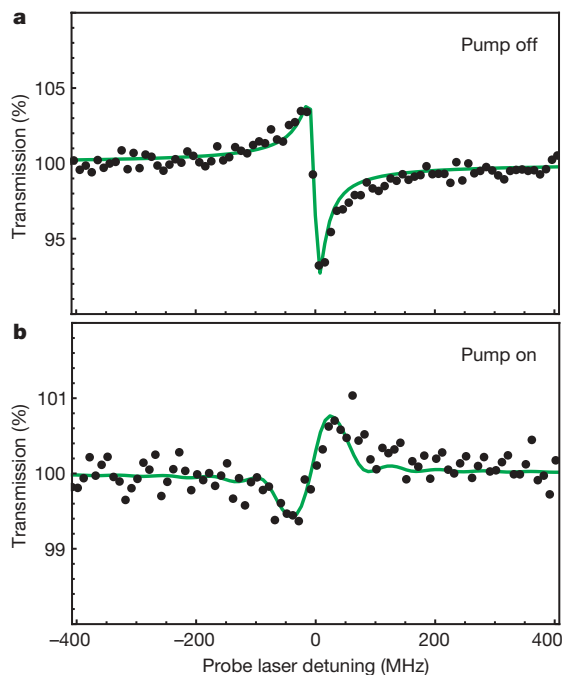


Figure 3 | Coherent scattering phase shift of π on population inversion. **a**, Filled circles, transmission spectrum of the probe beam for a single molecule in the ground state (pump off). By adjusting the polarization state of the incident light and an analyser in detection, the phase between the laser beam and the light scattered by the molecule could be adjusted to obtain a dispersive spectrum. **b**, Same measurement as in **a** but on a population-inverted molecule (pump on) yields a dispersive spectrum with 180° (π) phase shift. Solid curves are outcomes of calculations; see text for details.

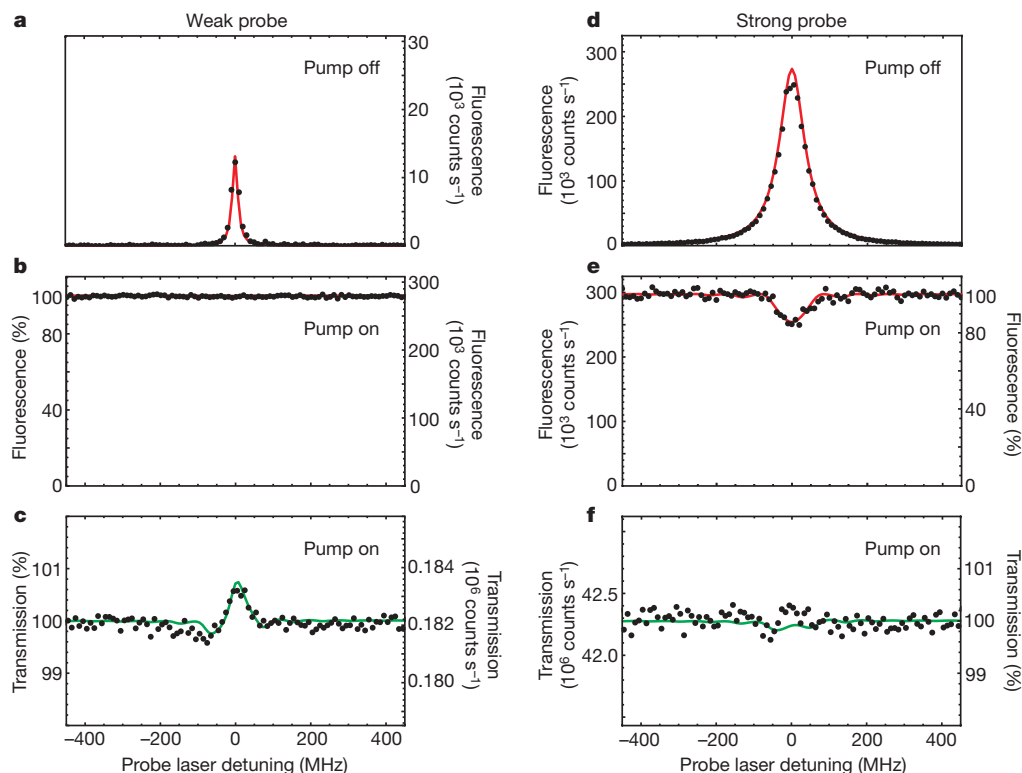


Figure 4 | The nonlinear response of a population-inverted molecule. Filled circles, spectra recorded with the CW laser power corresponding to saturation parameter $S = 0.05$ (left column) and $S = 22.3$ (right column). **a**, **d**, Fluorescence excitation spectra in the absence of pumping. In **a**, a natural linewidth of 17 MHz verifies that the Rabi frequency Ω is much smaller than the spontaneous decay rate Γ . **b**, **e**, Fluorescence of state $|2\rangle$ caused by a strong pump beam as a function of the CW laser frequency. In

modified to that displayed in Fig. 3b, revealing a π phase shift in the light scattered by the excited-state molecule. Hence, the single-emitter transistor has two output channels—one in transmission and one in reflection¹⁶—which are fed depending on whether the emitter is prepared in the excited or ground state, respectively.

Having established the coherent character of the amplification process, it is evident that a single-emitter transistor operates efficiently only in the unsaturated regime^{15,22}. We, thus, elaborate on the performance of this device as a function of the source power. A strong pump beam populates state $|2\rangle$ every 13 ns, comparable with the fluorescence lifetime of 9.5 ns (Fig. 1b). Therefore, if the probe beam power is kept well below the saturation level, the stimulated emission of state $|2\rangle$ is much weaker than its spontaneous emission¹⁵, so that a substantial Stokes-shifted fluorescence is registered on PD2 (see Fig. 1c). Figure 4a–c illustrates that under these conditions, tuning the frequency of the probe laser to the molecular ZPL does not lead to a notable depletion of population in $|2\rangle$, but it does cause a sizable amplification. The situation was very different when the probe beam was strong enough to power broaden the $|1\rangle \leftrightarrow |2\rangle$ transition, as represented by the fluorescence excitation spectrum in Fig. 4d. The data points in Fig. 4e and f show that now, the population of state $|2\rangle$ is clearly depleted by the probe laser, but the amplification of this beam is not significant. In this saturated regime (see equation (2) below), stimulated emission on the ZPL constitutes a very small part of the strong transmitted power and cannot be deciphered on its noisy base line. The depletion of fluorescence from level $|2\rangle$, on the other hand, becomes observable because it is a considerable fraction of the fixed total fluorescence, which is set by the pumping rate. Thus, we point out that although both laser-induced depletion of the excited state population²⁵ and light amplification¹⁵ are associated with stimulated emission, to observe the former it is sufficient to apply a high laser power, while direct detection of the latter has been

e, a strong probe laser depletes the population of $|2\rangle$. **c**, **f**, Transmission spectra recorded simultaneously with the data in **b** and **e**, respectively. A weak probe laser beam is amplified by a population-inverted molecule (**c**) but the effect of the molecule is negligible on a strong probe beam (**f**). All vertical axes present a quantitative account of the experimental detector signals. Solid curves are outcomes of calculations; see text for details.

made possible here only because of a strong coupling between the laser beam and the emitter.

The interaction of a multilevel molecule with classical light can be analysed using the formalism of the optical Bloch equations^{22,24}. Given the fast incoherent decays of $|3\rangle \rightarrow |2\rangle$ and $|4\rangle \rightarrow |1\rangle$, however, these decays and the pumping transition $|1\rangle \rightarrow |3\rangle$ can be expressed by rates, simplifying the problem to the coherent treatment of a two-level system. The imaginary part of the resulting off-diagonal density matrix element ρ_{21} is directly proportional to the electric field of the coherently scattered light on the ZPL resonance¹⁵, thus allowing us to calculate the power associated with its interference with the excitation field^{16,21,22}. Furthermore, the diagonal element ρ_{22} is proportional to the total power dissipated out of the excited state. To consider the case of pulsed population inversion, we applied periodic boundary conditions on the elements of ρ . The time dependence of ρ_{21} and ρ_{22} are depicted respectively by the black and red curves in Fig. 1b, and the inset shows the evolution of these quantities during the pulse. The solid curves in Figs 2, 3 and 4 display the outcome of our numerical calculations for pulsed excitation, which show excellent agreement with the experimentally obtained data. The high quantitative success of the fits in Figs 4a–c and 4d–f are particularly noteworthy, because each set of spectra was fitted simultaneously, sharing the values of the pump power, probe power, and collection efficiency where applicable.

It is instructive to present the steady-state solutions of ρ for the case of CW pumping, which can be formulated analytically as:

$$\rho_{22}^{\text{ss}} = \frac{\xi}{1+\xi} + \frac{1-\xi}{1+\xi} \frac{\Omega^2}{4\Delta^2 + (1+\xi)^2\Gamma^2 + 2\Omega^2} \quad (1)$$

$$\rho_{21}^{\text{ss}} = \frac{1-\xi}{1+\xi} \frac{\Omega[2\Delta - i\Gamma(1+\xi)]}{4\Delta^2 + (1+\xi)^2\Gamma^2 + 2\Omega^2} \quad (2)$$

Here the ratio $\xi = k/\Gamma$ provides a measure for the pumping strength, where k is the $|1\rangle \rightarrow |2\rangle$ pumping rate, Δ represents the frequency detuning between the probe laser and the ZPL, Ω is the Rabi frequency, and Γ denotes the spontaneous emission rate. The first term of ρ_{22}^{ss} yields the population of $|2\rangle$ due to pumping alone, that is, for $\Omega = 0$. One clearly sees that the second term of ρ_{22}^{ss} and ρ_{21}^{ss} change sign when ξ crosses the value of 1. The fraction of light removed or added to the transmitted probe laser beam on resonance and in the weak excitation regime turns out to be expressed by $R \propto (1-\xi)/(1+\xi)^2$, which assumes positive and negative values for attenuation and amplification, respectively. It follows that R becomes zero at $\xi = 1$ and takes on its minimum value (that is, maximum amplification) at $\xi = 3$. These results can be qualitatively extended to the case of pulsed population inversion if ξ is replaced by $\xi = kt_{\text{pul}}/(t_{\text{rep}}\Gamma)$, where t_{pul} and t_{rep} are the pulse on-time and repetition period, respectively. More quantitatively, for the parameters of our experiment, the crossover between attenuation and amplification takes place at $\xi \approx 1.2$, and the maximum value of amplification is reached at $\xi \approx 6$ for pulsed pumping. We remark in passing that the single-molecule transistor can also operate using a CW gate beam.

The analytical results for CW pumping also provide us with intuitive insight into the spectral features of the data in Fig. 2. First, we note that the linewidth of the amplified spectrum in Fig. 2e is more than twice as broad as the extinction spectrum recorded on the ground state in Fig. 2a. This is caused by the strong pumping rate k , which is necessary for counter-balancing spontaneous emission and achieving population inversion. A large k is also responsible for the reduction of the visibility from 7% for the extinction dip to 0.6% for the amplification peak because it provides a loss channel for the ground state and lowers the scattering cross-section of the $|1\rangle \leftrightarrow |2\rangle$ transition. The optimum ratio between amplification and extinction is found to be $-1/8$ at $\xi = 3$ for CW pumping, determined by the ratios of the minimum and maximum of R . Finally, we note

that the weak modulations observed at ± 76 MHz in Figs 2d, e, and 4c, f result from the periodic pump process.

The operation realm of single-emitter quantum optical transistors can be extended in several ways. We have shown that such a device can control a source beam that has a weaker flux than its saturated emission rate. To push the power range of the source to higher values, one could enhance the excited-state spontaneous emission rate by coupling to nano-antennas^{26,27} or simple microcavity geometries²⁸. This would also diminish the impact of Stokes-shifted fluorescence, which reduces the coherent scattering cross-section of dye molecules. At the other extreme, because the geometric coupling of a light beam to a single emitter can reach unity^{16,29}, it is expected that single-emitter transistors can also manipulate non-classical source beams with only a few photons. Indeed, preliminary experiments have demonstrated 10% attenuation of a light beam with as few as about 1,000 photons per second²². In addition, the gate power can be reduced to only a few tens of photons per pulse if the molecular population is inverted in a resonant pumping scheme through the narrow ZPL³⁰, instead of the broad $|1\rangle \leftrightarrow |3\rangle$ transition. Such a coherent pumping could also prepare superpositions of states $|1\rangle$ and $|2\rangle$, which would be then stamped onto photons scattered in the forward and backward directions. Given that a molecule only occupies a few nanometres in the solid state, it should be possible to package a huge number of single-emitter transistors in a nanoscopic area and exploit the inhomogeneous distribution of frequencies to operate many signals simultaneously.

Received 19 March; accepted 14 May 2009.

1. Tans, S. J., Verschuuren, A. R. M. & Dekker, C. Room-temperature transistor based on a single carbon nanotube. *Nature* **393**, 49–52 (1998).
2. Park, J. et al. Coulomb blockade and the Kondo effect in single-atom transistors. *Nature* **417**, 722–725 (2002).
3. Liang, W., Shores, M. P., Bockrath, M., Long, J. R. & Park, H. Kondo resonance in a single-molecule transistor. *Nature* **417**, 725–729 (2002).
4. Davidovich, L., Maali, A., Brune, M., Raimond, J. M. & Haroche, S. Quantum switches and nonlocal microwave fields. *Phys. Rev. Lett.* **71**, 2360–2363 (1993).
5. Harris, S. E. & Yamamoto, Y. Photon switching by quantum interference. *Phys. Rev. Lett.* **81**, 3611–3614 (1998).
6. Micheli, A., Daley, A. J., Jaksch, D. & Zoller, P. Single atom transistor in a 1d optical lattice. *Phys. Rev. Lett.* **93**, 140408 (2004).
7. Dawes, A. M. C., Illing, L., Clark, S. M. & Gauthier, D. J. All-optical switching in rubidium vapor. *Science* **308**, 672–674 (2005).
8. Chang, D. E., Sorensen, A. S., Demler, E. A. & Lukin, M. D. A single-photon transistor using nanoscale surface plasmons. *Nature Phys.* **3**, 807–812 (2007).
9. Vaishnav, J., Ruseckas, J., Clark, C. W. & Juzelunas, G. Spin field effect transistors with ultracold atoms. *Phys. Rev. Lett.* **101**, 265302 (2008).
10. Imamoglu, A., Schmidt, H., Woods, G. & Deutsch, M. Strongly interacting photons in a nonlinear cavity. *Phys. Rev. Lett.* **79**, 1467–1470 (1997).
11. Duan, L.-M. & Kimble, H. J. Scalable photonic quantum computation through cavity-assisted interactions. *Phys. Rev. Lett.* **92**, 127902 (2004).
12. Birnbaum, K. M. et al. Photon blockade in an optical cavity with one trapped atom. *Nature* **436**, 87–90 (2005).
13. Schuster, I. et al. Nonlinear spectroscopy of photons bound to one atom. *Nature Phys.* **4**, 382–385 (2008).
14. Shen, J.-T. & Fan, S. Strongly correlated two-photon transport in a one-dimensional waveguide coupled to a two-level system. *Phys. Rev. Lett.* **98**, 153003 (2007).
15. Loudon, R. *Quantum Theory of Light* (Oxford Univ. Press, 2000).
16. Zumofen, G., Mojarad, N. M., Sandoghdar, V. & Agio, M. Perfect reflection of light by an oscillating dipole. *Phys. Rev. Lett.* **101**, 180404 (2008).
17. Moerner, W. E. & Orrit, M. Illuminating single molecules in condensed matter. *Science* **283**, 1670–1676 (1999).
18. Moerner, W. E. & Kador, L. Optical detection and spectroscopy of single molecules in a solid. *Phys. Rev. Lett.* **62**, 2535–2538 (1989).
19. Orrit, M. & Bernard, J. Single pentacene molecules detected by fluorescence excitation in a *p*-terphenyl crystal. *Phys. Rev. Lett.* **65**, 2716–2719 (1990).
20. Plakhotnik, T. & Palm, V. Interferometric signatures of single molecules. *Phys. Rev. Lett.* **87**, 183602 (2001).
21. Gerhardt, I. et al. Strong extinction of a laser beam by a single molecule. *Phys. Rev. Lett.* **98**, 033601 (2007).
22. Wrigge, G., Gerhardt, I., Hwang, J., Zumofen, G. & Sandoghdar, V. Efficient coupling of photons to a single molecule and the observation of its resonance fluorescence. *Nature Phys.* **4**, 60–66 (2008).
23. Lettow, R. et al. Realization of two Fourier-limited solid-state single-photon sources. *Opt. Express* **15**, 15842–15847 (2007).

24. Lounis, B., Jelzko, F. & Orrit, M. Single molecules driven by strong resonant fields: hyper-Raman and subharmonic resonances. *Phys. Rev. Lett.* **78**, 3673–3676 (1997).
25. Klar, T., Jakobs, S., Dyba, M., Egner, A. & Hell, S. W. Fluorescence microscopy with diffraction resolution barrier broken by stimulated emission. *Proc. Natl Acad. Sci. USA* **97**, 8206–8210 (2000).
26. Kühn, S., Håkanson, U., Rogobete, L. & Sandoghdar, V. Enhancement of single molecule fluorescence using a gold nanoparticle as an optical nano-antenna. *Phys. Rev. Lett.* **97**, 017402 (2006).
27. Rogobete, L., Kaminski, F., Agio, M. & Sandoghdar, V. Design of nanoantennae for the enhancement of spontaneous emission. *Opt. Lett.* **32**, 1623–1625 (2007).
28. Chizhik, A. *et al.* Tuning the fluorescence emission spectra of a single molecule with a variable optical subwavelength metal microcavity. *Phys. Rev. Lett.* **102**, 073002 (2009).
29. Stobin'ska, M., Alber, G. & Leuchs, G. Perfect excitation of a matter qubit by a single photon in free space. *Europhys. Lett.* **86**, 14007 (2009).
30. Gerhardt, I. *et al.* Coherent state preparation and observation of Rabi oscillations in a single molecule. *Phys. Rev. A* **79**, 011402(R) (2009).

Acknowledgements This work was supported by the Swiss National Foundation (SNF) and ETH Zurich (QSIT, grant no. PP-01 07-02). We thank I. Gerhardt and G. Wrigge for their contributions to this project. V.S. thanks X. S. Xie for his hospitality at Harvard University during the writing process of this manuscript.

Author Information Reprints and permissions information is available at www.nature.com/reprints. Correspondence and requests for materials should be addressed to V.S. (vahid.sandoghdar@ethz.ch).

Giant tunnel electroresistance for non-destructive readout of ferroelectric states

V. Garcia^{1,2}, S. Fusil^{1,3}, K. Bouzehouane¹, S. Enouz-Vedrenne⁴, N. D. Mathur², A. Barthélémy¹ & M. Bibes¹

Ferroelectrics possess a polarization that is spontaneous, stable and electrically switchable¹, and submicrometre-thick ferroelectric films are currently used as non-volatile memory elements with destructive capacitive readout². Memories based on tunnel junctions with ultrathin ferroelectric barriers would enable non-destructive resistive readout³. However, the achievement of room-temperature polarization stability and switching at very low thickness is challenging^{4,5}. Here we use piezoresponse force microscopy at room temperature to show robust ferroelectricity down to 1 nm in highly strained BaTiO₃ films; we also use room-temperature conductive-tip atomic force microscopy to demonstrate resistive readout of the polarization state through its influence on the tunnel current^{6,7}. The resulting electroresistance effect scales exponentially with ferroelectric film thickness, reaching ~75,000% at 3 nm. Our approach exploits the otherwise undesirable leakage current—dominated by tunnelling at these very low thicknesses—to read the polarization state without destroying it. We demonstrate scalability down to 70 nm, corresponding to potential densities of >16 Gbit inch⁻². These results pave the way towards ferroelectric memories with simplified architectures, higher densities and faster operation, and should inspire further exploration of the interplay between quantum tunnelling and ferroelectricity at the nanoscale.

As ferroelectricity is a cooperative phenomenon, it is commonly accepted that there is a fundamental thickness limit (the critical thickness, t_c) below which ferroelectricity collapses⁸ owing to the depolarization field and/or finite-size effects⁹. This problem has been investigated theoretically, mostly through *ab initio* calculations that have predicted critical thicknesses of 2.4 nm for BaTiO₃ (BTO; ref. 4) and 1.2 nm for PbTiO₃ (ref. 10). Experimentally, the determination of t_c is challenging, as polarization versus electric-field (P - E) measurements are made difficult by leakage currents when the thickness decreases below a few tens of nanometres. Indications of a ferroelectric state may be inferred from diffraction studies, but to demonstrate the existence of a switchable polarization, piezoresponse force microscopy (PFM) is the technique of choice. For instance, a t_c of 1.2 nm has been found for PbTiO₃ films by X-ray scattering¹¹ and by X-ray photoemission diffraction¹⁰, and a t_c of 2.8 nm by PFM¹². For BiFeO₃ and La_{0.1}Bi_{0.9}MnO₃ films, a t_c of 2 nm was also found by PFM experiments^{13–15}. For BTO, P - E loops have been successfully measured in 5-nm films at 300 K (ref. 16) and in 3.5-nm films at 77 K (ref. 17), setting the current t_c in single films of this material.

Besides thickness, ferroelectric properties may also depend critically on external factors^{18,19} such as strain²⁰. Indeed, both the Curie temperature (T_C) and the spontaneous polarization of BTO can be increased dramatically by epitaxial strain—for example, up to a factor of ~2.5 with a compressive strain of 1.6% applied through epitaxial growth onto mismatched DyScO₃ substrates²⁰. The maximum

achievable strain (and thus T_C) is however limited by the accumulated elastic energy, so that very large strains are in principle restricted to very thin films.

As we are mostly interested in films thinner than a few nanometres, we selected (001)-oriented NdGaO₃ (NGO) single crystal substrates that impose a compressive strain of up to 3.2% on BTO. BTO films with thicknesses ranging between 1 nm and 50 nm were grown on NGO with a 30-nm-thick La_{0.67}Sr_{0.33}MnO₃ (LSMO) buffer. The interfaces between the layers are atomically smooth (as inferred from X-ray reflectometry measurements), and surfaces show terraces separated by ~4-Å-high steps (see the atomic force microscopy (AFM) mapping of Fig. 1a). Samples with BTO layers thicker than 5 nm were characterized by high-resolution X-ray diffraction 2θ - ω scans and reciprocal space maps. The widths of the rocking curves are typically lower than 0.01°, indicating an excellent structural quality for the different layers. Reciprocal space maps show that the pseudo-cubic (001)LSMO is always fully strained while the strain state of tetragonal (001)BTO changes with thickness. As can be seen in Fig. 1b, 50-nm-thick BTO films grown on LSMO/NGO are relaxed, with virtually bulk-like unit-cell parameters ($a = 3.987$ Å and $c = 4.040$ Å). However, as thickness decreases, the out-of-plane c parameter progressively increases, accompanied by a decrease of the in-plane a parameter. The strain state of the 2-nm sample was determined from high-resolution electron microscopy cross-section images (Fig. 1c). These images also reveal the high structural quality of the ultrathin BTO layers that appear to grow coherently onto the LSMO buffer. The analysis of the contrast periodicity in the growth direction and in the plane yields $c_{\text{BTO}} = 4.120 \pm 0.05$ Å and $a_{\text{BTO}} = 3.918 \pm 0.05$ Å, which corresponds to a c/a ratio (tetragonality) of 1.051. This is larger than the $c/a = 1.038$ obtained for 100-nm BTO films grown on DyScO₃ for which $T_C > 900$ K was reported²⁰. One may thus anticipate that such a highly strained state might counterbalance the detrimental influence of thickness reduction and preserve ferroelectricity at very low thickness.

Figure 2 shows the ferroelectric characterization of a BTO(1 nm)/LSMO(30 nm)/NGO sample. After applying a tip-LSMO poling voltage of ± 3.5 V along $4 \times 0.5 \mu\text{m}^2$ stripes, a large out-of-plane piezoresponse phase (OPP) contrast ($\sim 180^\circ$) is observed, indicating that ferroelectric domains with opposite polarizations have been written in the BTO film (Fig. 2b). We verified that poling does not influence the surface topography (Fig. 2a). The polarization in these domains can be switched back and forth by applying a 3.5 V voltage of opposite polarity (Fig. 2c). This phase contrast is perfectly stable for more than 72 h (Supplementary Fig. 2), which excludes charging effects as a possible origin²¹ and demonstrates that BTO films as thin as 1 nm are ferroelectric at room temperature. Thicker BTO films were similarly found to be ferroelectric. Figure 2d shows the hysteretic dependence of OPP with applied voltage for a 3-nm film, providing additional evidence for ferroelectricity at low BTO thickness. From the very small

¹Unité Mixte de Physique CNRS/Thales, 1 Av. A. Fresnel, Campus de l'Ecole Polytechnique, 91767 Palaiseau, France, and Université Paris-Sud, 91405 Orsay, France. ²Department of Materials Science, University of Cambridge, Cambridge CB2 3QZ, UK. ³Université d'Evry-Val d'Essonne, Bd. F. Mitterrand, 91025 Evry cedex, France. ⁴Thales Research & Technology, 1 Av. A. Fresnel, Campus de l'Ecole Polytechnique, 91767 Palaiseau, France.

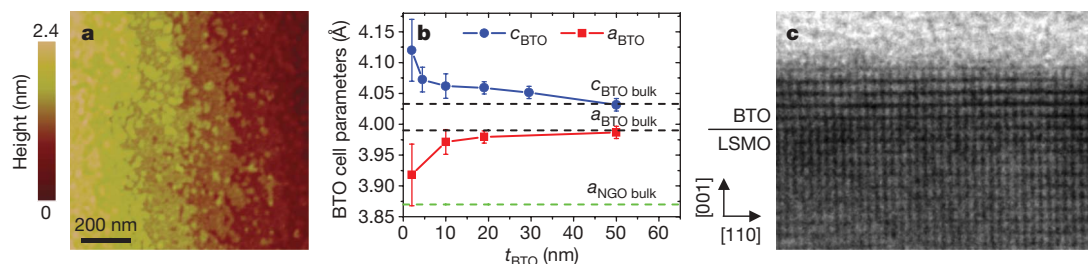


Figure 1 | Structural properties of BaTiO₃ (BTO) thin films. **a**, AFM topography of a 1-nm BTO film, showing terraces with one-unit-cell steps. **b**, Evolution of the out-of-plane (c_{BTO}) and in-plane (a_{BTO}) cell parameters of the BTO films deduced from high-resolution X-ray diffraction (thickness $t = 5$ –50 nm) and high-resolution electron microscopy ($t = 2$ nm). t_{BTO} , thickness of BTO film. Error bars correspond to the width at half-maximum in the reciprocal space maps or to the dispersion of cell parameters calculated

from various profiles of the high-resolution electron microscopy images. Horizontal dashed lines correspond to the cell parameters of bulk BTO and NGO. **c**, Transmission electron microscopy cross-section image of a 2-nm BTO/30-nm LSMO ($\text{La}_{2/3}\text{Sr}_{1/3}\text{MnO}_3$) bilayer grown on an NdGaO₃ substrate. The crystallographic directions are given in the pseudo-cubic notation.

PFM amplitude, we estimate a piezoelectric coefficient (d_{33}) of 2–5 pm V^{-1} . However, we point out that to measure reliable d_{33} values, measurements on top electrode pads are required to ensure a homogeneous distribution of the electric field lines. This d_{33} value, as well as the overall shape of the hysteresis cycle, can thus just be taken as rough estimates.

BTO films thinner than 4 nm were characterized by a laboratory-made conductive-tip atomic force microscope²² (CTAFM) with a 10^{-12} – 10^{-4} A current range; $3 \times 3 \mu\text{m}^2$ resistance maps were collected at a tip–LSMO bias voltage of 2 V. For all samples, the resistance is very homogeneous on this scale and increases exponentially with thickness (Fig. 3j), as expected for tunnelling through BTO.

Several authors have proposed that electrons tunnelling through a ferroelectric layer would be transmitted differently depending on the direction of the polarization, by means of several possible mechanisms^{3,6,7,23}. The resulting tunnel electroresistance (TER) effect may be very large and thus provide an efficient way to read the polarization state without destroying it. This is in contrast with conventional capacitive ferroelectric readout, which is destructive. Experimentally, an electroresistance of ~700% has been reported in ferroelectric tunnel

junctions, but could not unambiguously be attributed to polarization switching²⁴.

To investigate TER locally, we have adapted our scanning probe microscope to perform sequential ferroelectric poling, PFM imaging and CTAFM imaging of the poled domains. The resistance difference measured with the CTAFM between positively and negatively poled regions would correspond to the TER effect. The PFM and CTAFM mappings for 1-, 2- and 3-nm BTO films are displayed in Fig. 3a–f. For the 1-nm film, the sharp PFM phase contrast (Fig. 3a) corresponds to a moderate but visible change in the resistance (Fig. 3d). Resistance profiles (Fig. 3g) across the poled area reveal a resistance difference between the positively or negatively poled region of TER ~200%. As shown in Fig. 3e and h, the resistance contrast increases dramatically for the 2-nm sample and the TER attains ~10,000%. The TER is even larger for the 3-nm film, reaching a maximum of ~75,000% (see Fig. 3f and the resistance profile in Fig. 3i). The TER results for different BTO thicknesses are summarized in Fig. 3k; as can be appreciated, the TER increases exponentially with BTO film thickness, t_{BTO} .

The ferroelectric polarization has been proposed to influence the tunnel current through changes either in the density of states (DOS) of electrode–barrier interfaces³ or in the physical parameters of the tunnel barrier (height^{6,7}, thickness⁷, tunnelling mass⁷). As the tunnel transmission depends exponentially on the latter, the observed thickness dependence of the TER suggests that the polarization direction primarily affects the tunnel barrier characteristics rather than the DOS.

The small piezoelectric coefficient estimated for our ultrathin BTO films tends to disqualify the barrier thickness variation as the dominant origin of the TER. On the other hand, the thickness dependence of the TER is reminiscent of the predictions of refs 6 and 7. These electrostatic models assume that, if different electrode materials are used, the incomplete screening of the polarization charges at the electrode–barrier interfaces will lead to an asymmetric deformation of the barrier potential profile. Switching the polarization will produce two different average barrier heights and thus two different tunnel resistances, thereby defining a polarization-induced TER effect^{6,7}. Remarkably, as the tunnel resistance depends exponentially on the square root of the barrier height, even a small polarization-induced change in the tunnel barrier height will result in a large TER.

Recently, more sophisticated models have been proposed for epitaxial ferroelectric tunnel barriers, taking into account the influence of ferroelectric polarization on the complex electronic band structure²⁵. Depending on the polarization direction, the complex κ -loops (energy dependence of the wave vector κ of the evanescent states) are distorted²³, resulting in different values of the tunnel transmission coefficient with different coupling to the electrode electronic states. This type of approach is probably the best suited to describe our epitaxial heterostructures, and first-principles calculations of the

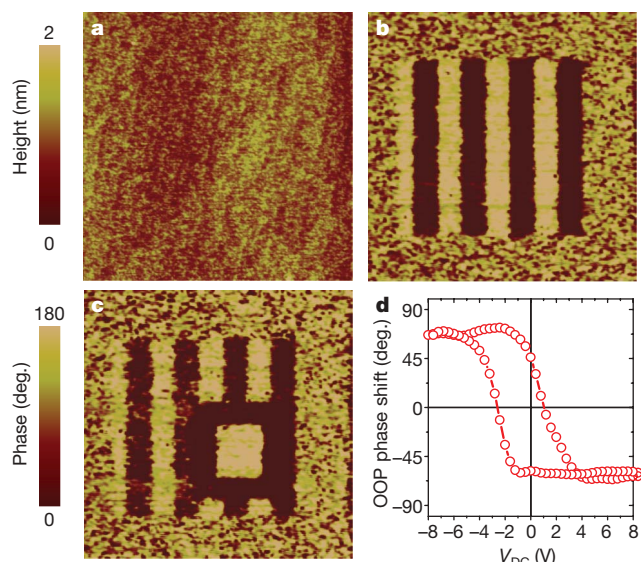


Figure 2 | Ferroelectricity of BTO ultrathin films. Demonstration of ferroelectricity for a 1-nm BTO film grown on top of a 30-nm LSMO electrode. **a**, Topography ($6 \times 6 \mu\text{m}^2$) and **b**, PFM out-of-plane (OOP) phase image after writing eight alternating positive (+3.5 V) and negative (−3.5 V) $4 \times 0.5 \mu\text{m}^2$ voltage stripes. **c**, A $2 \times 2 \mu\text{m}^2$ dark square is written on top of the pattern with +3.5 V, and a $1 \times 1 \mu\text{m}^2$ white square (−3.5 V) is subsequently written on top of that square. **d**, Hysteretic dependence of PFM phase with applied d.c. bias (V_{DC}) for a 3-nm BTO film.

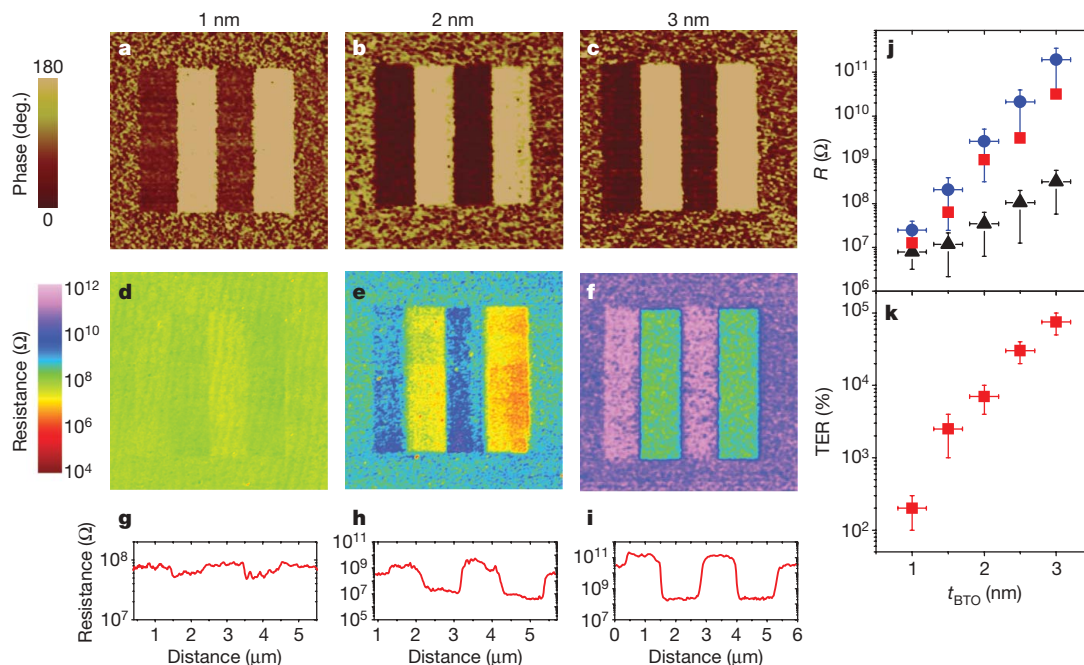


Figure 3 | Direct evidence for ferroelectricity-related giant TER with ultrathin strained BTO films. **a–f**, Parallel PFM phase image (**a–c**) and CTAFA resistance mapping (**d–f**) of four written ferroelectric stripes ($1 \times 4 \mu\text{m}^2$) for BTO films 1, 2 and 3 nm thick. **g–i**, Corresponding resistance profiles of the poled area. **j**, Thickness dependence of the resistance (R) of unpoled (red squares), and positively (black triangles) and negatively (blue

circles) poled, regions. An exponential increase with t_{BTO} is found, as expected for direct tunnelling. **k**, The TER also increases exponentially with t_{BTO} , reaching $\sim 75,000\%$ for the 3-nm film. In **j** and **k**, vertical error bars correspond to the standard deviation of the resistance distribution over selected areas (and corresponding TER variations), and the horizontal error bars to the thickness uncertainty from growth calibrations.

whole junction²³ would bring a valuable insight into the precise origin of the TER.

The very large TER effect that we have observed should make it possible to replace the destructive capacitive readout of state-of-the-art ferroelectric random access memories (FERAMs) by a simpler, non-destructive resistive readout scheme. To further assess the potential of this new concept for high-density data storage, we have explored the scalability of the TER effect by writing matrices of nanoscale dots and reading their TER. Figure 4a shows the OPP image of a 5×5 matrix of 70-nm dots written every 200 nm at a poling voltage of 3 V over an area previously poled homogeneously at -3 V, for a BTO thickness of 2 nm. This density of PFM-read dots is in the range of that reported²⁶ on thick $\text{Pb}(\text{Zr}_{0.2}\text{Ti}_{0.8})\text{O}_3$ films. Figure 4b displays the resistive readout of this matrix by CTAFA. A large resistance contrast between the background (high resistance) and the dots (low resistance) is visible for all dots. The average resistance difference corresponds to a TER of $\sim 10,000\%$, that is, the same value as in the micrometre-sized stripes of Fig. 3. This demonstrates the scalability of the TER effect to nanoscale devices.

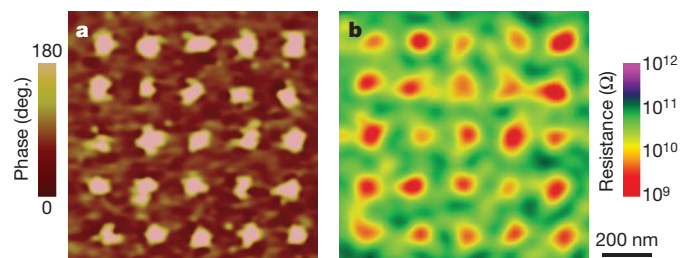


Figure 4 | Resistive readout of polarization state in high-density nanoscale ferroelectric dot arrays. A matrix of 25 dots has been obtained by applying $+3$ V pulses with a step of 200 nm over a previously written -3 V square. The 70-nm nanoscale dots are subsequently read by collecting PFM phase images (**a**) and CTAFA resistance maps (**b**).

We have demonstrated that highly strained BTO films retain robust room-temperature ferroelectricity down to 1 nm. The preservation of ferroelectricity at such low thickness enables the readout of the polarization state through its influence on the tunnelling resistance. The resistance contrast between polarization states increases exponentially with BTO thickness, reaching $\sim 75,000\%$ for 3-nm films at room temperature, and is scalable down to 70 nm, corresponding to densities greater than $16 \text{ Gbit inch}^{-2}$. These results show great promise for high density data storage, as efficient non-destructive resistive readout would greatly simplify FERAM architectures and reading protocol. This would enable densities close to those of phase change memories while potentially retaining the excellent endurance of current FERAMs.

METHODS SUMMARY

BTO/LSMO bilayers were grown by pulsed laser deposition on (001)NdGaO₃ (NGO) substrates using a KrF laser ($\lambda = 248 \text{ nm}$) with a fluence of 2 J cm^{-2} and a repetition rate of 1 Hz. 30-nm LSMO films were grown at 775°C and an oxygen pressure of 0.15 mbar. The subsequent growth of BTO with an oxygen pressure of 0.10 mbar was followed by one hour of annealing at 750°C in high oxygen pressure (500 mbar).

For films thicker than 5 nm, the unit-cell parameters were determined by high-resolution X-ray diffraction (Panalytical X'pert Pro) using Cu K α_1 radiation. For the 2-nm film, we used high-resolution transmission electron microscopy images collected on a Topcon 002B at 200 kV.

Scanning probe microscopy experiments were performed with a Digital Instruments Nanoscope IV set-up at room temperature in a nitrogen flow. PFM was carried out using CrPt tips at an excitation frequency of 4–7 kHz and an a.c. voltage of 1 V and Stanford Research SR830 external lock-in amplifiers. d.c. poling was performed with CrPt tips by applying a voltage between 3 and 5 V between the tip and the bottom electrode.

CTAFA measurements were carried out with the same set-up and a laboratory-made high bandwidth (5 kHz) current amplifier^{22,27}. The bias voltage between the tip and the bottom electrode was 1.5–2.5 V. Si tips coated with B-doped diamond were used to limit tip wear during successive scans. For Fig. 3, the same tip and same acquisition parameters were used for all samples. For other images (Fig. 4, Supplementary Figs 3 and 4) the setpoint was minimized to limit tip wear. For poling, PFM and CTAFA experiments, special care

was always taken to ensure that the surface morphology of the sample was unchanged before and after poling or scanning.

Received 4 February; accepted 11 May 2009.

Published online 31 May 2009.

1. Dawber, M., Rabe, K. M. & Scott, J. F. Physics of thin-film ferroelectric oxides. *Rev. Mod. Phys.* **77**, 1083–1130 (2005).
2. Scott, J. F. & Paz de Araujo, C. A. Ferroelectric memories. *Science* **246**, 1400–1405 (1989).
3. Tsybal, E. Y. & Kohlstedt, H. Tunneling across a ferroelectric. *Science* **313**, 181–183 (2006).
4. Junquera, J. & Ghosez, P. Critical thickness for ferroelectricity in perovskite ultrathin films. *Nature* **422**, 506–509 (2003).
5. Despont, L. *et al.* Direct evidence for ferroelectric polar distortion in ultrathin lead titanate perovskite films. *Phys. Rev. B* **73**, 094110 (2006).
6. Zhuravlev, M. Y., Sabirianov, R. F., Jaswal, S. S. & Tsybal, E. Y. Giant electroresistance in ferroelectric tunnel junctions. *Phys. Rev. Lett.* **94**, 246802 (2005).
7. Kohlstedt, H., Pertsev, N. A., Rodríguez Contreras, J. & Waser, R. Theoretical current-voltage characteristics of ferroelectric tunnel junctions. *Phys. Rev. B* **72**, 125341 (2005).
8. Kohlstedt, H., Pertsev, N. A. & Waser, R. Size effects on polarization in epitaxial ferroelectric films and the concept of ferroelectric tunnel junctions including first results. *Mater. Res. Soc. Symp. Proc.* **688**, C6.5 (2002).
9. Ghosez, P. & Junquera, J. in *Handbook of Theoretical and Computational Nanotechnology* Vol. 7 (Rieth, M. & Schommers, W.) 623–728 (American Scientific Publishers, 2006).
10. Despont, L. *et al.* Direct evidence for ferroelectric polar distortion in ultrathin lead titanate perovskite films. *Phys. Rev. B* **73**, 094110 (2006).
11. Fong, D. D. *et al.* Ferroelectricity in ultrathin perovskite films. *Science* **304**, 1650–1653 (2004).
12. Lichtensteiger, C. *et al.* Monodomain to polydomain transition in ferroelectric PbTiO_3 thin films with $\text{La}_{0.67}\text{Sr}_{0.33}\text{MnO}_3$ electrodes. *Appl. Phys. Lett.* **90**, 052907 (2007).
13. Béa, H. *et al.* Ferroelectricity down to at least 2 nm in multiferroic BiFeO_3 epitaxial thin films. *Jpn. J. Appl. Phys.* **45**, L187–L189 (2006).
14. Chu, Y. H. *et al.* Ferroelectric size effects in multiferroic BiFeO_3 thin films. *Appl. Phys. Lett.* **90**, 252906 (2007).
15. Gajek, M. *et al.* Tunnel junctions with multiferroic barriers. *Nature Mater.* **6**, 296–302 (2007).
16. Kim, Y. S. *et al.* Critical thickness of ultrathin ferroelectric BaTiO_3 films. *Appl. Phys. Lett.* **86**, 102907 (2005).
17. Petraru, A. *et al.* Wedgelike ultrathin epitaxial BaTiO_3 films for studies of scaling effects in ferroelectrics. *Appl. Phys. Lett.* **93**, 072902 (2008).
18. Takahashi, R., Grepstad, J. K., Tybell, T. & Matsumoto, Y. Photochemical switching of ultrathin PbTiO_3 films. *Appl. Phys. Lett.* **92**, 112901 (2008).
19. Thompson, C. *et al.* Imaging and alignment of nanoscale 180° stripe domains in ferroelectric thin films. *Appl. Phys. Lett.* **93**, 182901 (2008).
20. Choi, K. J. *et al.* Enhancement of ferroelectricity in strained BaTiO_3 thin films. *Science* **306**, 1005–1009 (2004).
21. Tybell, T., Ahn, C. H. & Triscone, J.-M. Ferroelectricity in thin perovskite films. *Appl. Phys. Lett.* **75**, 856–858 (1999).
22. Houzé, F., Meyer, R., Schneegans, O. & Boyer, L. Imaging the local electrical properties of metal surfaces by atomic force microscopy with conducting probes. *Appl. Phys. Lett.* **69**, 1975–1977 (1996).
23. Velev, J. P. *et al.* Magnetic tunnel junctions with ferroelectric barriers: predictions of four resistance states from first principles. *Nano Lett.* **9**, 427–432 (2009).
24. Rodríguez-Contreras, J. *et al.* Resistive switching in metal-ferroelectric-metal junctions. *Appl. Phys. Lett.* **83**, 4595–4597 (2003).
25. Velev, J. P., Duan, C.-G., Belashchenko, K. D., Jaswal, S. S. & Tsybal, E. Y. Effect of ferroelectricity on electron transport in $\text{Pt}/\text{BaTiO}_3/\text{Pt}$ tunnel junctions. *Phys. Rev. Lett.* **98**, 137201 (2007).
26. Paruch, P., Tybell, T. & Triscone, J.-M. Nanoscale control of ferroelectric polarization and domain size in epitaxial $\text{Pb}(\text{Zr}_{0.2}\text{Ti}_{0.8})\text{O}_3$ thin films. *Appl. Phys. Lett.* **79**, 530–532 (2001).
27. Planès, J., Houzé, F., Chrétien, P. & Schneegans, O. Conducting probe atomic force microscopy applied to organic conducting blends. *Appl. Phys. Lett.* **79**, 2993–2995 (2001).

Supplementary Information is linked to the online version of the paper at www.nature.com/nature.

Acknowledgements We thank H. Béa, C. Israel, M. Vickers and B. Warot-Fonrose for technical support, and H. Kohlstedt for discussions. This work was supported by the France-UK PMC Alliance programme, the French RTRA Triangle de la Physique, EU STRP Macomufi, EU STRP CoMePhS, UK EPSRC EP/E026206/I, the French ANR Femmes and the French ANR Alicante.

Author Information Reprints and permissions information is available at www.nature.com/reprints. Correspondence and requests for materials should be addressed to M.B. (manuel.bibes@thalesgroup.com).

The role of terrestrial plants in limiting atmospheric CO₂ decline over the past 24 million years

Mark Pagani¹, Ken Caldeira², Robert Berner¹ & David J. Beerling³

Environmental conditions during the past 24 million years are thought to have been favourable for enhanced rates of atmospheric carbon dioxide drawdown by silicate chemical weathering^{1–7}. Proxy records indicate, however, that the Earth's atmospheric carbon dioxide concentrations did not fall below about 200–250 parts per million during this period⁸. The stabilization of atmospheric carbon dioxide concentrations near this minimum value suggests that strong negative feedback mechanisms inhibited further drawdown of atmospheric carbon dioxide by high rates of global silicate rock weathering. Here we investigate one possible negative feedback mechanism, occurring under relatively low carbon dioxide concentrations and in warm climates, that is related to terrestrial plant productivity and its role in the decomposition of silicate minerals^{9–11}. We use simulations of terrestrial and geochemical carbon cycles and available experimental evidence to show that vegetation activity in upland regions of active orogens was severely limited by near-starvation of carbon dioxide in combination with global warmth over this period. These conditions diminished biotic-driven silicate rock weathering and thereby attenuated an important long-term carbon dioxide sink. Although our modelling results are semi-quantitative and do not capture the full range of biogeochemical feedbacks that could influence the climate, our analysis indicates that the dynamic equilibrium between plants, climate and the geosphere probably buffered the minimum atmospheric carbon dioxide concentrations over the past 24 million years.

Alkenone-based proxy records⁸ indicate that atmospheric carbon dioxide (CO₂) concentrations ranged between 1,000 and 1,500 parts per million (p.p.m.) from about 45 to 34 million years (Myr) ago (the middle to late Eocene epoch), decreased from ~34 to 24 Myr ago (the Oligocene epoch), and approached modern levels by ~24 Myr ago (the early Miocene epoch) (Fig. 1a). Long-term declines in ocean temperatures from the early Eocene leading to the appearance of small Antarctic ice sheets by the late Eocene¹², and a striking shift to colder high-latitude climates at ~34 Myr ago, are climate trends consistent with these CO₂ records (Fig. 1b). In contrast, the final 24 Myr of the Cenozoic era—a time known for periods of both global warmth and substantial ice accumulation—was characterized by relatively low atmospheric CO₂ concentrations⁸. Despite very different assumptions and uncertainties, this CO₂ history for the past 24 Myr or so is reinforced by other CO₂ estimates, including ocean pH reconstructions using the boron isotope composition of foraminifera¹³ (Fig. 1a), and low but variable CO₂ values based on the stomatal indices of fossil leaves¹⁴.

The drop in atmospheric CO₂ concentrations from ~50 to 24 Myr ago (Fig. 1a) was driven by a decrease in geologic CO₂ degassing and/or enhanced chemical weathering of silicate rocks¹⁵. Although there is no consensus regarding Cenozoic CO₂ degassing rates^{16–19}, most

spreading-rate estimates suggest that seafloor production (and CO₂ input) declined slightly^{17,18} or remained constant over the past 65 Myr (ref. 19), with no evidence for distinct changes in spreading rates during the Eocene or the Oligocene. In contrast, physical weathering rates of silicate rocks accelerated with surface uplift and erosion, as inferred by an increase in the global sedimentation rate of sandstones and shales with time¹⁵.

Orogenic reconstructions emphasize the past 65 Myr as a time of active tectonism (Fig. 1a). Himalayan surface uplift includes Andean-style ranges by ~60 Myr ago¹, near-modern elevations for some regions of southern Tibet by the Oligocene^{2,3}, and large changes in topographic relief and rates of denudation during the late Oligocene and Miocene¹. Andean surface uplift began sometime in the early Oligocene, with crustal thickening and exhumation during the late Oligocene^{4,5} and surface uplift in the late Miocene⁶. Finally, exhumation of the massive New Guinea arc occurred during the middle Miocene⁷, while surface uplift of the southern Alps of New Zealand was delayed until the latest Miocene to early Pliocene epoch⁵.

The decline in CO₂ at ~34 Myr ago required a small (that is, less than 0.01 gigatonnes of carbon per year) but sustained imbalance in the carbon cycle²⁰. A striking feature of Cenozoic tectonic activity is the scale of surface uplift and denudation of recent orogens during the past 24 Myr, as well as a lack of evidence for increased metamorphic and volcanic degassing²¹. The current paradigm of climate stability applied in all geochemical carbon simulations assumes a strong CO₂-driven weathering feedback that changes with temperature and soil CO₂ concentration and mitigates large changes in CO₂ over a few million years¹⁵. Indeed, the small variance in the mean atmospheric CO₂ trend for the past ~650,000 years requires a strong weathering feedback for the observed balance of carbon fluxes²². Rates of silicate weathering are modulated by the supply of weatherable minerals and by reaction kinetics, often ascribed to hydrology and temperature²³, with high chemical weathering rates observed in wet, warm regions experiencing active orogenesis. Accordingly, enhanced low-latitude tectonic activity and relative global warmth during the past 24 Myr should have led to a significant long-term imbalance in carbon fluxes and CO₂ drawdown. Contrary to this expectation, atmospheric CO₂ concentrations did not plunge to extremely low values (Fig. 1a), despite changes in climate and the creation of environments that rapidly consume atmospheric CO₂. To stabilize atmospheric CO₂ near its minimum value for over 20 Myr would necessitate either fortuitously balancing multi-million-year carbon fluxes (an unrealistic scenario given the magnitude of the carbon fluxes involved), or negative feedback mechanisms that opposed higher rates of silicate–chemical weathering and further CO₂ decline during the warmth of the early to middle Miocene.

Here, we identify one overlooked negative feedback mechanism occurring under relatively low CO₂ and in warm climates, related to

¹Department of Geology and Geophysics, Yale University, New Haven, Connecticut 06520, USA. ²Department of Global Ecology, Carnegie Institution of Washington, Stanford, California 94305, USA. ³Department of Animal and Plant Sciences, University of Sheffield, Sheffield S10 2TN, UK.

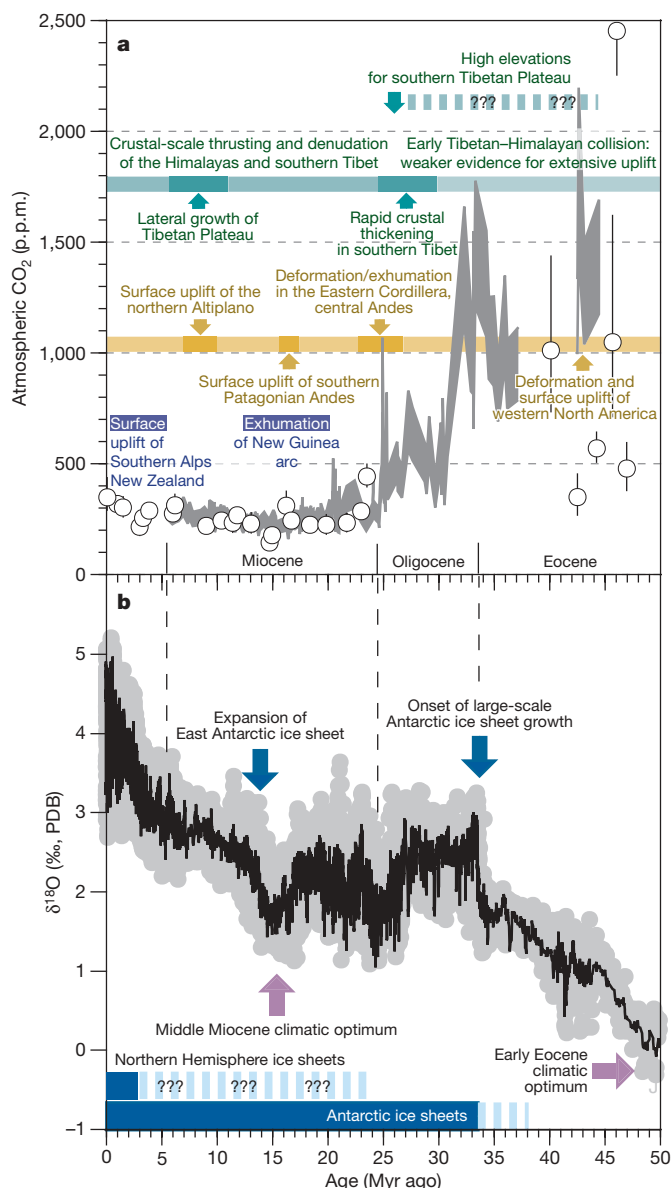


Figure 1 | The Earth's CO₂, tectonic and climatic history over the past 50 Myr. **a**, Proxy records of long-term changes in atmospheric CO₂ concentration. Shaded bands represent a range of alkenone-based atmospheric CO₂ estimates⁸. Open circles represent CO₂ estimates from boron isotope-pH reconstructions¹³. **b**, Long-term δ¹⁸O record from benthic foraminifera¹². p.p.m., parts per million. PDB, Pee Dee belemnite standard.

terrestrial plant productivity and its role in the decomposition of silicate minerals. The mechanistic basis for the relationship between terrestrial plant activity and chemical weathering is well understood^{9–11}. Rooted vascular plants, and their belowground mycorrhizal fungal partners, accelerate rates of chemical weathering by a factor of 1.5 to <10 through a variety of mechanisms associated with recently fixed organic carbon fluxes exported belowground. Biologically enhanced weathering occurs (1) when roots mechanically fracture minerals and increase the surface area available for dissolution, (2) as soil solution pH is lowered by the introduction of root-respired CO₂, organic carbon oxidation, organic acids and proton exchange during nutrient uptake, and (3) through chelation by organic ligands, secreted from rootlets and their associated microorganisms that act to lower the activity of metals and saturation states, leading to enhanced mineral dissolution and nutrient supply for plant growth. Further, canopy transpiration influences the rates of chemical reactions and microbial activity by increasing the

residence time of unsaturated soil water. Accordingly, global rates of silicate chemical weathering are linked to biologically enhanced weathering through the health of terrestrial ecosystems.

The dominant plants associated with high silicate-chemical weathering rates in upland regions use the C₃ photosynthetic pathway. However, the efficacy of C₃ photosynthesis is compromised under specific environmental conditions because the primary enzyme catalysing carbon fixation (Rubisco; ribulose-1,5-bisphosphate carboxylase/oxygenase) also reacts with diatomic oxygen, resulting in photorespiratory release of CO₂ and lower photosynthetic rates (as much as 30%–40% below modern CO₂ levels)²⁴. Photorespiration rates are amplified under low atmospheric CO₂/O₂ ratios, when O₂ significantly competes for the acceptor molecule ribulose biphosphate, and higher temperatures, which alter both the solubility of O₂ relative to CO₂ and the specificity of Rubisco in favour of O₂ (Fig. 2). Both environmental effects on the oxygenase activity of Rubisco are greatly diminished at high CO₂ by increased competitive inhibition of O₂ for ribulose biphosphate²⁵. These fundamental biochemical properties of leaves indicate that the photorespiratory burden of vegetation probably increased as CO₂ began to decline in

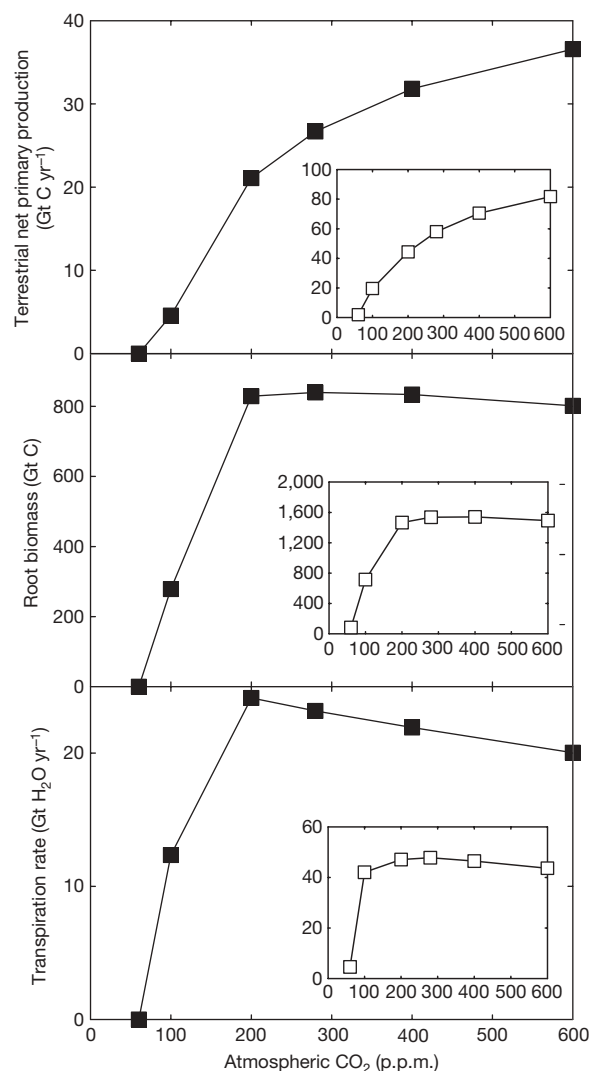


Figure 2 | Simulated dependence of vegetation activity on atmospheric CO₂ concentrations. All simulations used a dynamic global vegetation model and a pre-industrial climate. The main panels show global tropical forest responses; insets (axes units as for main panels) show the global terrestrial biosphere responses. The tropical forest canopy transpiration declines as atmospheric CO₂ concentrations rise above 200 p.p.m. because leaf area index is maximal and CO₂ induces stomatal closure. Gt, gigatonnes.

response to increased chemical weathering from orogenic uplift, especially during episodes of global warmth. Terrestrial vegetation activity would have decreased, weakening its feedback on silicate-rock weathering and offsetting the effect of orogenic uplift on the decrease of atmospheric CO₂.

We investigated the significance of this proposed feedback mechanism on ecosystem properties through simulations with a dynamic global vegetation model that includes representation of the above- and belowground carbon and nitrogen cycles at atmospheric CO₂ concentrations between 50 and 500 p.p.m. (ref. 26). Our results indicate that under present-day climate conditions, the tropical and global forest primary production and root biomass—two key ecosystem properties that enhance soil-weathering rates—decline abruptly at CO₂ concentrations below about 200 p.p.m. (Fig. 2). Similarly, global and tropical forest canopy transpiration rates are strongly diminished by falling atmospheric CO₂ concentrations. These results are supported by independent global-scale simulations of Miocene vegetation showing that forest productivity, particularly in warm tropical regions where photorespiration rates are highest, is strongly constrained by atmospheric CO₂ concentrations of 200–280 p.p.m. (ref. 26). As the minimum level of CO₂ (the level required to sustain C₃ plant growth and reproduction at the ecosystem level) is approached, key mechanisms that accelerate chemical weathering in actively weathering regions begin to slow, weakening the strength of a biologically mediated sink for CO₂ (Fig. 2).

The well-documented loss of forest cover and expansion of C₃ grasslands during the latest Oligocene to early Miocene²⁷ attest to environmental conditions unfavourable to forest productivity. Grasses have shallow root systems and symbiosis with arbuscular mycorrhizal fungi that do not secrete the low-molecular-weight organic acids involved in biotic weathering by ectomycorrhizal-dominated forests²⁸. Thus, this widespread replacement of forests by C₃ grasslands including grasses with the carbon-concentrating C₄ photosynthetic pathway probably further weakened the biotic weathering feedback.

The minimum CO₂ concentration that is critical for the natural ecosystem weathering feedback is not precisely known and its absolute value is likely to have changed with global mean temperature via its influence on respiration rates. Evidence from experiments and ice-core records suggest it lies between ≥ 100 and ≤ 190 p.p.m. during cooler global temperatures of the Pleistocene. The lower value is consistent with the minimum CO₂ concentration required for successful reproduction of a subtropical herb (tobacco needs ~ 100 p.p.m.; ref. 29). The upper estimate derives from Pleistocene ice-core studies that show that terrestrial vegetation repeatedly experienced and survived atmospheric CO₂ concentrations of ~ 180 p.p.m. over the last 650 kyr (ref. 22). This upper level is consistent with experimental results obtained from tropical and desert ecosystems in the Biosphere II facility in Oracle, Arizona, USA, that indicate an approximate ecological compensation point (defined as when net ecosystem exchange approaches zero) of 190 p.p.m. CO₂ (ref. 30). Given the influence of temperature on photorespiration rate, the ecological compensation point during warm intervals was probably achieved at higher CO₂ concentrations.

Geochemical carbon cycle models assume that C₃ plant growth promotes silicate-rock weathering even as the atmospheric CO₂ concentration approaches zero¹⁵. We evaluated the significance of including a more appropriate minimum CO₂ concentration for ecosystem weathering in a carbonate-silicate model by modifying the relationship between terrestrial primary productivity and atmospheric CO₂ using a well-established formulation for the effect of plants on soil CO₂ (see Methods Summary). Factors such as mountain uplift allow rock to weather more easily, so we introduce a dimensionless 'weatherability index' to represent the factor by which silicate-rock weathering is accelerated per unit area at constant atmospheric CO₂ (see Methods Summary). Figure 3 shows that as rocks weather more easily (owing to surface uplift, for example),

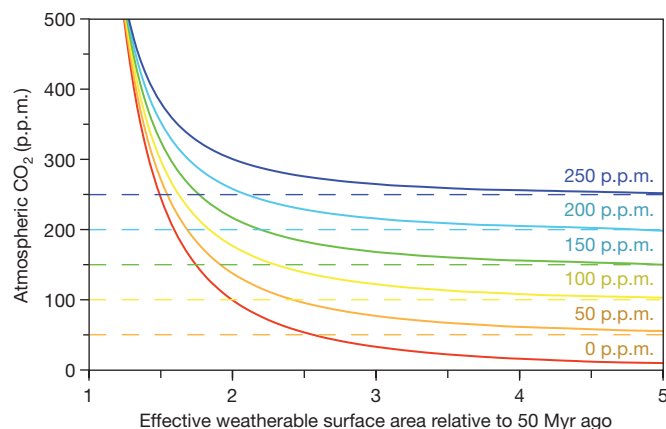


Figure 3 | Atmospheric CO₂, critical thresholds, and plant weathering. Atmospheric CO₂ predictions for critical CO₂ values ranging from 250 p.p.m. to 0 p.p.m. (see Methods Summary for details). Factors including the uplift and denudation of the Himalayas, Andes and New Guinea increased physical erosion and increased the amount of reactive mineral surface area exposed to chemical weathering. As conditions change and rocks weather more easily, the response of terrestrial plants helps buffer atmospheric CO₂ concentration above the critical threshold for vigorous plant growth.

atmospheric CO₂ decreases towards the critical CO₂ threshold below which plant activity does not contribute to enhanced silicate-rock weathering. As that threshold is approached, CO₂ drawdown due to biological weathering is attenuated, limiting the lower bound that CO₂ can fall to, and stabilizing atmospheric CO₂.

Our results for a range of CO₂ thresholds and availability of weatherable minerals (Fig. 3) show that critical CO₂ levels between ~ 150 and 250 p.p.m. effectively dampen CO₂ variability and yield CO₂ concentrations consistent with the lowest values observed for the past 24 Myr (Fig. 1a). Ecological CO₂ thresholds between about 24 and 5 Myr ago were probably higher than those during the Pleistocene, when healthy plant ecosystems are associated with CO₂ concentrations of ~ 190 p.p.m. However, these differences are anticipated, given that warmer-than-modern Neogene temperatures probably increased photorespiration rates and raised minimum CO₂ levels.

We recognize that our modelling results are semi-quantitative and do not capture the full range of biogeochemical feedbacks that could influence climate as CO₂ declines. For example, ecosystem turnover or demise due to CO₂ stress could affect erosion rates, soil stability, rock exposure, regional changes in albedo, and influence weathering rates and changes in CO₂. More elaborate carbon-cycle and climate-system feedbacks could potentially be determined using detailed biogeochemical modelling, but the present work clearly identifies the first-order response of terrestrial C₃ ecosystems to declining CO₂ levels and rising photorespiration rates as a severe reduction in the influence of plants on rock weathering and continued CO₂ drawdown. Therefore, we conclude that land plants strongly attenuated long-term CO₂ variability and helped prevent the onset of severe icehouse conditions during tectonically active periods of the Neogene. Ecological CO₂ thresholds are a fundamental component of long-term carbon-cycle dynamics, and are needed to explain the relative constancy of atmospheric CO₂ in the face of climate and tectonic change over at least the past 24 Myr.

METHODS SUMMARY

Vegetation modelling. Leaf-scale and global-scale simulations of the sensitivity of vegetation processes to atmospheric CO₂ and climate were performed with a mechanistic biochemical model of Rubisco kinetics and a global dynamic vegetation model, respectively. Equilibrium global simulations (500 years) were undertaken at specific atmospheric CO₂ concentrations using monthly pre-industrial surface climatology (monthly fields of temperature, precipitation and humidity) with a $2.5^\circ \times 2.5^\circ$ (latitude \times longitude) spatial resolution.

Land-plants and silicate-rock weathering. The silicate-rock weathering rate ($f_{\text{sw}, 50 \text{ Myr}}$) is represented as³¹:

$$f_{\text{sw}, 50 \text{ Myr}} = k_{50 \text{ Myr}} \times (f_{\text{land plants}})^{0.4} \quad (1)$$

where $f_{\text{land plants}}$ represents the effect of land plants on soil CO_2 levels and $k_{50 \text{ Myr}}$ represents all other factors influencing silicate-rock weathering rates (assumed constant).

A formulation for the effect of land plants on soil CO_2 levels for different critical CO_2 levels below which plant activity does not contribute to enhanced silicate-rock weathering (R_{crit})³² is expressed as:

$$f_{\text{land plants}, R_{\text{crit}}} = \left[\frac{R_{\text{CO}_2} - R_{\text{crit}}}{(R_{\text{half}} - R_{\text{crit}}) + (R_{\text{CO}_2} - R_{\text{crit}})} \right] \left(1 - \frac{1}{R_{\text{soil}, 0}} \right) + \left(\frac{R_{\text{CO}_2}}{R_{\text{soil}, 0}} \right) \quad (2)$$

where R_{CO_2} is the ratio of ancient atmospheric CO_2 relative to the pre-industrial CO_2 level. R_{half} is the atmospheric CO_2 level at which plants produce half of their maximum effect on silicate weathering; $R_{\text{soil}, 0}$ is the ratio of soil CO_2 to pre-industrial atmospheric CO_2 .

We adopt a $R_{\text{soil}, 0}$ value of 10 (ref. 32) and assume $R_{\text{half}} = 2R_{\text{CO}_2}$. For each value of R_{crit} , we identify the value of $k_{50 \text{ Myr}}$ that the same silicate-rock weathering rate produced when R_{CO_2} is at a value of 1,500 p.p.m., and denote it $k_{50 \text{ Myr}, R_{\text{crit}}}$. We then write the equation:

$$f_{\text{sw}, 50 \text{ Myr}} = A_{\text{rel}} \times k_{50 \text{ Myr}, R_{\text{crit}}} \times (f_{\text{land plants}, R_{\text{crit}}})^{0.4} \quad (3)$$

where A_{rel} represents the weatherable mineral surface area relative to that at 50 Myr ago. For Fig. 3, the value of A_{rel} was increased to represent the increase in reactive silicate-mineral surface area and atmospheric R_{CO_2} was solved by substituting equation (2) into equation (3).

Full Methods and any associated references are available in the online version of the paper at www.nature.com/nature.

Received 16 February; accepted 29 April 2009.

- Chung, S.-L. *et al.* Tibetan tectonic evolution inferred from spatial and temporal variations in post-collisional magmatism. *Earth Sci. Rev.* **68**, 173–196 (2005).
- Rowley, D. B. & Currie, B. S. Palaeo-altimetry of the late Eocene to Miocene Lunpola basin, central Tibet. *Nature* **439**, 677–681 (2006).
- DeCelles, P. G. *et al.* High and dry in central Tibet during the Late Oligocene. *Earth Planet. Sci. Lett.* **253**, 389–401 (2007).
- Gillis, R. J., Horton, B. K. & Grove, M. Thermochronology, geochronology, and upper crustal structure of the Cordillera Real: implications for Cenozoic exhumation of the central Andean plateau. *Tectonics* **25**, doi:10.1029/2005TC001887 (2006).
- Blisniuk, P. M. & Stern, L. A. Stable isotope paleoaltimetry: a critical review. *Am. J. Sci.* **305**, 1033–1074 (2005).
- Garzione, C. N., Molnar, P., Libarkin, J. C. & MacFaden, B. J. Rapid late Miocene rise of the Bolivian altiplano: evidence for removal of mantle lithosphere. *Earth Planet. Sci. Lett.* **241**, 543–556 (2006).
- Reusch, D. N. & Maasch, K. A. in *Tectonic Boundary Conditions for Climate Reconstruction* (eds Crowley, T. J. & Burke, K. C.) 261–276 (Oxford Monographs on Geology and Geophysics, No. 38, Oxford University Press, 1998).
- Pagani, M., Zachos, J. C., Freeman, K. H., Tipler, B. & Bohaty, S. Marked decline in atmospheric carbon dioxide concentrations during the Paleogene. *Science* **309**, 600–603 (2005).
- Moulton, K. L., West, J. & Berner, R. A. Solute flux and mineral mass balance approaches to the quantification of plant effects on silicate weathering. *Am. J. Sci.* **300**, 539–570 (2000).
- Andrews, J. A. & Schlesinger, W. H. Soil CO_2 dynamics, acidification and chemical weathering in a temperate forest with experimental CO_2 enrichment. *Glob. Biogeochem. Cycles* **15**, 149–162 (2001).
- Berner, E. K., Berner, R. A. & Moulton, K. L. Plants and mineral weathering: present and past. *Treatise Geochem.* **5**, 169–188 (2003).
- Zachos, J., Pagani, M., Sloan, L., Thomas, E. & Billups, K. Trends, rhythms, and aberrations in global climate: 65 Ma to present. *Science* **292**, 686–693 (2001).
- Pearson, P. N. & Palmer, M. R. Middle Eocene seawater pH and atmospheric carbon dioxide concentrations. *Science* **284**, 824–826 (1999).
- Kürschner, W. M., Kvacek, Z. & Dilcher, D. L. The impact of Miocene atmospheric carbon dioxide on climate and the evolution of terrestrial ecosystems. *Proc. Natl Acad. Sci. USA* **105**, 449–453 (2008).
- Berner, R. A. & Kothavala, Z. GEOCARB III: a revised model of atmospheric CO_2 over Phanerozoic time. *Am. J. Sci.* **301**, 182–204 (2001).
- Cogné, J. & Humler, E. Trends and rhythms in global seafloor generation rate. *Geochem. Geophys. Geosyst.* **7**, doi:10.1029/2005GC001148 (2004).
- Engelbreton, D. C., Kelley, K. P., Cashman, H. J. & Richards, M. A. 180 million years of subduction. *Geol. Soc. Am. Today* **2**, 93–95 (1992).
- Lowenstein, T. K., Timofeff, M. N., Brennan, S. T., Hardie, L. A. & Demicco, R. V. Oscillations in Phanerozoic seawater chemistry: evidence from fluid inclusions. *Science* **294**, 1086–1088 (2001).
- Rowley, D. B. Rate of plate creation and destruction: 180 Ma to present. *Geol. Soc. Am. Bull.* **114**, 927–933 (2002).
- Kerrick, D. M. & Caldeira, K. Metamorphic CO_2 degassing from orogenic belts. *Chem. Geol.* **145**, 213–232 (1998).
- Kerrick, D. M. & Caldeira, K. Was the Himalayan orogen a climatically significant coupled source and sink for atmospheric CO_2 during the Cenozoic? *Earth Planet. Sci. Lett.* **173**, 195–203 (1999).
- Zeebe, R. E. & Caldeira, K. Close mass balance of long-term carbon fluxes from ice-core CO_2 and ocean chemistry records. *Nature Geosci.* doi:10.1038/ngeo185 (2008).
- West, J., Galy, A. & Bickle, M. Tectonic and climatic controls on silicate weathering. *Earth Planet. Sci. Lett.* **235**, 211–228 (2005).
- Pearcy, R. W. & Ehleringer, J. Comparative ecophysiology of C_3 and C_4 plants. *Plant Pop. Biol.* **7**, 1–13 (1984).
- Ehleringer, J. R., Cerling, T. E. & Helliker, B. R. C_4 photosynthesis, atmospheric CO_2 , and climate. *Oecologia* **112**, 285–299 (1997).
- Beerling, D. J. & Woodward, F. *Vegetation and the Terrestrial Carbon Cycle: Modelling the First 400 Million Years* (Cambridge University Press, 2001).
- Jacobs, B. F., Kingston, J. D. & Jacobs, L. L. The origin of grass-dominated ecosystems. *Ann. Missouri Bot. Garden* **86**, 90–643 (1999).
- Taylor, L. L. *et al.* Biological weathering and the long-term carbon cycle: integrating mycorrhizal evolution and function into the current paradigm. *Geobiology* **7**, 171–191 (2009).
- Campbell, C. D., Sage, R. F., Kocacinar, F. & Way, D. A. Estimation of the whole-plant CO_2 compensation point of tobacco (*Nicotiana tabacum* L.). *Glob. Change Biol.* **11**, 1956–1967 (2005).
- Lin, G. *et al.* Ecosystem carbon exchange in two terrestrial ecosystem mesocosms under changing atmospheric CO_2 concentrations. *Oecologia* **119**, 97–108 (1999).

Supplementary Information is linked to the online version of the paper at www.nature.com/nature.

Acknowledgements Conversations with C. Garzione, M. Hren, J. Berry, and C. Osborne were greatly appreciated. This work was supported, in part, by NSF grant OCE-0095734 (to M.P.) and DOE grant DE-FG02-01ER15173 (to R.A.B.). D.J.B. gratefully acknowledges funding from the Leverhulme Trust and Natural Environment Research Council (NE/E015190/1), and through a Royal Society-Wolfson Research Merit Award. M.P. acknowledges support from the Yale Climate and Energy Institute.

Author Contributions All four authors were involved in drafting the paper, led by M.P. K.C. and R.A.B. developed and applied procedures for modelling biotic weathering by land plants, and D.J.B. undertook the leaf-scale and global-scale simulations of vegetation processes.

Author Information Reprints and permissions information is available at www.nature.com/reprints. Correspondence and requests for materials should be addressed to M.P. (mark.pagani@yale.edu).

METHODS

Leaf gas exchange calculations. Effects of temperature and atmospheric CO₂ on rates of leaf photosynthesis and photorespiration (Supplementary Fig. 1) were calculated using a mechanistic model of leaf carbon assimilation³³, with maximum rates of carboxylation and electron transport of 63 $\mu\text{mol m}^{-2} \text{s}^{-1}$ and 126 $\mu\text{mol m}^{-2} \text{s}^{-1}$, respectively. All calculations assumed a typical intercellular CO₂ concentration (0.7) multiplied by atmospheric CO₂ (ref. 34), with an irradiance of 1,000 $\mu\text{mol photons m}^{-2} \text{s}^{-1}$. The equations for rates of oxygenation and carboxylation (refs 26, 35) and the temperature sensitivities of relevant biochemical parameters³⁶ have previously been established.

The results of our leaf gas exchange calculations indicate a high sensitivity of photorespiratory CO₂ release rates to increases in temperature³⁵. The calculations further show that high-temperature effects are greatest at low (200 p.p.m.) atmospheric CO₂ concentrations and become diminished as CO₂ concentrations increase (Supplementary Fig. 1). Overall, these results, and the biochemical rationale for them described in the main text, underpin our hypothesis that as atmospheric CO₂ concentrations decline towards 200 p.p.m. in the long-term, photorespiratory CO₂ releases increase, to an extent enhanced by climatic warming.

Sheffield Dynamic Global Vegetation Model simulations. The Sheffield Dynamic Global Vegetation Model (SDGVM) simulates global patterns of net primary production (NPP), leaf area index (LAI) and the distribution of plant functional types from monthly inputs of temperature, precipitation, relative humidity and cloudiness, and global data sets of soil texture^{26,37}. Core modules of net photosynthesis, stomatal conductance, canopy transpiration, uptake of mineralized nitrogen and responses of these attributes to changes in soil water supply are detailed and rigorously evaluated against field observations^{26,37}. A key feature of the model is the coupling of above- and belowground carbon and nitrogen cycles. Litter production influences soil carbon and nitrogen pools via the Century soil nutrient cycling model³⁸, which in turn feed back to influence aboveground primary production.

SDGVM local- and global-scale predictions of NPP, LAI and global plant functional type distributions have been extensively and successfully evaluated against a wide range of measurements and field observations²⁶. SDGVM accurately reproduces actual site-specific observations and measurements of NPP and LAI for a range of forest types in the tropics and throughout Europe and North America^{26,37}. Simulations forcing SDGVM with an observed (ISLSCP) and simulated (HadCM2) modern-day 1° × 1° (latitude × longitude) climatology further indicate close global-scale agreement in both cases between calculated LAI values and satellite measurements of the normalized difference vegetation index, a measure of changes in the flux density of red light and far-red light²⁶. The SDGVM-simulated geographical distribution of plant functional types is in close agreement with maps of 'actual' vegetation²⁶. Global terrestrial NPP for the contemporary climate and CO₂ is estimated with SDGVM to be 62 Gt C yr⁻¹, in agreement with satellite-based estimates of about 55–60 Gt C yr⁻¹ (ref. 39).

The sensitivity of NPP predictions of SDGVM to CO₂ and climate is similar to those of other dynamic vegetation models^{40,41}. The CO₂ fertilization response of

NPP compares favourably to that reported in Free Air Carbon Dioxide Enrichment experiments for temperate forested sites in North America and Italy; a 19% (model) versus a 23% (observed) increase between 367 and 550 p.p.m. (ref. 42).

Global simulations of the geographical distribution of plant functional types (which depends on NPP, LAI and minimum temperature thresholds) for the cool, low-CO₂ glacial climate of the last ice age are in general agreement with reconstructed vegetation patterns (geographical locations and areal extent) from palaeo-evidence at the global scale and from palynological evidence for North America²⁶. Canopy LAI reductions and changes in forest cover in response to glacial CO₂ and climate are comparable to those of the TRIFFID⁴³ and BIOME3⁴⁴ dynamic global vegetation models. This indicates similar sensitivities to changes in the balance between canopy transpiration and NPP under a low atmospheric CO₂ concentration.

31. Berner, R. A. GEOCARBSULF; a combined model for Phanerozoic atmospheric O₂ and CO₂. *Geochim. Cosmochim. Acta* **70**, 5653–5664 (2006).
32. Volk, T. Feedbacks between weathering and atmospheric CO₂ over the last 100 million years. *Am. J. Sci.* **287**, 763–779 (1987).
33. Farquhar, G. D., von Caemmerer, S. & Berry, J. A. A biochemical model of photosynthetic CO₂ assimilation in leaves of C₃ species. *Planta* **149**, 78–90 (1980).
34. von Caemmerer, S. & Evans, J. R. Determination of the average partial pressure of CO₂ in chloroplasts from leaves of several C₃ plants. *Aust. J. Plant Physiol.* **18**, 287–305 (1991).
35. Sharkey, T. D. Estimating the rate of photorespiration in leaves. *Physiol. Plant.* **73**, 147–152 (1988).
36. Bernacchi, C. J., Singaas, E. L., Pimentel, C., Portis, A. R. & Long, S. P. Improved temperature response functions for models of Rubisco-limited photosynthesis. *Plant Cell Environ.* **24**, 253–259 (2001).
37. Woodward, F. I., Smith, T. M. & Emanuel, W. R. A global land primary productivity and phytogeography model. *Glob. Biogeochem. Cycles* **9**, 471–490 (1995).
38. Parton, W. J. *et al.* Observations and modeling of biomass and soil organic matter dynamics for the grassland biome worldwide. *Glob. Biogeochem. Cycles* **7**, 785–809 (1993).
39. Running, S. W. *et al.* A continuous satellite-derived measure of global terrestrial primary production. *Bioscience* **54**, 547–560 (2004).
40. Hickler, T. *et al.* CO₂ fertilization in temperate FACE experiments not representative of boreal and tropical forests. *Glob. Change Biol.* **14**, 1–12 (2008).
41. Sitch, S. *et al.* Evaluation of the terrestrial carbon cycle, future plant geography and climate-carbon cycle feedbacks using five dynamic global vegetation models (SDGVMs). *Glob. Change Biol.* **14**, 2015–2039 (2008).
42. Woodward, F. I. & Kelly, C. K. Responses of global plant diversity capacity to changes in carbon dioxide concentration and climate. *Ecol. Lett.* **11**, 1229–1237 (2008).
43. Cowling, S. A. *et al.* Simulated glacial and interglacial vegetation across Africa: implications for species phylogenies and trans-African migration of plants and animals. *Glob. Change Biol.* **14**, 827–840 (2008).
44. Cowling, S. A., Maslin, M. A. & Sykes, M. T. Paleovegetation simulations of lowland Amazonia and implications for neotropical allopatry and speciation. *Quat. Res.* **55**, 140–149 (2001).

Seismic reflection images of a near-axis melt sill within the lower crust at the Juan de Fuca ridge

J. Pablo Canales¹, Mladen R. Nedimović^{2,3}, Graham M. Kent⁴, Suzanne M. Carbotte³ & Robert S. Detrick¹

The oceanic crust extends over two-thirds of the Earth's solid surface, and is generated along mid-ocean ridges from melts derived from the upwelling mantle¹. The upper and middle crust are constructed by dyking and sea-floor eruptions originating from magma accumulated in mid-crustal lenses at the spreading axis^{2–6}, but the style of accretion of the lower oceanic crust is actively debated⁷. Models based on geological and petrological data from ophiolites propose that the lower oceanic crust is accreted from melt sills intruded at multiple levels between the Moho transition zone (MTZ) and the mid-crustal lens^{8–11}, consistent with geophysical studies that suggest the presence of melt within the lower crust^{12–16}. However, seismic images of molten sills within the lower crust have been elusive. Until now, only seismic reflections from mid-crustal melt lenses^{2,17,18} and sills within the MTZ have been described¹⁹, suggesting that melt is efficiently transported through the lower crust. Here we report deep crustal seismic reflections off the southern Juan de Fuca ridge that we interpret as originating from a molten sill at present accreting the lower oceanic crust. The sill sits 5–6 km beneath the sea floor and 850–900 m above the MTZ, and is located 1.4–3.2 km off the spreading axis. Our results provide evidence for the existence of low-permeability barriers to melt migration within the lower section of modern oceanic crust forming at intermediate-to-fast spreading rates, as inferred from ophiolite studies^{9,10}.

The Juan de Fuca ridge (JdFR) is a mid-ocean ridge in the northeast Pacific (Fig. 1), where spreading occurs at intermediate rates (56 mm yr⁻¹; ref. 20). The results presented here arise from a two-dimensional seismic reflection survey conducted in 2002 along the JdFR and its flanks^{19,21,22}. This survey imaged the top of an axial magma chamber (AMC) beneath all JdFR segments at depths of ~2–3 km (ref. 22). Reflections from the crust–mantle boundary (the Moho) were observed throughout much of the survey at 2,080 ± 100 ms crustal two-way travel time (TWTT), as well as sub-Moho reflections interpreted as gabbro lenses and possibly melt accumulations¹⁹ (Fig. 1).

Along the Cleft segment of the JdFR (Fig. 1), the top of the AMC is 2.0–2.3 km deep²¹ (Fig. 2b, f), and the Moho is imaged intermittently throughout the area²¹. Crustal travel times to the Moho decrease away from the axis and decrease northward, from ~2,550 ms at the south end to ~2,300 ms at the north end²¹ (Fig. 2a and Supplementary Fig. 1a). The exception to these general trends is a pronounced ~11-km-long area of anomalously large crustal travel times located ~3–5 km east of the spreading axis (Supplementary Fig. 1a), suggesting local crustal thickening, elevated crustal temperatures, presence of melt above the Moho, or a combination of any of these factors.

At the southern end of this anomaly, profiles 75 and 40 (Fig. 1) show a reflection event at 2,000 ms below the sea floor (Fig. 2a, b, d and h).

This event is located 1.4–3.2 km to the east of the spreading axis, in 50–114-kyr-old crust²⁰, extending ~2.4 km and ~1.8 km in the ridge-parallel and ridge-perpendicular directions, respectively. The reflection event must originate at depths of 5–6 km (for an average crustal velocity of 5–6 km s⁻¹ above this reflector) from layering that is likely to be at least ~100-m thick in order to be detected by our signal (which has a dominant frequency of 12 Hz and a dominant wavelength of 400–500 m at those depths). The origin of this event could be an anomalous Moho, a frozen sill of ultramafic material embedded in gabbros (such as a wehrlite intrusion²³), or a molten sill. On the basis of its amplitude variation with offset (AVO) response (Fig. 3) and on other considerations discussed below, we interpret this event as originating from a lower-crustal melt lens (LCML).

The possibility that the reflection event is an anomalously shallow Moho seems unlikely, because this implies abrupt crustal thinning by either a reduction in magma supply in a small area that is otherwise surrounded by large Moho travel times (Supplementary Fig. 1a), or

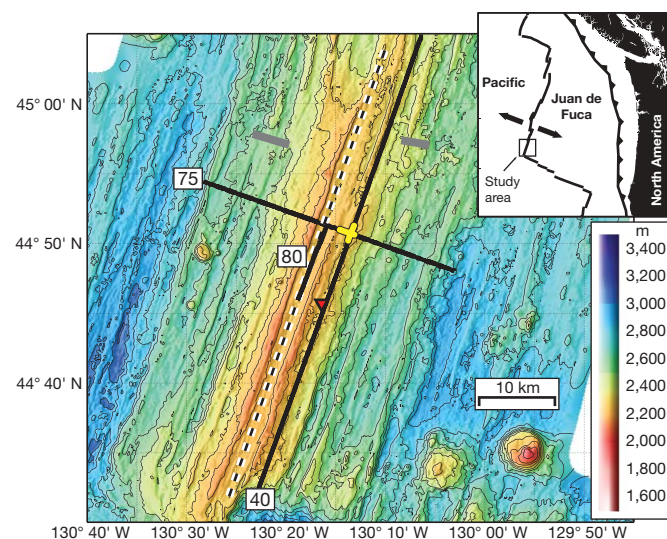


Figure 1 | Seismic reflection profiles located over a bathymetric map of the Cleft segment of the southern JdFR. Colours represent sea-floor depth in metres, with contours every 100 m. Numbered solid lines are seismic profiles shown in Figs 2 and 4. Dashed line locates the spreading axis. Yellow lines locate the plan-view extent of the LCML reflection event shown in Figs 2 and 4. Thick grey lines locate sub-Moho reflection events identified¹⁹ in the vicinity of Cleft segment. Red triangle locates low-temperature hydrothermal vents observed on the sea floor³⁰. Top-right inset shows location of the study area in the northeast Pacific. Names indicate tectonic plates; arrows indicate direction of sea-floor spreading.

¹Department of Geology and Geophysics, Woods Hole Oceanographic Institution, Woods Hole, Massachusetts 02543, USA. ²Department of Earth Sciences, Dalhousie University, Halifax, Nova Scotia B3H 4J1, Canada. ³Lamont-Doherty Earth Observatory of Columbia University, Palisades, New York 10964, USA. ⁴Scripps Institution of Oceanography, University of California San Diego, La Jolla, California 92093, USA.

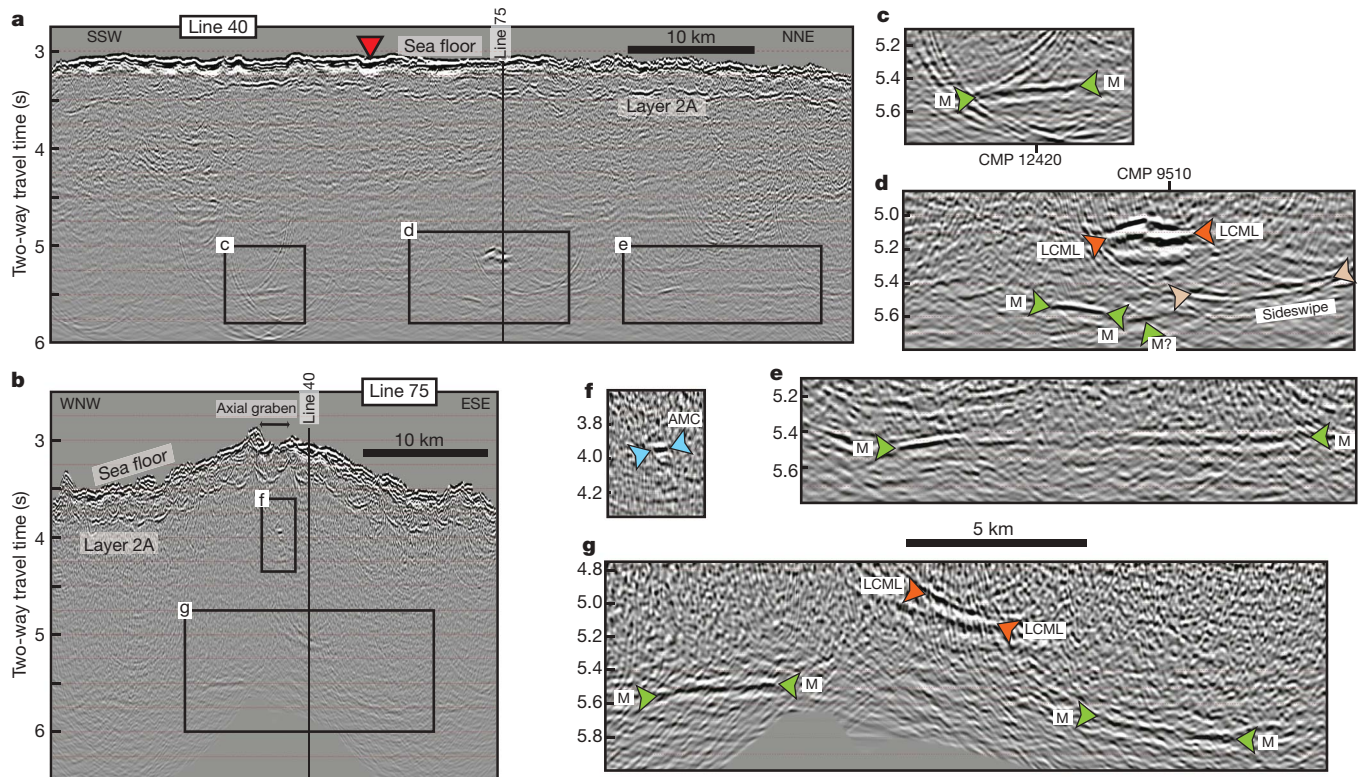


Figure 2 | Migrated seismic reflection profiles 40 and 75. **a**, Ridge-parallel profile 40 is located 3.3 km to the east of the spreading axis (Fig. 1). Vertical line, intersection with profile 75. Boxed areas are shown in detail in **c**, **d** and **e**. Red triangle, low-temperature hydrothermal vents observed on the sea floor³⁰. **b**, Ridge-perpendicular profile 75. Vertical line, intersection with profile 40. Spreading axis is within the labelled axial graben. Boxed areas are shown in detail in **f** and **g**. In **c–g**, main events are indicated with coloured arrows: top of axial magma chamber (AMC), lower-crustal melt lens

(LCML) and Moho (M). Vertical axes show two-way travel time in seconds for all panels. Scale bar at lower right is for **c–g**. Locations of CMP 12420 (Fig. 3a) and 9510 (Fig. 3b) are labelled in **c** and **d**, respectively. The event labelled as sideswipe in **d** is interpreted as such based on its steep hyperbolic diffraction character observed in the stacked image (Supplementary Fig. 2a, d), as well as in its higher frequency content relative to the lower-frequency, flat-lying Moho events. Unmigrated stack versions of the images shown here are presented in Supplementary Fig. 2.

by tectonic thinning or uplifting, for which there is no evidence in the sea-floor morphology. Average crustal TWTT to Moho observed along line 40 is 2,256 ms (Fig. 2a, c–e), which is 256 ms more than for the LCML event (Fig. 2d). In addition, a weak Moho event, which can be recognized in the pre-stack gathers at far offsets (Fig. 3b), appears to extend beneath the LCML (Fig. 2d). This indicates that the top of the LCML is located within the lower crust, about 850–900 m above the Moho (for a lower-crustal velocity of 6.8 km s^{-1}).

The LCML event displays a complex reflection pattern with two positive (black) peaks compared to one from the Moho reflection (Fig. 2d, g). This suggests that the LCML event was produced by a complex velocity structure (rather than a simple velocity increase/decrease), possibly associated with two or more sills or the roof and floor of a single sill. In this case, the polarity of the reflection of the LCML may not be useful to discriminate between positive or negative impedance contrasts, as one would expect from the ideal case of a simple sill intrusion¹⁸. In a first-order approximation, both the Moho and a frozen ultramafic sill should have identical impedance contrasts because they both represent ultramafic material sitting below gabbros. Therefore, minor amplitude interference effects aside, the comparison of the AVO responses of Moho and LCML events (Fig. 3d–f) observed in pre-stack gathers (Fig. 3a, b) can help determine if the LCML corresponds to a positive or a negative velocity contrast. Figure 3d–f shows that the P-wave reflecting off the LCML ($P_{\text{LCML}}P$) has higher amplitude than the Moho for offsets <3 km, and that the amplitude of the $P_{\text{LCML}}P$ decays more rapidly between 3 and 5 km offset while the Moho amplitude shows less variation across all offsets (Fig. 3f). The observed AVO response of the LCML resembles the predicted variation with offset of the reflection

coefficient for a P-wave reflecting off a low-velocity molten sill (Fig. 3f). In contrast, the observed AVO response of the Moho event is more consistent with the predicted variation with offset of the reflection coefficient for a P-wave reflecting off a high-velocity Moho or ultramafic sill (Fig. 3f). This suggests that the LCML reflection corresponds to a molten sill.

For a fully molten sill, one expects to observe at far offsets significant converted S-wave energy reflecting off the LCML¹⁸ ($P_{\text{LCML}}S$, Supplementary Fig. 3). We do not observe high-amplitude S-wave arrivals in the data, but we recognize a weak arrival at offsets larger than ~4.5 km between ~6.0 and 6.2 s, where the $P_{\text{LCML}}S$ is expected to be present (Fig. 3b, c). Although the weak amplitude of the $P_{\text{LCML}}S$ is more consistent with a ‘mush’ sill than a fully molten one (Supplementary Fig. 3), the observed AVO response of the $P_{\text{LCML}}P$ event suggests a melt-rich sill (other factors such as attenuation may be affecting the strength of the $P_{\text{LCML}}S$ event). However our data cannot distinguish between mush at the crystal scale and a set of molten sills that are smaller than the dominant wavelength of the seismic signal and encased in solid cumulates.

The largest crustal TWTT to Moho at the southern edge of the LCML event is 2,508 ms, which is 252 ms more than the average crustal TWTT observed along line 40. Assuming that this Moho travel-time anomaly is entirely caused by thickening of the lower crust beneath the LCML, it implies a local thickness anomaly of ~850–900 m (for a lower-crustal velocity of 6.8 km s^{-1}), placing the crust–mantle boundary 1,700–1,800 m beneath the LCML. Alternatively, the Moho travel-time anomaly could be due to a 45–50% reduction in P-wave velocity, implying a completely molten lowermost crust regardless of how melt is distributed and interconnected²⁴. These

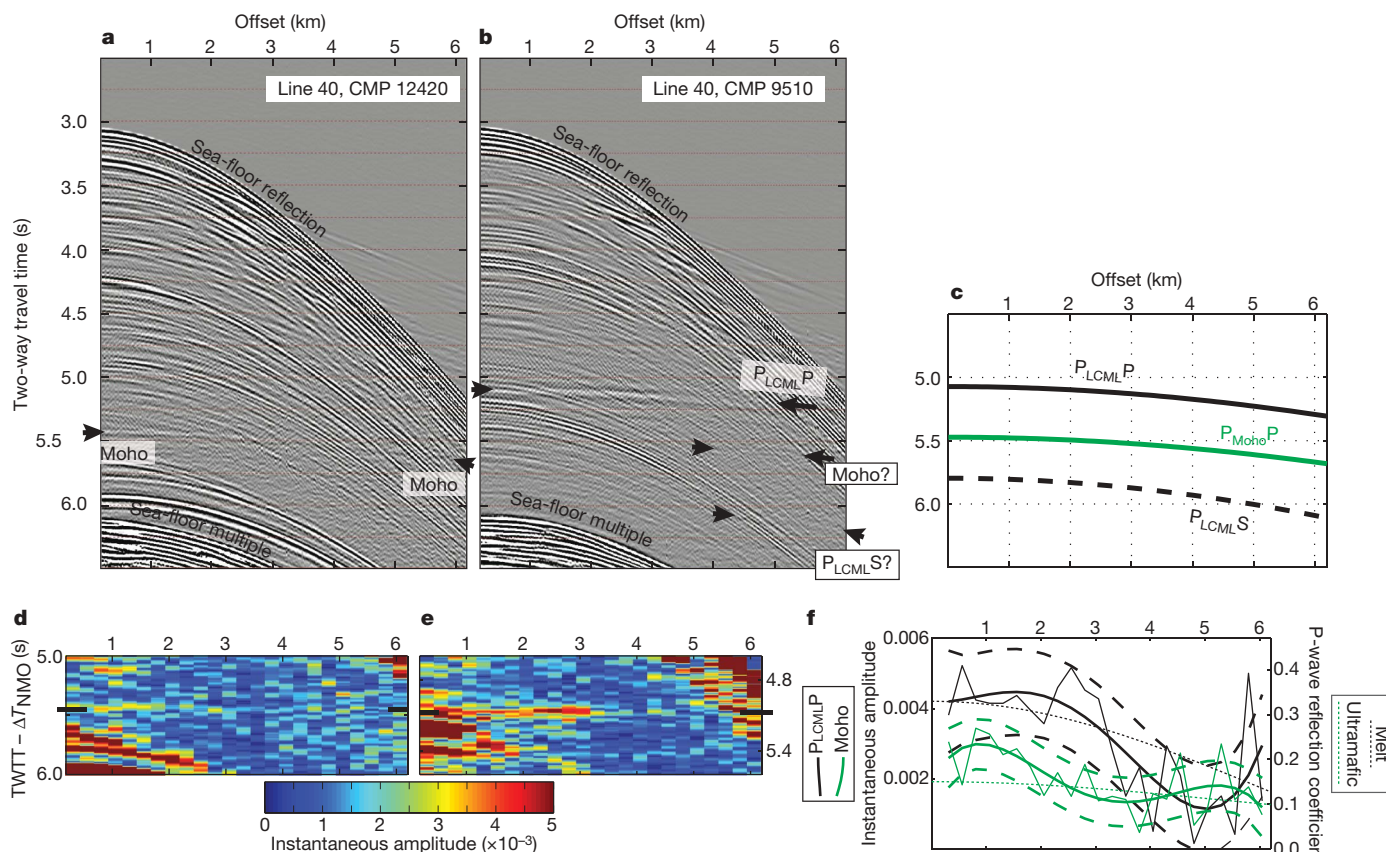


Figure 3 | Observed and modelled reflection amplitudes and travel times. **a, b**, CMP supergathers 12420 (**a**) and 9510 (**b**) from profile 40 (locations in Fig. 2c, d). P waves reflecting off the Moho and the LCML ($P_{LCML}P$) are indicated. Weak but coherent arrivals are observed in CMP 9510 at ~ 4.0 – 5.5 km offset between ~ 5.5 and 5.6 s, and at far offsets (>4.5 km) between ~ 6.0 and 6.2 s, and are tentatively interpreted as Moho reflections and S-converted waves reflecting off the LCML ($P_{LCML}S$), respectively. (The $P_{LCML}S$ would be converted back to P at the sea floor to be detected by the hydrophone streamer.) **c**, Predicted travel-time curves for Moho reflection, $P_{LCML}P$ and $P_{LCML}S$ (Methods). **d, e**, Instantaneous amplitude of CMP supergathers 12420 (**d**) and 9510 (**e**) within a 1-s window around the Moho and $P_{LCML}P$ arrivals, respectively (Methods). Vertical axis shows two-way travel time corrected for normal move-out (ΔT_{NMO}). **f**, AVO analysis of Moho and $P_{LCML}P$ events (green and black lines, respectively); amplitude

scale at left vertical axis. Thin solid lines, instantaneous amplitudes versus offset at a constant time of 5.445 s for CMP 12420, and 5.075 s for CMP 9510 (short thick lines in **d** and **e**, respectively). Thick solid lines, least-squares cubic fits (dashed lines are 50% confidence limits of the polynomial fits). The increase in instantaneous amplitude for CMP 9510 at offsets >5 km is due to interference of high-amplitude, steeply dipping sea-floor reflections and diffractions with the $P_{LCML}P$ event, and it does not accurately represent the AVO response of this event. Predicted P-wave reflection coefficients versus source–receiver offset (amplitude scale at right vertical axis) are shown for two scenarios (Methods): the lower medium is a molten sill (short-dashed black line, ‘melt’), or it represents mantle or a solid ultramafic sill (short-dashed green line, ‘ultramafic’). Horizontal axes in all panels are source–receiver offset.

two scenarios are end-member possibilities; most probably the travel-time anomaly below the LCML is due to both presence of melt and local thickening of the lower crust.

Melt migration from the mantle to the crust is thought to be a process of focused porous flow^{25,26}, although this may change at the MTZ as melts enter a conductively cooling regime and build up permeability barriers by crystallizing plagioclase, leading to the emplacement of melt sills within the MTZ¹¹. In contrast, porous flow may not be the dominant mechanism of melt migration above the MTZ²⁷, and lower-crustal sills could be fed by focused flow along channels originating at the MTZ melt sills^{10,11}. Several mechanisms have been proposed for the creation of permeability barriers that can allow the emplacement of melt sills at multiple levels within the lower crust, such as the presence of anorthosite bands, plagioclase-clinopyroxene-orthopyroxene saturation within crystallizing gabbros, or formation of low-porosity cumulate gabbros after melt extraction¹⁰. Our data cannot discriminate between these processes; however, the observation that the LCML is emplaced a few kilometres off the spreading axis allows us to hypothesize that here, the melt sill could have formed at a permeability barrier associated with a contrasting thermal regime above it, in a similar manner to the emplacement of the axial mid-crustal melt lens^{28,29}. The axial region of

fast-spreading ridges is characterized by a 5–7-km-wide zone of low seismic velocities¹⁴. The lateral boundaries of this region are interpreted as steep isotherms controlled by the transition from shallow hydrothermal circulation at the ridge axis to deep-penetrating hydrothermal fluid pathways just a few kilometres off the spreading axis¹⁴. Thus we interpret the off-axis deep melt sill imaged by our data to represent a deep freezing horizon that roughly follows the boundaries of an axial low-velocity zone.

The imaged LCML is wider than the shallow AMC lens (Fig. 2f, h and Fig. 4). However its along-axis extent is much more limited than the AMC (Fig. 4b), which extends along tens of kilometres beneath the ridge²¹. The along-axis continuity of AMC lenses observed at many spreading centres implies that mid-crustal melt sills are relatively steady-state features frequently replenished with magma from below. Therefore the limited spatial extent of the LCML, together with the absence of similarly sized lower-crustal reflections in the only three-dimensional seismic reflection study of a fast-spreading ridge published to date¹², suggests that lower-crustal melt sills are probably less frequently fed than AMC lenses, and/or that the LCML imaged in our data is uncommonly large.

The sea floor in the area where profiles 40 and 75 intersect is flatter, smoother, and has higher reflectivity than the surroundings

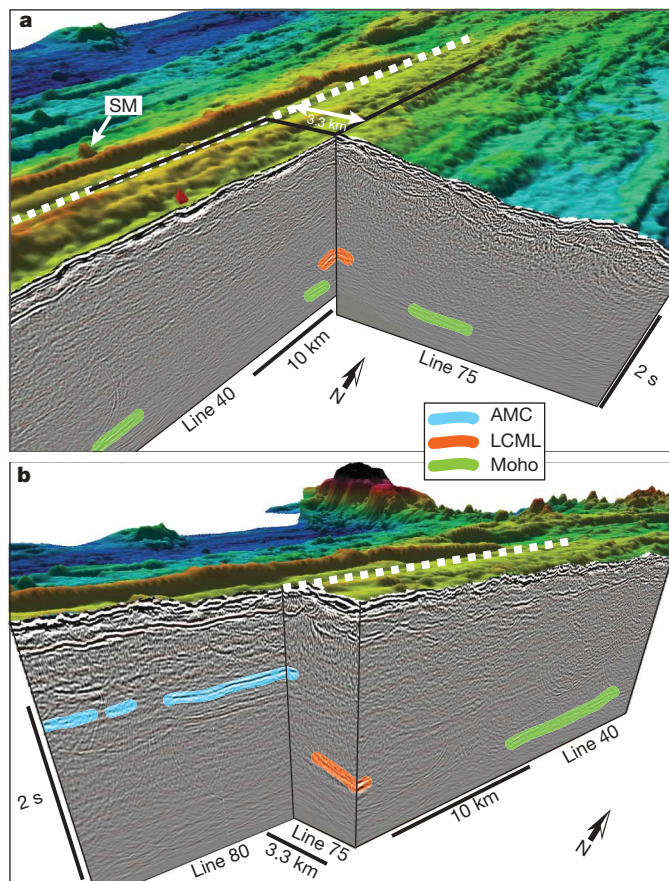


Figure 4 | Three-dimensional perspective of crustal structure and sea-floor topography. **a**, Southern and eastern parts of profiles 40 and 75, respectively, are shown hanging from the sea-floor topography. Moho and LCML events identified in Fig. 2 are emphasized with colour markers. White dashed line, spreading axis. SM, young-looking, near-axis seamount with chemistry distinct from the axial lava flows³⁰. Red triangle, low-temperature hydrothermal vents observed on the sea floor³⁰. Solid lines, profiles shown in **b**. **b**, Profile 80, northern part of profile 40, and central section of profile 75, all shown hanging from the sea-floor topography. Moho, LCML and AMC events identified in Fig. 2 are emphasized with colour markers. White dashed line, spreading axis, coincident with profile 80.

(Supplementary Fig. 1b–d), suggesting younger terrain and repaving of the sea floor. Lava flows up to 4 km off-axis emanating from ridge-parallel faults and fissures have been identified along the Cleft segment and interpreted as erupting from the edges of the AMC lens³⁰. In addition, the axial summit graben of Cleft segment is flanked by some small, young-looking near-axis seamounts with chemistry distinct from the axial lavas (Fig. 4a)³⁰. Observations by submersible vehicles have also reported the presence of low-temperature hydrothermal venting ~3.3 km east of the spreading axis³⁰ and ~10 km to the south of the LCML (Figs 1, 2a, 4a). Our discovery of lower-crustal melt sills at similar distances from the spreading axis in the same area suggests that deep lower-crustal melt lenses could also contribute to construction of the upper crust by off-axis sea-floor eruptions, and provide heat for off-axis hydrothermal circulation.

Our data provide evidence for a molten sill at present accreting the lower oceanic crust at the JdFR. The location of the sill within 50–114-kyr-old crust suggests that a crustal column formed at this section of the JdFR represents magmatic accretion over a time period of at least 100 kyr. Near-axis lower-crustal reflections have been previously reported at the East Pacific Rise³¹. However, their along-axis extent has not been explored and they were not interpreted as melt sills³¹. Our results imply the existence of low-permeability barriers to melt migration within the lower oceanic crust, in agreement with models based on observations at ophiolites^{9,10}, and indicate that

melt migration from the MTZ to the shallow AMC lens may not necessarily be as efficient as recently inferred from three-dimensional seismic reflection data¹². As the palaeo-conditions under which crustal sections exposed at ophiolites were formed are in most cases difficult to determine, there is some ambiguity about the extent to which ophiolites are analogues to modern oceanic crust³². Our results thus support the idea that some of the lower-crustal processes inferred from ophiolite settings do occur during the accretion of modern oceanic crust at intermediate-to-fast spreading rates. However, the uniqueness and limited extent of the imaged LCML compared to the mid-crustal melt lens suggests that large lower-crustal melt sills are rare and probably contribute a small fraction to the overall thickness of the lower crust, as suggested by numerical models and petrological constraints^{7,33}.

METHODS SUMMARY

Data processing. Acquisition parameters are described in refs 19, 21. Pre-stack processing consisted of *f-k* filtering, sorting into 80-fold common-midpoint (CMP) gathers, amplitude correction for spherical divergence, trace editing, band-pass filtering (2–7–20–40 Hz), velocity analysis and normal move-out correction. After stacking, data were muted below first sea-floor multiple, time migrated using stacking velocities, and muted above the sea-floor reflection. CMP supergathers were constructed by sorting 30 consecutive CMP gathers into fivefold constant-offset gathers, partial stacking, and band-pass filtering (2–7–20–40 Hz). **AVO analysis.** Instantaneous amplitudes were calculated on CMP supergathers after normal move-out correction to flatten the seismic events and partial stacking of traces within 250-m bins.

Full Methods and any associated references are available in the online version of the paper at www.nature.com/nature.

Received 23 June 2008; accepted 27 April 2009.

1. Forsyth, D. W. in *Mantle Flow and Melt Generation at Mid-Ocean Ridges* (eds Phipps Morgan, J., Blackman, D. K. & Sinton, J. M.) 1–65 (Geophysical Monograph Series Vol. 71, AGU, 1992).
2. Detrick, R. S. *et al.* Multi-channel seismic imaging of a crustal magma chamber along the East Pacific Rise. *Nature* **326**, 35–41 (1987).
3. Herron, T. J. *et al.* Structure of the East Pacific Rise crest from multichannel seismic reflection data. *J. Geophys. Res.* **83**, 798–804 (1978).
4. Karson, J. A. Geologic structure of the uppermost oceanic crust created at fast-to intermediate-rate spreading centers. *Annu. Rev. Earth Planet. Sci.* **30**, 347–384 (2002).
5. Perfit, M. R. & Chadwick, W. W. in *Faulting and Magmatism at Mid-Ocean Ridges* (eds Buck, W. R. *et al.*) 59–115 (Geophysical Monograph Series Vol. 106, AGU, 1998).
6. Sinton, J. M. & Detrick, R. S. Mid-ocean ridge magma chambers. *J. Geophys. Res.* **97**, 197–216 (1992).
7. MacLennan, J., Hulme, T. & Singh, S. C. Thermal models of oceanic crustal accretion: linking geophysical, geological and petrological observations. *Geochem. Geophys. Geosyst.* **5**, Q02F25, doi:10.1029/2003GC000605 (2004).
8. Kelemen, P. B., Koga, K. & Shimizu, N. Geochemistry of gabbro sills in the crust-mantle transition zone of the Oman ophiolite: implications for the origin of the oceanic lower crust. *Earth Planet. Sci. Lett.* **146**, 475–488 (1997).
9. Boudier, F., Nicolas, A. & Ildefonse, B. Magma chambers in the Oman ophiolite: fed from the top and the bottom. *Earth Planet. Sci. Lett.* **144**, 239–250 (1996).
10. Kelemen, P. B. & Aharonov, E. in *Faulting and Magmatism at Mid-Ocean Ridges* (eds Buck, W. R. *et al.*) 267–289 (Geophysical Monograph Series Vol. 106, AGU, 1998).
11. Korenaga, J. & Kelemen, P. B. Origin of gabbro sills in the Moho transition zone of the Oman ophiolite: implications for magma transport in the oceanic lower crust. *J. Geophys. Res.* **102**, 27729–27749 (1997).
12. Singh, S. C. *et al.* Seismic reflection images of the Moho underlying melt sills at the East Pacific Rise. *Nature* **442**, 287–290 (2006).
13. Crawford, W. C. & Webb, S. C. Variations in the distribution of magma in the lower crust and at the Moho beneath the East Pacific Rise at 9°–10°N. *Earth Planet. Sci. Lett.* **203**, 117–130 (2002).
14. Dunn, R. A., Toomey, D. R. & Solomon, S. C. Three-dimensional seismic structure and physical properties of the crust and shallow mantle beneath the East Pacific Rise at 9° 30'N. *J. Geophys. Res.* **105**, 23537–23555 (2000).
15. Garmann, J. Accumulations of melt at the base of young oceanic crust. *Nature* **340**, 628–632 (1989).
16. Wilcock, W. S. D., Solomon, S. C., Purdy, G. M. & Toomey, D. R. The seismic attenuation structure of a fast-spreading mid-ocean ridge. *Science* **258**, 1470–1474 (1992).
17. Mutter, J. C. *et al.* Seismic images of active magma systems beneath the East Pacific Rise between 17°05' and 17°35'S. *Science* **268**, 391–395 (1995).

18. Singh, S. C. *et al.* Melt to mush variations in crustal magma properties along the ridge crest at the southern East Pacific Rise. *Nature* **394**, 874–878 (1998).
19. Nedimović, M. R. *et al.* Frozen magma lenses below the oceanic crust. *Nature* **436**, 1149–1152 (2005).
20. Wilson, D. S. Confidence intervals for motion and deformation of the Juan de Fuca plate. *J. Geophys. Res.* **98**, 16053–16071 (1993).
21. Canales, J. P. *et al.* Upper crustal structure and axial topography at intermediate-spreading ridges: seismic constraints from the Southern Juan de Fuca Ridge. *J. Geophys. Res.* **110**, B12104, doi:10.1029/2005JB003630 (2005).
22. Carbotte, S. M. *et al.* Rift topography linked to magmatism at the intermediate spreading Juan de Fuca Ridge. *Geology* **34**, 209–212 (2006).
23. Jousset, D. & Nicolas, A. The Moho transition in the Oman ophiolite — relation with wehrlites in the crust and dunites in the mantle. *Mar. Geophys. Res.* **21**, 229–241 (2000).
24. Taylor, M. A. J. & Singh, S. C. Compositions and microstructure of magma bodies from effective medium theory. *Geophys. J. Int.* **149**, 15–21 (2002).
25. Aharonov, E., Whitehead, J., Kelemen, P. B. & Spiegelman, M. Channeling instability of upwelling melt in the mantle. *J. Geophys. Res.* **100**, 20433–20450 (1995).
26. Kelemen, P. B., Shimizu, N. & Salters, V. J. M. Extraction of mid-ocean ridge basalt from the upwelling mantle by focused flow of melt in dunite channels. *Nature* **375**, 747–753 (1995).
27. Korenaga, J. & Kelemen, P. B. Melt migration through the oceanic lower crust: a constraint from melt percolation modeling with finite solid diffusion. *Earth Planet. Sci. Lett.* **156**, 1–11 (1998).
28. Hooft, E. & Detrick, R. S. The role of density in the accumulation of basaltic melts at mid-ocean ridges. *Geophys. Res. Lett.* **20**, 423–426 (1993).
29. Phipps Morgan, J. & Chen, Y. J. The genesis of oceanic crust: magma injection, hydrothermal circulation, and crustal flow. *J. Geophys. Res.* **98**, 6283–6297 (1993).
30. Stakes, D. S. *et al.* The Cleft revealed: geologic, magnetic, and morphologic evidence for construction of upper oceanic crust along the southern Juan de Fuca Ridge. *Geochem. Geophys. Geosyst.* **7**, Q04003, doi:10.1029/2005GC001038 (2006).
31. Barth, G. A. & Mutter, J. C. Variability in oceanic crustal thickness and structure: multichannel seismic reflection results from the northern East Pacific Rise. *J. Geophys. Res.* **101**, 17951–17975 (1996).
32. Dilek, Y., Moores, E. M. & Furnes, H. in *Faulting and Magmatism at Mid-Ocean Ridges* (eds Buck, W. R. *et al.*) 153–176 (Geophysical Monograph Series Vol. 106, AGU, 1998).
33. Coogan, L. A. *et al.* Petrology and geochemistry of the lower ocean crust formed at the East Pacific Rise and exposed at Hess Deep: a synthesis and new results. *Geochem. Geophys. Geosyst.* **3**, 8604, doi:10.1029/2001GC000230 (2002).

Supplementary Information is linked to the online version of the paper at www.nature.com/nature.

Acknowledgements This research was supported by the US NSF. We thank the captain, crew and scientific party of RV *Maurice Ewing* Cruise 0207.

Author Contributions All authors participated in the data acquisition experiment. J.P.C. processed the data, interpreted them, and wrote the paper with contributions from all of the co-authors.

Author Information Reprints and permissions information is available at www.nature.com/reprints. Correspondence and requests for materials should be addressed to J.P.C. (jpcanales@whoi.edu).

METHODS

Travel-time curves. Travel-time curves were calculated assuming a one-dimensional model consisting of a 2,319-m-thick water layer ($v_p = 1,500 \text{ m s}^{-1}$), a 5,940-m-thick crustal layer above the LCML ($v_p = 6,000 \text{ m s}^{-1}$), and a 1,000-m-thick layer between the LCML and the Moho ($v_p = 5,000 \text{ m s}^{-1}$). Crustal Poisson's ratio is 0.25.

Reflection coefficients. Reflection coefficients were calculated by assuming two homogeneous, semi-infinite media separated by a flat interface. We considered two models with the same upper medium properties but different lower medium properties. For the upper medium representing the gabbroic lower crust, we use the following elastic parameters: $v_p = 6,500 \text{ m s}^{-1}$, $v_s = 3,550 \text{ m s}^{-1}$ and $\rho = 2,800 \text{ kg m}^{-3}$. These parameters represent average laboratory measurements made at room temperature and 200 MPa confining pressure in gabbros drilled at the Mid-Atlantic Ridge³⁴ after correcting for the expected elevated temperatures of the near-axis lower crust (900 °C; ref. 7), assuming that v_p decreases with temperature as $-0.57 \times 10^{-3} \text{ km s}^{-1} \text{ K}^{-1}$ (ref. 35) and a Poisson's ratio of 0.29 (refs 34, 36).

In the first model, the lower medium represents a melt sill. We use the definition of ref. 18: melt refers to liquid matrix with disconnected crystals, with $v_s \approx 0 \text{ km s}^{-1}$. We use the following elastic parameters: $v_p = 3,400 \text{ m s}^{-1}$ (ref. 18), $v_s = 0 \text{ m s}^{-1}$ and $\rho = 2,700 \text{ kg m}^{-3}$ (ref. 28).

In the second model, the lower medium represents ultramafic rocks. We use the following elastic parameters: $v_p = 7,700 \text{ m s}^{-1}$, $v_s = 4,400 \text{ m s}^{-1}$ and

$\rho = 3,200 \text{ kg m}^{-3}$. These parameters represent average values for wehrlite and harzburgite compositions³⁷ after correcting for the expected elevated temperatures of the near-axis lower crust (900 °C; ref. 7), assuming that v_p decreases with temperature as $-0.54 \times 10^{-3} \text{ km s}^{-1} \text{ K}^{-1}$ (ref. 35) and a Poisson's ratio of 0.26 (ref. 36).

The predicted reflection coefficients do not exactly reproduce the observed AVO responses because the simplified models do not include effects such as energy attenuation and cannot fully describe complex reflectivity. True reflection coefficients for the LCML and Moho could not be estimated from the sea-floor multiple-to-primary amplitude ratio due to sea-floor diffractions that interfere with the LCML at zero offset.

34. Miller, D. J. & Christensen, N. I. Seismic velocities of lower crustal and upper mantle rocks from the slow spreading Mid-Atlantic Ridge, south of the Kane transform zone (MARK). *Proc. ODP Sci. Res.* **153**, 437–454 (1997).
35. Christensen, N. I. Compressional wave velocities in rocks at high temperatures and pressures, critical thermal gradients, and crustal low-velocity zones. *J. Geophys. Res.* **84**, 6849–6857 (1979).
36. Christensen, N. I. Poisson's ratio and crustal seismology. *J. Geophys. Res.* **101**, 3139–3156 (1996).
37. Karson, J. A., Collins, J. A. & Casey, J. F. Geologic and seismic velocity structure of the crust/mantle transition in the Bay of Islands ophiolite complex. *J. Geophys. Res.* **89**, 6126–6138 (1984).

LETTERS

Neural mechanisms of rapid natural scene categorization in human visual cortex

Marius V. Peelen^{1,2,3}, Li Fei-Fei^{1,4} & Sabine Kastner^{1,2,3}

The visual system has an extraordinary capability to extract categorical information from complex natural scenes. For example, subjects are able to rapidly detect the presence of object categories such as animals or vehicles in new scenes that are presented very briefly^{1,2}. This is even true when subjects do not pay attention to the scenes and simultaneously perform an unrelated attentionally demanding task³, a stark contrast to the capacity limitations predicted by most theories of visual attention^{4,5}. Here we show a neural basis for rapid natural scene categorization in the visual cortex, using functional magnetic resonance imaging and an object categorization task in which subjects detected the presence of people or cars in briefly presented natural scenes. The multi-voxel pattern of neural activity in the object-selective cortex evoked by the natural scenes contained information about the presence of the target category, even when the scenes were task-irrelevant and presented outside the focus of spatial attention. These findings indicate that the rapid detection of categorical information in natural scenes is mediated by a category-specific biasing mechanism in object-selective cortex that operates in parallel across the visual field, and biases information processing in favour of objects belonging to the target object category.

In daily life we often look for particular object categories in our environment that are relevant for ongoing behaviour. For example, before crossing a street we look whether cars are near, perhaps not noticing other objects in the visual scene present at the same time, such as people walking on the other side of the street. Behavioural experiments have shown that such detection of familiar object categories in natural scenes is extremely rapid^{1,2}, and can be done even without focal attention³. These results indicate the existence of selection mechanisms for familiar object categories that operate independently of spatial attention.

In the present study, using functional magnetic resonance imaging (fMRI), we investigated neural mechanisms for extracting object category information from complex natural scenes. We proposed that the rapid detection of categorical information may be mediated by top-down mechanisms that bias processing in favour of the searched-for object category. These biasing mechanisms may lead to a filtering of the scene that effectively limits the visual representation of the scene to objects belonging to the task-relevant object category, thereby facilitating the rapid detection of the target category. To probe this hypothesis, we measured the influence of a category detection task (detecting either people or cars) on fMRI activity evoked by pictures of real-world scenes. Furthermore, given that behavioural studies have found evidence for parallel processing in rapid scene categorization^{3,6,7}, we asked whether such influences can be observed both inside and outside the focus of spatial attention.

A large (>2,000 pictures) set of photographs of outdoor scenes (cityscapes and landscapes; Supplementary Fig. 1) was selected for

the experiment. A subset of these scenes contained people or cars in natural, daily-life situations. As in natural vision, the visual appearances and spatial locations of the people and cars in these scenes were highly variable. For example, a scene could show a single person sitting on a bench in a park close to the camera, or could show a group of people walking on a street at a distance (Supplementary Fig. 1). On each trial, subjects briefly (~130 ms, see Methods) viewed four different simultaneously presented pictures (two along the vertical axis, and two along the horizontal axis⁸), followed immediately by perceptual masks presented at the same locations (Fig. 1). The task was to report the presence of either people ('body task') or cars ('car task') in the horizontally or vertically presented pictures, resulting in four different task combinations. These four combinations were always performed in separate functional runs to prevent confusion about the target category and task-relevant picture locations. We will refer to the task-relevant pictures as 'attended' pictures, and the task-irrelevant pictures as 'unattended' pictures. A separate analysis confirmed that subjects spatially attended the task-relevant pictures more than the task-irrelevant pictures, by showing spatially-specific attentional modulation in retinotopic visual cortex (see Supplementary Fig. 2). The content of the attended pictures was manipulated independently from the content of the unattended pictures, such that all possible pairings of scene types

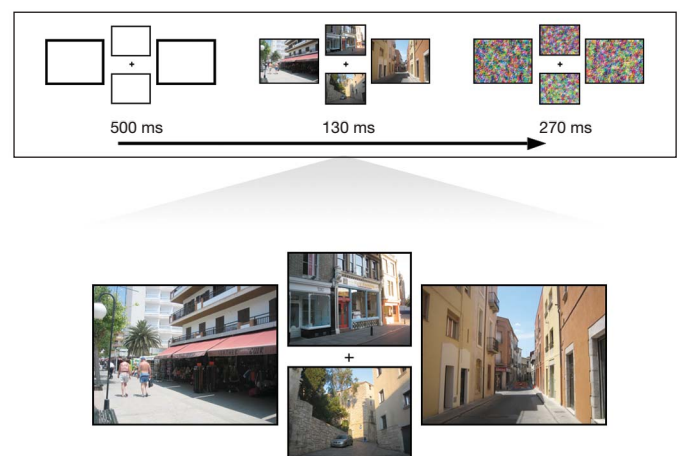


Figure 1 | Schematic overview of trial layout. Each trial started with a spatial cue indicating the relevant stimulus locations (which were held constant within a run). This was followed by the four pictures presented for, on average, 130 ms. Presentation time of the pictures was adjusted for each subject to arrive at ~80% accuracy. The pictures were followed by perceptual masks (270 ms). The next trial started, on average, 1,300 ms after the offset of the masks.

¹Department of Psychology, Princeton University, Princeton, New Jersey 08540, USA. ²Center for the Study of Brain, Mind, and Behavior, Princeton University, Princeton, New Jersey 08540, USA. ³Princeton Neuroscience Institute, Princeton University, Princeton, New Jersey 08540, USA. ⁴Department of Computer Science, Princeton University, Princeton, New Jersey 08540, USA.

were equally likely. This design allowed us to measure brain responses to attended and unattended pictures separately by means of selective averaging.

We analysed multi-voxel patterns of activation across the object-selective visual cortex, as these have been shown to be sensitive to object-category information^{9,10}. The object-selective visual cortex, often referred to as the lateral-occipital complex, was localized in each subject by contrasting responses to intact versus scrambled objects in a separate localizer scan¹¹. The analysis approach was to correlate response patterns evoked by the two scene types (containing either people or cars) in the main experiment with response patterns evoked by a different set of pictures of human bodies and cars presented in a separate experiment (Fig. 2; Methods Summary). Unlike the stimuli in the main experiment, this second set of stimuli consisted of isolated objects without scene context that were centrally presented. We expected to find, in the case of the car stimuli for example, a higher correlation between response patterns evoked by scenes containing cars with response patterns evoked by isolated car pictures (within-category comparison) than with response patterns evoked by isolated body pictures (between-category comparison). We found that response patterns indeed correlated more strongly for within-category comparisons than between-category comparisons ($T_9 = 4.1$, $P < 0.005$; Fig. 3a), a difference that tended to be stronger for the attended than the unattended pictures (main effect of attention: $F_{1,9} = 3.9$, $P = 0.08$). This suggests a high-level representation of object-category information that is invariant to the different viewing conditions, many of which are typically encountered in daily life.

Of central interest to the present study was the effect of search task on this category information. Notably, category information depended fully on search task (category \times task: $F_{1,9} = 13.5$, $P < 0.01$; Fig. 3a). During the body task, patterns of activation carried significant category information about bodies ($T_9 = 5.0$, $P < 0.001$), but not cars ($T_9 = -0.5$). Conversely, during the car task significant category information was present for cars ($T_9 = 2.9$, $P < 0.05$), but not for bodies ($T_9 = -1.8$). Furthermore, the category \times task interaction was independent of spatial attention (category \times task \times attention: $F_{1,9} = 0.1$, $P = 0.79$), and significant for both the attended ($F_{1,9} = 11.7$, $P < 0.01$) and the unattended pictures ($F_{1,9} = 10.5$, $P < 0.05$). For these analyses we sorted trials on the basis of the content of either the attended or the unattended pictures. Because the content of these two picture pairs was fully independent, the content of one picture pair was effectively 'averaged out' when

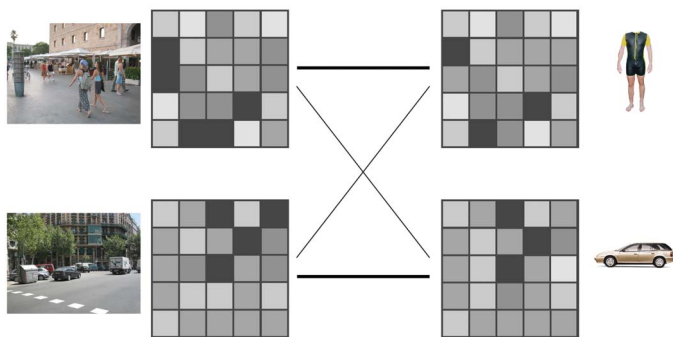


Figure 2 | Schematic overview of analysis approach. The approach of the multi-voxel pattern analysis was to correlate patterns of activation to conditions in the main experiment (depicted on the left) with patterns of activation to conditions in the category localizer (depicted on the right). The thickness of the lines between patterns indicates the hypothesized strengths of the correlations. For example, higher correlations were expected between patterns evoked by scenes containing people and isolated body pictures (within-category comparison) than with isolated car pictures (between-category comparison). This approach allowed us to measure the influence of search task and spatial attention on category information in visual cortex.

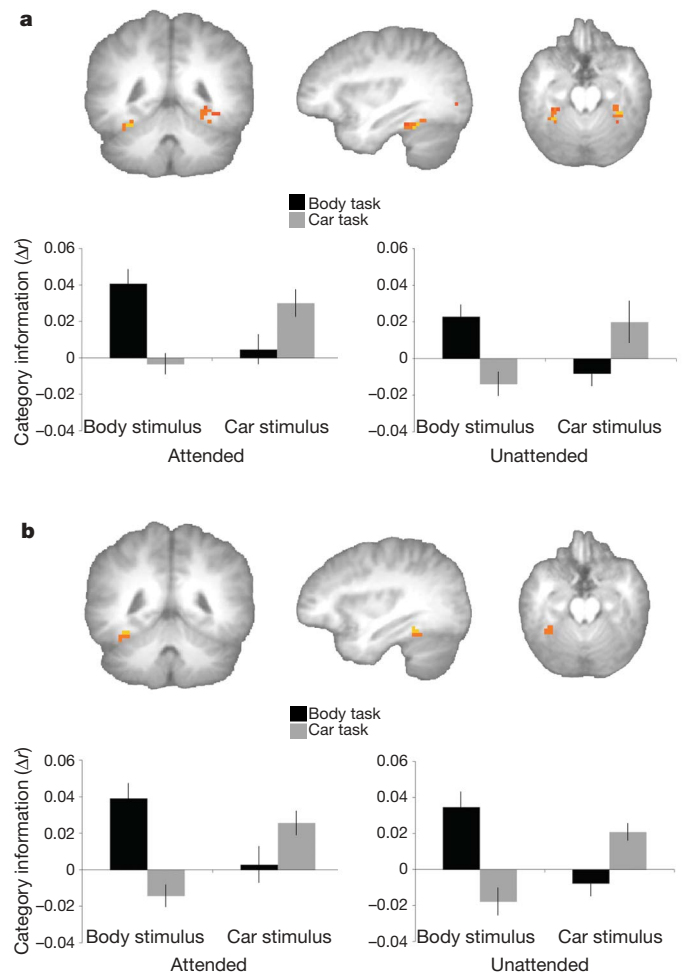


Figure 3 | Results of multi-voxel pattern analysis. **a**, The top panel shows the ventral cluster of object-selective cortex (intact versus scrambled objects) in a group-average analysis at $P < 0.005$ (Talairach coordinates of peak: $x = 35$, $y = -41$, $z = -18$). The lower panel shows category information as a function of category, task and attention in individually-defined object-selective cortex. Category information was calculated by taking the difference between within-category comparisons and between-category comparisons, and reflects the amount of category information in multi-voxel patterns of activation (see Fig. 2 and Methods Summary). Error bars indicate \pm s.e.m. **b**, The top panel shows the result of the category \times task contrast in the group-average searchlight analysis at $P < 0.005$ (uncorrected). The lower panel shows category information as a function of category, task and attention in the sphere surrounding the peak voxel of the activation from the group-average searchlight analysis (Talairach coordinates of peak: $x = 35$, $y = -44$, $z = -18$). Error bars indicate \pm s.e.m.

measuring responses to the other picture pair, and vice versa. To ensure further that the results we have described were not related to the simultaneously presented other picture pair, we calculated the category \times task interaction separately for the different simultaneously presented conditions. As expected, the category \times task interaction for the attended pictures did not depend on the content of the unattended pictures, and vice versa ($P > 0.1$, for both tests). Finally, to test whether these results were specific to higher-level visual cortex, we performed the same analyses in retinotopically defined visual areas V1, V2 and V3. None of these regions contained category information, and there were no significant effects of task or category ($P > 0.1$, for all tests).

These results indicate that body and car stimuli embedded in natural scenes were visually processed to a high level only when they were actively searched for. Objects belonging to the target category were processed up to the category level, even when they were presented

outside the focus of attention. In contrast, objects belonging to the irrelevant category were not represented at the category level, even when they were presented inside the focus of attention.

To investigate whether other regions in the brain may show similar effects to those observed in object-selective visual cortex, we used an information-based functional brain mapping approach, measuring patterns of activation throughout the brain by means of a spherical searchlight¹². Within a given sphere, we correlated patterns of activation to the conditions in the main experiment with patterns of activation to the separately presented isolated body and car stimuli, identical to the analysis in object-selective cortex. Individual subject data were spatially normalized, which allowed us to use a random-effects group analysis to test where in the brain search task influenced category information. The most significant category \times task interaction was found in the ventral temporal cortex, overlapping the object-selective visual cortex (Fig. 3b). The correlation values in the sphere surrounding the peak voxel of this cluster were very similar to those of the a priori defined object-selective region (Fig. 3). As expected (given the selection of the sphere), category information (within- versus between-category comparison) depended strongly on the search task (category \times task: $F_{1,9} = 34.9$, $P < 0.0005$; Fig. 3b). During the body task, patterns of activation carried significant information about bodies ($T_9 = 8.9$, $P < 0.00001$), but not cars ($T_9 = -0.6$), whereas for the car task, significant information was present for cars ($T_9 = 5.8$, $P < 0.0005$), but not (or negative) for bodies ($T_9 = -2.6$). The category \times task interaction was independent of attention (category \times task \times attention: $F_{1,9} = 0.1$, $P = 0.81$), and significant for both the attended ($F_{1,9} = 16.6$, $P < 0.005$) and the unattended pictures ($F_{1,9} = 35.6$, $P < 0.0005$). This analysis demonstrated that the effect of search task on category information was strongest in the ventral temporal cortex, and could be observed in a group-average analysis without defining individual a priori regions-of-interest.

The present results provide evidence for a neural mechanism of attentional selection at the level of object category. Notably, this mechanism in high-level visual cortex seems to operate across the visual field independent of spatial attention, similar to attentional selection mechanisms for simple features (for example, for colour or motion direction) in lower-level visual cortex^{13–15}. As such, it provides a neural basis for recent behavioural findings reporting an extraordinary capability of the human visual system to rapidly extract object category information from natural scenes, even outside the focus of spatial attention³. The selection mechanism described here may operate through the pre-activation of neurons representing the target category that subsequently biases the processing of the scene in favour of the target category¹⁶. Such an account of our data are in line with parallel models of visual search, in which a ‘search template’ biases the processing of a scene across the visual field in favour of objects that match the template^{17,18}. Given the variability in the visual characteristics and spatial locations of individual category exemplars in natural scenes, such search templates would need to be rather abstract, invariant to geometric and photometric changes, and spatially unspecific. Furthermore, successful performance in our task required extra, space-based, selection mechanisms to prevent responses to the task-irrelevant pictures (see Supplementary Table 1 and Supplementary Discussion). Our results indicate that these additional selection mechanisms (for example, the retinotopically specific spatial attention effects observed in the retinotopic visual cortex; see Supplementary Fig. 2) operate mostly independently from the object-category mechanism observed in activity patterns in object-selective cortex.

Furthermore, the finding that objects belonging to the irrelevant object category were poorly represented in high-level visual cortex, even when they were spatially attended, is consistent with the phenomenon of ‘change blindness’, the finding that we are mostly unaware of large changes to objects in natural scenes when the identity of the changed object is unknown in advance^{19–21}. Indeed, our results

provide evidence that, contrary to our subjective experience of a complete internal representation of the external world, the neural representation of real-world scenes is limited to those objects that are directly relevant for ongoing behaviour²².

Together, the present results provide a possible neural basis for both the limitations in our perception of real-world scenes and our remarkable ability for categorizing such scenes inside and outside the focus of spatial attention.

METHODS SUMMARY

Ten healthy adults (three females) participated in eight runs of the main experiment across two scanning sessions. In different runs, subjects performed one of two detection tasks on either the horizontal or the vertical pairs of pictures, resulting in four different run types. Within a scanning session, each of the presented pictures was unique. The same set of pictures was used in both sessions, such that across the two sessions the same pictures were presented in both detection tasks.

Activity patterns to the body and car conditions in the category localizer were correlated with activity patterns to the body and car scenes in the main experiment. This resulted in four correlations (for example, between body scenes in the main experiment and bodies in the localizer: $r_{\text{body(main)}_body(\text{localizer})}$). Within-category correlations are the correlations where categories matched (for example, $r_{\text{car(main)}_car(\text{localizer})}$), whereas between-category correlations are the correlations between non-matching categories (for example, $r_{\text{car(main)}_body(\text{localizer})}$). Category information was defined as the difference between within-category and between-category correlations. For example, category information (Δr) for the body stimuli (left two bars in Fig. 3) was calculated by: $(r_{\text{body(main)}_body(\text{localizer})}) - (r_{\text{body(main)}_car(\text{localizer})})$.

Functional (echo-planar imaging (EPI) sequence; 34 slices per volume; resolution = $3 \times 3 \times 3$ mm with 1 mm gap; repetition time (TR) = 2.0 s; time to echo (TE) = 30 ms; flip angle = 90°) and anatomical (MPRAGE sequence; 256 matrix; TR = 2.5 s; TE = 4.38 ms; flip angle, 8° ; $1 \times 1 \times 1$ mm resolution) images were acquired with a 3T Allegra MRI scanner (Siemens). Functional data were slice-time corrected, motion corrected, and low-frequency drifts were removed with a temporal high-pass filter (cutoff of 0.006 Hz). No spatial smoothing was applied.

Full Methods and any associated references are available in the online version of the paper at www.nature.com/nature.

Received 16 March; accepted 30 April 2009.

Published online 7 June 2009.

- Potter, M. C. Meaning in visual search. *Science* **187**, 965–966 (1975).
- Thorpe, S., Fize, D. & Marlot, C. Speed of processing in the human visual system. *Nature* **381**, 520–522 (1996).
- Li, F. F., VanRullen, R., Koch, C. & Perona, P. Rapid natural scene categorization in the near absence of attention. *Proc. Natl Acad. Sci. USA* **99**, 9596–9601 (2002).
- Broadbent, D. E. *Perception and Communication* (Oxford Univ. Press, 1958).
- Treisman, A. M. & Gelade, G. A feature-integration theory of attention. *Cognit. Psychol.* **12**, 97–136 (1980).
- Fei-Fei, L., VanRullen, R., Koch, C. & Perona, P. Why does natural scene categorization require little attention? Exploring attentional requirements for natural and synthetic stimuli. *Vis. Cogn.* **12**, 893–924 (2005).
- Rousselet, G. A., Fabre-Thorpe, M. & Thorpe, S. J. Parallel processing in high-level categorization of natural images. *Nature Neurosci.* **5**, 629–630 (2002).
- Wojciulik, E., Kanwisher, N. & Driver, J. Covert visual attention modulates face-specific activity in the human fusiform gyrus: fMRI study. *J. Neurophysiol.* **79**, 1574–1578 (1998).
- Cox, D. D. & Savoy, R. L. Functional magnetic resonance imaging (fMRI) “brain reading”: detecting and classifying distributed patterns of fMRI activity in human visual cortex. *Neuroimage* **19**, 261–270 (2003).
- Haxby, J. V. et al. Distributed and overlapping representations of faces and objects in ventral temporal cortex. *Science* **293**, 2425–2430 (2001).
- Malach, R. et al. Object-related activity revealed by functional magnetic resonance imaging in human occipital cortex. *Proc. Natl Acad. Sci. USA* **92**, 8135–8139 (1995).
- Kriegeskorte, N., Goebel, R. & Bandettini, P. Information-based functional brain mapping. *Proc. Natl Acad. Sci. USA* **103**, 3863–3868 (2006).
- Maunsell, J. H. & Treue, S. Feature-based attention in visual cortex. *Trends Neurosci.* **29**, 317–322 (2006).
- Motter, B. C. Neural correlates of attentive selection for color or luminance in extrastriate area V4. *J. Neurosci.* **14**, 2178–2189 (1994).
- Saenz, M., Buracas, G. T. & Boynton, G. M. Global effects of feature-based attention in human visual cortex. *Nature Neurosci.* **5**, 631–632 (2002).
- Chelazzi, L., Miller, E. K., Duncan, J. & Desimone, R. A neural basis for visual search in inferior temporal cortex. *Nature* **363**, 345–347 (1993).

17. Duncan, J. EPS mid-career award 2004: brain mechanisms of attention. *Q. J. Exp. Psychol. (Colchester)* **59**, 2–27 (2006).
18. Duncan, J. & Humphreys, G. W. Visual search and stimulus similarity. *Psychol. Rev.* **96**, 433–458 (1989).
19. O'Regan, J. K., Rensink, R. A. & Clark, J. J. Change-blindness as a result of 'mudsplashes'. *Nature* **398**, 34 (1999).
20. Rensink, R. A., O'Regan, J. K. & Clark, J. J. To see or not to see: the need for attention to perceive changes in scenes. *Psychol. Sci.* **8**, 368–373 (1997).
21. Simons, D. J. & Rensink, R. A. Change blindness: past, present, and future. *Trends Cogn. Sci.* **9**, 16–20 (2005).
22. O'Regan, J. K. Solving the "real" mysteries of visual perception: the world as an outside memory. *Can. J. Psychol.* **46**, 461–488 (1992).

Supplementary Information is linked to the online version of the paper at www.nature.com/nature.

Acknowledgements We thank P. Downing, U. Hasson, S. McMains, K. Norman, T. Stein and A. Treisman for suggestions on earlier versions of the manuscript, members of the Kastner laboratory for help with retinotopic mapping, and N. Oosterhof for help with data analysis. This work was supported by grants from the National Institutes of Health (2R01 MH64043, 1R01 EY017699, 2P50 MH-62196) to S.K., and a Microsoft Research New Faculty Fellowship and the F. Moss gift to L.F.-F.

Author Contributions M.V.P., in collaboration with L.F.-F. and S.K., conceived the experiment. M.V.P. acquired and analysed the data. M.V.P., L.F.-F. and S.K. interpreted the results and wrote the paper.

Author Information Reprints and permissions information is available at www.nature.com/reprints. Correspondence and requests for materials should be addressed to M.V.P. (mpeelen@princeton.edu).

METHODS

Stimuli. Two-thousand-and-fifty-six natural scene pictures were selected from an online database²³. Five-hundred-and-twelve pictures contained one or more people (but no cars), 512 pictures contained one or more cars (but no people), and 1,024 pictures contained no cars and no people. The pictures were mostly photographs of city streets. The position, viewpoint and size of the people and cars in the pictures were highly variable, mimicking real-world viewing conditions (see Supplementary Fig. 1 for sample pictures). Twelve different perceptual masks were created. Each was a coloured picture of a mixture of white noise at different spatial frequencies on which a naturalistic texture was superimposed²⁴.

All pictures were full-colour photographs reduced to 480 (vertical) \times 640 (horizontal) pixels. The pictures along the horizontal axis (size: $7.9^\circ \times 10.5^\circ$) were presented with an offset of 3.5° to the right or left of the central fixation cross. The pictures along the vertical axis (size: $4.5^\circ \times 6^\circ$) were presented with an offset of 0.5° above or below the central fixation cross.

General procedure. Each subject participated in one practice session and four scanning sessions. The first scanning session was used for mapping retinotopic visual areas. The second and third session consisted of four runs of the main experiment, two runs of the category pattern localizer, and two runs of the object-selective cortex localizer. The fourth session consisted of a position localizer to measure retinotopic representations corresponding to the picture positions in the main experiment. See Supplementary Methods for details of the localizer experiments. Data were analysed using the AFNI software package²⁵ and MATLAB (The MathWorks).

Main experiment. Each run started and ended with a fixation-only block of 14 s. The average trial duration was 2.2 s. Each trial started with a 500 ms presentation of four placeholders at the location of the to-be-presented pictures. The placeholders of the relevant locations (either the two horizontal, or the two vertical locations) were highlighted during this time, by increasing the width of the placeholder outline by 2 pixels ($\sim 0.05^\circ$). This was followed by the presentation of the four pictures for 130 ms on average. The presentation time of the pictures was individually determined on the basis of the performance in a separate session, and was held constant within a scanning session (see Supplementary Methods). A presentation of perceptual masks directly followed the picture presentations. The combined duration of picture and mask presentations was always 400 ms. A screen with the four placeholders followed the presentation of the masks for a duration of 950 to 1,650 ms (pseudo-randomly chosen, with intervals of 100 ms), with a mean duration of 1,300 ms.

On 20% of the trials (32 trials per run) only the masks (but no pictures) were presented, for 270 ms on average. On the remaining 128 trials, four simultaneously presented pictures were presented followed by four masks (each randomly selected from the total set of 12 masks). Each of the four scenes could contain either: people but no cars ('body'), cars but no people ('cars'); or no people and no cars ('none'). Within each pair of pictures (horizontal and vertical) there were eight possible combinations of these scene types: body–none, none–body, cars–none, none–cars, body–cars, cars–body, none–none and none–none. Each of these combinations was presented equally often. Trial order was randomized (without replacement).

Our research questions focused on the scene combinations that contained either people but no cars, or cars but no people. The other scene combinations were included in the design so that the irrelevant object category did not predict the presence or absence of the relevant object category.

In different runs, subjects performed one of two detection tasks ('body task' or 'car task') on either the horizontal or the vertical pairs of pictures, resulting in four different run types. The task was to press one button for the presence and another button for the absence of the target category in the relevant picture pair. The mapping of the two buttons (index and middle finger) to present and absent responses was counterbalanced across sessions and subjects. Subjects always performed two runs of the same task in a row, to prevent frequent switching from one target category to another. The order of the tasks was counterbalanced across sessions and subjects. In different runs, subjects performed the tasks on either the horizontal or vertical picture pairs, the order of which was held constant within a session, and which was counterbalanced across the two sessions.

Multi-voxel pattern analysis. For each subject, general linear models were created for the main experiment and the category pattern localizer experiment. One predictor (convolved with a standard model of the haemodynamic response function) modelled each condition. Regressors of no interest were also included to account for differences in the mean magnetic resonance signal across scans and for head motion within scans. Two separate regression analyses were run for the main experiment; with trials grouped based on either the task-relevant or task-irrelevant pairs of scene pictures. These regression analyses resulted, for each voxel, in a t -value for each condition in the main experiment and for each condition in the localizer. The t -values of conditions in the main experiment were correlated, across the voxels of a region of interest (ROI), with t -values of the body and car conditions in the localizer. The analyses were repeated using parameter estimates instead of t -values, which yielded highly similar results. The analysis was done for each subject and session separately. Correlations were Fisher-transformed before statistical testing: $0.5\ln[(1+r)/(1-r)]$. Correlations of the two sessions were averaged. For each subject, ROI and localizer condition, the average correlation across conditions in the main experiment was subtracted out to remove overall differences in correlations that were not of interest. Differences between the resulting voxelwise correlations were then tested using repeated-measures analysis of variance (ANOVA) and t -tests (two-tailed) with subject ($n = 10$) as random factor. All trials (correct and incorrect) were included in the analyses. We repeated all analyses on correct trials only, which yielded qualitatively similar but slightly less significant results (due to the smaller number of trials).

Searchlight analysis. A whole-brain pattern analysis was performed using a spherical searchlight¹². For each voxel in the brain we computed voxelwise correlations in a sphere of 10-mm radius (corresponding to 121 voxels) centred on this voxel. The voxelwise correlations were computed as described above. The correlation values from each sphere were Fisher-transformed and assigned to the centre voxel of this sphere. The correlations were computed for each subject and session separately. Results were transformed into Talairach space, the correlations of the two sessions were averaged for each subject, and random-effects group analyses were performed.

23. Russell, B. C., Torralba, A., Murphy, K. P. & Freeman, W. T. LabelMe: a database and web-based tool for image annotation. *Int. J. Comput. Vis.* **77**, 157–173 (2008).
24. Walther, D. B., Caddigan, E., Fei-Fei, L. & Beck, D. M. Natural scene categories revealed in distributed patterns of activity in the human brain. *J. Neurosci.* (in the press).
25. Cox, R. W. & Hyde, J. S. AFNI: software for analysis and visualization of functional magnetic resonance neuroimages. *Comput. Biomed. Res.* **29**, 162–173 (1996).

LETTERS

Cyclic AMP intoxication of macrophages by a *Mycobacterium tuberculosis* adenylate cyclase

Nisheeth Agarwal¹, Gyanu Lamichhane¹, Radhika Gupta¹, Scott Nolan¹ & William R. Bishai¹

With 8.9 million new cases and 1.7 million deaths per year, tuberculosis is a leading global killer that has not been effectively controlled^{1,2}. The causative agent, *Mycobacterium tuberculosis*, proliferates within host macrophages where it modifies both its intracellular and local tissue environment, resulting in caseous granulomas with incomplete bacterial sterilization^{3,4}. Although infection by various mycobacterial species produces a cyclic AMP burst within macrophages that influences cell signalling, the underlying mechanism for the cAMP burst remains unclear^{5–7}. Here we show that among the 17 adenylate cyclase genes present in *M. tuberculosis*, at least one (Rv0386) is required for virulence. Furthermore, we demonstrate that the Rv0386 adenylate cyclase facilitates delivery of bacterial-derived cAMP into the macrophage cytoplasm. Loss of Rv0386 and the intramacrophage cAMP it delivers results in reductions in TNF- α production via the protein kinase A and cAMP response-element-binding protein pathway, decreased immunopathology in animal tissues, and diminished bacterial survival. Direct intoxication of host cells by bacterial-derived cAMP may enable *M. tuberculosis* to modify both its intracellular and tissue environments to facilitate its long-term survival.

Bacterial pathogens have evolved highly specific mechanisms to proliferate in the host during infection. A common strategy is subversion of host cell signal transduction by the introduction of enzymes that modulate the levels of secondary messengers such as cAMP^{8,9}. Macrophages produce intracellular cAMP through G-protein-coupled receptor (GPCR)-adenylate cyclases (ACs)¹⁰. Increased cAMP stimulates protein kinase A (PKA), leading to the phosphorylation of cAMP response-element-binding protein (CREB), and subsequent transcriptional changes including modulation of cytokine expression^{11,12}.

To survive intracellularly, *M. tuberculosis* inhibits the host phagosome maturation process that is bactericidal for other organisms¹³ using mechanisms that are incompletely understood, but may include secreted proteins, lipids or polysaccharides^{14–16}. At the tissue level, *M. tuberculosis* elicits an immune response that results in caseous necrosis and the formation of solid granulomas¹⁷. These lesions, which are avascular and possibly hypoxic, may allow chronic contained infection^{18–20}.

The *M. tuberculosis* CDC1551 genome reveals 17 genes containing class III adenylate cyclase domains, a feature shared by pathogenic mycobacteria such as *Mycobacterium avium* (12 adenylate cyclases) and *Mycobacterium marinum* (31 adenylate cyclases). In contrast, *Escherichia coli*, *Pseudomonas aeruginosa*, *Corynebacterium glutamicum* and *Streptomyces coelicolor* only have one adenylate cyclase²¹. Although a member of the *M. tuberculosis* complex, *Mycobacterium microti*, has been reported to block phagosome maturation by cAMP production within macrophages⁷, the source and effects of cAMP during macrophage infection by mycobacteria remain unclear.

We observed that after a brief exposure to *M. tuberculosis*, J774 macrophage-like cells produced an intracellular cAMP burst, as previously reported with *M. tuberculosis* and other mycobacteria^{5–7}, which was ~threefold above baseline within 3 h (Fig. 1a). The cAMP burst, which is sustained for more than 16 h after infection, correlated with CREB phosphorylation in a dose-dependent manner (Fig. 1b), suggesting stimulation of the PKA–CREB pathway by cAMP. These responses were not increased above baseline in macrophages infected with heat-killed bacteria, indicating that live tubercle bacilli are required (Fig. 1c, d). Similar results were observed with human THP-1 macrophages (data not shown).

Because several signal transduction pathways may stimulate CREB phosphorylation, we evaluated CREB responses in the

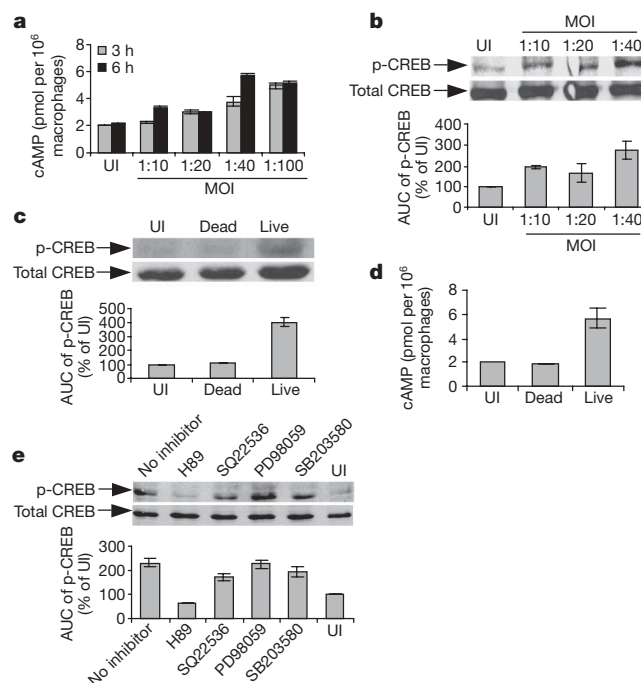


Figure 1 | The *M. tuberculosis*-induced macrophage cAMP burst and CREB phosphorylation pathway require live bacilli but not host GPCR-AC.

a, b, Intramacrophage cAMP levels in J774 cells after 3 or 6 h (**a**) and CREB-phosphorylation (p-CREB) after 16 h compared with uninfected (UI) cells (**b**), at several multiplicities of infection (MOIs). AUC, area under the curve of the densitometric scan. **c, d**, Dead (heat-killed) bacilli fail to produce a p-CREB response at 16 h (**c**) or a cAMP burst at 3 h (**d**) in J774 cells. **e**, Sixteen hour p-CREB accumulation after *M. tuberculosis* infection requires PKA, as shown using the inhibitor H89, but is not dependent on host GPCR-AC, as shown using the inhibitor SQ22536 (see Methods, text and Fig. 4e for details about other inhibitors). Data are mean \pm s.d. of multiple experiments ($n = 2$ in **b, c, e** and $n = 3$ in **a, d**).

¹Department of Medicine, Johns Hopkins School of Medicine, CRB2, Room 1.08, 1550 Orleans Street, Baltimore, Maryland 21231-1044, USA.

M. tuberculosis-infected macrophages using specific pharmacological inhibitors against pathways involving ERK1/2 (PD98059), p38 MAPK (SB203580), or PKA (H89). As seen in Fig. 1e, *M. tuberculosis*-stimulated CREB phosphorylation was inhibited by less than 15% by PD98059 or SB203580 despite the fact that control immunoblots showed sustained inhibition of the targeted MAPKs over the incubation period. In contrast, H89 uniquely blocked infection-induced CREB phosphorylation by >70%, indicating a need for PKA activation; similar results were observed with an independent PKA inhibitor (Supplementary Fig. 1). Next we tested the inhibition of host cell GPCR-AC using SQ22536. Surprisingly, despite exposure to concentrations of SQ22536 that completely blocked forskolin-stimulated host cell adenylate cyclase activity, only partial inhibition of *M. tuberculosis*-induced CREB phosphorylation was observed with this inhibitor (Fig. 1e). Also, GPCR-AC inhibition by SQ22536 did not reduce cAMP levels in *M. tuberculosis*-infected cells. These findings indicated that endogenous macrophage GPCR-AC (the presumed source of cAMP and subsequent PKA activation) was not required for *M. tuberculosis*-induced CREB phosphorylation, and thus suggested that there might be an alternative source of cAMP.

To address the possibility that a bacterial adenylate cyclase might contribute to the intramacrophage cAMP burst⁷, we measured cAMP production by *M. tuberculosis* in broth cultures and found notable levels both in the intracellular and extracellular compartments (Fig. 2a). Next, we constructed a recombinant *M. tuberculosis* strain overexpressing its endogenous phosphodiesterase (PDE) *Rv0805* (Mtb-PDE), and a corresponding empty-vector-containing control strain (Mtb-control). As detailed in the Methods, PCR with reverse transcription (RT-PCR) experiments confirmed an 8–12-fold overexpression of *Rv0805* in the Mtb-PDE strain compared to the Mtb-control strain. As predicted, overexpression of *Rv0805* significantly reduced intrabacterial cAMP both at early and late *in vitro* growth time points (Fig. 2b). Infection of macrophages with the Mtb-PDE strain showed that the overexpression of bacterial PDE—which is not

secreted (Supplementary Fig. 2) and does not possess a signal sequence or lipid-anchoring domain, suggesting export—significantly reduced intramacrophage cAMP concentrations (Fig. 2c) as well as CREB phosphorylation (Fig. 2d) in comparison to the Mtb-control strain. In light of the observation that *M. avium*-stimulated CREB phosphorylation results in tumour necrosis factor- α (TNF- α) secretion⁶, we also tested levels of TNF- α secretion by macrophages infected with the recombinant strains. As shown in Fig. 2e, infection with the Mtb-PDE strain resulted in ~fourfold less TNF- α secretion than with the Mtb-control strain. These results indicated that overexpression of a bacterial phosphodiesterase reduced intramacrophage cAMP levels as well as PKA-dependent events influenced by cAMP.

To investigate the role of *M. tuberculosis* adenylate cyclases in pathogenesis further, we studied eight *M. tuberculosis* mutants each with a transposon insertion in a unique adenylate cyclase gene (Supplementary Fig. 3)²². Mice were infected with a pooled inoculum containing each of the adenylate cyclase mutants plus a control transposon mutant, JHU-1864c, known to be attenuated for survival in mice. Lung homogenates from groups of mice killed at four time points were plated, and the recovered pooled colonies were used to prepare *M. tuberculosis* genomic DNA for quantitative PCR using mutant-specific primers (Supplementary Table 1) to evaluate the relative abundance of each mutant (Supplementary Fig. 4). One of the eight mutants competing for survival in mouse lungs—the mutant in *Rv0386* (JHU-0386), which encodes a cell-wall associated adenylate cyclase (Supplementary Fig. 5)—showed a pattern of survival decline over time similar to that of the known attenuated strain JHU-1864c (Fig. 3a). To confirm this observation, we complemented the *Rv0386* mutation (JHU-0386 COMP, Supplementary Fig. 6), and infected three strains of mice (BALB/c, C57BL/6 and C57BL/6 mice lacking the *Tnfa* gene (C57BL/6 *Tnfa*^{-/-})) by the aerosol route with the wild type, mutant, and complemented *M. tuberculosis* strains. As seen in Fig. 3b, the JHU-0386 mutant was significantly impaired for lung survival at late time points in immunocompetent mice (1.2 and 0.8 log units lower than wild type in BALB/c (at day 56) and in C57BL/6 (at day 28), respectively, $P < 0.05$ in both cases) and for dissemination to the spleen. In contrast, in mice lacking *Tnfa*, mutant and control strain proliferation was equivalent, indicating that the survival defect of JHU-0386 is dependent on host cell TNF- α .

We then tested macrophage cAMP levels with the *M. tuberculosis* mutant lacking the adenylate cyclase gene *Rv0386*. Infection with this mutant (which has an equivalent growth rate to wild type *in vitro* (data not shown) and in macrophages (Supplementary Fig. 7)), resulted in cAMP levels that were ~fivefold lower than those observed with wild-type *M. tuberculosis* (Fig. 3c). Similar results were observed in primary mouse macrophages (Supplementary Fig. 8a); moreover, the other seven adenylate cyclase mutants in the study failed to show an effect on intramacrophage cAMP levels (Supplementary Fig. 9). Providing an intact copy of the *Rv0386* gene to the JHU-0386 mutant by complementation restored intramacrophage cAMP levels to their wild-type levels, whereas complementation with a gene containing site-directed mutations producing two inactivating missense substitutions, N120Y and R124S, in the adenylate cyclase domain of *Rv0386* (JHU-0386 SDM-COMP) failed to restore the cAMP burst (Fig. 3c) despite being expressed at comparable levels to wild-type *Rv0386* (data not shown). Furthermore, loss or restoration of the *Rv0386* gene did not influence macrophage cGMP levels (Supplementary Fig. 10). These data show that *Rv0386* is required for full virulence in the mouse model. Notably, loss of this adenylate cyclase gene results in a macrophage infection that is devoid of a cAMP burst. Taken together and in the context of the SQ22536 inhibition studies and the phosphodiesterase overexpression experiment, our data indicate that *M. tuberculosis*-derived cAMP contributes to the macrophage cAMP burst and implicate the bacterial adenylate cyclase *Rv0386* in this process.

To investigate how the *M. tuberculosis* pathogenesis program might benefit by increasing intramacrophage cAMP levels, we

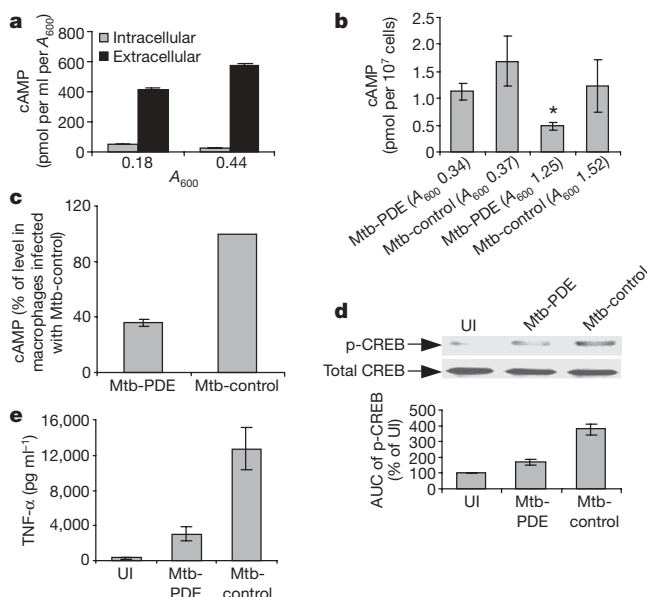


Figure 2 | Overexpression of phosphodiesterase *Rv0805* in *M. tuberculosis* reduces intramacrophage cAMP levels, CREB phosphorylation, and TNF- α secretion in infected J774 cells. **a, b**, *In vitro* cultures of *M. tuberculosis* secrete cAMP in the extracellular culture medium (**a**), and the Mtb-PDE strain shows reduced intrabacterial cAMP levels relative to the Mtb-control in early ($A_{600} \sim 0.35$) and late ($A_{600} > 1.25$) growth phases (**b**). **c–e**, Compared with the Mtb-control, Mtb-PDE-infected J774 cells show reduced intramacrophage cAMP levels (**c**), reduced CREB phosphorylation (**d**), and reduced TNF- α secretion (**e**). UI, uninfected. Data are mean \pm s.d. of multiple experiments ($n = 2$ in **d** and $n = 3$ in **a–c, e**). * $P < 0.05$, two-tailed Student's *t* test.

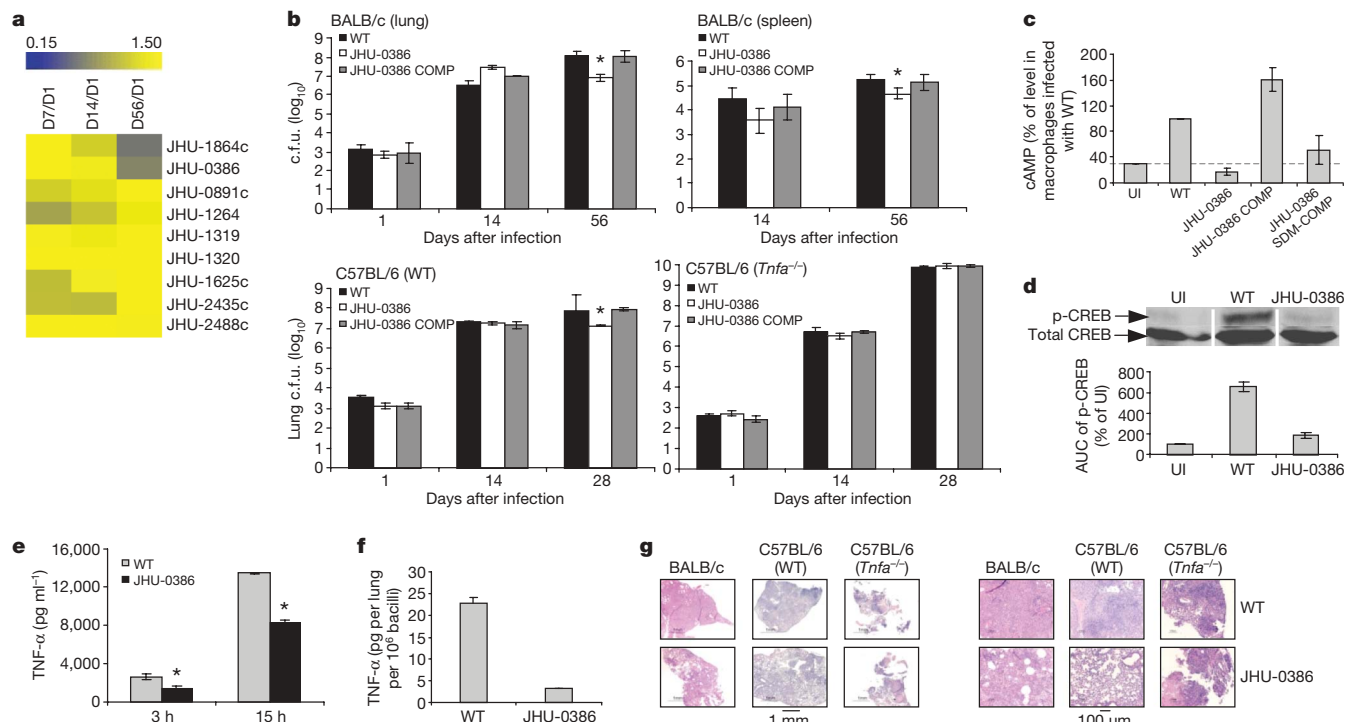


Figure 3 | The *M. tuberculosis* Rv0386 mutant shows reduced mouse virulence, and lower levels of intramacrophage cAMP, CREB phosphorylation, and TNF- α secretion. **a**, Pooled mouse infection reveals that the Rv0386 mutant shows a pattern of survival decline; colour intensity represents specific qPCR abundance relative to day 1 (D1). **b**, Single mutant infections show reduced Rv0386 mutant survival at day 56 in BALB/c (top) and at day 28 in C57BL/6 (bottom left) mouse tissues, but not in *Tnfa*-deficient mice (bottom right). c.f.u., colony-forming units; WT, wild type. **c–e**, In J774 cells, the Rv0386 mutant shows reduced intramacrophage cAMP levels at 3 h that are restored to wild-type levels by an intact complementing allele but not with site-directed mutations (SDM) in the adenylate cyclase

domain (**c**). The mutant also shows reduced CREB-phosphorylation at 16 h (**d**), and reduced TNF- α secretion at the indicated times (**e**). **f, g**, Moreover, after aerosol infection, reduced TNF- α levels are seen in lung homogenates of JHU-0386-infected BALB/c mice at day 14 (**f**), and reduced cellular infiltration and airway loss at day 56 (BALB/c) or day 28 (C57BL/6), but no histological differences are seen at day 28 in *Tnfa*^{-/-} C57BL/6 mice (**g**). Data are the mean values from several mice in **a** ($n = 4$), mean \pm s.d. from multiple mice in **b, f** ($n = 3$), or mean \pm s.d. of several experiments ($n = 2$ in **d**, $n = 3$ in **c, e**). * $P < 0.05$ between wild-type and JHU-0386 strains, by two-tailed Student's *t* test.

studied the signal transduction pathways during infection with the mutant lacking Rv0386. Macrophage infection by the Rv0386 mutant elicited sharply reduced CREB phosphorylation signals, equivalent to levels in uninfected macrophages (Fig. 3d), and reduced TNF- α secretion, 40–50% below wild-type levels (Fig. 3e). To evaluate the impact of these *in vitro* reductions in inflammatory markers during whole animal infections, we evaluated TNF- α levels in BALB/c mouse lung homogenates following aerosol infection with wild type or the Rv0386 mutant. As seen in Fig. 3f, lung TNF- α levels in the JHU-0386 mutant were nearly tenfold lower than those seen with the wild type. Concordantly, the histopathology of mouse lungs infected with the Rv0386 mutant showed considerably less airway consolidation and inflammatory damage than the corresponding wild-type-infected tissues in both immunocompetent mouse strains (BALB/c and C57BL/6), but were equally severe in C57BL/6 *Tnfa*^{-/-} mice (Fig. 3g).

To understand the mechanism of Rv0386 modulation of intramacrophage cAMP levels, we infected macrophages with *M. tuberculosis* strains pre-labelled with [¹⁴C]-glycerol, and followed radiolabelled (bacterial-derived) cAMP levels using silica gel (Fig. 4a, b) or poly-ethylenimine (PEI) cellulose (Fig. 4c, d) thin-layer chromatography (TLC). There was a significant reduction in radiolabelled (bacterial-derived) cAMP levels by 60–80% in macrophages infected with the Rv0386 mutant, but not in those infected with either the complemented Rv0386 mutant or wild-type *M. tuberculosis* (Fig. 4b, d). These data indicate that cAMP derived from *M. tuberculosis* carbon pools enters macrophages after infection, and that loss of the Rv0386 adenylate cyclase gene reduces the ability of *M. tuberculosis* to deliver bacterial-derived cAMP to the macrophage cytoplasm. On the basis of these findings, we propose that the Rv0386 gene product belongs

to a mycobacterial cAMP generation and delivery system that produces cAMP within the host phagosome and facilitates its transport into the host cytoplasm, leading to excess cAMP and a subversion of cellular signal transduction (Fig. 4e).

Although several extracellular bacterial pathogens have evolved virulence effectors for modulating host cellular cAMP levels, either through G-protein modifying ADP ribosylation or secreted adenylate cyclase exotoxins (Fig. 4e)²³, subversion of host cell cAMP signal transduction by pathogenic mycobacteria has not been examined with modern tools. Our data indicate that the intracellular pathogen *M. tuberculosis* possesses at least one adenylate cyclase (Rv0386) that is required for the intramacrophage cAMP burst after phagocytosis, and that in the absence of Rv0386, CREB phosphorylation, TNF- α secretion, tissue immunopathology, and mouse virulence are reduced (Fig. 4e). The full consequences of cAMP intoxication of macrophages by *M. tuberculosis* are not fully determined and may include other pathways, such as host cell apoptosis^{10,24}.

Our data indicate that the microbe subverts the host cAMP signal transduction system to influence immune cell function, and that one consequence of this mechanism is early secretion of the pro-inflammatory cytokine TNF- α . A growing body of literature supports the concept of TNF- α dysregulation in the immunopathogenesis of tuberculosis. Indeed, low levels of TNF- α are well-known to be required for immune containment of latent *M. tuberculosis*^{25,26}, whereas in active disease high levels of TNF- α contribute to caseation necrosis, the blockade of dendritic cell maturation, and the development of granulomas that could serve the pathogen's purposes by providing an avascular sanctuary from cell-mediated immunity^{27–29}. Although TNF- α secretion and granuloma formation are commonly

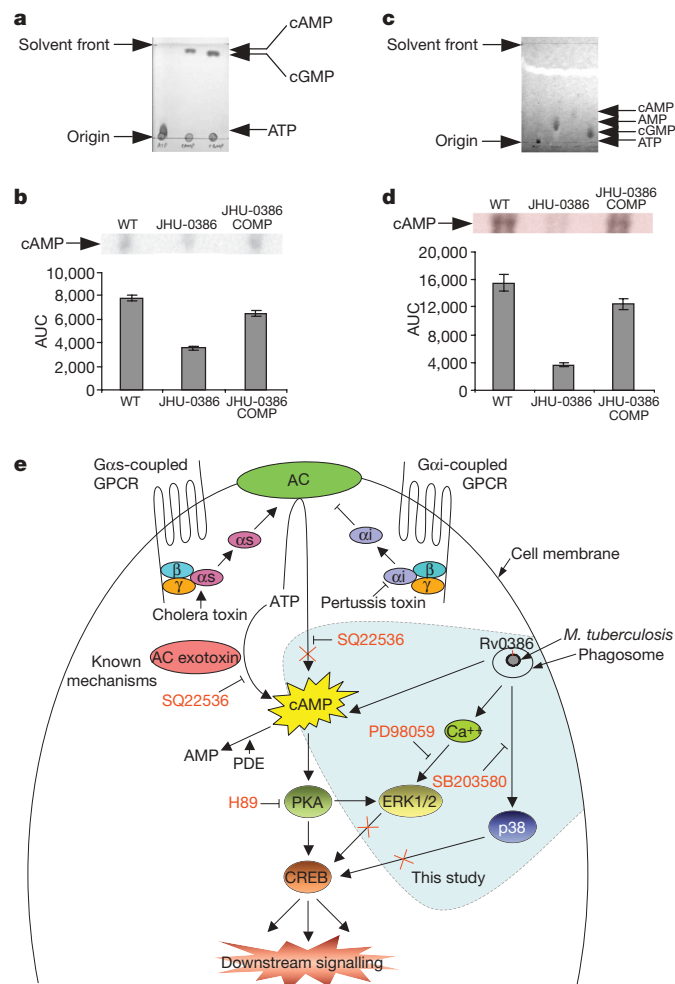


Figure 4 | Bacterial-derived cAMP enters the macrophage cytosol after infection. **a, c**, Silica gel TLC (**a**) and PEI cellulose chromatography (**c**) resolve the nucleotides indicated (ultraviolet visualization). **b, d**, After labelling *M. tuberculosis* strains with [14 C]-glycerol, J774 cells infected with the JHU-0386 mutant show significantly reduced bacterial-derived, radiolabelled cAMP in the intramacrophage compartment by silica gel TLC (**b**) or PEI cellulose separation (**d**) with autoradiography (top), and densitometric quantification (bottom). WT, wild type. Representative data of several experiments ($n = 2$ in **a, c**) or mean \pm s.d. ($n = 2$ in **b, d**) are shown. **e**, Pathways of intracellular cAMP intoxication by pathogenic bacteria. This study shows that the *M. tuberculosis* adenylate cyclase Rv0386 is required for the infection-associated macrophage cAMP burst as well as CREB phosphorylation. Red crosses indicate pathways shown not to be involved in the infection-associated cAMP burst. See Supplementary Text 1 for details. AC, adenylate cyclase.

associated with mycobacterial containment, emerging evidence suggests that microbial growth and dissemination are paradoxically enhanced through host granuloma formation mechanisms. Recently, for example, granuloma formation was found to enhance both bacterial growth and dissemination in a manner dependent on the bacterial *RD1* gene locus in the *M. marinum*–zebrafish model³⁰. Our data with *M. tuberculosis* in macrophages and mice support and extend this concept by showing that *M. tuberculosis* uses cAMP secretion to induce host TNF- α production, and that this results in more extensive lung disease and improved bacterial survival in immunocompetent mice. These findings suggest that *M. tuberculosis* elicits granuloma formation as part of its survival program.

METHODS SUMMARY

A detailed description of the bacterial strains, plasmids and growth conditions is provided in the full Methods. The PDE-overexpressing plasmid was constructed by cloning the gene encoding the phosphodiesterase of *M. tuberculosis*, Rv0805,

into the mycobacterial expression vector pSD5 under the control of the *hsp60* promoter. *M. tuberculosis* CDC1551 transformed with empty vector, pSD5-*hsp60* (Mtb-control), was used as a control strain in the experiments involving Mtb-PDE. The JHU-0386 mutant strain was complemented with either a wild-type or a mutant Rv0386 allele, called *SDMRv0386*, containing two missense mutations leading to N120Y and R124S substitutions in Rv0386. N120 and R124 are predicted active site residues for the adenylate cyclase domain of Rv0386, and their replacement destroys adenylate cyclase activity. Estimation of bacterial loads in mouse organs was performed by quantitative real-time PCR (qPCR) or by single-strain infection. For estimation by qPCR, a pool of *M. tuberculosis* mutants in 8 of the 17 adenylate cyclase genes was used to infect BALB/c mice by the aerosol route. Bacterial colonies obtained from lungs of four mice at different time points were used for the preparation of genomic DNA. Bacillary proliferation of a specific mutant strain in mice lungs over a period of 56 days after infection was estimated by comparing the fold-changes in the relative abundance of strain-specific PCR products in the pool at different days with its relative abundance in the genomic DNA pool at day 1 by performing 35-cycle qPCR experiments. Cyclic AMP levels in the intra- and extracellular compartments of *M. tuberculosis*, and in the cytoplasm of J774 macrophage-like cells infected with *M. tuberculosis*, were estimated by ELISA using the cAMP Enzyme Immunoassay kit (Assay Designs Inc.) and by silica gel 60 F₂₅₄ (Sigma) or cellulose PEI-F TLC (J.T. Baker Inc.). The levels of TNF- α secreted into the culture medium by infected macrophages or in the lung homogenates of infected mice were measured using a mouse TNF- α ELISA kit. Total and phosphorylated CREB levels in the macrophages were determined by immunoblotting using the clarified macrophage lysates with the respective antibodies and the luminol reagent. A detailed description of these methods is provided in the full Methods.

Full Methods and any associated references are available in the online version of the paper at www.nature.com/nature.

Received 1 April; accepted 30 April 2009.

Published online 10 June 2009.

- Dye, C. Global epidemiology of tuberculosis. *Lancet* **367**, 938–940 (2006).
- Wright, A. et al. Epidemiology of antituberculosis drug resistance 2002–07: an updated analysis of the Global Project on Anti-Tuberculosis Drug Resistance Surveillance. *Lancet* doi:10.1016/S0140-6736(09)60331-7 (in the press).
- Flannagan, R. S., Cosio, G. & Grinstein, S. Antimicrobial mechanisms of phagocytes and bacterial evasion strategies. *Nature Rev. Microbiol.* **7**, 355–366 (2009).
- Dannenborg, A. M. Jr. Immunopathogenesis of pulmonary tuberculosis. *Hosp. Pract. (Off. Ed.)* **28**, 51–58 (1993).
- Bai, G., Schaak, D. D. & McDonough, K. A. cAMP levels within *Mycobacterium tuberculosis* and *Mycobacterium bovis* BCG increase upon infection of macrophages. *FEMS Immunol. Med. Microbiol.* **55**, 68–73 (2009).
- Roach, S. K., Lee, S. B. & Schorey, J. S. Differential activation of the transcription factor cyclic AMP response element binding protein (CREB) in macrophages following infection with pathogenic and nonpathogenic mycobacteria and role for CREB in tumor necrosis factor α production. *Infect. Immun.* **73**, 514–522 (2005).
- Lowrie, D. B., Jackett, P. S. & Ratcliffe, N. A. *Mycobacterium microti* may protect itself from intracellular destruction by releasing cyclic AMP into phagosomes. *Nature* **254**, 600–602 (1975).
- Baker, D. A. & Kelly, J. M. Structure, function and evolution of microbial adenylate and guanylate cyclases. *Mol. Microbiol.* **52**, 1229–1242 (2004).
- Sands, W. A. & Palmer, T. M. Regulating gene transcription in response to cyclic AMP elevation. *Cell. Signal.* **20**, 460–466 (2008).
- Serezani, C. H., Ballinger, M. N., Aronoff, D. M. & Peters-Golden, M. Cyclic AMP: master regulator of innate immune cell function. *Am. J. Respir. Cell Mol. Biol.* **39**, 127–132 (2008).
- Johannessen, M. & Moens, U. Multisite phosphorylation of the cAMP response element-binding protein (CREB) by a diversity of protein kinases. *Front. Biosci.* **12**, 1814–1832 (2007).
- Servillo, G., Della Fazio, M. A. & Sassone-Corsi, P. Coupling cAMP signaling to transcription in the liver: pivotal role of CREB and CREM. *Exp. Cell Res.* **275**, 143–154 (2002).
- Pette, K. et al. Isolation of *Mycobacterium tuberculosis* mutants defective in the arrest of phagosome maturation. *Proc. Natl Acad. Sci. USA* **101**, 13642–13647 (2004).
- Walburger, A. et al. Protein kinase G from pathogenic mycobacteria promotes survival within macrophages. *Science* **304**, 1800–1804 (2004).
- Fratti, R. A., Chua, J., Vergne, I. & Deretic, V. *Mycobacterium tuberculosis* glycosylated phosphatidylinositol causes phagosome maturation arrest. *Proc. Natl Acad. Sci. USA* **100**, 5437–5442 (2003).
- Axelrod, S. et al. Delay of phagosome maturation by a mycobacterial lipid is reversed by nitric oxide. *Cell. Microbiol.* **10**, 1530–1545 (2008).
- Hunter, R. L., Jagannath, C. & Actor, J. K. Pathology of postprimary tuberculosis in humans and mice: contradiction of long-held beliefs. *Tuberculosis (Edinb.)* **87**, 267–278 (2007).

18. Tsai, M. C. *et al.* Characterization of the tuberculous granuloma in murine and human lungs: cellular composition and relative tissue oxygen tension. *Cell. Microbiol.* **8**, 218–232 (2006).
19. Timm, J. *et al.* Differential expression of iron-, carbon-, and oxygen-responsive mycobacterial genes in the lungs of chronically infected mice and tuberculosis patients. *Proc. Natl Acad. Sci. USA* **100**, 14321–14326 (2003).
20. Via, L. E. *et al.* Tuberculous granulomas are hypoxic in guinea pigs, rabbits, and nonhuman primates. *Infect. Immun.* **76**, 2333–2340 (2008).
21. Shenoy, A. R., Sivakumar, K., Krupa, A., Srinivasan, N. & Visweswariah, S. S. A survey of nucleotide cyclases in Actinobacteria: unique domain organization and expansion of the class III cyclase family in *Mycobacterium tuberculosis*. *Comp. Funct. Genomics* **5**, 17–38 (2004).
22. Lamichhane, G. *et al.* A postgenomic method for predicting essential genes at subsaturation levels of mutagenesis: application to *Mycobacterium tuberculosis*. *Proc. Natl Acad. Sci. USA* **100**, 7213–7218 (2003).
23. Ahuja, N., Kumar, P. & Bhatnagar, R. The adenylate cyclase toxins. *Crit. Rev. Microbiol.* **30**, 187–196 (2004).
24. von Kethen, A. & Brune, B. Attenuation of macrophage apoptosis by the cAMP-signaling system. *Mol. Cell. Biochem.* **212**, 35–43 (2000).
25. Keane, J. *et al.* Tuberculosis associated with infliximab, a tumor necrosis factor α -neutralizing agent. *N. Engl. J. Med.* **345**, 1098–1104 (2001).
26. Chakravarty, S. D. *et al.* Tumor necrosis factor blockade in chronic murine tuberculosis enhances granulomatous inflammation and disorganizes granulomas in the lungs. *Infect. Immun.* **76**, 916–926 (2008).
27. Bekker, L. G. *et al.* Immunopathologic effects of tumor necrosis factor alpha in murine mycobacterial infection are dose dependent. *Infect. Immun.* **68**, 6954–6961 (2000).
28. Clay, H., Volkman, H. E. & Ramakrishnan, L. Tumor necrosis factor signaling mediates resistance to mycobacteria by inhibiting bacterial growth and macrophage death. *Immunity* **29**, 283–294 (2008).
29. Hanekom, W. A. *et al.* *Mycobacterium tuberculosis* inhibits maturation of human monocyte-derived dendritic cells *in vitro*. *J. Infect. Dis.* **188**, 257–266 (2003).
30. Davis, J. M. & Ramakrishnan, L. The role of the granuloma in expansion and dissemination of early tuberculous infection. *Cell* **136**, 37–49 (2009).

Supplementary Information is linked to the online version of the paper at www.nature.com/nature.

Acknowledgements The support of National Institutes of Health (NIH) awards AI30036, AI36973 and AI37856 is gratefully acknowledged.

Author Contributions N.A. and W.R.B. designed the research. N.A. performed the experiments. R.G., S.N. and G.L. designed and contributed to the mouse experiments. N.A. and W.R.B. analysed the data and wrote the paper.

Author Information Reprints and permissions information is available at www.nature.com/reprints. Correspondence and requests for materials should be addressed to W.R.B. (wbishai@jhmi.edu).

METHODS

Bacterial strains, plasmids and growth conditions. In this study we used *Escherichia coli* strain DH5 α and *M. tuberculosis* CDC1551, as described earlier³¹. Details on the transposon insertion mutants of *M. tuberculosis* used in this study (Supplementary Fig. 3) may be found on the TARGET website of the Johns Hopkins University (<http://webhost.nts.jhu.edu/target/>). Plasmid pSD5-hsp60 (mycobacteria-*E. coli* shuttle vector for protein expression in *M. tuberculosis* from the strong mycobacterial promoter, *Phsp60*) was kindly provided by A. Tyagi, University of Delhi South Campus. Both *E. coli* and mycobacterial strains were grown as described³¹ from frozen glycerol stocks stored at -70°C . All reagents to grow mycobacteria were tested for the absence of endotoxin contamination using the E-Toxate assay (Sigma-Aldrich).

Overexpression of Rv0805 in *M. tuberculosis*. The gene encoding the PDE of *M. tuberculosis*, Rv0805 (ref. 32), was PCR-amplified from *M. tuberculosis* chromosomal DNA using gene-specific primers, PrRv0805(F) and PrRv0805(R) (Supplementary Table 1), using conditions described earlier³². The amplicons were cloned into the mycobacterial expression vector pSD5-hsp60 at the Nde I and Pst I sites. The resulting construct pSD5-hsp60_Rv0805 was sequenced and subsequently used to transform *M. tuberculosis* CDC1551. Overexpression of Rv0805 in the Mtb-PDE strain was confirmed by real-time RT-PCR as described previously³¹, using Rv0805-specific primer pairs (Rv0805_RT(F) and Rv0805_RT(R); Supplementary Table 1). *M. tuberculosis* CDC1551 transformed with empty vector, pSD5-hsp60 (Mtb-control), was used as a control strain in the experiments involving Mtb-PDE. For overexpression of Rv0805 fused with a C-terminal Flag tag, Rv0805 was PCR amplified by using gene-specific primers, PrRv0805(F) and Rv0805Flag(R) (Supplementary Table 1), and cloned into the mycobacterial expression vector pSD5-hsp60 as described earlier.

Expression of Rv0386-Flag in *M. tuberculosis*. To express the Rv0386 fused with the Flag tag at its C terminus in *M. tuberculosis*, a 3,762 base pair (bp) DNA fragment including the coding sequence of the Rv0386 gene, 459 bp of 5' sequence (including the gene's native promoter), and 24 bp of Flag sequence at the 3' end was PCR-amplified with the primers pGWRv0386_F and pGWRv0386 (Flag)_R (Supplementary Table 1). Using the Gateway cloning system (Invitrogen), these amplicons were cloned into the destination vector pGS202R, which is a hygromycin resistance (Hyg^R) derivative of mycobacterial integrating vector pMH94 containing LR recombination sites (G.L. and S.N., unpublished data). The resulting construct, pGS202R-Rv0386-Flag, was subjected to nucleotide sequencing and subsequently used to transform *M. tuberculosis* CDC1551. Candidate Hyg^R colonies were selected, and the presence of the intact Rv0386-Flag gene was identified by PCR and Southern blotting.

Construction of Rv0386 complementation strains. To complement the JHU-0386 mutant, a 3,738 bp DNA fragment including the coding sequence of the Rv0386 gene and 459 bp of 5' sequence (including the gene's native promoter) was amplified by PCR with primers pGWRv0386_F and pGWRv0386_R (Supplementary Table 1) and cloned into the destination vector, pGS202R, as described above. The resulting construct, pGS202R-Rv0386, was subjected to nucleotide sequencing and subsequently used to transform the *M. tuberculosis* JHU-0386 mutant strain which is kanamycin resistant (Kan^R). Candidate Hyg^R and Kan^R colonies were selected, and the presence of the intact complementing Rv0386 allele was identified by PCR and Southern blotting. We also constructed a mutant complementing Rv0386 allele, called SDMRv0386, which contains two missense mutations leading to N120Y and R124S substitutions in Rv0386. This was made with primer pairs pSDMRv0386_F and pSDMRv0386_R (Supplementary Table 1) together with pGS202R-Rv0386-Flag template DNA using QuikChange XL site-directed mutagenesis kit (Stratagene) according to the manufacturer's instructions. The resulting construct, pGS202R-SDMRv0386, was subjected to nucleotide sequencing and subsequently used to transform the *M. tuberculosis* JHU-0386 mutant strain.

Mycobacterial infection of mice and estimation of bacterial load by quantitative real-time PCR. A pool of *M. tuberculosis* mutants in 8 of 17 adenylate cyclase genes was used to infect BALB/c mice by the aerosol route, with an inoculum that implanted $\sim 3.7 \times 10^3$ c.f.u. in the lungs at day 1. Groups of four mice were killed at days 1, 7, 14 and 56 after infection, and the respective lung homogenates were plated on 7H11 agar medium to obtain mycobacterial colonies representing a heterogeneous population of different mutants residing in mouse lungs at each time point. Bacterial colonies obtained from lungs of four mice at each time point were scraped from 7H11 agar plates, pooled, and used for preparation of genomic DNA. Genomic DNA was prepared from pooled mycobacterial colonies, quantified by measuring absorbance at 260 nm, and used for quantitative real-time PCR (qPCR) experiments. Bacterial proliferation of specific mutant strains in mouse lungs over a period of 56 days after infection was estimated by comparing fold-changes in the relative abundance of each strain-specific PCR product in the pool at different days with their relative abundance

in the genomic DNA pool at day 1 by performing 35-cycle qPCR experiments. Each qPCR experiment was performed using 10 ng of genomic DNA prepared from the pooled mycobacterial colonies obtained from mouse lungs at each of the time points (day 1 and the following days), and a primer pair (containing transposon-specific primer SP1, and an adenylate-cyclase-specific primer; Supplementary Table 1) designed to amplify ~ 200 bp junctional DNA sequences specific for the transposon point of insertion of each adenylate cyclase mutant (Supplementary Fig. 3). Fold-changes in relative abundance of mutant-specific DNA were measured by normalizing PCR product abundance to that of *sigA*. qPCR values for a particular time point were normalized to that for day 1. Ratio values lower than one indicate reduced survival in the mouse lung at that time point.

Infection of mice with single mycobacterial strains. Single strain infections of 4–5-week-old BALB/c or C57BL/6 mice and 4–7-week-old *Tnfa*-deficient mice, 12956-*Tnfm1GK*/J, were performed with the JHU-0386, wild-type CDC1551 and JHU-0386 COMP strains of *M. tuberculosis* by the aerosol route, with an inoculum that implanted $\sim 10^3$ c.f.u. in the lungs of BALB/c or C57BL/6 and $\sim 10^2$ c.f.u. in the lungs of *Tnfa*-deficient mice, respectively, at day 1. Three mice from each group were subsequently killed at day 1 and weeks 2, 4 and 8 post-infection to determine the organ c.f.u. counts. Lung and spleen tissues were homogenized in their entirety in PBS, and colonies were enumerated on selective 7H11 plates after 3 weeks of incubation at 37°C .

Infection of macrophages with *M. tuberculosis*. Infection ratios were determined by fluorescence microscopy; live or heat-killed mycobacteria were tagged with Sulfo-NHS-Biotin (Pierce) and subsequently used for infection of J774 macrophage-like cells. For 3 h infections, macrophages were incubated with the inoculating mycobacterial suspension in RPMI for 3 h, followed by three washes with PBS; for 6 h infections, macrophages were incubated for a further 3 h after PBS washes. At the end of the infection at each time point, macrophages were fixed on coverslips and incubated with DyLight-488-conjugated streptavidin in 1% BSA, 0.1% saponin in PBS for 4 h. Fluorescent mycobacterial cells were visualized using fluorescence microscopy, and the level of infection was quantified by counting the number of cells infected in at least five fields per replicate. No fewer than 100 cells per replicate were counted. Macrophages infected with a 1:40 MOI for 3 h resulted in ~ 70 –80% of cells infected, and those with a 1:40 MOI for 6 h resulted in $>85\%$ of cells infected; cell viability remained $>75\%$ under all conditions as estimated by trypan blue staining. For infection of primary macrophages, bone marrow derived macrophages were isolated from 5–7-week-old BALB/c mice as described earlier⁶.

ELISA. For estimation of intramacrophage cAMP or cGMP levels, macrophages were seeded on 6-well plates at 5×10^5 cells per well for 24 h, and infected with mycobacteria for 3 h with a 1:40 MOI as described earlier before lysis. ELISAs were performed with the macrophage lysates by using Enzyme Immunoassay Kits (Assay Designs Inc.) according to the manufacturer's instructions. Intrabacterial cAMP levels in *M. tuberculosis* were estimated by generating a clarified bacterial lysate after heat lysis of bacterial suspensions in 0.1 M HCl. Prior to acid-heat lysis, dilutions of this suspension were spread on 7H11 agar plates for bacterial enumeration, and the intrabacterial cAMP levels in *M. tuberculosis* were estimated as pmol per 10^7 bacilli. Levels of TNF- α secreted into the culture medium by infected macrophages (MOI 1:100 for 3 h), or in lung homogenates of infected mice, were measured using the R&D Systems Quantikine Mouse TNF- α /TNFSF1A Immunoassay ELISA kit. For estimation of TNF- α in mouse lungs infected with a particular bacterial strain, equal volumes of lung homogenates from three infected mice were combined and used for TNF- α measurement.

***M. tuberculosis* cell lysate preparation.** *M. tuberculosis* cell lysates were prepared from mid-log-phase cultures in PBS by bead-beating followed by centrifugation at high speed for 10 min. The pellet fraction comprising cell envelope proteins was subsequently washed twice with PBS, suspended in SDS loading dye, and boiled for 5 min. The supernatant fraction corresponding to cytosolic proteins was passed through a 0.22 μm filter, mixed with SDS loading dye, and boiled for 5 min. For SDS-PAGE, equal amount of proteins from both the fractions were loaded onto SDS-PAGE gels.

Western blot analysis. Macrophages were seeded on 6-well plates at 5×10^5 cells per well, and 24 h later were infected with mycobacteria with a 1:40 MOI for 3 h, and subsequently subjected to three washes with PBS. Infections were then allowed to progress for 13 h. Total CREB or phosphorylated CREB western immunoreactivity of macrophage lysates was performed as described⁶. Levels of p-CREB were quantified by densitometry of anti-phosphorylated-CREB immunoblots from at least two independent experiments, and the values were obtained after normalization to the respective total CREB intensities. Anti-Flag western immunoreactivity of mycobacterial cell lysates was performed according to the manufacturer's instructions (Sigma).

Detection of cAMP in infected J774 macrophage-like cells by TLC. *M. tuberculosis* cell pellets were suspended in PBS containing 0.02% Tween-80 (PBS-T) and incubated with $1 \mu\text{Ci ml}^{-1}$ of [^{14}C]-glycerol at 37°C with shaking for 4 h. Subsequently, cells were pelleted, washed with PBS and suspended in complete 7H9 medium for overnight growth at 37°C . The next day, before infection, the labelled mycobacterial cell pellets were washed twice with PBS-T and suspended in RPMI. J774 macrophage-like cells were infected with radiolabelled mycobacteria with a 1:40 MOI for 3 h as described above. At the end of the infection, macrophages were lysed in 0.1 M HCl plus 0.05% Triton X-100 for 15 min on ice. The cell debris was separated by centrifugation at high speed, and the protein concentration in the lysate was estimated using Bradford's reagent. For comparisons between different samples, lysate volumes were adjusted for protein concentration, and equal protein amounts were spotted on the thin layer medium. Before spotting, lysate proteins were precipitated by boiling for 1 min in a dry block; after centrifugation at high speed, the supernatant was spotted on either Silica gel 60 F₂₅₄ (Sigma) or Cellulose PEI-F (J.T. Baker Inc.) TLC sheets ($20 \times 10 \text{ cm}$). Ascending chromatography was conducted for 1 h at room temperature (25°C)^{33,34}. Commercially available purified nucleotides were spotted alongside the samples to identify the position of cAMP and other nucleotides. Separated nucleotides were visualized with short-wave ultraviolet light. Radiolabelled cAMP fractions were visualized by autoradiography with a PhosphorImager (Molecular Dynamics).

Inhibitor treatment. The inhibitors were purchased from Calbiochem, reconstituted either in sterile, endotoxin-tested water or dimethylsulphoxide (DMSO) according to manufacturer's recommendations, and used at the following concentrations: H89 (50 μM), SQ22536 (200 μM), PD98059 (50 μM) and SB203580

(50 μM). DMSO was used at the same concentrations as the vehicle control. Another PKA-specific inhibitor, protein kinase A inhibitor fragment 14-22, myristoylated trifluoroacetate salt (PKA-I) was purchased from Sigma and used at 40 μM . Macrophages were treated with these inhibitors or DMSO 1 h before infection. For all inhibitors, a dose-response relationship was observed in relation to CREB phosphorylation (for H89 or SQ22536), ERK1/2 phosphorylation (for PD98059), or p38 phosphorylation (for SB203580) (data not shown), and the concentrations used in subsequent studies were chosen on the basis of the dose-response curve. None of the inhibitors used had a significant effect on macrophage uptake of mycobacteria.

Statistical analysis. Statistical significance was determined with the paired two-tailed Student's *t* test at $P < 0.05$ level of significance using InStat/Prism software.

31. Agarwal, N., Woolwine, S. C., Tyagi, S. & Bishai, W. R. Characterization of the *Mycobacterium tuberculosis* sigma factor SigM by assessment of virulence and identification of SigM-dependent genes. *Infect. Immun.* **75**, 452–461 (2007).
32. Shenoy, A. R., Sreenath, N., Podobnik, M., Kovacevic, M. & Visweswariah, S. S. The Rv0805 gene from *Mycobacterium tuberculosis* encodes a 3',5'-cyclic nucleotide phosphodiesterase: biochemical and mutational analysis. *Biochemistry* **44**, 15695–15704 (2005).
33. Higashida, H., Hossain, K. Z., Takahagi, H. & Noda, M. Measurement of adenylyl cyclase by separating cyclic AMP on silica gel thin-layer chromatography. *Anal. Biochem.* **308**, 106–111 (2002).
34. Böhme, E. & Schultz, G. Separation of cyclic nucleotides by thin-layer chromatography on polyethyleneimine cellulose. *Methods Enzymol.* **38**, 27–38 (1974).

Enhancing CD8 T-cell memory by modulating fatty acid metabolism

Erika L. Pearce¹, Matthew C. Walsh¹, Pedro J. Cejas¹, Gretchen M. Harms¹, Hao Shen², Li-San Wang^{1,3}, Russell G. Jones⁴ & Yongwon Choi¹

CD8 T cells, which have a crucial role in immunity to infection and cancer, are maintained in constant numbers, but on antigen stimulation undergo a developmental program characterized by distinct phases encompassing the expansion and then contraction of antigen-specific effector (T_E) populations, followed by the persistence of long-lived memory (T_M) cells^{1,2}. Although this predictable pattern of CD8 T-cell responses is well established, the underlying cellular mechanisms regulating the transition to T_M cells remain undefined^{1,2}. Here we show that tumour necrosis factor (TNF) receptor-associated factor 6 (TRAF6), an adaptor protein in the TNF-receptor and interleukin-1R/Toll-like receptor superfamily, regulates CD8 T_M -cell development after infection by modulating fatty acid metabolism. We show that mice with a T-cell-specific deletion of TRAF6 mount robust CD8 T_E -cell responses, but have a profound defect in their ability to generate T_M cells that is characterized by the disappearance of antigen-specific cells in the weeks after primary immunization. Microarray analyses revealed that TRAF6-deficient CD8 T cells exhibit altered expression of genes that regulate fatty acid metabolism. Consistent with this, activated CD8 T cells lacking TRAF6 display defective AMP-activated kinase activation and mitochondrial fatty acid oxidation (FAO) in response to growth factor withdrawal. Administration of the anti-diabetic drug metformin restored

FAO and CD8 T_M -cell generation in the absence of TRAF6. This treatment also increased CD8 T_M cells in wild-type mice, and consequently was able to considerably improve the efficacy of an experimental anti-cancer vaccine.

A prevailing paradigm in immunology is that antigenic signal strength drives progressive T-cell differentiation³. To investigate this model regarding T_M cells, we studied CD8 T-cell responses to bacterial infection in mice with a T-cell-specific deletion of TRAF6 (TRAF6- ΔT), a negative regulator of antigen-specific T-cell activation⁴. Despite having fewer total CD8 T cells (Supplementary Fig. 1), TRAF6- ΔT mice mounted normal ovalbumin (OVA)-specific T_E -cell responses to attenuated *Listeria monocytogenes* expressing OVA (LmOVA; Fig. 1a and Supplementary Fig. 2). To examine CD8 T_M cells in TRAF6- ΔT mice, we immunized with LmOVA and measured OVA-specific cells 60 days post-infection. Although OVA-specific T_E -cell responses were intact, CD8 T_M -cell generation in TRAF6- ΔT mice was severely compromised (Fig. 1b and Supplementary Fig. 3), even with tenfold higher or lower immunizing doses (not shown). In mice lacking *cbl-b*⁵, a different negative regulator of antigen-specific T-cell activation, T_M cells developed normally (Supplementary Fig. 4), indicating that failure of T_M -cell generation in TRAF6- ΔT mice cannot be entirely explained by loss of a negative regulator.

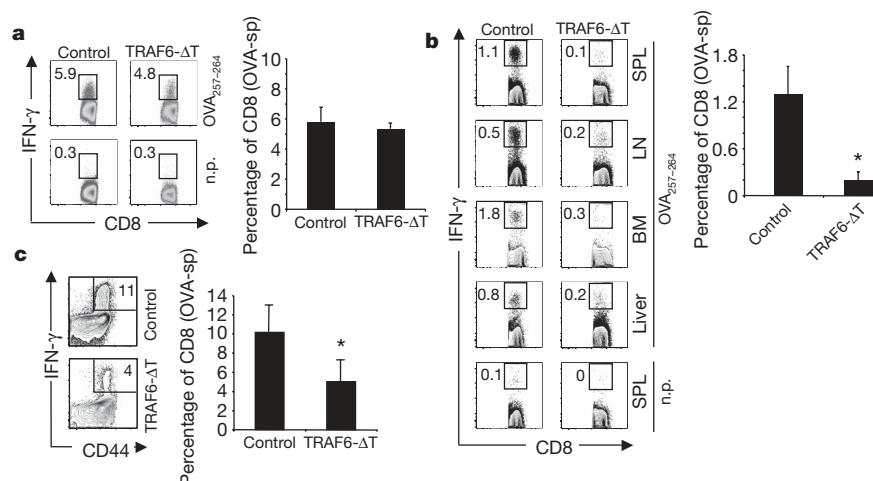


Figure 1 | TRAF6- ΔT mice mount normal T_E -cell responses, but have impaired T_M -cell development after immunization with *L. monocytogenes*. Control and TRAF6- ΔT mice were LmOVA-immunized and spleen (a) and (c) or spleen (SPL), lymph nodes (LN), and bone marrow (BM) (b) cells were restimulated with OVA peptide and analysed for intracellular interferon- γ (IFN- γ) 7 days (a, $n = 3$ –5 per group) or 60 days (b, $n = 3$ per group)

post-infection. n.p., no peptide. c, Sixty days post-immunization mice were challenged with LmOVA, and OVA-specific cells were analysed 7 days post-challenge ($n = 3$ per group). Dot plots and bar graphs show percentages of CD8 T cells producing IFN- γ (means and standard deviation); * $P = 0.02$ (b), 0.0005 (c).

¹Department of Pathology and Laboratory Medicine, ²Department of Microbiology, ³Penn Center for Bioinformatics, University of Pennsylvania School of Medicine, Philadelphia, Pennsylvania 19104, USA. ⁴McGill Cancer Centre, Department of Physiology, McGill University, Montreal, QC, H3G 1Y6, Canada.

A hallmark of T_M cells is the ability to mount accelerated recall responses to challenge infection. To confirm the impaired generation of CD8 T_M cells in TRAF6- ΔT mice, we challenged previously immunized control and TRAF6- ΔT mice with LmOVA and measured OVA-specific cells 7 days later. TRAF6- ΔT mice failed to respond robustly to re-infection, indicating that T_M cells may not have been generated and that the smaller OVA-specific population present in TRAF6- ΔT mice was a new primary response (Fig. 1c). To determine whether TRAF6- ΔT mice generate T_M cells, we transferred equal numbers of OVA-specific cells from previously immunized control and TRAF6- ΔT mice 28 days post-infection, at which time a small population of OVA-specific cells appeared to be present (Supplementary Fig. 3), and compared functionality on a per cell basis in response to challenge. We reasoned that naive donor cells transferred into immune-competent animals would not respond to infection because they would be vigorously outcompeted by endogenous naive cells, and only T_M donor cells would mount accelerated recall responses that could outcompete endogenous naive cells. At day 7 post-challenge, donor-derived OVA-specific secondary T_E cells from control mice represented 11% of the engrafted population whereas TRAF6- ΔT donor cells were undetectable (Supplementary Fig. 5), demonstrating a severe impairment in CD8 T_M -cell development in TRAF6- ΔT mice.

TRAF6- ΔT mice accumulate CD4 T cells and develop multi-organ inflammatory disease⁴. Because CD4 T cells can influence CD8 T-cell responses^{6–8} we wanted to rule out effects from the TRAF6-deficient CD4 T-cell compartment. To determine whether defective CD8 T_M -cell generation in TRAF6- ΔT mice was intrinsic to CD8 T cells, we crossed TRAF6- ΔT mice with major-histocompatibility-complex-class-I-restricted OVA-specific T-cell-receptor-transgenic OT-I mice. Because OT-I mice lack CD4 T cells, generation of OTI-TRAF6- ΔT mice allowed us to assay a pure population of uniformly naive TRAF6-deficient CD8 T cells (Supplementary Figs 6–8). We transferred OTI-TRAF6-wild type (WT) and OTI-TRAF6- ΔT cells into congenic recipients, which possess a normal CD4 T-cell compartment, and then immunized with LmOVA (Fig. 2a). By transferring only small numbers of transgenic cells we could measure endogenous OVA-specific cells at the same time as the engrafted donor response, allowing us to assume that most donor cells were activated⁹. In addition, following T-cell responses by serially bleeding allowed us to compare the kinetics of responding CD8 T cells within individual animals. Although both OTI-TRAF6-WT and OTI-TRAF6- ΔT donor cells mounted strong T_E -cell responses (days 4–6), OTI-TRAF6- ΔT cells were not maintained during contraction (days 10–21) and were undetectable by 3 weeks post-infection (Fig. 2b, c and Supplementary Fig. 9). Donor T_E cells from both genotypes exhibited similar expression of classical activation markers after primary immunization (Supplementary Figs 10 and 11); however, consistent with published data regarding killer cell lectin-like receptor 1 (KLRG1) as a marker for short-lived T_E cells that do not form T_M cells, a greater percentage of the OTI-TRAF6- ΔT T_E -cell population expressed higher levels of KLRG1 (Supplementary Fig. 12)¹⁰. After challenge infection, only donor OTI-TRAF6-WT T_M cells responded robustly (Fig. 2b, c and Supplementary Fig. 9). These results demonstrate that, although TRAF6 is dispensable for CD8 T_E -cell responses, TRAF6 signalling within CD8 T cells is crucial to T_M -cell generation.

Antigen-specific CD8 T cells responding to infection are not a homogenous population, but consist of small numbers of T_M -cell precursors that express interleukin 7 receptor (IL7R α ; ref. 11). In conjunction with this idea, numerous studies have delineated roles for the γ_c cytokines IL7 and IL15 as critical factors for CD8 T-cell homeostasis and T_M -cell development^{12–15}. Impaired γ_c cytokine signalling in TRAF6-deficient CD8 T cells could explain the defect in their ability to form T_M cells. We tested the ability of CD8 T_E cells to respond to IL15 and found that both OTI-TRAF6-WT and OTI-TRAF6- ΔT cells exhibit similar responsiveness to this cytokine

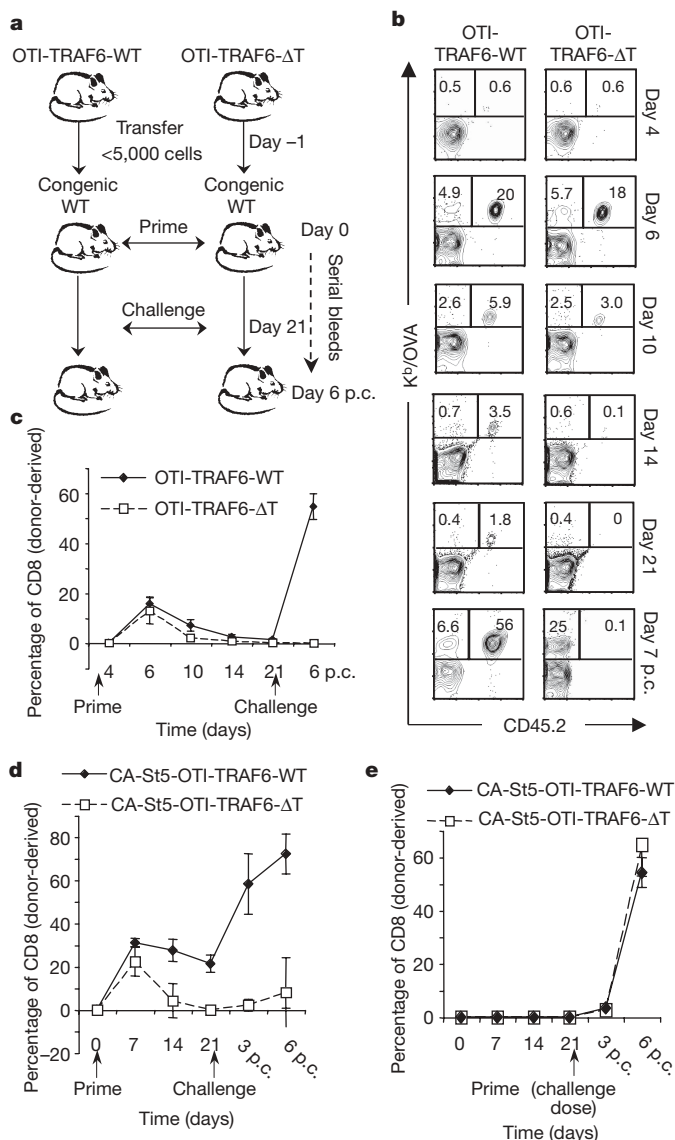


Figure 2 | TRAF6 intrinsically regulates CD8 T_M -cell generation. OT-I cells (<5,000) from OTI-TRAF6-WT and OTI-TRAF6- ΔT (CD45.2; **a–c**) or CA-St5-OTI-TRAF6-WT and CA-St5-OTI-TRAF6- ΔT mice (CD45.2; **d, e**) were transferred into CD45.1 recipients ($n = 5–9$ per group) and LmOVA-immunized. Three weeks post-transfer, immune (**a–d**) or unimmunized (**e**) mice were LmOVA-challenged. Mice were bled as indicated and cells were surface-stained. Dot plots show donor cells by CD45.2 and K^b/OVA tetramer (numbers indicate total CD8 T-cell percentages that are host- or donor-derived). Line graphs represent percentages of donor-derived CD8 T cells (means \pm standard deviation). p.c., post challenge.

(Supplementary Figs 13 and 14). To be sure that the lack of T_M -cell development by TRAF6-deficient CD8 T cells is not secondary to a defect in survival, and to investigate further a possible defect in γ_c cytokine signalling, we crossed OTI-TRAF6- ΔT mice to mice constitutively expressing an active form of Stat-5 (also known as Stat5b; CA-St5)¹⁶, a critical signalling molecule downstream of the γ_c cytokine receptor¹⁶. CD8 T cells expressing CA-St5 show augmented survival, proliferation and B-cell leukemia/lymphoma 2 (Bcl2) expression¹⁷, and CA-St5 mice exhibit selective expansion of memory-like CD8 T cells¹⁶. We transferred CA-St5-OTI-TRAF6-WT and CA-St5-OTI-TRAF6- ΔT cells into congenic mice, immunized, and followed the donor and host OVA-specific responses (Fig. 2d and Supplementary Fig. 15). Contraction of CA-St5-OTI-TRAF6-WT populations was reduced compared to control OT-I populations (Fig. 2c, d). Surprisingly, however, CA-St5-OTI-TRAF6- ΔT cells were not rescued from contracting to undetectable levels 3 weeks post-infection (Fig. 2d

and Supplementary Fig. 15). Importantly, we confirmed that CA-St5 expression in TRAF6-deficient CD8 T cells enhanced survival in an *ex vivo* survival assay (Supplementary Fig. 16), indicating that the severe contraction exhibited by the TRAF6-deficient OT-I population (Fig. 2c, d and Supplementary Fig. 15) and the ensuing lack of T_M -cell development is not secondary to a general survival defect. Animals primed with the challenge dose of bacteria 3 weeks post-transfer showed no differences in the T_E -cell response between the genotypes (Fig. 2e and Supplementary Fig. 15), indicating that the loss of TRAF6-deficient CD8 T cells is exaggerated in response to signals after infection, and not simply due to defects in homeostatic signals after transfer.

We used a systems biology approach to identify unique gene expression signatures between OTI-TRAF6-WT and OTI-TRAF6- ΔT CD8 T cells that could account for their differences in survival after infection. We performed microarray analyses for both genotypes 6 and 10 days post-transfer and infection (Supplementary Fig. 17). Owing to similar survival rates between OTI-TRAF6-WT and OTI-TRAF6- ΔT CD8 T cells during the peak of the T_E -cell response, but striking differences in survival during contraction, we reasoned that expression of genes related to survival might begin to diverge between genotypes at day 10 post-infection. We used the NIAID DAVID website (<http://david.abcc.ncifcrf.gov>) to look for pathways in the KEGG database that have significant overlaps with differentially expressed genes in our microarray experiment. We discovered that TRAF6-deficient cells from day 10 post-infection displayed defects in the expression of genes that function in several metabolic pathways, including fatty acid metabolism (Fig. 3a).

FAO is an important survival pathway in metabolically stressed cells¹⁸ and the removal of signals associated with infection, such as growth factor cytokines including IL2, induces metabolic stress in haematopoietic cells^{19,20}. Therefore, we tested the ability of OTI-TRAF6-WT and OTI-TRAF6- ΔT CD8 T cells to oxidize fatty acids

after withdrawal of the pro-proliferative growth factor cytokine IL2 *in vitro*. After IL2 withdrawal, only control OTI-TRAF6-WT CD8 T cells increased FAO to a high degree (Fig. 3b). Consistent with normal activation (Supplementary Fig. 18), activated control and TRAF6-deficient CD8 T cells increased glycolysis in response to IL2 (data not shown). Also, TRAF6-deficient CD8 T cells displayed normal upregulation of FAO in response to glucose withdrawal, indicating that cells are not completely unfit in the absence of TRAF6, but rather their inability to regulate catabolic fatty acid metabolism is due to the lack of a specific signal from growth factor (Supplementary Fig. 19). Importantly, although transgenic expression of CA-St5 did enhance T-cell survival after infection (Supplementary Fig. 16), it did not rescue the defect in FAO in TRAF6-deficient cells after growth factor withdrawal (Supplementary Fig. 20), indicating that FAO defects are not secondary to survival defects.

Proliferating T cells use glycolytic metabolism rather than FAO for energy generation^{21–23}, and growth factors enable this bias²⁴. In the absence of glucose, cells can survive in part by ceasing proliferation and switching to catabolic metabolism like FAO and autophagy^{18,20}. OTI-TRAF6- ΔT CD8 T cells were notably less capable of effecting this metabolic switch than OTI-TRAF6-WT CD8 T cells after IL2 withdrawal (Fig. 3c). This indicated that TRAF6-deficient CD8 T cells responding to infection are unable to survive contraction and persist as long-lived T_M cells due to an inability to properly engage pathways of FAO when growth factors such as IL2 become limiting after the peak of the immune response.

AMP-activated kinase (AMPK) and Akt are central regulators of FAO and glycolysis, respectively²³. Consistent with reduced FAO, TRAF6-deficient CD8 T cells have lower active AMPK levels after IL2 withdrawal (Fig. 3d). To investigate whether AMPK defects could underlie decreased FAO in TRAF6-deficient CD8 T cells, we measured the effect of the anti-diabetic drug metformin, which promotes AMPK activation²⁵, on FAO after IL2 withdrawal. Metformin increased

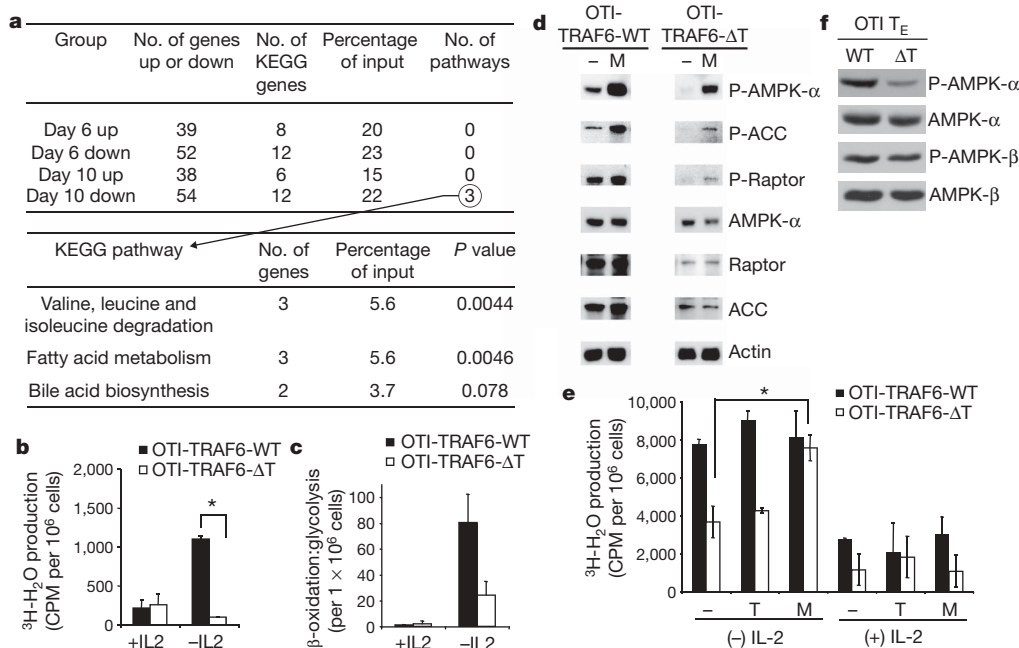


Figure 3 | TRAF6-deficient CD8 T cells display defects in fatty acid metabolism that can be corrected by metformin. **a**, OT-I cells (<5,000) from OTI-TRAF6-WT and OTI-TRAF6- ΔT mice (CD45.2) were transferred into CD45.1 recipients and immunized with LmOVA. Six ($n = 3$ per group) and 10 ($n = 5$ per group) days post-infection, donor cells were analysed by microarray (**a** and Supplementary Fig. 17). Tables were generated using NIAID DAVID and KEGG databases. **b**, FAO (measured as mitochondrial β -oxidation) of activated OTI-TRAF6-WT and OTI-TRAF6- ΔT cells post-IL2 withdrawal; * $P = 0.012$. **c**, Ratio of β -oxidation to glycolysis in activated

OTI-TRAF6-WT and OTI-TRAF6- ΔT cells post-IL2 withdrawal. **d**, Western analysis of cells 16 h post-IL2 withdrawal with and without metformin (M; acetyl CoA carboxylase (ACC, also known as Acaca) and raptor are examined as targets of AMPK). **e**, Mitochondrial β -oxidation of activated OTI-TRAF6-WT and OTI-TRAF6- ΔT cells with and without IL2, where cells received nothing (–), triciribine (T) or metformin (M) for 16 h, * $P = 0.003$. **f**, Western analysis of purified OTI-TRAF6-WT and OTI-TRAF6- ΔT T_E donor cells (7 days post-infection). All error bars show mean and standard deviation.

AMPK activation (Fig. 3d) and rescued FAO in TRAF6-deficient CD8 T cells (Fig. 3e). In contrast, FAO in TRAF6-deficient cells was unaffected by the Akt inhibitor triciribine (Fig. 3e), indicating that Akt may not regulate this metabolic pathway. These data support that FAO initiation after the peak of infection, accompanied by the reduction in T-cell survival signals, underlies T_M -cell development, and that commitment to this metabolic pathway is affected when TRAF6 is absent. In such a case, stimulating FAO in TRAF6-deficient CD8 T cells would rescue the observed defects and promote T_M cells. Consistent with this hypothesis, OTI-TRAF6- ΔT CD8 T cells had lower levels of active AMPK at the peak of the T_E -cell response (Fig. 3f).

To explore whether inducing FAO *in vivo* would rescue the observed defects in TRAF6-deficient CD8 T cells and promote T_M cells, we administered metformin daily after T-cell transfer and infection. Remarkably, metformin promoted survival not only of OTI-TRAF6- ΔT CD8 T cells throughout contraction but also of endogenous OVA-specific cells, resulting in enhanced T_M cells with the capacity to respond to re-infection (Fig. 4a and Supplementary Fig. 21). Metformin also promoted OTI-TRAF6-WT CD8 T-cell survival (Fig. 4b). Treatment with a second FAO-inducing drug^{26–28}, the mTOR (mammalian target of rapamycin, also known as FRAP1) inhibitor rapamycin, resulted in markedly increased T_M -cell development and ensuing recall response for both OTI-TRAF6- ΔT and OTI-TRAF6-WT CD8 T cells (Fig. 4a, b and Supplementary Fig. 21). Together these data strongly point towards the commitment to FAO as a key requirement for T_M -cell development, and the pharmacological modulation of this metabolic pathway as a potential target for vaccine design.

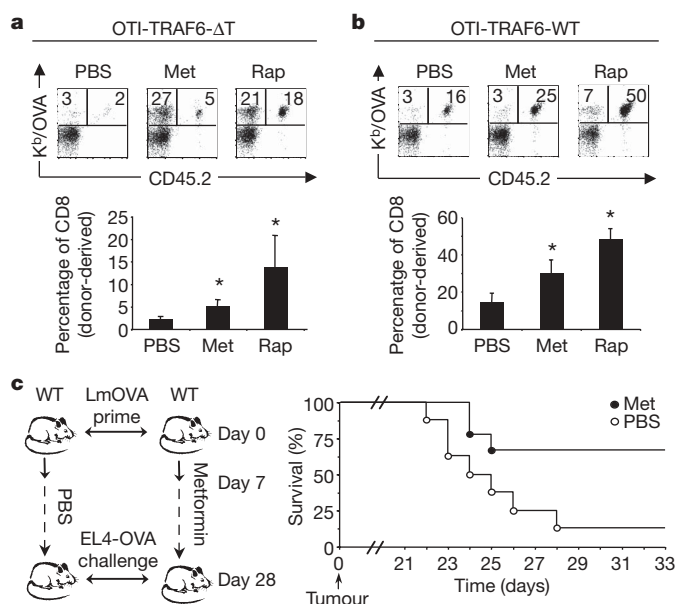


Figure 4 | Metformin treatment promotes T_M -cell generation and protective immunity after infection and tumour challenge. **a, b**, OT-I cells (<5,000) from OTI-TRAF6-WT and OTI-TRAF6- ΔT mice (CD45.2) were transferred into CD45.1 recipients and immunized with LmOVA. Eight days post-infection, mice were injected daily with PBS ($n = 7$ –9 per group), metformin ($n = 7$ –9 per group) or rapamycin ($n = 5$ per group) for 3 weeks and were then challenged with LmOVA. OVA-specific responses of host and donor cells in the blood were measured 5 days post-challenge. Dot plot numbers reflect the percentages of total CD8 T cells that are host- (left) or donor- (right) derived (OVA-specific). Bar graphs represent the percentage of CD8 T cells that are donor-derived (means and standard error). * P values (comparing to PBS) are 0.015 (Met) and 0.000038 (Rap) (**a**), and 0.0373 (Met) and 0.00028 (Rap) (**b**). **c**, C57BL/6 mice were immunized and daily injections of metformin or PBS began 7 days post-infection. Three weeks later, treatments ceased and mice were inoculated with EL4-OVA tumours. Tumours became palpable by 18 days post-inoculation and mice were killed when tumours reached 2 cm. The graph reflects percentage survival ($n = 9$, metformin; $n = 8$, PBS).

Promoting CD8 T_M -cell development is a major goal of vaccination. Our data showing increased CD8 T_M cells for donor OT-I and endogenous OVA-specific cells after metformin treatment indicated that commitment to FAO is generally important for CD8 T_M -cell development, and not only in settings of TRAF6-deficiency. This led us to the idea that pharmacological modulation of T-cell metabolism could enhance vaccine efficacy. To test this we used an experimental vaccine against an aggressive tumour²⁹. We immunized control mice with LmOVA and then began daily injections of PBS or metformin after the peak of the T_E -cell response. After 3 weeks, drug treatment ceased and mice were inoculated with EL4-OVA tumour cells (Fig. 4c). Metformin was administered after T_E -cell expansion to avoid the possibility of altering the T_E -cell response. To rule out direct effects of metformin on tumour growth, treatment was stopped 24 h before tumour injection. After EL4-OVA inoculation, 6 out of 9 metformin-treated mice survived >33 days compared to only 1 out of 8 PBS-treated mice (Fig. 4c). This increase in survival after metformin treatment correlated with an increase in T_M cells before tumour inoculation (Supplementary Fig. 22), indicating that metformin treatment enhanced T_M -cell generation resulting in greater protective anti-tumour immunity.

Proliferating T cells use glucose as their main energy source and suppress fatty acid metabolism, whereas quiescent cells (that is, naive and T_M) break down fatty acids, amino acids and glucose interchangeably for energy²³. As such, proliferating T_E cells display an anabolic signature typified by increased glycolytic metabolism, whereas T_M cells display a catabolic signature. This implies that during contraction there is an active conversion of cellular energy metabolism to generate T_M cells. Current models suggest that during contraction T cells compete for growth factors such as IL2, and we speculate that as these growth factors become limiting cells become stressed and undergo a metabolic transformation essential for T_M -cell generation. We propose a model in which TRAF6 has a critical role after infection by regulating a metabolic switch in CD8 T cells that promotes survival and development into long-lived T_M cells.

Investigating the role of TRAF6 in T_M -cell development led us to the surprising finding that energy metabolism can be pharmacologically manipulated during an immune response to promote CD8 T_M -cell generation and protective immunity. Although the exact mechanism of metformin-mediated CD8 T_M -cell enhancement remains unclear, our work indicates that metabolism-altering drugs hold promise as immunotherapeutics and command further study as modulators of T-cell responses. Metformin has been shown to inhibit tumour progression^{25,30}, although given our results it is unclear how metformin-regulated changes in T_M cells contribute to its anti-tumour properties. Our findings highlight a critical link between metabolic transitions and cell fate determination, and may have important implications for therapeutic and prophylactic vaccine development.

METHODS SUMMARY

TRAF6^{fllox/fllox}CD4-cre(–) (control) and TRAF6^{fllox/fllox}CD4-cre(+) (TRAF6- ΔT) were bred in-house (backcrossed more than ten generations to C57BL/6) and have been previously described⁴. C57BL/6 (WT) and OT-I transgenic mice were purchased from The Jackson Laboratory. OT-I mice were bred to TRAF6^{fllox/fllox}CD4-cre mice to generate control OT-I-TRAF6^{fllox/fllox}CD4-cre(–) or OT-I-TRAF6^{fllox/+}CD4-cre(+) mice (OTI-TRAF6-WT) and OT-I-TRAF6^{fllox/fllox}CD4-cre(+) (OTI-TRAF6- ΔT). Mice expressing the constitutively active Stat5 transgene (CA-St5)¹⁶ were provided by M. Farrar and bred to OT-I-TRAF6^{fllox/+}CD4-cre(+) mice to generate control OT-I-CA-St5-TRAF6^{fllox/fllox}CD4-cre(–) mice (OTI-CA-St5-TRAF6-WT) and OT-I-CA-St5-TRAF6^{fllox/fllox}CD4-cre(+) mice (OTI-CA-St5-TRAF6- ΔT). Age-matched control and TRAF6- ΔT mice were injected intravenously (i.v.) with a sub-lethal dose of 1×10^6 colony forming units (CFU) of recombinant attenuated *L. monocytogenes* (LmOVA) for primary immunizations and challenged i.v. with 1×10^7 CFU for secondary immunizations. CD45.1 congenic mice from OT-I adoptive transfer experiments were injected with a sub-lethal dose of 5×10^6 CFU of LmOVA for primary immunizations and were challenged i.v. with 5×10^7

CFU for secondary immunizations. Acute LmOVA infections are resolved and bacteria are cleared by day 7 in all mice. All *P* values were calculated using unpaired two-tailed Student's *t*-test.

Full Methods and any associated references are available in the online version of the paper at www.nature.com/nature.

Received 23 January; accepted 23 April 2009.
Published online 3 June 2009.

- Harty, J. T. & Badovinac, V. P. Shaping and reshaping CD8⁺ T-cell memory. *Nature Rev. Immunol.* **8**, 107–119 (2008).
- Prlic, M., Williams, M. A. & Bevan, M. J. Requirements for CD8 T-cell priming, memory generation and maintenance. *Curr. Opin. Immunol.* **19**, 315–319 (2007).
- Lanzavecchia, A. & Sallusto, F. Progressive differentiation and selection of the fittest in the immune response. *Nature Rev. Immunol.* **2**, 982–987 (2002).
- King, C. G. *et al.* TRAF6 is a T cell-intrinsic negative regulator required for the maintenance of immune homeostasis. *Nature Med.* **12**, 1088–1092 (2006).
- Bachmaier, K. *et al.* Negative regulation of lymphocyte activation and autoimmunity by the molecular adaptor Cbl-b. *Nature* **403**, 211–216 (2000).
- Shedlock, D. J. & Shen, H. Requirement for CD4 T cell help in generating functional CD8 T cell memory. *Science* **300**, 337–339 (2003).
- Sun, J. C. & Bevan, M. J. Defective CD8 T cell memory following acute infection without CD4 T cell help. *Science* **300**, 339–342 (2003).
- Janssen, E. M. *et al.* CD4⁺ T cells are required for secondary expansion and memory in CD8⁺ T lymphocytes. *Nature* **421**, 852–856 (2003).
- Badovinac, V. P., Haring, J. S. & Harty, J. T. Initial T cell receptor transgenic cell precursor frequency dictates critical aspects of the CD8⁺ T cell response to infection. *Immunity* **26**, 827–841 (2007).
- Joshi, N. S. *et al.* Inflammation directs memory precursor and short-lived effector CD8⁺ T cell fates via the graded expression of T-bet transcription factor. *Immunity* **27**, 281–295 (2007).
- Kaech, S. M. *et al.* Selective expression of the interleukin 7 receptor identifies effector CD8 T cells that give rise to long-lived memory cells. *Nature Immunol.* **4**, 1191–1198 (2003).
- Schluns, K. S., Williams, K., Ma, A., Zheng, X. X. & Lefrancois, L. Cutting edge: requirement for IL-15 in the generation of primary and memory antigen-specific CD8 T cells. *J. Immunol.* **168**, 4827–4831 (2002).
- Schluns, K. S., Kieper, W. C., Jameson, S. C. & Lefrancois, L. Interleukin-7 mediates the homeostasis of naive and memory CD8 T cells *in vivo*. *Nature Immunol.* **1**, 426–432 (2000).
- Tan, J. T. *et al.* Interleukin (IL)-15 and IL-7 jointly regulate homeostatic proliferation of memory phenotype CD8⁺ cells but are not required for memory phenotype CD4⁺ cells. *J. Exp. Med.* **195**, 1523–1532 (2002).
- Surh, C. D., Boyman, O., Purton, J. F. & Sprent, J. Homeostasis of memory T cells. *Immunol. Rev.* **211**, 154–163 (2006).
- Burchill, M. A. *et al.* Distinct effects of STAT5 activation on CD4⁺ and CD8⁺ T cell homeostasis: development of CD4⁺CD25⁺ regulatory T cells versus CD8⁺ memory T cells. *J. Immunol.* **171**, 5853–5864 (2003).
- Kelly, J. *et al.* A role for Stat5 in CD8⁺ T cell homeostasis. *J. Immunol.* **170**, 210–217 (2003).
- Buzzai, M. *et al.* The glucose dependence of Akt-transformed cells can be reversed by pharmacologic activation of fatty acid beta-oxidation. *Oncogene* **24**, 4165–4173 (2005).
- Rathmell, J. C., Vander Heiden, M. G., Harris, M. H., Frauwirth, K. A. & Thompson, C. B. In the absence of extrinsic signals, nutrient utilization by lymphocytes is insufficient to maintain either cell size or viability. *Mol. Cell* **6**, 683–692 (2000).
- Lum, J. J. *et al.* Growth factor regulation of autophagy and cell survival in the absence of apoptosis. *Cell* **120**, 237–248 (2005).
- Frauwirth, K. A. *et al.* The CD28 signaling pathway regulates glucose metabolism. *Immunity* **16**, 769–777 (2002).
- Jones, R. G. *et al.* The proapoptotic factors Bax and Bak regulate T cell proliferation through control of endoplasmic reticulum Ca²⁺ homeostasis. *Immunity* **27**, 268–280 (2007).
- Jones, R. G. & Thompson, C. B. Revving the engine: signal transduction fuels T cell activation. *Immunity* **27**, 173–178 (2007).
- Fox, C. J., Hammerman, P. S. & Thompson, C. B. Fuel feeds function: energy metabolism and the T-cell response. *Nature Rev. Immunol.* **5**, 844–852 (2005).
- Buzzai, M. *et al.* Systemic treatment with the antidiabetic drug metformin selectively impairs p53-deficient tumor cell growth. *Cancer Res.* **67**, 6745–6752 (2007).
- Sipula, I. J., Brown, N. F. & Perdomo, G. Rapamycin-mediated inhibition of mammalian target of rapamycin in skeletal muscle cells reduces glucose utilization and increases fatty acid oxidation. *Metabolism* **55**, 1637–1644 (2006).
- Peng, T., Golub, T. R. & Sabatini, D. M. The immunosuppressant rapamycin mimics a starvation-like signal distinct from amino acid and glucose deprivation. *Mol. Cell Biol.* **22**, 5575–5584 (2002).
- Brown, N. F., Stefanovic-Racic, M., Sipula, I. J. & Perdomo, G. The mammalian target of rapamycin regulates lipid metabolism in primary cultures of rat hepatocytes. *Metabolism* **56**, 1500–1507 (2007).
- Moore, M. W., Carbone, F. R. & Bevan, M. J. Introduction of soluble protein into the class I pathway of antigen processing and presentation. *Cell* **54**, 777–785 (1988).
- Huang, X. *et al.* Important role of the LKB1–AMPK pathway in suppressing tumorigenesis in PTEN-deficient mice. *Biochem. J.* **412**, 211–221 (2008).

Supplementary Information is linked to the online version of the paper at www.nature.com/nature.

Acknowledgements We thank C. Krawczyk, C. King, M. Farrar, Y. Paterson, Z.-K. Pan and E. J. Pearce. This work is supported in part by grants from the NIH (Y.C., H.S.), CIHR (R.G.J.) and an NCI Institutional Training Grant (E.L.P.).

Author Contributions E.L.P., M.C.W., R.G.J. and Y.C. designed the research and analysed the data. E.L.P., M.C.W., P.J.C., L.W. and G.M.H. performed experiments. E.L.P., M.C.W., H.S., R.G.J. and Y.C. contributed to the preparation of the manuscript. E.L.P. wrote the manuscript with M.C.W. and Y.C.

Author Information Microarray data is in the public repository Gene Expression Omnibus (GEO) under accession number GSE15750. Reprints and permissions information is available at www.nature.com/reprints. Correspondence and requests for materials should be addressed to Y.C. (ychoi3@mail.med.upenn.edu).

METHODS

Mice. *Cblb*^{-/-} mice were a gift from J. Penninger. B6.Ly5.2/Cr (CD45.1 congenic) mice were purchased from the National Cancer Institute. All animals were cared for according to the Animal Care Guidelines of the University of Pennsylvania.

Immunizations. We used the attenuated strain of recombinant LmOVA deleted for *actA* (LmOVA)³¹ throughout this paper for convention, however, challenging control and TRAF6-ΔT mice with 1×10^6 CFU of non-attenuated recombinant *Listeria* expressing OVA³², or priming and challenging CD45.1 congenic mice from an OT-I adoptive transfer with 1×10^5 CFU and 1×10^6 of recombinant *Listeria* expressing OVA, respectively, yielded similar results. To determine bacterial clearance, control and TRAF6-ΔT were immunized with 8×10^6 CFU LmOVA and CFU per spleen and liver were determined 2, 4 and 6 days after infection as described³¹. A total of 5×10^6 EL4-OVA (EG.7) tumour cells were injected into the right flank of mice as indicated.

Flow cytometry and intracellular cytokine staining. All fluorochrome-conjugated monoclonal antibodies were purchased from BD Pharmingen or eBioscience. All staining was performed as previously described³¹. For *ex vivo* intracellular cytokine staining, cells were cultured at 37 °C for 5 h in complete medium supplemented with 100 U ml⁻¹ of recombinant human IL2 and 1.0 μl ml⁻¹ GolgiStop, in either the presence or the absence of OVA_{257–264} peptide at 1.0 μg ml⁻¹. OVA-specific CD8⁺ T cells were also quantified by direct staining with H2-K^b/OVA_{257–264} (K^b/OVA) MHC-peptide tetramers, either by killing animals and collecting cells from organs or by collecting blood from a live animal (serial bleeds), as indicated.

Adoptive transfers. Spleenocytes from control and TRAF6-ΔT mice 28 days post-immunization were stained with K^b/OVA tetramer to determine numbers of OVA-specific CD8 T cells. Spleenocytes containing 1×10^4 of OVA-specific cells were transferred intravenously to recipient mice followed by challenge infection as indicated. For OT-I cell adoptive transfers, OT-I cells were obtained from the blood or the spleen and then stained with K^b/OVA tetramers to determine numbers of OT-I cells, and then <5,000 OT-I cells were transferred into recipient mice. Adoptive transfer experiments were done with either OTI-TRAF6^{fllox/fllox}CD4-cre(-) or OTI-TRAF6^{fllox/+}CD4-cre(+) cells, and this confirmed that CD4-cre-expressing cells are not rejected.

In vitro T-cell stimulation. Naive T cells were activated with anti-CD3 (1.0 μg ml⁻¹), anti-CD28 (0.5 μg ml⁻¹) and 100 U ml⁻¹ of IL2 for 3 or 4 days and then assayed as indicated.

Metabolism assays. All activated T cells were rested in the absence of IL2 for 3–4 h (rest period) before being cultured in the absence or presence of IL2 or glucose (withdrawal period). The glycolytic rate of T cells was determined by measuring the conversion of 5-³H-glucose to tritiated water, as described previously³³. In brief, *in vitro* activated OT-I cells were plated at 1×10^6 per ml in 24-well plates and cultured with and without glucose and with and without IL2 (100 U ml⁻¹) as indicated for 14–16 h. Cells were collected, washed twice and resuspended in either glucose-free or glucose-replete medium with and without 100 U ml⁻¹ of IL2 (RPMI, Gibco), and then incubated with 10 μm Ci of 5-³H-glucose (Perkin-Elmer) at 37 °C for 1 h. The reaction was stopped by adding HCl (0.1 M final). ³H₂O generated by enolase activity was separated from 5-³H-glucose by diffusion, and counts were measured using a 1450 Microbeta scintillation counter (Wallac). Measurement of mitochondrial-dependent β-oxidation of fatty acids was conducted as previously described with modifications³⁴. In brief, 1×10^6 activated OT-I cells were cultured with and without glucose and/or with and without IL2 (100 U ml⁻¹) as indicated for 14–16 h. [9,10-³H]-palmitic acid complexed to BSA (essentially fatty acid free; Sigma) was added to the cultures and incubated for 6–8 h. Mitochondrial-independent β-oxidation was assessed by measuring [9,10-³H]-palmitate oxidation in the presence of 200 μM etomoxir (Sigma), an irreversible inhibitor of carnitine palmitoyltransferase I (CPT1), the rate-limiting enzyme for mitochondrial import of long-chain fatty acids. Supernatant was applied to ion-exchange columns (Dowex 1X8–200, Sigma), and ³H₂O recovered by eluting the columns with water. One-fifth of the recovered ³H₂O was then used for scintillation counting. The rate of β-oxidation was calculated as the difference between oxidation counts in the presence or absence of etomoxir, and expressed as CPM per 1×10^6 cells.

Metformin (2 mM)³⁵ or triciribine (1 μM)³⁶ was added during the IL2 withdrawal period as indicated.

In vivo drug treatment. Mice were injected daily with 300 μl of PBS or metformin (250 mg kg⁻¹)³⁵ in 300 μl of PBS. Rapamycin was dissolved in PBS/5% DMSO and injected daily (1.5 mg kg⁻¹)³⁷. The PBS vehicle for these experiments also contained 5% DMSO. No effect between PBS and PBS/5% DMSO was detected.

Microarray. After OT-I cell adoptive transfer and LmOVA infection, splenocytes and blood were collected (at day 6 and 10 post-infection) from individual mice and donor cells were sorted (FACS Vantage, BD Bioscience) on the CD45.2 donor marker directly into Trizol LS (Invitrogen). RNA was extracted and samples were analysed using the Affymetrix Mouse Genome 430 2.0 Array at the University of Pennsylvania Microarray Core Facility. We first used the gcRMA package³⁸ from the Bioconductor software³⁹ to generate log₂ probesets expression levels. Hierarchical clustering showed that one of the samples is an outlier and is excluded in subsequent analyses. We used the limma software package⁴⁰ from Bioconductor to assess the effect of time (days 6 and 10) and genotype (WT and *Traf6*^{-/-}) by fitting the expression levels of each probeset *i* using R model specification 'expr ~ genotype * timepoint', which translates to the following model:

$$x_{ij} = m_i + a_i G_{ij} + b_i T_{ij} + r_i GT_{ij} + e_{ij}$$

where x_{ij} is the log₂ expression level in sample *j*, m_i is the overall mean log₂ expression level, G_{ij} is the indicator variable if sample *j* is *Traf6*^{-/-} ($G_{ij} = 1$ if sample *j* is *Traf6*^{-/-}, 0 otherwise), T_{ij} is the indicator variable if sample *j* is collected at day 10, and GT_{ij} is the genotype-time point interaction term ($GT_{ij} = 1$ if and only if $G_{ij} = 1$ and $T_{ij} = 1$), a_i , b_i and r_i are the coefficients of the genotype and time point effects to be estimated, and e_{ij} is the normally distributed error term. We determined whether probesets are differentially expressed between genotypes at day 6 (day 10) using the classifyTestsF function (nested F-test) from limma with default *P*-value cutoff 0.01 and generated Venn diagrams.

Western blot analysis. Cell lysate preparation, SDS-PAGE, electrophoretic transfer, immunoblotting and development using enhanced chemiluminescence were accomplished as previously described⁴¹. To isolate *ex vivo* T_E cells, OT-I cells were adoptively transferred into CD45.1 congenic mice followed by LmOVA infection. At day 7 post-infection donor cells were isolated (at 4 °C) by MACS purification (Miltenyi Biotech). All antibodies for western analysis were purchased from Cell Signaling. P-AMPK measures phosphorylation at Thr 172.

- Pearce, E. L. & Shen, H. Generation of CD8 T cell memory is regulated by IL-12. *J. Immunol.* **179**, 2074–2081 (2007).
- Foulds, K. E. *et al.* Cutting edge: CD4 and CD8 T cells are intrinsically different in their proliferative responses. *J. Immunol.* **168**, 1528–1532 (2002).
- Elstrom, R. L. *et al.* Akt stimulates aerobic glycolysis in cancer cells. *Cancer Res.* **64**, 3892–3899 (2004).
- Deberardinis, R. J., Lum, J. J. & Thompson, C. B. Phosphatidylinositol 3-kinase-dependent modulation of carnitine palmitoyltransferase 1A expression regulates lipid metabolism during hematopoietic cell growth. *J. Biol. Chem.* **281**, 37372–37380 (2006).
- Buzzai, M. *et al.* Systemic treatment with the antidiabetic drug metformin selectively impairs p53-deficient tumor cell growth. *Cancer Res.* **67**, 6745–6752 (2007).
- Karst, A. M., Dai, D. L., Cheng, J. Q. & Li, G. Role of p53 up-regulated modulator of apoptosis and phosphorylated Akt in melanoma cell growth, apoptosis, and patient survival. *Cancer Res.* **66**, 9221–9226 (2006).
- Albert, M. H., Yu, X. Z., Martin, P. J. & Anasetti, C. Prevention of lethal acute GVHD with an agonistic CD28 antibody and rapamycin. *Blood* **105**, 1355–1361 (2005).
- Wu, Z., Irizarry, R. A., Gentleman, R., Martinez-Murillo, F. & Spencer, F. A model-based background adjustment for oligonucleotide expression arrays. *J. Am. Stat. Ass.* **99**, 909–917 (2004).
- Gentleman, R. C. *et al.* Bioconductor: open software development for computational biology and bioinformatics. *Genome Biol.* **5**, R80 (2004).
- Smyth, G. K. In *Bioinformatics and Computational Biology Solutions Using R and Bioconductor* (eds Gentleman, R., Carey, V., Dudoit, S., Irizarry, R. & Huber, W.) 397–420 (Springer, 2005).
- Kobayashi, T. *et al.* TRAF6 is a critical factor for dendritic cell maturation and development. *Immunity* **19**, 353–363 (2003).

LETTERS

mTOR regulates memory CD8 T-cell differentiation

Koichi Araki¹, Alexandra P. Turner², Virginia Oliva Shaffer², Shivaprakash Gangappa², Susanne A. Keller³, Martin F. Bachmann³, Christian P. Larsen² & Rafi Ahmed¹

Memory CD8 T cells are a critical component of protective immunity, and inducing effective memory T-cell responses is a major goal of vaccines against chronic infections and tumours^{1–3}. Considerable effort has gone into designing vaccine regimens that will increase the magnitude of the memory response, but there has been minimal emphasis on developing strategies to improve the functional qualities of memory T cells⁴. Here we show that mTOR (mammalian target of rapamycin⁵, also known as FRAP1) is a major regulator of memory CD8 T-cell differentiation, and in contrast to what we expected, the immunosuppressive drug rapamycin has immunostimulatory effects on the generation of memory CD8 T cells. Treatment of mice with rapamycin following acute lymphocytic choriomeningitis virus infection enhanced not only the quantity but also the quality of virus-specific CD8 T cells. Similar effects were seen after immunization of mice with a vaccine based on non-replicating virus-like particles. In addition, rapamycin treatment also enhanced memory T-cell responses in non-human primates following vaccination with modified vaccinia virus Ankara. Rapamycin was effective during both the expansion and contraction phases of the T-cell response; during the expansion phase it increased the number of memory precursors, and during the contraction phase (effector to memory transition) it accelerated the memory T-cell differentiation program. Experiments using RNA interference to inhibit expression of mTOR, raptor (also known as 4932417H02Rik) or FKBP12 (also known as FKBP1A) in antigen-specific CD8 T cells showed that mTOR acts intrinsically through the mTORC1 (mTOR complex 1) pathway to regulate memory T-cell differentiation. Thus these studies identify a molecular pathway regulating memory formation and provide an effective strategy for improving the functional qualities of vaccine- or infection-induced memory T cells.

Rapamycin is an immunosuppressive drug commonly used in transplant recipients and specifically inhibits the intracellular kinase mTOR⁵. Several recent studies have shown that rapamycin has various effects on the immune system, such as inhibiting type I interferon production by plasmacytoid dendritic cells⁶, modulating T-cell trafficking⁷, and regulating Foxp3 expression in regulatory T cells^{8,9}. However, the role of the mTOR pathway in regulating CD8 T-cell responses is not known. To address this issue, we treated B6 mice with rapamycin during the course of an acute lymphocytic choriomeningitis virus (LCMV) infection, and monitored the virus-specific CD8 T-cell response (Fig. 1a). We made the surprising observation that rapamycin enhanced the LCMV-specific CD8 T-cell response. Increased numbers of antigen-specific CD8 T cells were seen in both lymphoid and non-lymphoid tissues (Fig. 1a and Supplementary Fig. 1). The most notable thing about this result was the decreased contraction of the T-cell response in the rapamycin treated group. Similar frequencies of virus-specific effector CD8 T cells were observed in both groups of mice at the peak of the T-cell response on day 8 post-infection, but there was minimal contraction of the T cells in the rapamycin treated group

(Fig. 1a). To determine whether the decreased T-cell contraction seen between days 8 to 30 post-infection in the rapamycin treated group was due to increased cell proliferation and/or reduced cell death, mice were infected with LCMV in the presence or absence of rapamycin and then given 5-bromodeoxyuridine (BrdU) during the T-cell contraction phase from days 10 to 22 (Supplementary Fig. 2). We found that there was minimal incorporation of BrdU by antigen-specific CD8 T cells in either group of mice, showing that the decreased contraction of T cells in the presence of rapamycin was not due to increased cell proliferation. Thus, it appears that the major effect of rapamycin is to enhance the survival of antigen-specific CD8 T cells.

We next examined the phenotype of the memory CD8 T cells present in the two groups of mice at day 36 post-infection (Fig. 1b). To investigate this, we performed phenotypic analysis of virus-specific memory CD8 T cells using four markers that are useful in defining memory CD8 T cells: CD127 (IL-7 receptor α and essential for memory T-cell maintenance^{10–13}), CD62L (lymph node homing receptor and associated with high proliferative capacity¹⁴), KLRG1 (inversely correlated with long lived memory cells^{15,16}), and Bcl2 (anti-apoptotic and expressed at high levels in memory T cells^{12,17}). Memory CD8 T cells generated in the presence of rapamycin expressed higher levels of CD127, CD62L and Bcl2, and had a higher frequency of KLRG1^{Low} cells compared to control mice (Fig. 1b and Supplementary Fig. 3). These data strongly suggested that inhibition of the mTOR pathway using rapamycin not only increased the magnitude of the virus-specific CD8 T-cell response (Fig. 1a) but also improved the functional qualities of the memory CD8 T cells, as memory cells with the phenotype (CD127^{High} CD62L^{High} Bcl2^{High} and KLRG1^{Low}) are associated with long-lived protective immunity^{14–16}. To test this directly, we examined the ability of these memory CD8 T cells to undergo homeostatic proliferation, a property essential for long-term memory maintenance, and to make recall responses upon re-exposure to antigen. As shown in Fig. 1c and d, virus-specific memory CD8 T cells generated in mice treated with rapamycin were superior to memory cells generated in untreated mice in both of these hallmark memory properties.

In the experiment shown in Fig. 1, mice were continuously treated with rapamycin during the entire course of the T-cell response (days –1 to 35 post-infection). We next examined how rapamycin would effect the CD8 T-cell response if it was only given during the T-cell expansion phase (days –1 to 8 post-infection). These results (Fig. 2a and b) were strikingly similar to what we had seen earlier (Fig. 1a); even if the rapamycin treatment was discontinued during the contraction phase (days 8–30), there was only minimal death of the effector CD8 T cells generated in the presence of the drug. Previous studies have shown that the day 8 effector CD8 T-cell population consists of two subsets; the terminal effector T cells (CD127^{Low}, KLRG1^{High}) that mostly die over the ensuing 2–4 weeks and the memory precursor cells (CD127^{High}, KLRG1^{Low}) that mostly survive and further differentiate to give rise to the pool of long-lived memory

¹Emory Vaccine Center and Department of Microbiology and Immunology, ²Emory Transplant Center and Department of Surgery, Emory University School of Medicine, Atlanta, Georgia 30322, USA. ³Cytos Biotechnology AG, Wagistrasse 25, 8952 Zürich-Schlieren, Switzerland.

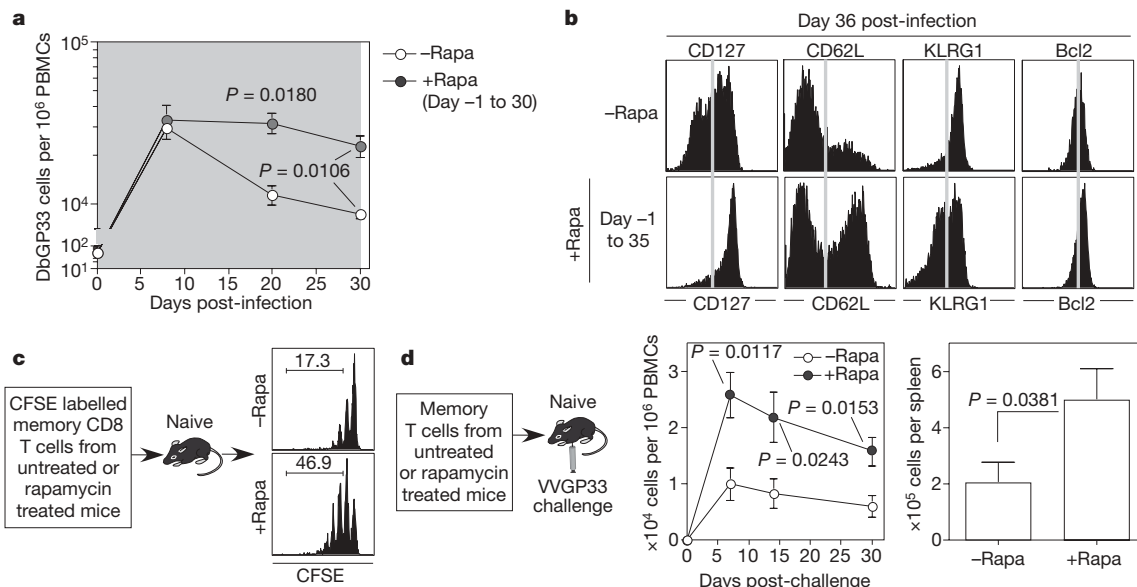


Figure 1 | Rapamycin enhances the number and quality of virus-specific memory CD8 T cells. **a**, Kinetics of endogenous GP33 epitope specific CD8 T cells in peripheral blood mononuclear cells (PBMCs) of LCMV-infected B6 mice treated with rapamycin (from day -1 to 30 post-infection; shaded area; +Rapa, $n = 6$ mice) or not treated (-Rapa, $n = 3$ mice). **b**, Phenotypic analysis of endogenous DbGP33 tetramer positive cells in the spleen at day 36 post-infection. **c**, GP33 epitope specific P14 transgenic memory CD8 T cells (day 34 post-infection) were generated in the presence or absence of rapamycin, CFSE labelled and then adoptively transferred into naive mice to

monitor their homeostatic proliferation. CFSE dilution of P14 cells at 30 days post-transfer is shown, and the number represents percentage of memory cells that divided more than twice. **d**, Memory P14 cells derived from rapamycin treated or untreated mice were adoptively transferred, and mice were challenged with vaccinia virus expressing the GP33 epitope (VVGPP3). Kinetics of P14 cells in PBMCs after challenge and the total P14 cell numbers in spleen on day 30 post-infection are shown (-Rapa, $n = 4$; +Rapa, $n = 6$). Data show mean and s.e.m.

cells^{10,15,16}. Our results suggested that rapamycin was enhancing the formation of these memory precursor cells. This was indeed the case, and day 8 virus-specific effector CD8 T cells generated in rapamycin treated mice contained a higher proportion of CD127^{High}KLRG1^{Low} cells and these cells also expressed higher levels of Bcl2 (Fig. 2c). However, we noticed that the phenotype of memory CD8 T cells at

day 36 post-infection was similar in the drug treated and control mice (Fig. 2d). This was different to the results obtained on continuous rapamycin treatment (compare Fig. 1b and Fig. 2d). Taken together, these results clearly show that rapamycin enhances the formation of memory precursors during the naive to effector T-cell differentiation phase, but these results also suggest that rapamycin may also regulate the effector to memory transition phase.

To test this hypothesis, we treated mice with rapamycin only during the T-cell contraction phase (days 8–35) following acute LCMV infection (Fig. 3). We found that the number of memory cells generated was not affected by the drug (Fig. 3a) but the phenotype of these memory CD8 T cells was notably different (Fig. 3b). Thus, rapamycin treatment during the effector to memory transition phase enhanced the memory differentiation program, resulting in a significantly higher number of virus-specific CD8 T cells with the phenotype characteristic of highly functional memory cells ($P < 0.0001$ – 0.0022 ; Fig. 3b). It was important to determine if this represented cell proliferation and outgrowth of a subset of effector CD8 T cells already expressing these memory markers, or if rapamycin truly increased the expression of these markers in the surviving effector T cells during this effector to memory differentiation phase. To address this issue, we transferred a highly purified (>99.7%) and CFSE-labelled population of day 8 CD62L^{Low} antigen-specific effector CD8 T cells into naive mice, and monitored both cell division and memory differentiation of these transferred effector cells in the presence or absence of rapamycin (Fig. 3c). We found that there was no cell division during this effector to memory transition phase (days 1–25 post-transfer) but that the memory T cells that differentiated in the presence of rapamycin re-expressed CD62L much faster (Fig. 3d and e). More importantly, these memory CD8 T cells were functionally superior and exhibited better recall responses and protective immunity (viral control) following challenge with vaccinia virus expressing the LCMV GP33 epitope (Fig. 3f–h). Thus, inhibiting mTOR during the effector to memory transition phase improved the functional qualities of memory T cells.

The results so far have shown that rapamycin can enhance both the magnitude and quality of the CD8 T-cell response following a

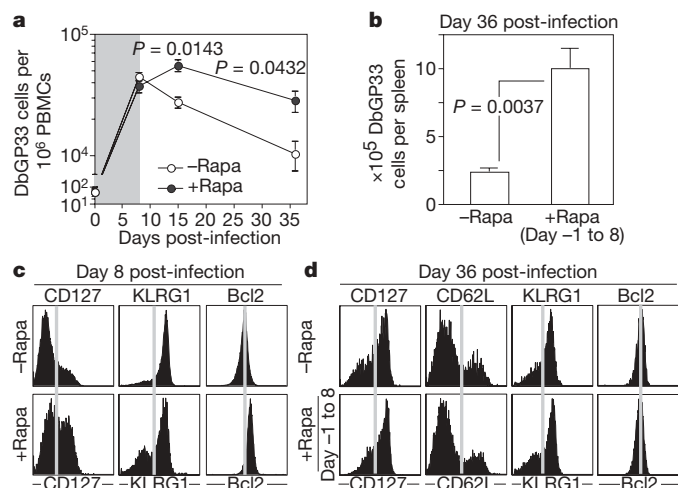


Figure 2 | Rapamycin treatment during T-cell expansion phase increases the number of memory precursors. **a**, Kinetics of endogenous GP33 epitope-specific CD8 T cells in PBMCs of LCMV-infected B6 mice treated with rapamycin (from day -1 to 8 post-infection; shaded area) ($n = 3$ – 6 , each time point). **b**, The average number of DbGP33 tetramer positive cells on day 36 post-infection in spleens of LCMV infected mice treated with rapamycin (-Rapa, $n = 9$; +Rapa day -1 to 8, $n = 3$). **c**, CD127, KLRG1 and Bcl2 expression on endogenous DbGP33 tetramer positive cells in PBMCs at 8 days post LCMV infection in B6 mice. Rapamycin was administered from day -1 to day 8 post-infection. **d**, Phenotypic analysis of DbGP33 tetramer positive cells in spleens of LCMV infected mice (rapamycin treatment from day -1 to 8 post-infection). Data show mean and s.e.m.

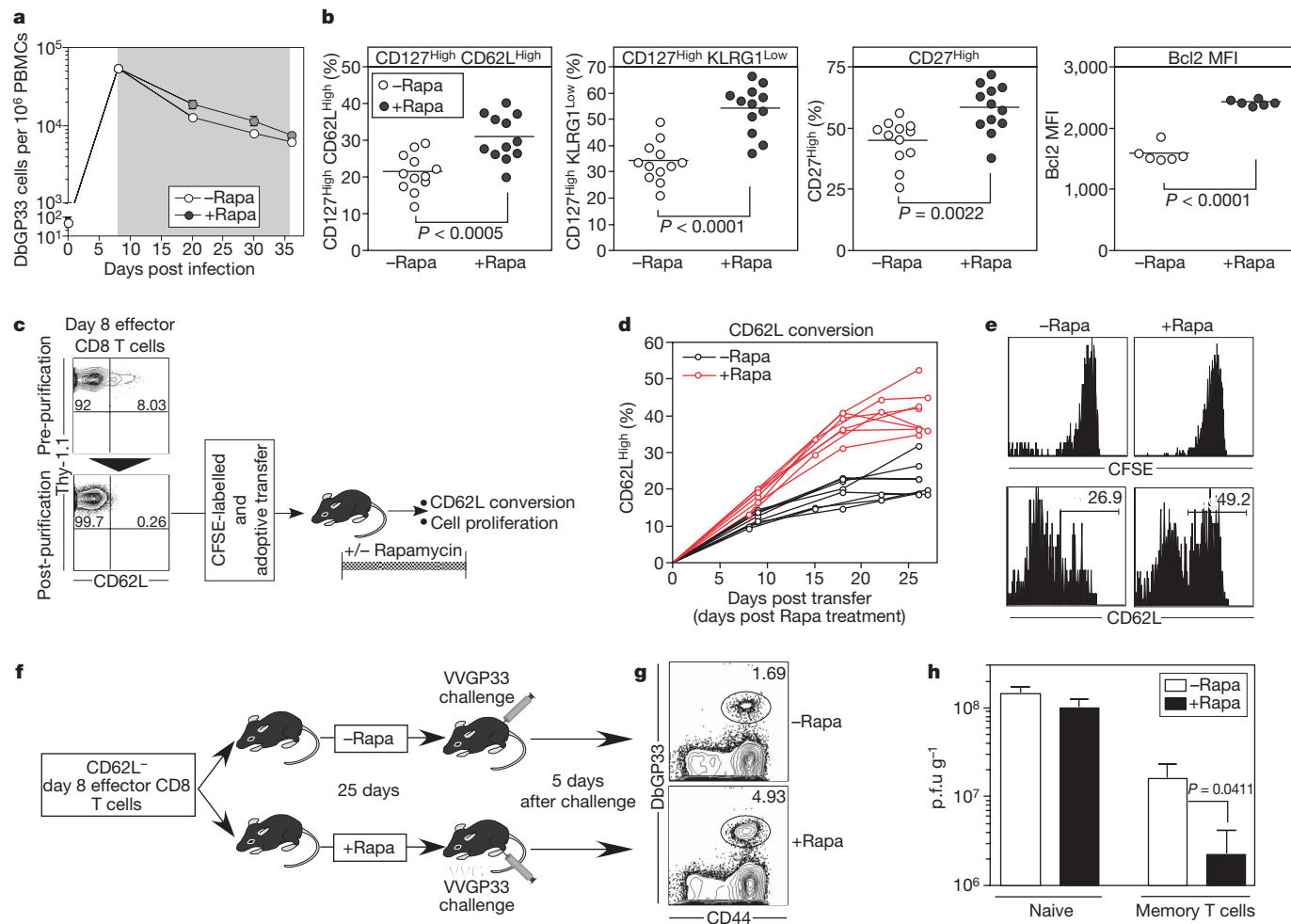


Figure 3 | Rapamycin treatment during effector to memory transition phase accelerates memory differentiation. **a**, Kinetics of endogenous GP33 epitope specific CD8 T cells in PBMCs of LCMV-infected B6 mice treated with rapamycin (from day 8 to 35 post-infection; shaded area) (–Rapa, $n = 9$ mice; +Rapa, $n = 9$). **b**, Phenotypic changes in endogenous DbGP33 tetramer positive CD8 T cells in spleen on day 36 post LCMV infection ($n = 12$; each group). B6 mice were treated with rapamycin during the effector to memory T-cell transition period (days 8–35 post-infection). MFI, mean fluorescence intensity. **c**, CD62L[–] day 8 P14 transgenic effector CD8 T cells were purified, labelled with CFSE, and then adoptively transferred into

primary viral infection. We next examined whether similar effects would be seen during a secondary response. As shown in Supplementary Fig. 4, rapamycin also enhanced recall responses when the drug treatment was only done during secondary LCMV infection. Thus, rapamycin regulates both primary and secondary T-cell responses, and this has important implications in designing strategies for improving memory T-cell qualities during prime-boost vaccine regimens.

To determine if our findings from the mouse model of LCMV infection could be generalized to other systems, we examined the effect of rapamycin following immunization of mice with a non-replicating vaccine. In these experiments, mice were vaccinated with virus-like particles (VLPs) derived from hepatitis B core antigen genetically fused to the LCMV GP33 epitope¹⁸. Rapamycin again enhanced both the magnitude and the quality of the VLP-induced memory CD8 T cells (Supplementary Fig. 5). It should be noted that the effects of rapamycin treatment were very long-lasting; memory T-cell numbers remained tenfold higher even 165 days after stopping the drug treatment (Supplementary Fig. 5a). We also tested the applicability of this approach in a non-human primate model. Rhesus macaques previously immunized with vaccinia virus were

boosted with modified vaccinia virus Ankara (MVA) in the presence or absence of rapamycin, and antigen-specific CD8 T-cell responses were analysed by intracellular IFN- γ staining. We found clear differences in frequencies of antigen-specific CD8 T cells between rapamycin treated and untreated monkeys. In the presence of rapamycin, maintenance of a higher number of memory CD8 T cells was observed (Supplementary Fig. 6a, b), and slower T-cell contraction was evident compared to control animals (Supplementary Fig. 6c). These results demonstrate that rapamycin enhances T-cell immunity in both mice and non-human primates following vaccination with either live or inactivated vaccines.

Our results clearly establish that mTOR is a major regulator of memory CD8 T-cell differentiation. However, a critical question that needs to be answered is whether mTOR is acting intrinsically in antigen-specific CD8 T cells to regulate memory differentiation, or if the observed effects of rapamycin on memory formation are mediated by some other cells of the immune system. It is important to resolve this issue, as mTOR is ubiquitously expressed by many cells and several recent studies have shown that rapamycin can modulate the functional properties of several other cells of the immune system^{6,8,9,19,20}. To address this question, we used a retrovirus based RNA

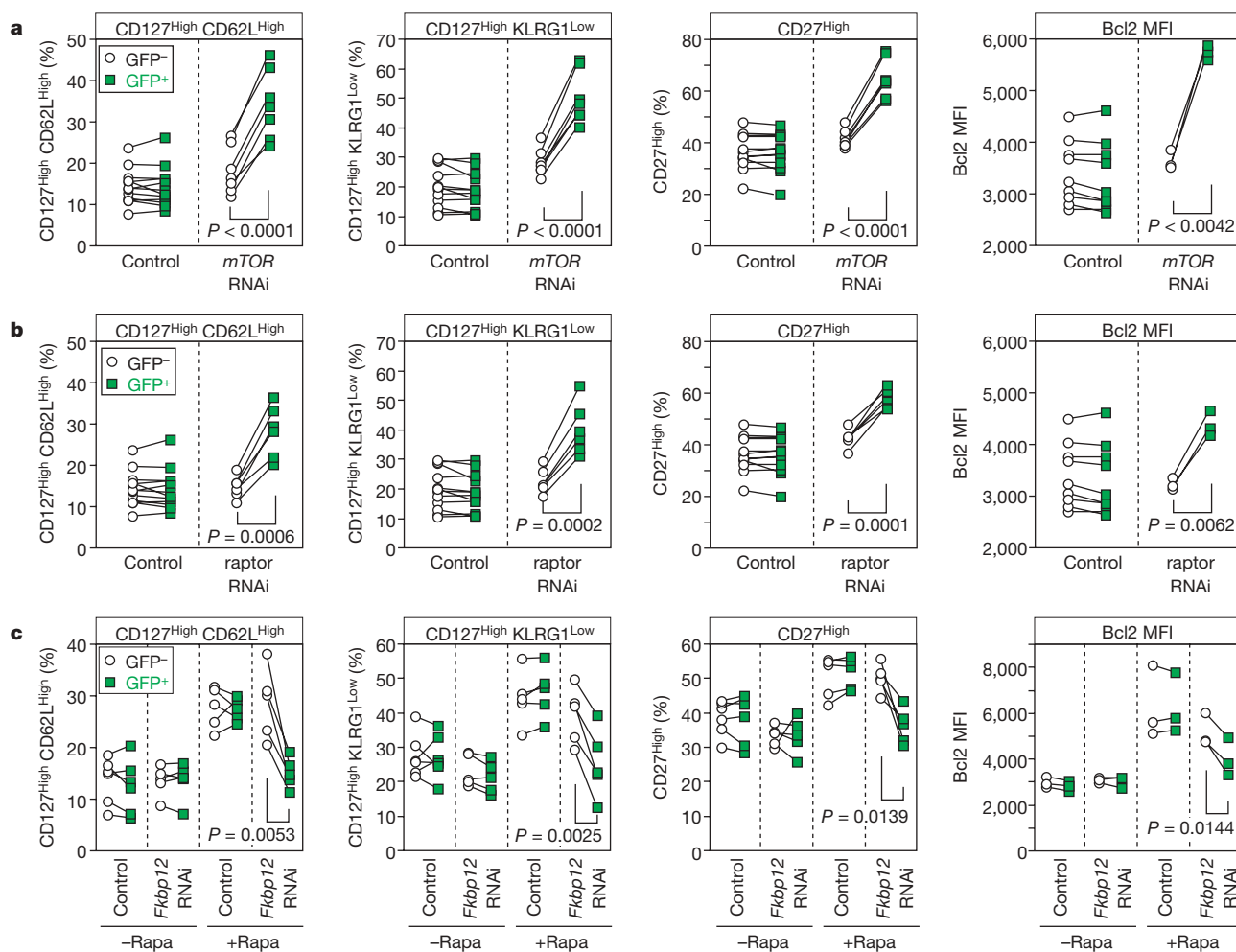


Figure 4 | *mTOR* acts intrinsically in antigen-specific CD8 T cells through the *mTORC1* pathway to regulate memory T-cell differentiation. Specific genes (*mTOR* or *raptor*) were knocked down using a retrovirus based RNAi system. Retrovirus transduced LCMV specific P14 transgenic CD8 T cells (marked by GFP expression) were adoptively transferred into naive mice, followed by LCMV infection. Phenotypic analysis of retrovirus transduced cells (GFP⁺) and non-transduced (GFP⁻) P14 cells in the PBMCs was performed on days 14–16 post infection. **a**, **b**, Each line shows expression of the indicated phenotypic markers on transduced and non-transduced

antigen-specific CD8 T cells in individual animals; **a**, *mTOR* RNAi, **b**, *raptor* RNAi. Same control data are shown in **a** and **b**. **c**, *Fkbp12* RNAi expressing retrovirus- or control retrovirus-transduced P14 transgenic CD8 T cells (marked by GFP expression) were adoptively transferred into naive mice, followed by LCMV infection. Half of the mice were treated with rapamycin throughout infection. Phenotypic analysis of retrovirus transduced cells (GFP⁺) and non-transduced (GFP⁻) P14 cells in the PBMCs was performed on days 14–16 post infection.

interference (RNAi) system to specifically knockdown various genes of the *mTOR* pathway (*mTOR*, *raptor*, *S6K1* (also known as *Rps6kb1*), *Eif4e* and *Fkbp12*) in antigen-specific CD8 T cells. Retroviruses marked by GFP and expressing RNAi for a particular gene or a control retrovirus were used to infect LCMV specific transgenic CD8 T cells (P14 cells); these transduced cells were then adoptively transferred into naive mice, followed by LCMV infection (Supplementary Fig. 7a). This system allows us to compare the phenotypic changes that occur during memory T-cell differentiation in GFP⁺ retrovirus transduced versus GFP⁻ non-transduced antigen-specific CD8 T cells in the same environment (that is, the same mouse; Supplementary Fig. 7b). Thus, any differences in memory differentiation that are seen between these two cell populations can be ascribed to the intrinsic effects of that particular gene in antigen-specific T cells.

In the initial set of experiments, we knocked down *mTOR* itself in antigen-specific CD8 T cells. We found that *mTOR* RNAi retrovirus-transduced GFP⁺ P14 cells showed significantly higher expression of the canonical memory T-cell markers (CD127, CD62L, Bcl2, CD27) and lower expression of KLRG1 compared to non-transduced or control vector transduced P14 cells (Fig. 4a). These data show that *mTOR* acts intrinsically in antigen-specific CD8 T cells to regulate

memory differentiation. However, as *mTOR* forms two distinct complexes, the rapamycin-sensitive *mTORC1* (*mTORC1*) and the rapamycin-insensitive *mTORC2*⁵, *mTOR* knockdown does not completely mimic rapamycin treatment. To distinguish between these two pathways, we knocked down the gene, *raptor*, that is an essential component of the *mTORC1* complex^{21,22}. As shown in Fig. 4b, inhibition of *raptor* in antigen-specific T cells gave results identical to those seen on knockdown of *mTOR*, thereby identifying the *mTORC1* complex as the regulator of memory differentiation. To gain more insight into mechanisms by which *mTOR* regulates memory formation, we examined the role of *S6K1* and *eIF4E*⁵. We found that knockdown of these *mTORC1* downstream effectors significantly enhanced memory CD8 T-cell differentiation (Supplementary Fig. 8). Thus, our results show that *mTOR* is exerting its effect through these two downstream molecules.

To further explore the role of *mTOR* in T-cell intrinsic versus external effects on memory differentiation, we made rapamycin-insensitive antigen-specific CD8 T cells by knockdown of the FKBP12 protein. This intracellular protein binds rapamycin and it is this FKBP12–rapamycin complex that inhibits the *mTORC1* pathway. Thus, by knocking down FKBP12 in P14 CD8 cells, we made these cells insensitive to any intrinsic effects of rapamycin but the

drug could still act effectively on all the other cells in the mouse. This system allows us to examine if inhibition of mTOR in other cells can effect memory CD8 T-cell differentiation. As shown in Fig. 4c, inhibiting mTOR in other cells when the antigen-specific cells themselves were rapamycin insensitive did not effect memory differentiation. The effect of rapamycin on memory differentiation almost disappeared on knockdown of FKBP12 from the P14 cells, and these cells did not show increased expression of the characteristic memory markers (CD127, CD62L, Bcl2, and so on; see rightmost column in Fig. 4c). Thus, taken together, the results shown in Fig. 4a–c establish that mTOR not only acts intrinsically in antigen-specific CD8 T cells but that inhibiting mTOR in other cells has minimal to no effect on memory T-cell differentiation.

During the past few years, considerable progress has been made in understanding the lineage relationships between naive, effector and memory T cells and in defining the phenotypic and functional changes that underlie memory CD8 T-cell differentiation^{1,23}. However, much less is known about the intracellular molecules and pathways that regulate the generation of memory T cells. In this study, we identify a molecular pathway that regulates memory T-cell differentiation, and provide a strategy for modulating the formation of memory cells. In particular, the ability to increase the functional qualities of memory T cells provides a new approach for enhancing the efficacy of vaccines against infectious diseases and cancer.

METHODS SUMMARY

Mice, viral infection, and VLP. C57BL/6j mice and Thy-1.1 P14 transgenic mice bearing the H-2D^b GP33 epitope specific TCR were used. Mice were intraperitoneally (i.p.) infected with LCMV Armstrong or recombinant vaccinia virus GP33 (VVGp33), which expresses the LCMV GP33 epitope. For VLP immunization, mice were subcutaneously given VLP genetically fused to LCMV GP33 epitope¹⁸.

Rhesus macaques and vaccination. Six rhesus macaques were inoculated with Dryvax (Wyeth) by scarification. At 105 days post Dryvax vaccination, animals were then vaccinated intramuscularly (i.m.) with MVA.

Administration of rapamycin. For the murine experiments, rapamycin (Wyeth) was administered i.p. daily. A relatively low dose of rapamycin was used during T-cell expansion phase because the higher dose inhibited T-cell responses (Supplementary Fig. 9). For the rhesus macaque experiments, rapamycin was administered daily i.m. to Dryvax immunized animals before MVA vaccination.

Generation and isolation of effector and memory T-cell subsets. Naive P14 transgenic T cells were adoptively transferred into B6 recipients (P14 chimaeric mice). Effector and memory P14 T cells were isolated from LCMV-infected P14 chimaeric mice. CD62L⁺ effector CD8 T cells were purified using anti-CD62L magnetic beads and a CD8 T cell isolation kit (Miltenyi Biotec).

Retrovirus based RNAi. The pMKO.1 GFP retroviral vector (Addgene plasmid 10676) was provided by W. Hahn. Double strand oligonucleotides for short hairpin RNA (shRNA) were cloned into pMKO.1 GFP. Recombinant retrovirus was made by transfection in 293T cells. Retrovirus transduced P14 cells were adoptively transferred into naive mice, then the mice were infected with LCMV Armstrong. The GFP⁺ P14 CD8 T cells were purified by FACS on day 7–8 post-infection, and then protein expression levels were analysed by western blotting (Supplementary Fig. 10).

Full Methods and any associated references are available in the online version of the paper at www.nature.com/nature.

Received 27 April; accepted 15 May 2009.

Published online 21 June 2009.

- Williams, M. A. & Bevan, M. J. Effector and memory CTL differentiation. *Annu. Rev. Immunol.* **25**, 171–192 (2007).
- Surh, C. D. & Sprent, J. Homeostasis of naive and memory T cells. *Immunity* **29**, 848–862 (2008).

- Klebanoff, C. A., Gattinoni, L. & Restifo, N. P. CD8⁺ T-cell memory in tumor immunology and immunotherapy. *Immunol. Rev.* **211**, 214–224 (2006).
- Seder, R. A., Darrah, P. A. & Roederer, M. T-cell quality in memory and protection: implications for vaccine design. *Nature Rev. Immunol.* **8**, 247–258 (2008).
- Wullschleger, S., Loewith, R. & Hall, M. N. TOR signaling in growth and metabolism. *Cell* **124**, 471–484 (2006).
- Cao, W. et al. Toll-like receptor-mediated induction of type I interferon in plasmacytoid dendritic cells requires the rapamycin-sensitive PI(3)K-mTOR-p70S6K pathway. *Nature Immunol.* **9**, 1157–1164 (2008).
- Sinclair, L. V. et al. Phosphatidylinositol-3-OH kinase and nutrient-sensing mTOR pathways control T lymphocyte trafficking. *Nature Immunol.* **9**, 513–521 (2008).
- Sauer, S. et al. T cell receptor signaling controls Foxp3 expression via PI3K, Akt, and mTOR. *Proc. Natl Acad. Sci. USA* **105**, 7797–7802 (2008).
- Haxhinasto, S., Mathis, D. & Benoist, C. The AKT-mTOR axis regulates de novo differentiation of CD4⁺Foxp3⁺ cells. *J. Exp. Med.* **205**, 565–574 (2008).
- Kaech, S. M. et al. Selective expression of the interleukin 7 receptor identifies effector CD8 T cells that give rise to long-lived memory cells. *Nature Immunol.* **4**, 1191–1198 (2003).
- Huster, K. M. et al. Selective expression of IL-7 receptor on memory T cells identifies early CD40L-dependent generation of distinct CD8⁺ memory T cell subsets. *Proc. Natl Acad. Sci. USA* **101**, 5610–5615 (2004).
- Schluns, K. S., Kieper, W. C., Jameson, S. C. & Lefrançois, L. Interleukin-7 mediates the homeostasis of naive and memory CD8 T cells *in vivo*. *Nature Immunol.* **1**, 426–432 (2000).
- Tan, J. T. et al. Interleukin (IL)-15 and IL-7 jointly regulate homeostatic proliferation of memory phenotype CD8⁺ cells but are not required for memory phenotype CD4⁺ cells. *J. Exp. Med.* **195**, 1523–1532 (2002).
- Wherry, E. J. et al. Lineage relationship and protective immunity of memory CD8 T cell subsets. *Nature Immunol.* **4**, 225–234 (2003).
- Sarkar, S. et al. Functional and genomic profiling of effector CD8 T cell subsets with distinct memory fates. *J. Exp. Med.* **205**, 625–640 (2008).
- Joshi, N. S. et al. Inflammation directs memory precursor and short-lived effector CD8⁺ T cell fates via the graded expression of T-bet transcription factor. *Immunity* **27**, 281–295 (2007).
- Grayson, J. M., Zajac, A. J., Altman, J. D. & Ahmed, R. Cutting edge: increased expression of Bcl-2 in antigen-specific memory CD8⁺ T cells. *J. Immunol.* **164**, 3950–3954 (2000).
- Storni, T. et al. Nonmethylated CG motifs packaged into virus-like particles induce protective cytotoxic T cell responses in the absence of systemic side effects. *J. Immunol.* **172**, 1777–1785 (2004).
- Ohtani, M. et al. Mammalian target of rapamycin and glycogen synthase kinase 3 differentially regulate lipopolysaccharide-induced interleukin-12 production in dendritic cells. *Blood* **112**, 635–643 (2008).
- Weichhart, T. et al. The TSC-mTOR signaling pathway regulates the innate inflammatory response. *Immunity* **29**, 565–577 (2008).
- Hara, K. et al. Raptor, a binding partner of target of rapamycin (TOR), mediates TOR action. *Cell* **110**, 177–189 (2002).
- Kim, D. H. et al. mTOR interacts with raptor to form a nutrient-sensitive complex that signals to the cell growth machinery. *Cell* **110**, 163–175 (2002).
- Kaech, S. M. & Wherry, E. J. Heterogeneity and cell-fate decisions in effector and memory CD8⁺ T cell differentiation during viral infection. *Immunity* **27**, 393–405 (2007).

Supplementary Information is linked to the online version of the paper at www.nature.com/nature.

Acknowledgements We thank B. T. Konieczny for technical assistance; D. Garber for providing us with the MVA; R. Amara for help developing rhesus macaque assays; W. Hahn for providing pMKO.1 GFP vector; and E. Strobert and P. L. Turner for technical assistance. This work was supported by NIH grants AI030048 (to R.A.) and N01-AI-50025 and AI040519 (to C.P.L.).

Author Contributions K.A. and R.A. designed mouse experiments; A.P.T., V.O.S., S.G. and C.P.L. designed macaque experiments; K.A. performed mouse experiments; A.P.T., V.O.S. and S.G. performed macaque experiments; K.A. and R.A. analysed mouse data; K.A., A.P.T., V.O.S., S.G. and C.P.L. analysed macaque data; S.A.K. and M.F.B. provided critical reagents; and K.A. and R.A. wrote the paper.

Author Information Reprints and permissions information is available at www.nature.com/reprints. Correspondence and requests for materials should be addressed to R.A. (rahmed@emory.edu).

METHODS

Mice, viral infection, VLP, and virus titrations. Twelve- to sixteen-week old C57BL/6j mice were purchased from The Jackson Laboratory. Thy-1.1 P14 transgenic mice bearing the DbGP33 specific TCR were fully backcrossed to C57BL/6 mice in our animal colony. LCMV Armstrong (2×10^5 p.f.u., i.p.) and recombinant vaccinia virus GP33 (VVGP33, 5×10^6 p.f.u., i.p.), which expresses the LCMV GP33 epitope, were used for infection. VVGP33 titres were determined in the ovary by plaque assay as described previously¹⁴. For VLP immunization, mice were subcutaneously given 50 µg of VLP, which was derived from the hepatitis B core antigen genetically fused to the LCMV gp33-41 epitope (KAVYNFATM) and packaged with CpG-ODN.

Administration of rapamycin in mice. Rapamycin (Wyeth) was administered to mice i.p. daily during the treatment period. Three different treatment periods were used: (1) throughout LCMV infection (day -1 before infection to the memory phase, day 35 post-infection); (2) the T-cell expansion phase (day -1 before infection to day 8 post-infection); or (3) T-cell contraction phase (day 8 to the memory phase, day 35 post-infection). The daily dose of rapamycin was $75 \mu\text{g kg}^{-1}$ (blood levels; $5\text{--}20 \text{ ng ml}^{-1}$) for treatments (1) and (2), and $600 \mu\text{g kg}^{-1}$ (blood levels; $40\text{--}100 \text{ ng ml}^{-1}$) for treatment (3) (the contraction phase treatment) because the higher dose ($600 \mu\text{g kg}^{-1}$) inhibits T-cell responses during the expansion phase of the CD8 T-cell response (Supplementary Fig. 9). Control mice received sham treatment during the same time periods described above (daily of injection of the buffer without rapamycin).

Rhesus macaques and vaccination. Six rhesus macaques (*Macaca mulatta*) were inoculated with Dryvax (Wyeth) by scarification in accordance with the US Food and Drug Administration guidelines. Briefly, a bifurcated needle was immersed in the vaccine suspension and used to poke the skin 15 consecutive times. At 105 days post Dryvax vaccination, animals were vaccinated with 10^8 p.f.u. MVA i.m.

Administration of rapamycin in rhesus macaques. Daily administration of rapamycin ($10\text{--}50 \mu\text{g kg}^{-1} \text{ d}^{-1}$) was given i.m. to three of the six Dryvax immunized rhesus macaques around 5 days before MVA vaccination. Blood levels of rapamycin were maintained within a range of $5\text{--}15 \text{ ng ml}^{-1}$. The other three macaques were left untreated as controls.

Generation and isolation of effector and memory T-cell subsets. To generate LCMV specific P14 effector T cells, mice into which 1×10^5 P14 naive T cells were adoptively transferred were infected with LCMV. On day 8 post-infection, effector P14 cells were isolated from the spleen, and CD62L⁺ CD8 T cells were purified using anti-CD62L magnetic beads and a CD8 T cell isolation kit (Miltenyi Biotec). These cells were then used for a CD62L conversion experiment and a protective immune response experiment. For the CD62L conversion experiment, CFSE labelled CD62L⁺ P14 effector cells ($7\text{--}10 \times 10^6$ cells) were adoptively transferred into naive mice. For the protective immune response experiment, 3×10^5 CD62L⁺ P14 effector cells were adoptively transferred into naive mice, and rapamycin was administered for 25 days. On day 28 post-transfer, mice were challenged with VVGP33 to examine protective immune responses. To obtain memory P14 cells generated in rapamycin treated mice, B6 mice into which 1×10^5 P14 naive T cells were adoptively transferred were infected with LCMV, and these mice were then treated with rapamycin from day -1 to day 33 post-infection. On day 34 post-infection, memory P14 T cells generated in the presence of rapamycin were isolated from the spleen. Control memory P14 cells were obtained using the same method without the rapamycin treatment. For the homeostatic experiment, CFSE labelled memory P14 cells (1×10^6 cells) obtained from either rapamycin treated or untreated mice were adoptively transferred into separate naive recipients. For the recall response experiment, 1×10^4 P14 memory T cells derived from either rapamycin treated or untreated mice were adoptively transferred into separate naive mice, and the day after transfer these mice were then infected with VVGP33. To investigate effects of rapamycin during secondary T-cell responses, 2.5×10^4 P14 memory T cells (>60 days post-infection) were

adoptively transferred into naive mice, and rapamycin treatment was started. The day after transfer, these mice were infected LCMV.

Flow cytometry. Flow cytometric analysis was performed on a LSRII, a CantoII, or a FACSCalibur (BD Biosciences). MHC class I tetramers were made as described previously²⁴. All antibodies for flow cytometry were purchased from BD biosciences except for CD127, KLRG1 and CD27. Antibodies to CD127 and CD27 were purchased from eBiosciences and anti-KLRG1 was purchased from Southern biotech. Single cell suspensions of spleen cells, lymph nodes, livers or PBMCs from mice were prepared and direct *ex vivo* staining was carried out as described previously¹⁴. For *in vivo* BrdU incorporation, LCMV-infected mice were fed 0.8 mg ml^{-1} BrdU in their drinking water every day. BrdU in virus-specific CD8 T cells was measured by a BrdU flow kit (BD Biosciences), according to the manufacturer's instructions. To detect vaccinia virus specific CD8 T cells generated in rhesus macaques, 1.5×10^6 PBMCs isolated by density gradient centrifugation were incubated at 37°C for 15 h with vaccinia virus at a multiplicity of infection of 1 in a volume of 300 µl RPMI containing 10% heat inactivated FBS. Brefeldin A ($5 \mu\text{g ml}^{-1}$) was added for the final 5 h of incubation. IFN- γ producing vaccinia virus specific CD8 T cells were detected by intracellular cytokine staining.

Retrovirus based RNAi. The pMKO.1 GFP retroviral vector (Addgene plasmid 10676) was kindly provided by W. Hahn. Double strand oligonucleotides for short hairpin RNA (shRNA) against *mTOR*, *raptor*, *Fkbp12*, *S6K1* and *Eif4e* were cloned into pMKO.1 GFP between AgeI and EcoRI sites. The sequences for *mTOR* shRNA are: 5'-CCGGGCCAGAAATCCATCCATTCTCGAGAATGAATGGATGGATTCTG GC-3' (antisense strand). The sequences for *raptor* shRNA are: 5'-CCGGGCCCGAGTCTGTGAATGTAATCTCGAGATTACATTCACAGACTC GGGCTTTTGTG-3' (sense strand) and 5'-AATTCAAAAAGCCCGAGTCTGTGAATGTAATCTCGAGATTACATTCACAGACTCGGGC-3' (antisense strand). The sequences for *Fkbp12* shRNA are: 5'-CCGGGCCAAACTGATAATCTCTCACTCGAGTGAGGAGATTATCAGTTTGGCTTTTGTG-3' (sense strand) and 5'-AATTCAAAAAGCCAACTGATAATCTCTCACTCGAGTGAGGAGATTATCAGTTTGGC-3' (antisense strand). The sequences for *S6K1* shRNA are: 5'-CCGGGCCATGGAACATTGTGAGAAATCTCGAGATTCTCACAATGTTCATGCTTTTGTG-3' (sense strand) and 5'-AATTCAAAAAGCATGGAACATGTGAGAAATCTCGAGATTCTCACAATGTTCCATGC-3' (antisense strand). The sequences for *Eif4e* shRNA are: 5'-CCGGCCGAAGATAGTGATTGGTTATCTCGAGATAACCAATCACTATCTTCGGTTTGTG-3' (sense strand) and 5'-AATTCAAAAACCGAAGATAGTGATTGGTTATCTCGAGATAACCAATCATATCTTCGG-3' (antisense strand). Recombinant retrovirus was made by co-transfection with pMKO.1 GFP and pCL-Eco (Imgenex) in 293T cells using TransIT-293 (Mirus). 48 h after transfection culture supernatants were collected. To transduce P14 cells with the recombinant retrovirus, P14 transgenic mice were infected with 1×10^6 p.f.u. of LCMV intravenously and 24 h later, P14 transgenic spleen cells were isolated and then spin-transduced at 37°C for 90 min with freshly collected retrovirus containing $8 \mu\text{g ml}^{-1}$ of polybrene (Sigma). 5×10^5 retroviral transduced P14 spleen cells were adoptively transferred into naive mice, followed by LCMV infection (2×10^5 p.f.u., i.p.). The GFP⁺ P14 CD8 T cells were purified by FACS on day 7–8 post infection, and then protein expression levels were analysed by western blotting (Supplementary Fig. 10).

Statistical analysis. For the statistical analysis of the RNAi experiments, a two-tailed paired Student's *t* test was used. To determine the statistical significance of the viral titres, we used a non-parametric Mann-Whitney test. All other statistical analysis was performed using a two-tailed unpaired Student's *t* test.

24. Murali-Krishna, K. *et al.* Counting antigen-specific CD8 T cells: a reevaluation of bystander activation during viral infection. *Immunity* **8**, 177–187 (1998).

Human ISL1 heart progenitors generate diverse multipotent cardiovascular cell lineages

Lei Bu^{1,2*}, Xin Jiang^{1,2*}, Silvia Martin-Puig^{1,2}, Leslie Caron^{1,2}, Shenjun Zhu¹, Ying Shao¹, Drucilla J. Roberts³, Paul L. Huang¹, Ibrahim J. Domian^{1,2} & Kenneth R. Chien^{1,2}

The generation and expansion of diverse cardiovascular cell lineages is a critical step during human cardiogenesis, with major implications for congenital heart disease. Unravelling the mechanisms for the diversification of human heart cell lineages has been hampered by the lack of genetic tools to purify early cardiac progenitors and define their developmental potential^{1–4}. Recent studies in the mouse embryo have identified a multipotent cardiac progenitor that contributes to all of the major cell types in the murine heart^{5–8}. In contrast to murine development, human cardiogenesis has a much longer onset of heart cell lineage diversification and expansion, suggesting divergent pathways. Here we identify a diverse set of human fetal ISL1⁺ cardiovascular progenitors that give rise to the cardiomyocyte, smooth muscle and endothelial cell lineages. Using two independent transgenic and gene-targeting approaches in human embryonic stem cell lines, we show that purified ISL1⁺ primordial progenitors are capable of self-renewal and expansion before differentiation into the three major cell types in the heart. These results lay the foundation for the generation of human model systems for cardiovascular disease and novel approaches for human regenerative cardiovascular medicine.

To localize ISL1⁺ heart cells during human cardiogenesis, we used immunofluorescence microscopy in serial sections of human fetal hearts at 11 and 18 weeks of gestation. ISL1⁺ cells were found in the right atrium and outflow tract (OFT), both second-heart-field (SHF)-derived structures (Fig. 1), as well as in the left atrial wall and appendage (Supplementary Fig. 1a). Thus, ISL1⁺ cells in the human fetal heart are found in a pattern that matches the known contribution of ISL1⁺ precursors to SHF derivatives in the murine fetal heart^{6,8,9}. Furthermore, we performed co-staining of ISL1 and the lineage-specific differentiation markers cardiac troponin T (cTNT (also called TNNT2), cardiomyocyte), smooth muscle myosin heavy chain (SMMHC (also called MYH11), smooth muscle cell) (Fig. 1) and the platelet/endothelial cell adhesion molecule (PECAM1, endothelial cell) (Supplementary Fig. 1b). Double-positive cells, expressing ISL1 as well as a lineage-specific differentiation marker, were identified as intermediates for the cardiomyocyte, smooth muscle and endothelial lineages. A unique subset of cells expressing ISL1, but not NKX2-5 or differentiated cardiac lineage markers, was observed in the right atrial wall and proximal OFT (Fig. 1 and Supplementary Fig. 1). In later-stage fetal hearts (18 weeks of gestation), the relative and total numbers of ISL1⁺ cells were significantly reduced (Supplementary Fig. 1c, d and data not shown). Collectively, these findings show that ISL1 is expressed over a long period of human cardiogenesis and suggest that a unique subset of primordial ISL1⁺ progenitors might give rise to downstream multipotent heart progenitors that contribute to the SHF-derived structures through differentiation into multiple lineage-restricted ISL1⁺ intermediates.

To study the early cell fate decisions taken by ISL1⁺ human cardiovascular progenitors, and to characterize embryonic stem (ES)-cell-derived human cardiac ISL1⁺ progenitors, we generated an *ISL1*- β -geo bacterial artificial chromosome (BAC) transgenic human ES cell line to genetically tag ISL1⁺ progenitors (Supplementary Fig. 2a). After 5–6 days of embryoid body (EB) formation, β -geo⁺ cells were detected by 5-bromo-4-chloro-3-indolyl- β -D-galactoside (X-gal) staining. Co-staining of X-gal and ISL1 (Fig. 2a, left panel) confirmed that β -geo expression driven by regulatory sequences present in the *ISL1* BAC recapitulated the expression pattern of the endogenous ISL1 protein. Single-cell-derived clones from EBs of human *ISL1*- β -geo BAC transgenic cells were observed on mouse cardiac mesenchymal cells after 5 days of *in vitro* expansion. Of these clones, 10 \pm 5% had focal β -geo activity (Fig. 2a, right panel).

To identify, purify and track the fate of human ES-cell-derived ISL1⁺ progenitors, we used lineage tracing with a Cre/loxP system to mark irreversibly *ISL1* expressing cells and their differentiated progeny in the context of *in vitro* human cardiac differentiation. The *ISL1*-cre knock-in human ES cell lines (using WA09 and HUES3 as parental human ES cell lines¹⁰) were identified by Southern blotting using a 5' probe and by 3' long-range polymerase chain reaction (PCR; Fig. 2b, c). Immunostaining assay documented that cre expression recapitulated endogenous *ISL1* expression (Supplementary Fig. 2b). The *ISL1*-cre cells were then co-transfected with a pCAG-flox-DsRed reporter plasmid and a pCAG-Flpase plasmid (Supplementary Fig. 2c). cre expression from the *ISL1* locus mediates the excision of the floxed stop sequence on the pCAG-flox-DsRed plasmid, resulting in the irreversible expression of the *DsRed*-MST (ref. 11; DsRed-MST is a variant DsRed protein) gene in ISL1⁺ progenitors and their differentiated progeny (Supplementary Fig. 2c). Approximately 20–30% of beating EBs in the *ISL1*-cre *DsRed* cells on day 16 after EB formation (EB day 16) expressed DsRed (Supplementary Fig. 2d and Supplementary Movie 1). Immunostaining displayed co-expression of *ISL1* and *DsRed* in the cells dissociated from day 8 EBs (Fig. 2d). The *ISL1*-cre *DsRed* cell-derived population also co-expressed *DsRed* and sarcomeric α -actinin (*ACTN2*) or cTNT (Fig. 2e), indicating that a portion of human cardiomyocytes was derived from ISL1⁺ cardiac progenitors.

RT-PCR analysis on human *ISL1*-cre *DsRed* EBs revealed a dynamic pattern of *DsRed* and cardiac marker expression (Fig. 3a). *DsRed* expression was undetectable in undifferentiated human ES cells, but increased along with the expression of *ISL1* during differentiation. The SHF-specific marker *TBX1* (ref. 12) and the cardiac transcription factor *NKX2-5* were not expressed until EB day 6 and 8, respectively. The late cardiac marker myosin heavy chain 6 (*MYH6*) was first detected on EB day 10 (Fig. 3a). Taken together, these results indicate

¹Cardiovascular Research Center, Massachusetts General Hospital, Charles River Plaza/CPZN 3208, 185 Cambridge Street, Boston, Massachusetts 02114, USA. ²Harvard Stem Cell Institute, Cambridge, Massachusetts 02138, USA. ³Pediatric Surgical Research Laboratories, Department of Surgery, Massachusetts General Hospital, Harvard Medical School, 185 Cambridge Street, Boston, Massachusetts 02114, USA.

*These authors contributed equally to this work.

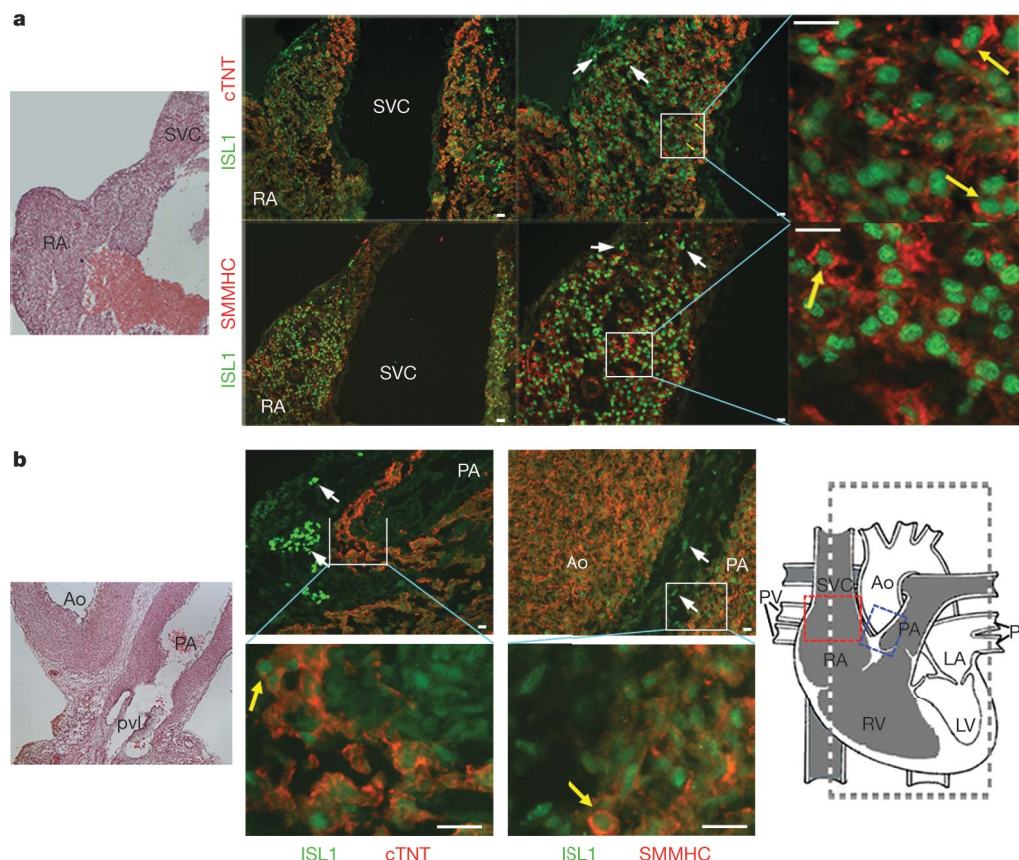


Figure 1 | Analysis of the *in vivo* expression of ISL1 in SHF-derived structures of the human fetal heart. Frozen sections from a human fetal heart at 11 weeks of gestation were stained with the indicated antibodies. A scheme shows the plane of the sections and anatomical labels.

a, b, Immunostaining of sections from right atrium/superior vena cava (RA/SVC; **a**) and the proximal OFT (**b**) with indicated antibodies. ISL1⁺ cells are

that the human EB differentiation program *in vitro* correlates with the normal human embryonic cardiac developmental program.

To obtain purified populations of ISL1⁺ cardiac progenitors, we isolated DsRed⁺ cells by fluorescence-activated cell sorting (FACS) on EB day 8 (Fig. 3b). RT-PCR analysis revealed that the expression of cardiac markers *ISL1* and *NKX2-5* is 30- and 8-fold higher in DsRed⁺ cells than in the DsRed⁻ population, respectively (Fig. 3c). Notably, both FACS and RT-PCR analyses demonstrated that DsRed⁺ cells do not express *KDR* when isolated on EB day 8 (Supplementary Fig. 3a, b).

To assess the differentiation potential of human ISL1⁺ progenitors, we performed clonal assays on single DsRed⁺ cells. We isolated DsRed⁺ cells from day 8 EBs and plated them at low density on mouse embryonic fibroblast (MEF) feeders. Colonies of DsRed⁺ cells were observed within 7 days at a cloning efficiency of 0.2–0.5% (Fig. 3d). We then performed RT-PCR analysis on 95 single DsRed⁺ cell-derived clones (Fig. 3e and Supplementary Table 1). Many of these clones, expressing *NKX2-5* alone or *ISL1* and *NKX2-5*, also expressed late cardiac markers (for example, *cTNT* and *SMMHC*), indicating that they are cardiac progenitors at intermediate stages of differentiation, consistent with our *in vivo* observations in the human fetal heart (Fig. 1). Clones expressing *ISL1* and *NKX2-5* are more effective (55%, 22 out of 40) at differentiating into the three major cardiovascular lineages and generating cardiomyocytes, as 90% of them (35 out of 40) co-express *cTNT* (Fig. 3e and Supplementary Table 1). Recent studies suggest that *KDR* and its mouse orthologue *Flk1* can label an enriched pool of early cardiac progenitors^{5,6,13–15}. Our results are consistent with these findings and

indicated by white arrows and transient intermediates, ISL1⁺cTNT⁺ and ISL1⁺SMMHC⁺, are indicated by yellow arrows. Scale bars: 50 μ m in the right panels of **a** and bottom panels of **b**; 25 μ m in the remaining panels. Ao, aorta; LA, left atrium; LV, left ventricle; PA, pulmonary artery; PV, pulmonary veins; pvl, pulmonary valve; RV, right ventricle.

further imply that the ISL1⁺NKX2-5⁺KDR⁺ cardiac progenitors derived from human ES cells may originally arise from an ISL1⁺KDR⁻ population (Supplementary Fig. 3a, b). However, in this study, *KDR* was not an effective single marker for isolating stage-specific cell populations, as it was expressed at multiple stages during cardiac differentiation (Supplementary Fig. 3c, d). Notably, *WT1*, the human orthologue of a recently identified mouse epicardium precursor marker, *Wt1* (refs 16, 17), was detectable in ISL1⁺NKX2-5⁺ and NKX2-5⁺ clones (Fig. 3e). Thus, human WT1⁺ progenitors may share a developmental origin with multipotent NKX2-5⁺ and/or ISL1⁺ cells. Confirmed by a two-colour system, DsRed⁺ colonies in the clonal assays were developed from single ISL1⁺ progenitors (Supplementary Fig. 4).

To evaluate the developmental potential of ISL1⁺ lineage cells, DsRed⁺-derived clones were dissociated for differentiation assays, which revealed contracting DsRed⁺ clusters on gelatin-coated plates (Supplementary Movies 2 and 3). Flow cytometry and immunocytochemistry analyses demonstrated that DsRed⁺ cells could give rise to the three major cardiac lineages: cardiomyocytes (4.2 \pm 0.3% cTNT⁺), endothelial cells (3.1 \pm 0.9% PECAM1⁺) and smooth muscle cells (44.1 \pm 15.7% SMTN⁺) (Fig. 3f).

Canonical Wnt pathways can promote the expansion of Is1⁺ cardiac progenitors in the mouse^{18–20}. In a similar manner, 6-bromoindirubin-3'-oxime (BIO)²¹ treatment resulted in a greater than 30% increase of human ISL1⁺ clones compared to cardiac mesenchymal cell control (Supplementary Fig. 5a, b). We then isolated human *ISL1-cre DsRed* cells from day 7 EBs, which were dissociated and plated on a plastic surface, MEF feeder cells, Wnt3a-secreting feeder

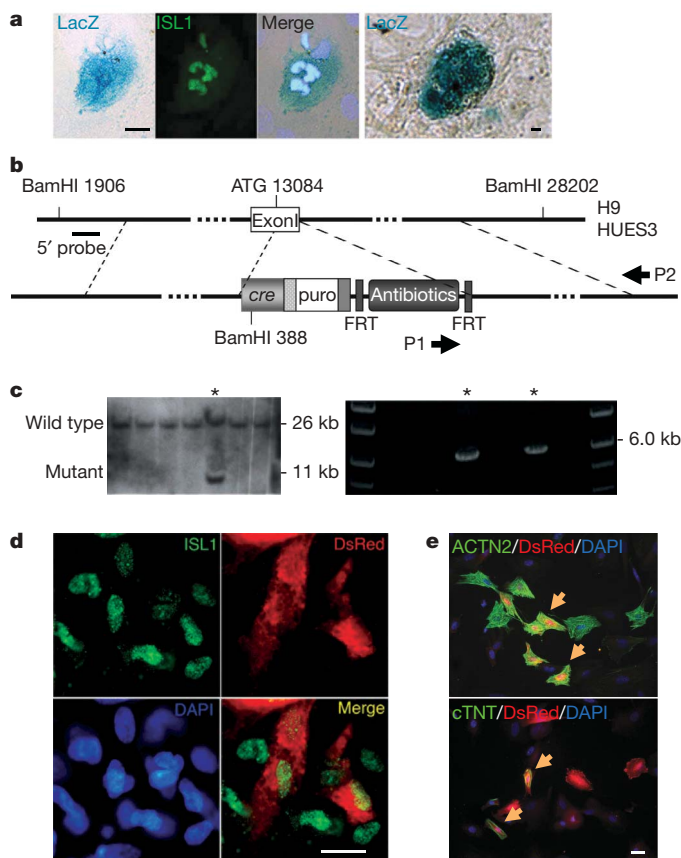


Figure 2 | ISL1 marks human ES-cell-derived cardiac progenitors. **a**, X-gal staining and immunostaining showing LacZ and ISL1 co-stained in human *ISL1-β-geo* BAC transgenic cells from EB day 6 (left); a β -geo⁺ colony was formed on cardiac mesenchymal cell feeders after an additional 5 days (right). Scale bars: 5 μ m. **b**, A diagram of the human *ISL1-cre* knock-in construct. **c**, Southern blotting and long-range PCR confirming the homologous integration of the human *ISL1-cre* knock-in construct. Primer pair P1/P2, indicated in **b**, was used for the long-range PCR. Asterisks indicate positive clones. **d**, Immunostaining showing the co-expression of *ISL1* and *DsRed* in the human *ISL1-cre* *DsRed* cells dissociated from day 8 EBs. **e**, Immunostaining showing the co-expression of *DsRed* and *ACTN2* or *cTNT* (orange arrows) in the human *ISL1-cre* *DsRed* cells from day 16 beating EBs. Scale bars: 5 μ m in **d** and **e**.

cells, or L feeder cells (Fig. 4a). No red clusters were formed on plastic surface or L feeders after 5 days of culture, whereas co-culturing with Wnt3a-secreting feeders resulted in an approximately sixfold increase in *DsRed*⁺ cell number and fivefold increase in *DsRed*⁺ clusters compared to those cultured on MEF feeders (Fig. 4a). *DsRed*⁺ cells expanded on Wnt3a feeders showed a higher expression of *ISL1* (Fig. 4b and Supplementary Fig. 5c). We performed a similar clonal assay on FACS-purified *DsRed*⁺ cells cultured on MEF feeders with Wnt3a-conditioned medium. At 12–14 days after plating, nearly 90% (28 out of 32) of clones maintained *ISL1* expression and around 20% (6 out of 32) of clones co-expressed the three cardiac lineage markers (Fig. 4c). After 10 days of differentiation, cTNT and SMMHC were detected in Wnt3a-expanded *DsRed*⁺ cells (Fig. 4d). Taken together, these results indicate that canonical Wnt ligands can promote the expansion and maintain the multipotency of human ES-cell-derived *ISL1*⁺ progenitors.

Our results demonstrate that a primordial human *ISL1*⁺ cardiac progenitor that is negative for KDR and NKX2-5 gives rise to a family of intermediate progenitors of multiple cardiac lineages, including the WT1⁺ epicardial lineage (Fig. 4e). Although KDR has been used as a marker to obtain populations of human ES-cell-derived progenitors that are enriched for *ISL1* expression¹³, as noted herein, *KDR* is widely expressed outside the heart, limiting its use to isolate and

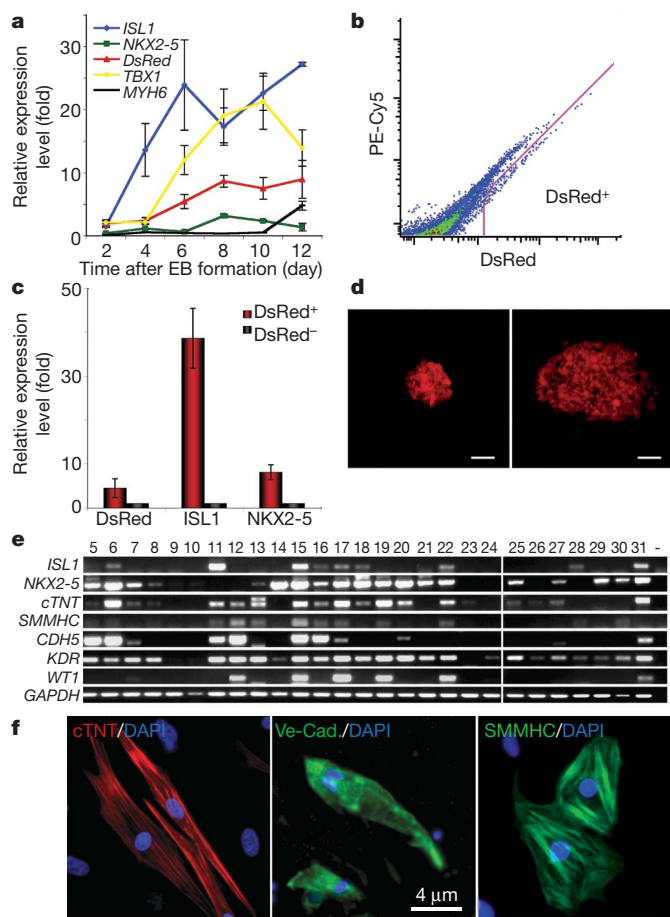
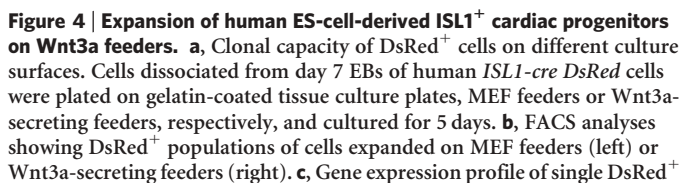


Figure 3 | Isolation and characterization of human ES-cell-derived *ISL1*⁺ cardiac progenitors and their progeny. **a**, Gene expression of the human *ISL1-cre* *DsRed* ES cells at different *in vitro* differentiation stages. **b**, FACS diagram to isolate *DsRed*⁺ cells from day 8 EBs of human *ISL1-cre* *DsRed* cells. **c**, Quantitative PCR (qPCR) showing gene expression of *DsRed*⁺ versus *DsRed*⁻ cells isolated from day 8 human *ISL1-cre* *DsRed* EBs. **d**, FACS-isolated *DsRed*⁺ cells from day 8 human *ISL1-cre* *DsRed* EBs formed colonies on MEF feeders after 7-day (left) and 14-day (right) co-culture. Scale bars: 10 μ m. **e**, Gene expression profile of single *DsRed*⁺ cell-derived clones. **f**, Immunostaining showing that single *DsRed*⁺ cell-derived clones give rise to three cardiovascular lineages after an additional 14 days of differentiation. Error bars in **a** and **c** indicate s.d. ($n = 3$).

clonally study purified populations of *ISL1*⁺ progenitors. In this study, via lineage tracing in human ES cells, we have directly labelled the *ISL1*⁺ cells, purified them to relative homogeneity, and tracked their downstream progeny. *ISL1* is expressed at the early stages of human cardiogenesis in a multipotent primordial progenitor, subsequently in a family of partially committed intermediate progenitors, and downregulated in the fully differentiated progeny (Fig. 4e). These *ISL1*⁺ progenitors give rise to both the right ventricle and inflow/outflow tracts, which are affected in several common forms of human cardiovascular malformations (for example, transposition of the great vessels, tricuspid atresia, tetralogy of Fallot), indicating their potential role in diverse forms of human congenital heart disease. In contrast to murine cardiogenesis, large numbers of multipotent *ISL1*⁺ progenitors persist during later stages of human fetal cardiogenesis, suggesting a stem cell paradigm for the exponential growth of the human fetal heart and outflow tract over many weeks, which may arise from expansion of the family of *ISL1*⁺ progenitors. Taken together, these studies suggest that human ES-cell-derived *ISL1*⁺ progenitors may provide new insights into human congenital heart disease, as well as novel model systems for human cardiovascular disease and new therapeutic approaches for adult cardiovascular defects.



d, Immunostaining showing that Wnt3a-expanded DsRed⁺ cells give rise to cardiomyocyte (cTNT⁺) and smooth muscle (SMMHC⁺) lineages after an additional 14 days of differentiation. Scale bars: 5 μ m in **a** and **d**. **e**, Model proposing a primordial ISL1⁺ progenitor generating a family of human multipotent cardiovascular lineages.

Human fetal heart immunohistochemistry. Human fetal hearts were obtained from authorized resources and embedded in OCT. Sections were stained with different antibody combinations as previously described^{6,18}. Haematoxylin and eosin (Sigma-Aldrich) staining was applied to adjacent slides to reveal tissue structures.

BAC recombinering and human ES cell genetic modification. Recombineering was performed as described²³ (see also <http://recombineering.ncicrf.gov/>). The β -geo cassette is integrated into the *ISL1* endogenous locus through homologous recombination. A new targeting BAC was constructed by replacing the β -geo reporter with a *cre-IRES-puro* cassette. An additional retrieving vector was made

for retrieving the final knock-in construct from the recombiner *ISL1-cre* BAC. Electroporation was performed as previously described^{10,24,25}, with modifications. The human ES cells were subjected to a single pulse at room temperature and plated on irradiated DR4 MEF feeders. Antibiotics selection was applied after 3 days.

Full Methods and any associated references are available in the online version of the paper at www.nature.com/nature.

1. Chien, K. R., Domian, I. J. & Parker, K. K. Cardiogenesis and the complex biology of regenerative cardiovascular medicine. *Science* **322**, 1494–1497 (2008).
2. Wu, S. M., Chien, K. R. & Mummery, C. Origins and fates of cardiovascular progenitor cells. *Cell* **132**, 537–543 (2008).
3. Martin-Puig, S., Wang, Z. & Chien, K. R. Lives of a heart cell: tracing the origins of cardiac progenitors. *Cell Stem Cell* **2**, 320–331 (2008).
4. Laugwitz, K. L., Moretti, A., Caron, L., Nakano, A. & Chien, K. R. Isl1 cardiovascular progenitors: a single source for heart lineages? *Development* **135**, 193–205 (2008).
5. Kattman, S. J., Huber, T. L. & Keller, G. M. Multipotent flk-1⁺ cardiovascular progenitor cells give rise to the cardiomyocyte, endothelial, and vascular smooth muscle lineages. *Dev. Cell* **11**, 723–732 (2006).
6. Moretti, A. *et al.* Multipotent embryonic isl1⁺ progenitor cells lead to cardiac, smooth muscle, and endothelial cell diversification. *Cell* **127**, 1151–1165 (2006).

7. Laugwitz, K. L. *et al.* Postnatal $Isl1^{+}$ cardioblasts enter fully differentiated cardiomyocyte lineages. *Nature* **433**, 647–653 (2005).
8. Cai, C. L. *et al.* $Isl1$ identifies a cardiac progenitor population that proliferates prior to differentiation and contributes a majority of cells to the heart. *Dev. Cell* **5**, 877–889 (2003).
9. Sun, Y. *et al.* $Isl1$ is expressed in distinct cardiovascular lineages, including pacemaker and coronary vascular cells. *Dev. Biol.* **304**, 286–296 (2007).
10. Cowan, C. A. *et al.* Derivation of embryonic stem-cell lines from human blastocysts. *N. Engl. J. Med.* **350**, 1353–1356 (2004).
11. Vintersten, K. *et al.* Mouse in red: red fluorescent protein expression in mouse ES cells, embryos, and adult animals. *Genesis* **40**, 241–246 (2004).
12. Xu, H. *et al.* $Tbx1$ has a dual role in the morphogenesis of the cardiac outflow tract. *Development* **131**, 3217–3227 (2004).
13. Yang, L. *et al.* Human cardiovascular progenitor cells develop from a KDR^{+} embryonic-stem-cell-derived population. *Nature* **453**, 524–528 (2008).
14. Ema, M. *et al.* Primitive erythropoiesis from mesodermal precursors expressing VE-cadherin, PECAM-1, Tie2, endoglin, and CD34 in the mouse embryo. *Blood* **108**, 4018–4024 (2006).
15. Motoike, T., Markham, D. W., Rossant, J. & Sato, T. N. Evidence for novel fate of $Flk1^{+}$ progenitor: contribution to muscle lineage. *Genesis* **35**, 153–159 (2003).
16. Zhou, B. *et al.* Epicardial progenitors contribute to the cardiomyocyte lineage in the developing heart. *Nature* **454**, 109–113 (2008).
17. Zhou, B., Gise, A., Ma, Q., Rivera-Feliciano, J. & Pu, W. T. $Nkx2-5$ - and $Isl1$ -expressing cardiac progenitors contribute to proepicardium. *Biochem. Biophys. Res. Commun.* **375**, 450–453 (2008).
18. Qyang, Y. *et al.* The renewal and differentiation of $Isl1^{+}$ cardiovascular progenitors are controlled by a Wnt/ β -catenin pathway. *Cell Stem Cell* **1**, 165–179 (2007).
19. Tzahor, E. Wnt/ β -catenin signaling and cardiogenesis: timing does matter. *Dev. Cell* **13**, 10–13 (2007).
20. Kwon, C. *et al.* Canonical Wnt signaling is a positive regulator of mammalian cardiac progenitors. *Proc. Natl Acad. Sci. USA* **104**, 10894–10899 (2007).
21. Meijer, L. *et al.* GSK-3-selective inhibitors derived from Tyrian purple indirubins. *Chem. Biol.* **10**, 1255–1266 (2003).
22. Xu, C. *et al.* Feeder-free growth of undifferentiated human embryonic stem cells. *Nature Biotechnol.* **19**, 971–974 (2001).
23. Lee, E. C. *et al.* A highly efficient *Escherichia coli*-based chromosome engineering system adapted for recombinogenic targeting and subcloning of BAC DNA. *Genomics* **73**, 56–65 (2001).
24. Zwaka, T. P. & Thomson, J. A. Homologous recombination in human embryonic stem cells. *Nature Biotechnol.* **21**, 319–321 (2003).
25. Davis, R. P. *et al.* Targeting a GFP reporter gene to the *MIXL1* locus of human embryonic stem cells identifies human primitive streak-like cells and enables isolation of primitive hematopoietic precursors. *Blood* **111**, 1876–1884 (2008).

Supplementary Information is linked to the online version of the paper at www.nature.com/nature.

Acknowledgements We thank C. Cowan for advice on human ES cell culture and electroporation; A. Nagy for providing the *DsRed-MST* plasmid; Y. Qyang for discussion and comments; E. Hansson for a critical reading of this manuscript; M. Lindsay and M. Ortega-Molina for help on human fetal heart anatomy; L. B. Prickett-Rice and K. Folz-Donahue for flow cytometry support; and Advanced Bioscience Resources for providing the human fetal tissues. S.M.P. is funded by Foundation Alfonso Martin Escudero, Spain. This study is supported by Harvard Stem Cell Institute and the Leducq Foundation.

Author Contributions L.B. and X.J. carried out most of the human ES cell experiments and analysed the data; S.M.-P. performed the analysis on the human fetal hearts, her contribution is similar in significance to the contributions of L.B. and X.J.; L.B. and K.R.C. designed the study; L.B., X.J., S.M.-P. and K.R.C. wrote the manuscript; L.C. performed a part of the differentiation study on *ISL1- β -geo* BAC transgenic cells and $ISL1^{+}$ expansion using wild-type human ES cells; S.Z. and Y.S. helped culture human ES cells and carried out some experiments; D.J.R. provided a part of the human fetal samples; P.L.H. provided advice on experiments; and I.J.D. provided pCAG-flox-DsRed plasmid and revised the manuscript.

Author Information Reprints and permissions information is available at www.nature.com/reprints. Correspondence and requests for materials should be addressed to K.R.C. (krchien@partners.org).

METHODS

Human fetal heart immunohistochemistry. Human fetal hearts were obtained from authorized sources. The pericardium was removed and the tissue was freshly fixed in 4% PFA at 4 °C overnight. The heart was washed four times with 1× PBS at 4 °C and embedded in OCT after going through a sucrose gradient. Eight-micrometre sections were stained with different antibody combinations as previously described^{6,18}. Primary antibodies used for staining are: anti-ISL1 mouse monoclonal antibody (Developmental Studies Hybridoma Bank), anti-cTNT rabbit polyclonal antibody (Abcam), anti-SMMHC rabbit polyclonal antibody (Biomedical Technologies), anti-NKX2-5 rabbit polyclonal antibody (Santa Cruz) and anti-KDR/Flk1 rabbit polyclonal antibody (Upstate). Alexa-Fluor-488- or Alexa-Fluor-594-conjugated secondary antibodies were purchased from Molecular Probes. Haematoxylin and eosin (Sigma-Aldrich) staining was applied to adjacent slides to reveal tissue structures.

Human ES cell culture. Human ES cells H9 (WiCell Research Institute, NIH code WA09) and HUES3 (Harvard University) were maintained in standard human ES culture as described^{10,22}. To generate embryoid bodies for *in vitro* differentiation, human ES cells were treated with 0.5 mg ml⁻¹ dispase (Gibco) at 37 °C for 20 min. Cells were then suspended in human ES cell differentiation medium (DMEM/F12 (Gibco) containing 18% FBS (BenchMark), 0.1 mM NEAA (Gibco), 2 mM L-glutamine (Gibco), 5.5 mM 2-mercaptoethanol (Sigma) and 50 µg ml⁻¹ ascorbic acid (Sigma)), transferred to 6-well ultra low cluster plates (Costar) and cultured at 37 °C with 5% CO₂.

BAC recombineering. Recombineering was performed as described²³ (see also <http://recombineering.ncifcrf.gov/>). Briefly, human BAC clone CTD-2314G24, which contains all exons of the *ISL1* gene and extends from 100.7 kb upstream to 26.1 kb downstream of the translation start site, was introduced into *Escherichia coli* strain SW102. A targeting vector was constructed with two 350-bp homologous arms and a β-geo reporter followed by an antibiotics cassette providing resistance in both eukaryotes and prokaryotes. The targeting vector was linearized and electroporated into SW102 containing BAC CTD-2314G24 and activated recombinases. The transformed bacteria were plated on LB plates with appropriate antibiotics and incubated at 32 °C for 18–24 h. Selected clones were picked and subjected to PCR to confirm successful recombination.

Construction of knock-in vector. A new targeting vector was constructed by replacing the β-geo reporter of above targeting vector with a *cre-IRES-puro* cassette. Recombineering was performed by introducing the new vector into SW102 containing BAC CTD-2314G24 and activated recombinases described

above. An additional retrieving vector containing a 500-bp fragment at 5' of the 9.2-kb 5' arm and a 500-bp fragment at 3' of the 5.5-kb 3' arm homologous to *ISL1* exon 1 was made for retrieving the final knock-in construct from the recombinereed *ISL1-cre* BAC.

Electroporation transfection. Electroporation was performed as previously described^{10,24,25} with modifications. Human *ISL1-β-geo* BAC and *ISL1-cre* knock-in vector were linearized by lambda terminase (Epicentre Biotechnologies) and restriction enzymes, respectively, and sterilized by ether extraction. Human ES cells were trypsinized and filtered through 100-µm cell strainers. Cells were then centrifuged and re-suspended in human ES cell culture medium with 1× PBS. A total of 15–30 µg of linearized DNAs was added into re-suspended human ES cells. The cells were subjected to a single 320 V, 200 µF pulse (BioRad GenePulser Xcell CE module) at room temperature and plated on irradiated DR4 MEF feeders. Antibiotics selection was applied 3 days after electroporation. Southern blotting and long-range PCR confirmed the homologous integration of the human *ISL1-cre* knock-in construct. Genomic DNA was digested with BamHI restriction enzyme and a 500-bp fragment upstream of the 5' homologous arm was used as 5' probe. The human *ISL1-cre* knock-in lines have a 26-kb wild-type band and a 11-kb mutant band.

Flow cytometry. Embryoid bodies were dissociated into single cells using 0.25% trypsin-EDTA and stained with DAPI. Forward scatter (FSC) versus side scatter (SSC) and forward scatter height (FSC-H) versus forward scatter width (FSC-W) were used to exclude debris and doublet. DAPI positive population, representing dead cells, was excluded during FACS (BD FACSAria). DsRed⁺ cells were isolated from day 8 EBs. Sorting data were analysed using FlowJo software (Treestart). Anti-KDR antibody was purchased from R&D Systems.

Clonal assay. The sorted cells were plated on 24-well plates with irradiated MEF feeders and cultured in human B27 medium (DMEM/F12 (Gibco) containing 5% KOSR (Invitrogen), 1× human B27 supplements (Gibco, supplied as 50× stock), 5 ng ml⁻¹ of human recombinant basic FGF (Millipore) and 10 ng ml⁻¹ of human EGF (Sigma)). After 10–14 days of culture, colonies were picked, dissociated and seeded on fibronectin-coated chamber slides for differentiation.

RT-PCR. Total RNA was isolated using the Absolutely RNA Nanoprep kit (Stratagene) and was reverse transcribed using the iScript cDNA Synthesis kit (BioRad). Primer sequences and PCR conditions are available upon request. qPCR was performed on MasterCycler EP RealPlex (Eppendorf) using iQ SYBR Green SuperMix (BioRad). Standard deviations (s.d.) of the means in qPCR experiments were obtained from three independent experiments.

LETTERS

A parallel circuit of LIF signalling pathways maintains pluripotency of mouse ES cells

Hitoshi Niwa^{1,2,3}, Kazuya Ogawa¹, Daisuke Shimosato^{1,2} & Kenjiro Adachi¹

The cytokine leukaemia inhibitory factor (LIF) integrates signals into mouse embryonic stem (ES) cells to maintain pluripotency. Although the Jak–Stat3 pathway is essential and sufficient to mediate LIF signals^{1,2}, it is still unclear how these signals are linked to the core circuitry of pluripotency-associated transcription factors, consisting of *Oct3/4* (also called *Pou5f1*), *Sox2* and *Nanog*^{3,4}. Here we show that two LIF signalling pathways are each connected to the core circuitry via different transcription factors. In mouse ES cells, *Klf4* is mainly activated by the Jak–Stat3 pathway and preferentially activates *Sox2*, whereas *Tbx3* is preferentially regulated by the phosphatidylinositol-3-OH kinase–Akt and mitogen-activated protein kinase pathways and predominantly stimulates *Nanog*. In the absence of LIF, artificial expression of *Klf4* or *Tbx3* is sufficient to maintain pluripotency while maintaining the expression of *Oct3/4*. Notably, overexpression of *Nanog* supports LIF-independent self-renewal of mouse ES cells in the absence of *Klf4* and *Tbx3* activity. Therefore, *Klf4* and *Tbx3* are involved in mediating LIF signalling to the core circuitry but are not directly associated with the maintenance of pluripotency, because ES cells keep pluripotency without their expression in the particular context.

Self-renewal of mouse ES cells under conventional culture conditions depends on the LIF-induced activation of the signal transducer Gp130, with withdrawal of LIF resulting in the induction of differentiation⁵. In the absence of LIF, either the artificial activation of Stat3 (ref. 2) or the overexpression of *Nanog*^{6,7} is sufficient to support ES self-renewal. Stat3 is activated by Jak kinase associated with Gp130, but the connection between Stat3 and *Nanog* has not been confirmed. Bioinformatic studies have identified several transcription factors as the putative targets of the core circuitry transcription factor Oct3/4 (ref. 8). Of these transcription factors, *Klf4* and *Tbx3* were found to possess the ability to support self-renewal of E14tg2a-derived *Rex1-Gfp-BSD/Oct3/4-Ecsp-pac* ES cells (hereafter called OCRG9 cells)⁹ in the absence of LIF, comparable to that of *Nanog* (Fig. 1a). These ES cells proliferate in the presence of puromycin, indicating active transcription from the *Oct3/4* promoter, but express GFP from the *Rex1* (also called *Zfp42*) promoter at lower frequency than the parental OCRG9 ES cells. *Klf4* encodes a krüppel-like zinc-finger transcription factor, which is required for the establishment of pluripotency in somatic cells¹⁰, delays differentiation in embryoid body culture¹¹, and acts as a cofactor of Oct3/4 and Sox2 to activate a particular set of target genes¹². *Tbx3* encodes T-box transcription factors, which are probably required to maintain pluripotency, as suggested by RNA-interference-mediated loss-of-function assays¹³. Transfection of one of these genes into CCE-derived MGZ5 ES cells¹⁴ using the integrated copy of the transgene also resulted in the reproducible derivation of LIF-independent clones (data not shown). However, no stable transfectants were recovered when MGZ5 ES cells

were transfected with *Tbx3* and *Klf4* using the episomal vector system that confers high expression level of the transgene¹, indicating the tight dosage effect of these genes (data not shown).

The morphology of ES cells supported by *Klf4*, *Tbx3* or *Nanog* (hereafter called *Klf4*-, *Tbx3*- or *Nanog*-ES cells, respectively) in the absence of LIF is indistinguishable from that of parental ES cells cultured with LIF (Fig. 1b). These cells continue to propagate for more than 1 month while maintaining constant proliferation ratios slightly slower than that of parental ES cells cultured with LIF (Fig. 1c). When the floxed transgene of *Klf4* (Fig. 1d) was transfected

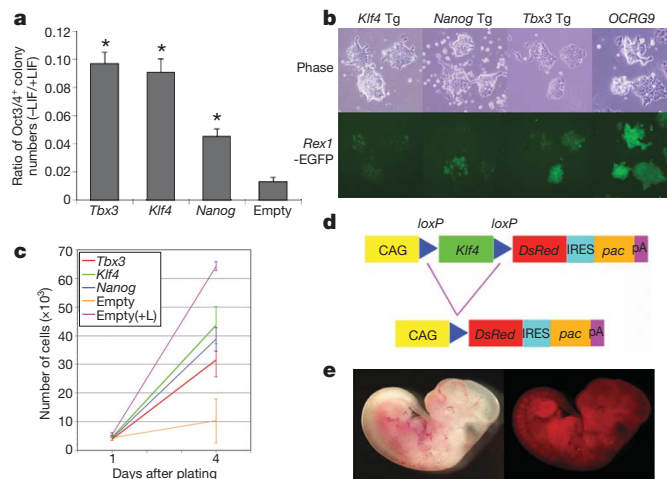


Figure 1 | *Tbx3* and *Klf4* support LIF-independent self-renewal of mouse ES cells. **a**, Generation of primary stem-cell colonies from ES cells transfected with *Tbx3*, *Klf4* and *Nanog* expression vectors in the absence of LIF. Shown are the ratios of the numbers of primary stem-cell colonies with Oct3/4–CFP expression, with or without LIF, resulting from transfection of 1×10^7 OCRG9 cells. Error bars indicate standard deviation. Asterisk, $P < 0.05$, t -test ($n = 3$). **b**, Transgenic (Tg) ES cells grown in the absence of LIF. Expression of the stem-cell marker *Rex1* was shown by the GFP reporter. **c**, Proliferation ratio of transgenic ES cells in the absence of LIF. 1×10^5 ES cells were seeded in a 90-mm dish in the presence of puromycin, which selects for Oct3/4-expressing cells, and the numbers of cells were counted after 1 or 4 days. Error bars indicate standard deviation ($n = 3$). **d**, Design of the removable transgene expression vector. *Klf4* cDNA flanked by loxP was placed under the control of the constitutively active CAG expression unit. Stable transfectants were selected by expression of the puromycin resistance gene (*pac*) translated from the internal ribosome entry site (IRES). Transient transfection of the *cre* expression vector excised *Klf4*, resulting in the expression of *DsRed*. **e**, Chimaeric embryo at embryonic day 12.5 produced from DsRed⁺ ES cells. EB5 ES cells carrying the floxed *Klf4* transgene were maintained without LIF for 1 month followed by excision of *Klf4* by transient expression of *cre*, resulting in the generation of DsRed⁺ ES cells.

¹Laboratory for Pluripotent Cell Studies, RIKEN Center for Developmental Biology, 2-2-3 Minatogima-minamimachi, Chuo-ku, Kobe 6500047, Japan. ²Laboratory for Development and Regenerative Medicine, Kobe University Graduate School of Medicine, 7-5-1 Kusunokicho, Chuo-ku, Kobe 6500017, Japan. ³JST, CREST, Sanbancho, Chiyoda-ku, Tokyo, 1020075, Japan.

into ES cells, these cells continued to propagate in the absence of LIF for 1 month. When the expression vector for *cre* recombinase was transiently transfected into these cells to excise the floxed *Klf4* transgene, the *DsRed* transgene was activated and the cells became LIF dependent and recovered the ability to generate normal embryoid bodies (data not shown). When these ES cells were injected into blastocysts, followed by transplantation into the uteri of pseudopregnant mice, they gave rise to chimaeric embryos in which *DsRed*-expressing cells contributed to the entire embryonic part (Fig. 1e). Similar results were observed for *Tbx3* (Supplementary Fig. 1). In both cases, before transgene excision, the transgenic ES cells were resistant to treatment with a Jak inhibitor or to stable expression of *Stat3F* (ref. 1), the dominant-negative form of *Stat3*, in the absence of LIF (data not shown). These results confirm that, as with *Nanog*^{6,7}, the expression of *Klf4* or *Tbx3* is absolutely sufficient to support self-renewal of ES cells in the absence of LIF.

To determine how these three transcription factors, which have the same activity, connect with each other, we measured expression levels of each endogenous transcript in transgenic ES cells cultured in the absence of LIF for 4 days (Fig. 2a). Downregulation of *Socs3*, a direct target of *Stat3* (ref. 15), as well as the loss of active *Stat3* (Fig. 2c) confirmed the removal of the LIF signal. *Oct3/4* expression was maintained at its normal level¹⁶ in all three transgenic ES cell lines. In contrast, *Sox2* expression level in *Nanog*- and *Tbx3*-ES cells was comparable to that in ES cells cultured in the absence of LIF for 4 days, suggesting that its expression is not maintained; *Nanog* is maintained only in *Tbx3*-ES cells. Because we previously found that the unique function of *Sox2* is the maintenance of *Oct3/4* expression¹⁷, these

results suggest that *Nanog* has the ability to maintain *Oct3/4* independent of *Sox2*, as previously suggested¹⁸, in *Tbx3*- and *Nanog*-ES cells. *Tbx3* expression was maintained in *Tbx3*-ES cells, but not in *Klf4*- and *Nanog*-ES cells, and *Klf4* expression was not maintained in all three transgenic ES cells. These characteristic expression patterns of *Tbx3*, *Klf4* and *Nanog* in each transgenic ES cell line were confirmed by protein expression levels (Fig. 2b). These findings suggest that there is a hierarchy in the functions of these transcription factors, in which *Tbx3* and *Klf4* are upstream whereas *Nanog* is downstream of *Tbx3*, to activate *Oct3/4* expression for proper self-renewal. Indeed, the hierarchical regulations of multiple pluripotency-associated genes were observed in the transgenic ES cells, in which some were commonly maintained but others were not (Supplementary Fig. 2).

Immunostaining of ES cells with specific antibodies showed that *Tbx3*, *Klf4* and *Nanog* were heterogeneously expressed (Fig. 2d). To characterize their expression pattern, we applied the *Rex1* marker system to distinguish two subpopulations in ES cells⁹. In OCRG9 ES cells, as previously reported, 80% of ES cells express GFP, which monitors *Rex1* expression. We found that 75%, 50% and 30% of ES cells express *Klf4*, *Nanog* and *Tbx3*, respectively (Fig. 2e), and that their expression was not always coordinated, although 24% of cells were triple-positive (Fig. 2f). Such obscure correlation between their nuclear localization patterns might reflect the fact that their complex regulation does not simply depend on the LIF-dependent cascade in the conventional culture condition but is also modulated by other signals. In contrast, *Oct3/4* expression was quite homogeneous, as determined by monitoring the *Oct3/4*-CFP fusion product expressed from the modified genomic allele (Fig. 2d). Therefore, the fluctuating

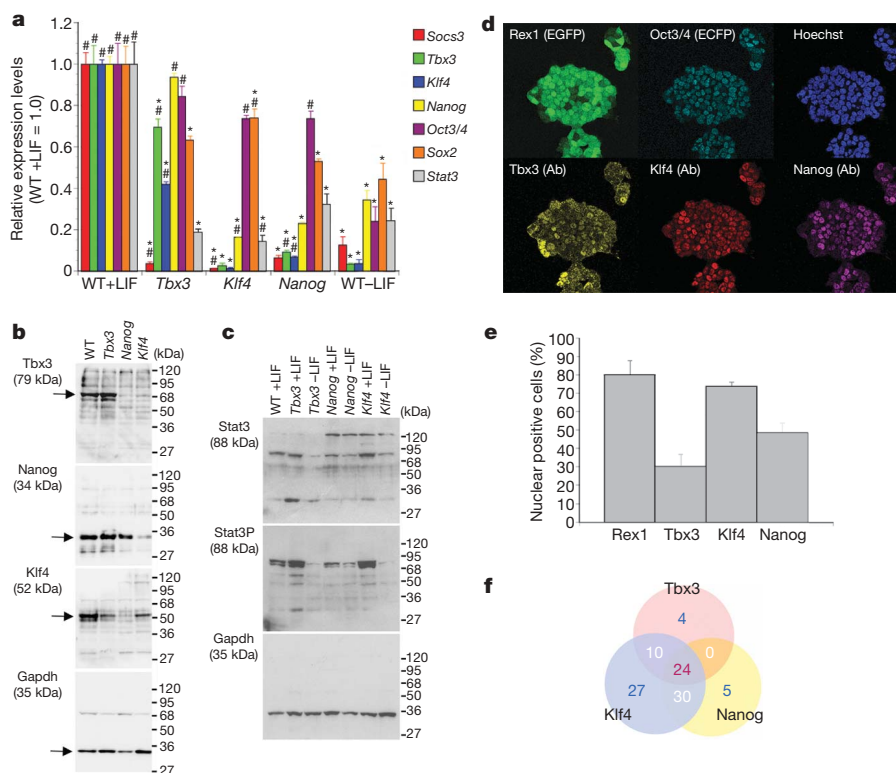


Figure 2 | Expression of pluripotency-associated transcription factors in LIF-independent ES cell lines. **a**, Quantitative RT-PCR analysis of transgenic ES cells cultured without LIF for 4 days. The level of expression of each transcript in parental ES cells cultured with LIF was set at 1.0. The expression levels in parental ES cells cultured without LIF for 4 days are also shown. Error bars indicate standard deviation. Asterisk, difference from wild type with LIF ($P < 0.05$; $n = 3$); hash, difference from wild type without LIF ($P < 0.05$; $n = 3$). **b**, Western blot analyses for the expression of *Tbx3*, *Nanog* and *Klf4* in transgenic ES cells cultured without LIF. **c**, Western blot analyses for the expression of phosphorylated *Stat3* (*Stat3P*) in transgenic ES cells

cultured with or without LIF. **d**, Confocal microscopic images of multiply immunostained *Rex1-Gfp/Oct3/4-Cfp* ES cells. *Tbx3*, *Klf4* and *Nanog* were detected in parallel by Alexa 546, 594 and 647, respectively. Original magnification, $\times 63$. **e**, Proportional analysis of gene expression in ES cells. Numbers of *Rex1*-GFP positive cells and cells carrying nuclear signals for *Tbx3*, *Klf4* or *Nanog*, as assessed by immunostaining, were counted in four independent confocal microscopy images ($n = 547$). Error bars indicate standard deviation of four images. **f**, Venn diagram of the expression patterns of *Tbx3*, *Klf4* and *Nanog*.

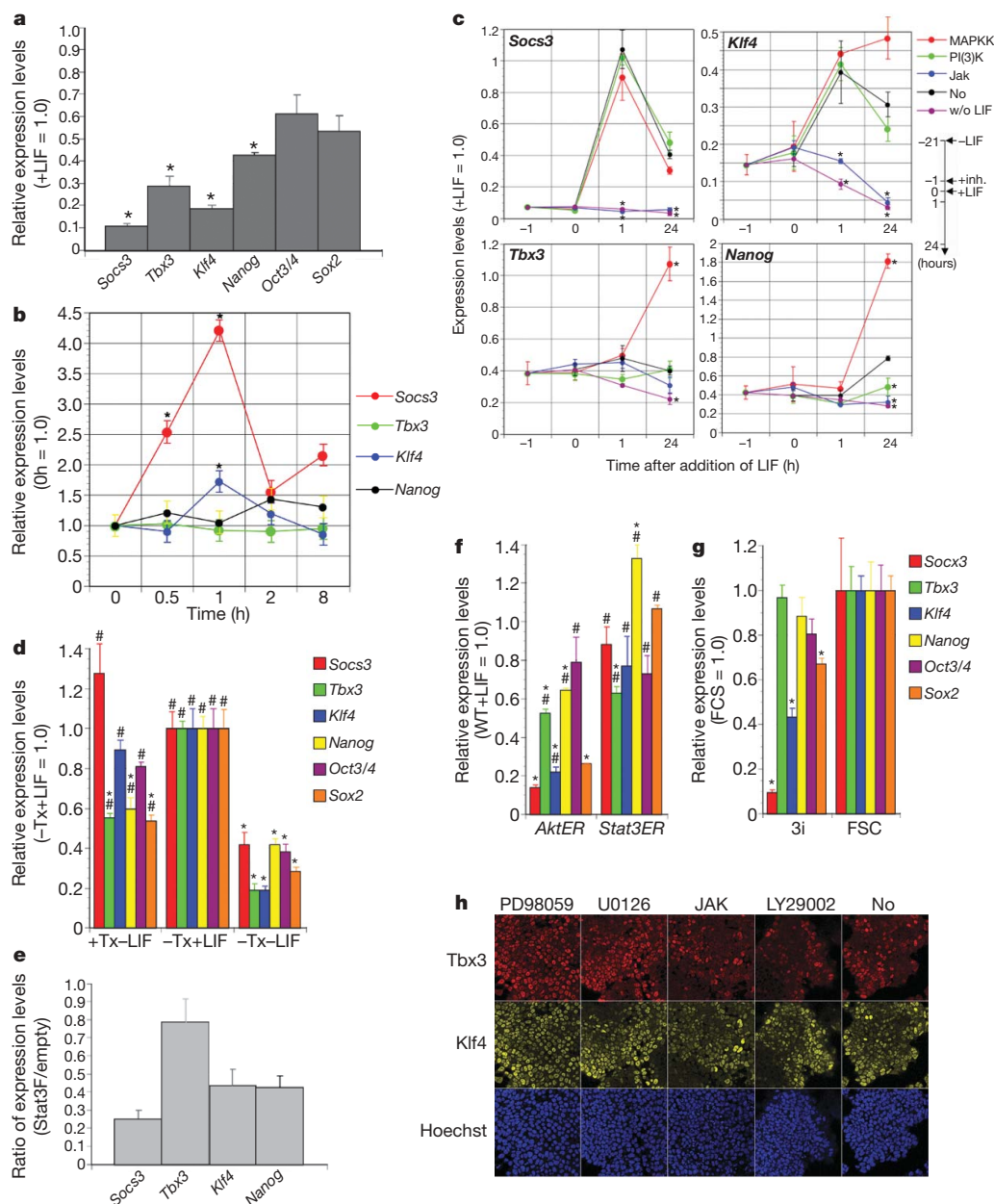


Figure 3 | Pathway-specific effects of LIF signals on the expression of *Tbx3* and *Klf4*. **a**, Quantitative RT-PCR analysis of gene expression in EB5 ES cells after withdrawal of LIF for 24 h. The level of expression of each in EB5 ES cells cultured with LIF was set at 1.0. Error bars indicate standard deviation. Asterisk, $P < 0.05$; $n = 3$. **b**, Kinetics of gene activation by LIF. EB5 ES cells were cultured without LIF for 21 h. LIF was added (set at time = 0) and gene expression was estimated by quantitative RT-PCR. Error bars indicate standard deviation. Asterisk, $P < 0.05$ from the expression levels at 0 ($n = 4$). **c**, Sensitivity of LIF-mediated upregulation to pathway-specific inhibitors. EB5 ES cells were cultured without LIF for 21 h. An inhibitor of Jak (Jak inhibitor I), PI(3)K (LY29002) or MAPKK (U0126) was added 1 h before the addition of LIF (set at time = 0). Expression levels of *Socs3*, *Klf4* and *Tbx3* at 0, 1 and 24 h after addition of LIF were estimated by quantitative RT-PCR. Error bars indicate standard deviation. Asterisk, $P < 0.05$ ($n = 4$) from the expression levels without inhibitors (No). w/o LIF indicates no addition of LIF at any time. **d**, Response to the activation of Stat3. ES cells stably expressing *Stat3ER* were cultured with 4HT without LIF (+Tx-LIF), without 4HT with LIF (-Tx+LIF), or without both 4HT and LIF (-Tx-LIF) for 4 days, and gene expression was estimated by quantitative RT-PCR. Error bars indicate standard deviation. Asterisk,

difference from the expression in -Tx+LIF ($P < 0.05$; $n = 3$); hash, difference from the expression in -Tx-LIF ($P < 0.05$; $n = 3$). **e**, Response to the inhibition of Stat3. EB5 ES cells were transfected with CAG-*Stat3F*-IP or CAG-IP, and the transient transfectants were selected by incubation with puromycin for 24–48 h. Expression levels at 48 h were estimated by quantitative RT-PCR. The ratios of expression level in *Stat3F* and empty transfectants are shown. Error bars indicate their standard deviation ($n = 3$). **f**, Quantitative PCR analysis of LIF-independent ES cells carrying *AktER* or *Stat3ER*. Transgenic ES cells were cultured without LIF in the presence of 4HT for 3 weeks and analysed. The expression levels in EB5 ES cells cultured with LIF were set at 1.0. Error bars indicate their standard deviation. Asterisk, difference from wild type plus LIF ($P < 0.05$; $n = 3$); hash, difference from wild type without LIF ($P < 0.05$; $n = 3$). **g**, Quantitative PCR analysis of OECG9 ES cells cultured in 3i inhibitor cocktail (ref. 23) or fetal calf serum (FCS)-containing medium. Error bars indicate standard deviation. Asterisk, $P < 0.05$ from the expression level in FCS ($n = 4$). **h**, *Tbx3* localization in ES cells treated with pathway-specific inhibitors. OECG9 ES cells cultured with LIF were treated with the indicated inhibitors for 24 h, and *Tbx3* and *Klf4* were localized by immunostaining.

expression of the upstream transcription factors converged to a constant expression, maintaining a steady state of self-renewal.

The ability to replace the requirement for LIF suggests that these transcription factors have physiological properties, even in the presence of LIF signalling. To test these properties, we evaluated the rapid transcriptional responsiveness to the activation of the LIF signal in ES cells. ES cells were cultured without LIF for 21 h to remove the LIF signal, resulting in significant repression of *Socs3*, *Klf4*, *Tbx3* and *Nanog* expression, but not *Oct3/4* and *Sox2* expression (Fig. 3a). LIF was subsequently added and the expression levels of these genes were monitored (Fig. 3b). *Socs3*, a direct target of Stat3, was upregulated at 0.5 h, decreased at 2 h and then maintained at a moderate level. *Klf4* showed a similar time course, although its magnitude of upregulation was smaller. In contrast, *Tbx3* and *Nanog* showed no significant response to LIF in this time period. These data suggest that *Klf4* looks most closely regulated by the LIF signal in these three genes.

We also assessed the intracellular signal pathways involved in activation of each gene. The LIF signal has been shown to activate three pathways: Jak–Stat3, phosphatidylinositol-3-OH kinase (PI(3)K)–Akt and mitogen-activated protein kinase (MAPK)¹⁹. Among them, the Jak–Stat3 pathway is solely regulated by LIF in ES cells, but the other two are regulated by multiple pathways. We incubated cells with specific inhibitors of each pathway before LIF stimulation, confirmed the effects by western blot of the signal components (Supplementary Fig. 3), and assessed their effects on early induction events (Fig. 3c). Upregulation of *Socs3* at 1 h was completely cancelled by the Jak inhibitor but not by the others, indicating that *Socs3* expression is solely dependent on the Jak–Stat3 pathway. Upregulation of *Klf4* was also specifically prevented by the Jak inhibitor. Notably, the MAPK-kinase (MAPKK) inhibitor upregulated *Tbx3* and *Nanog* at 24 h (Fig. 3c). Differential dependence on the Jak–Stat3 pathway was confirmed by direct modulation of Stat3 activity in ES cells. ES cells carrying a *Stat3ER* transgene, which is activated by 4-hydroxy tamoxifen (4HT)², were cultured with or without 4HT in the absence of LIF for 4 days and the gene expression levels were compared to that of the cells cultured in the presence of LIF. This comparison revealed that *Socs3* and *Klf4* were maintained by Stat3ER but *Tbx3* and *Nanog* were not (Fig. 3d). In contrast, when the Stat3 activity was inhibited by transient overexpression of the dominant-negative form of Stat3 (ref. 1), *Socs3*, *Klf4* and *Nanog* were significantly repressed but *Tbx3* expression was not affected (Fig. 3e). These data indicate that *Tbx3* expression is not mainly regulated by Stat3.

The PI(3)K–Akt pathway is partly regulated by LIF but is also activated by the insulin/insulin-like growth factor as well as the constitutive activity of Eras in ES cells²⁰. To test its impact on the pattern of gene expression, we analysed the gene expression pattern in ES cells maintained by a constitutively active form of Akt with a myristoylated signal in the absence of LIF²¹. In these ES cells, *Tbx3* and *Nanog*, as well as *Oct3/4*, showed normal expression, whereas *Klf4* and *Sox2* were not maintained (Fig. 3f). The expression pattern of these genes as well as other markers is quite similar to that of *Tbx3*-ES cells (Fig. 2a and Supplementary Fig. 2). These observations are consistent with the report that *Nanog* is regulated by the PI(3)K–Akt pathway²². Moreover, they strongly suggest that *Tbx3* expression is partly regulated by the PI(3)K–Akt pathway under the control of the LIF signal.

Why were *Tbx3* and *Nanog* upregulated at the late stage by LIF in the presence of MAPKK inhibitor? The MAPK pathway was recently shown to be activated by the FGF signal in ES cells, destabilizing its pluripotent state; complete blockage of MAPKK in combination with inhibition of glycogen synthase kinase 3 β (GSK3 β) was sufficient to support self-renewal in the absence of LIF²³. We found that *Tbx3* and *Nanog* were well maintained in ES cells cultured in this condition (Fig. 3g), and inhibition of MAPKK resulted in the accumulation of Tbx3 protein in nuclei from 8 h (data not shown) and reached to the maximum level after 24 h (Fig. 3h). Because *Tbx3*-ES cells express

endogenous *Tbx3* (Fig. 2a), *Tbx3* might be positively autoregulated. Therefore, if the MAPK pathway stimulates the nuclear export of Tbx3, its inhibition would result in the nuclear accumulation of Tbx3, resulting in the maintenance of its expression via autoregulation. The nuclear localization of Tbx3 may be regulated by multiple signals, as accumulation of Tbx3 protein in nuclei was also observed in ES cells cultured on feeder cells, and the stimulation of nuclear localization of Tbx3 protein is dependent on protein synthesis (data not shown).

We have shown that the LIF signal is integrated into the core regulatory circuitry of pluripotency via two parallel pathways: the Jak–Stat3, which activates *Klf4* and then *Sox2* but not *Nanog*, and the PI(3)K–Akt pathway, which activates *Tbx3* and then preferentially *Nanog* (Fig. 4). These pathways should be regarded as the principal ones; however, there should also be some minor pathways because *Sox2* regulation is not completely exclusive and the long-term culture of ES cells supported by Stat3ER without LIF resulted in the recovery of a normal gene expression pattern (Fig. 3f). The regulation of proliferation is separable from these parallel pathways because the activation of both by the transgenic expression of *Tbx3* and *Klf4* was not sufficient to recover the normal growth ratio, although *Stat3ER*-ES cells can proliferate normally in the absence of LIF (data not shown). Construction of such parallel circuitry might confer robustness on the transcription factor network, making *Klf4*, *Tbx3* and *Nanog* dispensable in ES cells and/or early embryogenesis^{24–26}. This dispensability may also be due to the overlapping function of similar molecules, because *Klf2*, *Tbx4* (data not shown) and *Klf5* (ref. 27) can also support LIF-independent self-renewal. The function of *Klf4* and *Tbx3* may therefore be limited to their connection of the LIF signal with the core circuitry, because *Oct3/4* is maintained without activation of *Klf4* and *Tbx3* in *Nanog*-ES cells. Notably, a similar expression pattern has been observed in epiblast-derived pluripotent stem cells (EpiSCs) derived from primitive ectoderm, which were maintained by activin and Fgf2²⁸, consistent with the expression of *Oct3/4*, *Sox2* and *Nanog*, suggesting that different sets of transcription factors can bridge the various extracellular signals and the unique core transcription factors. Indeed, the recent reports show that *Nanog* expression is maintained by the Smad2/3 pathway under the control of activin in

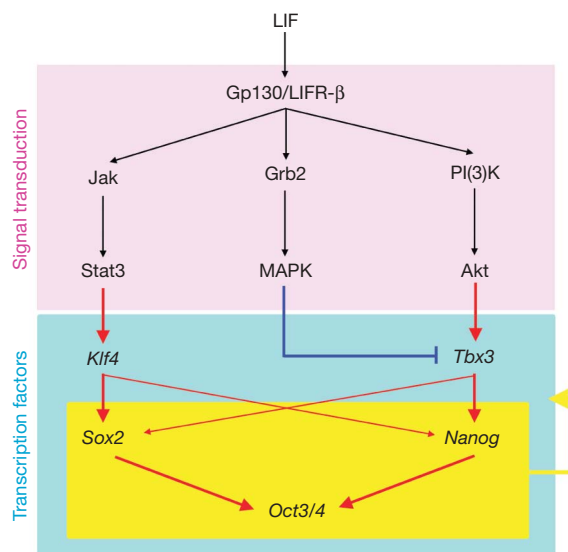


Figure 4 | Diagram of the parallel circuitry of the LIF signal pathways integrating into the transcription factor network. The Jak–Stat3 pathway activates *Klf4*, whereas the PI(3)K–Akt pathway stimulates the transcription of *Tbx3*. The MAPK pathway antagonizes the nuclear localization of Tbx3. *Klf4* and *Tbx3* mainly activate *Sox2* and *Nanog*, respectively, and maintain expression of *Oct3/4*. Transcription of all these transcription factors is positively regulated by *Oct3/4*, *Sox2* and *Nanog*, which may confer robustness and stable expression in the absence of all signals.

EpiSCs²⁹. Such a functional hierarchy of transcription factors might explain the robustness of the transcription factor network in maintaining pluripotency. To our knowledge, this is the first dissection of the functional hierarchy of transcription factors that maintains self-renewal of mouse ES cells.

METHODS SUMMARY

Construction of expression vectors. Mouse *Klf4* and *Tbx3* cDNAs were amplified from ES cell cDNA using the primers shown in Supplementary Table 1. These cDNAs were subsequently sequenced and subcloned into pCAG-IP¹⁴, pCAG-IN (in which *pac* in pCAG-IP was replaced by *neo*), and pCAG-flox-DsRedT4-IP³⁰ expression vectors.

ES cell culture. All ES cell cultures, stable transfections and chimera formations were performed as described³⁰. Selection drugs, inducers and inhibitors were used at the following concentrations: 1 µg ml⁻¹ puromycin (Sigma); 150 µg ml⁻¹ G418 (Sigma); 1 µM 4HT (Sigma); 10 µM Jak inhibitor I (Carbiochem); 5 µM LY294002 (Sigma); 25 µM PD98059 (Promega); 10 µM U0126 (Carbiochem).

Quantitative PCR. To quantify the amounts of transcripts, cDNAs were synthesized from 1 µg of total RNA using ReverTra Ace (Toyobo), and cDNA aliquots equivalent to 2.5 ng RNA were evaluated by quantitative PCR using a BioRad iCycler and the primers in Supplementary Table 1. All samples were tested in triplicate, and the results of each were normalized relative to *Gapdh* expression. The mean relative amounts of each transcript were calculated.

Immunostaining. Immunostaining was performed as described⁹, using the following antibodies and dilutions: goat anti-Tbx3 (Santa Cruz, 17871), 1:300; rabbit anti-Tbx3 (antisera prepared by ourselves), 1:1,000; rabbit anti-Klf4 (Santa Cruz, 20691), 1:300; goat anti-Klf4 (R&D, AF3158); rat anti-Nanog (eBioscience, MLC-51), 1:100; and mouse anti-Oct3/4 (Santa Cruz, 5279), 1:1,000.

Received 21 February; accepted 5 May 2009.

- Niwa, H., Burdon, T., Chambers, I. & Smith, A. Self-renewal of pluripotent embryonic stem cells is mediated via activation of STAT3. *Genes Dev.* **12**, 2048–2060 (1998).
- Matsuda, T. *et al.* STAT3 activation is sufficient to maintain an undifferentiated state of mouse embryonic stem cells. *EMBO J.* **18**, 4261–4269 (1999).
- Niwa, H. How is pluripotency determined and maintained? *Development* **134**, 635–646 (2007).
- Jaenisch, R. & Young, R. Stem cells, the molecular circuitry of pluripotency and nuclear reprogramming. *Cell* **132**, 567–582 (2008).
- Burdon, T., Smith, A. & Savatier, P. Signalling, cell cycle and pluripotency in embryonic stem cells. *Trends Cell Biol.* **12**, 432–438 (2002).
- Mitsui, K. *et al.* The homeoprotein Nanog is required for maintenance of pluripotency in mouse epiblast and ES cells. *Cell* **113**, 631–642 (2003).
- Chambers, I. *et al.* Functional expression cloning of Nanog, a pluripotency sustaining factor in embryonic stem cells. *Cell* **113**, 643–655 (2003).
- Sharov, A. A. *et al.* Identification of *Pou5f1*, *Sox2*, and *Nanog* downstream target genes with statistical confidence by applying a novel algorithm to time course microarray and genome-wide chromatin immunoprecipitation data. *BMC Genomics* **9**, 269 (2008).
- Toyooka, Y., Shimosato, D., Murakami, K., Takahashi, K. & Niwa, H. Identification and characterization of subpopulations in undifferentiated ES cell culture. *Development* **135**, 909–918 (2008).
- Takahashi, K. & Yamanaka, S. Induction of pluripotent stem cells from mouse embryonic and adult fibroblast cultures by defined factors. *Cell* **126**, 663–676 (2006).
- Li, Y. *et al.* Murine embryonic stem cell differentiation is promoted by SOCS-3 and inhibited by the zinc finger transcription factor Klf4. *Blood* **105**, 635–637 (2005).

- Nakatake, Y. *et al.* Klf4 cooperates with Oct3/4 and Sox2 to activate the Lefty1 core promoter in embryonic stem cells. *Mol. Cell. Biol.* **26**, 7772–7782 (2006).
- Ivanova, N. *et al.* Dissecting self-renewal in stem cells with RNA interference. *Nature* **442**, 533–538 (2006).
- Niwa, H., Masui, S., Chambers, I., Smith, A. G. & Miyazaki, J. Phenotypic complementation establishes requirements for specific POU domain and generic transactivation function of Oct-3/4 in embryonic stem cells. *Mol. Cell. Biol.* **22**, 1526–1536 (2002).
- Auernhammer, C. J., Bousquet, C. & Melmed, S. Autoregulation of pituitary corticotroph SOCS-3 expression: characterization of the murine SOCS-3 promoter. *Proc. Natl Acad. Sci. USA* **96**, 6964–6969 (1999).
- Niwa, H., Miyazaki, J. & Smith, A. G. Quantitative expression of Oct-3/4 defines differentiation, dedifferentiation or self-renewal of ES cells. *Nature Genet.* **24**, 372–376 (2000).
- Masui, S. *et al.* Pluripotency governed by Sox2 via regulation of Oct3/4 expression in mouse embryonic stem cells. *Nature Cell Biol.* **9**, 625–635 (2007).
- Pan, G., Li, J., Zhou, Y., Zheng, H. & Pei, D. A negative feedback loop of transcription factors that controls stem cell pluripotency and self-renewal. *FASEB J.* **20**, 1730–1732 (2006).
- Paling, N. R., Wheadon, H., Bone, H. K. & Welham, M. J. Regulation of embryonic stem cell self-renewal by phosphoinositide 3-kinase-dependent signaling. *J. Biol. Chem.* **279**, 48063–48070 (2004).
- Takahashi, K., Murakami, M. & Yamanaka, S. Role of the phosphoinositide 3-kinase pathway in mouse embryonic stem (ES) cells. *Biochem. Soc. Trans.* **33**, 1522–1525 (2005).
- Watanabe, S. *et al.* Activation of Akt signaling is sufficient to maintain pluripotency in mouse and primate embryonic stem cells. *Oncogene* **25**, 2697–2707 (2006).
- Storm, M. P. *et al.* Regulation of Nanog expression by phosphoinositide 3-kinase-dependent signalling in murine embryonic stem cells. *J. Biol. Chem.* **282**, 6265–6273 (2007).
- Ying, Q. L. *et al.* The ground state of embryonic stem cell self-renewal. *Nature* **453**, 519–523 (2008).
- Katz, J. P. *et al.* The zinc-finger transcription factor Klf4 is required for terminal differentiation of goblet cells in the colon. *Development* **129**, 2619–2628 (2002).
- Davenport, T. G., Jerome-Majewska, L. A. & Papaioannou, V. E. Mammary gland, limb and yolk sac defects in mice lacking *Tbx3*, the gene mutated in human ulnar mammary syndrome. *Development* **130**, 2263–2273 (2003).
- Chambers, I. *et al.* Nanog safeguards pluripotency and mediates germline development. *Nature* **450**, 1230–1234 (2007).
- Ema, M. *et al.* Kruppel-like factor 5 is essential for blastocyst development and the normal self-renewal of mouse ESCs. *Cell Stem Cell* **3**, 555–567 (2008).
- Tesar, P. J. *et al.* New cell lines from mouse epiblast share defining features with human embryonic stem cells. *Nature* **448**, 196–199 (2007).
- Vallier, L. *et al.* Activin/Nodal signalling maintains pluripotency by controlling Nanog expression. *Development* **136**, 1339–1349 (2009).
- Ogawa, K. *et al.* Activin-Nodal signaling is involved in propagation of mouse embryonic stem cells. *J. Cell Sci.* **120**, 55–65 (2007).

Supplementary Information is linked to the online version of the paper at www.nature.com/nature.

Acknowledgements We thank T. Nakano for providing the *AktER* expressing ES cells.

Author Contributions H.N. conceived the study; H.N. and K.O. designed and executed experiments; D.S. performed embryo manipulation; K.A. contributed experimental advice; and H.N. interpreted experiments and wrote the paper.

Author Information Reprints and permissions information is available at www.nature.com/reprints. Correspondence and requests for materials should be addressed to H.N. (niwa@cdb.riken.jp).

Genome-wide silencing in *Drosophila* captures conserved apoptotic effectors

Su Kit Chew^{1†}, Po Chen¹, Nichole Link¹, Kathleen A. Galindo¹, Kristi Pogue¹ & John M. Abrams¹

Apoptosis is a conserved form of programmed cell death firmly established in the aetiology, pathogenesis and treatment of many human diseases. Central to the core machinery of apoptosis are the caspases and their proximal regulators. Current models for caspase control involve a balance of opposing elements, with variable contributions from positive and negative regulators among different cell types and species¹. To advance a comprehensive view of components that support caspase-dependent cell death, we conducted a genome-wide silencing screen in the *Drosophila* model. Our strategy used a library of double-stranded RNAs together with a chemical antagonist of Inhibitor of apoptosis proteins (IAPs) that simulates the action of native regulators in the Reaper and Smac (also known as Diablo) families². Here we present a highly validated set of targets that is necessary for death provoked by several stimuli. Among these, *Tango7* is identified as a new effector. Cells depleted for this gene resisted apoptosis at a step before the induction of effector caspase activity, and the directed silencing of *Tango7* in *Drosophila* prevented caspase-dependent programmed cell death. Unlike known apoptosis regulators in this model system³, *Tango7* activity did not influence stimulus-dependent loss of *Drosophila* DIAP1 (also known as *th* and *IAP1*), but instead regulated levels of the apical caspase *Dronc* (*Nc*). Similarly, the human *Tango7* counterpart, PCID1 (also known as EIF3M), impinged on caspase 9, revealing a new regulatory axis affecting the apoptosome.

Mammalian Smac proteins are thought to be functional orthologues of the *Drosophila* IAP antagonists referred to as RHG proteins (Reaper, Head involution defective, and Grim, as well as Sickie and Jafrac2)³. Therefore, we tested the possibility that a small molecule Smac-mimetic⁴ might simulate the action of RHG proteins in *Drosophila* cells. Like RHG proteins⁵, the Smac-mimetic compound specifically bound DIAP1—a central brake against caspases³ (Fig. 1a). In *Drosophila* cell lines, the Smac-mimetic compound induced stereotypical apoptosis (Fig. 1b and Supplementary Movie 1), which was completely reversed either by peptide caspase inhibitors or by RNA interference (RNAi) depletion of the apical caspase *Dronc* (Fig. 1c), mirroring haemocytes lacking apoptosomal genes^{6,7}. Together, the findings establish the Smac-mimetic compound as a molecular mimetic of RHG proteins.

We conducted an RNAi-based genome-scale screen to identify essential apoptotic determinants using the Smac-mimetic compound as a proximal apoptogenic stimulus (Fig. 2a and Methods). Our platform used S2R+ cells and a library of double-stranded (ds)RNAs targeting 13,071 annotated genes in *Drosophila* genome build 3 (Fig. 2a and Methods) to capture targets that prevent Smac-mimetic-induced killing when silenced (Fig. 2c). Each dsRNA (Supplementary Table 4) was tested in triplicate. The effects were typically reproducible (Fig. 2b), and assay quality, measured by Z-factor values, was consistently high⁸.

Using both plate and position mean-centring analyses (Methods), we identified 42 candidate genes with protective activity that met or exceeded a stringent z-score ≥ 3.1 threshold ($P < 0.001$). This collection includes the expected benchmark targets *Dronc*, *Dark* (also known

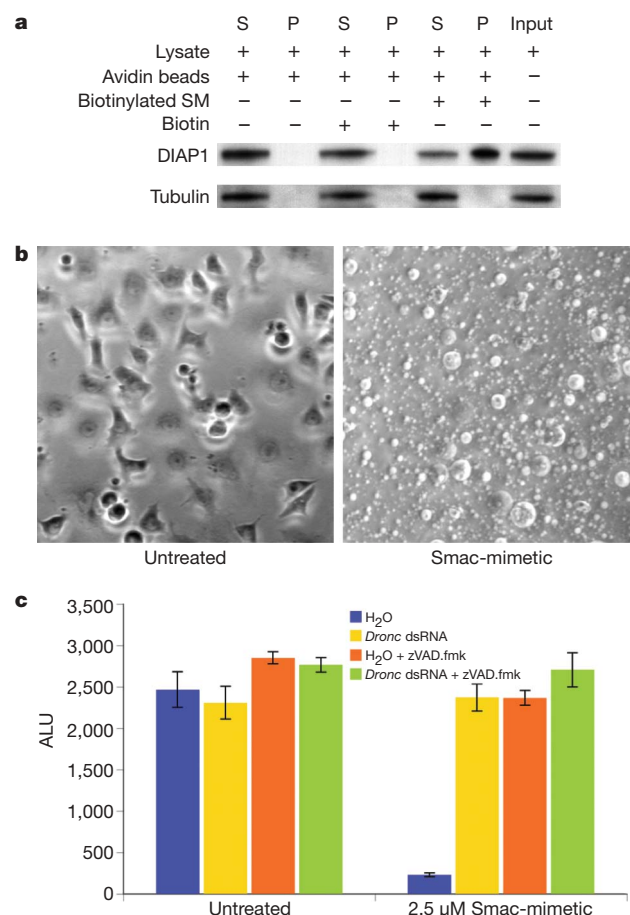


Figure 1 | A Smac-mimetic compound exerts broad cross-species IAP antagonist activity. **a**, Cell lysates were incubated with biotinylated Smac-mimetic (SM) or biotin. Pellets (P) of avidin-conjugated beads and supernatants (S) were probed with anti-DIAP1 or anti-tubulin antibodies. **b**, Smac-mimetic induces apoptotic blebbing in S2R+ cells within 6 h of treatment (Supplementary Movie 1). Twenty-four hour treatment with Smac-mimetic triggers similar effects in other fly cell lines and *ex vivo* primary cells^{6,7}. Original magnification, $\times 40$. **c**, After the treatments indicated, viability was measured using CellTiter-Glo. zVAD.fmk is a broad-range caspase inhibitor. ALU, arbitrary luminescence units; data are mean \pm s.d., $n = 3$ sample wells.

¹Department of Cell Biology, University of Texas Southwestern Medical Center, Dallas, Texas 75390, USA. [†]Present address: Wellcome Trust Sanger Institute, Hinxton, Cambridge CB10 1HH, UK.

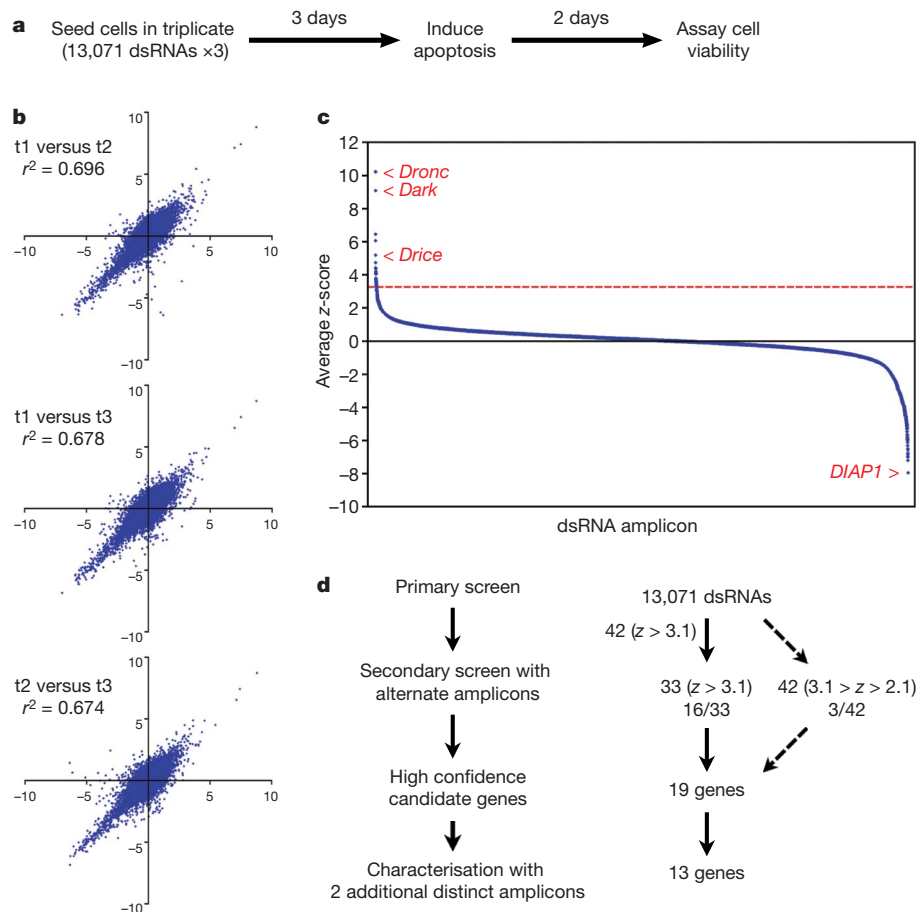


Figure 2 | A genome-wide screen captures apoptogenic effectors. **a**, Screen schematic is shown. **b**, Plate mean-centred z-scores for triplicate samples of each dsRNA (t1, t2 and t3) plotted against each other (r^2 denotes correlation coefficient). **c**, Average position mean-centred z-score plotted in rank

format. Arrowheads highlight known 'landmark genes' with pro- and anti-apoptotic activity. The dotted line is $z = 3.1$. **d**, Schematic for validation of candidates.

Table 1 | Characterization of high-rank candidate genes

Gene (human)	Description	UV		Cycloheximide	
		Amplicon 1	Amplicon 2	Amplicon 1	Amplicon 2
Control					
AmpR	Bacteria gene	0 ± 3.3		0 ± 3.5	
Known benchmarks					
<i>Dronc</i> (CASP9*)	Apical caspase	63.5 ± 4.9 ($P = 1.6 \times 10^{-10}$)		71.4 ± 1.8 ($P = 7.6 \times 10^{-13}$)	
<i>Dark</i> (APAF1*)	Caspase activation adaptor	55 ± 7.8 ($P = 1.9 \times 10^{-8}$)		47 ± 19.8 ($P = 0.00019$)	
Candidates					
<i>Drice</i> (CASP3*)	Effector caspase	59 ± 7.5 ($P = 7.3 \times 10^{-9}$)	30.1 ± 8.5 ($P = 1.1 \times 10^{-5}$)	67.2 ± 12.4 ($P = 1.6 \times 10^{-7}$)	48.9 ± 24.2 ($P = 0.00063$)
<i>Hrb27C</i> (DAZAP1)	Ribonucleoprotein	59.9 ± 6.5 ($P = 2.0 \times 10^{-9}$)	54.7 ± 4.5 ($P = 3.7 \times 10^{-10}$)	40.4 ± 16.8 ($P = 0.00019$)	27.1 ± 29.5 ($P = 0.049$)
<i>Enok</i> (MYST3)	Histone acetyltransferase	57.7 ± 5.4 ($P = 7.6 \times 10^{-10}$)	38.1 ± 4.4 ($P = 1.2 \times 10^{-8}$)	47.6 ± 14.7 ($P = 1.6 \times 10^{-5}$)	24.1 ± 13.1 ($P = 0.0014$)
<i>SNF4Aγ</i> (PRKAG1)	SNF4/AMP-activated kinase	12 ± 10 ($P = 0.019$)	22.1 ± 3.5 ($P = 5.2 \times 10^{-7}$)	8.7 ± 6.3 ($P = 0.015$)	17 ± 4.3 ($P = 2.1 \times 10^{-5}$)
<i>CG32626</i> (AMPD2)	AMP deaminase	18.3 ± 4.4 ($P = 1.0 \times 10^{-5}$)	14.9 ± 2.4 ($P = 4.8 \times 10^{-6}$)	7.4 ± 3.9 ($P = 0.0062$)	2.6 ± 7.6 ($P = 0.46$)
<i>CG40084</i> (CNNM2)	Cystathionine β-synthase domain	9.6 ± 9.2 ($P = 0.037$)	9.9 ± 2.9 ($P = 0.00026$)	5.4 ± 3.3 ($P = 0.020$)	6.1 ± 10.1 ($P = 0.19$)
<i>Atpx†</i> (ATP1A3)	Na ⁺ , K ⁺ -ATPase α-subunit	22.1 ± 3.9 ($P = 1.0 \times 10^{-6}$)	-12.9 ± 28.8 ($P = 0.30$)	4.8 ± 11.3 ($P = 0.34$)	-2.7 ± 2.8 ($P = 0.17$)
<i>CG7275</i> (WDSOF1)	WD40, Sof1 domains	27.9 ± 1.2 ($P = 3.0 \times 10^{-9}$)	30.9 ± 4 ($P = 5.0 \times 10^{-8}$)	9.5 ± 7.6 ($P = 0.020$)	14.4 ± 7 ($P = 0.0011$)
<i>Tango7</i> (PCID1)	PCI domain	66 ± 7.7 ($P = 3.2 \times 10^{-9}$)	68 ± 7.4 ($P = 1.7 \times 10^{-9}$)	58.4 ± 9.9 ($P = 8.6 \times 10^{-8}$)	60.9 ± 10.7 ($P = 1.1 \times 10^{-7}$)
<i>Myb</i> (MYBL2*)	Myb oncogene-like transcription factor	16.4 ± 4.3 ($P = 2.5 \times 10^{-5}$)	20.8 ± 3.1 ($P = 5.4 \times 10^{-7}$)	12 ± 9.8 ($P = 0.018$)	10.8 ± 17.6 ($P = 0.17$)
<i>eIF5</i> (EIF5)	Translation initiation factor	28.4 ± 5.9 ($P = 1.2 \times 10^{-6}$)	13.1 ± 2.3 ($P = 1.3 \times 10^{-5}$)	19 ± 2.9 ($P = 1.2 \times 10^{-6}$)	9.7 ± 9 ($P = 0.033$)
<i>Ikbl</i> (STK11*)	Ser/Thr kinase	5.7 ± 5.4 ($P = 0.051$)	36.7 ± 11.2 ($P = 1.7 \times 10^{-5}$)	3.4 ± 4 ($P = 0.15$)	10.6 ± 22.1 ($P = 0.27$)
<i>Sktl</i> (PIP5K1A*)	PIP5-kinase	16.1 ± 3.8 ($P = 1.4 \times 10^{-5}$)	19.4 ± 3.2 ($P = 1.3 \times 10^{-6}$)	17.7 ± 4.6 ($P = 2.1 \times 10^{-5}$)	16.2 ± 9.3 ($P = 0.0025$)

Caspase activity was measured 6 h after treatment with 90 mJ cm⁻² UVC or 250 μM cycloheximide. The percentage of caspase activity was calculated relative to control mean (100%) for each experiment. Data shown are the mean percentage inhibition ± s.d. from two independent experiments ($n = 3$ wells for each experiment). P values for two-tail t -tests were calculated by comparing the percentage inhibition of each gene with the control for each treatment. High consistency and reproducibility across amplicons indicate requisite functions in apoptosis.

* Human genes involved in cell death/survival pathways.

† Only amplicon 1 significantly affects ultraviolet-stimulated caspase activation. The specificity of amplicon 1 or ATPα to rescuing ATP viability and caspase activation has not been tested.

as *Ark*) and the effector caspase *Drice* (also known as *Ice*) (Fig. 2c, Table 1 and Supplementary Table 1).

Thirty-three of the 42 candidate genes with a z -score greater than 3.1 were retested using a different dsRNA amplicon (Fig. 2d)⁹. To examine the biological relevance of this threshold, 42 targets conferring less potent activity ($2.1 < z < 3.1$) were also retested (Supplementary Table 2). Nineteen candidates retested at least 3.1 standard deviations above the control mean, 16 of which had $z > 3.1$ in the original screen, whereas only three that survived this retest standard originally had $2.1 < z < 3.1$. Hence, our initial z -score threshold was experimentally relevant and predictive for reproducibility across different dsRNA amplicons.

We selected a set of 13 priority targets (Table 1) for further characterization on the basis of conservation and/or suggested links to human disease or development. For these, our validation strategy applied different assay methods, distinct apoptotic triggers and alternative non-overlapping dsRNAs^{10,11}. We assessed new amplicons

targeting each candidate by measuring effector caspase activity after ultraviolet light or cycloheximide challenge, two well-established apoptotic stimuli¹². These data (Table 1) discriminate several target groups including (1) genes that exert substantial activity across several stimuli (*Drice*, *Hrb27C*, *enok* and *Tango7*), (2) stimulus-dependent genes (*CG32626* and *CG7275*), and (3) genes with mild but statistically significant activity (*SNF4Aγ*, *eIF5* and *skt*).

Depletion of *Tango7* (*CG8309*) prevented killing induced by several apoptotic stimuli. Non-overlapping dsRNAs that target this gene (*Tango7* dsRNA1 and dsRNA2) conferred protective activity comparable to benchmark amplicons that silence *Dronc* and *Dark* (Table 1 and Fig. 3b). When tracked over a 22 h time course after ultraviolet challenge, more than 95% of control cells initiated blebbing and died. However, like samples depleted for *Dronc*, cells that were silenced for *Tango7* were similarly prevented from apoptotic blebbing when directly visualized over this same period (Fig. 3a and Supplementary Movies 2–4). Together with DEVDase (caspase 3/7-like

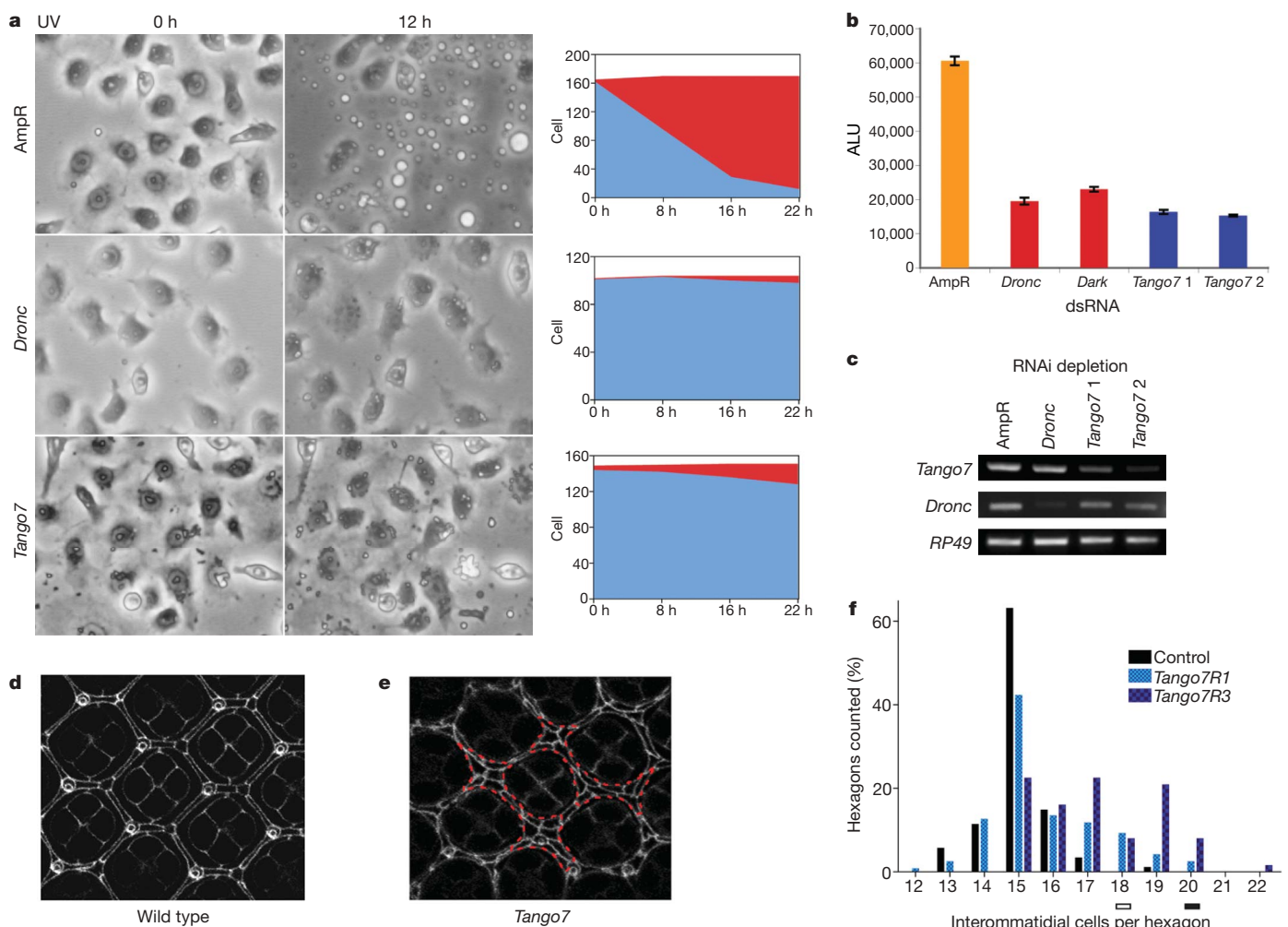


Figure 3 | *Tango7* is an effector of apoptosis. **a**, Left, time-lapse microscopy (original magnification, $\times 40$) of dsRNA-treated cells after ultraviolet (UV) exposure (see Supplementary Movies 2–4). AmpR refers to an irrelevant control dsRNA targeting B-lactamase. Right, cumulative counts (y -axis) of live (blue) or dead (red) cells. Similar results were observed using *Tango7* dsRNA1 (shown here) or *Tango7* dsRNA2 (data not shown). **b**, DEVDase activity 6 h after UV irradiation in RNAi-depleted cells. *Tango7* 1 and 2 are non-overlapping dsRNA amplicons targeting the *Tango7* transcript (see Methods). Data are mean \pm s.d., $n = 3$ different sample wells. **c**, Semi-quantitative RT-PCR detects relative transcript levels of *Tango7*, *Dronc* and the control *RP49* (also known as *RpL32*) in dsRNA-treated cells as in **a**. **d–f**, Caspase-dependent cell death in the pupal eye (original

magnification, $\times 63$). Transgenic dsRNAs silencing *Tango7* (**e**) or an irrelevant control (5887R1) (**d**) were targeted using the *gmr*-GAL4 eye ‘driver’ (see refs 13, 14 and Methods). Extra interommatidial cells shown (**e**, outlined red) are from *Tango7*R1. **f**, In control retinas, most (63%) hexagonal assemblies had stereotypical numbers of interommatidial cells (15). Less than 5% showed ≥ 17 cells per ommatidia ($n = 87$). *Tango7*R1 produced 28% of ommatidia with ≥ 17 cells ($n = 118$), and a minority (40%) showed stereotypical numbers. *Tango7*R3 produced 77% of ommatidia bearing ≥ 16 cells ($n = 62$). Differences between control and *Tango7* are significant by two-tailed unpaired t -test (*Tango7*R1 $P = 0.0002$; *Tango7*R3 $P < 0.0001$). The bars under the x -axis indicate values for *Dark* and *Dronc*²⁸ (solid) or for *Drice* (open)¹⁴.

activity) assays in Fig. 3b, our results indicate that *Tango7* acts before effector caspase activation and before steps involved in apoptotic blebbing.

The combined results from several amplicons and three distinct assays validate *Tango7* as an apoptogenic effector in S2R+ cells. To test the relevance of *Tango7* during programmed cell death (PCD) *in vivo*, *Tango7* dsRNAs were targeted to the pupal retina where excessive interommatidial cells are eliminated through caspase-dependent cell death³. Two different insertions of the 8309R1 transgene (*Tango7R1* and *Tango7R3*) were compared to an irrelevant control dsRNA transgene (Methods). Like retinas mutated for apical or effector caspases^{13,14}, retinas expressing either *Tango7R1* or *Tango7R3* retained statistically significant numbers of extra interommatidial cells (Fig. 3d–f). This effect was similar to animals lacking *Drice*¹⁴ and was not seen with an irrelevant dsRNA strain from the same collection. Depletion of *Tango7* in the wing also prompted a range of defects that were consistent with failures in post-eclosion cell death and similar to canonical PCD mutants^{6,13,15,16} (Supplementary Fig. 1a–d). Low-penetrance phenotypes not shared with other PCD mutants suggest that *Tango7* may not be dedicated to apoptotic functions. Unlike canonical cell death mutants, occasional scars appeared in a minority of adult retinas silenced for *Tango7* (Supplementary Fig. 1e, f), and hence extra interommatidial cells could conceivably arise through activity unrelated to cell death. However, because scars are not evident in pupal stages, these infrequent defects manifest long after pruning of interommatidial cells, and are more likely to reflect pleiotropic roles for *Tango7* in cells that are not fated to die.

To investigate the mode of apoptosis regulation by *Tango7*, core determinants were investigated. Notably, *Tango7* did not affect basal or stimulus-dependent loss of DIAP1 protein levels (Fig. 4a)—a central point of control commonly observed during canonical apoptosis signalling in *Drosophila*³. Levels of the apoptosomal protein Dark were also unaffected (Fig. 4a). In contrast, silencing of *Tango7* caused a marked decline in pro-Dronc levels (Fig. 4b). This relationship was also observed in the Dark-depleted state (Fig. 4b), which causes pro-Dronc accumulation to unusually high steady-state concentrations¹⁷. Therefore, under a wide dynamic range, *Tango7* positively regulates levels of this caspase. The findings also implicate a post-transcriptional mechanism linking *Tango7* activity to Dronc protein levels, because within the limits of our semiquantitative PCR with reverse transcription (RT-PCR) assay, the treatments had little or no effect on *Dronc* messenger RNA abundance (Fig. 3c).

To examine whether the relationship between *Tango7* and *Dronc* (Fig. 4b) reflects a conserved regulatory axis, we tested whether *PCID1*—the human orthologue of *Tango7*—might similarly affect caspase 9. Human T98G cells¹⁸ or IMR90E1A cells¹⁹ were treated with gene-specific short-interfering (siRNAs), and steady-state levels of pro-caspase 9 were determined. As in *Drosophila*, a similar relationship between human counterparts was exposed in cell lines of distinct origins (Fig. 4c). Here, *PCID1* siRNAs caused a repression of pro-caspase 9 levels, with effects that were analogous to siRNAs that directly target caspase 9. To explore the links between *PCID1* and apoptosis further, siRNA-treated cells were challenged with an apoptogenic stimulus (ultraviolet light) and tested for induction of effector caspase activity. As shown in Fig. 4d, silencing either *PCID1* or *CASP9* attenuated stimulus-dependent DEVDase. Furthermore, co-silencing of both targets reduced activity comparable to depletion of the pro-apoptotic effector, Bak²⁰. Hence, in cells in which the levels of caspase 9 are rate-limiting, *PCID1* is a relevant determinant of caspase activity. We also measured ATP in these experiments (data not shown), and by this criterion, neither *CASP9* siRNAs nor *PCID1* siRNAs appeared cytoprotective. However, this result was anticipated, because unlike caspase-inhibited fly cells³, mammalian cells often die by alternate forms of cell death when caspase activity is blocked^{20,21}.

The highly validated gene set in Table 1 presents new opportunities for understanding how cells integrate death signals and execute

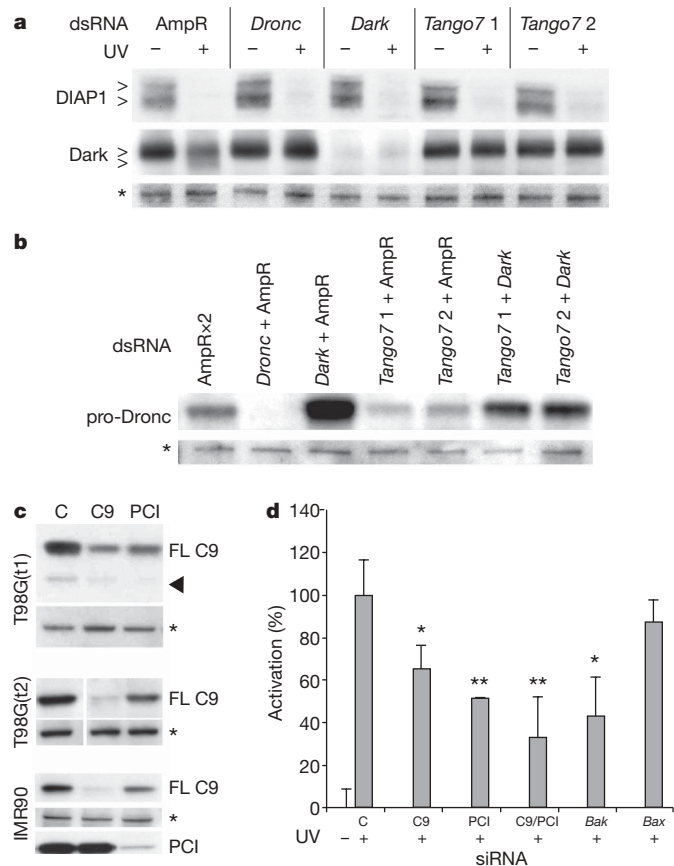


Figure 4 | *Tango7* and its human orthologue regulate apoptosomal caspases. **a**, S2R+ cells treated with indicated dsRNAs were analysed untreated (–) or after ultraviolet (UV) challenge (+). The same blot was probed with anti-Dark and anti-DIAP1 antibodies. Anti-DIAP1 detects full-length and modified forms (open arrowheads)²⁹. Anti-Dark detects full-length and cleaved Dark proteins (open arrowheads)⁷. The asterisk denotes a nonspecific, anti-DIAP1 band as a loading control. **b**, S2R+ cells treated with indicated dsRNAs were probed with anti-Dronc antibody. The asterisk denotes a nonspecific band as a loading control. In three independent experiments, compared to control (AmpR×2, see Methods), relative reductions in pro-Dronc band intensity for *Tango7* 1 + AmpR and *Tango7* 2 + AmpR were 63–86% and 53–85%, respectively. Compared to the *Dark* + AmpR-treated cells, relative reductions in band intensity for co-silencing *Tango7* 1 + *Dark* and *Tango7* 2 + *Dark* were 36–61% and 33–54%, respectively. **c**, Human T98G or IMR90E1A cells were treated with siRNAs targeting *PCID1* (PCI), *CASP9* (C9), or a non-target control (C). Pro-caspase 9 (FL C9), cleaved caspase 9 (arrowhead) and *PCID1* were detected. Asterisks denote nonspecific, loading-control bands. Two independent trials with the T98G line (T98G(t1) and T98G(t2)) are shown. **d**, IMR90E1A cells transfected with siRNAs targeting *PCID1*, *CASP9*, *Bak* or *Bax* were subsequently UV-challenged and assayed for DEVDase activity. C9/PCI samples received siRNAs targeting both *CASP9* and *PCID1*. Triplicate data were normalized against cells transfected with non-targeting control siRNAs (C) treated in parallel. Error bars show s.d. * $P < 0.05$, ** $P < 0.01$, Student's *t*-test (two-tailed). Three independent trials gave similar results. C9 or PCI siRNAs had negligible effects on basal DEVDase, because in the absence of UV challenge, DEVDase activity varied on average 2.3% (C9 siRNA) or 1.6% (PCI siRNA) relative to control.

apoptogenic responses. Like all RNAi screens, only rate-limiting targets were captured and *Drosophila* effectors not present in S2R+ cells were missed. Of note, *Dark*, *Dronc* and *Drice* dsRNAs were recovered among the top candidates, providing reassurance for the logistics of our platform. Targets recovered through our screen exposed previously unknown modalities that support apoptosis, but the extent to which most of these generalize beyond the original *Drosophila* culture system is not known. In principle, even the effector featured here, *Tango7*, might regulate caspase-dependent cell

death and *Dronc* only in S2R+ cells. However, this is quite unlikely for at least two reasons. First, when *Tango7* is silenced in the retina, the exact same cells that persist are those that are known to die via caspase-dependent, canonical pathways. Second, our *Drosophila* studies successfully predicted cross-species apoptogenic activity for the counterpart of *Tango7* in human cells of distinct origin.

Tango7 depletion uniquely illustrates how cell survival can be sustained (despite stimulus-dependent loss of DIAP1, Fig. 4a), exposing a new axis of regulation that bypasses a common apoptotic switch in flies and, instead, affects the apoptosome³. We found no evidence for a physical association between *Tango7* and *Dronc* protein (data not shown), and despite less severe effects on pro-*Dronc* levels, rescue by dsRNAs targeting *Tango7* were generally comparable to those targeting *Dronc*. Hence, *Tango7* could affect the post-translational processing or sub-cellular localization of pro-*Dronc*. Alternatively, *Tango7* could impact other apoptotic effectors, exerting effects beyond simply *Dronc* regulation. Consistent with these possibilities, *Tango7* was linked to Golgi activity²², but because genes needed for general Golgi functions were not recovered here, links between *Tango7* and *Dronc* evidently do not reflect compromised Golgi. Whatever the mechanism, this regulatory axis seems to be conserved because the human *Tango7* counterpart, *PCID1*, similarly regulated caspase 9 levels and DEVDase in human cells (Fig. 4c). In a recent study of pancreatic cancers²³, *PCID1* expression was repressed at least sixfold in all five patient tumours profiled. Furthermore, *PCID1* was also implicated as a determinant of herpes simplex virus susceptibility²⁴. It will be important to determine whether these possible links to human disease reflect apoptosis-related activity or, perhaps, non-apoptotic functions reported for caspase 9 (ref. 25).

METHODS SUMMARY

RNAi screen and validation. Eighteen-thousand cells in serum/antibiotic-free Schneider's media were seeded in each well containing 0.5 µg dsRNA (Ambion Silencer RNAi library or synthesized dsRNA), and incubated for 1 h before adding 100 µl serum-supplemented media. After 3 days, the media was replaced with Smac-mimetic-containing media. Cell viability was assayed 2 days later using CellTiter-Glo (Promega) in a plate reader (Envision multimode). Every assay plate included four control wells containing *Dronc* dsRNA. Of the 429 sample plates assayed in the screen, 76% (325 plates) had excellent assay quality ($Z \geq 0.5$) and only 2% were unacceptable ($Z < 0$). The Z-factor for each plate⁸ and plate mean-centred z-score for each well ($n = 92$ sample wells) were calculated. To correct for systematic bias/edge effects²⁶, the position mean-centred z-score for each well is calculated by its plate mean-centred z-score minus the position average, divided by the position standard deviation ($n = 143$ plates per triplicate). Genes with $z > 3.1$ ($P < 0.001$) from either plate mean or position mean-centred normalizations were considered together as primary candidates. For secondary screens and subsequent RNAi experiments, dsRNA synthesis and treatment were as described^{9,27} (Supplementary Table 3). In brief, cells were cultured for 72 h to deplete target gene product before analysis. Effector caspase (DEVDase) activity was measured using Caspase3/7-Glo (Promega) 6 h after apoptosis stimulation.

Full Methods and any associated references are available in the online version of the paper at www.nature.com/nature.

Received 8 October 2007; accepted 24 April 2009.

Published online 31 May 2009.

- Salvesen, G. S. & Abrams, J. M. Caspase activation—stepping on the gas or releasing the brakes? Lessons from humans and flies. *Oncogene* **23**, 2774–2784 (2004).
- Verhagen, A. M. & Vaux, D. L. Cell death regulation by the mammalian IAP antagonist Diablo/Smac. *Apoptosis* **7**, 163–166 (2002).
- Hay, B. A. & Guo, M. Caspase-dependent cell death in *Drosophila*. *Annu. Rev. Cell Dev. Biol.* **22**, 623–650 (2006).
- Li, L. *et al.* A small molecule Smac mimic potentiates TRAIL- and TNF α -mediated cell death. *Science* **305**, 1471–1474 (2004).
- Shi, Y. Caspase activation, inhibition, and reactivation: a mechanistic view. *Protein Sci.* **13**, 1979–1987 (2004).
- Chew, S. K. *et al.* The apical caspase *dronc* governs programmed and unprogrammed cell death in *Drosophila*. *Dev. Cell* **7**, 897–907 (2004).
- Akdemir, F. *et al.* Autophagy occurs upstream or parallel to the apoptosome during histolytic cell death. *Development* **133**, 1457–1465 (2006).
- Zhang, J. H., Chung, T. D. & Oldenburg, K. R. A simple statistical parameter for use in evaluation and validation of high throughput screening assays. *J. Biomol. Screen.* **4**, 67–73 (1999).
- Boutros, M. *et al.* Genome-wide RNAi analysis of growth and viability in *Drosophila* cells. *Science* **303**, 832–835 (2004).
- Kulkarni, M. M. *et al.* Evidence of off-target effects associated with long dsRNAs in *Drosophila melanogaster* cell-based assays. *Nature Methods* **3**, 833–838 (2006).
- Ma, Y., Creanga, A., Lum, L. & Beachy, P. A. Prevalence of off-target effects in *Drosophila* RNA interference screens. *Nature* **443**, 359 (2006).
- Zimmermann, K. C., Ricci, J. E., Droin, N. M. & Green, D. R. The role of ARK in stress-induced apoptosis in *Drosophila* cells. *J. Cell Biol.* **156**, 1077–1087 (2002).
- Xu, D. *et al.* The CARD-carrying caspase *Dronc* is essential for most, but not all, developmental cell death in *Drosophila*. *Development* **132**, 2125–2134 (2005).
- Muro, I. *et al.* The *Drosophila* caspase Ice is important for many apoptotic cell deaths and for spermatid individualization, a nonapoptotic process. *Development* **133**, 3305–3315 (2006).
- Link, N. *et al.* A collective form of cell death requires homeodomain interacting protein kinase. *J. Cell Biol.* **178**, 567–574 (2007).
- Rodriguez, A. *et al.* Dark is a *Drosophila* homologue of Apaf-1/CED-4 and functions in an evolutionarily conserved death pathway. *Nature Cell Biol.* **1**, 272–279 (1999).
- Muro, I., Hay, B. A. & Clem, R. J. The *Drosophila* DIAP1 protein is required to prevent accumulation of a continuously generated, processed form of the apical caspase DRONC. *J. Biol. Chem.* **277**, 49644–49650 (2002).
- Weinmann, L. *et al.* A novel p53 rescue compound induces p53-dependent growth arrest and sensitises glioma cells to Apo2L/TRAIL-induced apoptosis. *Cell Death Differ.* **15**, 718–729 (2008).
- Matapurkar, A. & Lazebnik, Y. Requirement of cytochrome c for apoptosis in human cells. *Cell Death Differ.* **13**, 2062–2067 (2006).
- Kroemer, G. & Martin, S. J. Caspase-independent cell death. *Nature Med.* **11**, 725–730 (2005).
- Colell, A. *et al.* GAPDH and autophagy preserve survival after apoptotic cytochrome c release in the absence of caspase activation. *Cell* **129**, 983–997 (2007).
- Bard, F. *et al.* Functional genomics reveals genes involved in protein secretion and Golgi organization. *Nature* **439**, 604–607 (2006).
- Jones, S. *et al.* Core signaling pathways in human pancreatic cancers revealed by global genomic analyses. *Science* **321**, 1801–1806 (2008).
- Perez, A. *et al.* A new class of receptor for herpes simplex virus has heptad repeat motifs that are common to membrane fusion proteins. *J. Virol.* **79**, 7419–7430 (2005).
- Murray, T. V. *et al.* A non-apoptotic role for caspase-9 in muscle differentiation. *J. Cell Sci.* **121**, 3786–3793 (2008).
- Malo, N. *et al.* Statistical practice in high-throughput screening data analysis. *Nature Biotechnol.* **24**, 167–175 (2006).
- Clemens, J. C. *et al.* Use of double-stranded RNA interference in *Drosophila* cell lines to dissect signal transduction pathways. *Proc. Natl Acad. Sci. USA* **97**, 6499–6503 (2000).
- Mendes, C. S. *et al.* Cytochrome c-d regulates developmental apoptosis in the *Drosophila* retina. *EMBO Rep.* **7**, 933–939 (2006).
- Ditzel, M. *et al.* Degradation of DIAP1 by the N-end rule pathway is essential for regulating apoptosis. *Nature Cell Biol.* **5**, 467–473 (2003).

Supplementary Information is linked to the online version of the paper at www.nature.com/nature.

Acknowledgements We thank X. Tu, L. Durham, L. Lum, P. Beachy, M. Roth, X. Wang, P. Harran, Y. Lazebnik, D. Dorris, the University of Texas Southwestern Medical Center (UTSW) High Throughput Screening laboratory and the Live Cell Imaging facility for technical and material support; Bloomington Stock Center, K. Basler, National Institute of Genetics (NIG) stock center (Japan) for fly lines; K. White, B. Hay and the Hybridoma Bank for antibodies; V. Malhotra for the pMT-Tango7 plasmid; J. Seeman and the Wang laboratory for discussions; and M. Allen for administrative support. This work was supported by grants from the National Institute of General Medical Sciences, the National Institute on Alcohol Abuse and Alcoholism and the UTSW High Impact/High Risk Grant Program. N.L. is supported by a National Research Service Award.

Author Contributions S.K.C., N.L., P.C., K.A.G. and K.P. planned and performed experiments and analysed results. All authors discussed results. J.M.A. planned experiments, analysed results and wrote the paper together with S.K.C., aided by contributions from N.L. and P.C.

Author Information Reprints and permissions information is available at www.nature.com/reprints. Correspondence and requests for materials should be addressed to J.M.A. (john.abrams@utsouthwestern.edu).

METHODS

Fly stocks. *Tango7R1* denotes the GAL4-responsive RNAi line targeting *CG8309* with a genotype *w; P{UAS-8309R-1}/2* on the second chromosome (NIG). This transgene was mobilized by standard methods and an insertion, designated *Tango7R3*, was recovered on the third chromosome. *3523R2* denotes the GAL4-responsive *CG3523* RNAi line *w; P{UAS-3523R-2}/3* (stock ID 3523R-2, NIG). *5887R1* denotes the GAL4-responsive *CG5887* RNAi line *w; P{UAS-5887R-1}* (stock ID 5887R-1, NIG). For pupal eye analyses, genotypes for *Tango7* are *UAS-dicer2/+; gmr-GAL4/UAS-Tango7R1*, or *UAS-dicer2/+; gmr-GAL4/+; UAS-Tango7R3/+*; or as control, *UAS-dicer2/+; gmr-GAL4/UAS-5887R1*. The three independent wing-specific *vestigial*-GAL4 driver lines, *vg-GAL4#1* denotes *y¹ w¹¹¹⁸; P{w⁺mC = vgM-GAL4.Exel}/3* (stock ID 8223, Bloomington), *vg-GAL4#2* denotes *P{w⁺mC = vgMQ-GAL4.Exel}/1*, *y¹ w¹¹¹⁸* (stock ID 8231, Bloomington) and *vg-GAL4#3* denotes *y w hsp70-flp; P{mini w⁺, GAL4}vgBE P{mini w⁺, UAS-flp}*; *P{y⁺, hsp70-cd2} P{mini w⁺, FRT}/79 P{ry⁺, hsp70-neo, FRT}/82 P{mini w⁺, hsp70-HA-gfp, smo⁺}*.

Cell culture, ultraviolet challenge and western analyses. S2R+ cells were cultured in Schneider's media with 10% FBS, 25 U ml⁻¹ penicillin, 25 µg ml⁻¹ streptomycin at 25 °C (all cell culture reagents from Invitrogen, except FBS from Atlas Biologicals). Unless otherwise indicated, media in all procedures refer to the above. T98G and IMR90E1A cells were cultured in DMEM supplemented with 10% FBS. For western analysis, samples were lysed in buffer A with 1% Triton X-100. Blots were probed with 1:1,000 anti-DIAP1 (gift from K. White), 1:1,000 anti-Dronc (gift from B. Hay), 1:1,000 anti-Dark², 1:5,000 anti-tubulin (E7, Developmental Studies Hybridoma Bank). *Drosophila* cells treated with two dsRNAs were exposed to 15 µg ml⁻¹ of each indicated dsRNA, for a total dsRNA concentration of 30 µg ml⁻¹. AmpR×2 denotes cells exposed to 30 µg ml⁻¹ of control AmpR dsRNA. Cells were analysed either untreated or 6 h after ultraviolet challenge (90 mJ cm⁻²). Relative changes in band intensity were obtained by comparing integrated densitometric values. Human cells were collected 5 days after siRNA transfection, and 10 µg total protein was separated by 10% SDS-PAGE. Caspase 9 and PCID1 levels were analysed using anti-caspase 9 (Cell Signaling) and anti-PCID1 (Proteintech Group, Inc.) antibodies.

Smac-mimetic binding. Cells were lysed in 20 mM HEPES-potassium hydroxide, pH 7.5, 10 mM KCl, 1.5 mM MgCl₂, 1 mM sodium EDTA, 1 mM sodium EGTA, 1 mM dithiothreitol (buffer A), 1% Triton X-100 buffer with protease inhibitors (Roche). Biotinylated-Smac-mimetic or biotin alone was incubated with avidin-conjugated beads and 10 mg ml⁻¹ BSA in PBS for 4 h at 4 °C. The beads were then incubated with precleared lysate (~1–2 mg protein) overnight before analysis.

Primary and secondary RNAi screen. The primary screen was optimized for S2R+ cells and conducted using a 'direct soaking' protocol, together with the Silencer *Drosophila* RNAi library (Ambion/Applied Biosystems) targeting 13,071 genes from *Drosophila* genome build 3. Sequences for all dsRNAs in the library are available in Supplementary Table 4. The RNAi library or synthesized dsRNAs were plated in 96-well microplates (Corning) using Beckman FX liquid handlers. Every assay plate included four control wells containing *Dronc* dsRNA. Each well

contained 0.5 µg dsRNA in 20 µl of SF900 media. Eighteen-thousand cells in 30 µl serum/antibiotic-free Schneider's media were seeded into each well and incubated for 1 h before adding 100 µl media. After 3 days, the media was replaced with 80 µl 2.5 µM Smac-mimetic media. Cell viability was assayed 2 days later using CellTiter-Glo (Promega) in a plate reader (Envision multi-mode). The plate mean-centred z-score for each well is its luminescence value minus the plate average, divided by the plate standard deviation (*n* = 92 sample wells). The Z-factor for each plate was calculated as described⁸. Low quality (*Z* < 0) plates were excluded from subsequent secondary retests and analyses. To correct for systematic bias/edge effects²⁶, the position mean-centred z-score for each well is calculated by its plate mean-centred z-score minus the position average, divided by the position standard deviation (*n* = 143 plates per triplicate). Average position mean-centred z-score for each amplicon is calculated from the individual position mean-centred z-scores of the triplicates. Genes with *z* > 3.1 from either plate mean or position mean-centred normalizations were considered together as primary candidates. For secondary screens and subsequent RNAi experiments, dsRNA synthesis and treatment was as described^{9,27} (Supplementary Table 3). Cells were cultured for 72 h to deplete target gene product before analysis. Effector caspase (DEVDase) activity was measured using Caspase3/7-Glo (Promega) 6 h after apoptosis stimulation according to manufacturer's instructions.

Time-lapse microscopy. Cells pretreated with dsRNAs were tracked by time-lapse microscopy for 22 h after ultraviolet exposure (90 mJ cm⁻² UVC). Photomicrographs were captured at 6-min intervals on a Zeiss Axiovert 200M inverted microscope equipped with a Marzhauser programmable stage, a Nikon DXM1200F camera and controlled by Metamorph software (Molecular Devices). Movie images were assembled and analysed using ImageJ (NIH). At least 100 cells were tracked in each treatment. Dead cells are scored by morphology of rounding up, blebbing or fragmentation into corpses.

Pupal eye analyses. White prepupae were isolated at 0 h and aged 46–48 h at 25 °C. To outline cell borders, pupal eyes were dissected and stained with mouse anti-DiscsLarge (Developmental Studies Hybridoma Bank, 1:1,000) and anti-mouse Fluorecein (Vector Laboratories, 1:250) as described previously^{6,15}. Interommatidial cell counts were modified from ref. 30. Hexagonal units connecting six 'ommatidia centres' that completely surround one ommatidium were counted. Secondary or tertiary pigment cells inside or partly inside hexagonal assemblies were counted as a single cell.

siRNA transfection. siRNAs to *CASP9* and *PCID1* were ON-TARGETplus SMARTpool siRNA, and the control siRNA used was ON-TARGETplus Non-targeting pool (Dharmacon). T98G and IMR90E1A cells were transfected with 64 nM siRNAs targeting the genes indicated using Dharmafect Duo (Dharmacon) and Optimem according to manufacturer's instructions. Pools contain four siRNAs for each indicated gene. After 5 days, transfected cells were challenged with ultraviolet light (100 mJ cm⁻²). Effector caspase (DEVDase) activity was measured using Caspase3/7-Glo (Promega) 18 h after ultraviolet stimulation.

LETTERS

The pluripotency factor Oct4 interacts with Ctcf and also controls X-chromosome pairing and counting

Mary E. Donohoe^{1,2,3,*†}, Susana S. Silva^{1,2,3,*}, Stefan F. Pinter^{1,2,3}, Na Xu^{1,2,3} & Jeannie T. Lee^{1,2,3,4}

Pluripotency of embryonic stem (ES) cells is controlled by defined transcription factors^{1,2}. During differentiation, mouse ES cells undergo global epigenetic reprogramming, as exemplified by X-chromosome inactivation (XCI) in which one female X chromosome is silenced to achieve gene dosage parity between the sexes^{3–5}. Somatic XCI is regulated by homologous X-chromosome pairing^{6,7} and counting^{8–10}, and by the random choice of future active and inactive X chromosomes. XCI and cell differentiation are tightly coupled¹¹, as blocking one process compromises the other^{8,12} and dedifferentiation of somatic cells to induced pluripotent stem cells is accompanied by X chromosome reactivation². Recent evidence suggests coupling of *Xist* expression to pluripotency factors occurs¹³, but how the two are interconnected remains unknown. Here we show that Oct4 (also known as Pou5f1)¹⁴ lies at the top of the XCI hierarchy, and regulates XCI by triggering X-chromosome pairing and counting. Oct4 directly binds *Tsix* and *Xite*, two regulatory noncoding RNA genes of the X-inactivation centre^{15,16}, and also complexes with XCI trans-factors, Ctcf and Yy1 (ref. 17), through protein–protein interactions. Depletion of Oct4 blocks homologous X-chromosome pairing and results in the inactivation of both X chromosomes in female cells. Thus, we have identified the first trans-factor that regulates counting, and ascribed new functions to Oct4 during X-chromosome reprogramming.

XCI has been reliably modelled in female mouse ES cells, which carry two active X chromosomes but will inactivate one when induced to differentiate into embryoid bodies *ex vivo*. Given the tight linkage between XCI and differentiation^{2,8,11,12}, XCI must in principle be regulated by factors that control pluripotency. Using bioinformatic analysis, here we have surveyed the X chromosome inactivation centre (*Xic*) for pluripotency factor binding sites, and found one Sox2 and two Oct4 motifs in a 15-kilobase (kb) region of *Tsix* and *Xite*^{6,8,9} that contains two enhancers for *Tsix*, the antisense repressor of *Xist*¹⁸ (Fig. 1a, b). One Oct4 site occurs within the bipartite enhancer, adjacent to the Ctcf–Yy1 binding motif ('site E'), ~1.0 kb downstream of Ctcf–Yy1 ('site D')^{17,19}. Within *Xite*, a composite Oct4–Sox2 site resides within DNaseI hypersensitive sites of the 1.2-kb enhancer^{16,18}.

In electrophoretic mobility shift assays (EMSA) using purified recombinant Oct4 protein (rOct4) and ³²P-labelled *Tsix* and *Xite* oligonucleotide probes, we observed specific protein–DNA complexes that were supershifted by anti-Oct4 antibodies (Fig. 1c–e). The interactions were competed away by excess cold oligonucleotides, and were not detected when mutated probes were used. In contrast, recombinant Sox2 protein (rSox2) did not bind *Tsix* (data not shown) but specifically bound *Xite* (Fig. 1c, e). Mixing rSox2 and rOct4 together with *Xite* resulted in a further mobility shift, suggesting that the pluripotency factors co-occupied the *Xite* motif. The Sox2–*Xite*

complex was supershifted by anti-Sox2 antibodies, competed away by excess cold oligonucleotides, and abolished by *Xite* mutation. These results indicated that Oct4 and Sox2 specifically bind *Tsix* and *Xite* *in vitro*.

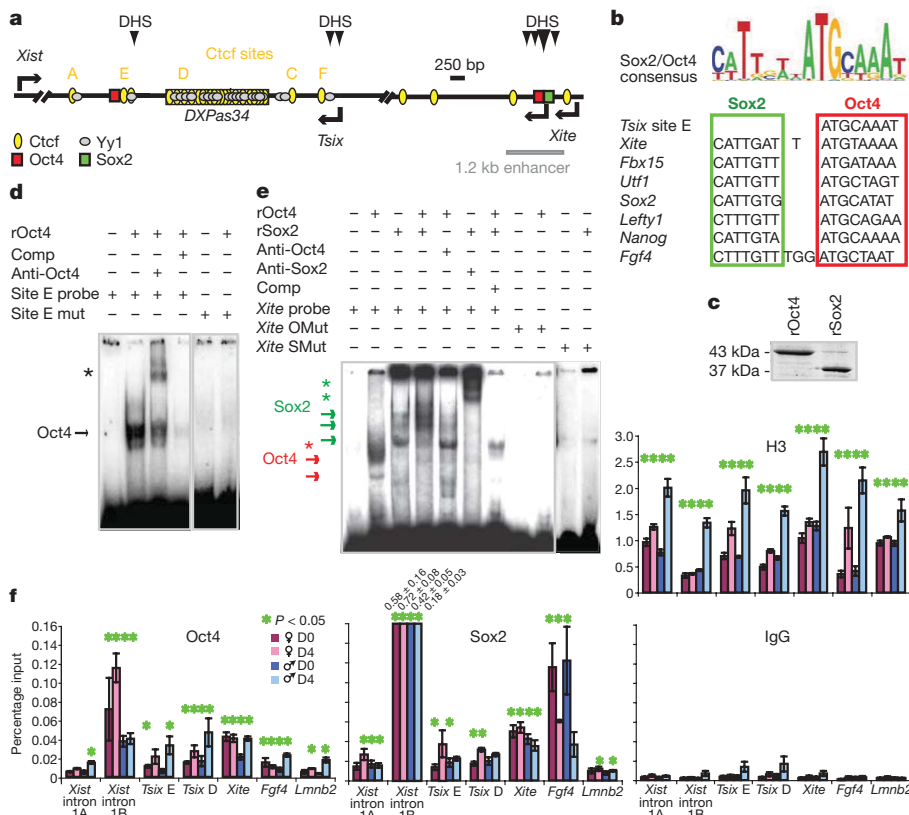
To investigate *in vivo* binding, we performed quantitative chromatin immunoprecipitation (ChIP) and observed binding at sites predicted by bioinformatic analysis and verified by EMSA (Fig. 1f). In male and female ES cells, both Oct4 and Sox2 bound *Tsix* and *Xite* chromatin above background (IgG control ChIP). Because EMSA did not show direct binding of Sox2 to *Tsix*, the Sox2–*Tsix* complex may occur indirectly by known looping interactions between *Tsix* and *Xite*²⁰. Although *Xist* intron 1B (ref. 13) showed the greatest pull-down by Oct4 and Sox2, ChIP levels at *Tsix* and *Xite* were comparable to that for the positive control *Fgf4*. Binding to the unrelated *Lmn2* locus was low, as was binding to a control region ~600 base pairs (bp) upstream of intron 1B (intron 1A). These data demonstrated that *Xite* strongly binds Oct4 and Sox2, and that *Tsix* binds Oct4 *in vivo*.

Notably, Oct4 and Sox2 sites occur near previously defined sites for Ctcf^{9,21,22} and Yy1 (refs 17, 23, 24) (Fig. 1a). Ctcf regulates X-chromosome pairing²⁵ and, together with Yy1, controls XCI choice by transactivating *Tsix*¹⁷. Given the proximity of Oct4 and Sox2 to Ctcf–Yy1 sites, we carried out glutathione S-transferase (GST) pull-down experiments to determine whether the factors interact. ³⁵S-labelled Oct4 bound GST-fused Ctcf but not Yy1 (Fig. 2a). To map binding domains, we tested Ctcf–GST fusions for binding to ³⁵S-labelled Oct4, and observed interaction through the zinc-finger region of Ctcf (amino acids 284–583). To map Oct4 domains, we co-transfected Flag–Oct4 fusions with full-length Ctcf, co-immunoprecipitated with anti-Flag antibodies, and observed interaction through the amino terminus of Oct4 (Fig. 2b). Reciprocal native co-immunoprecipitations in ES cells confirmed endogenous Ctcf–Oct4 interactions (Fig. 2c). We concluded that Oct4 and Ctcf interact *in vitro* and *in vivo*.

Next, we tested whether Sox2 directly interacts with Ctcf or Yy1. In GST pull-down assays, ³⁵S-labelled Yy1 bound GST–Sox2 but not GST–Oct4 (Fig. 2d). Reciprocally, ³⁵S-labelled Sox2 bound full-length GST–Yy1 (Fig. 2e). Domain mapping showed that this interaction occurred through the zinc-finger of Yy1 (amino acids 313–414) and the HDAC domain (amino acids 170–200). These data showed that Yy1 directly binds Sox2, whereas Oct4 directly binds Ctcf. Given that Yy1 interacts with Ctcf¹⁷ and Ctcf interacts with Oct4, we asked whether Yy1 could indirectly interact with Oct4 by overexpressing tagged proteins in HEK cells. When Flag-tagged Oct4 was co-transfected with haemagglutinin (HA)-tagged Yy1 alone, Flag–Oct4 did not efficiently co-immunoprecipitate Yy1; however, when Flag–Oct4 and HA–Yy1 were co-transfected with Myc-tagged Ctcf, Flag–Oct4 readily co-immunoprecipitated Yy1 (Fig. 2f;

¹Howard Hughes Medical Institute, ²Department of Molecular Biology, Massachusetts General Hospital, ³Department of Genetics, Harvard Medical School, ⁴Department of Pathology, Massachusetts General Hospital, Boston, Massachusetts 02114, USA. [†]Present address: Burke Medical Research Institute, Weill Cornell Medical College, White Plains, New York 10605, USA.

*These authors contributed equally to this work.



endogenous proteins were probably expressed at insufficient levels for detection). These results indicate that Oct4 forms a multifactor complex *in vivo* and interacts with Yy1 through Ctf. The complex may also include Sox2, as it interacts with Oct4 and Yy1.

Because of the transcriptional roles of Ctf and Yy1 at *Tsix*¹⁷ and the unique temporal expression pattern of *Tsix*¹⁵, the Oct4–Sox2 sites may also transactivate *Tsix* and regulate XCI through their intrinsic developmental specificity. Indeed, Oct4 and Sox2 were downregulated contemporaneously with *Xite* and *Tsix*, correlating with the upregulation of *Xist* (Supplementary Fig. 1). Luciferase reporter assays showed that whereas the 1.2-kb enhancer stimulated *Tsix* promoter activity almost fourfold in ES cells, mutating the Oct4 and Sox2 motifs abolished stimulation (Fig. 2g), supporting the role of Oct4 and Sox2 in *Tsix* transactivation. Consistent with this, short interfering (siRNA) knockdown of *Oct4* markedly reduced *Tsix* and *Xite* RNA levels in female ES cells (Fig. 2h). In contrast, knocking down *Ctcf* did not compromise expression, and knocking down *Sox2* slightly increased RNA levels in this context (Sox2 may have a less crucial role than Oct4). Thus, Oct4 is required to transactivate *Tsix* *in vivo*. Previous genetic analysis suggested that the *Xite* enhancer is active in day 0 cells, but acts principally during differentiation to maintain *Tsix* expression on one X chromosome and thereby ensure selection of only one active X chromosome¹⁶. In support of this, stimulation of the *Tsix*–reporter fusion is enhanced \sim threefold from day 2 to 6, the timeframe during which choice takes place (Fig. 2i). We propose that Oct4 transactivates *Tsix/Xite*, and that its binding directly controls the developmental timing of XCI.

We next asked what mechanistic aspects of XCI might be regulated by Oct4. Given that X-chromosome pairing is one of the earliest events of XCI^{6,7}, and that Oct4 sites occur within the *Tsix/Xite* pairing region^{6,25}, we investigated whether Oct4 controlled pairing. We knocked down *Oct4* by siRNA nucleofection of day 2 female ES cells, collected embryoid bodies on day 4, confirmed protein depletion (Fig. 3a), verified initiation of differentiation (Supplementary Fig. 2), and measured normalized distances (ND) between the two *Xic* genes (Fig. 3b, c). In control day 4 cells, \sim 22% of nuclei showed inter-*Xic*

distances of <0.1 normalized distances ($<1.0 \mu\text{m}$ approximately). Oct4-knockdown cells showed a significant reduction in such interactions, as 7% of nuclei demonstrated normalized distance <0.1 (Fig. 3c, d). The extent of reduction was similar to that observed in *Ctcf* knockdowns, a protein known to be required for pairing²⁵. In contrast, knocking down Sox2 had no obvious effect on pairing—supporting the idea that, whereas Sox2 binds *Xite* and can transactivate *Tsix*, it may be functionally redundant with Oct4 and have a lesser role during XCI. We concluded that Oct4 is essential for X–X chromosome pairing.

Because pairing has been proposed to regulate counting and choice^{6,7}, we next addressed whether Oct4 impacts these processes. In male cells, knocking down Oct4, Sox2, and *Ctcf* had no obvious effect on *Xist* expression during differentiation into embryoid bodies (Fig. 4a, b). This result differs from a recent study reporting ectopic *Xist* expression when a tetracycline-controlled, overexpressed *Oct4* transgene is downregulated in male ES cells¹³. The difference might be attributed to experimental variation, such as the use of different cell lines, methods of Oct4 repression, and methods of ES differentiation. Intriguingly, however, we observed an aberrant number of *Xist* RNA foci in female embryoid bodies when Oct4 was knocked down (Fig. 4c). Not only did Oct4-deficient cells show a higher frequency of *Xist* upregulation, but \sim 20% of *Xist*⁺ nuclei showed biallelic expression (Fig. 4c, d). Biallelic expression was not observed in the control, *Ctcf*-knockdown, or Sox2-knockdown cells (Fig. 4c, d and data not shown). We excluded aneuploidy as a cause of the two *Xist* foci, as DNA fluorescence *in situ* hybridization (FISH), carried out on the same nuclei, demonstrated two *Xic* and two chromosome 1 DNA signals and thereby confirmed two X chromosomes in a diploid background (Fig. 4c).

Real-time quantitative reverse transcription PCR (qRT–PCR) corroborated increased *Xist* expression in Oct4-knockdown cells (Fig. 4e). In the wild-type 16.7 line, XCI is normally skewed towards inactivating the 129 allele instead of the *Mus musculus castaneus* X chromosome (evidenced by an 80:20 *Xist* RNA ratio) due to the ‘*Xce* modifier effect’²⁶. We reasoned that if there was increased biallelic *Xist* expression, we should observe increased expression from

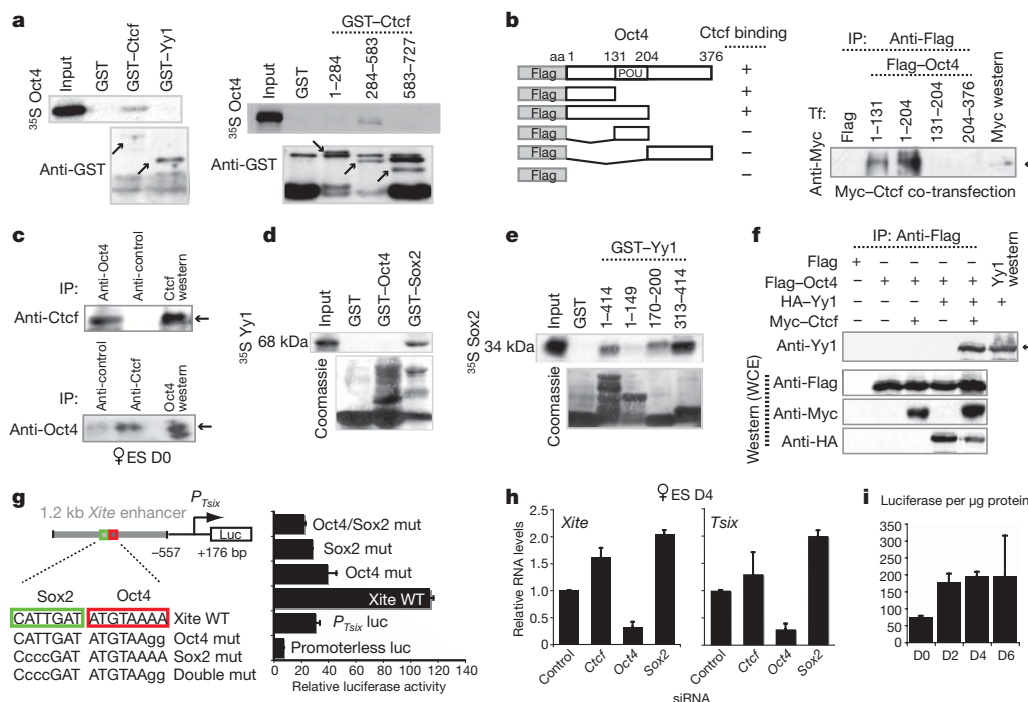


Figure 2 | Oct4-Ctcf and Sox2-Yy1 interactions, and *Tsix* transcriptional activation. **a**, Testing mammalian GST fusions of full-length Yy1 and Ctcf or Ctcf domains (amino acids indicated) for interaction with ³⁵S-labelled Oct4. Bottom panels, anti-GST western control. Arrows denote specific protein fusions. **b**, HEK cells were cotransfected with Myc-Ctcf and indicated Flag-tagged Oct4 fragments. Whole cell extracts (WCE) were immunoprecipitated (IP) with anti-Flag antibodies before western blotting with anti-Myc antibodies. The arrow denotes Ctcf protein. aa, amino acids; Tf, transfectant. **c**, Reciprocal co-immunoprecipitation to **b**. Top, immunoprecipitation with anti-Oct4 or control antibodies to test interaction with endogenous Ctcf. Arrow marks Ctcf detected by anti-Ctcf western analysis. Bottom, immunoprecipitation with anti-Ctcf or control antibodies to test interaction with endogenous Oct4. Arrow marks Oct4 detected by anti-Oct4 western. Doublet bands and mobility differences may reflect isoforms due to post-translational modifications. D0, day 0. **d**, Yy1 (³⁵S-labelled) binding to Sox2 but not Oct4 revealed by GST-fusion analysis. Bottom, Coomassie staining to reveal GST-fusion proteins. **e**, Domain

mapping of Yy1 binding to Sox2. Mobility differences may reflect post-translational modifications. **f**, Overexpression and co-immunoprecipitation of Flag-Oct4, Myc-Ctcf and HA-Yy1 in indicated combinations in HEK cells. Two 6-well plates of HEK cells were transfected with 8 µg of tagged constructs and collected 35 h later for co-immunoprecipitation analysis. Western blots of the co-immunoprecipitation (top panel) and whole cell extracts (bottom three panels) were performed using indicated antibodies. **g**, Oct4 and Sox2 confer developmental specificity to the *Xite* enhancer. Map of luciferase (luc) expression vector fused to the *Tsix* major promoter (*P_{Tsix}*) and the 1.2-kb enhancer. Mutations (mut; denoted by lower-case letters) of the Oct4/Sox2 motifs in the enhancer compromised *P_{Tsix}* activity in transiently transfected male day 0 ES cells. Error bars, s.d. **h**, qRT-PCR for *Xite* and *Tsix* RNA after knocking down the indicated factors. Levels are normalized to β-actin levels. Error bars, s.d. **i**, Luciferase analysis of cells carrying the wild-type enhancer shows enhanced *P_{Tsix}* activity after differentiation. Cells were differentiated in duplicate and luciferase levels were normalized to total protein levels.

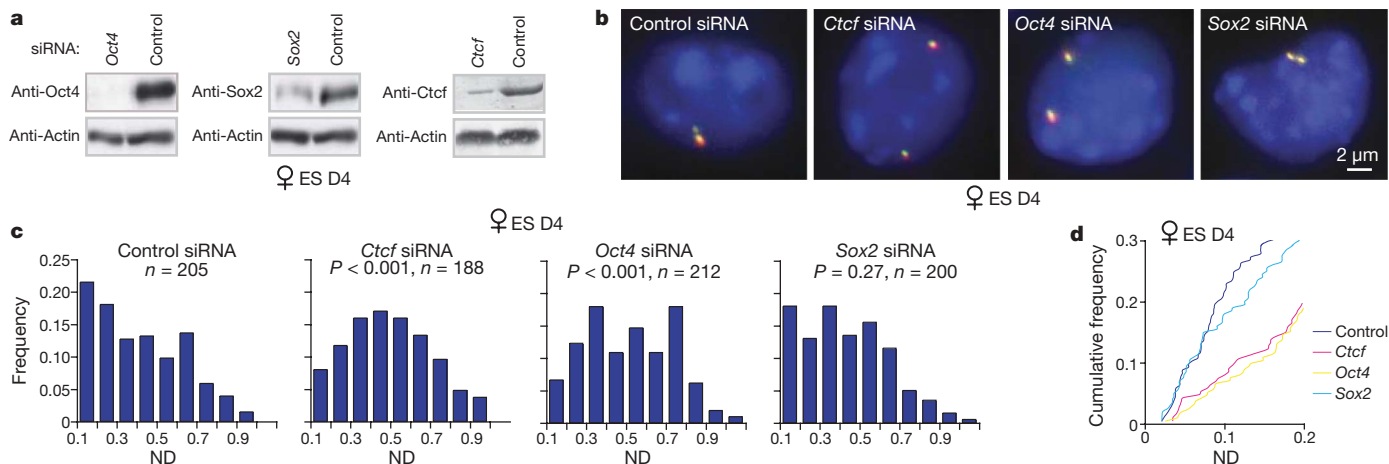


Figure 3 | Oct4 knockdown disrupts X-X pairing and results in aberrant *Xist* expression in female ES cells. **a**, Western analysis confirms knockdown of indicated proteins in wild-type female ES cells nucleofected with siRNAs on day 2 and collected on day 4 (D4). **b**, Representative images of *Xic*-*Xic* localization in knockdown cells using a two-probe combination of pSxn (*Tsix*, green) and pSx9 (*Xist*, red). To ensure signal specificity, only those foci with overlapping red and green signals are scored. **c**, Distribution of X-X

chromosome distances in knockdown cells as indicated. *n*, nuclei counted. ND denotes *Xic*-*Xic* distance (*d*), in which $d = 2 \times (\text{nuclear area}/\pi)^{0.5}$. The significant differences between samples and control siRNA were calculated using the Kolmogorov-Smirnov test—a non-parametric test to determine whether two data sets have a similar distribution (SPSS 13.0 software). **d**, Cumulative frequency curves of the analysis carried out in **c**. ND 0.0–0.2 are shown.

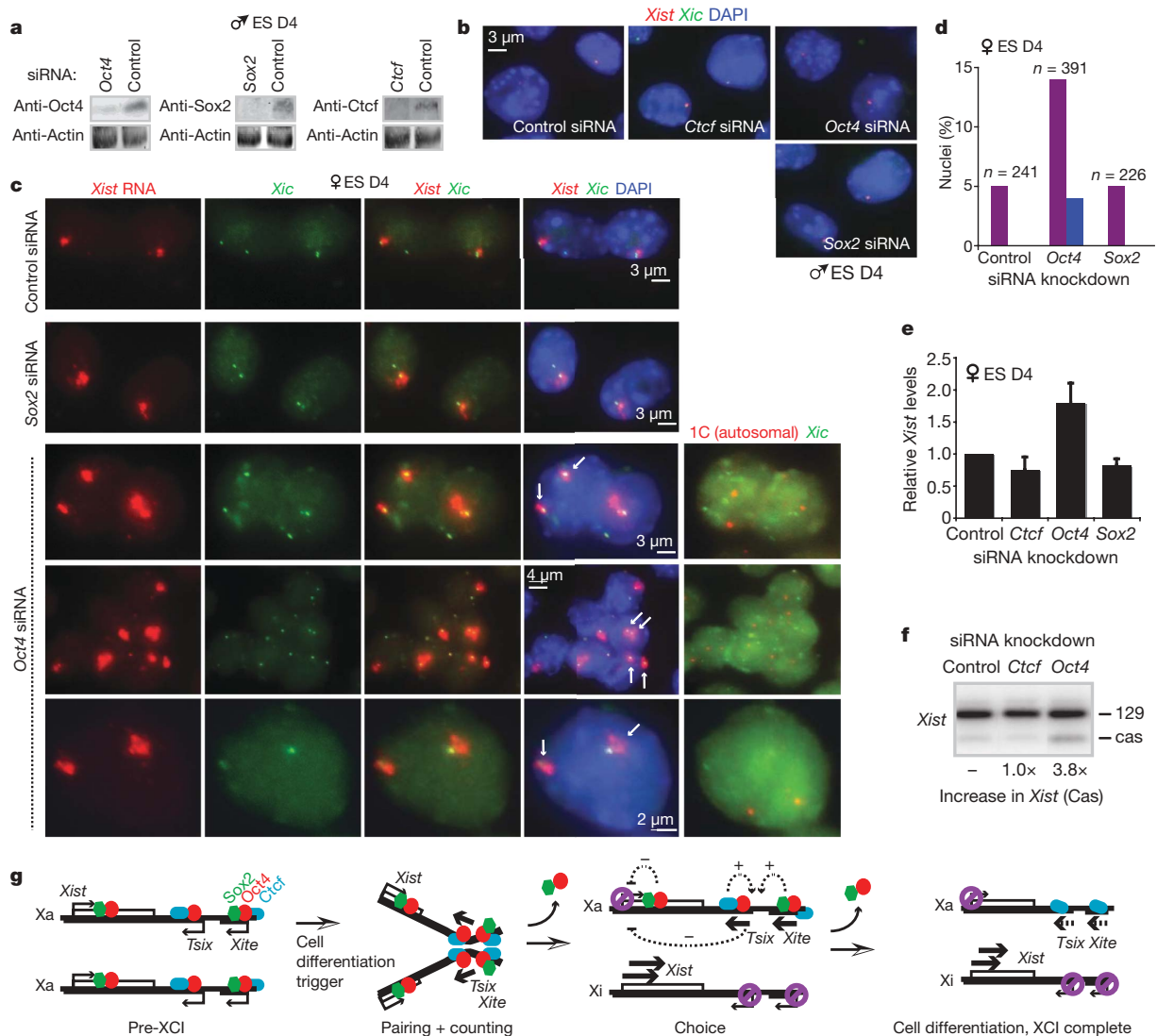


Figure 4 | Ectopic *Xist* expression from both X chromosomes in Oct4-deficient ES cells. **a**, Western analysis confirms knockdown of indicated proteins in wild-type male ES cells nucleofected on day 2 and collected on day 4 (D4). **b**, RNA/DNA FISH analysis for *Xist* RNA (red) and *Xic* DNA (green) after indicated knockdowns in day 4 male ES cells. **c**, RNA/DNA FISH shows ectopic *Xist* upregulation in Oct4 but not Sox2 or control female knockdown cells on day 4. Three representative fields of Oct4-deficient cells are shown. *Xist* RNA, red; *Xic* DNA (pSxn probe), green. After RNA/DNA FISH for *Xist/Xic*, cells were hybridized with a chromosome 1 (1C, red) and a

Xic (green) probe, showing that each nucleus with two *Xist* clusters is diploid. Note that original *Xist* RNA signals were destroyed in second-round FISH. White arrows show double *Xist* expression. **d**, The percentage of cells with one (purple) versus two (blue) *Xist* RNA clusters on day 4. **e**, Quantitative RT-PCR of *Xist* RNA in day 4 female knockdown cells. **f**, Allele-specific RT-PCR of *Xist* in day 4 female knockdown cells. 129, *M. musculus* and Cas, *M. m. castaneus* alleles. **g**, Model of dynamic and multifaceted regulation of XCI by Oct4. Xa, active X chromosome; Xi, inactive X chromosome; +, activating; -, repressive. See text for detailed discussion.

the *M. m. castaneus* allele. Allele-specific RT-PCR showed that expression of the *M. m. castaneus* allele was increased fourfold relative to the 129 allele (Fig. 4f). (Both alleles showed increased expression, but because of the *Xce* effect, the 129 allele maintained greater expression even as the *M. m. castaneus* allele proportionally increased.) Thus, RNA FISH and RT-PCR demonstrated that *Xist* becomes biallelically expressed in a fraction of female cells when Oct4 is deficient. This anomaly suggested a defect in counting that is consistent with the fact that the tightly linked process of pairing is also aberrant (Fig. 3).

To exclude the possibility that loss of pairing and ectopic *Xist* expression on day 4 could be due to accelerated differentiation in Oct4-depleted cells, we performed nucleofection on day 0 female cells and analysed pairing on day 1. Neither precocious pairing (Supplementary Fig. 3a–c) nor premature *Xist* activation (Supplementary Fig. 3d, e) was seen. On day 1, female cells normally would not have initiated XCI, but ~4% of Oct4-knockdown cells and ~1% of Sox2-knockdown cells showed weak *Xist* upregulation (Supplementary Fig. 3d, e). However, the *Xist* RNA clusters were generally

sparse and diffuse (Supplementary Fig. 3e, arrow) and distinctly different from *Xist* clusters of wild-type and Oct4-knockdown cells on day 4. Therefore, the loss of pairing and the aberrant counting were not due to precocious differentiation caused by Oct4 depletion. We concluded that Oct4 not only transactivates *Tsix/Xite* but also regulates X-chromosome pairing and counting. Notably, Oct4 is the first trans-factor identified for counting.

We have ascribed new functions to Oct4 and propose that Oct4 links cell differentiation to X-chromosome programming by controlling pairing and counting. Our data agree with a recent study proposing Oct4 as a regulator of XCI¹³. This study hypothesized that Oct4 binds *Xist* intron 1 and directly represses *Xist*. In contrast, our data indicate that Oct4 binds and directly activates *Xite/Tsix*, which would in turn repress *Xist*. Direct effects on *Xite/Tsix* are supported by EMSA and transcription assays (Figs 1 and 2), but concurrent *Tsix* down-regulation and *Xist* upregulation in Oct4-knockdown cells (Supplementary Fig. 4) are consistent with both models. Taken together, the two studies suggest that Oct4 may both activate *Xite/Tsix* and

repress *Xist* in parallel. Our model (Fig. 4g) proposes that, in pre-XCI cells, Oct4 binds the 5' ends of *Xite* and *Tsix* to transactivate the antisense transcript and thereby inhibit *Xist*. At the same time, Oct4 binds internal sites within *Xist* (and *Tsix*, as *Xist* and *Tsix* overlap), repressing *Xist* either directly or through *Tsix*. When cell differentiation is initially triggered, Oct4, together with Ctf, promotes X–X chromosome pairing through *Tsix/Xite* and ensures correct counting and mutually exclusive choice of the active and inactive X chromosome. On the future inactive X chromosome, Oct4 binding would be lost as Oct4 levels decrease, *Tsix* is downregulated, and *Xist* is induced; on the future active X chromosome, residual Oct4 would enable its transient persistence on *Tsix*, maintenance of *Tsix* expression, and inhibition of *Xist* in cis. Thus, the intrinsic developmental specificity of Oct4—active in pluripotent cells and downregulated in differentiating cells—controls the timing of XCI by triggering pairing and counting. By molecularly linking XCI to differentiation through Oct4–*Tsix/Xite* interactions, our study reveals a complex network involved in epigenetic reprogramming of the X chromosome in stem cells.

METHODS SUMMARY

Cell lines. The 16.7 female and J1 male ES lines, fibroblasts, and culture conditions have been described¹⁵.

EMSA. EMSA were performed¹⁷ using rOct4 and rSox2 made from full-length mouse complementary DNAs cloned into pET-47 (Novagen), expressed in bacteria, purified using a nickel column, and desalted using a PD-10 column (GE Healthcare). See full-length Methods for nucleotide sequences. Supershifts were carried out with anti-Oct4 and anti-Sox2 antibodies (H134 and 17320, respectively; Santa Cruz).

GST pull-downs and co-immunoprecipitations. Bacterial and mammalian GST fusions are described in the full Methods. Two micrograms of DNA was transfected into HEK 293A cells (Lipofectamine 2000, Invitrogen), cells were collected at 46–48 h for GST pull-down assays as described¹⁷. See full Methods and figure legends for co-immunoprecipitation details.

Chromatin immunoprecipitations. ChIP analyses were carried out as described²⁷ and the results were averaged for three independent biological replicates. ChIP antibodies included anti-Oct4 (8628, Santa Cruz), anti-Sox2 (17320, Santa Cruz), normal goat IgG (2028, Santa Cruz), and anti-H3 (1791, Abcam). Quantitative PCR was performed using an iCycler iQ real-time PCR detection system (Bio-Rad) by amplifying with primer pairs listed in the full-length Methods.

Luciferase assays. NS11 (no promoter:luciferase), NS65 (–557/+176 *Tsix* promoter:luciferase), and NS135 (1.2-kb *Xite* enhancer plus –557/+176 *Tsix* promoter:luciferase) have been described¹⁸. Mutant vectors were constructed by PCR mutagenesis of NS135 to yield: mutated *Oct4* XiteL, 5'–CCAGGTCTGCA TTGATATGTAAGGTAAGCACTTCTGTC–3'; and mutated *Sox2* XiteL, 5'–CC AGGTCTGCCCGATATGTAAGTAAGCACTTCTGTC–3'; and doubly mutated *Oct4* and *Sox2*, 5'–CCAGGTCTGCCCGATATGTAAGGTAAGCACTTCTGTC–3'. Mutated nucleotides are underlined. Thirty micrograms of linearized construct was electroporated into male and female ES cells, and G418-resistant colonies were pooled for the assay.

Knockdown analyses. Murine *Oct4*, *Sox2*, *Ctcf* and control SMARTpool siRNAs (Dharmacon) were nucleofected at 0.8 μM with the Amaxa Nucleofection System, and collected 24–48 h later for expression or pairing analyses.

FISH and pairing assays. FISH and pairing analyses were performed as described previously⁶.

Full Methods and any associated references are available in the online version of the paper at www.nature.com/nature.

Received 16 September 2008; accepted 28 April 2009.

Published online 17 June 2009.

1. Takahashi, K. & Yamanaka, S. Induction of pluripotent stem cells from mouse embryonic and adult fibroblast cultures by defined factors. *Cell* **126**, 663–676 (2006).
2. Maherali, N. *et al.* Directly reprogrammed fibroblasts show global epigenetic remodeling and widespread tissue contribution. *Cell Stem Cell* **1**, 55–70 (2007).
3. Wutz, A. & Gribnau, J. X inactivation explained. *Curr. Opin. Genet. Dev.* **17**, 387–393 (2007).
4. Lucchesi, J. C., Kelly, W. G. & Panning, B. Chromatin remodeling in dosage compensation. *Annu. Rev. Genet.* **39**, 615–651 (2005).

5. Payer, B. & Lee, J. T. X chromosome dosage compensation: how mammals keep the balance. *Annu. Rev. Genet.* **42**, 733–772 (2008).
6. Xu, N., Tsai, C. L. & Lee, J. T. Transient homologous chromosome pairing marks the onset of X inactivation. *Science* **311**, 1149–1152 (2006).
7. Bacher, C. P. *et al.* Transient colocalization of X-inactivation centres accompanies the initiation of X inactivation. *Nature Cell Biol.* **8**, 293–299 (2006).
8. Lee, J. T. Regulation of X-chromosome counting by *Tsix* and *Xite* sequences. *Science* **309**, 768–771 (2005).
9. Morey, C. *et al.* The region 3' to *Xist* mediates X chromosome counting and H3 Lys-4 dimethylation within the *Xist* gene. *EMBO J.* **23**, 594–604 (2004).
10. Monkhorst, K., Jonkers, I., Rentmeester, E., Grosveld, F. & Gribnau, J. X inactivation counting and choice is a stochastic process: evidence for involvement of an X-linked activator. *Cell* **132**, 410–421 (2008).
11. Monk, M. & Harper, M. I. Sequential X chromosome inactivation coupled with cellular differentiation in early mouse embryos. *Nature* **281**, 311–313 (1979).
12. Silva, S. S., Rowntree, R. K., Mekhoubad, S. & Lee, J. T. X-chromosome inactivation and epigenetic fluidity in human embryonic stem cells. *Proc. Natl Acad. Sci. USA* **105**, 4820–4825 (2008).
13. Navarro, P. *et al.* Molecular coupling of *Xist* regulation and pluripotency. *Science* **321**, 1693–1695 (2008).
14. Nichols, J. *et al.* Formation of pluripotent stem cells in the mammalian embryo depends on the POU transcription factor Oct4. *Cell* **95**, 379–391 (1998).
15. Lee, J. T. & Lu, N. Targeted mutagenesis of *Tsix* leads to nonrandom X inactivation. *Cell* **99**, 47–57 (1999).
16. Ogawa, Y. & Lee, J. T. *Xite*, X-inactivation intergenic transcription elements that regulate the probability of choice. *Mol. Cell* **11**, 731–743 (2003).
17. Donohoe, M. E., Zhang, L. F., Xu, N., Shi, Y. & Lee, J. T. Identification of a Ctf cofactor, Yy1, for the X chromosome binary switch. *Mol. Cell* **25**, 43–56 (2007).
18. Stavropoulos, N., Rowntree, R. K. & Lee, J. T. Identification of developmentally specific enhancers for *Tsix* in the regulation of X chromosome inactivation. *Mol. Cell Biol.* **25**, 2757–2769 (2005).
19. Chao, W., Huynh, K. D., Spencer, R. J., Davidow, L. S. & Lee, J. T. CTCF, a candidate trans-acting factor for X-inactivation choice. *Science* **295**, 345–347 (2002).
20. Tsai, C. L., Rowntree, R. K., Cohen, D. E. & Lee, J. T. Higher order chromatin structure at the X-inactivation center via looping DNA. *Dev. Biol.* **319**, 416–425 (2008).
21. Ohlsson, R., Renkawitz, R. & Lobanenkov, V. V. CTCF is a uniquely versatile transcription regulator linked to epigenetics and disease. *Trends Genet.* **17**, 520–527 (2001).
22. West, A. G., Gaszner, M. & Felsenfeld, G. Insulators: many functions, many mechanisms. *Genes Dev.* **16**, 271–288 (2002).
23. Park, K. & Atchison, M. L. Isolation of a candidate repressor/activator, NF-E1 (YY-1, δ), that binds to the immunoglobulin κ 3' enhancer and the immunoglobulin heavy-chain μ E1 site. *Proc. Natl Acad. Sci. USA* **88**, 9804–9808 (1991).
24. Shi, Y., Lee, J. S. & Galvin, K. M. Everything you have ever wanted to know about Yin Yang 1. *Biochim. Biophys. Acta* **1332**, F49–F66 (1997).
25. Xu, N., Donohoe, M. E., Silva, S. S. & Lee, J. T. Evidence that homologous X-chromosome pairing requires transcription and Ctf protein. *Nature Genet.* **39**, 1390–1396 (2007).
26. Avner, P. & Heard, E. X-chromosome inactivation: counting, choice and initiation. *Nature Rev. Genet.* **2**, 59–67 (2001).
27. Lee, T. I., Johnstone, S. E. & Young, R. A. Chromatin immunoprecipitation and microarray-based analysis of protein location. *Nature Protocols* **1**, 729–748 (2006).
28. Chen, X. *et al.* Integration of external signaling pathways with the core transcriptional network in embryonic stem cells. *Cell* **133**, 1106–1117 (2008).

Supplementary Information is linked to the online version of the paper at www.nature.com/nature.

Acknowledgements We thank N. Stavropoulos and J. Lopilato for their contributions to the early phase of this work. We also thank J. Zhao, J. A. Erwin and J. Ahn for critical reading of the manuscript and all laboratory members for stimulating discussion. This work was funded by a National Institutes of Health grant to J.T.L. (GM58839). J.T.L. is an Investigator of the Howard Hughes Medical Institute.

Author Contributions M.E.D. designed, performed and analysed the *Xite/Tsix* bioinformatics screen, EMSA, tests of protein–protein interactions, luciferase assays, knockdowns and qRT–PCR; S.S.S. designed, performed and analysed the pairing and counting experiments; and S.F.P. designed, performed and analysed the *Xist* bioinformatics screen and the quantitative ChIP assays. N.X. participated in initial pairing analyses. J.T.L. formulated, analysed and directed the study and wrote the paper.

Author Information Reprints and permissions information is available at www.nature.com/reprints. Correspondence and requests for materials should be addressed to J.T.L. (lee@molbio.mgh.harvard.edu).

METHODS

Cell lines and antibodies. The wild-type 16.7 female and J1 male ES lines, fibroblasts, and culture conditions have been described¹⁵.

EMSA. EMSA were performed using 10 fmol of annealed oligonucleotides as described¹⁷ using purified recombinant Oct4 and Sox2 proteins. Full-length mouse *Oct4* and *Sox2* were generated by PCR, cloned in-frame into a *Lac*-inducible histidine-tagged pET-47 vector (Novagen), expressed in bacterial cells after IPTG induction, then purified using a nickel column (Invitrogen), and desalted using a PD-10 column (GE Healthcare). The oligonucleotides used were: site E, 5'-GTAATACCTATGCAAAATTCTTACCTG-3'; mutated Oct4 site E, 5'-GTAA TACCTATGCAAGCCTTACCTG-3'; XiteL, 5'-CCAGGTGTGCATTGATATG TAAAATAAGCACTTCTGTC-3'; mutated *Oct4* XiteL, 5'-CCAGGTCTGC ATTGATATGTAAGGTAAGCACTTCTGTC-3'; and mutated Sox2 XiteL, 5'-CCAGGTCTGCCCGATATGTAATAAGCACTTCTGTC-3'. Mutated nucleotides are underlined. Supershifts or neutralizations were carried out with 1 µl of high concentration anti-Oct4 and anti-Sox2 antibodies (Santa Cruz).

GST pull-downs. Bacterial GST-Oct4 and GST-Sox2 fusion plasmids were constructed using PCR. The GST-Yy1 plasmids have been described¹⁷. All bacterial GST fusion proteins were prepared as described¹⁷, whereas the mammalian EF-1-driven GST-fusion plasmids were cloned with PCR-amplified full-length Yy1, Ctf, Ctf N terminus (amino acids 1–284), Ctf zinc-finger (amino acids 284–583), and Ctf carboxy terminus (amino acids 583–727). Myc-Ctf was constructed by PCR-amplifying full-length mouse Ctf and cloning in-frame into a pCMV-myc vector (Clontech). For pull-down assays, 2 µg of DNA were transfected into HEK293A cells using Lipofectamine 2000 (Invitrogen), cells were collected 46–48 h later and lysed in RIPA buffer with protease inhibitors, and GST fusion proteins extracted using GST-agarose beads (Sigma). Fusion proteins were confirmed by Coomassie staining or western blot analysis using an anti-GST antibody (Covance). All GST pull-downs were performed using ³⁵S-labelled *in vitro*-translated Oct4 and Sox2 for detection.

Chromatin immunoprecipitations. ChIP analyses were carried out as described²⁷ on day 0 and 4 male and female ES cells, and the results were averaged for three independent biological replicates. ChIP antibodies included anti-Oct4 (8628, Santa Cruz), anti-Sox2 (17320, Santa Cruz), normal goat IgG (2028, Santa Cruz), and anti-H3 (1791, Abcam). Quantitative PCR was performed using an iCycler iQ real-time PCR detection system (Bio-Rad) by amplifying with primer pairs specific to *Xist* intron 1A (p63/p64), intron 1B (p65/p66), *Tsix* site E (p73/p74), site D (p71/p72), *Xite* (p77/p78), positive control *Fgf4* (p57/p58), and negative control *Lmn2* (p89/p90) with a distance of >0.5 kb from any potential *Oct4* or *Sox2* consensus sites. Primer sequences were: p57, AGACTTCTGA GCAACCTCCCGAA; p58, CAACTGTCTTCTCCCAACACTCT; p63, CTGA AGATGGTGATGGCGAGTTG; p64, AAAGAGTTCCTCCCAATTAGTGTCC TG; p65, ATGTTTCTTTTGAAGCAGTTACTTGATC; p66, CATTGTCTGG CTCTCTAGGTGATAATAC; p71, CGTAGAGATGGTTGGCTAAAATGTT AC; p72, CCCTGATGTGAGTGTGTGGATTG; p73, TTAATGTTCAAGTTTT CAATTCCGAAGAGAAG; p74, GTTGTCTGCCTACTAACACAGGTAAG; p77, CAAGGTTGGGAACAAGGTATATCAGG; p78, GGACAAGGGACAGAA GTGCTTATTTTAC; p89, ACTCCATAATTATCTCTGATGTC; p90, GAC AGGCTAAGTAAAGGATGTCTATTTTC.

Luciferase assays. The reporter constructs NS11 (no promoter:luciferase), NS65 (–557/+176 *Tsix* promoter:luciferase), and NS135 (1.2-kb *Xite* enhancer plus –557/+176 *Tsix* promoter:luciferase) have been previously described¹⁸. The mutant luciferase vectors were constructed using NS135 as a template and PCR mutagenesis was performed with the QuikChange kit (Stratagene) with the following oligonucleotides: mutated *Oct4* XiteL, 5'-CCAGGTCTG CATTGATATGTAAGGTAAGCACTTCTGTC-3'; and mutated *Sox2* XiteL, 5'-CCAGGTCTGCCCGATATGTAATAAGCACTTCTGTC-3'. After sequential PCRs, the doubly mutated *Oct4* and *Sox2* sites consist of the sequence: 5'-CCAGGTCTGCCCGATATGTAAGGTAAGCACTTCTGTC-3'. The mutated

nucleotides are underlined. The stably integrated transgenes were generated by electroporating 30 µg of linearized construct into 10⁷ male and female wild-type ES cells at 240 V, 900 µF using the Bio-Rad GenePulser. After selection with 300 µg ml^{–1} of G418 for 8–9 days, resistant colonies were pooled. The luciferase assays and normalizations have been described¹⁷.

Co-immunoprecipitation assays. In Fig. 2f, HEK293T cells were cotransfected with Flag-Oct4, Myc-Ctf and HA-Yy1 mammalian expression vectors using Lipofectamine 2000 (Invitrogen). Lysates were collected with 350 mM NaCl, 50 mM HEPES, pH 7.4, 0.1% NP-40, 1 mM dithiothreitol (DTT), 1 mM EDTA, 1 mM PMSF, and 1× Complete Protease Inhibitor Cocktail (Roche Diagnostics). Anti-Flag antibodies (Sigma) were added as appropriate and incubated with the lysate for 6 h, followed by addition of a mixture of protein A plus G agarose and washing. In Fig. 2c, the endogenous interactions were detected using day 0 ES whole cell extracts incubated for 6 h with anti-Ctf (Upstate) or anti-Oct4 (Santa Cruz) and bound to a mixture of protein A plus G agarose. Immunoprecipitates were then western blotted and probed with anti-Oct4, anti-Yy1, or anti-Ctf antibodies, western blots were probed for anti-Myc (Covance), anti-HA (Santa Cruz), and anti-Flag, and detected by secondary antibodies conjugated to horseradish peroxidase (Western Lightning Chemiluminescence Kit; PerkinElmer Life Sciences) or to IR (LiCor).

Gene silencing by RNA interference and expression analysis. The murine *Oct4*, *Sox2*, *Ctf* and control SMARTpool siRNAs were purchased from Dharmacon. siRNAs were nucleofected into day 2 wild-type female ES cells at 0.8 µM with the Amaxa Biosystems Nucleofector/Mouse ES Nucleofector kit and collected 46–48 h later. Western analysis of whole cell extracts confirmed protein knockdown. RNA was prepared using Trizol (Invitrogen) and reverse transcribed to cDNA using random hexamers or appropriate strand-specific primers. Two-hundred nanograms of cDNA was amplified with SYBR Green using the Bio-Rad iCycler iQ real-time detection system. PCR was performed as described using 5' and 3' β-actin primers¹⁷, and *Xite* primers (Xite5', AGGGACTGAACGCTGCTAGT; Xite3', AGACATCTGCAAGGATTAGATGG). Allele-specific RT-PCR was carried out with NS33 and NS60 for *Xist* as described²⁹ and probed with internal oligonucleotide XSP1 (*Xist*). *Oct4*, *Foxd3*, *Rex1* and *Nanog* primers were as previously described³⁰.

FISH and pairing assays. For the day 4 FISH and pairing analysis, ES cells were nucleofected with siRNA on day 2 and collected and fixed in 4% paraformaldehyde/PBS on day 4. For day 1 analysis, cells were nucleofected on day 0 and processed on day 1 after 24 h of siRNA treatment. RNA/DNA and DNA FISH were performed as described using labelled fluorescein-12-dUTP or cy3-dUTP by nick translation (Roche). pSxn (*Tsix*) was used as probe to detect the *Xic*, pSx9 for *Xist* RNA, and BAC probe 1C for chromosome 1. Analysis of pairing was accomplished by capturing digital images with a Nikon microscope, recording slide coordinates for serial FISH experiments, and processing with Volocity software (Improvision) as described previously⁶. Z-sections were taken at 0.2 µm intervals and three-dimensional images were projected on a two-dimensional plane. OpenLab software was used to analyse *Xic*–*Xic* distances (*x*) and the nuclear areas (*A*). Normalized distance (ND) is defined as x/d , in which *d* is the nuclei diameter, characterized as $2(A/\pi)^{0.5}$. All pairing assays were carried out using a two-probe combination of pSxn and pSx9 to ensure signal specificity. Only those foci with overlapping pSxn and pSx9 signals were scored as a *Xic* signal. Furthermore, only female nuclei with two resolvable X-chromosome signals were included in the overall counts.

29. Stavropoulos, N., Lu, N. & Lee, J. T. A functional role for *Tsix* transcription in blocking *Xist* RNA accumulation but not in X-chromosome choice. *Proc. Natl Acad. Sci. USA* **98**, 10232–10237 (2001).

30. Toyooka, Y., Shimosato, Y., Murakami, K., Takahashi, K. & Niwa, H. Identification and characterization of subpopulations in undifferentiated ES cell culture. *Development* **135**, 909–913 (2008).

Q&A

Pierluigi Nicotera is the founding director of the new German Centre for Neurodegenerative Diseases in Bonn, Germany.



What do you hope to accomplish at the centre?

We want to promote clinical and fundamental research in neurodegenerative disease as well as in public health. The core centre is in Bonn with other locations throughout the country. As director of the centre, I cannot micromanage individual projects, but I will decide the strategy and priority of the programmes together with the leaders of each individual location. Overall, I will be responsible for the centre's scientific delivery and more directly for the activities at the Bonn site, which also comprises the Cologne and Jülich locations.

Have you been interested in neurodegenerative disease for a long time?

When I was quite young, I was captivated by the idea of man on the Moon. The popular dream of most every child in the 1950s and 60s was to become an astrophysicist. But as we grow up, there are other influences. The father of a school friend was a doctor who treated patients with

Parkinson's disease, and no one knew then what caused it or what genetic mutations were involved. I became fascinated, initially by stroke and, more recently, by the mechanisms that underlie neurodegenerative disease and how the connections between neurons are affected.

What are the key findings of your research thus far?

I began formulating the reasons for cell death and clarified the mechanism that causes calcium to be lethal for cells, which led to discoveries of fundamental processes in cells.

Were you surprised to be offered this position?

I had heard that this centre was being created and that they were looking for a director, but it wasn't until late last year that the offer materialized from the German Ministry of Education and Research. I thought it was a unique opportunity because there is tremendous funding for research, up to €66 million (US\$91 million) a year.

Each site is already well recognized for excellent science, so the centre can count on a high-profile group of scientists.

What motivates you in your work?

There is a continuous challenge to cure human illness. When I go to bed I think, 'What did I do today? Did I help anyone to progress?' With neurodegenerative diseases, we ask, 'When will we have a new drug?' Developing new treatments takes a long time. The idea of progress — going forward and discovering new things, never standing still — is central for me.

Do you have a secret for scientific success?

What's the definition of success? Winning the Nobel Prize? Making a new medicine? It's difficult to say. I would propose that it depends on the degree of happiness and satisfaction the scientific work gives to an individual, and I am very happy in what I do. ■

Interview by Karen Kaplan

IN BRIEF

Competitive edge

Four US federal legislators want the nation's National Academies to identify how its research universities can remain internationally competitive. In a 22 June letter, Senators Barbara Mikulski (Democrat, Maryland) and Lamar Alexander (Republican, Tennessee) and Representatives Bart Gordon (Democrat, Tennessee) and Ralph Hall (Republican, Texas) ask the academies to assess universities' organizational, intellectual and financial capacity and their collaborations with other national research groups. Academies spokesperson Sara Frueh said the organization's leaders will now discuss how to conduct such a study.

Brain research

Stanford University's School of Medicine in California has received a US\$10-million grant over five years from the National Institute of Mental Health in Bethesda, Maryland, to help establish and operate a Silvio O. Conte Center for Neuroscience Research. The new centre, in Palo Alto, will focus on studying neuroplasticity, or the capacity of the brain to change as a result of experience. Robert Malenka, the Stanford professor of psychiatry and behavioural science who will direct the centre, said he expects the grant to support 14 to 18 researchers, including postdocs, and hopes the centre will begin operating this autumn. Conte Centres are typically set up to operate for ten years.

Green economy

Green jobs will be key for economic recovery, says a report from the Heinrich Böll Foundation in Washington DC. The report, released in collaboration with the Worldwatch Institute, also in Washington DC, says that a green economy will help to battle climate change and drive job growth. At the 23 June report launch, Jürgen Trittin, a member of the German Parliament, said that clean-tech investment in Germany had created 120,000 jobs in the past three years. Michael Peck, head of wind-turbine manufacturer Gamesa in Alava, Spain, said that the US wind-power sector already employs more people than the coal industry. However, some analysts have noted that incentives to encourage green jobs may eliminate more jobs than they create (see *Nature* 459, 1156; 2009).

POSTDOC JOURNAL

The simple life



I became a biologist because I wanted to travel to exotic places and save endangered species. This may not be the ideal place for such an admission, but there it is — my own inconvenient truth. Although this was the naive notion of a working-class adolescent, unacquainted with academia, I have been lucky enough to travel from Outer Mongolia to the Outer Hebrides to work on fascinating species — from voles, to pikas, to Tasmanian devils.

Now I find myself the full-time mom of a three-year-

old; my field-work wings clipped. My husband Brett has the postdoc and gets to see the cool stuff — coyotes, bobcats, salamanders and rattlesnakes. But motherhood has its benefits. I get to spend my days bouncing on giant inflatable castles with my son Kai, splashing around in the fun pool and hiking the trails of San Francisco Bay in search of snails, squirrels and fox poop.

Some days I would gladly trade toddler-dom for sampling parasitized frogs with Brett, but this forced distance from academia has helped me realize

that, somewhere along the winding road of my career, I lost sight of my reasons for studying biology in the first place. With the help of Kai and the snails, I am starting to see the natural world as I did when I was a kid — all the wonder, all the possibilities. I know I still want to be a biologist when I grow up. ■

Joanne Isaac was a postdoc studying the effect of climate change on biodiversity at James Cook University in Townsville, Australia. She is now in the United States so that her husband can complete a postdoc.

MULTIPLE FATES

Despite the economic downturn, US universities are seeking faculty members with stem-cell expertise. That doesn't mean times are easy. **Monya Baker** investigates.

At first glance, stem-cell researchers in the United States have much to celebrate. Former president George W. Bush's restrictions on funding stem-cell research are expected to end on 7 July, on the orders of President Barack Obama. That's also when the National Institutes of Health (NIH) will release new guidelines for human embryonic stem-cell (ESC) research. These could make hundreds more cell lines eligible for federal funding — which is good news for stem-cell researchers.

Other policies, meanwhile, provide a more direct stimulus. The American Recovery and Reinvestment Act of 2009 includes a one-time cash injection of \$10.4 billion for the NIH, some of which will be used to support stem-cell science. And the California Institute for Regenerative Medicine (CIRM), a \$3-billion, 10-year state initiative in San Francisco, has already awarded more than \$760 million for building new labs, training more scientists, and for stem-cell research projects.

"Any increase at NIH will lead to some increase of stem-cell funding because stem-cell research fits in so many of the centres and institutions here," says Story Landis, head of the NIH Stem Cell Task Force. She notes that some of the stimulus money will be awarded to postdocs, and \$100 million can go to sweeten start-up packages for junior faculty members.

But this flurry of good news is tempered by sobering economic realities. As scientists need years of focused training, an unsustained burst of funding in a particular field may lead to institutions competing for existing scientists rather than encouraging people to develop

new specialties. "In the short term," says James Fossett, associate professor at the Rockefeller College of Public Affairs and Policy in Albany, New York, "it's going to be a good time to be a stem-cell scientist — if you are already one."

State restrictions

As federal policy becomes more permissive, some states, including Georgia, Mississippi, and Texas, introduced legislation that would actually restrict stem-cell research and funding, notes Christopher Scott, who heads the programme for stem cells in society at Stanford University in California. Other states that have been financing such research have less incentive to do so. "If I was a young scientist, I would look very closely at the state I'm going to, the NIH funding in that state, and the possibility that Obama might not be there in four years," he says.

Still, there's no question that stem-cell research, both embryonic and non-embryonic, has surged worldwide. At the end of 2004, membership of the International Society for Stem Cell Research (ISSCR), based in Deerfield, Illinois, was 1,350; by mid-2009, it had more than doubled to over 2,900, of whom nearly 60% are in North America. Many are young: more than 40% identify

themselves as graduate students or postdocs.

And their job prospects aren't totally reliant on new funding. Five North American universities that recently advertised junior faculty positions for stem-cell scientists had funded the new posts, at least in part, with reallocations from institutional or departmental budgets. Other funding came

from grants, philanthropists and state governments. (One institute, the University of California, Riverside, later put its search on hold because of the state's budget crisis.)

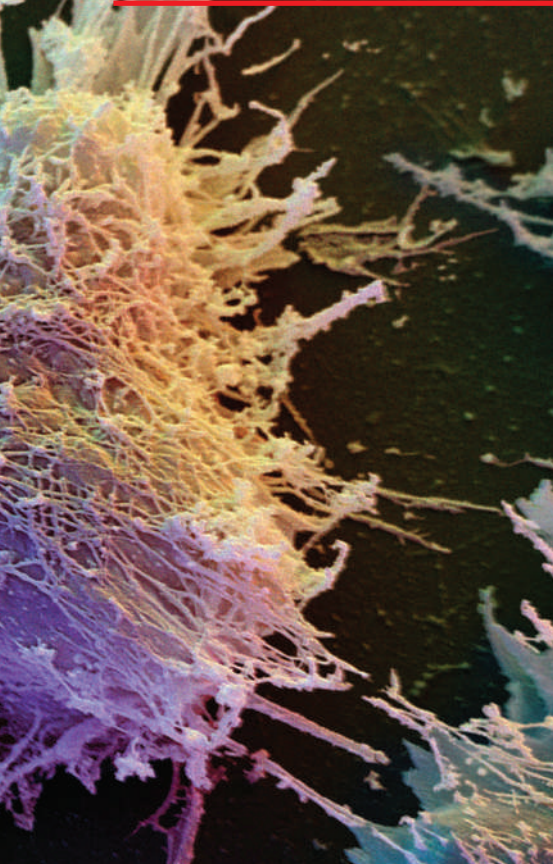
Search-committee members Asrar Malik of the University of Illinois in Chicago and Ina Dobrinski of the University of Calgary, Alberta, felt that more people were applying and that they were better qualified for the jobs than in previous years. Both attributed this to growth in the field, although Dobrinski thought hiring freezes elsewhere might also be a contributing factor.

"We're hiring a bunch of stem-cell scientists," says Shlomo Melmed, dean of

medical faculty at Cedars-Sinai Medical Center in Los Angeles. "Now that there is such a lot of emphasis on stem-cell biology, we're going to have a big, big need to prove to the taxpayer that this does have benefits to patients." The centre has already recruited Clive Svendsen from the University



"Companies are rushing to set up programmes."
— Mahendra Rao



D. SCHARF/SCIENCE FACTION/CORBIS

of Wisconsin, Madison, to lead a new regenerative-medicine institute, and it plans to hire three more senior-level and three junior-level faculty members. Existing investigators have CIRM and NIH funds, Melmed says, but the institute will open with funds from philanthropists and the centre's own budget.

VERSATILE CELLS SEEK SIMILAR SCIENTISTS

Whether applicants are looking for positions in academia or in industry, experience working with finicky cells can make resumés stand out. As cell therapies move toward the clinic, skill with cells will be more in demand, says Walter Funk, a former employee of biotech company Geron of Menlo Park, California, and a consultant to the biotech industry.

"That's going to require an additional set of skills — cell banking, cell manufacturing, regulatory affairs — just to produce the cells needed for clinical study," says Funk.

Even if the goal is to use cells for drug screening or disease modelling instead of cell therapies, homogeneous cell products will be essential. California's Stanford University and Universities of California in Berkeley and San Francisco are all establishing core facilities for growing stem cells.

Geoff Sargent's stem-cell expertise won him a job setting up a pluripotent-stem-cell lab with the California Pacific Medical Center Research Institute in San Francisco. But more important than any particular skill, he says, is a willingness to move beyond one's comfort zone.

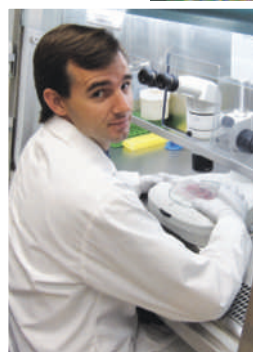
"Companies evolve," says Sargent, who lost his job at Advanced Cell Technology when the firm shut down its facilities in Alameda,

(He declined to reveal exact amounts.)

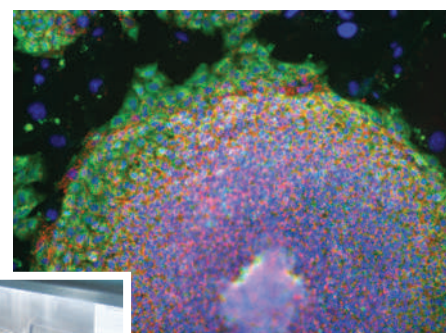
Researcher Pablo Ross, from the cellular reprogramming lab at Michigan State University in East Lansing, is looking for his next position. He has encountered fewer faculty positions, but a higher percentage earmarked for stem cells. "Many departments that were not very interested in [induced pluripotent stem cells] and ESCs are now interested in adding to their programmes," Ross says. He already has job offers and more interviews scheduled.

Translational research seems to generate particular enthusiasm. In the face of California's budget crisis and its reliance on state bond sales, CIRM has focused on plans to fund projects that prepare stem-cell technologies for clinical trials. In December, it plans to give out \$20 million apiece to up to 12 teams, with the aim of starting clinical trials in four years.

But finding stem-cell positions remains challenging for some, says Hanna Mikkola, an assistant professor at the University of California, Los Angeles, who chairs the junior investigators committee of the ISSCR. The society's annual meeting — to be held on 8–11 July in Barcelona, Spain — has several events that target young scientists. Along with providing information from journal editors and funding agencies on how to craft successful submissions, these events will also advise people on how to get jobs within those



Pablo Ross (left) sees interest in induced pluripotent stem cells (above) increasing.



S. SUHR, E. CHANG, P. ROSS, AND J. CIBELLI/DEPT ANIMAL SCI., MSU

organizations. On the upside, Mikkola notes that limited funds can prompt more rigorous thinking and even fuel interdisciplinary research. Her advice for researchers is to let their passion for science

keep discouragement at bay.

Eager industry

Large pharmaceutical companies could provide the sharpest short-term increase in job opportunities, says Mahendra Rao, vice-president of research in regenerative medicine and stem-cell technologies at Invitrogen, a division of California-based Life Technologies in Carlsbad. "They are all rushing to establish stem-cell programmes," he says.

The easing of restrictions plus recent approvals by the US Food and Drug Administration for ESC trials could increase investments in regenerative medicine, says Rao, especially by companies with big research budgets and shrinking product pipelines. GlaxoSmithKline and Harvard University, for instance, announced a \$25-million deal last year. Pfizer has launched a regenerative medicine unit in Cambridge, UK, where policies governing ESC research are both friendlier and more predictable than in the United States. In May, the company announced an investment of \$100 million in stem-cell research. Rao doubts that tool and reagent companies will expand their stem-cell departments much, but scientific successes, friendlier policies and approval for clinical trials will eventually increase interest from venture capitalists. This could mean that start-ups, too, will begin hiring.

Regardless, scientists still seem to find ways to pursue exciting science, says Landis. When President Bush closed off federal funding for ESC lines created after August 2001, there were fears that output and the supply of new researchers would dry up.

"If you look at the continuing growth in the stem-cell literature, it's not as big a concern," Landis says. "I think the field has exploded." ■

Monya Baker is editor of *Nature Reports Stem Cells*.

California. "They'll start out with research, and then when they get to therapeutics, they need different skill sets."

Shifts are happening across the entire stem-cell field, says Thorsten Schlaeger, head of the human embryonic-stem-cell core facility at Harvard Medical School. Today, more researchers than ever before have experience in culturing pluripotent stem cells, but practitioners will need to adapt to having many more types of cells available. Career planning requires acknowledging that the techniques in demand today might not be sought after tomorrow.

"To a student it could appear that this is a field to be in forever," Schlaeger says, "but you could be behind the curve if you're thinking of what's great now." Stem-cell researchers will need to be as flexible as the cells they study.

Asked what expertise Pfizer will be seeking for positions in its new regenerative medicine unit, Ruth McKernan, the unit's chief scientific officer, says she wants candidates whose scientific curiosity extends beyond the narrow area of their training. Intellectual agility will be more important than any particular technique, she says. "We don't know what we'll have them doing a year from hire."

M.B.

A Breederax for Dalia

All play and no work is a recipe for disaster.

Janett L. Grady

Suddenly awake, Dalia opened her eyes into a spin of light. The light was blinding, so she closed her eyes again and lay in the soft shadows behind her lids. She remembered the night, the wine and Odok's wail. In the shadowy spin, fixed in despair, Dalia held on to the slender hope that she had remembered a dream.

Needing to know, she opened her eyes, crawled from her bed and staggered across the room. Sure enough, Odok was on his bunk. She had put him there, after crushing his skull with the empty bottle of wine. It was not a dream. She had killed him, and there on the floor was the bottle. She glared at it and then back at the lifeless body, and took a deep breath to slow the spin and focus her eyes. She was now faced with requesting a replacement.

She gazed down at the Breederax now without purpose. She glanced at the tell-screen, at the pigs on deck two, and shuddered at the thought of doing Odok's job.

Minutes later, feeling more in control of her balance, Dalia hurried into the cockpit and slumped into her seat. She sat there for a moment, listening to the hum, staring out at the endless void. She reached for the Ceres cell, then changed her mind. Cerulia was closer than Klausttron, but the Klaustrons were more likely to have a replacement. At the dawn of time, these religious beings had created the first Breederax, and through the eons the Breederax had been reinvented throughout the Universe. She grabbed the Klauss cell, waited for the yellow light and then hit the translate button. The yellow light blinked once. When the green light came on, a voice boomed, coming as if from an iron vault: "Identification?" Dalia cringed.

"Don't shout," she said. "I'm not hard of hearing." No response. "Freighter 666T3," she said, "from Earth. Mission, pigs to the fourth quadrant, coordinates 42C3-fix-84K2. Power, telesun 6, two reactors and one cobalt booster."

"Oh, thou wretched mucilid!" boomed the voice, louder than before. "What is it this time, thou mucilaginous monstrosity?"

"Up yours," Dalia replied. "Turn it down, will you?"

"Oh, very well," said the voice in a lower tone. "What is it the excrescent humanoid would like this time around?"

"I need a new Breederax," she said. "I'll even settle for one of yours."

"Hearken to Klausttron power, thou

puling coagulum, thou snivellous emulsion! In the magnificence of illuminating currents, the gods bestow mercy on thee."

"Get a life," Dalia shot back.

"Do you have a Breederax, or not?"

"Thou..."

"Stuff it," she said.

"Can you have one ready?"

"Oh, I suppose so, but you'll have to give a report as to what happened to the one assigned. Trade requirements, you know."

"What do you mean, *trade requirements*?"

"New rule. K-Council wants a report."

"Fine. What do you want to know?"

"I want to know what happened."

"He wouldn't do what I wanted, so I stopped his clock."

"I see. Male or female?"

"I said 'he', damn it, and 'he' means male. What else?"

"Chemical or genetic?"

"Chemical."

"Of Earth construction, I suppose."

"Not exactly. I picked him up on Europa, an icy rock not all that far from Earth."

"I know Europa," said the voice with an air of disgust. "They're evil, lecherous fools."

"Fine. What else do you want to know?"

"Was it... was he compatible?"

The thought of how compatible Odok had been caused Dalia to shift in her seat. She recalled how satisfied she had been. "Yes," she answered after the pause. "At least most of the time."

"I see," said the voice. "Was he changeable or fixed?"

"Changeable."

"Duties?"

"Servant, maintenance and companion."

"Companion is understood, thou vicious vermin. Thy sinful existence is well known."

"Fine," she said. "What else do you want to know?"

"That'll do it," said the voice. "When are you going to get here?"

"I ought to be there in about..." Dalia paused and glanced up at the time charts. "... 18 months," she said. "One quick stay in the Chamber of Life, then 17 months."

"Why the Chamber?" asked the voice.

"You sound young."

"Trying to stay that way," Dalia replied.



JACEY

"I drank some alcohol and there's an organ or two that might wear out. You know, the liver and so forth. I want to make sure I'm healthy enough to handle a Klausttron Breederax... so make sure it's new and working right."

"Blasphemous!" boomed the voice. "They all work right!"

"Let's hope so," said Dalia. "Oh, and make sure he'll do what he's told."

"Genetic, or do you want it chemical?"

"Gen takes too long," she said. "You'd never have him ready. Make it chemical."

"Is that all, or does the lusty humanoid want more?"

Dalia thought about it. Odok's alterability had worked fairly well, chemical implants had modified bone structure, muscle tone, body weight and the contours of his face every 24 hours or so. Europa's scientists had failed, however, even after it became known that human females functioned most efficiently when companioned with a quiet, subservient Breederax.

"Make sure he'll do what I tell him," said Dalia, "no matter what."

"Ours," said the voice, "are more obedient than Europa's."

"Fine. Have him ready. I'll be there as soon as I can."

"Thou..."

Dalia put the cell in its cradle and hit the off switch. She got up and walked into the cabin.

She glared down at the mess. Odok, his head a shambles, was no longer able to satisfy her natural cravings. She gathered his lifeless form into her arms, carried it across the room, and heaved 185 pounds through a vent marked TRASH.

"Chips and circuits," she said aloud, and she watched as Odok sailed away. "Drunk or not," she said, "slopping hogs was part of your job."

Janett L. Grady is a retired senior citizen who writes from Palmer, Alaska. Her work has appeared in magazines all over the United States, and in a few based in Canada and the United Kingdom.